Understanding Dinuclear Synergy in Sustainable Polymerisation Catalysis

Francesca Fiorentini



University College

Department of Inorganic Chemistry

University of Oxford

July 2024

A thesis submitted in partial fulfilment of the requirements for the degree of Doctor of Philosophy in Chemistry

Declaration

The work presented in this thesis was conducted between September 2020 and July 2024 at the University of Oxford. This is the work of the author unless otherwise stated.

The copyright of this thesis rests with the author and is made available under a Creative Commons Attribution Non-Commercial No Derivatives license. Researchers are free to copy, distribute or transmit the thesis on the condition that they attribute it, that they do not use it for commercial purposes and that they do not alter, transform or build-upon it. For any reuse or distribution, researchers must make clear to others the license terms of this work.



Francesca Fiorentini

Abstract

This thesis describes the development of novel heterodinuclear catalysts for sustainable polymerisations, including epoxide/CO_2 and epoxide/anhydride ring-opening copolymerisations (ROCOP), and the ring-opening polymerisation (ROP) of *rac*-lactide. Structure-performance correlations of the mixed-metal catalysts are conducted with the aim to better understand the origins of intermetallic synergy.

Chapter Two explores a series of heterodinuclear catalysts comprising Co(III)M(I/II), where M(I/II) = Na(I), K(I), Rb(I), Cs(I), Ca(II), Sr(II), Ba(II), which are evaluated for three different polymerisations, by assessment of rate constants, turn over frequencies, polymer selectivity and control. This allows for comparisons of performances both within and between catalysts containing Group I and II metals for CO_2/propene oxide (PO) ring-opening copolymerization (ROCOP), PO/phthalic anhydride (PA) ROCOP and lactide (LA) ring-opening polymerization (ROP). The data reveal new structure-performance correlations that apply across all three polymerisations: catalysts featuring s-block metals of lower Lewis acidity show higher rates and selectivity. The epoxide/heterocumulene ROCOPs both show exponential activity increases vs. Lewis acidity (measured by the p*K*a of $[M(OH_2)_m]^{n+}$), whilst the lactide ROP activity and CO_2/epoxide selectivity show linear increases. Such clear structure-activity/selectivity correlations are very unusual, yet are fully rationalised by the polymerization mechanisms and the chemistry of the catalytic intermediates. The general applicability across three different polymerizations is significant for future exploitation of catalytic synergy and provides a framework to improve other catalysts.

Chapter Three explores two heterodinuclear catalysts featuring either Al(III) or Co(III) with s-block metals (Al(III)M(I/II) and Co(III)M(I/II); M(I/II) = Na(I), K(I), Rb(I), Ca(II), Sr(II), Ba(II)) for PO/CO_2 ROCOP and/or cyclohexene oxide (CHO)/PA ROCOP. These catalysts feature flexible ether binding pockets, which allows the incorporation of larger, more weakly Lewis acidic metals such as Rb(I), allowing a greater range of Lewis acidities to be investigated. The Co(III)M(I/II) catalyst series was

tested for both PO/CO_2 and CHO/PA ROCOP, while the Al(III)M(I/II) series was tested for CHO/PA ROCOP. In all three cases, correlations between activity/selectivity and s-block metal pK_a were observed that were comparable to those reported in Chapter Two. For PO/CO_2 ROCOP, the most active catalyst was the Co(III)K(I) combination; the Co(III)Rb(I) catalyst was less active, but had a comparable selectivity. On the contrary, for CHO/PA ROCOP the most active combination for both catalyst series featured Rb(I). The subtle variations in catalyst performance are discussed and the general trends across different reactions and catalyst types are substantiated.

Chapter Four investigates three heterodinuclear Co(III)K catalysts, featuring very similar coordination chemistries, with different intermetallic separations. The catalysts are compared for the ring-opening copolymerization (ROCOP) of PO with CO_2 or with PA. The catalyst with a fixed, wide intermetallic separation, $L_{wide}CoK(OAc)_2$ (Co-K = 8.06 Å), shows very high activity for PO/PA ROCOP, but is inactive for PO/CO2 ROCOP. On the other hand, the catalyst with a fixed, narrow intermetallic separation, $L_{short}CoK(OAc)_2$ (Co-K, 3.59 Å), shows high activity for PO/CO_2 ROCOP, but is much less active for PO/PA ROCOP. A bicomponent catalyst system, comprising a monometallic complex $L_{mono}CoOAc$ used with an equivalent of KOAc[18-crown-6], shows high activity for both PO/CO_2 and PO/PA ROCOP, provided the catalyst concentration is sufficiently high, but underperforms at low catalyst loadings. It is proposed through kinetic investigations that the two lead catalysts, $L_{wide}CoK(OAc)_2$ and $L_{short}CoK(OAc)_2$, operate by different mechanisms for PO/PA and PO/CO_2 ROCOP. The new 'wide' separation catalyst, $L_{wide}CoK(OAc)_2$ shows some of the best performances yet reported for PO/PA ROCOP, and suggests other catalysts featuring larger intermetallic separations should be targeted for epoxide/anhydride copolymerisations.

Acknowledgments

First, I would like to thank Charlotte for giving me the opportunity to do my PhD in her group, and for her guidance over the last four years. Your encouragement, insights and expertise have been invaluable both for the research presented in this thesis, and for my development as a chemist and researcher.

Thanks next go to the members of the Williams group (past and present) for providing a great working environment. In particular, thank you to Arron for supervising me when I first started, and still answering my questions even after having long left the group. Special thanks go to Kat for being a top friend, alongside colleague, and fielding many a chemistry-related voice note; to Kam for (literally) always being there, and keeping me company on many trips to fill up my water bottle. Thanks to Freya for dealing with me in my first foray into supervising, and for being such an amazing student! Thanks also go to Bonny, Nora, Kristian, Holly, and Wouter for providing many opportunities to procrastinate and chat.

I would also like to thank my friends outside of Oxford – Christy, Liv, and Billy – for providing excuses to leave the city and picking up my phone calls. Thank you also to my family for always being supportive and loving. Finally, thank you to Thirushan for putting up with me and my desire to visit (almost) every restaurant in Oxford, always listening to my complaining, and giving annoyingly excellent advice. I miss you and (visa-permitting) I will join you in Boston soon!

List of Publications

Eisenhardt, K. H. S.; **Fiorentini, F**.; Williams, C. K. Opportunities to Replace Co(III) By Al(III) or Fe(III) in Polymerisation Catalysts. **2024**, *Submitted Manuscript*

Fiorentini, F.; Eisenhardt, K. H. S.; Deacy, A. C.; Williams, C. K. Synergic Catalysis: The Importance of Intermetallic Separation in Co(III)K(I) Catalysts for Ring Opening Copolymerizations. *J. Am. Chem. Soc.* **2024**, *146* (33), 23517-23528

Eisenhardt, K. H. S.; **Fiorentini, F**.; Lindeboom, W.; Williams, C. K. Quantifying CO_2 Insertion Equilibria for Low-Pressure Propene Oxide and Carbon Dioxide Ring Opening Copolymerization Catalysts. *J. Am. Chem. Soc.* **2024**, *146* (15), 10451-10464

Shellard, E. J. K.; Diment, W. T.; Resendiz-Lara, D. A.; **Fiorentini, F.**; Gregory, G. L.; Williams, C. K. Al(III)/K(I) Heterodinuclear Polymerization Catalysts Showing Fast Rates and High Selectivity for Polyester Polyols. *ACS Catal.* **2024**, *14* (3), 1363-1374

Fiorentini, F.; Diment, W. T.; Deacy, A. C.; Kerr, R. W. F.; Faulkner, S.; Williams, C. K. Understanding catalytic synergy in dinuclear polymerization catalysts for sustainable polymers. *Nat. Commun.* **2023**, *14* (1), 4783

Diment, W. T.; Lindeboom, W.; **Fiorentini, F**.; Deacy, A. C.; Williams, C. K. Synergic Heterodinuclear Catalysts for the Ring-Opening Copolymerization (ROCOP) of Epoxides, Carbon Dioxide, and Anhydrides. *Acc. Chem. Res.* **2022**, *55* (15), 1997-2010

Abbreviations

Å	Angstrom ($1x10^{-10}$ m)	D	Diffusion coefficient
AGE	Allyl glycidyl ether	$Đ$	Dispersity
alt	Alternating	ΔG	Change in Gibbs free energy
Ar	Aryl	ΔH	Enthalpy change
AcOH	Acetic acid	ΔS	Entropy change
ATR-IR	Attenuated Total Reflectance Infrared	DGA	Diglycolic anhydride
β-BDI	β-Diimine	DFT	Density functional theory
BDM	Benzene dimethanol	DOSY	Diffusion-ordered NMR spectroscopy
BO	Butylene oxide	Equiv.	Equivalents
Bz	Benzoate	Et	Ethyl
cm	centimeter	FT	Fourier transform
C	Curie constant	g	Gram
°C	Degrees Celsius	GA	Glutaric anhydride
Cat.	Catalyst	GPC	Gel permeation chromatography
$CDCl_3$	Deuterated chloroform	h	Hour
CHC	Cyclohexene carbonate	HMBC	Heteronuclear multiple bond correlation
CHD	Trans-cyclohexane-1,2-diol	HSQC	Heteronuclear single quantum coherence
CHO	Cyclohexene oxide	IR	Infrared
COSY	Correlated spectroscopy	k	Rate coefficient
Conv.	Conversion	K	Kelvin
CPO	Cyclopentene oxide	kcal	Kilocalories
CTA	Chain transfer agent	kg	Kilograms
CV	Cyclic voltammetry	k_{obs}	Observed rate coefficient
LA	Lactide	k_P	Polymerisation rate coefficient
L	Ligand	Ph	Phenyl

PLA	Polylactide	PO	Propene oxide
LO	Limonene oxide	ppm	Parts per million
min	Minute	PC	Propene carbonate
μ	Magnetic moment	PPO	Poly(propene oxide)
μ_B	Bohr magneton	PPC	Poly(propene carbonate)
μ_{SO}	Spin-only magnetic moment	PPN	Bis(triphenylphosphine)imine
MA	Maleic anhydride	rt	Room temperature
MALDI	Matrix-assisted laser desorption ionisation	R	Generic substituent
Me	Methyl	R^2	Coefficient of determination
MeCN	Acetonitrile	RDS	Rate-determining step
MeOD-d_4	Deuterated methanol	RHS	Right-hand side
MeOH	Methanol	ROCOP	Ring-opening copolymerization
mg	Milligram	ROP	Ring-opening polymerization
MO	Menthene oxide	s	Second
mol	Mole	*S*	Spin quantum number
Mn	Number-average molecular mass	SQUID	Superconducting quantum interference device
NBA	Norbornene anhydride	t	Time
NMR	Nuclear magnetic resonance	θ	Weiss constant
OAc	Acetate	T	Temperature
P	Polymer chain	THF-d_4	Deuterated tetrahydrofuran
PA	Phthalic anhydride	THPA	cis-1,2,3,6-Tetrahydrophthalic anhydride
PCHC	Poly(cyclohexene carbonate)	ToF	Time of flight
PCHO	Poly(cyclohexene oxide)	TOF	Turnover frequency
τ	Structural parameter	TON	Turnover number
tBu	*tert*-Butyl	UV-vis	Ultraviolet-visible spectroscopy
TCA	Tricyclic anhydride	V	Volt
THF	Tetrahydrofuran	vCHO	4-Vinyl-1-cyclohexene oxide

vs.	Versus
X	Generic co-ligand
χm	Molar magnetic susceptibility
XAS	X-ray absorption spectroscopy
XRD	X-ray diffraction

Table of Figures, Schemes, Tables, and Equations

Chapter One: Introduction

Figure 1.1 Step-growth polycondensation of bisphenol A (BPA) and phosgene to produce polycarbonate (top), and ring-opening copolymerisation of epoxides and CO_2 to produce polycarbonates (bottom).

Figure 1.2 Step-growth and ring-opening copolymerisation synthetic routes to produce polyesters.

Figure 1.3 ROCOP of epoxides with anhydrides (LHS) and CO_2 (RHS).

Figure 1.4 Mechanism for the ROP of lactide

Figure 1.5 Three types of homogeneous catalysts: bicomponent systems, tethered catalysts, and dinuclear catalysts.

Figure 1.6 Top: Structures of examples of salen catalysts for epoxide/CO_2; bottom: Proposed mechanism for the ROCOP of PO/CO_2 catalysed by a metal salen complex.

Figure 1.7 Examples of bicomponent catalyst systems for epoxide/CO_2 ROCOP (LHS) and epoxide/anhydride ROCOP (RHS).

Figure 1.8 Structure, performance, and mechanism of a tethered Co(III) salen – piperidinium catalyst for epoxide/CO_2 ROCOP.

Figure 1.9 A: PO/CO_2 ROCOP to form PPC and PO/PA/CO_2 terpolymerisation to form an ABA block copolymer; B: structure and performance of a tethered Co(III) salen – tertiary ammonium catalyst for epoxide/CO_2 and epoxide/anhydride ROCOP.

Figure 1.10 A. Scheme for PO/CPMA ROCOP; B. Catalyst structures and performances of a binary Al(III) salen – PPNCl catalyst system, and of a tethered Al(III) salen – tris(dialkylamino)cyclopropenium catalyst for epoxide/anhydride ROCOP

Figure 1.11 Structure and performance of a tethered Al(III) porphyrin – quaternary ammonium catalyst for epoxide/CO_2 ROCOP.

Figure 1.12 A. Structure and performance of a tethered borane – quaternary ammonium catalyst for epoxide/CO_2 ROCOP; B. proposed mechanism for CHO/CO_2 ROCOP.

Figure 1.13 A. Structure of Zn(II)BDI catalysts for epoxide/CO_2 and epoxide/anhydride ROCOP; B. Correlation between activity of the catalysts for epoxide/CO_2 (blue squares) and epoxide/anhydride (red triangles) ROCOP and increasing steric bulk of the ligand; C. proposed dinuclear mechanism for CHO/CO_2 ROCOP.

Figure 1.14 Structure and performances of heterodinuclear catalysts for epoxide/CO_2 ROCOP where M = Zn(II), Fe(III), Co(II), and Mg(II).

Figure 1.15 Calculated energies of intermediates and transition states for the ROCOP of CHO and CO_2 catalysed by a dizinc catalyst.

Figure 1.16 Structures and performances of tethered Zn(II)BDI catalysts for CHO/CO_2 ROCOP.

Figure 1.17 Structures and activities of examples of di- and tri-nuclear Co(III), Al(III), and Cr(III) catalysts for epoxide/CO_2 and epoxide/anhydride ROCOP.

Figure 1.18 Top: Al(III) porphyrin catalysts tethered to a poly(methyl methacrylate) (PMMA) oligomeric backbone for PO/CO_2 ROCOP. Bottom: Dinuclear Al(III) porphyrin catalyst featuring a naphthalene backbone.

Figure 1.19 A. Structure and performance of a Zn(II)Mg(II) catalyst for CHO/CO_2 ROCOP; B. Comparison of activities of homodinuclear Zn(II)Zn(II) and Mg(II)Mg(II) catalysts, heterodinuclear Zn(II)Mg(II) catalyst, and a 50:50 mixture of the homodinuclear catalysts for CHO/CO_2 ROCOP; C. Proposed mechanism for CHO/CO_2 ROCOP catalysed by Zn(II)Mg(II) showing the chain-shuttling mechanism.

Figure 1.20 Structures and performances of Co(II)Mg(II) and Fe(II)Mg(II) catalysts for CHO/CO_2 ROCOP.

Figure 1.21 A. Structures of related Co(III)K(I) catalysts for epoxide/CO_2 ROCOP; B. Comparison of the two catalysts for PO/CO_2 ROCOP under varying temperatures and CO_2 pressures.

Figure 1.22 Proposed dinuclear metallate mechanism for PO/CO_2 ROCOP catalysed by L_{closed}Co(III)K(I) and L_{open}Co(III)K(I).

Figure 1.23 Structures and performances of Al(III)K(I) and Al(III)Rb(I) catalysts for CHO/PA ROCOP.

Figure 1.24 Top: Structures and performances of heterodinuclear catalysts for LA ROP; botton: proposed dinuclear mechanism for LA ROP.

Figure 1.25 A. Catalyst structures and B. Activity and physical parameters (BDE = M-O bond dissociation energy; HC = hydrolysis constant; WERC = water exchange rate constant) across the tested metal series for a Co_3Ln catalyst system (top) and a Mg(II)M catalyst (bottom).

Figure 1.26 A. Co(II)Mg(II) catalyst structure; B. enthalpic and entropic contributions to $\Delta G^{\ddagger}$ of the Co(II)Co(II), Mg(II)Mg(II), and Co(II)Mg(II) dinuclear catalysts for CHO/CO_2 ROCOP; C. Proposed rate-determining transition state for CHO/CO_2 ROCOP catalysed by Co(II)Mg(II).

Figure 1.27 A. Co(III)K(I) catalyst structure with varying imine bridge structures; B. Correlations of activity (blue squares; LHS) and selectivity (red triangles; RHS) for PO/CO_2 ROCOP with Co(II/I) reduction potential.

Figure 1.28 A. Tethered Co(III) salen catalyst with varying tether length; B. Correlations between tether length and activity and selectivity for polycarbonate; C. Proposed mechanism for propagation of PO/CO_2 ROCOP catalysed by the tethered Co(III) salen system.

Figure 1.29 A. Structure of tethered di-borane and quaternary ammonium catalyst for CHO/CO_2 ROCOP with changing linker length and quaternary ammonium steric bulk; B. Correlations between activity and spacer length, and of selectivity for polycarbonate and B-N-B angle (dictated by steric bulk around the quaternary ammonium centre).

Figure 1.30 A. Structure of tethered borane – quaternary phosphonium catalyst for CHO/CO_2 ROCOP; B. Activities (bars) and Lewis acidity (measured by Gutmann-Beckett method; pink squares), and enthalpic (blue diamonds) and entropic (green circles) contributions to $\Delta H^{\ddagger}$ for the catalysts with varying linker lengths.

Figure 1.31 A. Structures of tri-Cr(III) tethered salen catalysts for epoxide/anhydride ROCOP with varying intermetallic separations; B. Correlation of activity with increasing intermetallic separation.

Figure 1.32 Summary of catalyst structures and polymerisations investigated in Chapters two to four.

Chapter Two: Understanding Metallic Synergy in Dinuclear Polymerisation Catalysis

Figure 2.1 Synthesis of Co(III)M(I/II) where M(I/II) = Na(I), K(I), Rb(I), Cs(I), Ca(II), Sr(II), Ba(II). i) $Co(OAc)_2$, M(I)(OAc) or $M(II)(OAc)_2$, MeCN, 1 h; ii) ethylene diamine, MeCN, 16 h; iii) Acetic acid, MeCN, air, 72 h.

Figure 2.2 ^{1}H NMR spectra of the dialdehyde proligand (bottom) and Co(III)Ba(II) (top) showing the disappearance of the proligand phenol (purple), shifting of the aldehyde/imine (orange), aromatic (pink and green), broadening of the ether peaks (yellow), and appearance of the acetate peak (red).

Figure 2.3 Variable temperature NMR spectra of Co(III)Ca(II) between 298 – 190 K (top to bottom) showing the appearance of a new acetate peak at 230 K (o) and the splitting of the original acetate peak (m) into two singlets (m′ and m′′).

Figure 2.4 Solid state IR spectrum of Co(III)Ba(II) with assigned peaks.

Figure 2.5 Solid state structures of Co(III)M(II) (M(II) = Ca(II), Sr(II), Ba(II); clockwise from top LHS) determined by X-ray crystallography. Thermal ellipsoids drawn at 40% probability, solvent molecules and hydrogen atoms omitted for clarity.

Figure 2.6 Solid state and chemical structures of Co(III)Ba(II), alongside key C-O bond lengths, showing Co(III) centre metallate character.

Figure 2.7 Solid state structures of Co(III)Ca(II) (LHS), Co(III)K(I) (middle), and Co(III)Rb(I) (RHS) showing the importance of size match between the 18-crown-6 cavity and the s-block metal cation.

Table 2.1 Scheme and Data for propene oxide (PO)/CO_2 ROCOP using the Co(III)M(I/II) catalysts, where PPC is poly(propene carbonate) and PC is propene carbonate. Reaction conditions: catalyst (0.025 mol%, 3.6 mM), PO (5 mL, 14.3 M), 1,2-cyclohexane diol (0.5 mol%, 71 mM), 20 bar CO_2, 50 °C.

Table 2.2 Scheme and Data for Propene Oxide (PO)/Phthalic Anhydride (PA) ROCOP with Co(III)M(II) and Co(III)M(I) catalysts. [a] Reaction conditions: Catalyst (0.1 mol%, 0.0143 mM), PA (10 mol%, 1.43 mM), PO (1 mL, 14.3 M), 50 °C.

Table 2.3 Scheme and Data for *rac*-Lactide (LA) Ring Opening Polymerization Scheme Using the Co(III)M(II or I) Catalysts. Reaction conditions: catalyst (0.1 mol%, 14.3 mM), *rac*-LA (10 mol%, 1.43 M), PO (1 mL, 14.3 M), 50 °C.

Figure 2.8 A. Plots of k_{obs} and TOF against s-block M(I) or M(II) pK_a value for PO/CO_2 ROCOP catalysed by Co(III)M(I/II) with the structure of the key intermediate, i.e. rate

determining intermediate; B. Plot of selectivity against s-block metal pK_a value with the key intermediate that determines selectivity for polycarbonate over cyclic carbonate; C. Catalytic cycle for PO/CO_2 ROCOP catalysed by Co(III)M(I/II).

Figure 2.9 A. Plot of k_{obs} and TOF against pK_a of the s-block metal for PO/PA ROCOP catalysed by Co(III)M(I/II) and the key intermediate that determines activity; B. Catalytic cycle for PO/PA ROCOP catalysed by Co(III)M(I/II).

Figure 2.10 A. Plot of k_{obs} and TOF against pK_a of the s-block metal for *rac*-LA ROP catalysed by Co(III)M(I/II) and the key intermediate that determines activity; B. Plot of P_i against pK_a of the s-block metal for *rac*-LA ROP catalysed by Co(III)M(I/II) and the key intermediate that determines isotacticity; C: Catalytic cycle for *rac*-LA ROP catalysed by Co(III)M(I/II).

Figure 2.11 Proposed targets for future work, featuring stronger crown ether donors (LHS) and weaker Lewis acid s-block metals (RHS).

Chapter Three: Mechanistic Investigations of Heterodinuclear Sustainable Polymerisation Catalysts using s-Block Metal Lewis Acidity

Figure 3.1 Summary of aims for Chapter Three, with the comparison of the structure of the catalyst series from Chapter Two.

Figure 3.2 Synthesis of L_1Al(III)M(I/II) (M(I/II) = Ca(II), Sr(II), Ba(II), Na(I), K(I), Rb(I)); i) MeOH, rt, 16 h; ii) $AlEt_3$, THF, rt, N_2, 2 h; iii) AcOH, THF, rt, 16 h; iv) M(I/II)$(OAc)_{2-3}$, THF, rt, 16 h.

Figure 3.3 Stacked ^{1}H NMR spectra of L_1Al(III)Ca(II) (top) and H_2L_1 (bottom) showing disappearance of the phenolic proton resonance (purple), appearance of acetate resonances (red), and shifting of the imine resonance (orange).

Figure 3.4 Solid-state IR spectrum of L_1Al(III)Ca(II).

Figure 3.5 Solid state structure and selected bond lengths and angles of L_1Al(III)Ca(II) determined by single crystal X-ray diffractometry. Thermal ellipsoids are shown at 50% probability, and solvent molecules and protons are omitted for clarity.

Figure 3.6 Synthesis of L_2Co(III)M(I/II) (M(I/II) = Ca(II), Sr(II), Ba(II), Na(I), K(I)), Rb(I); i) MeOH, rt, N_2, 16 h; ii) $Co(OAc)_2$, M(I/II)$(OAc)_{1-2}$, MeCN, N_2, rt, 16 h; iii) air, rt, 16 h; 48 – 72% yield.

Figure 3.7 Stacked ^{1}H NMR spectra of L_1Al(III)Ca(II) (top) and H_2L_1 (bottom) showing disappearance of the phenolic proton resonance (purple), appearance of acetate resonances (red), and shifting of the imine (orange) and ether (yellow) resonances.

Figure 3.8 Solid-state IR spectrum of L_2Co(III)Ca(II).

Figure 3.9 LHS: Stacked ^{1}H NMR spectra for CHO/PA ROCOP catalysed by L_1Al(III)Na(I) (from 3 mins (pink) to 30 mins (purple)) showing the decay of the resonances corresponding to PA, and the growth in resonances corresponding to polyester; RHS: plot of [PA] against time for CHO/PA ROCOP catalysed by L_1Al(III)Ca(II) from which k_{obs} and TOF were calculated.

Table 3.1 Data for the ROCOP of cyclohexene oxide (CHO) and phthalic anhydride (PA) with the $L_1Al(III)M(I/II)$ catalysts.

Figure 3.10 A. Plot of activity (TOF and k_{obs}) of $L_1Al(III)M(I/II)$ for CHO/PA ROCOP against pK_a of the incorporated s-block metal aqua complex; B. Proposed mechanism of CHO/PA ROCOP catalysed by $L_1Al(III)M(I/II)$; C. Rationalisation of the increase in activity seen with decreasing s-block metal Lewis acidity.

Figure 3.11 LHS: Stacked FTR-IR spectra at various time-points (from 0 h (pink) to 20 h (purple)) of PO/CO_2 ROCOP catalysed by $L_2Co(III)Ba(II)$ showing the growth of peaks corresponding to polycarbonate (1750 cm^{-1}) and cyclic carbonate (1810 cm^{-1}); RHS: Plot of $ln([PO]_t/[PO]_0)$ against time for PO/CO_2 ROCOP catalysed by $L_2Co(III)Rb(I)$ from which k_{obs} and TOF are calculated.

Table 3.2 Data for the ROCOP of propene oxide (PO) and CO_2 with the $L_2Co(III)M(I/II)$ catalysts.

Figure 3.12 A. Plot of activity (TOF and k_{obs}) of $L_2Co(III)M(I/II)$ for PO/CO_2 ROCOP against pK_a of the incorporated s-block metal aqua complex; B. Proposed mechanism of PO/CO_2 ROCOP catalysed by $L_2Co(III)M(I/II)$, highlighting the key rate-determining intermediate; C. Rationalisation of the increase in activity seen with decreasing s-block metal Lewis acidity.

Figure 3.13 A. Proposed mechanism of PO/CO_2 ROCOP catalysed by $L_2Co(III)M(I/II)$, showing the key selectivity-determining intermediate; B. Plot of selectivity of $L_2Co(III)M(I/II)$ for PO/CO_2 ROCOP against pK_a of the incorporated s-block metal aqua complex; C. Rationalisation of the increase in selectivity seen with decreasing s-block metal Lewis acidity up to $L_2Co(III)Na(I)$, followed by a plateau.

Table 3.3 Data for the ROCOP of cyclohexene oxide (CHO) and phthalic anhydride (PA) with the $L_2Co(III)M(I/II)$ catalysts.

Figure 3.14 A. Plot of activity of PO/CO_2 ROCOP catalysed by $L_2Co(III)M(I/II)$ against pK_a of the incorporated s-block metal aqua complex, alongside a simplified mechanism for the polymerisation, highlighting the reversible nature of CO_2 insertion; B. Plot of activity of CHO/PA ROCOP catalysed by $L_2Co(III)M(I/II)$ against pK_a of the incorporated s-block metal aqua complex, alongside a simplified mechanism for the polymerisation, highlighting the irreversible nature of PA insertion; C. Structures of key rate-determining intermediates for PO/CO_2 (LHS) and CHO/PA (RHS) ROCOP, showing that the weak Lewis acidity of Rb(I) leads to decarboxylation for PO/CO_2 ROCOP but an enhancement in activity for CHO/PA ROCOP.

Chapter Four: The Effect of Intermetallic Separation in Co(III)K Heterodinuclear Catalysts for Ring-Opening Copolymerisations

Figure 4.1 A. Schemes for the ring-opening copolymerisation of cyclohexene oxide (CHO) with CO_2 or phthalic anhydride (PA); B. Analysis of literature dinuclear catalysts for CHO/CO_2 or CHO/PA ROCOP, identifying optimal intermetallic separations within those structures. Activity (turn over frequency, TOF) for catalysts for CHO/CO_2 ROCOP (CO_2 pressures > 5 bar) (LHS y-axis, purple squares and circles) and for CHO/PA ROCOP (RHS y-axis, green diamonds and triangles) is plotted

against intermetallic separation (from solid-state structures or calculated by DFT). Catalysts requiring co-catalysts (e.g PPNCl) have an added cross.

Figure 4.2 Leading catalysts by their intermetallic separations and the proposed rationale for metallic synergy.

Figure 4.3 A. Structures of the catalysts tested for PO/PA and PO/CO_2 ROCOP. X = OAc. B. Schemes for the tested ring-opening polymerizations of propene oxide with phthalic anhydride or CO_2.

Figure 4.4 Synthesis of H_2L_{wide} from benzo-18-crown-6. i) H_2SO_4, HNO_3, $CHCl_3$, 0 °C to rt, 2 days, 84% ; ii) Pd/C, 1.5 bar H_2, MeOH, rt, 5 days iii) 3,5-ditertbutylbenzaldehyde, MeOH, N_2, 65 °C, 3 days, 87% (from dinitrobenzo-18-crown-6).

Figure 4.5 Synthesis of $L_{wide}CoK(OAc)_2$ from H_2L_{wide}; i) KOAc, MeOH, N_2, reflux, 1 h, ii) $Co(OAc)_2$, N_2, rt iii) AcOH, MeOH, air, rt, 4 h.

Figure 4.6 Comparison of ^{1}H NMR spectra of H_2L_{wide} (top) and $L_{wide}CoK(OAc)_2$ (bottom) showing the disappearance of the phenol resonance (purple), appearance of the acetate resonance (red), and broadening of the crown ether resonances (yellow circles)

Figure 4.7 A. ^{1}H NMR spectrum of $L_{wide}CoK(OAc)_2$ in $CDCl_3$ showing broad and paramagnetically-shifted peaks; B. Proposed structures of $L_{wide}CoK(OAc)_2$ in non-donating (LHS) and donating (RHS) solvents.

Figure 4.8 Plots of inverse of molar susceptibility (χ_m) against temperature (A) and molar susceptibility and temperature ($\chi_m T$) against temperature (B) for $L_{wide}CoK(OAc)_2$.

Figure 4.9 RHS: Solid-state IR spectrum of H_2L_{wide} (top; black) and $L_{wide}CoK(OAc)_2$ (bottom; green) between 4500 – 500 cm^{-1} showing all peaks; LHS: IR spectrum of H_2L_{wide} and $L_{wide}CoK(OAc)_2$ between 1700 – 1200 cm^{-1} to show imine and acetate stretches.

Figure 4.10 Overlaid UV-vis spectra of H_2L_{wide} (black) and $L_{wide}CoK(OAc)_2$ (green) in DCM.

Figure 4.11 MALDI-ToF mass spectrometry of $L_{wide}CoK(OAc)_2$. The predominant peak at 870.07 m/z corresponds to $[L_{wide}Co(II)K(I)]^+$ (RHS), the isotopic distribution of which is in agreement with the calculated distribution (LHS).

Figure 4.12 Solid-state structures of $L_{wide}NiKOAc$ obtained by single crystal diffraction showing the half-dimer (A) and dimeric structure (B) of the complex. Solvent molecules and hydrogen atoms omitted for clarity, ellipsoids drawn at 40% probability.

Figure 4.13 Synthesis of $L_{mono}CoOAc$: i) MeOH, reflux, N_2, 2 h, 72% yield; ii) $Co(OAc)_2$, MeOH, reflux, N_2, 1 h; iii) AcOH, air, rt, 16 h, 92% yield.

Figure 4.14 Synthesis of $L_{short}CoK(OAc)_2$ from the dialdehyde proligand: i) $Co(OAc)_2$, KOAc, MeCN, rt, 1 h, N_2; ii) *ortho*-phenylene diamine, rt, 16 h, N_2; iii) AcOH, air, rt, 72 h, 64% yield.

Figure 4.15 ^{1}H NMR spectrum of a representative PO/PA ROCOP reaction showing integrals and/or regions for PA monomer, polyester, BDM, mesitylene (10 eq. used as an internal standard), and polyether for the calculation of conversion, which is in

turn used to calculate the turnover number (TON) and turnover frequency (TOF), and selectivity for polyester. P = polymer.

Table 4.1 Data for the ROCOP of propene oxide (PO) and phthalic anhydride (PA) for the three catalysts.

Figure 4.16 Representative molar mass distributions of poly(PO-*alt*-PA) formed by $L_{wide}CoK(OAc)_2$ with 20 equivalents of BDM (A) and no chain transfer agent (B) added to the polymerisation; representative plot of experimental and theoretical molar mass, and dispersity against conversion for poly(PO-*alt*-PA) formation by $L_{wide}CoK(OAc)_2$ (C); plot of PA conversion against time for PO/PA ROCOP polymerised by $L_{mono}CoOAc$ + KOAc[18-crown-6] showing its initiation time (D).

Figure 4.17 ^1H NMR spectrum of a representative PO/CO_2 ROCOP reaction showing integrals for mesitylene (10 eq. used as an internal standard), polycarbonate, cyclic carbonate, and polyether for the calculation of conversion, which is in turn used to calculate the turnover number (TON) and turnover frequency (TOF), and selectivity for CO_2 and polymer.

Table 4.2 Data for the ROCOP of propene oxide (PO) and CO_2 for the three catalysts.

Figure 4.18 Top: Comparison of the three catalysts in terms of activities (and selectivities, where relevant) for PO/PA ROCOP (LHS) and PO/CO_2 ROCOP (RHS). Reaction conditions: PO/PA ROCOP: 1:20:400:1000 ([a] 1:20:400:4000) $[catalyst]_0$:$[BDM]_0$:$[PA]_0$:$[PO]_0$, neat, 60 °C; PO/CO_2 ROCOP: 1:20:4000 ([b]1:20:1000) $[catalyst]_0$:$[CHD]_0$:$[PO]_0$, neat, 50 °C, 20 bar CO_2.

Figure 4.19 Cyclic voltammetry traces for $L_{wide}CoK(OAc)_2$ (LHS) and $L_{mono}CoOAc$ (RHS).

Table 4.3 Summary of Co(III/II) redox potentials and ROCOP activities/selectivities for the three tested catalysts, and for an analogue of $L_{short}CoK(OAc)_2$ with a chlorinated phenyl amine backbone.

Figure 4.20 Proposed structures of the three dinuclear catalyst systems during polymerization with changing intermetallic separation

Figure 4.21 Plots of k_{obs} against $[PO]_0$ (A) and $[PA]_0$ (B) showing linear correlations, indicating first-order dependencies of rate on the concentration of each monomer.

Figure 4.22 Plots used for the determination of polymerisation rate dependence with respect to the concentration of PA. A: Exponential decay of [PO] against time; B: linear plots of $\ln([PO]_t/[PO]_0)$ with varying concentrations of PA; C: plot of $\ln(k_{obs})$ against $\ln([PA]_0)$ with a gradient of 1.10; D: polymerisation half-life against [PA] showing it stays constant with varying [PA].

Figure 4.23 Plots used for the determination of the rate dependence with respect to catalyst concentration. A: plots of $\ln[PA]_t/[PA]_0)$ against time with varying catalyst concentrations; B: plot of k_{obs} against initial catalyst concentration.

Equation 4.1 $$rate = k_P[\text{catalyst}]^1[PO]^1[PA]^1$$

Figure 4.24 DOSY NMR experiment of $L_{wide}CoK(OAc)_2$ in MeOD-d_4 indicating a monomeric species.

Figure 4.25 Proposed mechanism for PO/PA ROCOP catalysed by $L_{wide}CoK(OAc)_2$.

Figure 4.26 Comparison of the three Co(III)K(I) catalysts against high-performance literature catalysts for PO/PA ROCOP (for conditions see Figure S4.18).

Figure 4.27 Turnover frequencies (TOFs) and polyester selectivity for polymerizations using different monomer pairs, from LHS reactions combine PO with different anhydride (purple data), whilst the RHS show PA with various epoxides (green data).

Chapter Five: Outlook and Future Work

Figure 5.1 Bio-derived epoxides, anhydrides, and cyclic esters which have been reported for ring-opening co-polymerisations and ring-opening polymerisations.

Figure 5.2 Representative results from Gutmann-Beckett studies using TPPO in MeCN-d_4.

Figure 5.3 Proposed structures of complexes featuring Co(III) or Al(III) in combination with Ce(III) or Eu(III) in different ligand scaffolds, with the aim of exploring electron donation from the ligand ether moieties into the f-block elements.

Figure 5.4 Proposed novel Co(III)K(I) catalyst structure which may have a flexible intermetallic separation.

Table of Contents

Declaration 2

Abstract 3

Acknowledgements 5

List of Publications 6

Abbreviations 7

Table of Figures, Schemes, and Tables 10

Chapter One: Introduction 23

1.1 Polycarbonate and Polyester Plastics 24

1.2 Polymer Synthetic Routes 25

1.2.1 Polycarbonates 25

1.2.2 Polyesters 27

1.3 Ring-Opening Polymerisation and Copolymerisation Mechanisms 28

1.3.1 Ring-Opening Copolymerisation of Epoxides and CO_2 or Anhydrides 28

1.3.1.1 Selectivity 29

1.3.2 Ring-Opening Polymerisation of Lactide 30

1.4 Catalysts 31

1.4.1 Homogeneous Catalysts 31

1.4.1.1 Bicomponent Catalysts 32

1.4.1.2 Tethered Catalysts 36

1.4.1.3 Dinuclear Catalysts 40

1.4.1.3.1 Origins of a Dinuclear Mechanism 40

1.4.1.3.2 Homonuclear Catalysts 42

1.4.1.3.3 Heteronuclear Catalysts 48

1.5 Structure-Activity Relationships 56

1.5.1 Role of Metals 58

1.5.2 Internuclear Separation 60

1.6 Aims and Objectives 65

1.7 References 67

Chapter Two: Understanding Metallic Synergy in Dinuclear Polymerisation Catalysis 78

2.1 Introduction 79

2.2 Aims 79

2.3 Results and Discussion 81

2.3.1 Catalyst Synthesis and Characterisation 81

2.3.1.1 NMR Spectroscopy 82

2.3.1.1.1 Variable Temperature ^{1}H NMR Spectroscopy 83

2.3.1.2 Infrared Spectroscopy 84

2.3.1.3 Single Crystal X-Ray Crystallography 85

2.3.2 Polymerisation Catalysis 88

2.3.2.1 Ring-Opening Copolymerisation of Propene Oxide and CO_2 88

2.3.2.2 Ring-Opening Copolymerisation of Propene Oxide and Phthalic Anhydride 89

2.3.2.3 Ring-Opening Polymerisation of *rac*-Lactide 91

2.3.3 Discussion 93

2.4 Conclusions and Further Work 100

2.5 References 102

Chapter Three: Mechanistic Investigations of Heterodinuclear Sustainable Polymerisation Catalysts using s-Block Metal Lewis Acidity 107

3.1 Introduction 108

3.2 Aims 109

3.3 Results and Discussion 110

3.3.1 L_1Al(III)M(I/II) Synthesis and Characterisation 110

3.3.1.1 Synthesis 110

3.3.1.2 NMR Spectroscopy 111

3.3.1.3 Infrared Spectroscopy 112

3.3.1.4 Single Crystal X-Ray Crystallography 113

3.3.2 L_2Co(III)M(I/II) Synthesis and Characterisation 115

3.3.2.1 Synthesis 115

3.3.2.2 NMR Spectroscopy 116

3.3.2.3 Infrared Spectroscopy 117

3.3.4 Ring-Opening Copolymerisation Catalysis 118

3.3.4.1 Ring-Opening Copolymerisation of Cyclohexene Oxide with Phthalic Anhydride using L_1Al(III)M(I/II) 118

3.3.4.2 Ring-Opening Copolymerisation of Propene Oxide with CO_2 using L_2Co(III)M(I/II) 121

3.3.4.3 Ring-Opening Copolymerisation of Cyclohexene Oxide with Phthalic Anhydride using L_2Co(III)M(I/II) 125

3.4 Conclusions and Future Work 129

3.5 References 131

Chapter Four: The Effect of Intermetallic Separation in Co(III)K Heterodinuclear Catalysts for Ring-Opening Copolymerisations 133

4.1 Introduction 134

4.2 Aims 137

4.3 Results and Discussion 139

4.3.1 Catalyst Synthesis and Characterisation 139

4.3.1.1 Synthesis and Characterisation of L_{wide}CoK(OAc)$_2$ 139

4.3.1.1.1 Synthesis 139

4.3.1.1.2 NMR Spectroscopy 141

4.3.1.1.3 SQUID Magnetometry 143

4.3.1.1.4 Infrared Spectroscopy 144

4.3.1.1.5 UV-Vis Spectroscopy 145

4.3.1.1.5 MALD-ToF Mass Spectrometry 146

4.3.1.1.6 Single Crystal Diffractometry 147

4.3.1.2 Synthesis of L_{mono}CoOAc 148

4.3.1.3 Synthesis of L_{short}CoK(OAc)$_2$ 149

4.3.2 Ring-Opening Copolymerisation Results 150

4.3.2.1 Ring-Opening Copolymerisation of Propene Oxide and Phthalic Anhydride 150

4.3.2.2 Ring-Opening Copolymerisation of Propene Oxide and CO_2 154

4.3.3 Electronic vs. Intermetallic Separation Effects 157

4.3.4 Kinetic and Mechanistic Investigations of L_{wide}CoK(OAc)$_2$ 161

4.3.5 Literature Catalyst Comparison 168
4.3.6 Monomer Scope of $L_{wide}CoK(OAc)_2$ 170
4.4 Conclusions and Future Work 172
4.5 References 174
Chapter Five: Outlook and Future Work 178
5.1 Outlook and Challenges 179
5.1.1 Renewable Feedstocks 179
5.1.2 Measuring and Using Metal Synergy 180
5.1.2.1 Measuring Lewis Acidity 180
5.1.2.2 Exploiting Intermetallic Separation 183
5.2 References 185
Chapter Six: Experimental 187
6.1 General Procedures 188
6.1.1 NMR Spectroscopy 188
6.1.2 Elemental Analysis 188
6.1.3 Mass Spectrometry 189
6.1.4 UV-Vis Spectroscopy 189
6.1.5 SQUID Magnetometry 189
6.1.6 X-Ray Diffractometry 189
6.1.7 Cyclic Voltammetry 190
6.1.8 Gel Permeation Chromatography 190
6.1.9 Epoxide/CO_2 Ring-Opening Copolymerisations 190
6.1.10 Epoxide/Anhydride Ring-Opening Copolymerisations 191
6.1.11 *rac*-Lactide Ring-Opening Polymerisations 191
6.2 Chapter Two 192
6.2.1 Co(III)M(I) (M(I) = Na, K, Rb, Cs) Catalysts 192
6.2.2 Co(III)M(II) (M(II) = Ca, Sr, Ba) Catalysts 192
6.2.2.1 Co(III)Ca(II) 193
6.2.2.2 Co(III)Sr(II) 194

6.2.2.3 Co(III)Ba(II) 195
6.3 Chapter Three 196
6.3.1 Dinitrobenzo[18-crown-6] 196
6.3.2 H_2L_{wide} 197
6.3.3 $L_{wide}CoK(OAc)_2$ 198
6.3.4 $L_{mono}CoOAc$ 199
6.3.5 $L_{short}CoK(OAc)_2$ 200
6.4 Chapter Four 201
6.4.1 H_2L_1 201
6.4.2 L_1Al(III)M(I) (M(I) = Na, K, Rb) Catalysts 201
6.4.3 L_1Al(III)Ca(II) Catalyst 201
6.4.4 H_2L_2 202
6.4.5 L_2Co(III)M(I) (M(I) = Na, K, Rb) Catalysts 202
6.4.6 L_2Co(III)M(II) (M(II) = Ca, Sr, Ba) Catalysts 202
6.4.6.1 L_2Co(III)Ca(II) 203
6.4.6.2 L_2Co(III)Sr(II) 204
6.4.6.3 L_2Co(III)Ba(II) 205
6.5 References 206
Appendix 207

Chapter One

Introduction

1.1 Polycarbonate and Polyester Plastics

Plastics have revolutionised human society, and play a ubiquitous role across the global economy due to their low cost and weight, and stability. In the words of Giulio Natta, in the introduction to Herman F. Mark's *Giant Molecules* "if our age were to be named for the materials that characterize it – as were the Stone and Bronze Ages of the past – this might be known as the age of plastics."[1]

Over the course of the 20th and 21st centuries, global production of plastics has increased substantially. In 2022, over 400 million tonnes of plastic were produced globally, of which 91% were virgin plastics produced from petrochemicals.[2] This reliance on petrochemicals results in a significant carbon footprint associated with the plastics industry, which accounted for 3% of global greenhouse emissions in 2019.[3] While mechanical recycling is often discussed as a method to reduce this carbon footprint, only approximately 9% of the plastics we use are currently recycled.[2] Of the remaining 91%, a small proportion is incinerated (12%) while the vast majority accumulates in the environment in landfill, oceans, etc. (79%).[2] One issue with mechanical recycling is that the recycled plastics have inferior mechanical properties to virgin plastics, limiting their use.[4] Chemical recycling to monomer is an alternative recycling process, which is receiving increasing interest.[5] Using a catalyst, polymers are broken down into their starting monomer/s which can then be used to produce plastics which are indistinguishable from virgin plastics.

In view of a circular plastic economy, the following aims should be prioritised[6]:

1) To produce polymers from renewable resources, such as bio-derived feedstocks or waste CO_2.
2) To target polymers which can be reused, recycled, and/or remanufactured.
3) To target biodegradable polymers for applications where they cannot be recovered and recycled (e.g. in formulations, films, and environmentally dispersed wastes), to avoid accumulation in the environment.

Polycarbonates and polyesters are already used for various applications, at both high and low molecular weights, such as food packaging, rigid plastics, polyurethane foams, biomedical devices, and drug delivery.[7-11] Furthermore, they are good candidates for a future circular plastics economy because:

1) They can be produced from bio-derived diols, diacids, epoxides, anhydrides, cyclic esters and/or CO_2.[12-14]
2) Specific examples of polycarbonates and polyesters have been shown to be chemically recyclable back to monomer.[5, 15, 16]
3) Their oxygenated nature often allows their biodegradation.[13, 17]

1.2 Polymer Synthetic Routes

1.2.1 Polycarbonates

In industrial settings, polycarbonates are predominantly produced via step-growth polycondensation, typically of bisphenol A with phosgene or diphenyl carbonate (Figure 1.1, top).[8] This method of production is rather energy-intensive and atom inefficient due to the production of small molecule by-products, which must be removed during the polymerisation to drive conversion. To achieve high molecular weight polymers, very high conversions of monomer are needed. Due to the poor control of the polymerisation, the resultant polycarbonates have high dispersities which prevents the formation of block copolymers and complicates structure-performance insights.

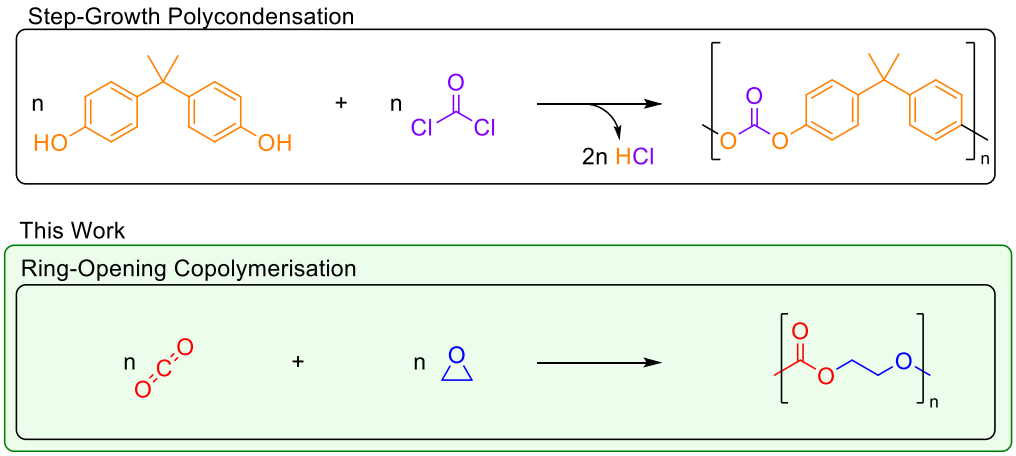


Figure 1.1. Step-growth polycondensation of bisphenol A (BPA) and phosgene to produce polycarbonate (top), and ring-opening copolymerisation of epoxides and CO_2 to produce polycarbonates (bottom).

An alternative method for polycarbonate synthesis is the ring-opening copolymerisation (ROCOP) of epoxides and CO_2 (Figure 1.1, bottom). This method is attractive as it utilises CO_2, which is a waste product of many industrial processes, and may provide a financial incentive to CO_2-capture.[18] A growing number of epoxides can be bio-derived, opening up the possibility of fully sustainably-derived polycarbonates. There is a limited range of catalysts which have been reported for this process, the best of which can show very high activities, selectivities, and control ($Đ < 1.20$).[14, 19] A high priority area are those which can operate at low CO_2 pressures (< 5 bar), as they are able to be used in conventional manufacturing plants.

1.2.2 Polyesters

Polyesters are also predominantly produced industrially by step-growth polycondensation of diesters or diacids with diols, or via the polycondensation of hydroxyl acids (Figure 1.2, top).[8]

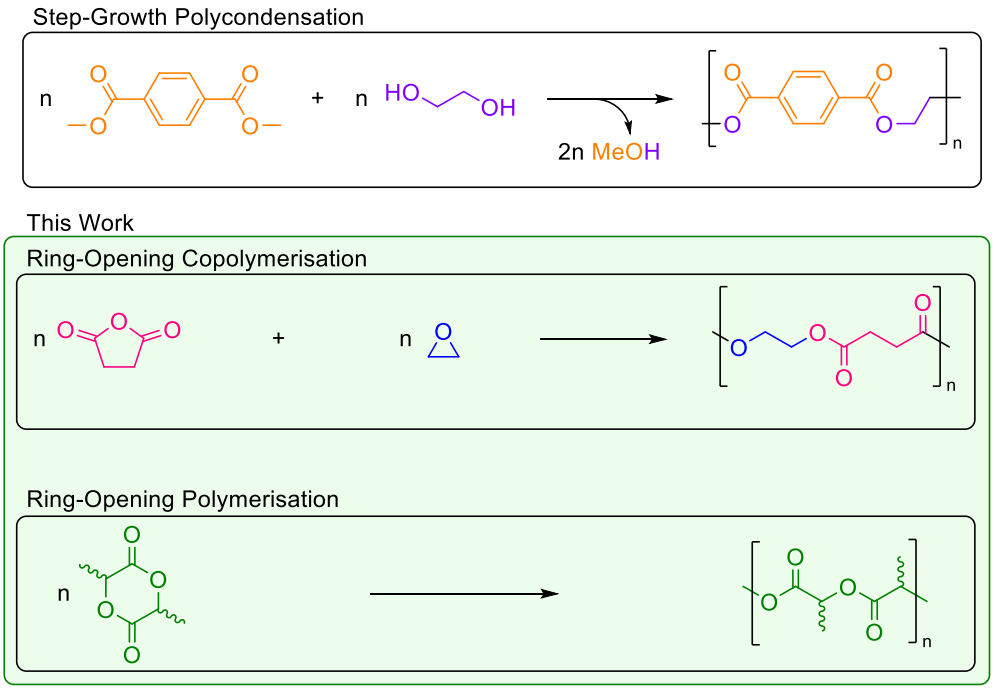


Figure 1.2. Step-growth and ring-opening copolymerisation synthetic routes to produce polyesters.

The ROCOP of epoxides and anhydrides is an alternative route to polyesters, and it may be more attractive as it is 100% atom-economical, offers options for bio-derived monomers, and polyesters with a wide range of backbones (e.g. aliphatic, aromatic, functionalised) are feasible (Figure 1.2, middle).[14]

The related ring-opening polymerisation (ROP) of cyclic esters is also an attractive candidate for polyester synthesis (Figure 1.2, bottom). The ROP of lactide (LA), produced from starch harvested from crops, for example sugar cane, is used to produce poly(lactic acid) (PLA) at scale commercially; PLA is the largest volume bioderived polymer, produced at ~ 200,000 tonnes globally in 2019.[13] PLA is a thermoplastic used in packaging, fibres, and biomedical applications.[8, 12, 20]

Both ROP and ROCOP are living polymerisations and can be used to produce polyesters with controlled molar masses ($Đ < 1.20$).

1.3 Ring-Opening Polymerisation and Copolymerisation Mechanisms

1.3.1 Ring-Opening Copolymerisation of Epoxides and CO_2 or Anhydrides

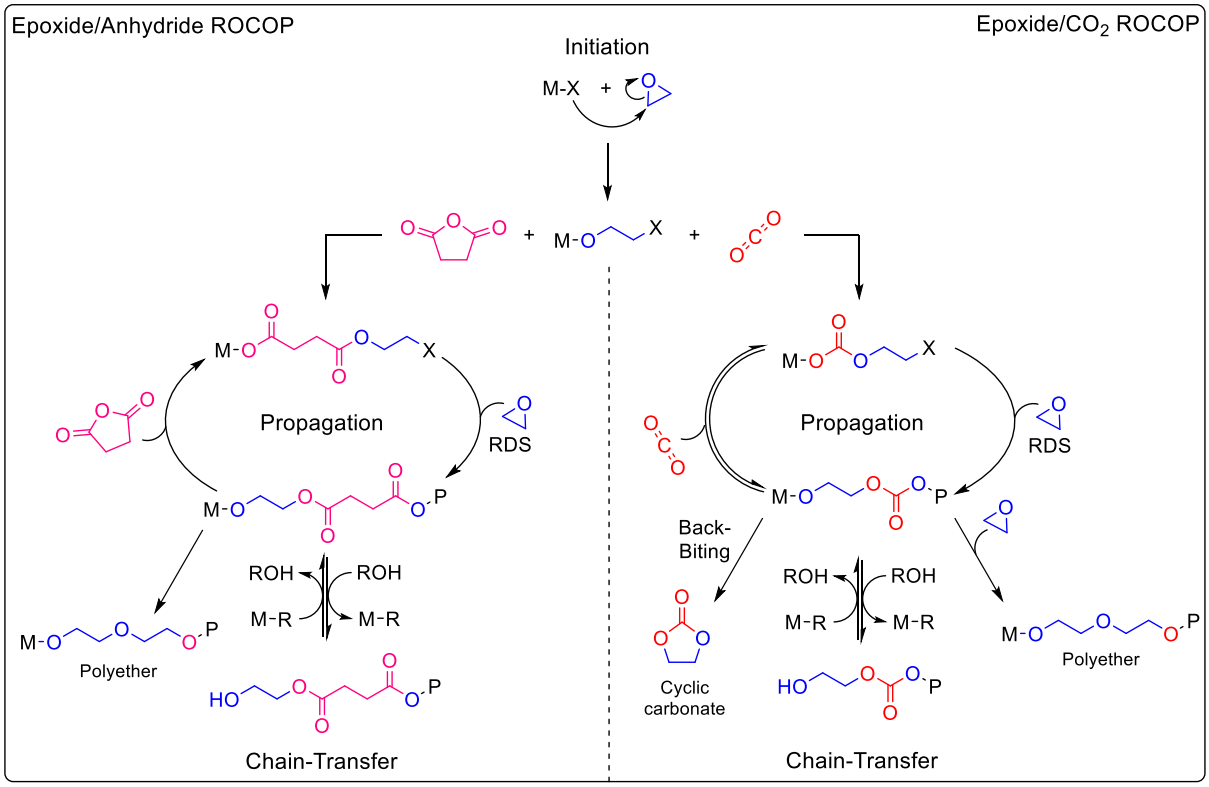


Figure 1.3. ROCOP of epoxides with anhydrides (LHS) and CO_2 (RHS).

The ROCOPs of epoxides with CO_2 or anhydrides proceed through related pathways (Figure 1.3):

1) Initiation

The two polymerisation mechanisms share the same initial step. An initiating group bound to the catalyst (either a catalyst co-ligand or introduced by the addition of an initiator) ring-opens a molecule of epoxide, to form a highly reactive alkoxide intermediate. Common examples of initiating groups include halides, acetates, and alkoxide

groups. Highly reactive initiating groups are desirable to allow rapid initiation, which is essential in a living polymerisation.

2) Propagation — The alkoxide intermediate (generated from initiation) then undergoes insertion of CO_2 or anhydride, depending on the polymerisation. This insertion forms a carbonate or carboxylate intermediate, respectively, which can then ring-open another epoxide to reform the alkoxide intermediate. This is generally the rate-determining step, but depends on the catalyst and conditions.

3) Chain-Transfer — Protic species (ROH), termed chain-transfer agents (CTAs), are often added as they undergo rapid and reversibly exchange with the alkoxide intermediates. These CTAs control the overall polymer molar mass and end-group chemistry, whilst ensuring narrow molar mass distributions.[21] Commonly, CTAs are diols, such as *trans*-1,2-cyclohexane diol (CHD) or benzene dimethanol (BDM).

1.2.1.1 Selectivity

1) Polyether — In both copolymerisations, ether linkage formation can occur if the alkoxide intermediate ring-opens another epoxide molecule, instead of inserting CO_2 or cyclic anhydride. Incorporation of ether linkages into the polycarbonates/polyesters affect their properties. The selective incorporation of ether linkages into polycarbonates and polyesters is currently being investigated by various groups, but is outside the scope of this thesis, where ether linkages are undesirable.[22, 23]

2) Cyclic By-product

For epoxide/CO_2 ROCOP, another undesired by-product is cyclic carbonate. This may form if the alkoxide intermediate undergoes intramolecular attack on the carbonate linkage adjacent to the chain-end. The cyclic carbonate is formed, and a chain-shortened alkoxide intermediate is re-formed. Cyclic carbonates are undesirable as they are difficult to remove due to their high boiling points (> 200 °C) and may alter the resultant polycarbonate/polyester properties.

Cyclic carbonate formation is favoured by high temperatures (since it is the thermodynamic product of epoxide/CO_2 coupling) and low CO_2 pressures (since CO_2 insertion is an equilibrium process, lower pressures favour higher alkoxide intermediate concentrations, which increases the rate of back-biting).[24]

1.3.2 Ring-Opening Polymerisation of Lactide

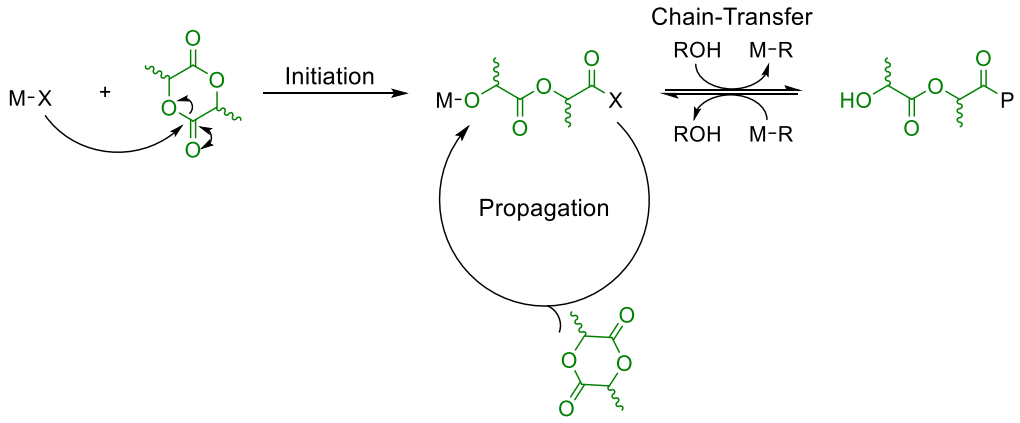


Figure 1.4 Mechanism for the ROP of lactide.

The ROP of lactide proceeds through a similar mechanism (Figure 1.4):

1) Initiation	Again, the catalyst co-ligand is often the initiating group, and initiates the polymerisation by ring-opening the monomer, resulting in an alkoxide propagating intermediate.
2) Propagation	The alkoxide intermediate generated from initiation attacks and ring-opens another monomer, reforming a chain-lengthened alkoxide intermediate.
3) Chain-Transfer	Protic species (ROH) which are added to the polymerisations can rapidly and reversibly exchange with the alkoxide chain-end, allowing control of the polymer molar mass and end-groups while maintaining narrow dispersity distributions.

1.4 Catalysts

While the three polymerisations described herein have related mechanisms, catalysts that are highly active and/or selective for one polymerisation will not necessarily have the same performance across all three reactions – indeed, very few catalysts are reported for all three processes. This sub-section will cover key catalysts reported across the three polymerisation fields, i.e. catalysts that were note-worthy at the time of reporting, due to high activity and selectivity, and/or providing insights into the polymerisation mechanism.

1.4.1 Homogeneous Catalysts

While heterogeneous catalysts are traditionally preferred for industrial applications due to their ease of synthesis, low cost, simplicity of separation, and recyclability, this thesis focusses on the development of homogeneous catalysts as they facilitate the investigation of polymerisation mechanisms due to their relative ease of characterisation and well-defined active sites. This can improve understanding of the factors which underpin highly-active and/or highly-selective polymerisation catalysts. Polymerisations using homogeneous catalysts tend to be better-controlled

compared to heterogeneous systems, resulting in polymers with improved selectivities and narrower weight distributions.

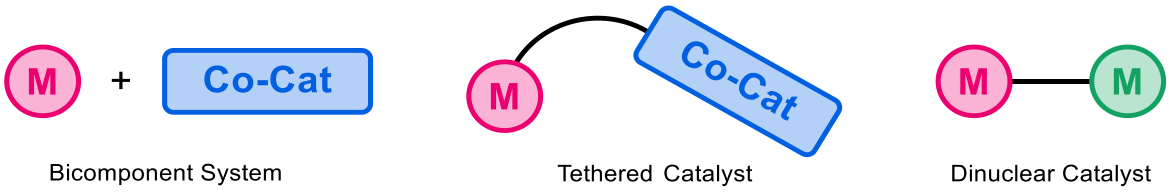


Figure 1.5. Three types of homogeneous catalysts: bicomponent systems, tethered catalysts, and dinuclear catalysts.

Homogeneous catalysts for ring-opening copolymerisations can generally be divided into three categories (Figure 1.5):

1) Bicomponent systems: these feature metal complexes (or organocatalyst) that are combined with an organic co-catalyst, or metal catalysts which operate via a dimeric polymerisation mechanism.
2) Tethered catalysts: these feature a metal complex (or organocatalyst) and organic co-ligand which have been combined into the same molecule to increase the probability of the two components encountering in solution.
3) Dinuclear catalysts: these utilise dinucleating ligands, where two metals are bound within the same complex in such a way that they operate in synergy with each other. Trinuclear catalysts have also been reported, but are rarer.

The following sub-section will explore the history of the development of these three catalyst categories, focussing in particular on high-performance or otherwise notable catalysts.

1.4.1.1 Bicomponent Catalysts

Some of the first well-defined catalysts for epoxide/CO_2 and epoxide/anhydride ROCOP were metal(III) porphyrin complexes (Cr, Co, Al), which were used in combination with quaternary ammonium salt co-catalysts to improve their performance.[25-27] Even with the addition of the co-

catalyst, these porphyrin complexes generally show low activities in comparison to other metal catalysts.

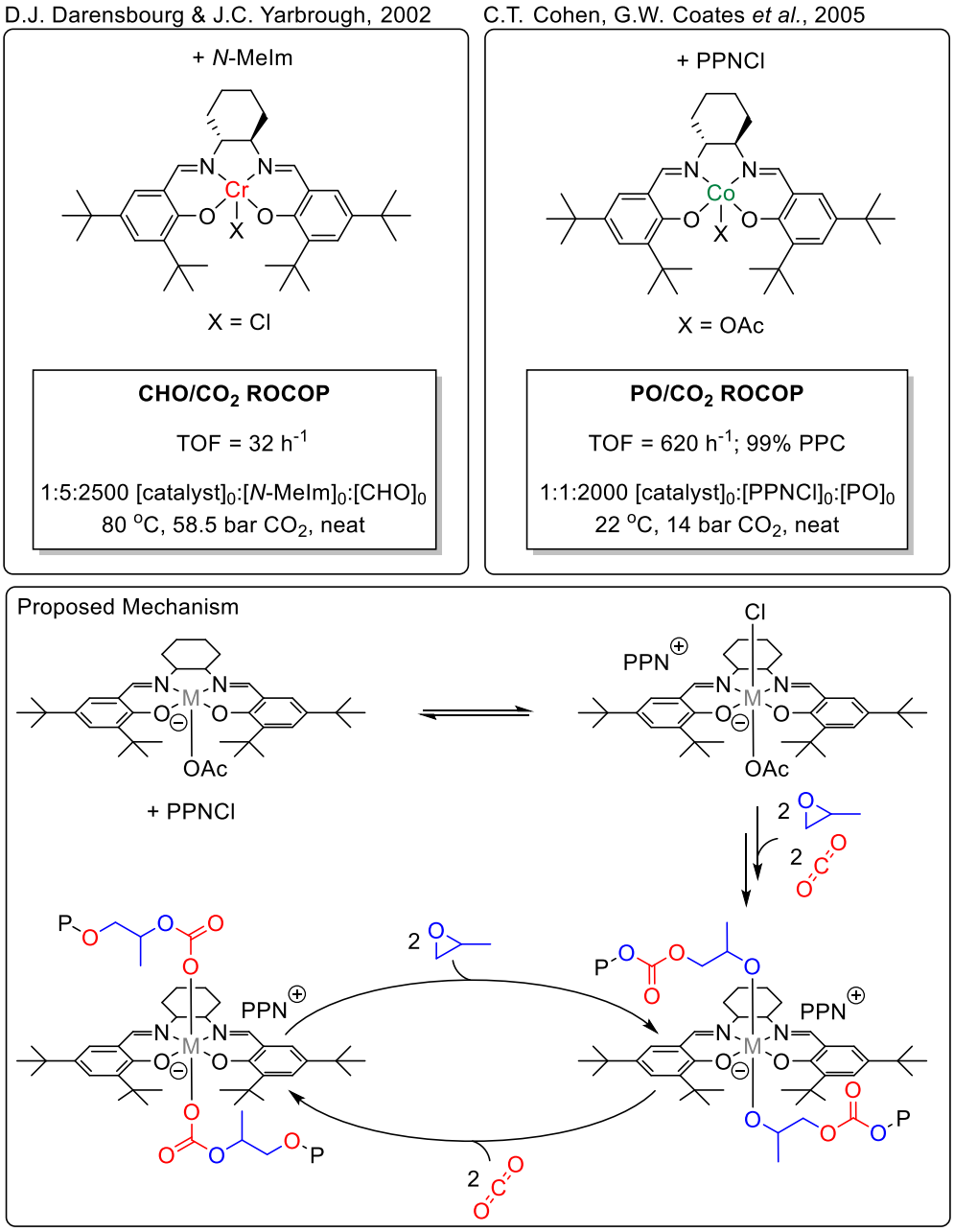


Figure 1.6. Top: Structures of examples of salen catalysts for epoxide/CO_2; bottom: Proposed mechanism for the ROCOP of PO/CO_2 catalysed by a metal salen complex.[28, 29]

One of the most widely researched class of catalysts for the ROCOP of epoxides with CO_2 or anhydrides is the metal salens. Darensbourg and co-workers reported a Cr(III) salen catalyst for CHO/CO_2 ROCOP in 2002.[28] It had an activity of 10 h^{-1} for CHO/CO_2 ROCOP which rose to 32 h^{-1} upon the addition of 5 equiv. relative to catalyst of *N*-methyl imidazole (1:2500 [catalyst]$_0$:[CHO]$_0$,

80 °C, 58.5 bar CO_2; Figure 1.6 Top LHS). Coates and co-workers later reported a related Co(III) salen for PO/CO_2 ROCOP which was able to achieve good activities and selectivities when combined with an equivalent of PPNCl (TOF = 620 h^{-1}, 99% PPC, 1:1:2000 $[catalyst]_0$:$[PPNCl]_0$:$[PO]_0$, 22 °C, 14 bar CO_2; Figure 1.6 top RHS).[29] Duchateau and co-workers reported an investigation on the effects of metal, ligand, and co-catalyst for epoxide/anhydride ROCOP.[30] They found that the most active combination for CHO/PA ROCOP was a Cr(III) salphen catalyst with an equivalent of PPNCl (TOF = 245 h^{-1} , 1:1:250:250 $[catalyst]_0$:$[PPNCl]_0$:$[PA]_0$:$[CHO]_0$, 110 °C).

It was proposed that the co-catalyst anion can coordinate to the metal centre *trans* to the propagating polymer chain, labilising the carbonate intermediate in the rate-determining step. Since this anion can act as initiator, they proposed two polymer chains can propagate from one catalyst metal centre simultaneously (Figure 1.6 bottom).[28, 29, 31] The addition of PPNCl, and other co-catalysts, is proposed to indirectly increase the thermal stability of Co(III) polymerisation catalysts, since thermal deactivation of these catalysts occurs due to the reduction of the Co(III) centre of the alkoxide intermediate to Co(II).[32, 33] As PPNCl increases the rate of CO_2 insertion into the alkoxide, the lifetime of the alkoxide intermediate is decreased, and so thermal deactivation decreases.

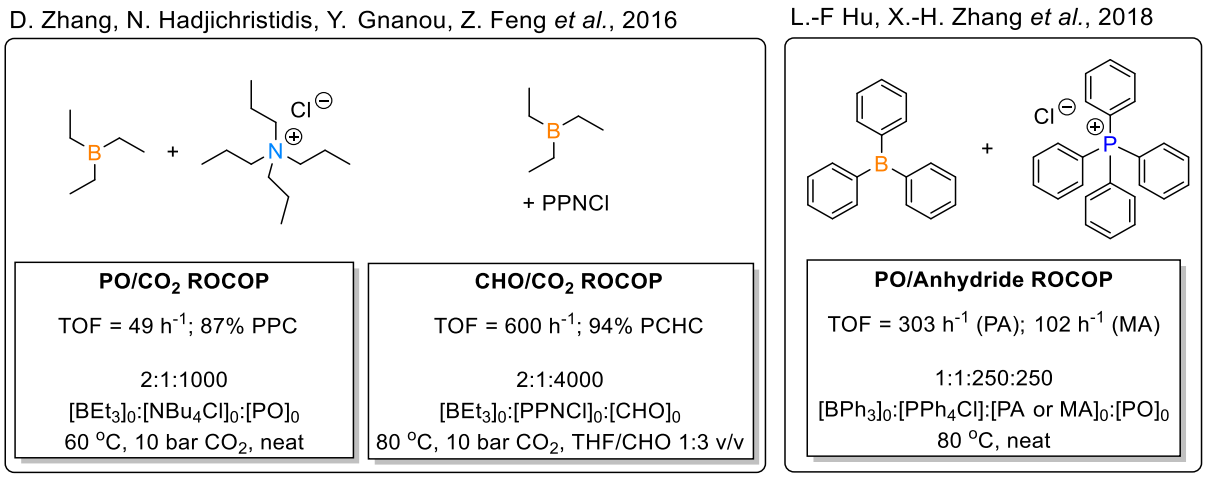


Figure 1.7. Examples of bicomponent catalyst systems for epoxide/CO_2 ROCOP (LHS) and epoxide/anhydride ROCOP (RHS).[34, 35]

Bicomponent organoborane/co-catalyst systems were first reported in 2016, by Feng, Gnanou, Hadjichristidis and co-workers for the ROCOP of both PO and CHO with CO_2. They used triethylborane in combination with various onium and phosphazenium salts (Figure 1.7 LHS).[34] The most active combination for PO/CO_2 ROCOP was triethyl borane with tetrabutyl ammonium chloride, but it shows low activities at low loading (TOF = 49 h^{-1}, 87% PPC, 2:1:1000 $[BEt_3]_0$:$[Bu_3NCl]_0$:$[PO]_0$, neat, 60 °C, 10 bar CO_2). For CHO/CO_2 the most active combination was with PPNCl (TOF = 600 h^{-1}, 94% PCHC, 2:1:4000 $[BEt_3]_0$:$[PPNCl]_0$:[CHO], THF/CHO (1:3 v/v), 80 °C, 10 bar CO_2).

In 2018, Zhang and co-workers reported a triphenyl borane/tetraphenyl phosphonium chloride catalyst system for the ROCOP of PO with PA or maleic anhydride (MA) (TOF = 303 h^{-1} (PO/PA), 102 h^{-1} (PO/MA), 1:1:100:350 $[BPh_3]_0$:$[PPh_4Cl]_0$:[PA or MA]$_0$:$[PO]_0$, 80 °C, neat; Figure 1.7, RHS).[35]

While the use of PPNCl has allowed the development of highly active and selective catalysts, it is expensive, toxic, and corrosive to steel. As such, catalysts should be developed which obviate or limit the use of such co-catalysts.

1.4.1.2 Tethered Catalysts

To address the low activities of bicomponent catalyst systems at low concentrations, tethered catalyst-co-catalyst systems have been targeted by various groups, where the ionic co-catalyst is bound by a flexible linker to the catalyst.

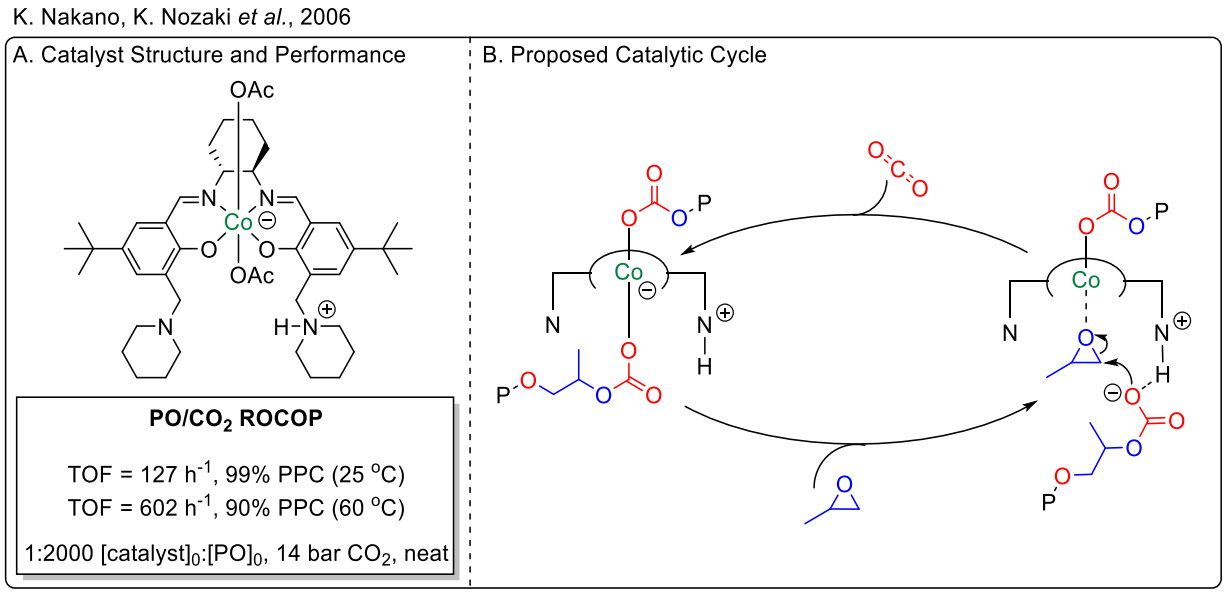


Figure 1.8. Structure, performance, and mechanism of a tethered Co(III) salen – piperidinium catalyst for epoxide/CO_2 ROCOP.[36]

Nozaki and co-workers were the first to report such a catalyst system in 2006, with a Co(III) salen complex tethered to two piperidinium co-catalysts (Figure 1.8A).[36] The catalyst was highly active and selective for PO/CO_2 ROCOP: it achieved a TOF of 127 h^{-1} with 99% PPC selectivity at only 25 °C, under 14 bar CO_2 pressure (1:2000 $[catalyst]_0$:$[PO]_0$). When the polymerisation was conducted at 60 °C the activity increased to 602 h^{-1}, although the selectivity for polycarbonate decreased slightly to 90%. It was proposed that the piperidinium co-catalysts improve the selectivity of the polymerisation by moderating the nucleophilicity of the carbonate chain-end by protonation, preventing it from undergoing back-biting to form the cyclic carbonate (Figure 1.8B).

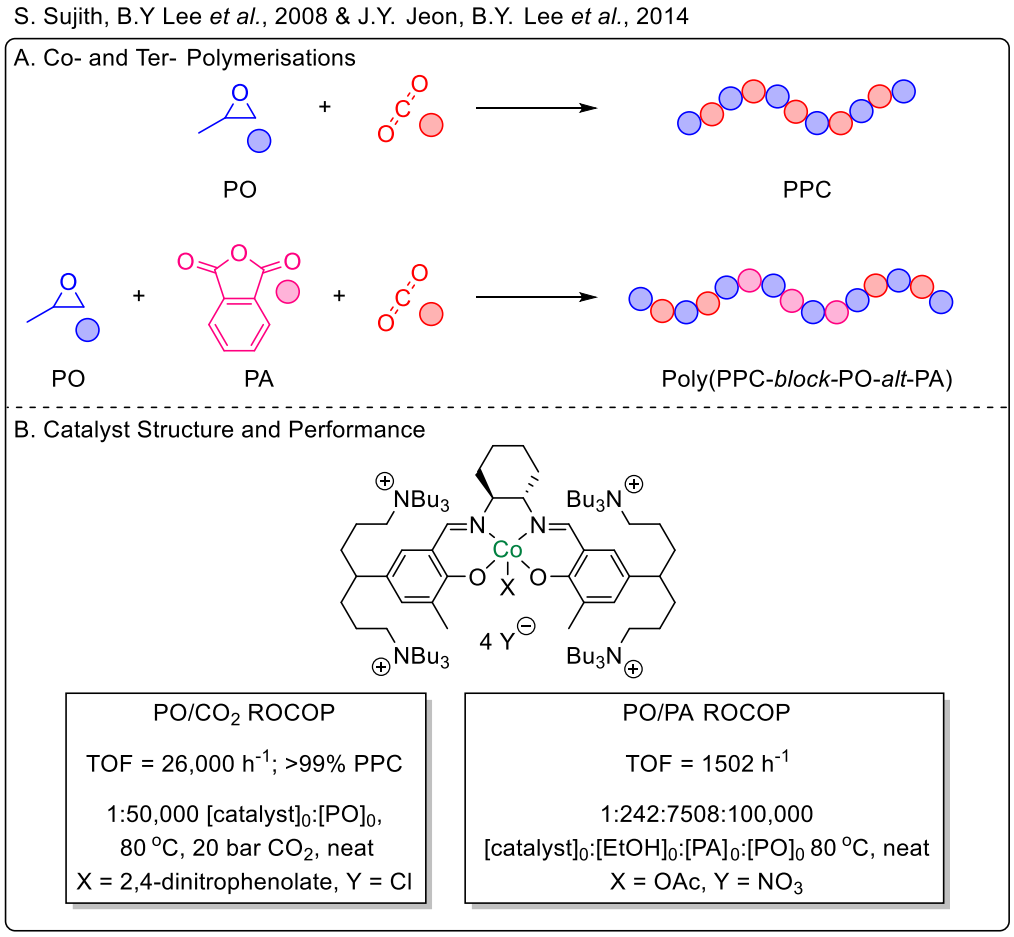


Figure 1.9. A: PO/CO_2 ROCOP to form PPC and PO/PA/CO_2 terpolymerisation to form an ABA block copolymer; B: structure and performance of a tethered Co(III) salen – tertiary ammonium catalyst for epoxide/CO_2 and epoxide/anhydride ROCOP.[37, 38]

Lee and co-workers reported a related catalyst, again for PO/CO_2 ROCOP, with four tertiary ammonium co-catalyst subunits tethered to a Co(III) salen complex (Figure 1.9).[37] The catalyst showed a TOF of up to 26,000 h^{-1} at 80 °C, with >99% polymer selectivity (1:50,000 $[catalyst]_0:[PO]_0$, 20 bar). Further, they recovered and recycled the catalyst by filtration through silica, followed by elution with $NaBF_4$ in MeOH. The catalyst was later used for the terpolymerisations of PO, CO_2, and PA to form a block copolymer.[39] For PO/PA ROCOP, the catalyst had a TOF of 1502 h^{-1} (1:242:7,508:100,000 $[catalyst]_0:[EtOH]_0:[PA]_0:[PO]_0$, 80 °C). While this is substantially lower than its activity for PO/CO_2 ROCOP, it is excellent for the field.

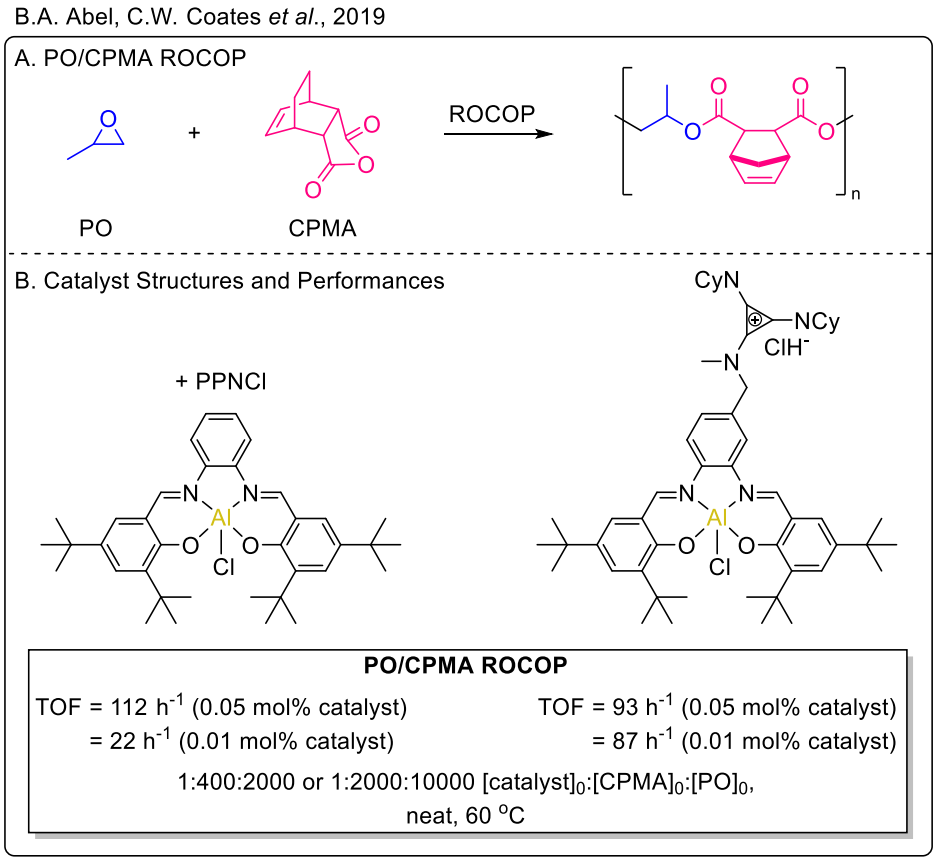


Figure 1.10. A. Scheme for PO/CPMA ROCOP; B. Catalyst structures and performances of a binary Al(III) salen – PPNCl catalyst system, and of a tethered Al(III) salen – tris(dialkylamino)cyclopropenium catalyst for epoxide/anhydride ROCOP.[40]

In 2019, Coates and co-workers reported an Al(III) salen catalyst with a tethered tris(dialkylamino)cyclopropenium moiety for PO/carbic anhydride (CPMA) ROCOP (TOF = 93 h^{-1}, 1:400:2000 $[catalyst]_0:[CPMA]_0:[PO]_0$, 60 °C, neat; Figure 1.10).[40] The catalyst showed a comparable activity to the bicomponent Al(III) salen/PPNCl catalyst system at high loadings, and maintained its activity at high dilution, while the activity of the bicomponent catalyst system decreased to only 20% of its original activity.

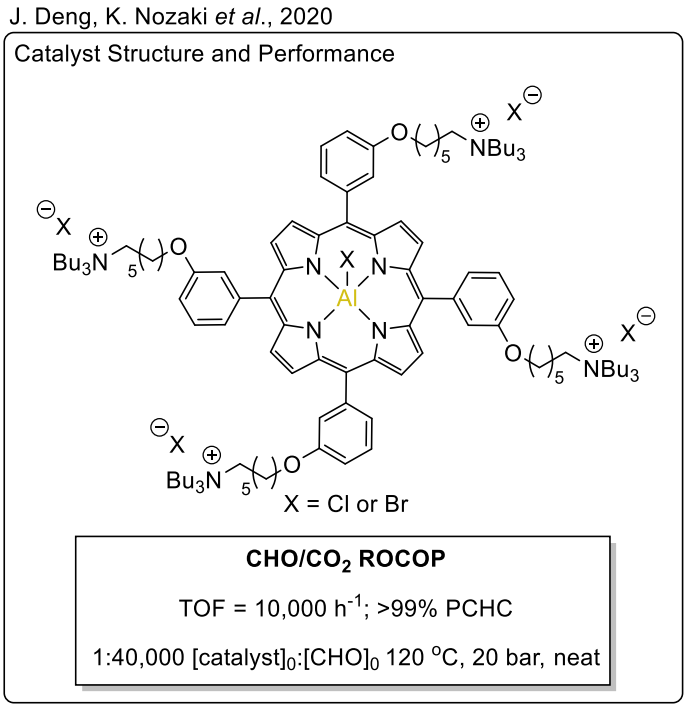


Figure 1.11. Structure and performance of a tethered Al(III) porphyrin – quaternary ammonium catalyst for epoxide/CO_2 ROCOP.[41]

Nozaki and co-workers extended this tethering approach to design an Al(III) porphyrin complex (Figure 1.11).[41] The Al(III) porphyrin featured four tethered tertiary ammonium co-catalysts and was highly active for CHO/CO_2 ROCOP, with a TOF of 10,000 h^{-1} at 120 °C, under 20 bar CO_2 pressure (>99% PCHC, 1:40,000 $[catalyst]_0:[CHO]_0$). Again, they proposed that the cationic tertiary ammonium co-catalysts prevented backbiting by stabilising the carbonate chain-end, ensuring that it does not diffuse into the bulk solution.

Catalyst-co-catalyst tethering is not only limited to metal complexes – in 2020 Wu and colleagues reported a tethered organoborane/quaternary ammonium catalyst for CHO/CO_2 ROCOP (Figure 1.12A).[42] It was an effective catalyst, with a TOF of up to 1,583 h^{-1} with full selectivity for PCHC (1:10,000 $[catalyst]_0:[CHO]_0$, 120 °C, 20 bar CO_2, neat). During the polymerisation, the borane is proposed to coordinate and activate the monomer, while the quaternary ammonium co-catalyst stabilises the carbonate chain-end (Figure 1.12B).

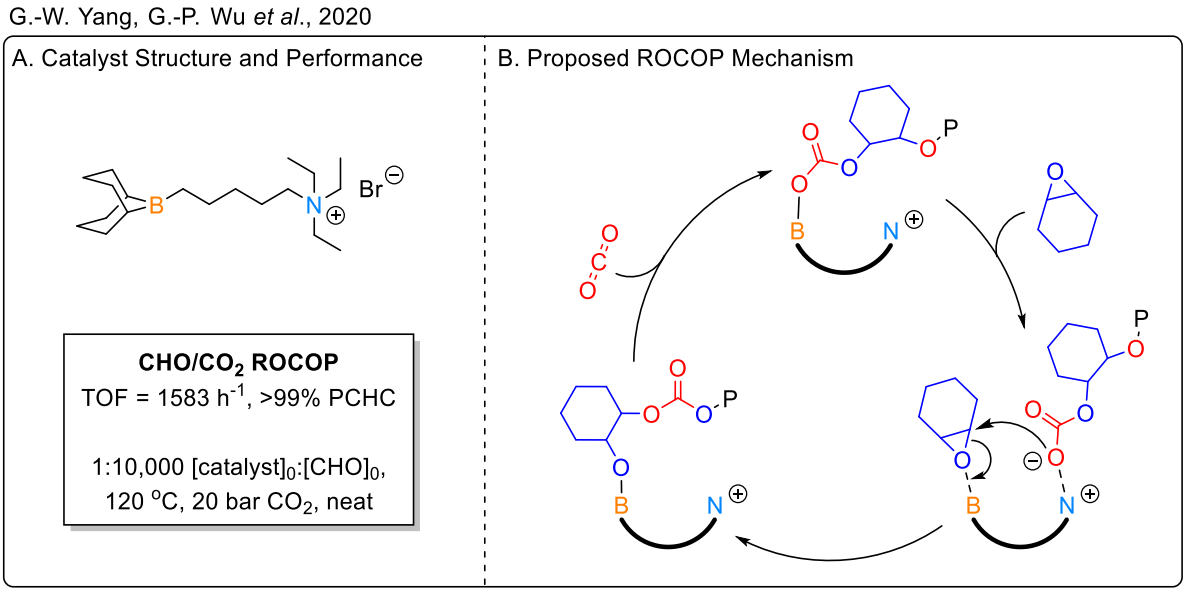


Figure 1.12. A. Structure and performance of a tethered borane – quaternary ammonium catalyst for epoxide/CO_2 ROCOP; B. proposed mechanism for CHO/CO_2 ROCOP.[42]

1.4.1.3 Dinuclear Catalysts

1.4.1.3.1 Origins of a Dinuclear Mechanism

Early studies of zinc β-diimidate (BDI) catalysts for CHO/CO_2 ROCOP indicated that the most active catalysts featured ligands with intermediate steric bulk, as these were proposed to form loosely-bound dimers in solution (Figure 1.13A).[43] Too little steric bulk, and the dimers formed were too tightly-bound and inactive, and if the steric bulk was too high the species existed in a monomer – dimer equilibrium which decreased the rate of polymerisation (Figure 1.13B). As such, a dinuclear mechanism was proposed where the nucleophile (carbonate) and electrophile (epoxide) were bound by separate Zn(II) centres (Figure 1.13C). Close proximity of the two metal centres allows the rate-determining step – epoxide ring-opening – to proceed, thus enhancing the rate of polymerisation. These catalysts were also active for epoxide/anhydride ROCOP, and – again – the most active catalysts were those with intermediate steric bulk, suggesting a similar dinuclear mechanism (Figure 1.13C).[44]

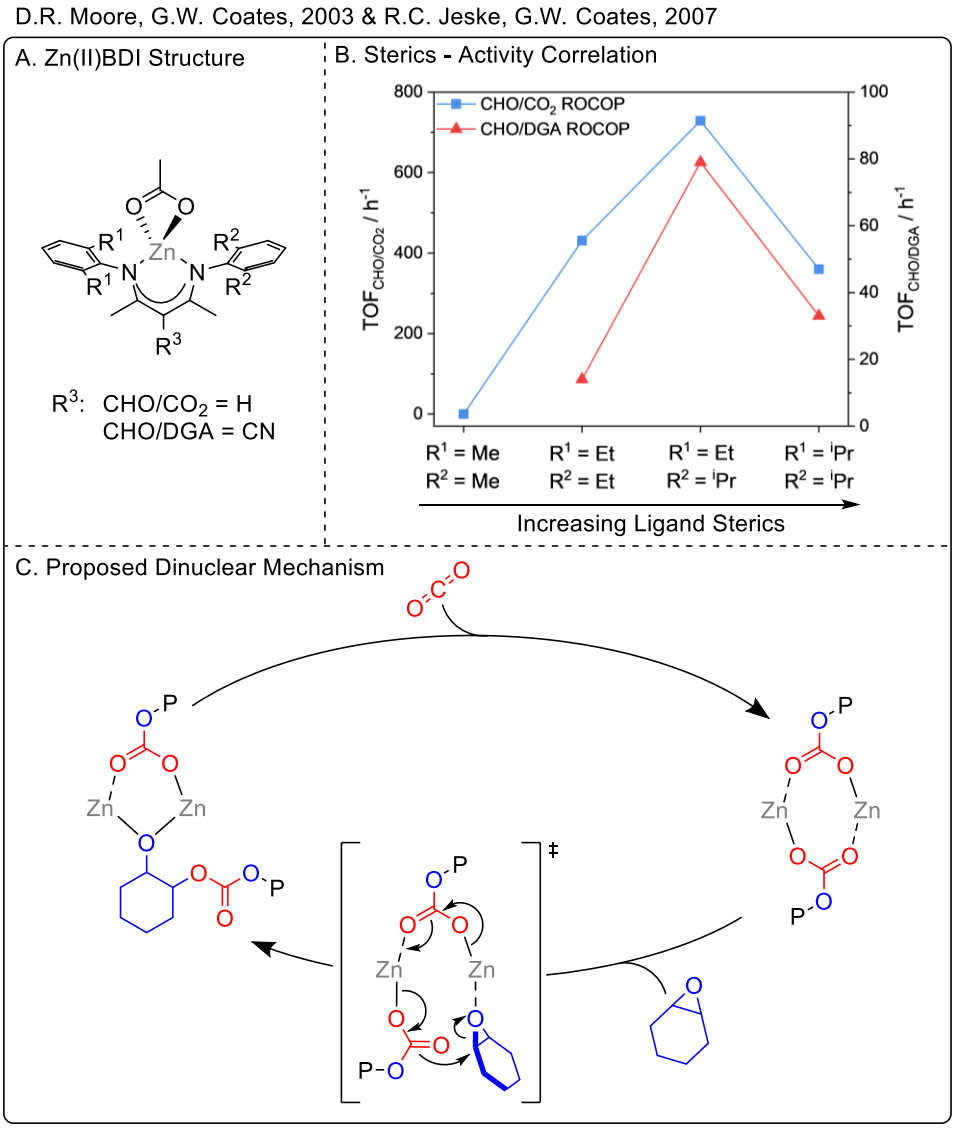


Figure 1.13. A. Structure of Zn(II)BDI catalysts for epoxide/CO_2 and epoxide/anhydride ROCOP; B. Correlation between activity of the catalysts for epoxide/CO_2 (blue squares) and epoxide/anhydride (red triangles) ROCOP and increasing steric bulk of the ligand; C. proposed dinuclear mechanism for CHO/CO_2 ROCOP.[43, 44]

In 2002, Hillmyer and Tolman reported a higher activity for a dinuclear Fe(III) catalyst compared to its analogous mononuclear Fe(III) catalyst for L-LA ROP.[45] The dinuclear catalyst showed first-order rate-dependence with respect to catalyst concentration, while the mononuclear catalyst showed rate-dependence on the concentration of catalyst of approximately a half. While this was not proposed in the article, this difference in rate and the kinetics of LA ROP catalysed by the dinuclear and mononuclear catalysts may, in hindsight, indicate a dinuclear mechanism.

1.4.1.3.2 Homonuclear Catalysts

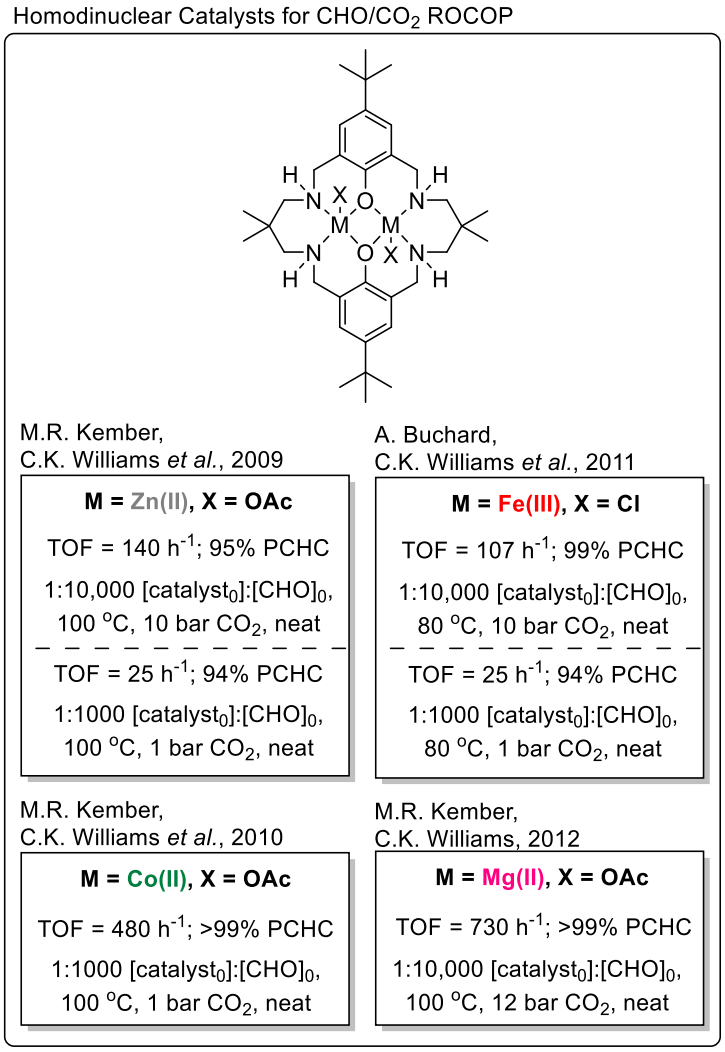


Figure 1.14. Structure and performances of heterodinuclear catalysts for epoxide/CO_2 ROCOP where M = Zn(II), Fe(III), Co(II), and Mg(II).[46-49]

Many researchers thereafter targeted dinuclear catalysts for these polymerisations, where a multinucleating ligand is used to coordinate multiple metal centres within the same catalyst complex.

Between 2009 – 2012, our group reported various dinuclear catalysts for CHO/CO_2 ROCOP with Zn(II)Zn(II), Fe(III)Fe(III), Co(II)Co(II), and Mg(II)Mg(II) metal combinations (Figure 1.14).[46-49] These catalysts utilised a macrocyclic ligand which consistently gives complexes with intermetallic separations of approximately 3 – 4 Å. Many of these catalysts were active at atmospheric CO_2

pressures, which was rare at the time. In particular, the Mg(II)Mg(II) metal combination was amongst the most active, with a TOF of 730 h^{-1} and perfect polycarbonate selectivity (1:10,000 $[catalyst]_0$:$[CHO]_0$, 100 °C, neat, 12 bar CO_2), and the Co(II)Co(II) combination showed a TOF of 480 h^{-1} and, again, perfect polycarbonate selectivity at only 1 bar CO_2 pressure (1:1000 $[catalyst]_0$:$[CHO]_0$, 100 °C, neat).[48, 49]

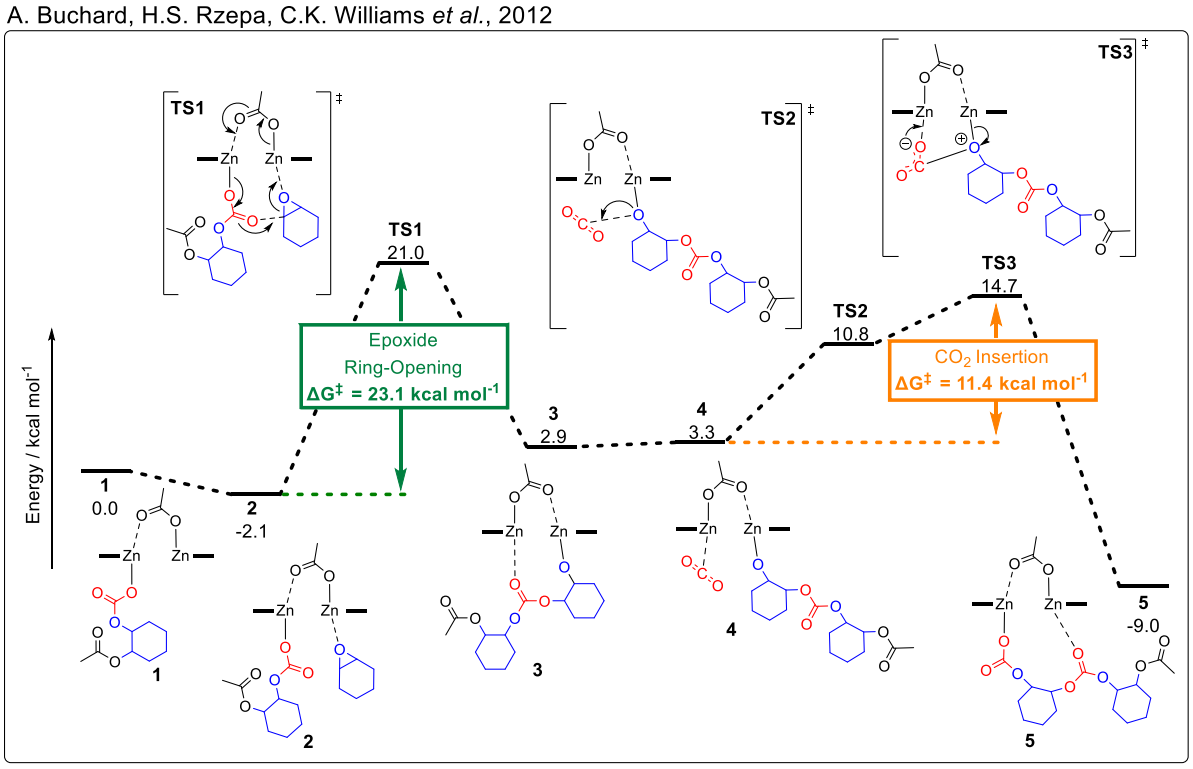


Figure 1.15. Calculated energies of intermediates and transition states for the ROCOP of CHO and CO_2 catalysed by a dizinc catalyst.[50]

A kinetic investigation of CHO/CO_2 ROCOP with the Zn(II)Zn(II) catalyst showed first-order rate dependence on the concentration of catalyst and epoxide, but zero-order rate-dependence on carbon dioxide pressure between 1 – 40 bar.[51] The rate-determining step was therefore proposed as CHO ring-opening by a Zn(II)-carbonate, which was supported by a later DFT investigation.[50] This DFT investigation suggested a "chain-shuttling" mechanism, where the propagating polymer chain is exchanged twice during the catalytic cycle (Figure 1.15). In the rate-determining step, one Zn(II) centre binds the carbonate nucleophile, while the other Zn(II) centre binds epoxide monomer. Epoxide ring-opening occurs with $\Delta G^{\ddagger}$ = + 23.1 kcal mol^{-1}, forming an alkoxide intermediate which

is bound to one of the Zn(II) centres. CO_2 then weakly coordinates to the other Zn(II) centre, and the alkoxide intermediate reacts with the CO_2 with $\Delta G^{\ddagger}$ = +11.4 kcal mol^{-1}. It can be seen that in this mechanism the two Zn(II) centres have distinct roles in the rate-determining step: 1) to coordinate and active epoxide, and 2) to provide a labile, nucleophilic carbonate species.

In 2013, Rieger and co-workers reported a di-Zn(II) catalyst ligated by a macrocycle comprising of two BDI ligands (Figure 1.16, LHS).[52] The catalyst had excellent activity and selectivity for CHO/CO_2 ROCOP (TOF = 7587 h^{-1} (20 bar CO_2), 9130 h^{-1} (40 bar CO_2), 1:4000 [catalyst]$_0$:[CHO]$_0$, 100 °C, 1:1 v/v toluene/CHO). The flexibility of the methylene bridges was proposed to be important, with a DFT study suggesting that the intermetallic separations of key intermediates in the catalytic cycle were closer than the separation of the starting catalyst (4.50 – 5.66 Å vs. 7.77 Å respectively).

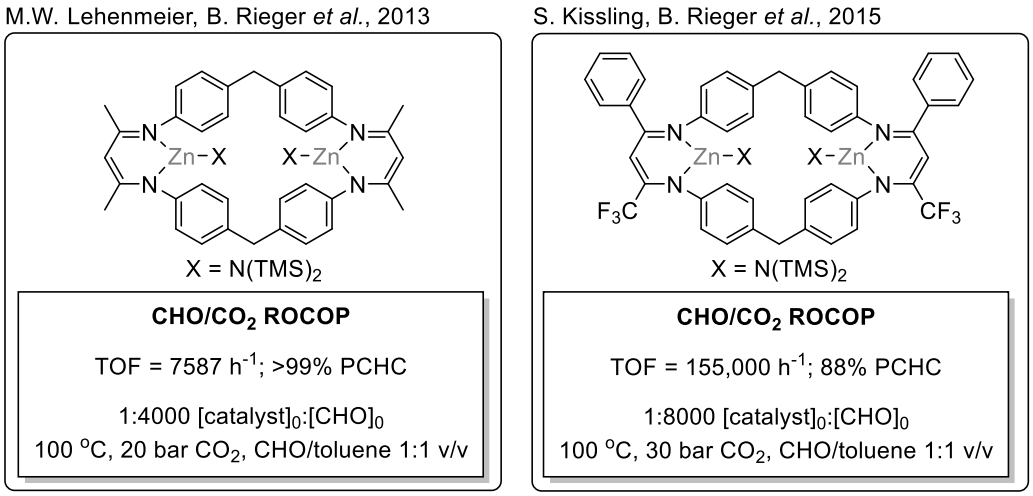


Figure 1.16. Structures and performances of tethered Zn(II)BDI catalysts for CHO/CO_2 ROCOP.[52, 53]

Introduction of electron-withdrawing trifluoromethyl groups, and phenyl groups, to the ligand scaffold enhanced the catalytic activity (Figure 1.16, RHS).[53] Under optimised conditions it achieved a TOF of 155,000 h^{-1}, although the proportion of carbonate linkages vs. epoxide was relatively low at 88% (1:8000 [catalyst]$_0$:[CHO]$_0$, 100 °C, 30 bar CO_2, toluene/CHO 1:1 v/v). The increase in activity with the electron-withdrawing groups was attributed to higher Zn(II) Lewis acidity, improving epoxide activation.

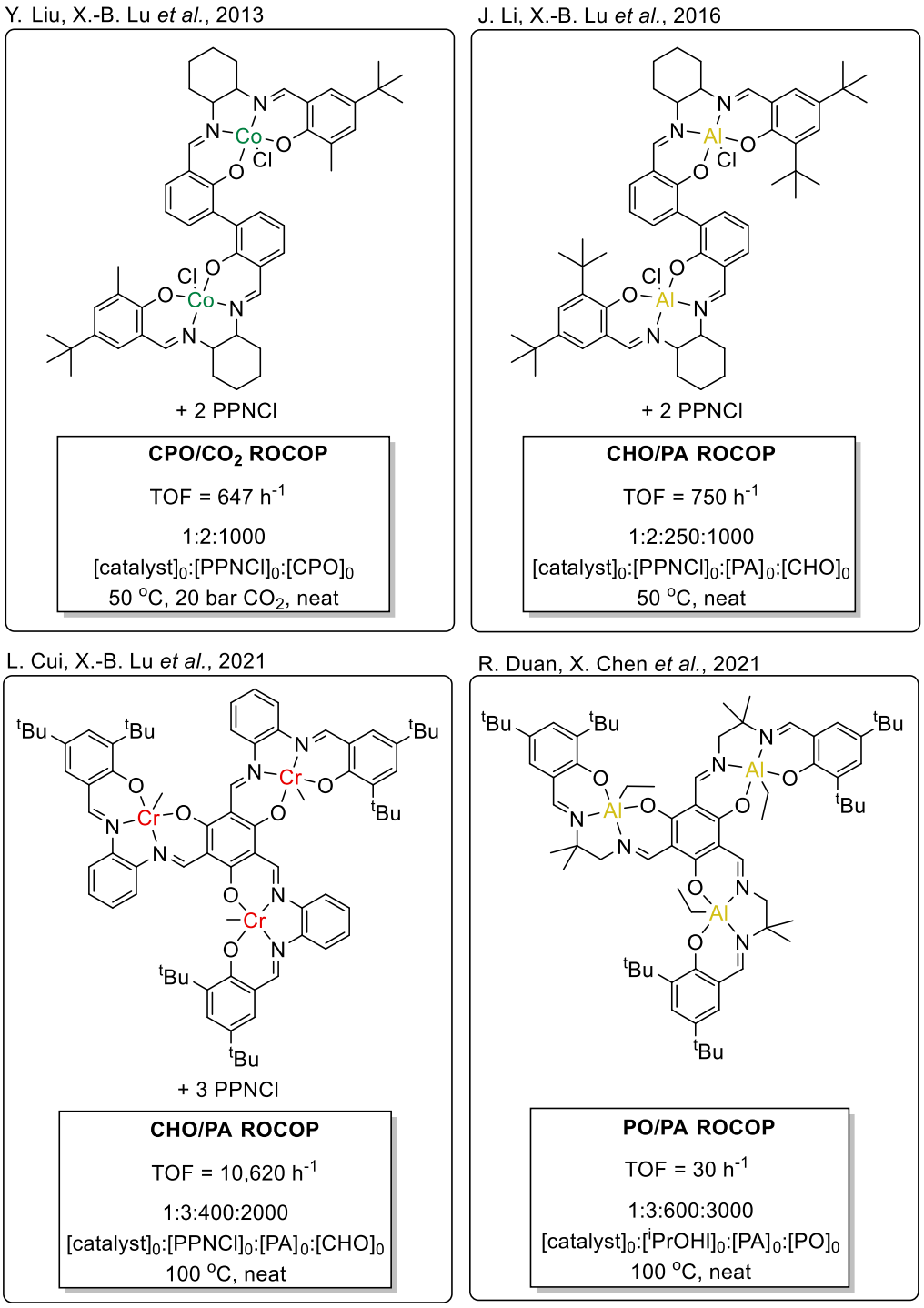


Figure 1.17. Structures and activities of examples of di- and tri-nuclear Co(III), Al(III), and Cr(III) catalysts for epoxide/CO_2 and epoxide/anhydride ROCOP.[54-57]

Many other di- and trinuclear catalysts have since been reported for epoxide/CO_2 and epoxide/anhydride ROCOP, and LA ROP.[54-61] A notable class of such catalysts feature M(III) salens tethered together by a central aromatic ring, resulting in multinuclear catalysts with relatively large intermetallic separations (typically 7 – 8 Å; Figure 1.17). These catalyst systems show activities

greater than those of monometallic M(III) salens, even when normalised with respect to the number of metal centres in the catalyst. As such, metal synergy is proposed, which is generally attributed to electronic communication between the metal centres, via the aromatic ligand system, increasing the electrophilicity of the metal centres.[57]

Notable examples of these catalyst systems include a dinuclear Co(III) catalyst for CPO/CO_2 ROCOP (TOF = 647 h^{-1}; 1:2:1000 $[catalyst]_0$:$[PPNCl]_0$:$[CPO]_0$, 50 °C, 20 bar CO_2, neat; Figure 1.17 top LHS), a similar Al(III) catalyst for CHO/PA ROCOP (TOF = 750 h^{-1}; 1:2:250:1000 $[catalyst]_0$:$[PPNCl]_0$:$[PA]_0$:$[CHO]_0$, 50 °C, neat; Figure 1.17 top RHS), and a trinuclear Cr(III) catalyst for CHO/PA ROCOP (TOF = 10620 h^{-1}; 1:3:400:2000 $[catalyst]_0$:$[PPNCl]_0$:$[PA]_0$:$[CHO]_0$, 100 °C, neat; Figure 1.17 bottom LHS).[54-56] A related tri-Al(III) catalyst was reported in 2021 by Chen and co-workers which was active for PO/PA ROCOP without the addition of PPNCl, albeit with a low TOF of 30 h^{-1} (1:3:600:3000 $[catalyst]_0$:$[^iPrOH]_0$:$[PA]_0$:$[PO]_0$, 100 °C, neat; Figure 1.17 bottom RHS).[57]

Wang and co-workers have reported various multinuclear catalysts featuring Al(III) porphyrin units (Figure 1.18).[62-64] In 2022, they reported a comb-shaped metallic oligomer catalyst for the production of poly(ether carbonate) polyols, featuring Al(III) porphyrin catalysts tethered to a poly(methyl methacrylate) (PMMA) oligomeric backbone (Figure 1.18, top).[64] Polymerisations were conducted in neat PO with varying starting proportions of CO_2, and the catalyst was shown to fully convert both epoxide and CO_2 to produce poly(ether carbonates) in the presence of 1000 equivalents of diacid (sebacic acid), with the proportion of carbonate linkages varying from 7 – 43% (TOF = 2500 – 1250 h^{-1}, 1:1:3,500-27,000:50,000 $[Al]_0$:$[PPNCl]_0$:$[diacid]_0$:$[CO_2]_0$:$[PO]_0$, 50 °C, neat).

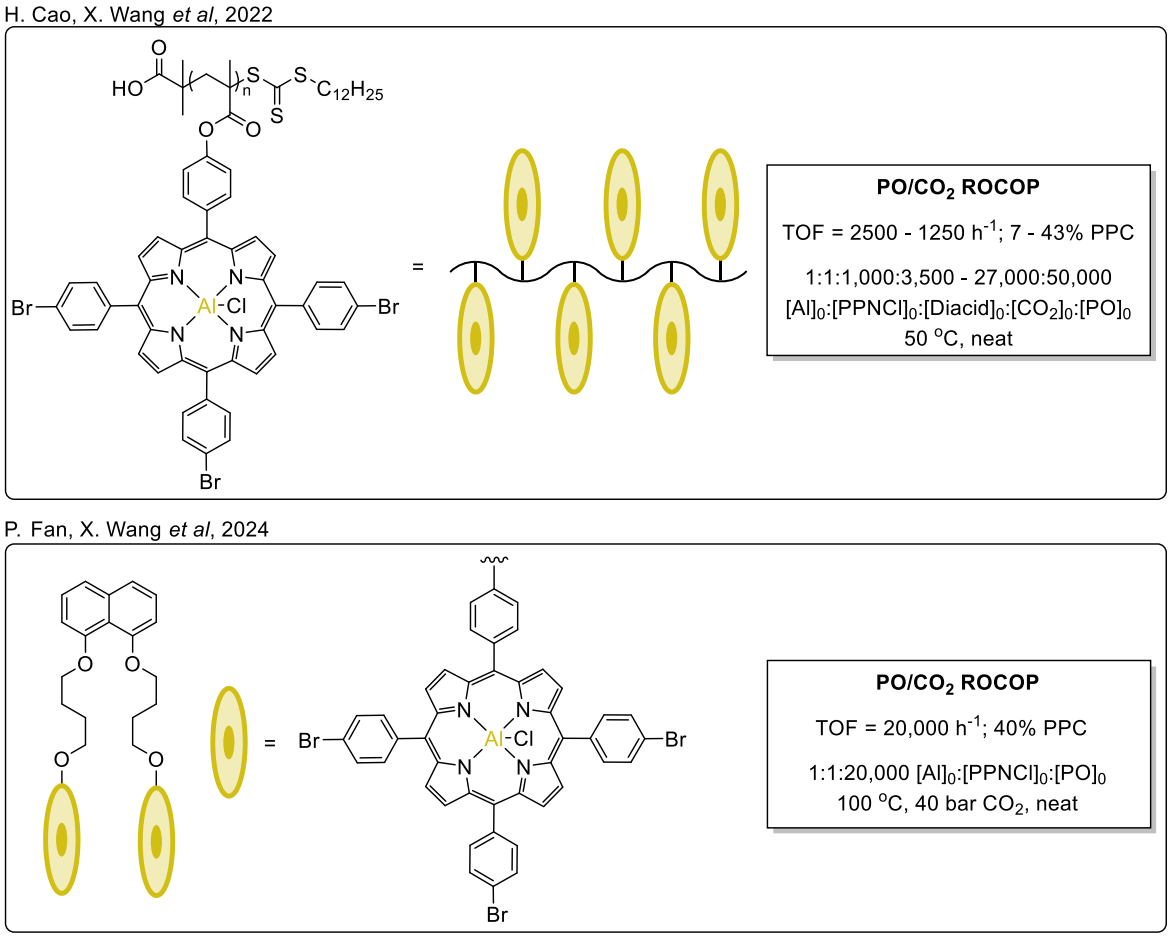


Figure 1.18. Top: Al(III) porphyrin catalysts tethered to a poly(methyl methacrylate) (PMMA) oligomeric backbone for PO/CO_2 ROCOP.[64] Bottom: Dinuclear Al(III) porphyrin catalyst featuring a naphthalene backbone.[63]

This year, the same group reported a series of dinuclear Al(III) porphyrin catalysts tethered to various acene backbones for the synthesis of poly(ether carbonate) polyols (Figure 1.18, bottom).[63] The most active of these catalysts featured a naphthalene backbone, achieving an activity of 20,000 h^{-1} at 100 °C, with 40% carbonate linkages but perfect polymer selectivity (1:1:20,000 $[Al]_0$:$[PPNCl]_0$:$[PO]_0$, 40 bar CO_2, neat). It should be noted that the activity is reported per Al(III) centre, whereas activities of multinuclear catalysts are generally reported per catalyst unit; as such, the TOF per catalyst molecule is 40,000 h^{-1}. This activity is exceptional, and it is highly unusual for a catalyst to maintain perfect polymer selectivity at such high temperatures. When the temperature is increased above 100 °C, the catalyst starts to produce cyclic carbonate. The high activity and polymer

selectivity of this catalyst was attributed to the flexibility of the catalyst tethers, allowing the intermetallic separation to vary throughout the polymerisation.[63]

1.4.1.3.3 Heteronuclear Catalysts

The chain-shutting ROCOP mechanism discussed before inspired the development of heterodinuclear complexes, as it follows that metal combinations could be chosen that are well-suited to each of the distinct, arguably opposite (i.e. epoxide activation vs. nucleophile labilisation), roles. The first of these investigations targeted a Zn(II)Mg(II) catalyst, ligated by the same macrocyclic ligand discussed before (Figure 1.19A).[65] This heterodinuclear catalyst had a greater activity for CHO/CO_2 ROCOP than the Zn(II)Zn(II) and Mg(II)Mg(II) homodinuclear analogues, as well as a greater activity than a 1:1 mixture of the two homodinuclear catalysts (Figure 1.19B). This result made clear that heterodinuclear synergy might be a useful tool for the design of highly active polymerisation catalysts.

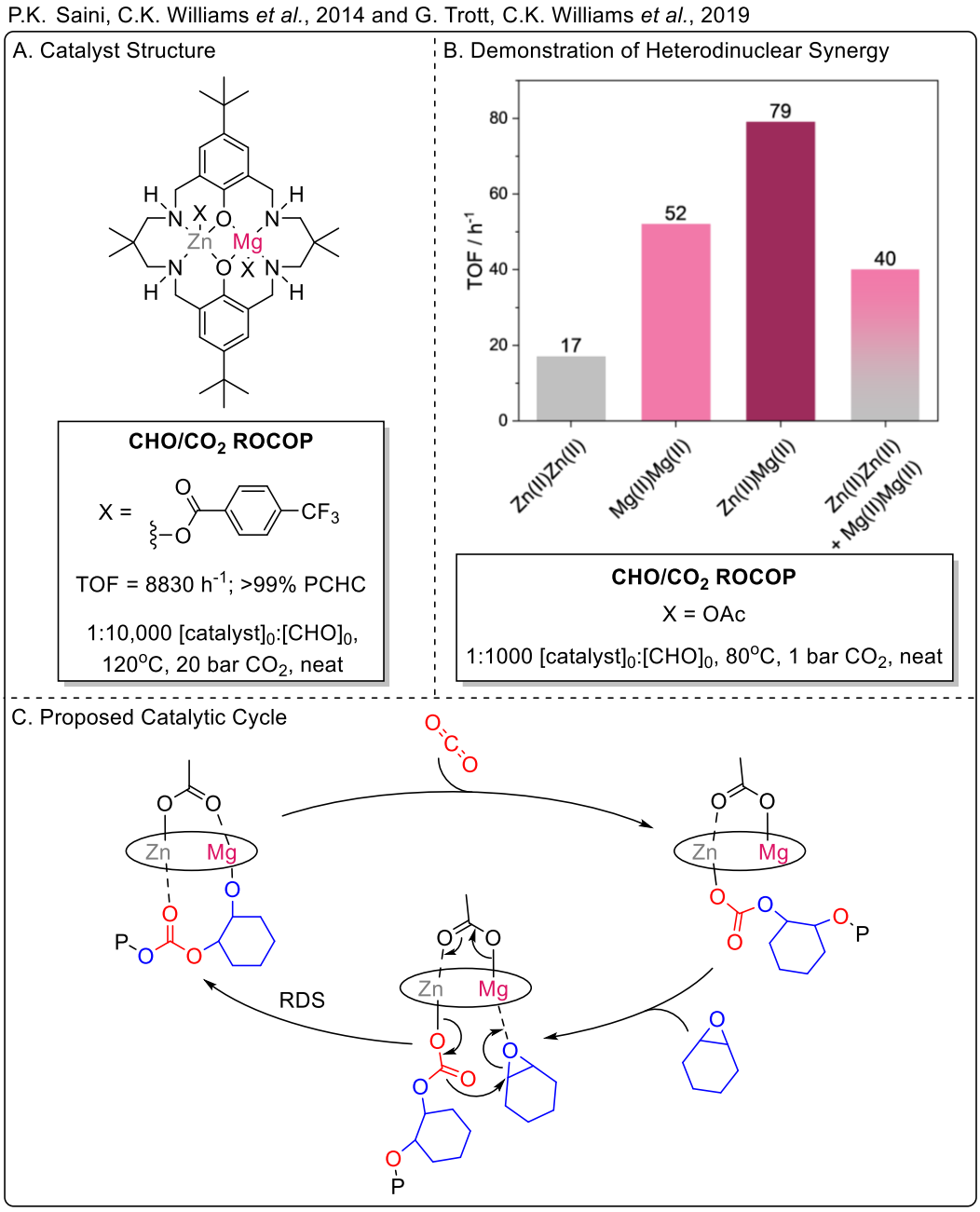


Figure 1.19. A. Structure and performance of a Zn(II)Mg(II) catalyst for CHO/CO_2 ROCOP; B. Comparison of activities of homodinuclear Zn(II)Zn(II) and Mg(II)Mg(II) catalysts, heterodinuclear Zn(II)Mg(II) catalyst, and a 50:50 mixture of the homodinuclear catalysts for CHO/CO_2 ROCOP; C. Proposed mechanism for CHO/CO_2 ROCOP catalysed by Zn(II)Mg(II) showing the chain-shuttling mechanism.[65, 66]

Optimisation of the co-ligands and reaction conditions resulted in a Zn(II)Mg(II) catalyst with CF_3-substituted benzoate co-ligands which had a TOF of up to 8830 h^{-1} for CHO/CO_2 ROCOP when the temperature and pressure were increased to 120 °C and 20 bar, respectively (Figure 1.19A).[66]

A DFT study of the Zn(II)Mg(II) catalyst and its homodinuclear analogues indicated that, in the rate-determining step, the Zn(II) centre was responsible for providing a labile carbonate nucleophile, while the Mg(II) centre was responsible for activating epoxide monomer (Figure 1.19C).[66]

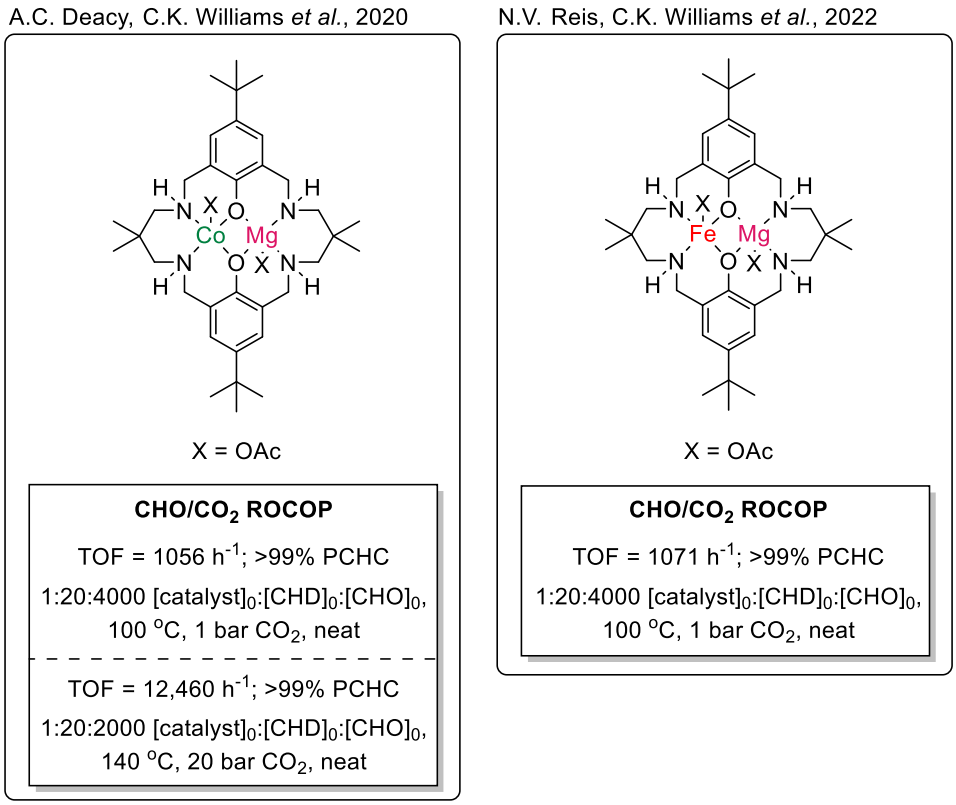


Figure 1.20. Structures and performances of Co(II)Mg(II) and Fe(II)Mg(II) catalysts for CHO/CO_2 ROCOP.[67, 68]

Other metal combinations for CHO/CO_2 ROCOP were subsequently investigated, but while some combinations showed excellent activities, not all combinations were synergic.[67-70] Explaining the lack of synergy was tentatively attributed to poor size-match between the ligand and metals in the case of Zn(II)M(I/II) (M(I/II) = Group I and II metal) combinations.[69]

A highly-active Co(II)Mg(II) catalyst for CHO/CO_2 ROCOP was reported in 2020, with a TOF of up to 12460 h^{-1} at 140 °C, while maintaining perfect selectivity for polycarbonate (1:20:2000 $[catalyst]_0:[CHD]_0:[CHO]_0$, 20 bar CO_2, neat; Figure 1.20, LHS).[67] Other M(II)Mg(II) combinations were investigated in a following report, which demonstrated that the Fe(II)Mg(II) catalyst showed comparable activity and selectivity to the Co(II)Mg(II) catalyst at 1 bar CO_2 pressure (1071 h^{-1} and

1056 h^{-1} respectively, >99% PCHC, 1:20:4000 [catalyst]$_0$:[CHD]$_0$:[CHO]$_0$, 100 °C, 1 bar CO_2, neat; Figure 1.20, RHS).[68]

Catalysts incorporating Group I and II metals are highly attractive due to their low cost, high natural abundance, low toxicity, and lack of colour. As such, ligand systems featuring oxygenated binding pockets were targeted to optimise their coordination.

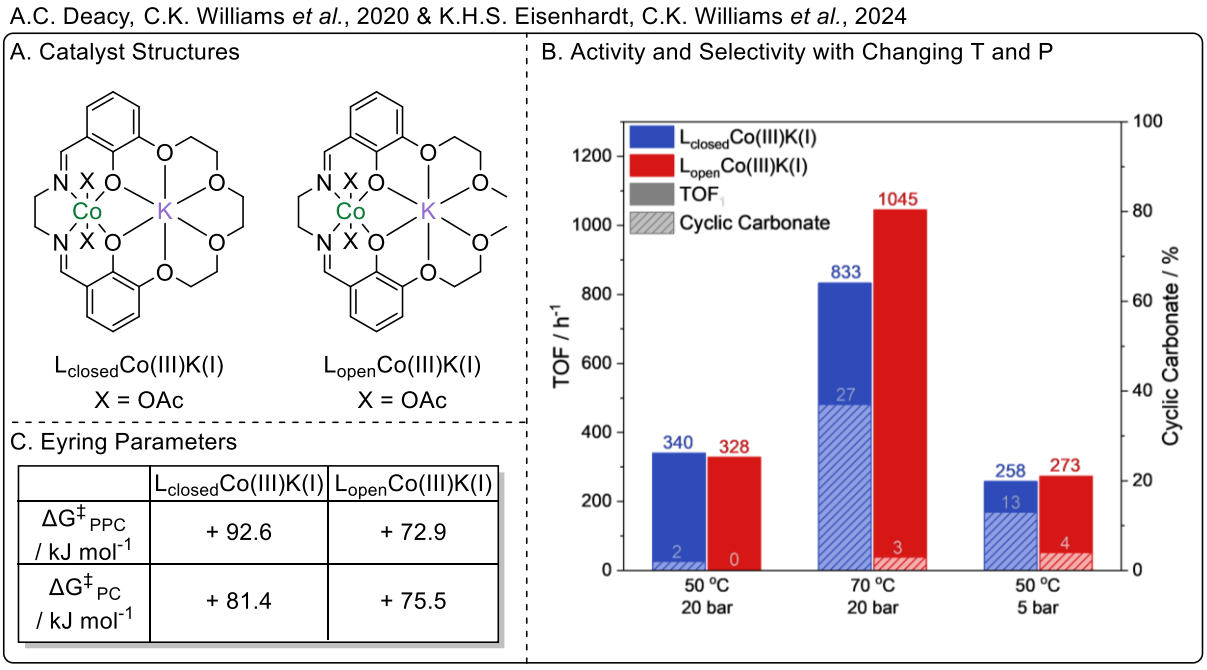


Figure 1.21. A. Structures of related Co(III)K(I) catalysts for epoxide/CO_2 ROCOP; B. Comparison of the two catalysts for PO/CO_2 ROCOP under varying temperatures and CO_2 pressures.[71, 72]

In 2020, we reported a series of Co(III)M(I) (M(I) = Na, K, Rb, Cs) catalysts for the ROCOP of PO and CO_2 (Figure 1.21A, L_{closed}Co(III)K(I)).[71] These were the first heterodinuclear catalysts for this polymerisation. In general, PO/CO_2 ROCOP is demanding when compared to the ROCOP of cyclic epoxides and CO_2, due to the reduced ring-strain associated with the aliphatic epoxide. The Co(III)K(I) catalyst was the most active, which was attributed at the time to the size-match between the K(I) centre and the oxygenated ligand binding pocket. The Co(III)K(I) complex was an excellent catalyst for PO/CO_2 ROCOP, with a TOF of 340 h^{-1} at 50 °C and 20 bar CO_2 pressure, up to 800 h^{-1} at 70 °C and 30 bar CO_2 pressure (1:20:4000 [catalyst]$_0$:[CHD]$_0$:[PO]$_0$, neat).

The performance of this catalyst was improved by severing one of the ligand ether carbon-carbon bonds, to create an "open" analogue (Figure 1.21A, L_{open}Co(III)K(I)).[72] While their performances at 50 °C and 20 bar CO_2 were comparable, L_{open}Co(III)K(I) maintains a high selectivity and activity even at elevated temperatures and reduced CO_2 pressures (Figure 1.21B). The high activity of L_{open}Co(III)K(I) was attributed to it having an experimentally measured $\Delta G^{\ddagger}$ almost 20 kcal mol^{-1} lower than that of L_{closed}Co(III)K(I) (Figure 1.21C).[24, 71, 72]

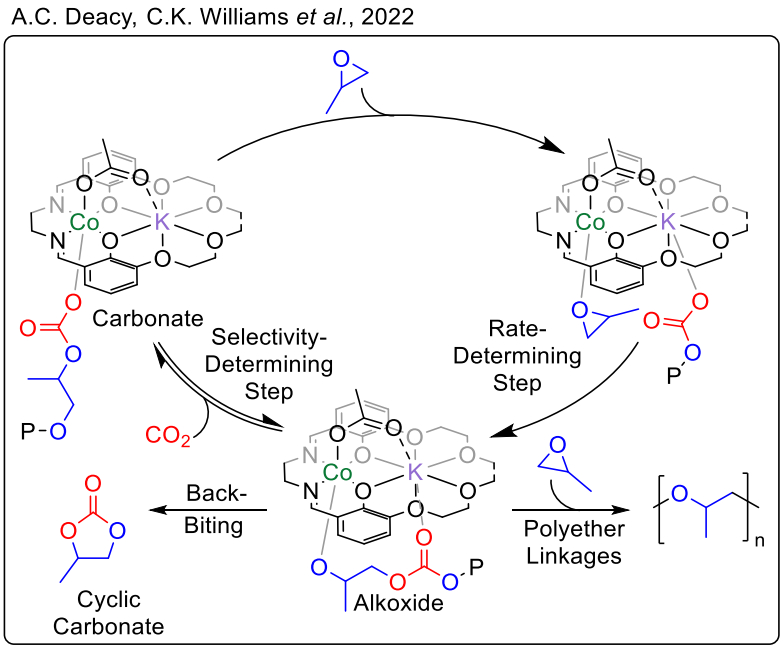


Figure 1.22. Proposed dinuclear metallate mechanism for PO/CO_2 ROCOP catalysed by L_{closed}Co(III)K(I) and L_{open}Co(III)K(I).[24]

A DFT study of L_{closed}Co(III)K(I) proposed a "dinuclear metallate" mechanism, where the rate-determining step is nucleophilic attack of a Co(III)-bound epoxide molecule by a K(I)-bound carbonate species (Figure 1.22).[24] This results in the formation of an alkoxide intermediate, which rapidly but reversibly inserts CO_2 to re-form the carbonate intermediate. This CO_2 insertion equilibrium was coined the "selectivity-determining step", as cyclic carbonate by-product formation is proposed to occur exclusively from the alkoxide intermediate. As such, the decrease in selectivity with increasing temperature and decreasing pressure can be explained by this CO_2 insertion equilibrium. At high temperatures, cyclic carbonate formation is favoured due to it being the

thermodynamic product of epoxide/CO_2 coupling. At low CO_2 pressures, the CO_2 insertion equilibrium shifts towards the alkoxide intermediate, from which cyclic carbonate can form.

The high selectivity of L_{open}Co(III)K(I) at low CO_2 pressures was attributed to a higher equilibrium constant, relative to L_{closed}Co(III)K(I), lying towards the carbonate intermediate even at lower CO_2 pressures. At high temperatures, the high selectivity for L_{open}Co(III)K(I), compared to L_{closed}Co(III)K(I), is attributed to the greater difference in the barriers to back-biting and polycarbonate propagation. For L_{closed}Co(III)K(I), the barrier to cyclic carbonate formation was measured to be lower than that of polycarbonate propagation (+81.4 vs. + 92.6 kJ mol^{-1}, respectively). For L_{open}Co(III)K(I), the opposite is seen; the barrier to polycarbonate propagation is lower than that of cyclic carbonate formation (+72.9 vs. +75.5 kJ mol^{-1}), favouring the formation of polycarbonate over cyclic carbonate even at higher temperatures (Figure 1.21C).[24, 72]

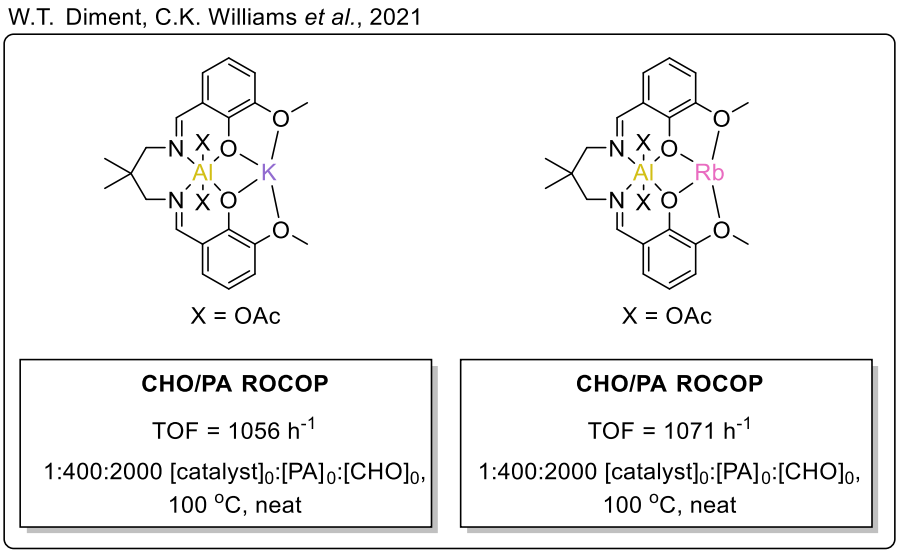


Figure 1.23. Structures and performances of Al(III)K(I) and Al(III)Rb(I) catalysts for CHO/PA ROCOP.[73]

A related Al(III)M(I) catalyst series for epoxide/anhydride ROCOP was reported in 2021 (Figure 1.23).[73] The Al(III)K(I) and Al(III)Rb(I) catalysts were the most active, with comparable activities (TOF = 1136 h^{-1} and 1072 h^{-1} respectively, 1:400:2000 $[catalyst]_0:[PA]_0:[CHO]_0$, 100 °C, neat).

While many high-performance monometallic LA ROP catalysts have been reported in the literature, heterodinuclear catalysts showing enhanced rates from intermetallic synergy have only recently been reported.

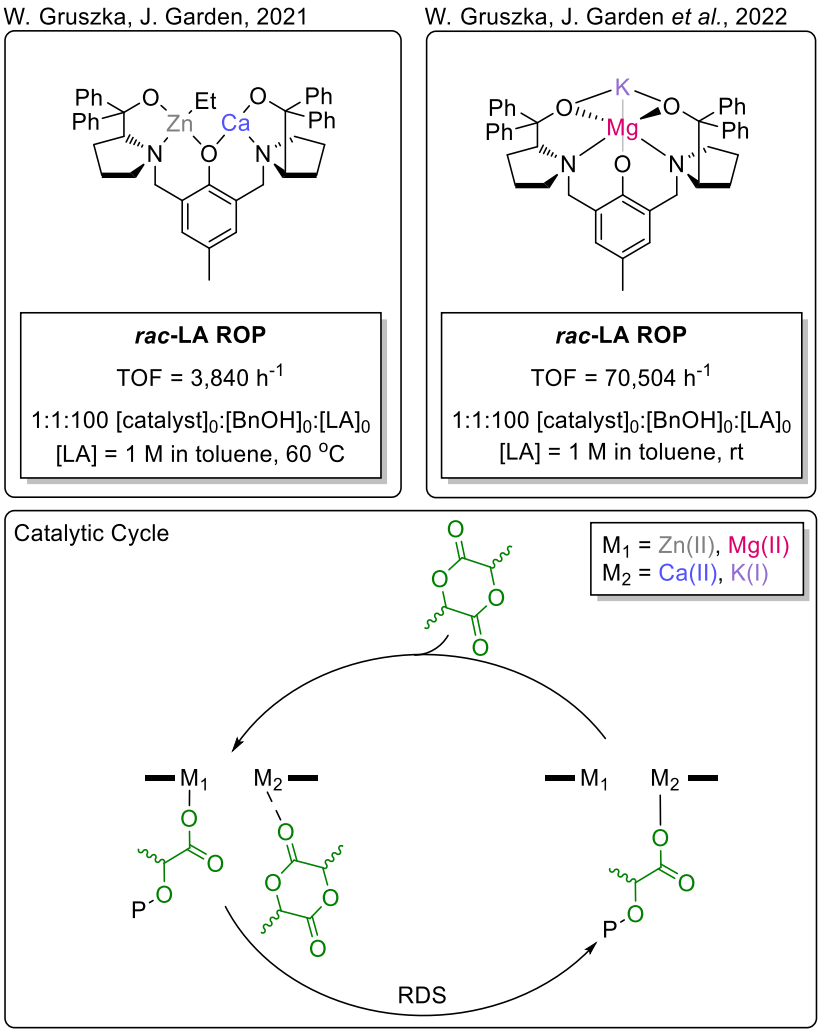


Figure 1.24. Top: Structures and performances of heterodinuclear catalysts for LA ROP; botton: proposed dinuclear mechanism for LA ROP.[74, 75]

Garden and co-workers reported various heterodinuclear catalysts for LA ROP, including a Zn(II)Ca(II) heterodinuclear catalyst coordinated by a prophenol ligand (Figure 1.24A LHS).[75] This catalyst had a TOF of 3,840 h^{-1} at 60 °C, and was more active than analogous Zn(II)Zn(II) and Zn(II)Mg(II) catalysts (1:1:100 $[catalyst]_0$:$[BnOH]_0$:$[LA]_0$, $[LA]_0$ = 1 M in toluene, 60 °C). The higher activity was attributed to the larger ionic radius of the Ca(II) centre, allowing greater surface area for monomer coordination in the rate-determining step (Figure 1.24B). The same group also reported

a K(I)Mg(II) catalyst, using the same ligand structure, which was able to convert 98 equivalents of *rac*-LA in 5 s at room temperature, corresponding to a TOF of 70,504 h^{-1} (1:1:100 $[catalyst]_0$:$[BnOH]_0$:$[LA]_0$, $[LA]_0$ = 1 M in toluene, rt; Figure 1.24, upper RHS).[76]

1.5 Structure-Activity Relationships

Although intermetallic synergy is often used to explain the high activities and selectivities of multinuclear polymerisation catalysts, it is very rarely systematically explored and understood. Even when series of catalysts are synthesised, with systematic variation of structural factors (e.g. metal combinations, ligand structure), structure-activity correlations can be challenging to find.

Ideally, structure-activity relationships would be built upon parameters that can be measured directly in the active catalyst species, during catalysis, using *in-situ* or *operando* measurements.[77-79] Generally, these are spectroscopic in nature, such as IR, Raman, NMR, UV-vis, and XAS.[79] This can be challenging, due to the low concentration of catalyst used during catalysis compared to the concentration of reactants, products, solvent, etc.; the short-lived nature of catalyst intermediates; and the formation of mixtures of species during catalysis, resulting in complex data which can be difficult to interpret. In particular, *operando* studies of homogeneous catalysts are far underrepresented compared to those with heterogeneous catalysts.[79]

Structure-activity relationships can also be investigated through characterisation of the synthesised pro-catalyst. These can include, for example, bond lengths or intermetallic separations measured by X-ray diffraction, or calculated from DFT; chemical shifts from NMR spectroscopy; redox half-potentials measured by cyclic voltammetry; positions and/or intensities of transitions in UV-vis and IR spectroscopies.

Often, structure-activity relationships are instead explored with structural, thermodynamic, and/or kinetic parameters that are intrinsic to specific metals, rather than the catalyst itself. Common examples include: ionic radii (determined from X-ray crystallography of ionic lattices); electronegativity (calculated from bond dissociation energies); metal hydrolysis constants (i.e. pK_a of the metal aqua complex; traditionally measured by pH titrations); bond dissociation energies (traditionally measured via calorimetry); oxophilicity/thiophilicity (measured by bond dissociation

enthalpies of M-O and M-S bonds); water exchange rate constants (measured using variable pressure NMR spectroscopy experiments).[80-84]

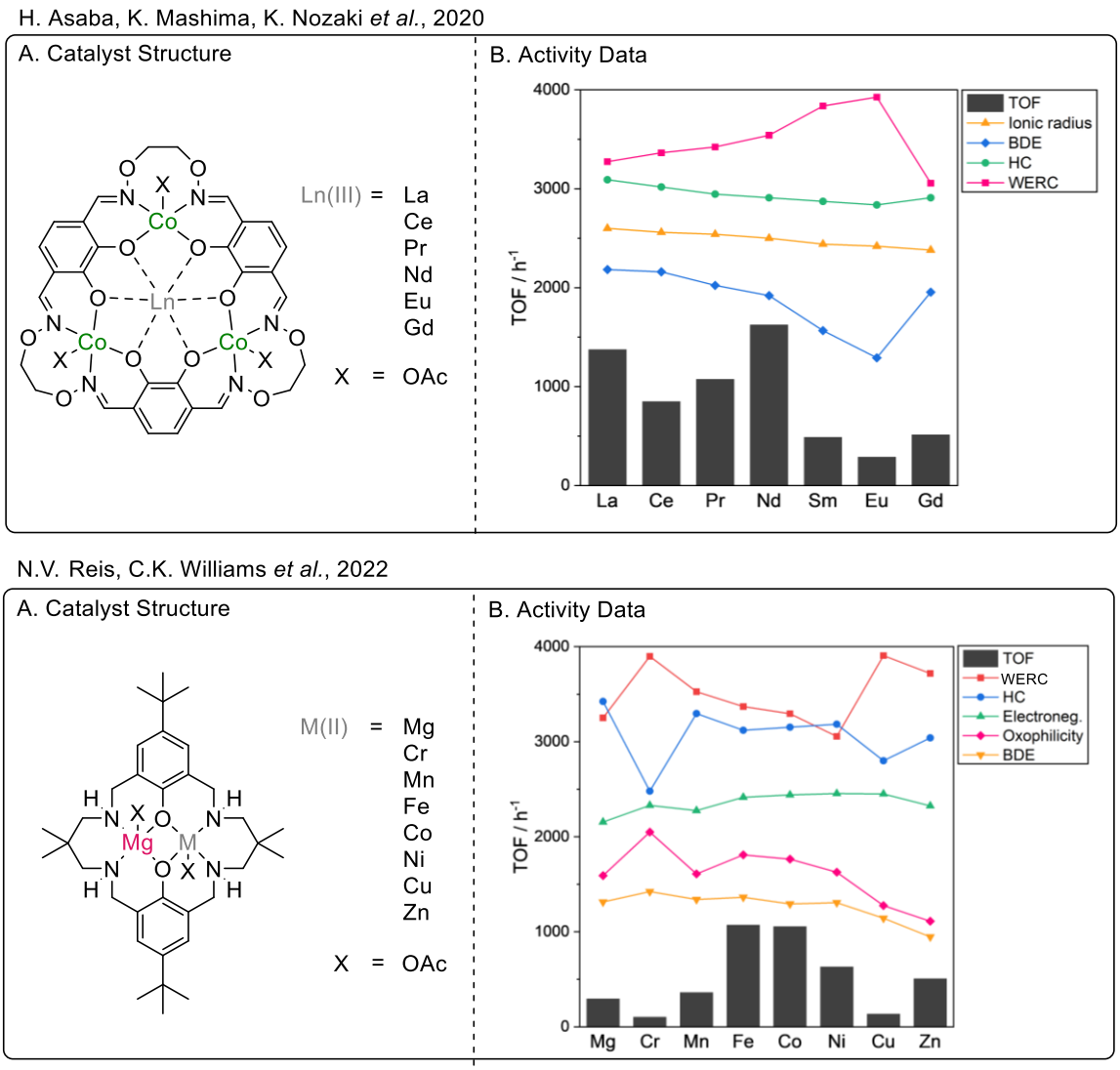


Figure 1.25. A. Catalyst structures and B. Activity and physical parameters (BDE = M-O bond dissociation energy; HC = hydrolysis constant; WERC = water exchange rate constant) across the tested metal series for a Co_3Ln catalyst system (top) and a Mg(II)M catalyst (bottom).[68, 85]

For example, Mashima and co-workers synthesised a series of tetranuclear Ln(III)Co(II)$_3$ (Ln(III) = La, Ce, Pr, Nd, Eu, Gd) catalysts for CHO/CO_2 ROCOP but could not find any correlation between activity and lanthanide ionic radius, bond dissociation energies, hydrolysis constant, or water exchange rates (Figure 1.25 top).[85]

Our group investigated a series of Mg(II)M(II) (M(II) = Mg, Cr, Mn, Fe, Co, Ni, Cu, Zn) catalysts, also for CHO/CO_2 ROCOP, but no correlation could be found between activity and M(II) ionic radius, bond dissociation energy, water exchange constant, electronegativity, or oxophilicity (Figure 1.25 bottom).[85]

1.5.1 Role of Metals

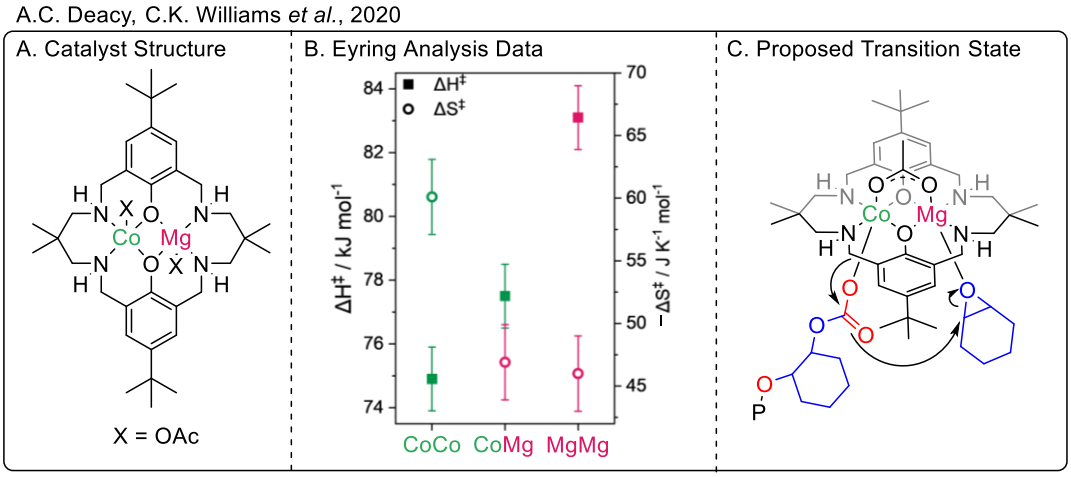


Figure 1.26. A. Co(II)Mg(II) catalyst structure; B. enthalpic and entropic contributions to ΔG‡ of the Co(II)Co(II), Mg(II)Mg(II), and Co(II)Mg(II) dinuclear catalysts for CHO/CO_2 ROCOP; C. Proposed rate-determining transition state for CHO/CO_2 ROCOP catalysed by Co(II)Mg(II).[67]

In 2020, we reported a Co(II)Mg(II) catalyst which showed excellent activities for the ROCOP of CHO and CO_2 (TOF = 12,460 h^{-1} (140 °C), 3,200 (100 °C) and >99% polycarbonate selectivity; 1:20:4000 $[catalyst]_0$:$[CHD]_0$:$[CHO]_0$, neat CHO, 20 bar CO_2; Figure 1.26A).[67] Eyring analysis of the heterodinuclear catalyst and its homodinuclear analogues revealed the roles of each of the metals (Figure 1.26B). The Co(II) centre reduces the enthalpic barrier to epoxide ring-opening, which was attributed to the highly nucleophilic Co(II)-carbonate, while the Mg(II) centre reduces the entropy change (i.e. makes it less negative), perhaps due to its low bond directionality when coordinating epoxide (Figure 1.26C).

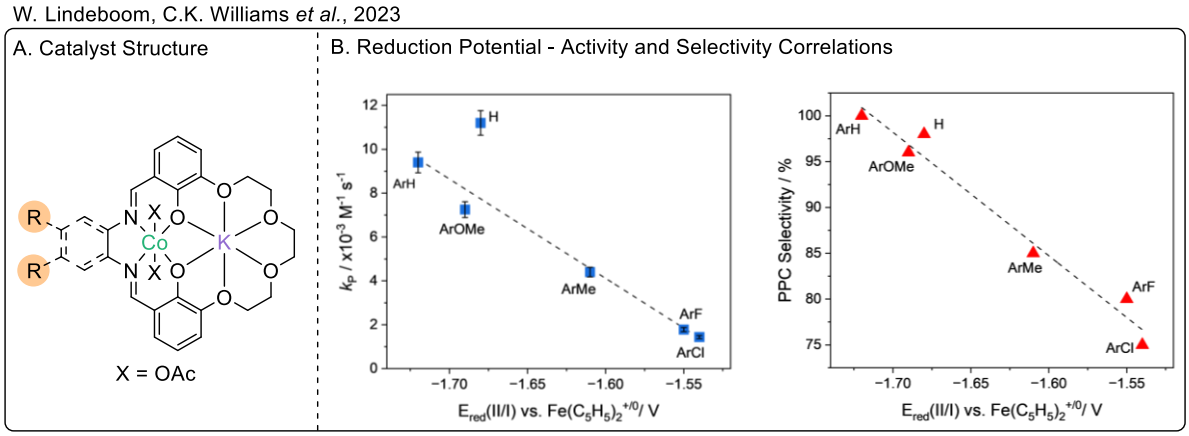


Figure 1.27. A. Co(III)K(I) catalyst structure with varying imine bridge structures; B. Correlations of activity (blue squares; LHS) and selectivity (red triangles; RHS) for PO/CO_2 ROCOP with Co(II/I) reduction potential.[86]

The role of the Co(III) centre in the previously-discussed Co(III)K(I) catalyst for PO/CO_2 ROCOP was investigated in a series of related Co(III)K(I) complexes, with phenylene imine linkers furnished with electron donating/withdrawing groups (Figure 1.27A).[86] The electron-density of the Co(III) centre was measured by cyclic voltammetry, and the data showed that relatively electron-rich Co(III) centres resulted in improved activities and selectivities for PO/CO_2 ROCOP (Figure 1.27B). This was attributed to the electron-rich Co(III) centres destabilising the key transition state of the rate-determining step.

1.5.2 Internuclear Separation

In multinuclear polymerisation catalysts, another key parameter that has been investigated is the separation between active centres.

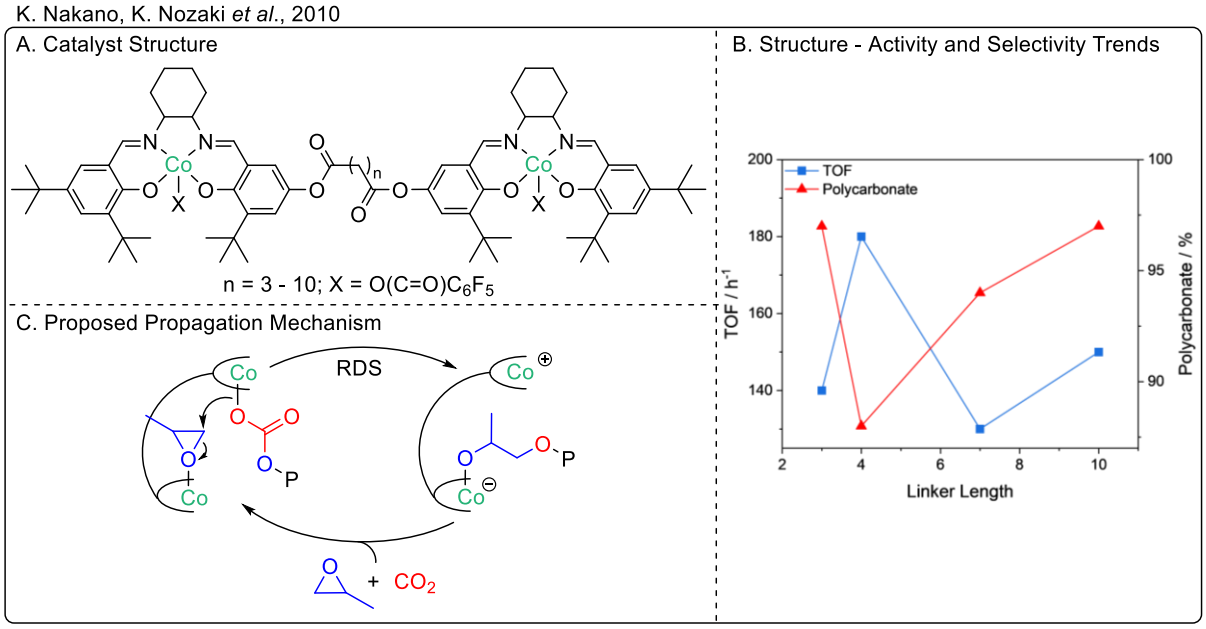


Figure 1.28. A. Tethered Co(III) salen catalyst with varying tether length; B. Correlations between tether length and activity and selectivity for polycarbonate; C. Proposed mechanism for propagation of PO/CO_2 ROCOP catalysed by the tethered Co(III) salen system.[87]

In 2010, Nozaki published a series of dinuclear Co(III) salen catalysts for PO/CO_2 ROCOP (Figure 1.27A).[87] The length of the linker between Co(III)-salen subunits was systematically varied between 3 – 10 carbons, with the highest activity achieved with n = 4 (Figure 1.28B). While this linker length maximised the rate for epoxide/CO_2 ROCOP, it also maximised the rate of epoxide homopolymerisation as this catalyst gave the lowest selectivity for polycarbonate over polyether (Figure 1.28B). This observation was explained by invoking a dinuclear mechanism, where one cobalt centre binds epoxide, and the other bind the carbonate chain-end in the rate-determining step (Figure 1.28C). The linker length must allow flexibility for the Co centres to be arranged in closer proximity in the rate-determining step.

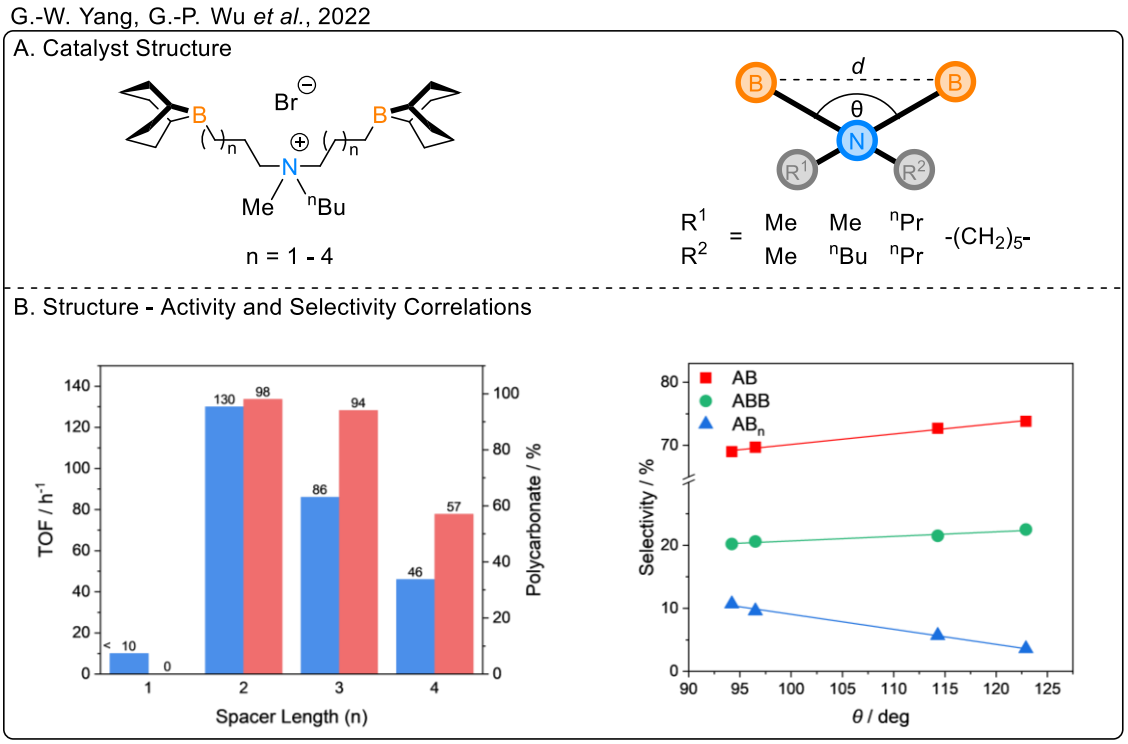


Figure 1.29. A. Structure of tethered di-borane and quaternary ammonium catalyst for CHO/CO_2 ROCOP with changing linker length and quaternary ammonium steric bulk; B. Correlations between activity and spacer length, and of selectivity for polycarbonate and B-N-B angle (dictated by steric bulk around the quaternary ammonium centre).[23]

In 2022, Wu and co-workers reported a series of tethered diborane-ammonium species with varying linker lengths between the active centres for CHO/CO_2 ROCOP (Figure 1.28A, LHS).[23] They found that the C_4 linker (n = 2) resulted in the greatest activity and selectivity for polycarbonate formation (Figure 1.29B, LHS). They also found that increasing the steric bulk around the quaternary ammonium moiety, while keeping the length of the linker the same, increased the B-B separation, and by extension the B-N-B angle (measured by single-crystal X-ray diffraction; Figure 1.28A, RHS). They were able to directly correlate this B-N-B angle to the selectivity for ether incorporation into the polycarbonate produced by the series of catalysts (Figure 1.29B, RHS). With increasing B-N-B angle (i.e. increasing steric bulk) the selectivity for polycarbonate linkages, and for individual polyether linkages (ABB, where A = CO_2 and B = epoxide) increase, while the proportion of extended polyether segments (ABB_n where and n ≥ 3) decreased.

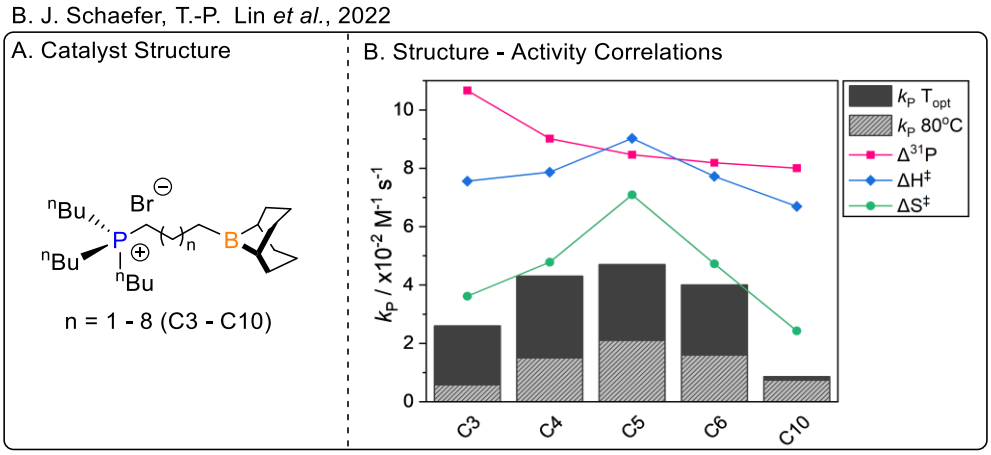


Figure 1.30. A. Structure of tethered borane – quaternary phosphonium catalyst for CHO/CO_2 ROCOP; B. Activities (bars) and Lewis acidity (measured by Gutmann-Beckett method; pink squares), and enthalpic (blue diamonds) and entropic (green circles) contributions to $\Delta H^{\ddagger}$ for the catalysts with varying linker lengths.[88]

A similar study, published in 2022 by Lin and co-workers, investigated the effect of changing linker length on tethered borane/quaternary phosphonium catalysts for CHO/CO_2 ROCOP (Figure 1.30A).[88] They also found that there was an optimum linker length of C_5 (n = 3; Figure 1.30B). They explored the roots of this trend by measuring the Lewis acidity of the catalysts by using the Guttman-Beckett method. This involves measuring the ^{31}P NMR spectrum of the catalyst combined with triethylphosphate (TEP); coordination of the catalyst will cause the TEP chemical shift to shift proportionally to its Lewis acidity. They also performed Eyring analysis on each catalyst to calculate $\Delta H^{\ddagger}$ and $\Delta S^{\ddagger}$ of rate-determining epoxide ring-opening. The Lewis acidity of the catalyst systems decrease with increasing linker length, but this does not correlate with activity. There seems to be a trade-off between $\Delta H^{\ddagger}$ and $\Delta S^{\ddagger}$; favourable (i.e. small and positive) $\Delta H^{\ddagger}$ values seem to be accompanied by unfavourable (i.e. more negative) $\Delta S^{\ddagger}$ values, and vice-versa. The most active catalyst, with a C_5 linker, has a relatively favourable $\Delta S^{\ddagger}$ of – 88 J K^{-1} mol^{-1}, but a relatively unfavourable $\Delta H^{\ddagger}$ of + 67.7 kJ mol^{-1}. The authors suggest that the C_5 linker stabilises the carbonate resting-state due to this P-B separation, but that the conformational entropy change due to the catalyst structural rearrangement going from the resting state to more "open" transition state is less negative.

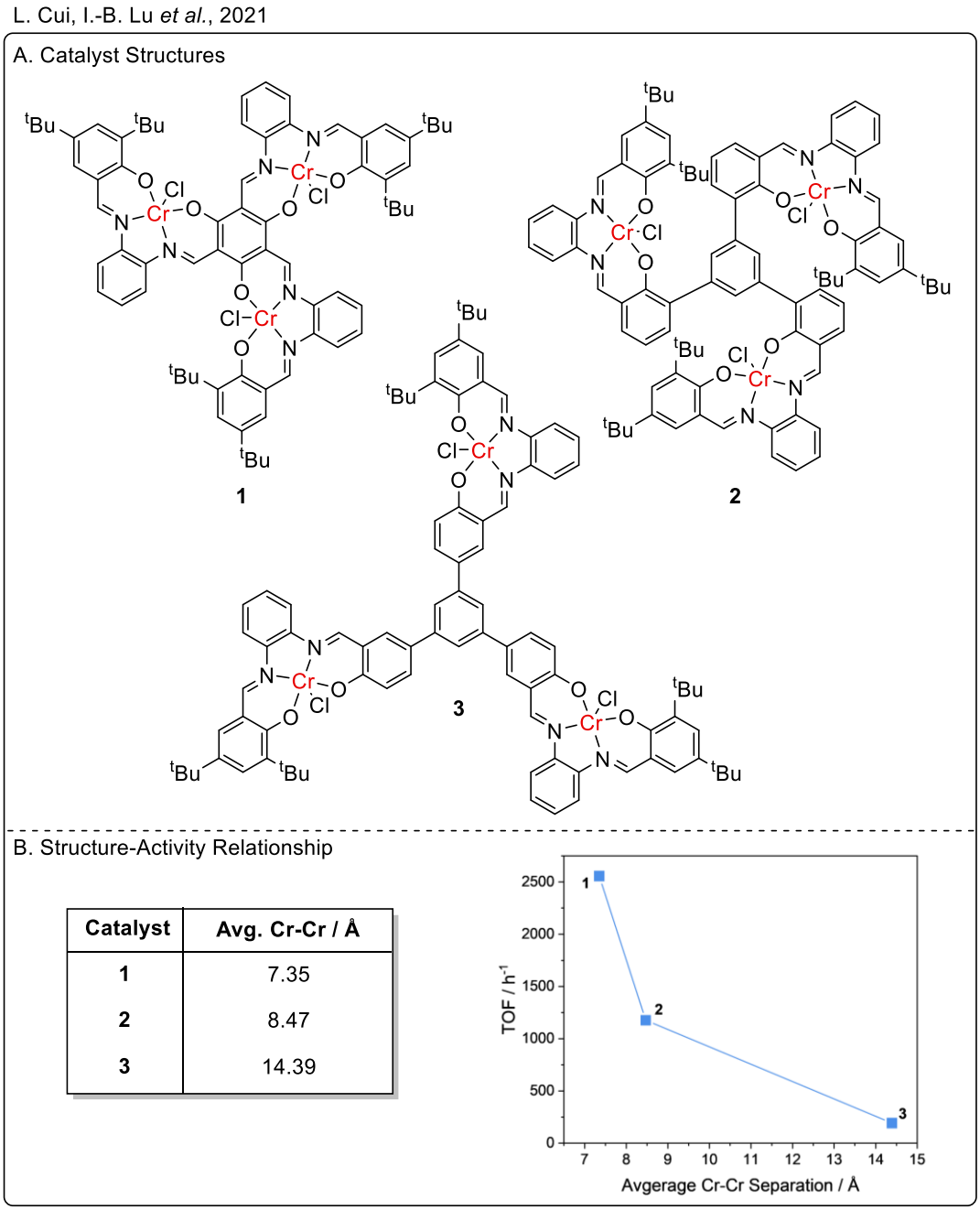


Figure 1.31. A. Structures of tri-Cr(III) tethered salen catalysts for epoxide/anhydride ROCOP with varying intermetallic separations; B. Correlation of activity with increasing intermetallic separation.[56]

Lu and co-workers investigated a series of trinuclear Cr(III) salphen catalysts for the ROCOP of various epoxides and anhydrides in 2021.[56] The average intermetallic separation between the three Cr(III) centres was systematically increased from 7.35 – 14.39 Å (calculated by DFT) by altering the aromatic tethered-salphen ligand (Figure 1.31A). They found that the most active catalyst for CHO/CO_2 ROCOP showed the narrowest intermetallic separation (**1**; Cr-Cr = 7.35 Å; 1:3:1200:6000

[catalyst]$_0$:[PPNCl]$_0$:[PA]$_0$:[CHO]$_0$, 60 °C, neat), while the larger intermetallic separation catalysts had reduced activities. In particular, the catalyst with an intermetallic separation of 14.39 Å has a markedly reduced activity of 192 h^{-1} (1:3:1200:6000 [catalyst]$_0$:[PPNCl]$_0$:[PA]$_0$:[CHO]$_0$, 60 °C, neat; Figure 1.31B). This was attributed to this catalyst undergoing CHO/PA ROCOP via a predominantly monometallic mechanism.

1.6 Aims and Objectives

This thesis will focus on exploring structure-activity relationships in dinuclear catalysts for the ring-opening copolymerisation of epoxides with CO_2 or anhydrides, and for the ring-opening polymerisation of *rac*-lactide. Robust and general structure-activity and/or structure-selectivity relationships are lacking in polymerisation catalysis, but should be prioritised to aid in the design of future catalysts. Chapters two to four will explore the effects of s-block metal Lewis acidity, and of intermetallic separation, for sustainable polymerisation catalysts (Figure 1.32).

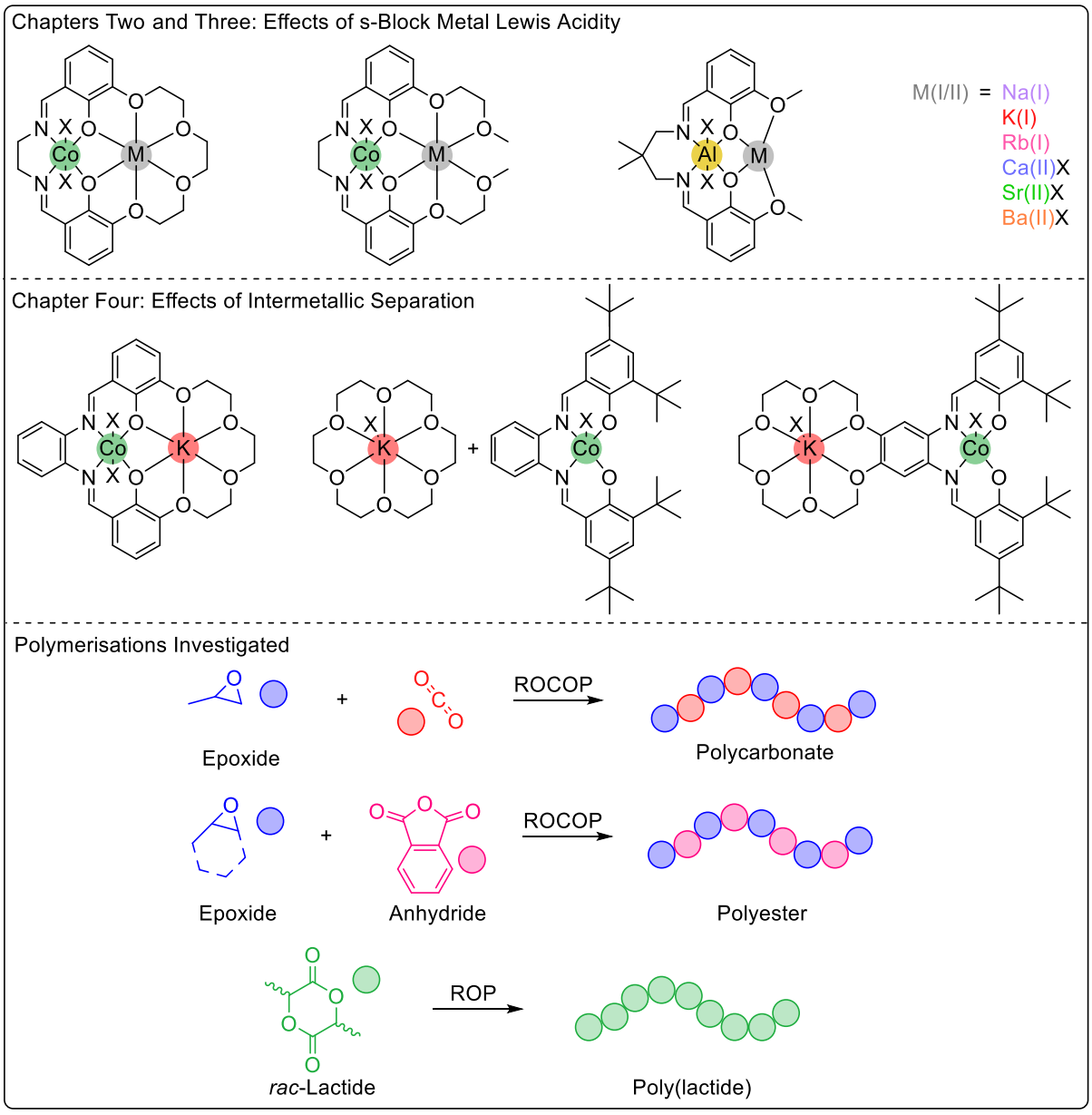


Figure 1.32. Summary of catalyst structures and polymerisations investigated in Chapters two to four.

Chapter two will focus on a series of Co(III)M(I/II) catalysts, where M(I/II) = Na(I), K(I), Rb(I), Cs(I), Ca(II), Sr(II), and Ba(II), and explore their activities and selectivities for the ROCOP of PO and CO_2, of PO and PA, and for the ROP of *rac*-LA. Their performances will be compared to s-block metal Lewis acidity, ionic radius, and ligand binding strength, to determine whether any structure-activity correlations can be observed, and then related to the mechanism of polymerisation.

Chapter three will build upon Chapter Two by further exploring trends of activity and selectivity for epoxide/CO_2 and epoxide/anhydride ROCOP for two catalyst systems featuring different metal combinations and ligand scaffolds. The catalysts feature flexible ligand backbones, allowing the incorporation of larger s-block metals, as this allows the exploration of a wider range of Lewis acidities.

Chapter four will compare a series of three Co(III)K(I) catalysts for the ROCOP of PO and CO_2, and of PO and PA. The three catalysts consist of 1) a catalyst with a wide, fixed, intermetallic separation, 2) one with a narrow, fixed, intermetallic separation, and lastly 3) a bicomponent catalyst system, (Co(III) salen used in conjunction with a K(OAc)-18-crown-6 adduct) which is proposed to have a variable intermetallic separation. The effects of intermetallic separation on the performance of each catalyst for the targeted polymerisations is explored, and the mechanism of the novel wide intermetallic separation catalyst is explored for PO/PA ROCOP.

1.7 References

(1) Mark, H. F. *Giant Molecules*; Time-Life International, 1966.

(2) *Plastics - the Fast Facts 2023*. Plastics Europe, 2023. https://plasticseurope.org/knowledge-hub/plastics-the-fast-facts-2023/ (accessed 2024 May 27).

(3) Ritche, H. *How much of global greenhouse gas emissions come from plastics?* Our World in Data, 2023. https://ourworldindata.org/ghg-emissions-plastics (accessed 2024 May 27).

(4) Schyns, Z. O. G.; Shaver, M. P. Mechanical Recycling of Packaging Plastics: A Review. *Macromol. Rapid Commun.* **2021**, *42* (3), 2000415.

(5) Coates, G. W.; Getzler, Y. D. Y. L. Chemical recycling to monomer for an ideal, circular polymer economy. *Nat. Rev. Mater.* **2020**, *5* (7), 501-516.

(6) Vidal, F.; van der Marel, E. R.; Kerr, R. W. F.; McElroy, C.; Schroeder, N.; Mitchell, C.; Rosetto, G.; Chen, T. T. D.; Bailey, R. M.; Hepburn, C.; et al. Designing a circular carbon and plastics economy for a sustainable future. *Nature* **2024**, *626* (7997), 45-57.

(7) Washington, K. E.; Kularatne, R. N.; Karmegam, V.; Biewer, M. C.; Stefan, M. C. Recent advances in aliphatic polyesters for drug delivery applications. *WIREs Nanomedicine and Nanobiotechnology* **2017**, *9* (4), e1446.

(8) Zhang, X.; Fevre, M.; Jones, G. O.; Waymouth, R. M. Catalysis as an Enabling Science for Sustainable Polymers. *Chem. Rev.* **2018**, *118* (2), 839-885.

(9) von der Assen, N.; Bardow, A. Life cycle assessment of polyols for polyurethane production using CO_2 as feedstock: insights from an industrial case study. *Green Chem.* **2014**, *16* (6), 3272-3280.

(10) Sulley, G. S.; Gregory, G. L.; Chen, T. T. D.; Peña Carrodeguas, L.; Trott, G.; Santmarti, A.; Lee, K.-Y.; Terrill, N. J.; Williams, C. K. Switchable Catalysis Improves the Properties of CO_2-Derived

Polymers: Poly(cyclohexene carbonate-b-ε-decalactone-b-cyclohexene carbonate) Adhesives, Elastomers, and Toughened Plastics. *J. Am. Chem. Soc.* **2020**, *142* (9), 4367-4378.

(11) Kirillova, A.; Yeazel, T. R.; Asheghali, D.; Petersen, S. R.; Dort, S.; Gall, K.; Becker, M. L. Fabrication of Biomedical Scaffolds Using Biodegradable Polymers. *Chem. Rev.* **2021**, *121* (18), 11238-11304.

(12) Zhu, Y.; Romain, C.; Williams, C. K. Sustainable polymers from renewable resources. *Nature* **2016**, *540* (7633), 354-362.

(13) Balla, E.; Daniilidis, V.; Karlioti, G.; Kalamas, T.; Stefanidou, M.; Bikiaris, N. D.; Vlachopoulos, A.; Koumentakou, I.; Bikiaris, D. N. Poly(lactic Acid): A Versatile Biobased Polymer for the Future with Multifunctional Properties—From Monomer Synthesis, Polymerization Techniques and Molecular Weight Increase to PLA Applications. In *Polymers*, 2021; Vol. 13.

(14) Diment, W. T.; Lindeboom, W.; Fiorentini, F.; Deacy, A. C.; Williams, C. K. Synergic Heterodinuclear Catalysts for the Ring-Opening Copolymerization (ROCOP) of Epoxides, Carbon Dioxide, and Anhydrides. *Acc. Chem. Res.* **2022**, *55* (15), 1997-2010.

(15) McGuire, T. M.; Deacy, A. C.; Buchard, A.; Williams, C. K. Solid-State Chemical Recycling of Polycarbonates to Epoxides and Carbon Dioxide Using a Heterodinuclear Mg(II)Co(II) Catalyst. *J. Am. Chem. Soc.* **2022**, *144* (40), 18444-18449.

(16) McGuire, T. M.; Buchard, A.; Williams, C. Chemical Recycling of Commercial Poly(l-lactic acid) to l-Lactide Using a High-Performance Sn(II)/Alcohol Catalyst System. *J. Am. Chem. Soc.* **2023**, *145* (36), 19840-19848.

(17) Artham, T.; Doble, M. Biodegradation of Aliphatic and Aromatic Polycarbonates. *Macromolecular Bioscience* **2008**, *8* (1), 14-24.

(18) Langanke, J.; Wolf, A.; Hofmann, J.; Böhm, K.; Subhani, M. A.; Müller, T. E.; Leitner, W.; Gürtler, C. Carbon dioxide (CO_2) as sustainable feedstock for polyurethane production. *Green Chem.* **2014**, *16* (4), 1865-1870.

(19) Bhat, G. A.; Darensbourg, D. J. Coordination complexes as catalysts for the coupling reactions of oxiranes and carbon dioxide. *Coord. Chem. Rev.* **2023**, *492*, 215277.

(20) Madhavan Nampoothiri, K.; Nair, N. R.; John, R. P. An overview of the recent developments in polylactide (PLA) research. *Bioresour. Technol.* **2010**, *101* (22), 8493-8501.

(21) Darensbourg, D. J. Chain transfer agents utilized in epoxide and CO2 copolymerization processes. *Green Chem.* **2019**, *21* (9), 2214-2223.

(22) Kerr, R. W. F.; Williams, C. K. Zr(IV) Catalyst for the Ring-Opening Copolymerization of Anhydrides (A) with Epoxides (B), Oxetane (B), and Tetrahydrofurans (C) to Make ABB- and/or ABC-Poly(ester-alt-ethers). *J. Am. Chem. Soc.* **2022**, *144* (15), 6882-6893.

(23) Yang, G.-W.; Xu, C.-K.; Xie, R.; Zhang, Y.-Y.; Lu, C.; Qi, H.; Yang, L.; Wang, Y.; Wu, G.-P. Precision copolymerization of CO2 and epoxides enabled by organoboron catalysts. *Nature Synthesis* **2022**, *1* (11), 892-901.

(24) Deacy, A. C.; Phanopoulos, A.; Lindeboom, W.; Buchard, A.; Williams, C. K. Insights into the Mechanism of Carbon Dioxide and Propylene Oxide Ring-Opening Copolymerization Using a Co(III)/K(I) Heterodinuclear Catalyst. *J. Am. Chem. Soc.* **2022**, *144* (39), 17929-17938.

(25) Takeda, N.; Inoue, S. Polymerization of 1,2-epoxypropane and copolymerization with carbon dioxide catalyzed by metalloporphyrins. *Die Makromolekulare Chemie* **1978**, *179* (5), 1377-1381.

(26) Bernard, A.; Chatterjee, C.; Chisholm, M. H. The influence of the metal (Al, Cr and Co) and the substituents of the porphyrin in controlling the reactions involved in the copolymerization of

propylene oxide and cyclic anhydrides by porphyrin metal(III) complexes. *Polymer* **2013**, *54* (11), 2639-2646.

(27) Aida, T.; Inoue, S. Catalytic reaction on both sides of a metalloporphyrin plane. Alternating copolymerization of phthalic anhydride and epoxypropane with an aluminum porphyrin-quaternary salt system. *J. Am. Chem. Soc.* **1985**, *107* (5), 1358-1364.

(28) Darensbourg, D. J.; Yarbrough, J. C. Mechanistic Aspects of the Copolymerization Reaction of Carbon Dioxide and Epoxides, Using a Chiral Salen Chromium Chloride Catalyst. *J. Am. Chem. Soc.* **2002**, *124* (22), 6335-6342.

(29) Cohen, C. T.; Chu, T.; Coates, G. W. Cobalt Catalysts for the Alternating Copolymerization of Propylene Oxide and Carbon Dioxide: Combining High Activity and Selectivity. *J. Am. Chem. Soc.* **2005**, *127* (31), 10869-10878.

(30) Hosseini Nejad, E.; van Melis, C. G. W.; Vermeer, T. J.; Koning, C. E.; Duchateau, R. Alternating Ring-Opening Polymerization of Cyclohexene Oxide and Anhydrides: Effect of Catalyst, Cocatalyst, and Anhydride Structure. *Macromolecules* **2012**, *45* (4), 1770-1776.

(31) Inoue, S. Immortal polymerization: The outset, development, and application. *J. Polym. Sci., Part A: Polym. Chem.* **2000**, *38* (16), 2861-2871.

(32) Xia, W.; Salmeia, K. A.; Vagin, S. I.; Rieger, B. Concerning the Deactivation of Cobalt(III)-Based Porphyrin and Salen Catalysts in Epoxide/CO2 Copolymerization. *Chem. Eur. J.* **2015**, *21* (11), 4384-4390.

(33) Ren, W.-M.; Liu, Z.-W.; Wen, Y.-Q.; Zhang, R.; Lu, X.-B. Mechanistic Aspects of the Copolymerization of CO2 with Epoxides Using a Thermally Stable Single-Site Cobalt(III) Catalyst. *J. Am. Chem. Soc.* **2009**, *131* (32), 11509-11518.

(34) Zhang, D.; Boopathi, S. K.; Hadjichristidis, N.; Gnanou, Y.; Feng, X. Metal-Free Alternating Copolymerization of CO2 with Epoxides: Fulfilling "Green" Synthesis and Activity. *J. Am. Chem. Soc.* **2016**, *138* (35), 11117-11120.

(35) Hu, L.-F.; Zhang, C.-J.; Wu, H.-L.; Yang, J.-L.; Liu, B.; Duan, H.-Y.; Zhang, X.-H. Highly Active Organic Lewis Pairs for the Copolymerization of Epoxides with Cyclic Anhydrides: Metal-Free Access to Well-Defined Aliphatic Polyesters. *Macromolecules* **2018**, *51* (8), 3126-3134.

(36) Nakano, K.; Kamada, T.; Nozaki, K. Selective Formation of Polycarbonate over Cyclic Carbonate: Copolymerization of Epoxides with Carbon Dioxide Catalyzed by a Cobalt(III) Complex with a Piperidinium End-Capping Arm. *Angew. Chem. Int. Ed.* **2006**, *45* (43), 7274-7277.

(37) S, S.; Min, J. K.; Seong, J. E.; Na, S. J.; Lee, B. Y. A Highly Active and Recyclable Catalytic System for CO_2/Propylene Oxide Copolymerization. *Angew. Chem. Int. Ed.* **2008**, *47* (38), 7306-7309.

(38) Jeon, J. Y.; Eo, S. C.; Varghese, J. K.; Lee, B. Y. Copolymerization and terpolymerization of carbon dioxide/propylene oxide/phthalic anhydride using a (salen)Co(III) complex tethering four quaternary ammonium salts. *Beilstein J Org Chem* **2014**, *10*, 1787-1795.

(39) Jeon, J. Y.; Eo, S. C.; Varghese, J. K.; Lee, B. Y. Copolymerization and terpolymerization of carbon dioxide/propylene oxide/phthalic anhydride using a (salen)Co(III) complex tethering four quaternary ammonium salts. *Beilstein J. Org. Chem.* **2014**, *10*, 1787-1795.

(40) Abel, B. A.; Lidston, C. A. L.; Coates, G. W. Mechanism-Inspired Design of Bifunctional Catalysts for the Alternating Ring-Opening Copolymerization of Epoxides and Cyclic Anhydrides. *J. Am. Chem. Soc.* **2019**, *141* (32), 12760-12769.

(41) Deng, J.; Ratanasak, M.; Sako, Y.; Tokuda, H.; Maeda, C.; Hasegawa, J.-y.; Nozaki, K.; Ema, T. Aluminum porphyrins with quaternary ammonium halides as catalysts for copolymerization of cyclohexene oxide and CO2: metal–ligand cooperative catalysis. *Chem. Sci.* **2020**, *11* (22), 5669-5675.

(42) Yang, G.-W.; Zhang, Y.-Y.; Xie, R.; Wu, G.-P. Scalable Bifunctional Organoboron Catalysts for Copolymerization of CO2 and Epoxides with Unprecedented Efficiency. *J. Am. Chem. Soc.* **2020**, *142* (28), 12245-12255.

(43) Moore, D. R.; Cheng, M.; Lobkovsky, E. B.; Coates, G. W. Mechanism of the Alternating Copolymerization of Epoxides and CO2 Using β-Diiminate Zinc Catalysts: Evidence for a Bimetallic Epoxide Enchainment. *J. Am. Chem. Soc.* **2003**, *125* (39), 11911-11924.

(44) Jeske, R. C.; DiCiccio, A. M.; Coates, G. W. Alternating Copolymerization of Epoxides and Cyclic Anhydrides: An Improved Route to Aliphatic Polyesters. *J. Am. Chem. Soc.* **2007**, *129* (37), 11330-11331.

(45) O'Keefe, B. J.; Breyfogle, L. E.; Hillmyer, M. A.; Tolman, W. B. Mechanistic Comparison of Cyclic Ester Polymerizations by Novel Iron(III)−Alkoxide Complexes: Single vs Multiple Site Catalysis. *J. Am. Chem. Soc.* **2002**, *124* (16), 4384-4393.

(46) Kember, M. R.; Knight, P. D.; Reung, P. T. R.; Williams, C. K. Highly Active Dizinc Catalyst for the Copolymerization of Carbon Dioxide and Cyclohexene Oxide at One Atmosphere Pressure. *Angew. Chem. Int. Ed.* **2009**, *48* (5), 931-933.

(47) Buchard, A.; Kember, M. R.; Sandeman, K. G.; Williams, C. K. A bimetallic iron(iii) catalyst for CO2/epoxide coupling. *Chem. Commun.* **2011**, *47* (1), 212-214.

(48) Kember, M. R.; White, A. J. P.; Williams, C. K. Highly Active Di- and Trimetallic Cobalt Catalysts for the Copolymerization of CHO and CO2 at Atmospheric Pressure. *Macromolecules* **2010**, *43* (5), 2291-2298.

(49) Kember, M. R.; Williams, C. K. Efficient Magnesium Catalysts for the Copolymerization of Epoxides and CO2; Using Water to Synthesize Polycarbonate Polyols. *J. Am. Chem. Soc.* **2012**, *134* (38), 15676-15679.

(50) Buchard, A.; Jutz, F.; Kember, M. R.; White, A. J. P.; Rzepa, H. S.; Williams, C. K. Experimental and Computational Investigation of the Mechanism of Carbon Dioxide/Cyclohexene Oxide Copolymerization Using a Dizinc Catalyst. *Macromolecules* **2012**, *45* (17), 6781-6795.

(51) Jutz, F.; Buchard, A.; Kember, M. R.; Fredriksen, S. B.; Williams, C. K. Mechanistic Investigation and Reaction Kinetics of the Low-Pressure Copolymerization of Cyclohexene Oxide and Carbon Dioxide Catalyzed by a Dizinc Complex. *J. Am. Chem. Soc.* **2011**, *133* (43), 17395-17405.

(52) Lehenmeier, M. W.; Kissling, S.; Altenbuchner, P. T.; Bruckmeier, C.; Deglmann, P.; Brym, A.-K.; Rieger, B. Flexibly Tethered Dinuclear Zinc Complexes: A Solution to the Entropy Problem in CO2/Epoxide Copolymerization Catalysis? *Angew. Chem. Int. Ed.* **2013**, *52* (37), 9821-9826.

(53) Kissling, S.; Lehenmeier, M. W.; Altenbuchner, P. T.; Kronast, A.; Reiter, M.; Deglmann, P.; Seemann, U. B.; Rieger, B. Dinuclear zinc catalysts with unprecedented activities for the copolymerization of cyclohexene oxide and CO_2. *Chem. Commun.* **2015**, *51* (22), 4579-4582.

(54) Liu, Y.; Ren, W.-M.; Liu, J.; Lu, X.-B. Asymmetric Copolymerization of CO2 with meso-Epoxides Mediated by Dinuclear Cobalt(III) Complexes: Unprecedented Enantioselectivity and Activity. *Angew. Chem. Int. Ed.* **2013**, *52* (44), 11594-11598.

(55) Li, J.; Liu, Y.; Ren, W.-M.; Lu, X.-B. Asymmetric Alternating Copolymerization of Meso-epoxides and Cyclic Anhydrides: Efficient Access to Enantiopure Polyesters. *J. Am. Chem. Soc.* **2016**, *138* (36), 11493-11496.

(56) Cui, L.; Ren, B.-H.; Lu, X.-B. Trinuclear salphen–chromium(III)chloride complexes as catalysts for the alternating copolymerization of epoxides and cyclic anhydrides. *J. Polym. Sci.* **2021**, *59* (16), 1821-1828.

(57) Duan, R.; Zhou, Y.; Huang, Y.; Sun, Z.; Zhang, H.; Pang, X.; Chen, X. A trinuclear salen–Al complex for copolymerization of epoxides and anhydride: mechanistic insight into a cocatalyst-free system. *Chem. Commun.* **2021**, *57* (1), 133-136.

(58) Liu, Y.; Ren, W.-M.; Liu, C.; Fu, S.; Wang, M.; He, K.-K.; Li, R.-R.; Zhang, R.; Lu, X.-B. Mechanistic Understanding of Dinuclear Cobalt(III) Complex Mediated Highly Enantioselective Copolymerization of meso-Epoxides with CO2. *Macromolecules* **2014**, *47* (22), 7775-7788.

(59) Yu, I.; Acosta-Ramírez, A.; Mehrkhodavandi, P. Mechanism of Living Lactide Polymerization by Dinuclear Indium Catalysts and Its Impact on Isoselectivity. *J. Am. Chem. Soc.* **2012**, *134* (30), 12758-12773.

(60) Fliedel, C.; Vila-Viçosa, D.; Calhorda, M. J.; Dagorne, S.; Avilés, T. Dinuclear Zinc–N-Heterocyclic Carbene Complexes for Either the Controlled Ring-Opening Polymerization of Lactide or the Controlled Degradation of Polylactide Under Mild Conditions. *ChemCatChem* **2014**, *6* (5), 1357-1367.

(61) Normand, M.; Roisnel, T.; Carpentier, J. F.; Kirillov, E. Dinuclear vs. mononuclear complexes: accelerated, metal-dependent ring-opening polymerization of lactide. *Chem. Commun.* **2013**, *49* (99), 11692-11694.

(62) Chen, P.; Zhou, H.; Cao, H.; Zhuo, C.; Liu, S.; Wang, X. Polymeric catalyst with polymerization-enhanced Lewis acidity for CO2-based copolymers. *Chin. Chem. Lett.* **2023**, *34* (12), 108630.

(63) Fan, P.; Liu, S.; Zhang, R.; Zhuo, C.; Gao, F.; Pang, X.; Chen, X.; Wang, X. Rigid-Flexible Binuclear Catalysts: Boosting Activity for Copolymerization of CO2 and Propylene Oxide. *Macromolecules* **2024**, *57* (12), 5702-5711.

(64) Cao, H.; Zhang, R.; Zhou, Z.; Liu, S.; Tao, Y.; Wang, F.; Wang, X. On-Demand Transformation of Carbon Dioxide into Polymers Enabled by a Comb-Shaped Metallic Oligomer Catalyst. *ACS Catal.* **2022**, *12* (1), 481-490.

(65) Saini, P. K.; Romain, C.; Williams, C. K. Dinuclear metal catalysts: improved performance of heterodinuclear mixed catalysts for CO2–epoxide copolymerization. *Chem. Commun.* **2014**, *50* (32), 4164-4167.

(66) Trott, G.; Garden, J. A.; Williams, C. K. Heterodinuclear zinc and magnesium catalysts for epoxide/CO2 ring opening copolymerizations. *Chem. Sci.* **2019**, *10* (17), 4618-4627.

(67) Deacy, A. C.; Kilpatrick, A. F. R.; Regoutz, A.; Williams, C. K. Understanding metal synergy in heterodinuclear catalysts for the copolymerization of CO_2 and epoxides. *Nat. Chem.* **2020**, *12* (4), 372-380.

(68) Reis, N. V.; Deacy, A. C.; Rosetto, G.; Durr, C. B.; Williams, C. K. Heterodinuclear Mg(II)M(II) (M=Cr, Mn, Fe, Co, Ni, Cu and Zn) Complexes for the Ring Opening Copolymerization of Carbon Dioxide/Epoxide and Anhydride/Epoxide. *Chem. Eur. J.* **2022**, *28* (14), e202104198.

(69) Deacy, A. C.; Durr, C. B.; Garden, J. A.; White, A. J. P.; Williams, C. K. Groups 1, 2 and Zn(II) Heterodinuclear Catalysts for Epoxide/CO2 Ring-Opening Copolymerization. *Inorg. Chem.* **2018**, *57* (24), 15575-15583.

(70) Deacy, A. C.; Durr, C. B.; Williams, C. K. Heterodinuclear complexes featuring Zn(ii) and M = Al(iii), Ga(iii) or In(iii) for cyclohexene oxide and CO2 copolymerisation. *Dalton Trans.* **2020**, *49* (1), 223-231.

(71) Deacy, A. C.; Moreby, E.; Phanopoulos, A.; Williams, C. K. Co(III)/Alkali-Metal(I) Heterodinuclear Catalysts for the Ring-Opening Copolymerization of CO_2 and Propylene Oxide. *J. Am. Chem. Soc.* **2020**, *142* (45), 19150-19160.

(72) Eisenhardt, K. H. S.; Fiorentini, F.; Lindeboom, W.; Williams, C. K. Quantifying CO2 Insertion Equilibria for Low-Pressure Propene Oxide and Carbon Dioxide Ring Opening Copolymerization Catalysts. *J. Am. Chem. Soc.* **2024**, *146* (15), 10451-10464.

(73) Diment, W. T.; Gregory, G. L.; Kerr, R. W. F.; Phanopoulos, A.; Buchard, A.; Williams, C. K. Catalytic Synergy Using Al(III) and Group 1 Metals to Accelerate Epoxide and Anhydride Ring-Opening Copolymerizations. *ACS Catal.* **2021**, *11* (20), 12532-12542.

(74) Gruszka, W.; Garden, J. A. Advances in heterometallic ring-opening (co)polymerisation catalysis. *Nat. Commun.* **2021**, *12* (1), 3252.

(75) Gruszka, W.; Sha, H.; Buchard, A.; Garden, J. A. Heterometallic cooperativity in divalent metal ProPhenol catalysts: combining zinc with magnesium or calcium for cyclic ester ring-opening polymerisation. *Catal. Sci. Technol.* **2022**, *12* (4), 1070-1079.

(76) Gruszka, W.; Garden, J. A. Salt additives as activity boosters: a simple strategy to access heterometallic cooperativity in lactide polymerisation. *Chem. Commun.* **2022**, *58* (10), 1609-1612.

(77) Chung, R.; Hein, J. E. The More, The Better: Simultaneous In Situ Reaction Monitoring Provides Rapid Mechanistic and Kinetic Insight. *Top. Catal.* **2017**, *60* (8), 594-608.

(78) Diebolt, O.; van Leeuwen, P. W. N. M.; Kamer, P. C. J. Operando Spectroscopy in Catalytic Carbonylation Reactions. *ACS Catal.* **2012**, *2* (11), 2357-2370.

(79) Köhnke, K.; Wessel, N.; Esteban, J.; Jin, J.; Vorholt, A. J.; Leitner, W. Operando monitoring of mechanisms and deactivation of molecular catalysts. *Green Chem.* **2022**, *24* (5), 1951-1972.

(80) Luo, Y.-R. *Comprehensive handbook of chemical bond energies*; CRC Press, 2007.

(81) Shannon, R. D. Revised effective ionic radii and systematic studies of interatomic distances in halides and chalcogenides. *Acta Crystallographica Section A* **1976**, *32* (5), 751-767.

(82) Kepp, K. P. A Quantitative Scale of Oxophilicity and Thiophilicity. *Inorg. Chem.* **2016**, *55* (18), 9461-9470.

(83) Kumar, A.; Blakemore, J. D. On the Use of Aqueous Metal-Aqua pK_a Values as a Descriptor of Lewis Acidity. *Inorg. Chem.* **2021**, *60* (2), 1107-1115.

(84) Lincoln, S. F. Mechanistic Studies of Metal Aqua Ions: A Semi-Historical Perspective. *Helv. Chim. Acta* **2005**, *88* (3), 523-545.

(85) Asaba, H.; Iwasaki, T.; Hatazawa, M.; Deng, J.; Nagae, H.; Mashima, K.; Nozaki, K. Alternating Copolymerization of CO_2 and Cyclohexene Oxide Catalyzed by Cobalt–Lanthanide Mixed Multinuclear Complexes. *Inorg. Chem.* **2020**, *59* (12), 7928-7933.

(86) Lindeboom, W.; Deacy, A. C.; Phanopoulos, A.; Buchard, A.; Williams, C. K. Correlating Metal Redox Potentials to Co(III)K(I) Catalyst Performances in Carbon Dioxide and Propene Oxide Ring Opening Copolymerization. *Angew. Chem. Int. Ed.* **2023**, *62* (37), e202308378.

(87) Nakano, K.; Hashimoto, S.; Nozaki, K. Bimetallic mechanism operating in the copolymerization of propylene oxide with carbon dioxide catalyzed by cobalt–salen complexes. *Chem. Sci.* **2010**, *1* (3), 369-373.

(88) Schaefer, J.; Zhou, H.; Lee, E.; Lambic, N. S.; Culcu, G.; Holtcamp, M. W.; Rix, F. C.; Lin, T.-P. Tertiary and Quaternary Phosphonium Borane Bifunctional Catalysts for CO_2/Epoxide Copolymerization: A Mechanistic Investigation Using In Situ Raman Spectroscopy. *ACS Catal.* **2022**, *12* (19), 11870-11885.

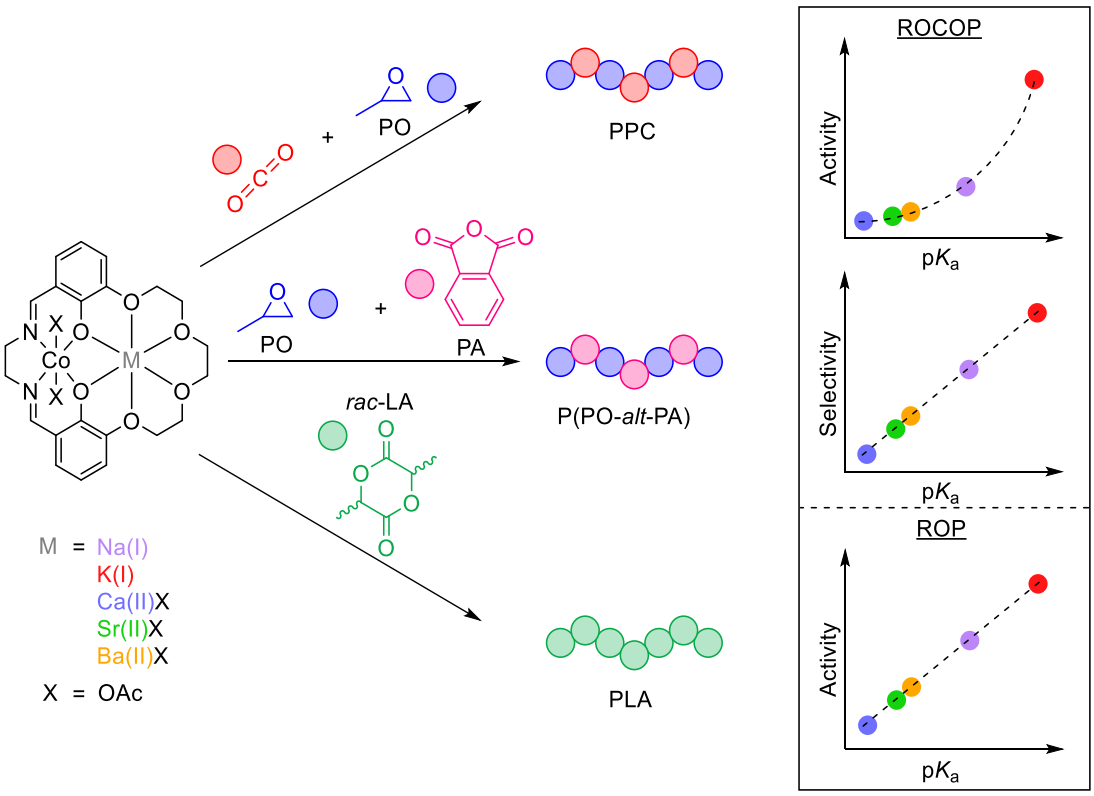
Chapter Two

Understanding Metallic Synergy in Dinuclear Polymerisation Catalysis

The work described in this chapter is reported in "*Understanding catalytic synergy in dinuclear polymerisation catalysts for sustainable polymers*"

F. Fiorentini, W.T. Diment, A.C. Deacy, R.W.F. Kerr, C.K. Williams

Nat. Commun., 2023, 14 (1), 4783



2.1 Introduction

Heterodinuclear synergy is often employed to enhance the performance of many catalysts containing Earth-abundant elements. s-Block metals in particular have a wide precedent of use in synergic catalysis, including organic reactions such as Grignard, hydroelementation, Wittig, and addition processes.[1-3] They are also used as promoters in heterogeneous catalysis, such as for nitrogen activation.[4] s-Block metal complexes and salts have been widely reported for various polymerisation catalyses, including for olefin polymerisations, and for cyclic ester, ether and switchable ring-opening polymerisations.[5-11]

In 2020, our group reported a highly active and selective Co(III)K(I) heterodinuclear catalyst for PO/CO_2 ROCOP.[12] It was the first heterodinuclear catalyst reported for this challenging polymerisation, and subsequent kinetic experiments and DFT calculations invoked a 'dinuclear metallate' mechanism to rationalise its high performance (Figure S2.1).[13] However, an understanding of the structure-performance relationships within the catalyst were lacking, as was understanding of the reason why K(I) outperformed the other Group I metals tested.

Also in 2020, we reported a highly-active Co(II)Mg(II) catalyst for the ring-opening copolymerisation of CHO and CO_2.[14] Detailed kinetic experiments allowed elucidation of the foundations of the metal synergy in this catalyst; the Co(II) centre reduced the enthalpy of the rate-determining step transition state, while the Mg(II) centre reduced its entropy. As such, the two metals have distinct roles in the polymerisation. This finding is rare in the field of polymerisation catalysis, with structure-activity relationships and understandings of metal synergy remaining few and far between. For example, various studies of multinuclear catalysts for epoxide/CO_2 and epoxide/anhydride ROCOP involving combinations of s-block, p-block, lanthanide, or transition metals showed no correlation of activity or selectivity with various metal properties such as metallic ionic radii, bond dissociation energies, water exchange constants, electronegativity, oxophilicity, or pK_a values.[15-18]

2.2 Aims

The aim of this chapter is to investigate the underpinnings of heterometallic synergy which gives rise to the high performance of a previously-reported Co(III)K(I) catalyst. While it was shown to be the most active out of a series of Co(III)M(I) catalysts (where M(I) = Na(I), K(I), Rb(I), Cs(I)), insights into the origins behind this performance trend were lacking.

To investigate the structure-activity trends of this catalyst system, a second series of Co(III)M(II) catalysts were be synthesised, where M(II) = Ca(II), Sr(II), Ba(II). The novel catalyst series were characterised by NMR spectroscopy, IR spectroscopy, and X-ray diffractometry.

The two series of catalysts were tested for PO/CO_2 ROCOP, PO/PA ROCOP, and *rac*-LA ROP. By comparing catalyst performances across such a range of polymerisations, each of which feature different intermediates, any trends in activity and/or selectivity can be fully studied and understood. The selection of both Group I and II metals will allow the effects of metal properties such as ionic radius and Lewis acidity (measured by the pK_a of the $[M(OH_2)_n]^{m+}$ complex in water) to be investigated independently of each other.

2.3 Results and Discussion

2.3.1 Catalyst Synthesis and Characterisation

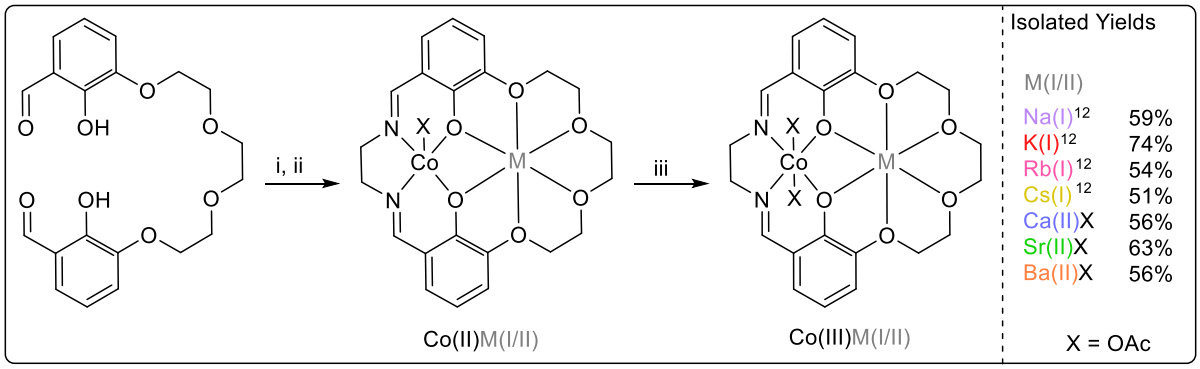


Figure 2.1. Synthesis of Co(III)M(I/II) where M(I/II) = Na(I), K(I), Rb(I), Cs(I), Ca(II), Sr(II), Ba(II). i) $Co(OAc)_2$, M(I)(OAc) or $M(II)(OAc)_2$, MeCN, 1 h; ii) ethylene diamine, MeCN, 16 h; iii) Acetic acid, MeCN, air, 72 h.

The two series of catalysts were synthesised by combining the dialdehyde proligand with $Co(OAc)_2$ and the respective M(I) or M(II) acetate salt in acetonitrile, under an inert atmosphere (Figure 2.1).[12] The mixture was stirred at room temperature for an hour, followed by addition of ethylene diamine in one portion and stirring for 16 h. The resultant Co(II)M(I/II) complex was oxidised to the desired Co(III) species by addition of acetic acid in air, and stirring for 72 h. The complexes were purified by precipitation from dichloromethane with diethyl ether and isolated as brown powders in good yields (51 – 74%) and were characterised by ^{1}H, $^{13}C\{^{1}H\}$, COSY, HSQC, HMBC NMR spectroscopy, IR spectroscopy, and single crystal X-ray diffraction (Figures 2.2 – 2.5, Figures S2.2 – 2.19). Purity of each complex was confirmed by elemental analysis.

2.3.1.1 NMR spectroscopy

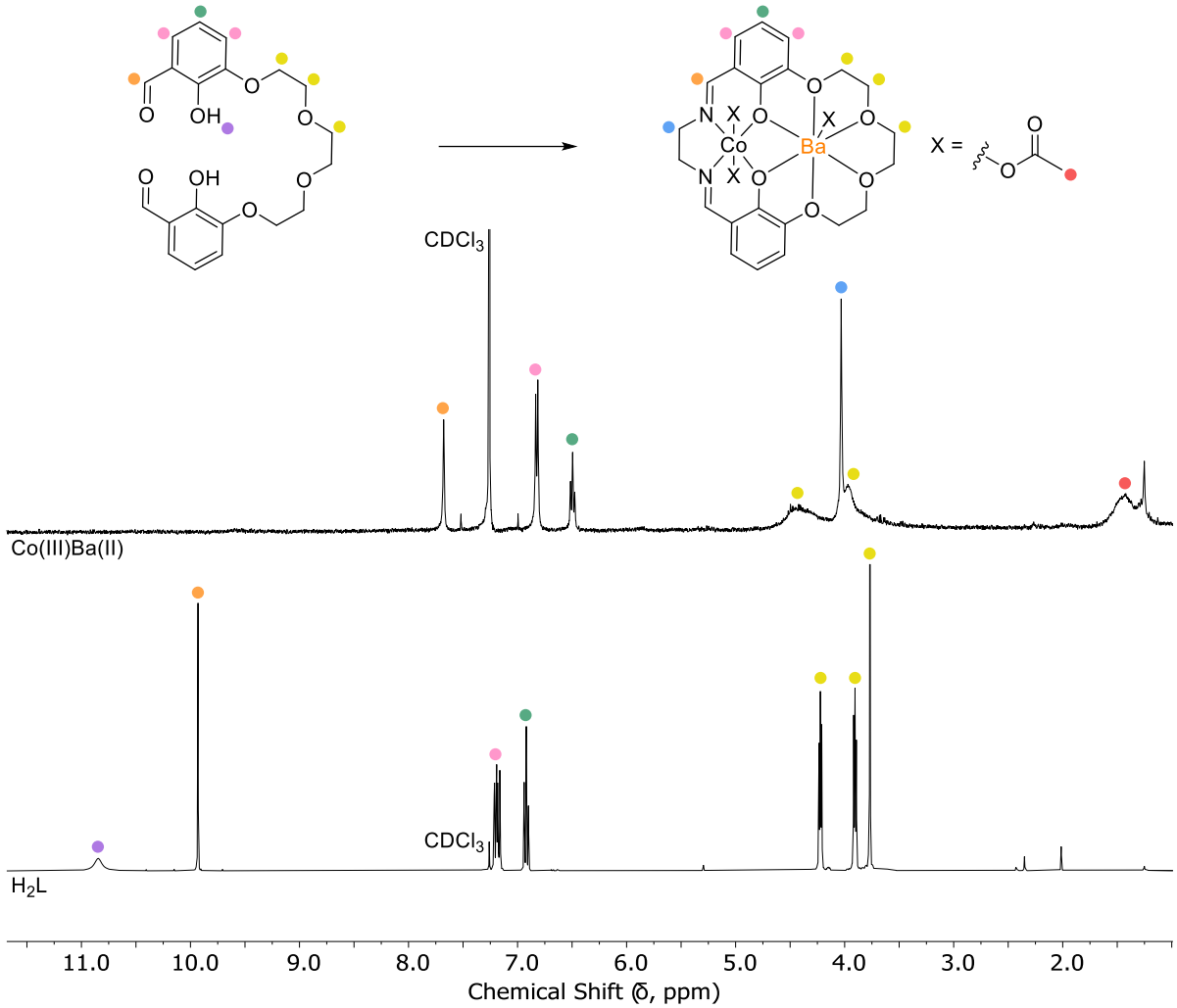


Figure 2.2. ^{1}H NMR spectra of the dialdehyde proligand (bottom) and Co(III)Ba(II) (top) showing the disappearance of the proligand phenol (purple), shifting of the aldehyde/imine (orange), aromatic (pink and green), broadening of the ether peaks (yellow), and appearance of the acetate peak (red).

Successful synthesis of each Co(III)M(II) complex was confirmed by ^{1}H and $^{13}C\{^{1}H\}$ NMR spectroscopy in $CDCl_3$ (Figure 2.2). The phenolic resonance present in the proligand disappears (10.85 ppm (^{1}H); purple in Figure 2.2), and resonances corresponding to the ethylene bridge (4.33 ppm (^{1}H), 58.6 ppm (^{13}C), blue in Figure 2.2) and acetate co-ligand (1.37 ppm (^{1}H), 23.7 and 179.3 ppm (^{13}C), red) appear. The aldehyde (9.93 ppm (^{1}H), 195.9 ppm (^{13}C); orange (bottom) in Figure 2.2) resonance in the proligand shifts significantly as it becomes an imine in the complex (7.68 ppm (^{1}H), 165.8 ppm (^{13}C); orange (top) in Figure 2.2). The crown ether region of the ligand (yellow in Figure 2.2) broadens significantly due to the fluxionality of this region.

2.3.1.1.1 Variable Temperature ^{1}H NMR Spectroscopy

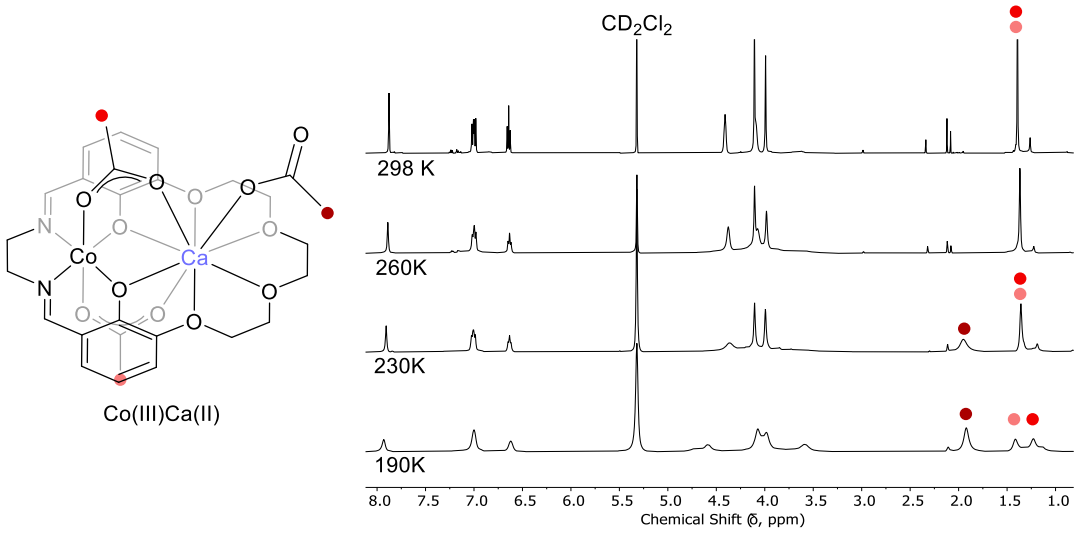


Figure 2.3. Variable temperature NMR spectra of Co(III)Ca(II) between 298 – 190 K (top to bottom) showing the appearance of a new acetate peak at 230 K (o) and the splitting of the original acetate peak (m) into two singlets (m′ and m′′).

At 25 °C (298K), the Co(III)M(II) complexes all show ^{1}H NMR spectra with acetate resonances with relative integrals of six protons, rather than the expected nine which would correspond to three acetate co-ligands (Figure 2.3). When the ^{1}H NMR spectrum of the Co(III)Ca(II) complex is recorded at 230 K, a new resonance at 1.99 ppm is observed (dark red circle; Figure 2.3). This is proposed to correspond to an acetate co-ligand, terminally bound to the Ca(II) centre. At 25 °C (298K), this acetate co-ligand is very fluxional, resulting in broadening of its corresponding peak such that it is indistinguishable from the baseline. When the temperature is further reduced to 190 K, the original acetate peak splits into two (red and pale red circles; Figure 2.3). This is proposed to correspond to two bridging acetate co-ligands, which become inequivalent at low temperatures. This proposed structure agrees with the solid-state structures obtained from single crystal X-ray diffraction (Figure 2.5).

2.3.1.2. Infrared Spectroscopy

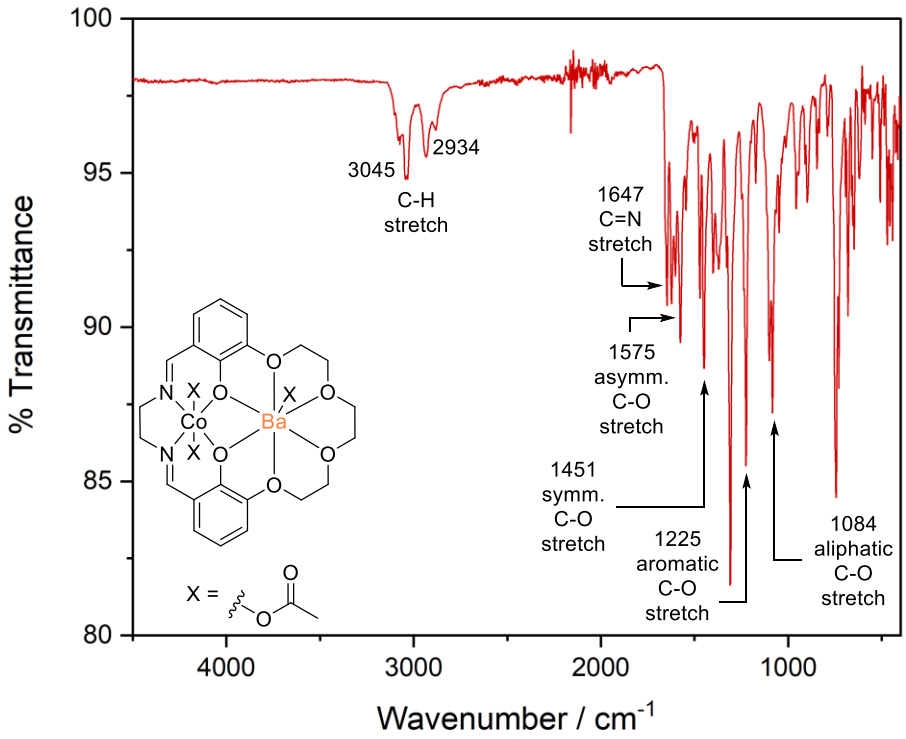


Figure 2.4. Solid state IR spectrum of Co(III)Ba(II) with assigned peaks.

The solid-state IR spectra of the novel complexes are consistent with the IR spectra reported for the Co(III)M(I) complexes, and with spectra reported for other complexes using the same macrocyclic ligand.[12, 19] The IR spectra of the Co(III)M(II) complexes show peaks for C-H stretches (2926 – 3045 cm^{-1}), imine C=N stretches (1647 – 1648 cm^{-1}), acetate C-O asymmetric and symmetric stretches (1575 – 1585 cm^{-1} and 1451 – 1455 cm^{-1} respectively), aromatic C-O stretches (1225 – 1242 cm^{-1}) and aliphatic C-O stretches (1084 – 1086 cm^{-1}; Figure 2.4). Measuring the difference in wavenumber of asymmetric and symmetric acetate C-O stretches can give an indication of the coordination mode of the acetate co-ligands. A difference of less than 200 cm^{-1} may indicate κ^2 coordination, whereas a difference greater than 200 cm^{-1} can imply κ^1 coordination.[20] Each of the complexes show differences in asymmetric and symmetric acetate C-O stretches of between 124 – 130 cm^{-1}, indicating that the predominant mode of acetate coordination is κ^2, which is consistent with the solid-state structures (*vide infra*).

2.3.1.3 Single Crystal X-Ray Crystallography

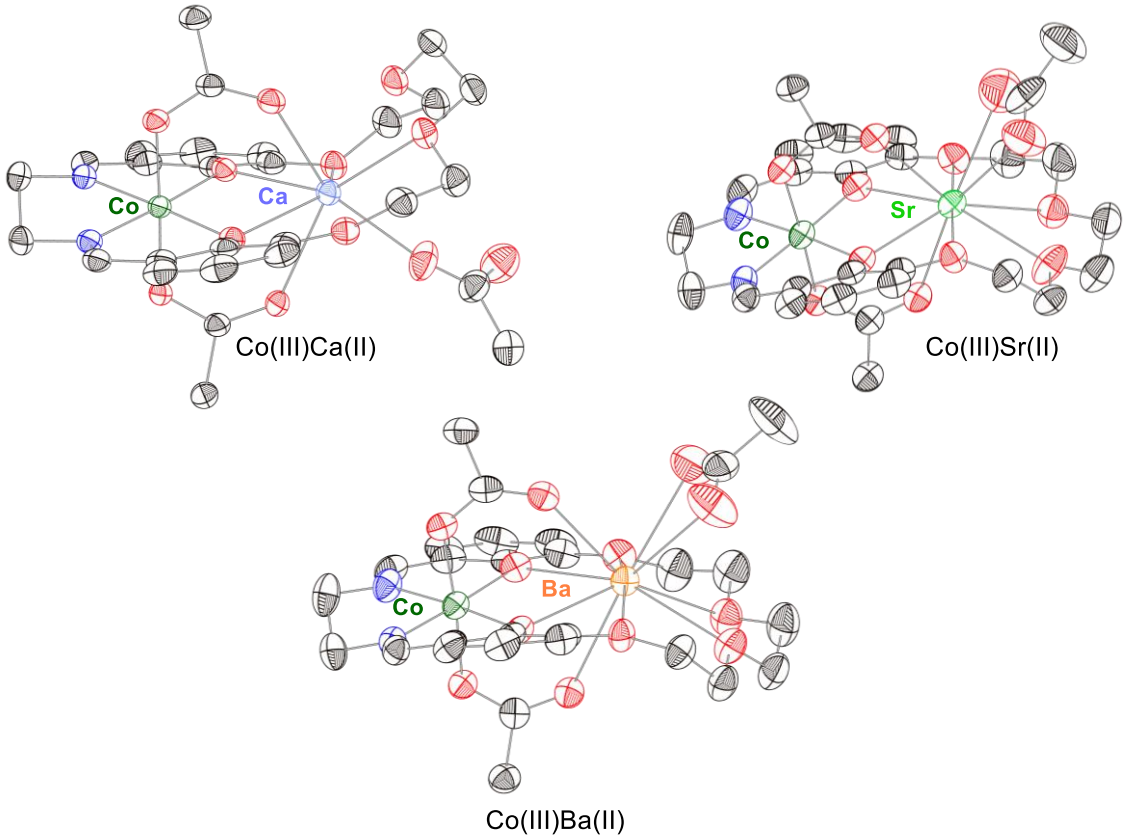


Figure 2.5. Solid state structures of Co(III)M(II) (M(II) = Ca(II), Sr(II), Ba(II); clockwise from top LHS) determined by X-ray crystallography. Thermal ellipsoids drawn at 40% probability, solvent molecules and hydrogen atoms omitted for clarity.

Single crystals suitable for X-ray crystallography were grown by slow evaporation of diethyl ether into a solution of the respective complex in dichloromethane.

Each Co(III)M(II) complex crystallises as the monomeric, heterodinuclear species with Co(III) coordinated within the Schiff base binding pocket and the Group II metal centre within the ether pocket (Figure 2.5). Each Co(III) centre shows octahedral geometry, coordinating to two Schiff base nitrogen donors, two phenoxide oxygens, and two acetate co-ligands which bridge between the Co(III) and M(II) centres. The Co(III) centres show cobaltate character, where the acetate co-ligands coordinate as anions in each case, as can be seen by the bond lengths between C(1) and O(7) and O(8), and C(2) and O(9) and O(10) (Figure 2.6). Metallate species have been previously invoked as the active catalytic species for various ring-opening polymerisations and ring-opening

copolymerisations but are rarely structurally characterised.[21-24] The Group II metal centre coordination numbers range from nine (Co(III)Ca(II)) to ten (Co(III)Sr(II) and Co(III)Ba(II)). Each of the Group II metal centres coordinate to two phenoxide oxygens, two aromatic ether oxygens, two aliphatic ether oxygens, and two bridging acetates. The Ca(II) centre in Co(III)Ca(II) coordinates a third, terminally-bound acetate, while the larger Sr(II) and Ba(II) centres in Co(III)Sr(II) and Co(III)Ba(II) respectively coordinate this third acetate co-ligand in a κ^2 fashion, where the acetate is doubly-coordinated to the Group II metal centre.

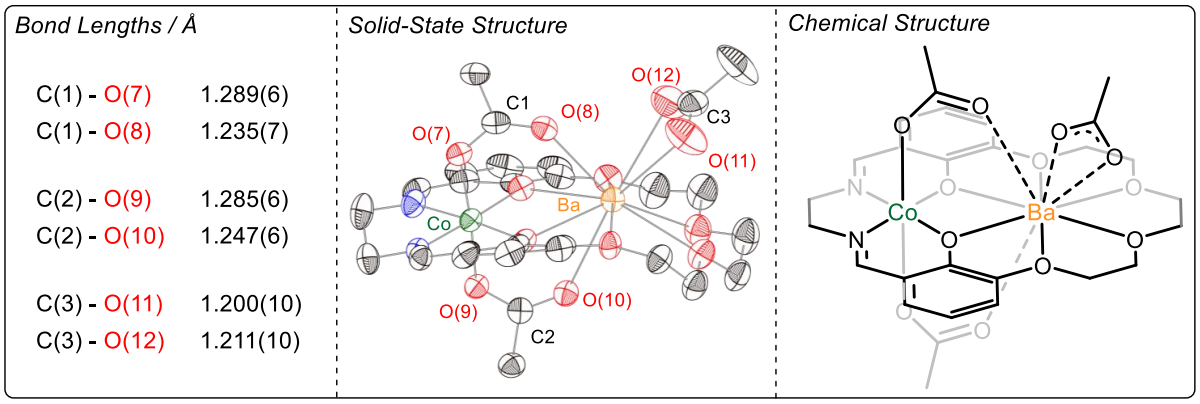


Figure 2.6. Solid state and chemical structures of Co(III)Ba(II), alongside key C-O bond lengths, showing Co(III) centre metallate character.

All complexes have intermetallic separations between 3 – 4 Å, which has previously been shown to allow intermetallic synergy in both biological and synthetic catalytic systems (Co(III)Ca(II) = 3.2774(7) Å, Co(III)Sr(II) = 3.4743(6) Å, Co(III)Ba(II) = 3.6198(8) Å).[11]

When these solid-state structures are considered alongside the structures of the previously-reported Co(III)M(I) complexes (M(I) = Na(I), K(I), Rb(I)), the importance of size-match between the s-block metal and the ether binding pocket is clear (Figure 2.7). K(I), Sr(II), and Ba(II) all have similar ionic radii to the ether cavity, and as such they coordinate within the plane of the ligand, with minimal distortion of the crown ether backbone (ionic radii: K(I) = 1.46 Å, Sr(II) = 1.36 Å, Ba(II) = 1.52 Å).[25] Na(I) and Ca(II) have smaller ionic radii than the ether cavity, which results in distortion of the crown ether backbone to minimise M(I/II)-O bond lengths (ionic radii: Na(I) = 1.12 Å, Ca(II) = 1.18 Å).[25] Rb(I) and Cs(I) have larger ionic radii than the macrocyclic cavity, resulting in the formation of

dimeric species in the solid state, and aggregates in solution, respectively (ionic radii: Rb(I) = 1.66 Å, Cs(I) = 1.81 Å).[25]

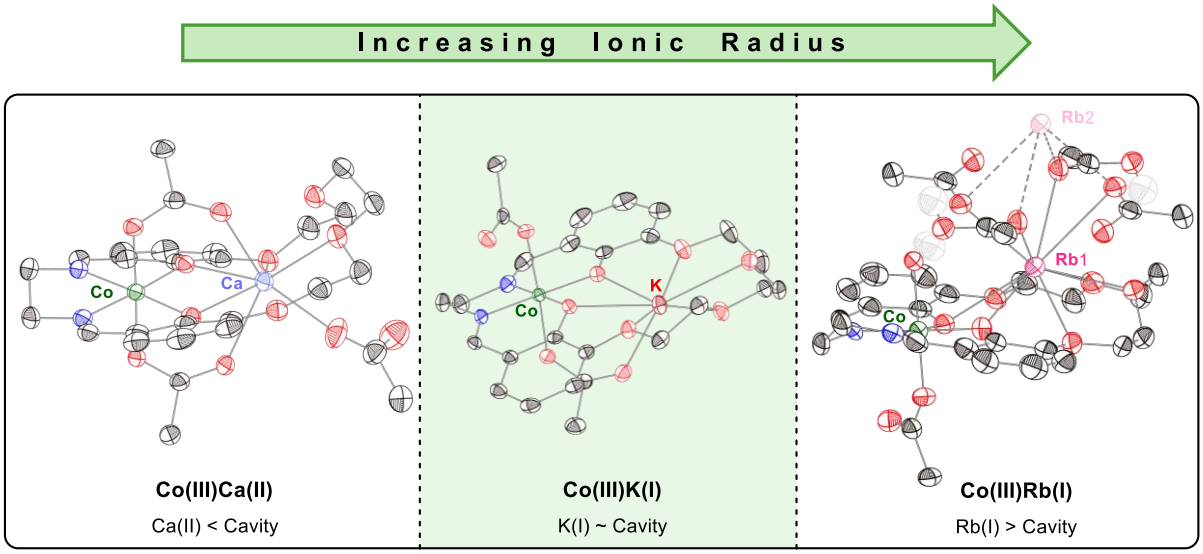


Figure 2.7. Solid state structures of Co(III)Ca(II) (LHS), Co(III)K(I) (middle), and Co(III)Rb(I) (RHS) showing the importance of size match between the 18-crown-6 cavity and the s-block metal cation.

2.3.2 Polymerisation Catalysis

2.3.2.1 Ring-Opening Copolymerisation of Propene Oxide and CO_2

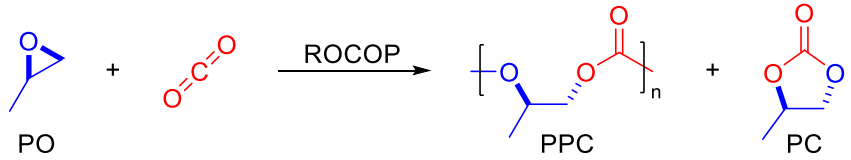


Table 2.1. Scheme and Data for propene oxide (PO)/CO_2 ROCOP using the Co(III)M(I/II) catalysts, where PPC is poly(propene carbonate) and PC is propene carbonate. Reaction conditions: catalyst (0.025 mol%, 3.6 mM), PO (5 mL, 14.3 M), 1,2-cyclohexane diol (0.5 mol%, 71 mM), 20 bar CO_2, 50 °C.

Entry	Catalyst	TON [a]	CO_2 / % [b]	PPC / % [c]	TOF / h^{-1} [d]	k_{obs} / x 10^{-3} s^{-1} [e]	M_n [$Đ$] / g mol^{-1} [f]
1	Co(III)Ca(II)	194 ± 10	93	38 ± 4	5 ± 1	0.36 ± 0.02	700 [1.17]
2	Co(III)Sr(II)	889 ± 44	97	50 ± 5	23 ± 2	1.79 ± 0.14	2100 [1.07]
3	Co(III)Ba(II)	856 ± 43	97	61 ± 6	30 ± 2	2.16 ± 0.17	2500 [1.11]
4	Co(III)Na(I)	600 ± 30	>99	79 ± 2	104 ± 8	7.52 ± 0.60	2300 [1.08]
5	Co(III)K(I)	1360 ± 68	>99	98 ± 2	528 ± 42	38.20 ± 3.06	5900 [1.10]
6	Co(III)Rb(I)	1240 ± 62	>99	91 ± 3	88 ± 7	6.37 ± 0.51	6500 [1.07]
7	Co(III)Cs(I)	1080 ± 54	>99	84 ± 3	88 ± 7	6.34 ± 0.51	5600 [1.08]

[a] Turnover number (TON) = moles PO consumed / moles catalyst. PO conversion determined from ^{1}H NMR spectra integrals for PPC (4.92 ppm), PC (4.77 ppm) and PPO (3.46-3.64 ppm), using mesitylene internal standard (0.05 mol%, 36 mM). [b] Selectivity for CO_2 conversion, determined from PO conversion to PPC + PC / overall PO conversion (using NMR integrals). [c] Selectivity for PPC formation, determined as PO conversion to PPC / overall PO conversion (using NMR integrals). [d] Turnover frequency (TOF) are determined from 5 – 20% conversions, in all cases (Table S2.1 and S2.2, Equation S2.1). [e] Calculated from linear ln([PO]t/[PO]0) vs. time plots (Figures S2.20 – S2.22). [f] Determined by GPC, in THF, at 30 °C, using narrow molecular weight polystyrene calibrants.

The novel Co(III)M(II) complexes were tested for the ROCOP of PO and CO_2, using 1:20:4000 [catalyst]$_0$:[*trans*-cyclohexane diol]$_0$:[PO]$_0$ in neat epoxide, at 50 °C and 20 bar CO_2. *trans*-Cyclohexane diol (CHD) is used as a chain transfer agent to control the molar mass of the resultant polymer; polyols with molar masses below 6000 g mol^{-1} are targeted for polyurethane, surfactant and resin

applications. The activities of the Co(III)M(II) catalysts are compared to those of the previously-reported Co(III)M(I) catalysts to elucidate effects of the s-block metal on catalysis.

The novel Co(III)M(II) catalysts are all moderately active for PO/CO_2 ROCOP. The most active of the series is Co(III)Ba(II) and the least active is Co(III)Ca(II), with turnover frequencies (TOFs) between 5 – 30 h^{-1}, corresponding to k_{obs} values between 0.36 – 2.16 × 10^{-3} s^{-1} (entries 1 – 3, Table 2.1). While CO_2 uptakes are very high for all the catalysts (≥ 93%), the selectivity for polycarbonate over cyclic carbonate range from moderate for Co(III)Ba(II) to very low for Co(III)Ca(II) (61 – 38%; entries 1 – 3, Table 2.1). The polycarbonate produced from each catalyst show narrow (1.07 – 1.17), monomodal molar mass distributions by GPC, indicating well-controlled polymerisations (Figures S2.23 – S2.25).

When these results are compared to the activities of the previously-reported Co(III)M(I) catalysts, it can be seen that the Co(III)M(I) catalysts outperform the Co(III)M(II) catalysts in terms of activity, and selectivity for polycarbonate over cyclic carbonate (entries 4 – 7, Table 2.1). It is evident from considering these two data series together that catalyst performance cannot be explained by trends in ionic radius or, by extension, ligand binding affinity (Figures S2.26 and S2.27). The most active catalyst of the series is Co(III)K(I), but while Co(III)Sr(II) and Co(III)Ba(II) feature s-block metal cations of similar ionic radii, and greater ligand binding affinities, their catalytic performances are significantly inferior.

2.3.2.2 Ring-Opening Copolymerisation of Propylene Oxide and Phthalic Anhydride

To further explore the applicability of the catalytic system, and attempt to understand trends within the system, the catalysts were tested for other polymerisations.

The ROCOP of epoxides and anhydrides is an attractive, controlled route for the synthesis of polyesters with variable structures and properties, due to the wide range of commercial monomers, many of which are, or can be, bio-derived.[26, 27] Unlike cyclic ester ROP, its favourable polymerisation thermodynamics allow high yields of polyesters, since the reaction is not equilibrium-limited.

The catalysts were tested for epoxide/anhydride ROCOP using PO and phthalic acid (PA), since both monomers are commercially available and can be bioderived. Loadings of 1:100:1000 $[Cat]_0$:$[PA]_0$:$[PO]_0$ (i.e. 0.1 mol% catalyst, 10 mol% PA) were used, at 50 °C in neat epoxide. Aliquots were taken at regular time points to determine conversion of PA to polyester by ^{1}H NMR spectroscopy, and the molar mass of the resultant polyester by GPC.

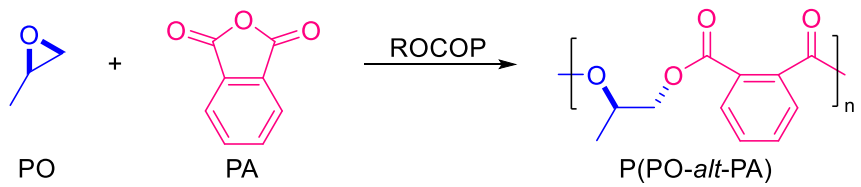


Table 2.2. Scheme and Data for Propene Oxide (PO)/Phthalic Anhydride (PA) ROCOP with Co(III)M(II) and Co(III)M(I) catalysts. [a]Reaction conditions: Catalyst (0.1 mol%, 0.0143 mM), PA (10 mol%, 1.43 mM), PO (1 mL, 14.3 M), 50 °C.

Entry [a]	Catalyst	TON [b]	Polyester / % [c]	TOF / h^{-1} [d]	k_{obs} / x 10^{-6} M^{-1} s^{-1} [e]	M_n [Đ] / g mol^{-1} [f]
1	Co(III)Ca(II)	88 ± 2	> 99	4 ± 2	17.4 ± 7.4	4600 [1.13] 11600 [1.02]
2	Co(III)Sr(II)	87 ± 1	> 99	3 ± 1	10.5 ± 3.2	5100 [1.08]
3	Co(III)Ba(II)	84 ± 1	> 99	3 ± 1	11.2 ± 3.6	6000 [1.11]
4	Co(III)Na(I)	88 ± 2	> 99	12 ± 1	45.8 ± 1.6	4200 [1.12]
5	Co(III)K(I)	89 ± 1	> 99	31 ± 1	122.7 ± 4.2	4500 [1.11]

[b] TON determined by ^{1}H NMR spectroscopy using integrals for PA (8.10 – 7.85 ppm) and P(PO-*alt*-PA) (7.75 – 7.40 ppm), in this case TON = conversion. [c] Selectivity for polyester determined by ^{1}H NMR spectroscopy using integrals for P(PO-*alt*-PA) and any PPO (3.46 – 3.64 ppm. [d] Turnover frequency (TOF) is reported from gradients of conversion vs. time plots, from 5 – 20% conversions, in all cases (Table S2.3 and S2.4, Equation S2.2). [e] Rate coefficient is the gradient of linear fits to plots of $[PA]_t$ vs. time (Figure S2.28). [f] Determined by GPC, in THF, at 30 °C, using narrow dispersity polystyrene calibrants.

Again, the catalysts tested show a wide range of activities (TOFs = 31 – 4 h^{-1}, k_{obs} = 122.7 – 17.4 × 10^{-3} M^{-1} s^{-1}; Table 2.2). The most active catalyst was Co(III)K(I) as before, followed by Co(III)Na(I), which both outperform the Co(III)M(II) catalysts. Plots of polyester molar mass against PA conversion are linear, and molar mass dispersities remain low and consistent throughout the reaction, indicating that the polymerisations are well-controlled (Figures S2.29 – S2.38).

2.3.2.3 Ring-Opening Polymerisation of *rac*-Lactide

Polylactide (PLA) is produced from LA, which is derived from the fermentation of starch-rich crops such as maize, and is the world-leading bioderived polymer with applications as a packaging material, in fibres, and as plastics.[28-30] Furthermore, it is recyclable, degradable, and compostable, and as such its end-of-life options are less problematic than for most petrochemical-derived plastics.

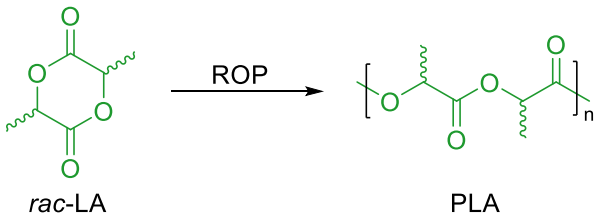


Table 2.3. Scheme and Data for *rac*-Lactide (LA) Ring Opening Polymerization Scheme Using the Co(III)M(II or I) Catalysts. Reaction conditions: catalyst (0.1 mol%, 14.3 mM), *rac*-LA (10 mol%, 1.43 M), PO (1 mL, 14.3 M), 50 °C.

Entry	Catalyst	TON [a]	TOF / h^{-1} [b]	k_{obs} / × 10^{-3} s^{-1} [c]	M_n [Đ] / g mol^{-1} [d]	P_i [e]
1	Co(III)Ca(II)	91	42 ± 4	0.21 ± 0.02	3300 [1.22]	0.52
2	Co(III)Sr(II)	95	212 ± 12	1.04 ± 0.06	4700 [1.23]	0.59
3	Co(III)Ba(II)	97	147 ± 10	0.72 ± 0.05	5600 [1.61]	0.60
4	Co(III)Na(I)	88	670 ± 22	3.29 ± 0.21	4100 [1.30]	0.63
5	Co(III)K(I)	90	912 ± 83	4.48 ± 0.41	4800 [1.23]	0.72

[a] TON determined by ^{1}H NMR spectroscopy through comparison of resonances associated with *rac*-LA (4.99 – 5.09 ppm, 2 H) and PLA (5.10 – 5.26 ppm, 2H). [b] Turnover frequency (TOF) between 5 – 70% = k_{obs} x 203.48 x10^3 s h^{-1} (Table S2.5 and S2.6, Equation S2.3). [c] Calculated from the gradient of the linear region of the plot of ln([*rac*-LA]$_t$/[*rac*-LA]$_0$) vs. time for Co(III)Na(I) and Co(III)K(I); due to the slow initiation time for Co(III)Ca(II), Co(III)Sr(II) and Co(III)Ba(II) k_{obs} was determined by fitting a sigmoidal function to the plot of [PLA] v. time of the form [PLA] = A(1-exp(-k_{obs}t))^s (Figures S2.39 – S2.43).[31] [d] Determined by gel permeation chromatography (GPC) in THF at 30 °C, using narrow dispersity polystyrene standards, using a correction factor (0.58).[32] [e] Determined by ^{1}H{^{1}H} NMR spectroscopy.

The catalysts were tested using 1:100:1000 [cat]$_0$:[*rac*-LA]$_0$:[PO]$_0$ (i.e. 0.1 mol% catalyst, 1.43 M *rac*-LA) at 50 °C in neat epoxide. PO was used as the polymerisation solvent to furnish the catalyst with alkoxide initiators to allow LA ROP to occur; the acetate co-ligands of each complex cannot initiate LA ROP.[33-35] LA ROP was the only polymerisation to occur; no polyether linkages from PO ROP

were observed by ^{1}H NMR spectroscopy. Aliquots were taken at regular time intervals to determine *rac*-LA conversion to PLA by ^{1}H NMR spectroscopy, and the PLA molar mass by GPC.

In-line with the previous polymerisations, the most active of the series is Co(III)K(I), with a TOF of 912 h^{-1}, and a corresponding k_{obs} of 4.48 × 10^{-3} s^{-1} (Table 2.3). Again, the Co(III)M(I) catalysts outperform those featuring Group II metal cations. For each polymerisation, plots of the molar mass of resultant PLA against the conversion of *rac*-LA are linear, and dispersities of the PLA are low and consistent throughout the reactions (Figures S2.44 – S2.53). As such, it can be seen that the reactions are well-controlled. The PLA produced by the tested catalysts were mostly atactic, although the most active catalyst, Co(III)K(I), produced PLA with a moderate isotacticity (P_i = 0.72).

By investigating both Group I and Group II metal cations, the data clearly shows that the observed activity trends cannot be rationalised by ionic radius (Figure S2.54). While K(I) and Ba(II) have similar ionic radii (1.46 Å and 1.52 Å respectively), Co(III)K(I) has an activity that is 6 × greater than that of Co(III)Ba(II) (TOF = 912 and 147 h^{-1}, k_{obs} = 4.48 and 0.72 × 10^{-3} s^{-1} respectively).[25]

2.3.3 Discussion

Each of the three polymerisations were examined to elucidate trends in the activity and selectivity data that were previously outlined. As discussed previously, the synthesis of, and testing of both Co(III)M(I) and Co(III)M(II) catalyst series has shown that the polymerisation data cannot be explained by trends in ionic radius. Instead, our focus shifted to the pK_a of the s-block metals, which is commonly used as a measure of metal Lewis acidity (i.e. the pK_a of the $[M(OH_2)_n]^{m+}$ complex in water, also known as pK_w). Recently, Blakemore and co-workers were able to determine the pK_a of various aqua complexes metal cations by using a modified Guttmann-Beckett method in acetonitrile.[36] The chemical shift of a triphenylphosphine oxide (TPPO) ^{31}P NMR spectroscopy probe was measured in MeCN-d_3 in the presence of metal triflate salts. These shifts were correlated to previously-reported, traditionally-measured pK_a values of the same metal cation aqua complexes. Using this method, they were able to determine the pK_a of cations such as K(I), Rb(I), and Cs(I) which are difficult to determine in water due to their low Lewis acidity.

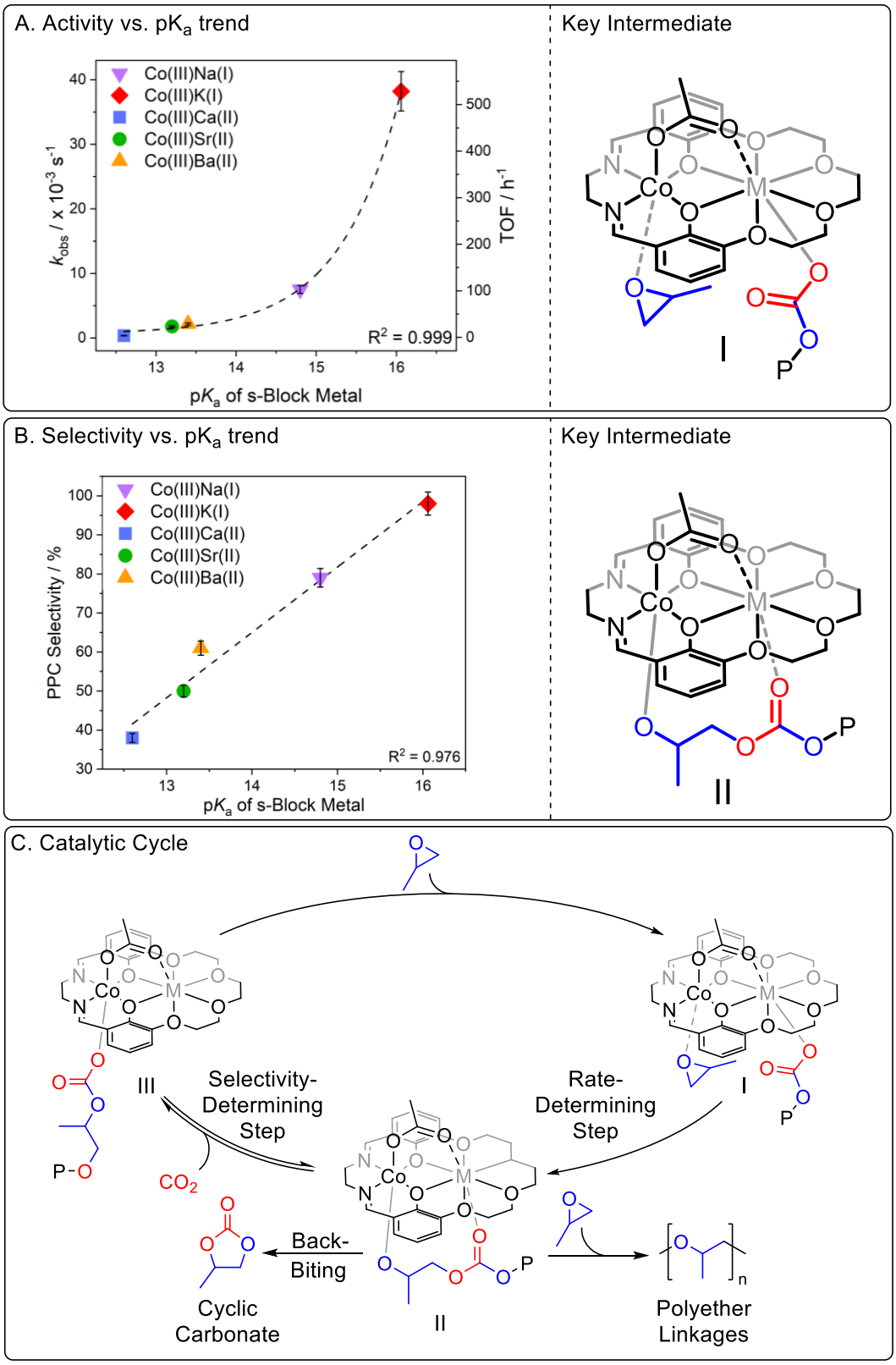


Figure 2.8. A. Plots of k_{obs} and TOF against s-block M(I) or M(II) pK_a value for PO/CO_2 ROCOP catalysed by Co(III)M(I/II) with the structure of the key intermediate, i.e. rate determining intermediate; B. Plot of selectivity against s-block metal pK_a value with the key intermediate that determines selectivity for polycarbonate over cyclic carbonate; C. Catalytic cycle for PO/CO_2 ROCOP catalysed by Co(III)M(I/II).

When the activity of each catalyst for PO/CO_2 ROCOP is plotted against the pK_a of the relevant s-block metal a clear trend is observed, where activity increases exponentially with increasing pK_a (i.e. decreasing Lewis acidity; Figure 2.8A). The data is well-fitted to an exponential function ($R^2 > 0.99$), and plots of ln(TOF) or ln(k_{obs}) against ln(pK_a) are linear, confirming the exponential nature of the correlation (Figure S2.55 and S2.56). When the selectivity for polycarbonate over cyclic carbonate is plotted against the pK_a of the s-block metal, a linear increase is seen with decreasing Lewis acidity (Figure 2.8B).

Kinetic and DFT investigations of PO/CO_2 ROCOP using the Co(III)K(I) catalyst indicate that the rate-determining step is ring-opening of a Co(III)-bound epoxide by a K(I)-bound carbonate group (Figure 2.8C).[12, 13] The selectivity for polymer over cyclic carbonate is determined by the equilibrium between the alkoxide and carbonate intermediates during CO_2 insertion, since the cyclic carbonate formation occurs from the alkoxide intermediate, as it has a lower barrier than cyclic carbonate formation from the carbonate intermediate.[13] Applying the insights from this DFT investigation to the current catalysts can be used to rationalise the performances. The more weakly Lewis acidic s-block metal are proposed to result in a more loosely-bound, labile nucleophilic carbonate in the rate-determining step. In the DFT study of Co(III)K(I), a weak interaction is seen between the s-block metal and an adjacent carbonate group in the alkoxide intermediate. A weakly Lewis acidic s-block metal may perhaps weaken the coordination to this carbonate group, destabilising the alkoxide intermediate relative to the carbonate intermediate. It may be that this helps to drive the equilibrium for CO_2 insertion towards the carbonate, enhancing CO_2 insertion and, therefore, reaction selectivity. Furthermore, stronger coordination that would be expected with a more Lewis acidic metal may activate the carbonyl group towards nucleophilic attack from the alkoxide chain-end (i.e. back-biting). Thus, we expect that the incorporation of weak Lewis acids, such as K(I), into the catalytic system increases the selectivity of the catalyst either by enhancing CO_2 insertion, and by increasing the barrier to back-biting, or by a combination of both factors.

Rb(I) and Cs(I) catalysts do not fit the trends since their radii are too large to be effectively coordinated within the macrocycle (Figures S2.57 and S2.58). This results in aggregation effects which has a detrimental impact on the polymerisation performance of the catalysts (Rb(I) = 1.56 Å, Cs(I) = 1.71 Å, vs. K = 1.46 Å).[12, 25]

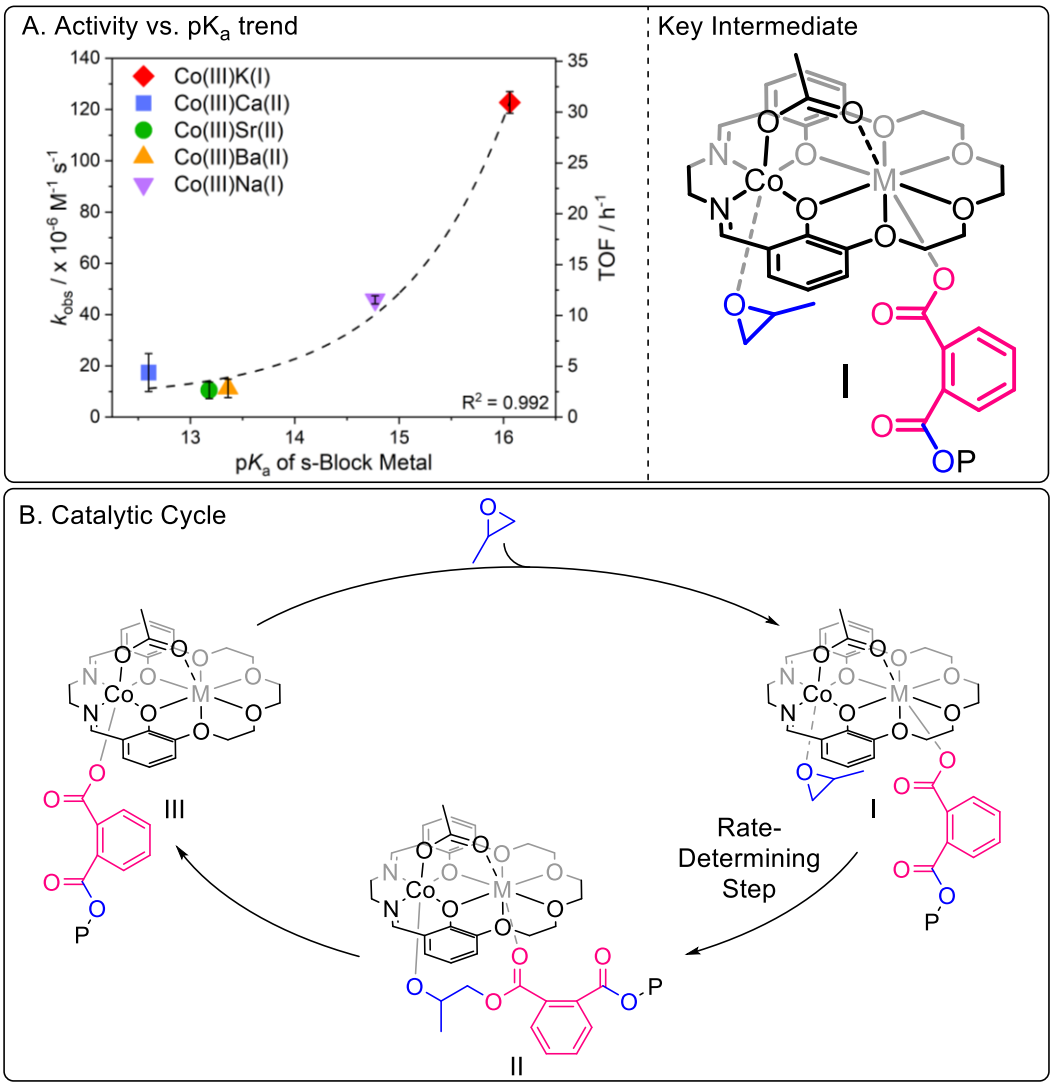


Figure 2.9. A. Plot of k_{obs} and TOF against pK_a of the s-block metal for PO/PA ROCOP catalysed by Co(III)M(I/II) and the key intermediate that determines activity; B. Catalytic cycle for PO/PA ROCOP catalysed by Co(III)M(I/II).

Plotting the activity data for PO/PA ROCOP against pK_a of the relevant s-block metal reveals a related trend; the activity of the catalysts increases exponentially with decreasing s-block metal Lewis acidity (Figure 2.9A). Again, the suitability of the exponential fit has been confirmed by linear plots of ln(TOF) or ln(k_{obs}) against ln(pK_a) (Figures S2.59 and S2.60).

Related heterodinuclear catalytic systems for epoxide/anhydride ROCOP show first-order kinetics in catalyst and epoxide, and a zero-order dependence of rate on anhydride concentration.[11] The linear conversion vs. time plots seen for these Co(III)M(I/II) catalysts when the polymerisations are conducted in an excess of epoxide confirms zero-order kinetics in anhydride concentration (Figure S2.28). When the excess in epoxide is reduced from 1:100:1000 $[cat]_0$:$[PA]_0$:$[PO]_0$ to 1:100:150, a first-order conversion vs. time trace is seen, which is confirmed by a linear plot of $\ln([PO]_t/[PO]_0)$ against time, confirming first-order dependence on epoxide (Figure S2.61 and S2.62).

Such kinetic results (first order dependence on [epoxide], zero-order dependence on [anhydride]) have been rationalised for similar catalysts using DFT and reactivity investigations by invoking rate-limiting ring-opening of epoxide by an s-block metal-carboxylate.[21] For this series of catalysts, a "dinuclear metallate" mechanism, related to that for PO/CO_2 ROCOP, is proposed (Figure 2.9B). In this proposed mechanism, the rate-limiting step involves ring-opening of a Co(III)-bound epoxide by a carboxylate intermediate bound to the s-block metal cation. This mechanism will be used to try to explain the observed activity trends. As such, more weakly Lewis acidic s-block metals should result in a more labile carboxylate intermediates, accelerating the rate-determining step.

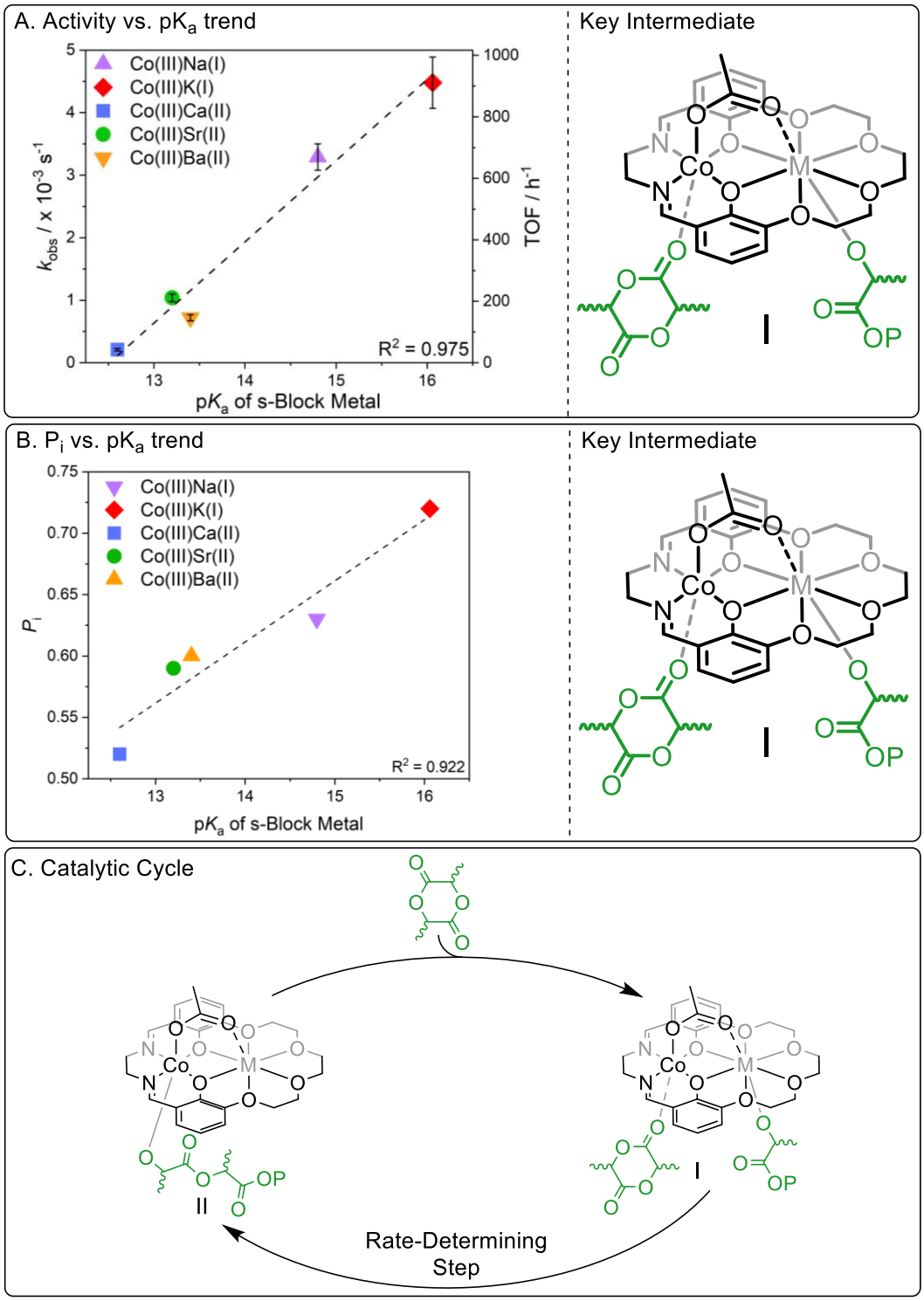


Figure 2.10. A. Plot of k_{obs} and TOF against pK_a of the s-block metal for *rac*-LA ROP catalysed by Co(III)M(I/II) and the key intermediate that determines activity; B. Plot of P_i against pK_a of the s-block metal for *rac*-LA ROP catalysed by Co(III)M(I/II) and the key intermediate that determines isotacticity; C: Catalytic cycle for *rac*-LA ROP catalysed by Co(III)M(I/II).

Finally, analysis of the *rac*-LA ROP activity data shows a linear increase with increasing pK_a of the s-block metal (Figure 2.10A). The mechanism for LA ROP is quite well-established; the rate-

determining step almost always involves nucleophilic attack of a LA unit by a metal-alkoxide intermediate.[37] This mechanism is indicated here because the rate of polymerisation shows first-order dependence on concentration of [LA], as can be seen by linear plots of $\ln([LA]_t/[LA]_0)$ against time (Figures S2.39 and S2.40). For the current series of catalysts, we propose that LA is coordinated to the Co(III) centre, while the alkoxide intermediate is bound to the s-block metal cation in the rate-determining step (Figure 2.10C). The data is consistent with such a proposed mechanism, since weakly Lewis acidic s-block metals should destabilise the alkoxide intermediate, enhancing its nucleophilicity and therefore increasing the rate of polymerisation. Interestingly, there is also a linear increase in the degree of isotacticity, P_i, with increasing pK_a of the s-block metal (Figure 2.10B).

The difference in correlation fits should be noted: steps involving bidentate intermediates, such as carbonates or carboxylates, seem to lead to exponential trends, while those involving monodentate intermediates, such as alkoxides, seem to result in linear trends. As such, the selectivity for PO/CO_2 ROCOP, and the activity and degree of isotacticity for *rac*-LA ROP, which are determined by alkoxide intermediates, show linear trends with increasing pK_a values of the s-block metals.

2.4 Conclusions and Further Work

A series of novel heterodinuclear Co(III)M(II) (M(II) = Ca(II), Sr(II), Ba(II)) complexes were synthesised, characterised and tested for PO/CO_2 and PO/PA ROCOP, and *rac*-LA ROP.

Clear structure-activity trends for each catalysis were observed by plotting the activity or selectivity for each polymerisation against the pK_a of the s-block metal aqua complex, using values determined by Blakemore and co-workers.[36] These correlations help to infer upon the origins of metal synergy in these heterodinuclear catalysts; the most active catalyst combined Co(III) with the weakly Lewis acidic K(I). The activity and selectivity trends were consistent with the previously proposed dinuclear metallate mechanism; the weak Lewis acidity of K(I) results in destabilisation, and, therefore, labilisation of the nucleophilic species in the rate determining step of each polymerisation, increasing the catalytic activity. For PO/CO_2 ROCOP, K(I) is proposed to increase the selectivity for polycarbonate by enhancing CO_2 insertion and also increasing the barrier to cyclic carbonate.

These results are important to each of the three fields of polymerisation investigated, since they highlight future routes to highly active and selective catalysts. In particular, this work might be relevant to the field of cyclic ester ring-opening polymerisation catalysis, where activity trends are commonly rationalised by metal ionic radii and by steric effects.[8-10, 37] These activity data might be better explained by comparison to metal pK_a values, and to establish such effects it's very useful to correlate Group I and II catalysts (most prior work only makes comparisons within a group). More broadly, the analysis technique described herein should be tested for other catalytic systems that involve heterodinuclear catalysis with s-block metals, and might elucidate the roots of high activities and/or selectivities.

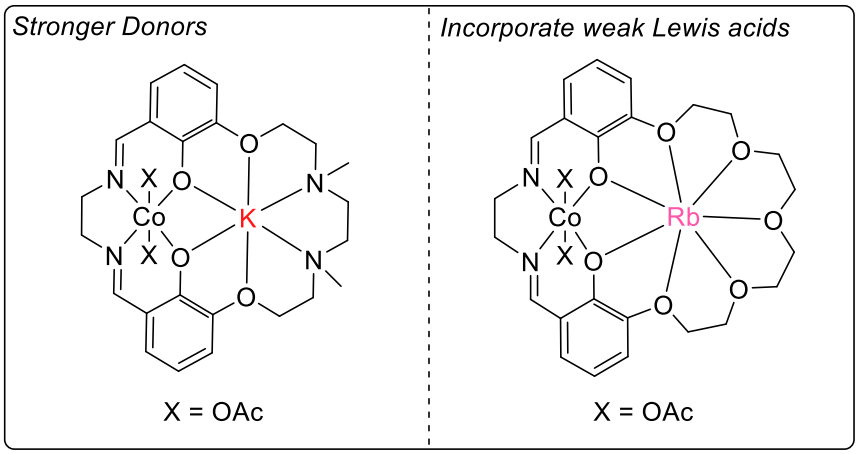


Figure 2.11. Proposed targets for future work, featuring stronger crown ether donors (LHS) and weaker Lewis acid s-block metals (RHS).

Future work with this catalytic system should focus on decreasing the Lewis acidity of the s-block metal by ligand modifications, or accommodating weaker Lewis acids within the macrocyclic ligand (Figure 2.11). The former could involve replacing some of the aliphatic oxygen donors with nitrogen donors. The nitrogen donors should donate more electron density into the K(I) centre, decreasing its Lewis acidity further. While the heavier Group I elements are weaker Lewis acids than K(I), they are too large to accommodate within the 18-crown-6 binding pocket. To accommodate these larger Group I metal cations within the crown ether pocket, a ligand could be synthesised to mimic a 21-crown-7 binding pocket. This should allow the coordination of heavier, weaker Lewis acidic metal cations, such as Rb(I), without the formation of aggregates. Although it must be considered that such catalysts need to be significantly more active than K(I) analogues to account for the increase in molar mass.

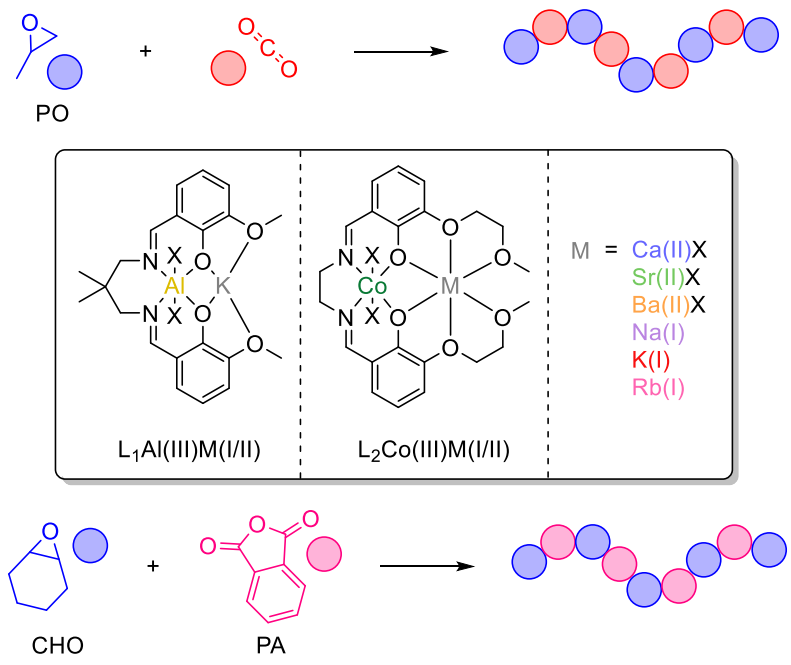
2.5 References

(1) Gil-Negrete, J. M.; Hevia, E. Main group bimetallic partnerships for cooperative catalysis. *Chem. Sci.* **2021**, *12* (6), 1982-1992.
(2) Hill, M. S.; Liptrot, D. J.; Weetman, C. Alkaline earths as main group reagents in molecular catalysis. *Chem. Soc. Rev.* **2016**, *45* (4), 972-988.
(3) Gentner, T. X.; Mulvey, R. E. Alkali-Metal Mediation: Diversity of Applications in Main-Group Organometallic Chemistry. *Angew. Chem. Int. Ed.* **2021**, *60* (17), 9247-9262.
(4) Connor, G. P.; Holland, P. L. Coordination chemistry insights into the role of alkali metal promoters in dinitrogen reduction. *Catal. Today* **2017**, *286*, 21-40.
(5) Cai, Z.; Xiao, D.; Do, L. H. Fine-Tuning Nickel Phenoxyimine Olefin Polymerization Catalysts: Performance Boosting by Alkali Cations. *J. Am. Chem. Soc.* **2015**, *137* (49), 15501-15510.
(6) Chiu, H.-C.; Pearce, A. J.; Dunn, P. L.; Cramer, C. J.; Tonks, I. A. β-Oxo-δ-diimine Nickel Complexes: A Comparison of Tautomeric Active Species in Ethylene Polymerization Catalysis. *Organometallics* **2016**, *35* (12), 2076-2085.
(7) Xia, X.; Suzuki, R.; Takojima, K.; Jiang, D.-H.; Isono, T.; Satoh, T. Smart Access to Sequentially and Architecturally Controlled Block Polymers via a Simple Catalytic Polymerization System. *ACS Catal.* **2021**, *11* (10), 5999-6009.
(8) Zhang, X.; Jones, G. O.; Hedrick, J. L.; Waymouth, R. M. Fast and selective ring-opening polymerizations by alkoxides and thioureas. *Nat. Chem.* **2016**, *8* (11), 1047-1053.
(9) Jadrich, C. N.; Pane, V. E.; Lin, B.; Jones, G. O.; Hedrick, J. L.; Park, N. H.; Waymouth, R. M. A Cation-Dependent Dual Activation Motif for Anionic Ring-Opening Polymerization of Cyclic Esters. *J. Am. Chem. Soc.* **2022**, *144* (19), 8439-8443.
(10) Saito, T.; Aizawa, Y.; Yamamoto, T.; Tajima, K.; Isono, T.; Satoh, T. Alkali Metal Carboxylate as an Efficient and Simple Catalyst for Ring-Opening Polymerization of Cyclic Esters. *Macromolecules* **2018**, *51* (3), 689-696.
(11) Diment, W. T.; Lindeboom, W.; Fiorentini, F.; Deacy, A. C.; Williams, C. K. Synergic Heterodinuclear Catalysts for the Ring-Opening Copolymerization (ROCOP) of Epoxides, Carbon Dioxide, and Anhydrides. *Acc. Chem. Res.* **2022**, *55* (15), 1997-2010.
(12) Deacy, A. C.; Moreby, E.; Phanopoulos, A.; Williams, C. K. Co(III)/Alkali-Metal(I) Heterodinuclear Catalysts for the Ring-Opening Copolymerization of CO_2 and Propylene Oxide. *J. Am. Chem. Soc.* **2020**, *142* (45), 19150-19160.
(13) Deacy, A. C.; Phanopoulos, A.; Lindeboom, W.; Buchard, A.; Williams, C. K. Insights into the Mechanism of Carbon Dioxide and Propylene Oxide Ring-Opening Copolymerization Using a Co(III)/K(I) Heterodinuclear Catalyst. *J. Am. Chem. Soc.* **2022**, *144* (39), 17929-17938.
(14) Deacy, A. C.; Kilpatrick, A. F. R.; Regoutz, A.; Williams, C. K. Understanding metal synergy in heterodinuclear catalysts for the copolymerization of CO_2 and epoxides. *Nat. Chem.* **2020**, *12* (4), 372-380.
(15) Reis, N. V.; Deacy, A. C.; Rosetto, G.; Durr, C. B.; Williams, C. K. Heterodinuclear Mg(II)M(II) (M=Cr, Mn, Fe, Co, Ni, Cu and Zn) Complexes for the Ring Opening Copolymerization of Carbon Dioxide/Epoxide and Anhydride/Epoxide. *Chem. Eur. J.* **2022**, *28* (14), e202104198.
(16) Asaba, H.; Iwasaki, T.; Hatazawa, M.; Deng, J.; Nagae, H.; Mashima, K.; Nozaki, K. Alternating Copolymerization of CO_2 and Cyclohexene Oxide Catalyzed by Cobalt–Lanthanide Mixed Multinuclear Complexes. *Inorg. Chem.* **2020**, *59* (12), 7928-7933.
(17) Lindeboom, W.; Fraser, D. A. X.; Durr, C. B.; Williams, C. K. Heterodinuclear Zn(II), Mg(II) or Co(III) with Na(I) Catalysts for Carbon Dioxide and Cyclohexene Oxide Ring Opening Copolymerizations. *Chem. Eur. J.* **2021**, *27* (47), 12224-12231.
(18) Deacy, A. C.; Durr, C. B.; Kerr, R. W. F.; Williams, C. K. Heterodinuclear catalysts Zn(II)/M and Mg(II)/M, where M = Na(I), Ca(II) or Cd(II), for phthalic anhydride/cyclohexene oxide ring opening copolymerisation. *Catal. Sci. Technol.* **2021**, *11* (9), 3109-3118.
(19) Reath, A. H.; Ziller, J. W.; Tsay, C.; Ryan, A. J.; Yang, J. Y. Redox Potential and Electronic Structure Effects of Proximal Nonredox Active Cations in Cobalt Schiff Base Complexes. *Inorg. Chem.* **2017**, *56* (6), 3713-3718.

(20) Thevenon, A.; Cyriac, A.; Myers, D.; White, A. J. P.; Durr, C. B.; Williams, C. K. Indium Catalysts for Low-Pressure CO_2/Epoxide Ring-Opening Copolymerization: Evidence for a Mononuclear Mechanism? *J. Am. Chem. Soc.* **2018**, *140* (22), 6893-6903.
(21) Diment, W. T.; Gregory, G. L.; Kerr, R. W. F.; Phanopoulos, A.; Buchard, A.; Williams, C. K. Catalytic Synergy Using Al(III) and Group 1 Metals to Accelerate Epoxide and Anhydride Ring-Opening Copolymerizations. *ACS Catal.* **2021**, *11* (20), 12532-12542.
(22) Lalrempuia, R.; Underhaug, J.; Törnroos, K. W.; Le Roux, E. Anionic hafnium species: an active catalytic intermediate for the coupling of epoxides with CO_2? *Chem. Commun.* **2019**, *55* (50), 7227-7230.
(23) Raman, S. K.; Deacy, A. C.; Pena Carrodeguas, L.; Reis, N. V.; Kerr, R. W. F.; Phanopoulos, A.; Morton, S.; Davidson, M. G.; Williams, C. K. Ti(IV)–Tris(phenolate) Catalyst Systems for the Ring-Opening Copolymerization of Cyclohexene Oxide and Carbon Dioxide. *Organometallics* **2020**, *39* (9), 1619-1627.
(24) Yoo, J.; Na, S. J.; Park, H. C.; Cyriac, A.; Lee, B. Y. Anion variation on a cobalt(III) complex of salen-type ligand tethered by four quaternary ammonium salts for CO_2/epoxide copolymerization. *Dalton Trans.* **2010**, *39* (10), 2622-2630.
(25) Shannon, R. D. Revised effective ionic radii and systematic studies of interatomic distances in halides and chalcogenides. *Acta Crystallographica Section A* **1976**, *32* (5), 751-767.
(26) Longo, J. M.; Sanford, M. J.; Coates, G. W. Ring-Opening Copolymerization of Epoxides and Cyclic Anhydrides with Discrete Metal Complexes: Structure–Property Relationships. *Chem. Rev.* **2016**, *116* (24), 15167-15197.
(27) Paul, S.; Zhu, Y.; Romain, C.; Brooks, R.; Saini, P. K.; Williams, C. K. Ring-opening copolymerization (ROCOP): synthesis and properties of polyesters and polycarbonates. *Chem. Commun.* **2015**, *51* (30), 6459-6479.
(28) Zhang, X.; Fevre, M.; Jones, G. O.; Waymouth, R. M. Catalysis as an Enabling Science for Sustainable Polymers. *Chem. Rev.* **2018**, *118* (2), 839-885.
(29) Inkinen, S.; Hakkarainen, M.; Albertsson, A.-C.; Södergård, A. From Lactic Acid to Poly(lactic acid) (PLA): Characterization and Analysis of PLA and Its Precursors. *Biomacromolecules* **2011**, *12* (3), 523-532.
(30) Zhu, Y.; Romain, C.; Williams, C. K. Sustainable polymers from renewable resources. *Nature* **2016**, *540* (7633), 354-362.
(31) Joly, D.; Carpentier, R. Sigmoidal reduction kinetics of the photosystem II acceptor side in intact photosynthetic materials during fluorescence induction. *Photochem. Photobiol. Sci.* **2009**, *8* (2), 167-173.
(32) Kowalski, A.; Duda, A.; Penczek, S. Polymerization of l,l-Lactide Initiated by Aluminum Isopropoxide Trimer or Tetramer. *Macromolecules* **1998**, *31* (7), 2114-2122.
(33) Rosetto, G.; Deacy, A. C.; Williams, C. K. Mg(ii) heterodinuclear catalysts delivering carbon dioxide derived multi-block polymers. *Chem. Sci.* **2021**, *12* (37), 12315-12325.
(34) Sulley, G. S.; Gregory, G. L.; Chen, T. T. D.; Peña Carrodeguas, L.; Trott, G.; Santmarti, A.; Lee, K.-Y.; Terrill, N. J.; Williams, C. K. Switchable Catalysis Improves the Properties of CO_2-Derived Polymers: Poly(cyclohexene carbonate-b-ε-decalactone-b-cyclohexene carbonate) Adhesives, Elastomers, and Toughened Plastics. *J. Am. Chem. Soc.* **2020**, *142* (9), 4367-4378.
(35) Stößer, T.; Mulryan, D.; Williams, C. K. Switch Catalysis To Deliver Multi-Block Polyesters from Mixtures of Propene Oxide, Lactide, and Phthalic Anhydride. *Angew. Chem. Int. Ed.* **2018**, *57* (51), 16893-16897.
(36) Kumar, A.; Blakemore, J. D. On the Use of Aqueous Metal-Aqua pK_a Values as a Descriptor of Lewis Acidity. *Inorg. Chem.* **2021**, *60* (2), 1107-1115.
(37) Gruszka, W.; Garden, J. A. Advances in heterometallic ring-opening (co)polymerisation catalysis. *Nat. Commun.* **2021**, *12* (1), 3252.

Chapter Three

Mechanistic Investigations of Heterodinuclear Sustainable Polymerisation Catalysts using s-Block Metal Lewis Acidity



3.1 Introduction

As was discussed in Chapter Two, clear trends were observed between the activity and (where relevant) selectivity of a Co(III)M(I/II) catalyst series (M(I/II) = Na(I), K(I), Ca(II), Sr(II), Ba(II)) for PO/CO_2 ROCOP, PO/PA ROCOP, and *rac*-LA ROP. The most active catalyst for each polymerisation was the Co(III)K(I) combination. This was attributed to the correlation with lower s-block metal Lewis acidity, which may labilise the K-oxygenate nucleophile in the rate-determining step of each polymerisation.[1] Some key questions still remain, including whether these correlations are relevant to other ROCOP catalysts:

1) Can similar correlations be observed with different ROCOP catalyst featuring, e.g., different ligand architectures or metal combinations?
2) Can improved activities be achieved by incorporating larger, more weakly Lewis acidic metals which were too large to coordinate within the ether pocket of the original macrocycle (e.g. Rb(I))?
3) Can these correlations between s-block metal Lewis acidity and activity/selectivity be used to gain insights into the mechanisms of the copolymerisations?

3.2 Aims

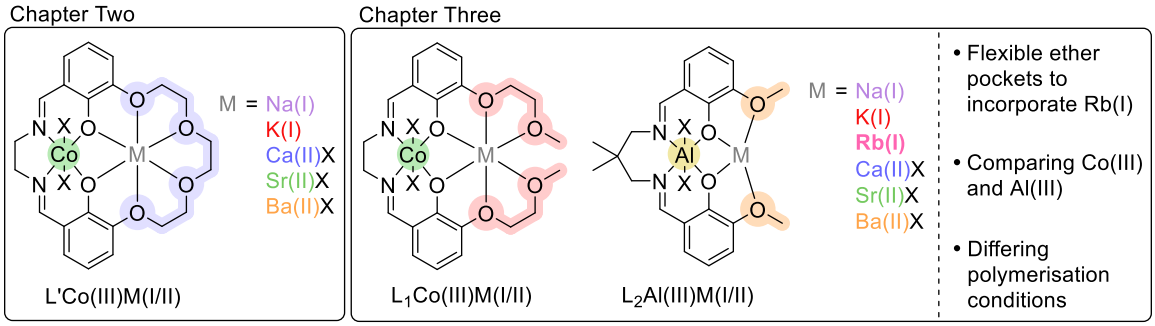


Figure 3.1. Summary of aims for Chapter Three, with the comparison of the structure of the catalyst series from Chapter Two.

In this chapter, the mechanisms of two catalysts for epoxide/CO_2 and/or epoxide/anhydride ROCOP are explored, guided by an s-block metal Lewis acidity scope study. The catalysts feature flexible, acyclic ether binding pockets, within which the s-block metals coordinate (Figure 3.1). This ligand flexibility should allow the incorporation of larger, more weakly Lewis acidic metals (e.g. Rb), allowing a greater range of Lewis acidities to be investigated. Varying M(III), monomer combinations, and reaction conditions allow further insight into the generality of any catalyst structure – performance trends.

3.3 Results and Discussion

3.3.1 L_1Al(III)M(I/II) Synthesis and Characterisation

3.3.1.1 Synthesis

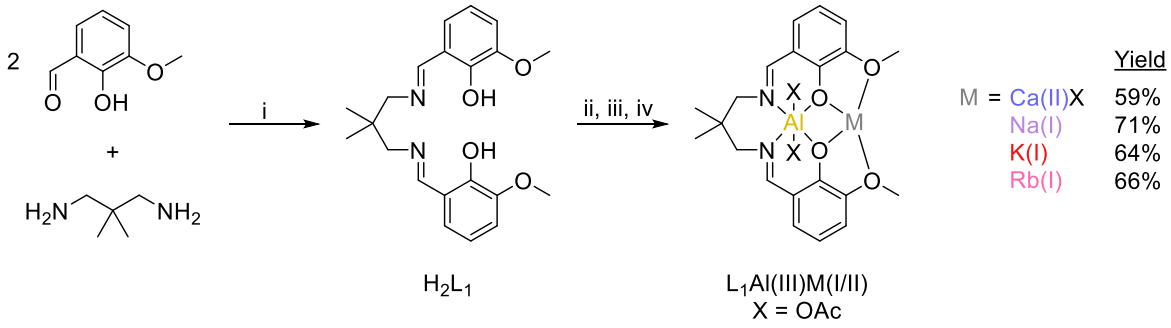


Figure 3.2. Synthesis of L_1Al(III)M(I/II) (M(I/II) = Ca(II), Sr(II), Ba(II), Na(I), K(I), Rb(I)); i) MeOH, rt, 16 h; ii) $AlEt_3$, THF, rt, N_2, 2 h; iii) AcOH, THF, rt, 16 h; iv) M(I/II)$(OAc)_{2\text{-}3}$, THF, rt, 16 h.

H_2L_1 was synthesised by combining two equivalents of *ortho*-vanillin with one equivalent of 2,2-dimethyl propane-1,3-diamine in methanol and stirring at room temperature for 16 h (Figure 3.2).[2] The resultant solution was evaporated *in vacuo* to give H_2L_1 as a yellow-orange solid in quantitative yield.

To a solution of H_2L_1 in THF, under a N_2 atmosphere, was added $AlEt_3$ in one portion.[2] The resultant solution was stirred for 2 h, followed by the addition of AcOH to produce the monometallic Al(III) acetate complex, which formed as a pale-yellow precipitate (Figure 3.2). The mixture was stirred for 16 h, after which the respective s-block metal acetate was added, and the mixture was stirred for 16 h. The precipitate changed colour from pale yellow to white, corresponding to the coordination of the s-block metal. The desired L_1Al(III)M(I/II) complex was isolated by filtration and washed with cold THF to produce the pure catalyst in yields between 59 – 71% (Figure 3.2). The novel L_1Al(III)Ca(II) catalyst was characterised by ^{1}H, ^{13}C{^{1}H}, COSY, HSQC, and HMBC NMR spectroscopy, IR spectroscopy, and single crystal X-ray diffraction (Figures 3.3 – 3.5, S3.1 – 3.5). Catalyst purity was determined by elemental analysis. Spectroscopic and elemental analysis of the L_1Al(III)M(I) catalysts were in accordance with those in the literature.[2]

Attempts to synthesise the Sr(II) and Ba(II) analogues were unsuccessful, as purification of the crude product by filtration and washing with THF led to degradation of the desired complexes by ^{1}H NMR spectroscopy. Further attempts to synthesise and isolate these complexes will be made using solvents that have been thoroughly dried before use, as the presence of trace water may result in the de-coordination of the s-block metal in the case of these complexes.

3.3.1.2 NMR Spectroscopy

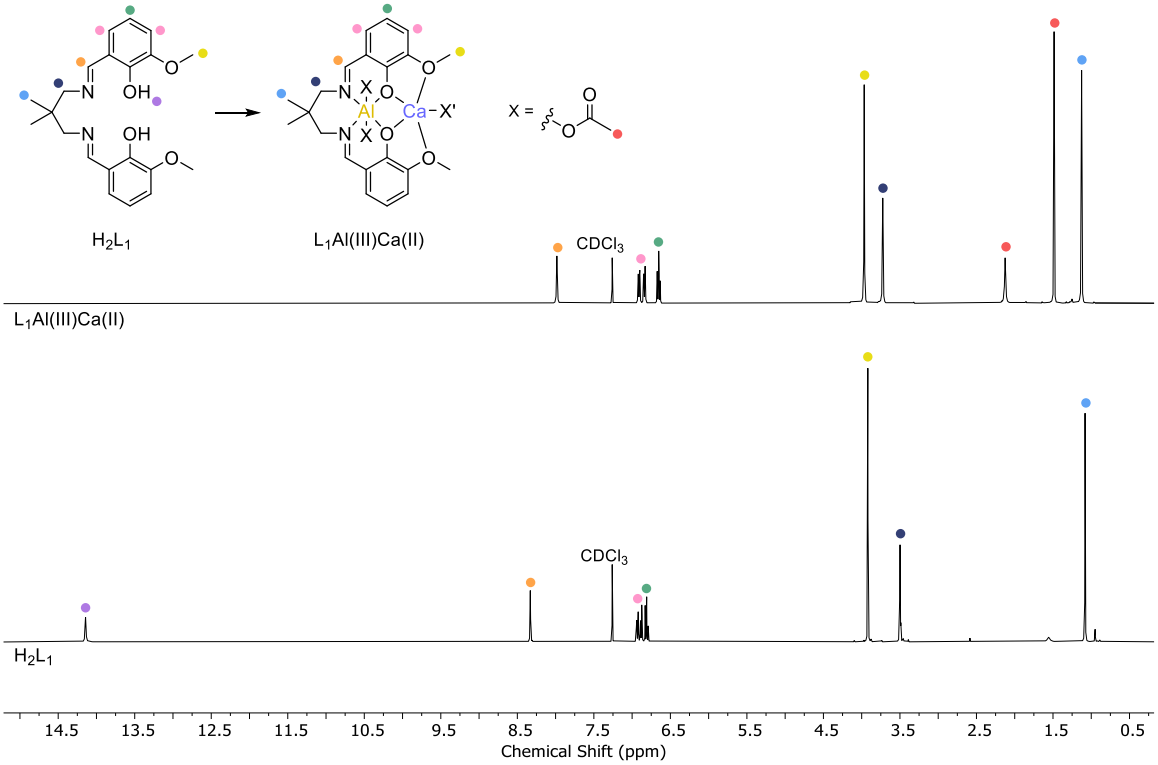


Figure 3.3. Stacked ^{1}H NMR spectra of L_1Al(III)Ca(II) (top) and H_2L_1 (bottom) showing disappearance of the phenolic proton resonance (purple), appearance of acetate resonances (red), and shifting of the imine resonance (orange).

Catalyst synthesis was confirmed by ^{1}H NMR spectroscopy, by the disappearance of the phenolic proton resonance of the proligand (13.57 ppm, purple circle in Figure 3.3), appearance of acetate resonances (2.13 – 1.49 ppm, red circles in Figure 3.3), and shifting of the imine resonance from 8.33 ppm to 7.98 – 7.90 ppm with coordination of the Al(III) centre. For L_1Al(III)Ca(II), two sets of acetate resonances can be observed in both the ^{1}H (2.13 and 1.49 ppm) and ^{13}C{^{1}H} (182.7, 176.0, 24.4, 24.3 ppm) NMR spectra (Figure S3.1 and S3.3). These are assigned as two acetates which are bound to

the Al(III) centre (1.49 ppm (^{1}H), and 176.0, 24.3 ppm (^{13}C{^{1}H}) and one acetate which is bound to the Ca(II) centre (2.13 ppm (^{1}H), and 182.7, 24.3 ppm (^{13}C{^{1}H}). The L$_{1}$Al(III)M(I) catalysts only have two acetate co-ligands due to charge balancing, leading to only one set of acetate co-ligands in the ^{1}H and ^{13}C{^{1}H} NMR spectra, which suggests that both acetate co-ligands are bound to the Al(III) centre.

3.3.1.3 Infrared Spectroscopy

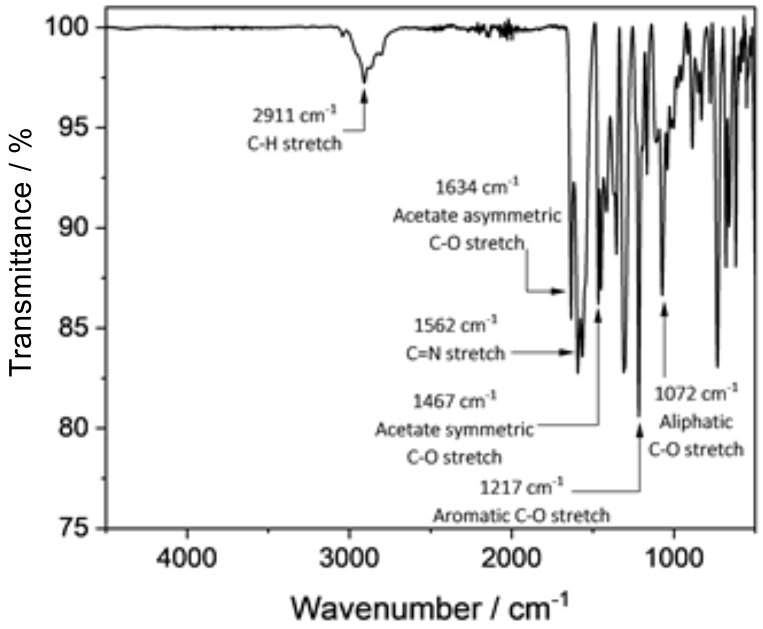
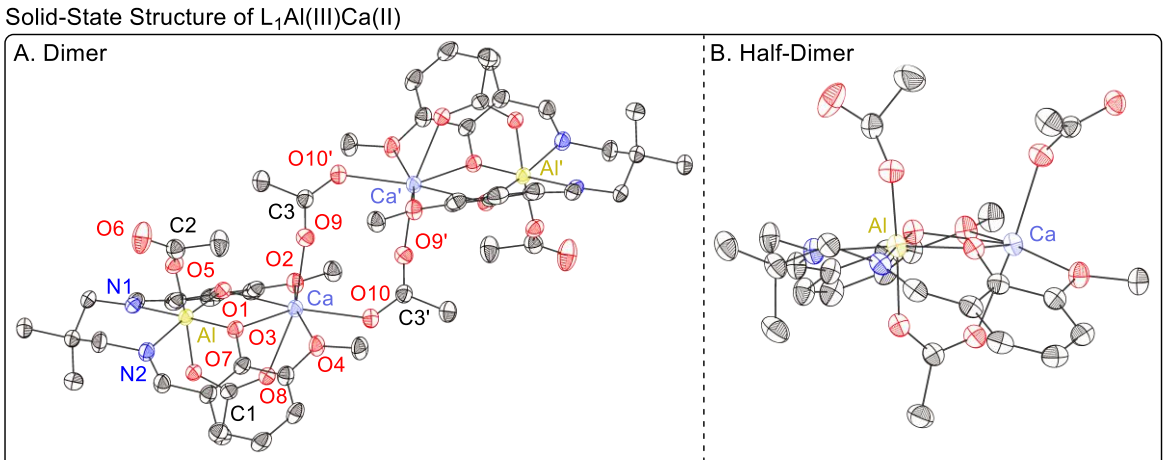


Figure 3.4. Solid-state IR spectrum of L$_{1}$Al(III)Ca(II).

The novel L$_{1}$Al(III)Ca(II) complex was characterised by IR spectroscopy, where absence of the ligand phenol O-H stretch (typically between 3200 – 3500 cm^{-1}) indicates successful coordination of Al(III) in the ligand scaffold (Figure 3.4). Absorbances corresponding to C-H bond stretches, imine C=N stretch, acetate C-O stretches, and aromatic and aliphatic C-O stretches can be observed (Figure 3.4).

3.3.1.4 Single Crystal X-Ray Crystallography



C. Selected Bond Lengths and Angles

Bond	Length / Å
Al-Ca	3.3487(5)
O7-C1	1.2822(18)
C1-O8	1.2471(18)
O9-C3	1.2592(19)
C3-O10'	1.2547(19)
O5-C2	1.293(2)
C2-O6	1.233(9)

Atoms	Angle / º
N1-Al-N2	89.88(5)
O5-Al-O7	176.14(5)
O1-Al-O3	89.21(5)
O2-Ca-O1	76.63(4)
O1-Ca-O3	65.58(3)
O3-Ca-O4	66.06(3)
O4-Ca-O10	64.05(3)
O9-Ca-O8	165.28(4)

Figure 3.5. Solid state structure and selected bond lengths and angles of L1Al(III)Ca(II) determined by single crystal X-ray diffraction. Thermal ellipsoids are shown at 50% probability, and solvent molecules and protons are omitted for clarity.

Single crystals of L1Al(III)Ca(II) suitable for X-ray diffraction experiments were grown by vapour diffusion of hexane into a solution of the complex in chloroform. L1Al(III)Ca(II) crystallises as the heterodinuclear complex with an Al(III)-Ca(II) intermetallic separation of 3.349 Å (Figure 3.5). It forms a dimeric structure in the solid-state, where two acetates bridge between the Ca(II) centres of two heterodinuclear units (Figure 3.5A). Al(III) forms a distorted octahedron, coordinating to two imine and two phenoxide donors of the ligand, and two acetate co-ligands *trans* to each other (Figure 3.5B). It shows aluminate character, as shown by the shorter acetate C-O bond lengths where the oxygen is coordinated to the Al(III) centre, compared to the C-O bond lengths where the oxygen is either uncoordinated or coordinated to Ca(II) (Figure 3.5C).[2, 3] The Ca(II) centre adopts a seven-coordinate, distorted pentagonal bipyramid geometry, coordinating to two phenoxide and two

aromatic ether donors from the ligand, one acetate bridging with the Al(III) centre, and two acetate co-ligands bridging with the other Ca(II) centre of the dimer.

As discussed previously, in the ^{1}H and $^{13}C\{^{1}H\}$ NMR spectra of L_1Al(III)Ca(II) two acetate environments can be observed, and these were assigned as two acetates bound to the Al(III) centre, and one bound to the Ca(II) centre. In the solid-state structures, three acetate environments can be observed: one is terminally bound to the Al(III) centre, a second bridges between the Al(III) and Ca(II) centres within a single complex, and the third bridges between Ca(II) centres of two complexes. Perhaps, in the solution-phase, the terminal and bridging acetates bound to the Al(III) centre are able to exchange on the time-scale of NMR spectroscopy, leading to a single environment.

Low-temperature ^{1}H NMR spectroscopic experiments should be performed in the future to explore whether the two Al(III)-bound acetate environments can be distinguished. DOSY NMR spectroscopy experiments should also be performed on L_1Al(III)Ca(II) in a donating solvent (e.g. THF-d_4, MeOD-d_4) to determine whether the complex is likely to be monomeric or dimeric during polymerisation.

3.3.2 $L_2Co(III)M(I/II)$ Synthesis and Characterisation

3.3.2.1 Synthesis

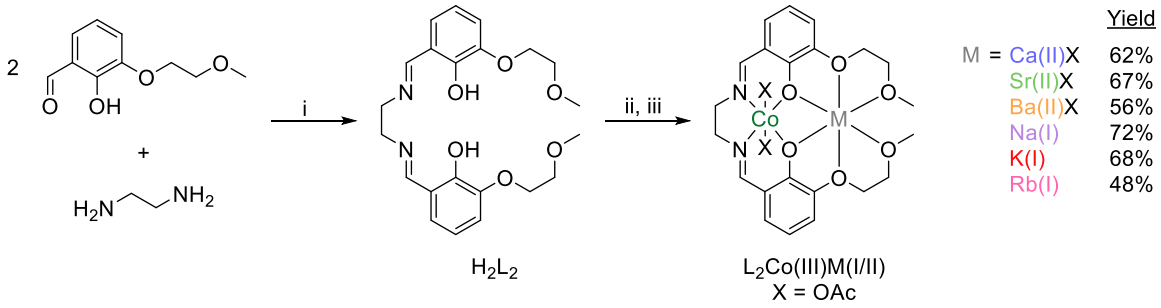


Figure 3.6. Synthesis of $L_2Co(III)M(I/II)$ (M(I/II) = Ca(II), Sr(II), Ba(II), Na(I), K(I)), Rb(I); i) MeOH, rt, N_2, 16 h; ii) $Co(OAc)_2$, $M(I/II)(OAc)_{1\text{-}2}$, MeCN, N_2, rt, 16 h; iii) air, rt, 16 h; 48 – 72% yield.

H_2L_2 was synthesised by combining two equivalents of the aldehyde precursor with an equivalent of ethylene diamine, in methanol at room temperature (Figure 3.6).[4] The solution was stirred for 16 h, after which H_2L_2 formed as a yellow, fluffy precipitate. The solid was isolated by filtration, and washed with cold methanol, to give H_2L_2 in 52% yield.

$L_2Co(III)M(I/II)$ was synthesised by combining H_2L_2 with $Co(OAc)_2$ and the respective s-block metal acetate in MeCN, under a N_2 atmosphere (Figure 3.6).[4] The mixture was stirred at room temperature for 16 h, giving a bright red solution. The Co(II) centre was oxidised to Co(III) by stirring the solution open to air for 16 h. The $L_2Co(III)M(I/II)$ complexes were purified by precipitation (dichloromethane/pentane) and isolated as pale brown solids with yields between 48 – 72%. In all cases, the complexes were characterised by ^1H, $^{13}C\{^1H\}$, COSY, HSQC, and HMBC NMR spectroscopy, and IR spectroscopy (Figures 3.7, 3.8, and S3.3.6 – S3.16). Catalyst purity was determined by elemental analysis. Spectroscopic characterisation of previously reported $L_2Co(III)M(I)$ catalysts were in accordance with data provided in the literature.[4]

3.3.2.2 NMR Spectroscopy

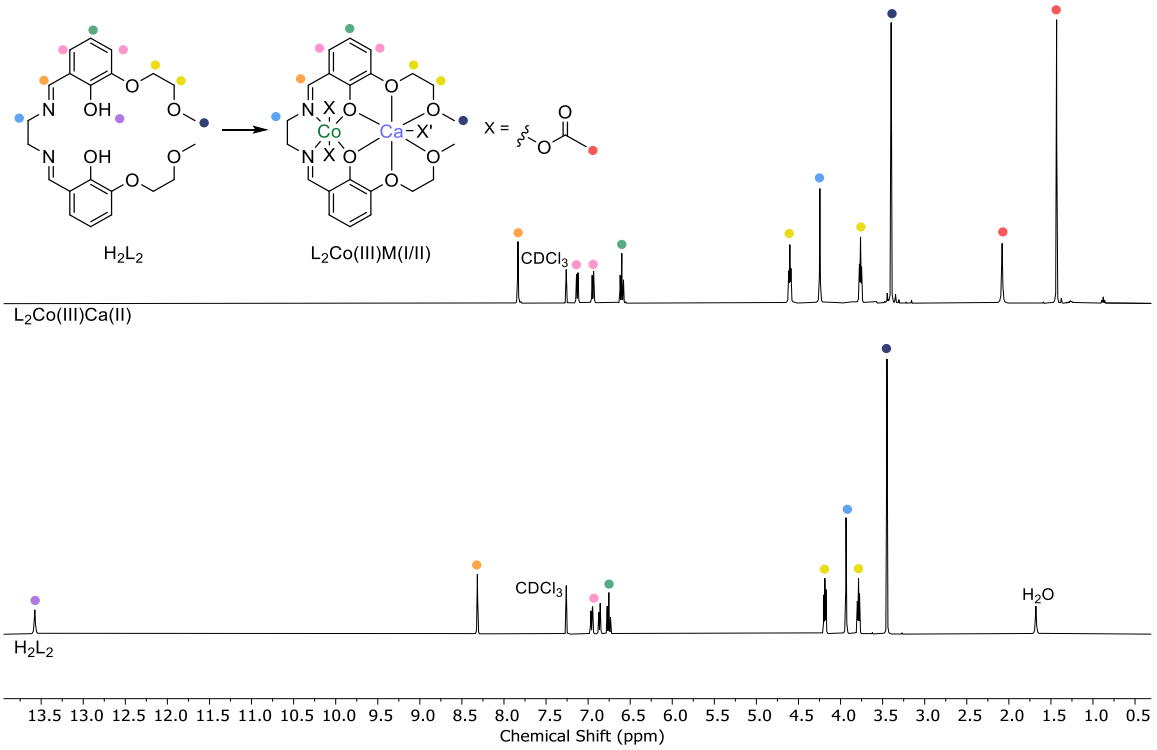


Figure 3.7. Stacked ^{1}H NMR spectra of L_1Al(III)Ca(II) (top) and H_2L_1 (bottom) showing disappearance of the phenolic proton resonance (purple), appearance of acetate resonances (red), and shifting of the imine (orange) and ether (yellow) resonances.

Successful synthesis of the L_2Co(III)M(I/II) catalysts could be determined by ^{1}H NMR spectroscopy by the disappearance of the phenolic proton (purple, Figure 3.7), indicating Co(III) coordination, and shifting of the ether resonances (yellow, Figure 3.7), indicating coordination of the s-block metal. Acetate resonances (red, Figure 3.7) can also be observed upon successful synthesis of the catalyst. As with L_1Al(III)Ca(II), the L_2Co(III)M(II) catalysts show two acetate resonances in the ^{1}H and ^{13}C{^{1}H} NMR spectra, which are proposed to correspond to two acetates which are bound to the Co(III) centre, and one acetate which is bound to the Group II metal.

3.3.2.3 Infrared Spectroscopy

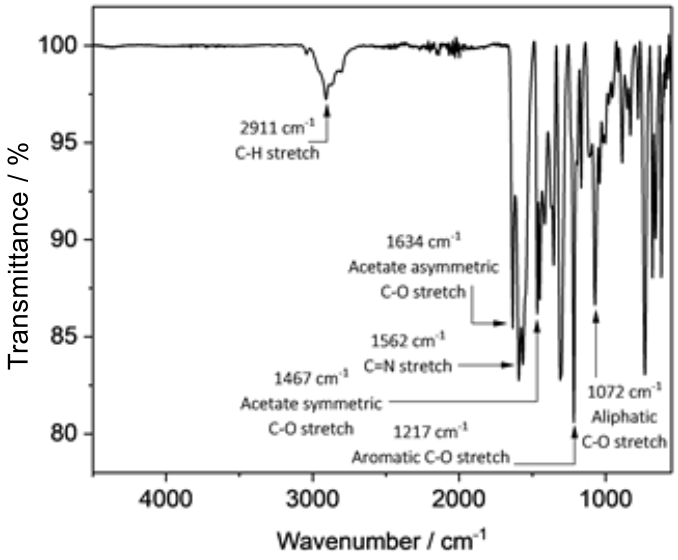


Figure 3.8. Solid-state IR spectrum of $L_2Co(III)Ca(II)$.

Successful coordination of the Co(III) centre within the ligand Schiff base binding pocket can be observed by IR spectroscopy, by the absence of a phenol O-H stretch (typically between 3200 – 3500 cm^{-1}; Figure 3.8). Absorbances corresponding to C-H stretch, imine C=N stretch, acetate C-O stretches, and aromatic and aliphatic C-O stretches can be observed (Figure 3.8).

3.3.4 Ring-Opening Copolymerisation Catalysis

3.3.4.1 Ring-Opening Copolymerisation of Cyclohexene Oxide with Phthalic Anhydride using L1Al(III)M(I/II)

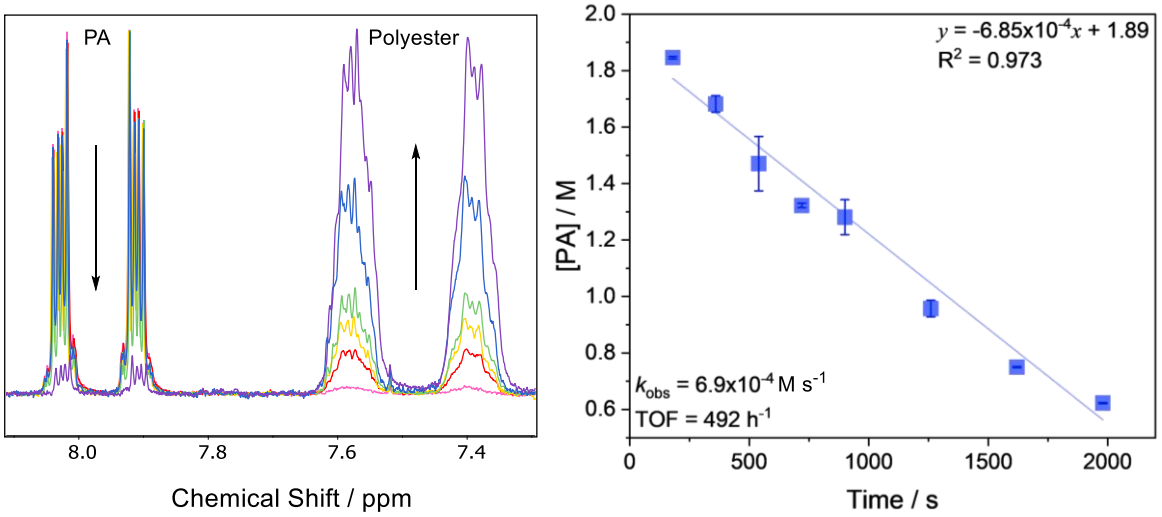


Figure 3.9. LHS: Stacked ^{1}H NMR spectra for CHO/PA ROCOP catalysed by L1Al(III)Na(I) (from 3 mins (pink) to 30 mins (purple)) showing the decay of the resonances corresponding to PA, and the growth in resonances corresponding to polyester; RHS: plot of [PA] against time for CHO/PA ROCOP catalysed by L1Al(III)Ca(II) from which k_{obs} and TOF were calculated.

The L1Al(III)M(I/II) catalyst series was tested for the ROCOP of CHO and PA under the following conditions: 1:400:2000 $[catalyst]_0$:$[PA]_0$:$[CHO]_0$, neat epoxide, 100 °C. Reactions were conducted in air-tight vials, and the reaction progression was monitored by removing aliquots at regular intervals, which were analysed by ^{1}H NMR spectroscopy to observe the decay in the resonance for PA, and the growth in the resonance for polyester (Figure 3.9, LHS). Reactions were conducted in duplicate, from which standard errors were calculated. Observed rate coefficients (k_{obs}) and turnover frequencies (TOFs) were calculated from linear fits of plots of [PA] against time (Figure 3.9, RHS).

Table 3.1. Data for the ROCOP of cyclohexene oxide (CHO) and phthalic anhydride (PA) with the L_1Al(III)M(I/II) catalysts.[a]

	Catalyst	Time / h	TON [b]	TOF [c] / h^{-1}	k_{obs} [d] / × 10^{-4} s^{-1}	M_n [$Đ$] [e] / g mol^{-1}
1	L_1Al(III)Na(I)	0.5	349	655 ± 7	9.1 ± 0.9	5200 [1.10]
2	L_1Al(III)K(I)	0.3	364	1080 ± 11	15 ± 2	5700 [1.09]
3	L_1Al(III)Rb(I)	0.3	379	1150 ± 11	16 ± 2	5800 [1.11]
4	L_1Al(III)Ca(II)	0.6	276	492 ± 5	6.9 ± 0.7	4000 [1.07]

[a] Reaction conditions: 1:400:2000 $[catalyst]_0$:$[PA]_0$:$[CHO]_0$, 100 °C, neat. [b] Turnover number (TON) = moles of CHO consumed/moles of catalyst, determined by ^{1}H NMR spectroscopy by integrating the peaks for PA (8.10 – 7.85 ppm), Poly(CHO-*alt*-PA) (7.75 – 7.40 ppm), and PCHO (3.46 – 3.64 ppm). [c] Turnover frequencies (TOFs) were calculated between 5 – 70% conversion in each case (Tables S1 and S2, equation S1). [d] Observed rate coefficients (k_{obs}) were calculated from linear fits to plots of [PA] against time (Figure 4.8 RHS). [e] Determined by GPC, in THF, at 30 °C, using narrow molecular weight polystyrene calibrants.

The L_1Al(III)M(I/II) catalyst series follows the same trend of activity against s-block metal Lewis acidity as seen in Chapter 2; there is an exponential increase in the activity of the catalysts with decreasing Lewis acidity (i.e. increasing pK_a of the aqua complex of the s-block metal; Table 3.1, Figure 3.10A).[5] Suitability of the exponential fit was confirmed by a plot of ln(k_{obs}) against ln(pK_a of $[M(OH_2)_n]^{m+}$), which shows a linear correlation (Figure S3.17). Attempting to correlate activity with ionic radius gives an inferior fit (Figure S3.18).[6] The L_1Al(III)Rb(I) catalyst is the fastest of the series, although it is only marginally more active than the K(I) analogue (TOF = 1150 h^{-1} and 1080 h^{-1} respectively). All the catalysts were fully selective for polyester, with narrow dispersities indicative of well-controlled polymerisations (Figure S3.19). Polyester molar masses were significantly lower than the calculated theoretical molar masses (e.g. $M_{n,\,theo}$ for L_1Al(III)K(I) = 29,800 g mol^{-1}) but this is likely due to protic impurities in the epoxide and anhydride (diol and diacid respectively) acting as initiators/chain transfer agents during the polymerisations.

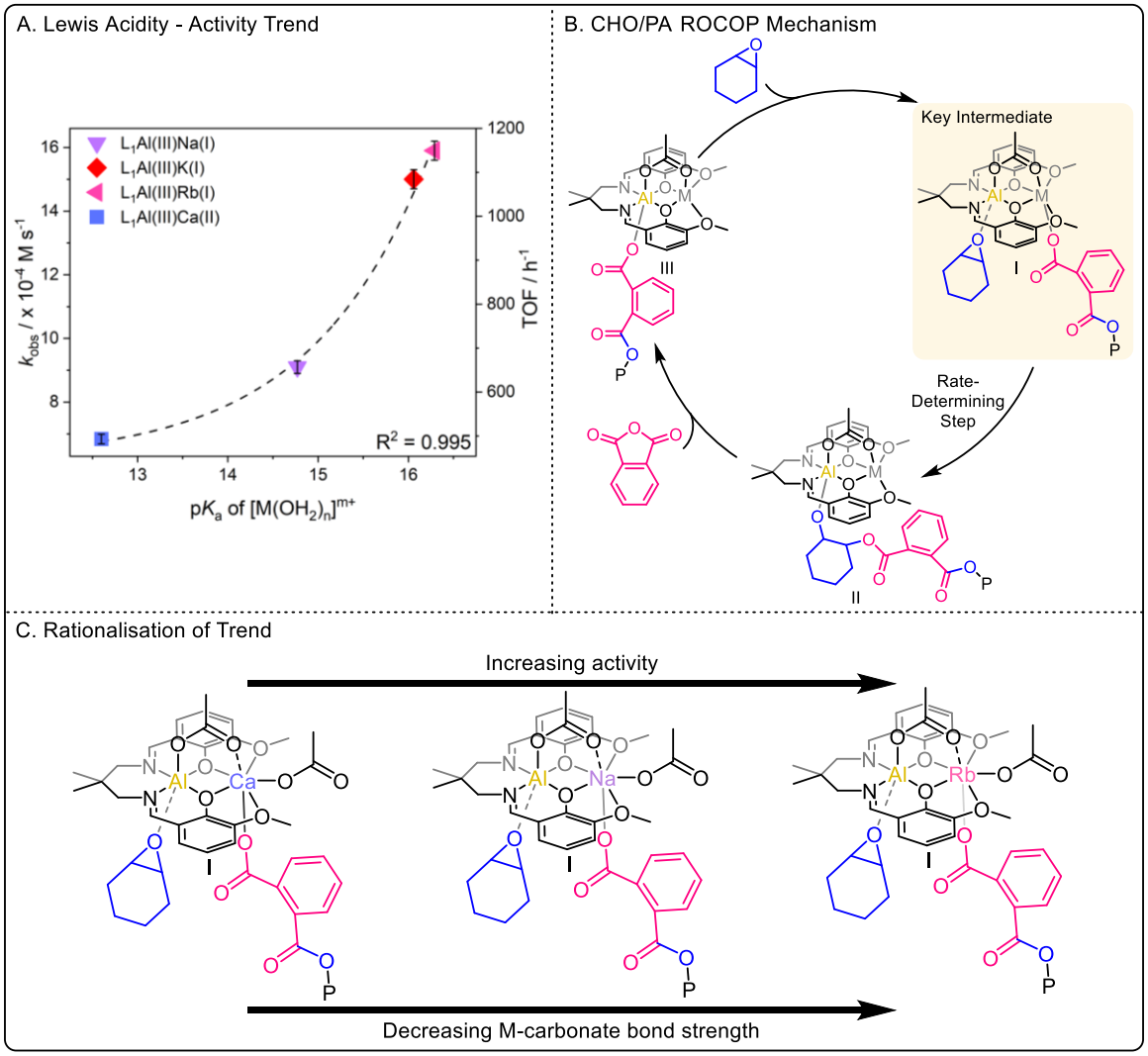


Figure 3.10. A. Plot of activity (TOF and k_{obs}) of L1Al(III)M(I/II) for CHO/PA ROCOP against pK_a of the incorporated s-block metal aqua complex; B. Proposed mechanism of CHO/PA ROCOP catalysed by L1Al(III)M(I/II); C. Rationalisation of the increase in activity seen with decreasing s-block metal Lewis acidity.

The L1Al(III)M(I/II) complexes are proposed to catalyse the ROCOP of CHO and PA via a dinuclear metallate mechanism.[2,7] In such a mechanism, the rate-determining step consists of Al(III)-epoxide ring-opening by a nucleophilic M-carboxylate species (Figure 3.10B). The resultant alkoxide rapidly inserts an equivalent of PA to reform the carboxylate species, completing the catalytic cycle. The observed trend in activity with changing s-block metal Lewis acidity may be rationalised by the more weakly Lewis acidic metals (K(I), Rb(I)) resulting in a more labile M-carboxylate nucleophile in the rate-determining step (Figure 3.10C).

3.3.4.2 Ring-Opening Copolymerisation of Propene Oxide with CO_2 using $L_2Co(III)M(I/II)$

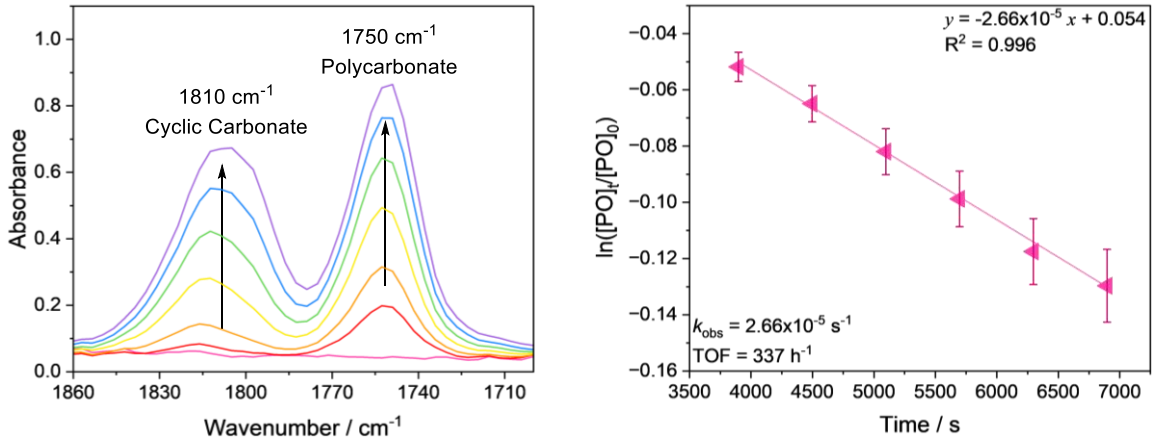


Figure 3.11. LHS: Stacked FTR-IR spectra at various time-points (from 0 h (pink) to 20 h (purple)) of PO/CO_2 ROCOP catalysed by $L_2Co(III)Ba(II)$ showing the growth of peaks corresponding to polycarbonate (1750 cm^{-1}) and cyclic carbonate (1810 cm^{-1}); RHS: Plot of $\ln([PO]_t/[PO]_0)$ against time for PO/CO_2 ROCOP catalysed by $L_2Co(III)Rb(I)$ from which k_{obs} and TOF are calculated.

The $L_2Co(III)M(I/II)$ catalyst series was tested for the ROCOP of PO and CO_2 under 13 bar CO_2 pressure, at 50 °C. The polymerisations were conducted in an autoclave fitted with an *operando* FTR-IR probe, allowing monitoring of the formation of polycarbonate (1750 cm^{-1}) and cyclic carbonate (1810 cm^{-1}; Figure 3.11 LHS). Once the reaction was complete, the catalyst was quenched by exposure to air and addition of approximately 10 equivalents of benzoic acid. The final conversion of epoxide was determined by ^1H NMR spectroscopy of an aliquot, using mesitylene as an internal standard. Observed rate coefficients (k_{obs}) and turnover frequencies (TOFs) were calculated from linear fits of plots of $\ln([PO]_0/[PO]_t)$ against time (Figure 3.11 RHS).

Table 3.2. Data for the ROCOP of propene oxide (PO) and CO_2 with the $L_2Co(III)M(I/II)$ catalysts. [a]

	Catalyst	Time / h	TON [b]	TOF_{PPC} [c] / h^{-1}	k_{obs} [d] / × 10^{-6} M^{-1} s^{-1}	PPC [e] / %	M_n [$Đ$] [f] / g mol^{-1}
1	$L_2Co(III)Na(I)$	5.6	680	96 ± 1	7.5 ± 0.8	91	3200 [1.08]
2	$L_2Co(III)K(I)$	3.0	1091	460 ± 50	36.0 ± 4	97	5900 [1.07]
3	$L_2Co(III)Rb(I)$	4.0	785	341 ± 30	27.0 ± 3	96	4200 [1.10]
4	$L_2Co(III)Ca(II)$	63.7	1237	6 ± 1	0.5 ± 0.1	25	3500 [1.21]
5	$L_2Co(III)Sr(II)$	46.9	1285	12 ± 1	0.9 ± 0.1	48	3700 [1.16]
6	$L_2Co(III)Ba(II)$	21.3	1200	20 ± 2	16.0 ± 2	55	3200 [1.13]

[a] Reaction conditions: 1:20:4000 $[catalyst]_0$:$[CHD]_0$:$[PO]_0$ in neat epoxide, 20 bar CO_2, 50 °C. [b] Turnover number (TON) = moles of PO consumed/moles of catalyst, determined by ^{1}H NMR spectroscopy by integrating resonances corresponding to PPC (4.92 ppm), PC (4.77 ppm) and PPO (3.46-3.64 ppm), using mesitylene internal standard (0.05 mol%, 36 mM). [c] Turnover frequencies (TOFs) are determined between 5 – 20% conversion in all cases (Tables S3 and S4, Equation S2). [d] Observed rate coefficients (k_{obs}) were calculated from linear fits to plots of $\ln([PO]_t/[PO]_0)$ against time (Figure 4.10 LHS). [e] PPC selectivity (i.e. selectivity for PPC over PC and PPO) determined by ^{1}H NMR spectroscopy. [f] Determined by GPC, in THF, at 30 °C, using narrow molecular weight polystyrene calibrants.

Again, the $L_2Co(III)M(I/II)$ catalyst series shows an exponential increase in activity with increasing s-block metal aqua complex pK_a from Ca(II) to K(I) followed by a drop in activity for Rb(I) (Table 3.2, Figure 3.12A). The suitability of the exponential fit for the catalyst series (excluding the $L_2Co(III)Rb(I)$ combination) was confirmed by a linear fit to the plot of $\ln(k_{obs})$ against ln(pK_a of $[M(OH_2)_n]^{m+}$) (Figure 3.20). Plots of activity and selectivity of each catalyst against the ionic radius of the incorporated s-block metal showed no correlation, indicating that the change in activity observed is not due to the changing s-block metal ionic radius, as is often invoked in the literature for many catalysts for ROCOP or ROP (Figures S3.21 and S3.22 respectively).[8-11]

Interestingly, for $L_2Co(III)M(I/II)$, the K(I) catalyst has a greater activity than the Rb(I) catalyst. This result is in contrast to the $L_1Al(III)M(I/II)$ catalyst series, where the Rb(I) catalyst had a slightly greater activity than the K(I) catalyst. The selectivity for polycarbonate varies widely across the series, ranging from only 25% for the Ca(II) catalyst, to 97% for the K(I) catalyst. All the tested catalysts had perfect CO_2 uptake (i.e. no ether linkages could be detected by ^{1}H NMR spectroscopy)

and the polycarbonates produced had narrow dispersities, and molar masses close to theoretical values (Figure S3.23).

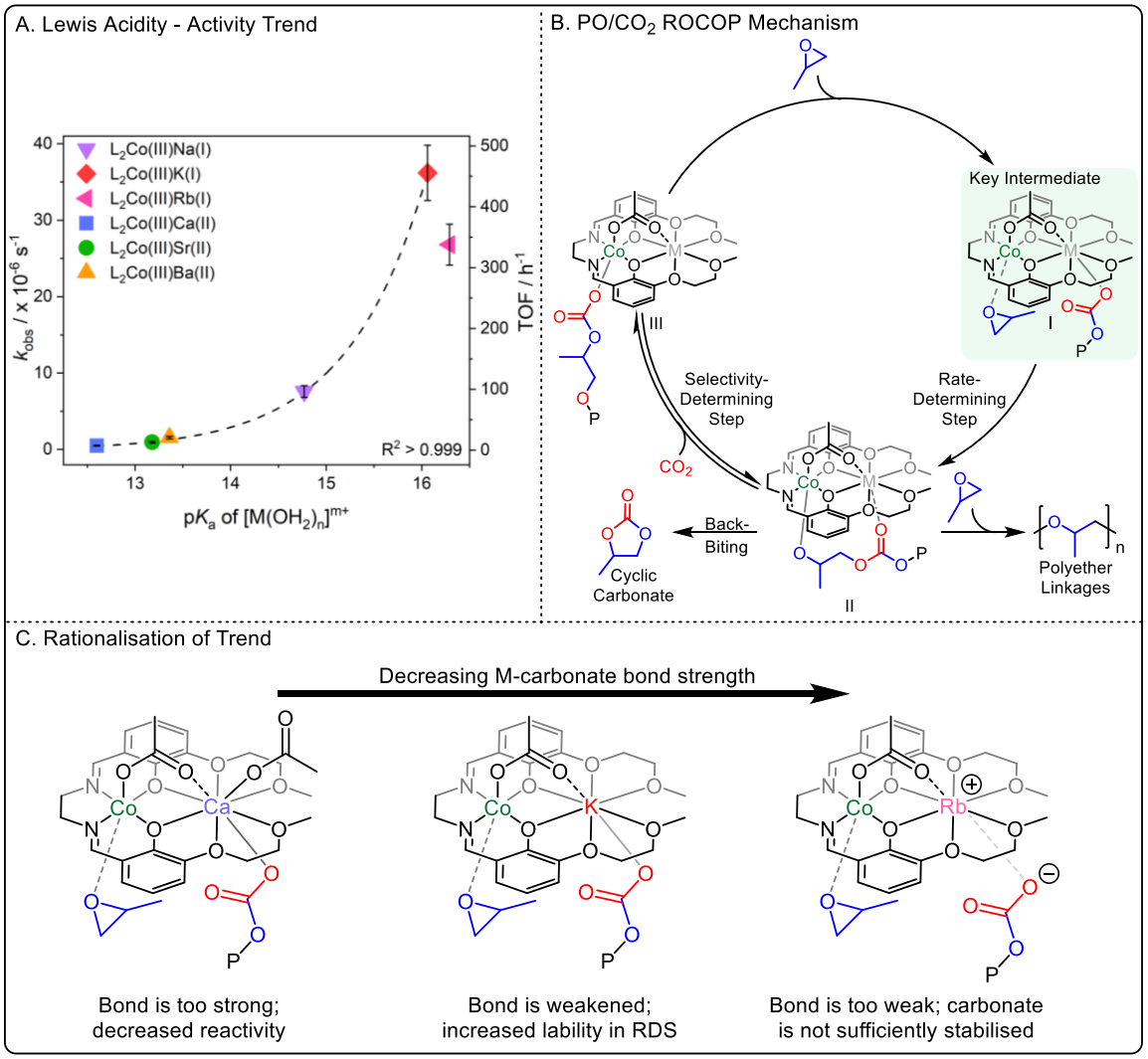


Figure 3.12. A. Plot of activity (TOF and k_{obs}) of L2Co(III)M(I/II) for PO/CO2 ROCOP against pK_a of the incorporated s-block metal aqua complex; B. Proposed mechanism of PO/CO2 ROCOP catalysed by L2Co(III)M(I/II), highlighting the key rate-determining intermediate; C. Rationalisation of the increase in activity seen with decreasing s-block metal Lewis acidity.

The proposed mechanism for PO/CO2 ROCOP catalysed by L2Co(III)M(I/II) is, again, a dinuclear metallate mechanism, where the rate determining step is epoxide ring-opening by a nucleophilic s-block metal carbonate intermediate (Figure 3.12B).[4] Subsequent CO2-insertion is determined by an equilibrium between the alkoxide and carbonate intermediates; this is often referred to as the "selectivity-determining step", as the cyclic carbonate by-product is proposed to be formed exclusively from the alkoxide intermediate.[4, 12]

The exponential increase in activity with decreasing Lewis acidity from Ca(II) to K(I) can be rationalised by progressive weakening of the bond between the s-block metal and the carbonate species, resulting in labilisation of the nucleophile in the rate-determining step. Perhaps Rb(I) is so weakly Lewis acidic that the carbonate is not sufficiently stabilised, resulting in decarboxylation of the carbonate chain-end, reducing the catalytic activity (Figure 3.12C).

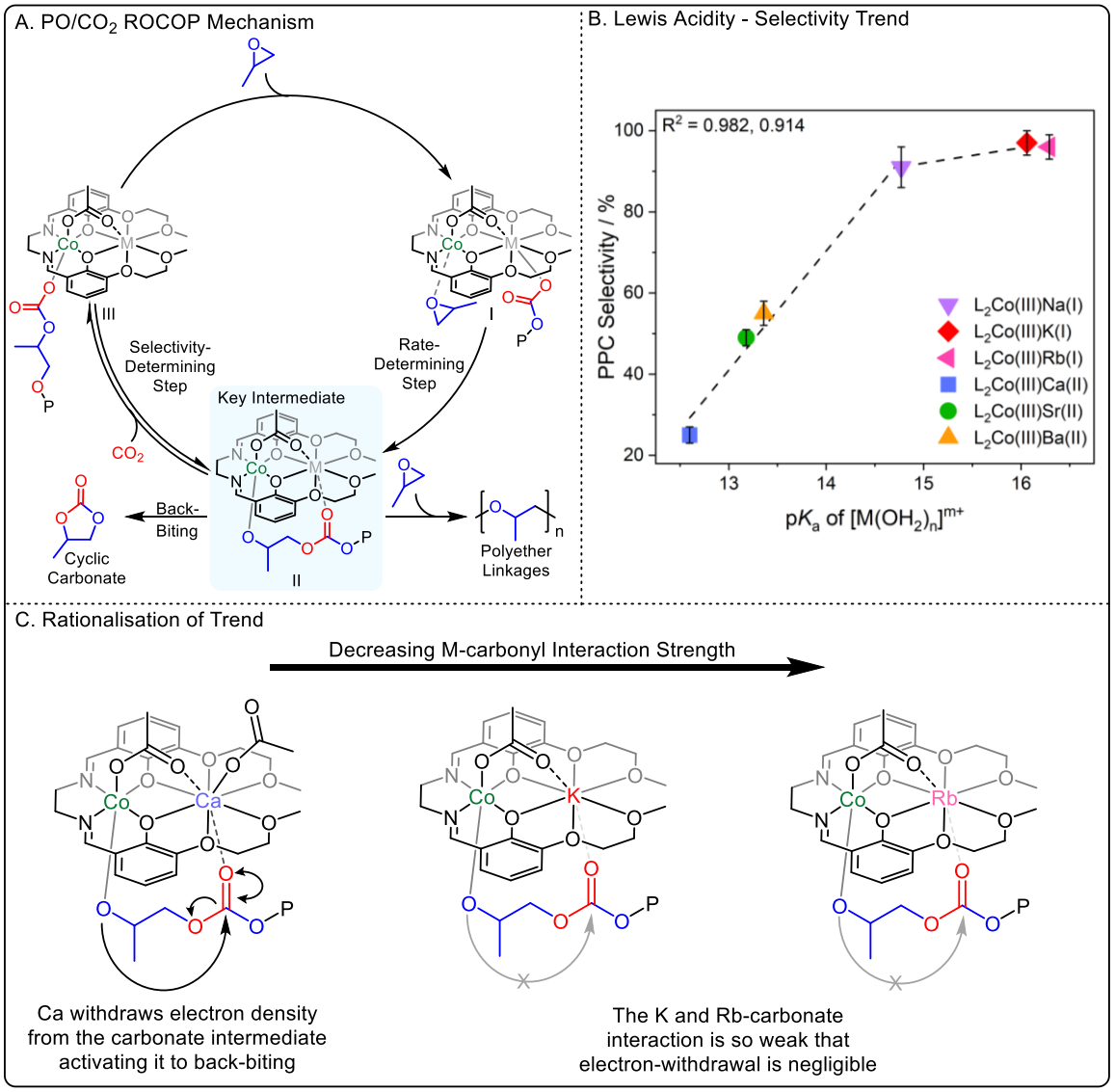


Figure 3.13. A. Proposed mechanism of PO/CO_2 ROCOP catalysed by L_2Co(III)M(I/II), showing the key selectivity-determining intermediate; B. Plot of selectivity of L_2Co(III)M(I/II) for PO/CO_2 ROCOP against pK_a of the incorporated s-block metal aqua complex; C. Rationalisation of the increase in selectivity seen with decreasing s-block metal Lewis acidity up to L_2Co(III)Na(I), followed by a plateau.

Selectivity shows a different trend with Lewis acidity. As the Lewis acidity decreases from Ca(II) to Na(I) there is a linear increase in the selectivity from 25% to 91%, after which there is a plateau in

the selectivity; L_2Co(III)K(I) and L_2Co(III)Rb(I) have essentially identical selectivities within error (96% and 97% respectively; Figure 3.13B).

According to DFT calculations on a related Co(III)K(I) complex, there may be a weak interaction between the s-block metal and the carbonyl adjacent to the alkoxide chain-end. This interaction may withdraw electron density from the carbonyl, activating it to intramolecular back-biting, decreasing the barrier to the formation of cyclic carbonate. As the Lewis acidity of the s-block metal decreases from Ca(II) to Na(I), this interaction would be expected to weaken, resulting in an increase in selectivity. Perhaps the K(I) and Rb(I) centres are so weakly Lewis acidic that the s-block metal-carbonate interactions are sufficiently weak for the electron withdrawal to be negligible, resulting in the observed plateau in selectivity (Figure 3.13C).

4.3.4.3 Ring-Opening Copolymerisation of Cyclohexene Oxide with Phthalic Anhydride using L_2Co(III)M(I/II)

There are multiple possible explanations for the difference in the position of the "maximum" in activity in the plots of Lewis acidity vs. activity for L_1Al(III)M(I/II) and L_2Co(III)M(I/II), but the source of the differences can be divided into two broad factors: either due to A) the difference in the catalysts (s-block metal coordination environment, nature of the trivalent metal, etc.) and/or B) the difference in the polymerisations (CHO vs. PO, epoxide/anhydride vs. epoxide/CO_2). To investigate the source of this difference, the L_2Co(III)M(I/II) catalysts were tested for CHO/PA ROCOP under the same conditions as the L_1Al(III)M(I/II) series was tested, although with twice the catalyst concentration to allow reactions to be conducted within more reasonable timeframes, and at a reduced temperature of 60 °C, as the Co(III) centre may be unstable to thermal reduction above this temperature over long reaction times (Table 3.3).[4]

Table 3.3. Data for the ROCOP of cyclohexene oxide (CHO) and phthalic anhydride (PA) with the L_2Co(III)M(I/II) catalysts. [a]

	Catalyst	Time / h	TON [b]	TOF [c] / h^{-1}	k_{obs} [d] / × 10^{-5} M s^{-1}	M_n [$Đ$] [e] / g mol^{-1}
1	Co(III)Na(I)	5.0	143	28 ± 2	3.9 ± 0.3	4400 [1.10]
2	Co(III)K(I)	0.5	157	287 ± 7	39.9 ± 0.9	4800 [1.15]
3	Co(III)Rb(I)	0.7	192	300 ± 19	42 ± 3	5700 [1.14]
4	Co(III)Ca(II)	63.5	54	1 ± 0.1	0.117 ± 0.007	2200 [1.20]
5	Co(III)Sr(II)	62.5	109	2 ± 0.2	0.22 ± 0.03	3000 [1.25]
6	Co(III)Ba(II)	27.5	134	5 ± 0.6	0.66 ± 0.08	3300 [1.21]

[a] Reaction conditions: 1:200:1000 $[catalyst]_0$:$[PA]_0$:$[CHO]_0$, 100 °C, neat. [b] Turnover number (TON) = moles of CHO consumed/moles of catalyst, determined by ^{1}H NMR spectroscopy by integrating the peaks for PA (8.10 – 7.85 ppm), Poly(CHO-*alt*-PA) (7.75 – 7.40 ppm), and PCHO (3.46 – 3.64 ppm). [c] Turnover frequencies (TOFs) were calculated between 5 – 70% conversion in each case (Tables S5 and S6, equation S3). [d] Observed rate coefficients (k_{obs}) were calculated from linear fits to plots of [PA] against time (Figure 4.8 RHS). [e] Determined by GPC, in THF, at 30 °C, using narrow molecular weight polystyrene calibrants.

Again, an exponential increase in activity with decreasing Lewis acidity was observed, which was confirmed by a double-logarithm plot, and plotting activity against ionic radius did not show correlation (Figures S3.24 and S3.25, respectively). All the catalysts produce polyesters that are monomodal by GPC, with narrow dispersities (Figure S3.26).

Interestingly, in this case the L_2Co(III)Rb(I) catalyst shows a greater activity than the L_2Co(III)K(I) catalyst. This seems to suggest that the key factor which changes the relative activities of the K(I) and Rb(I) catalysts is the nature of the ROCOP; i.e. whether it is epoxide/anhydride or epoxide/CO_2 ROCOP (Figure 3.14A and B).

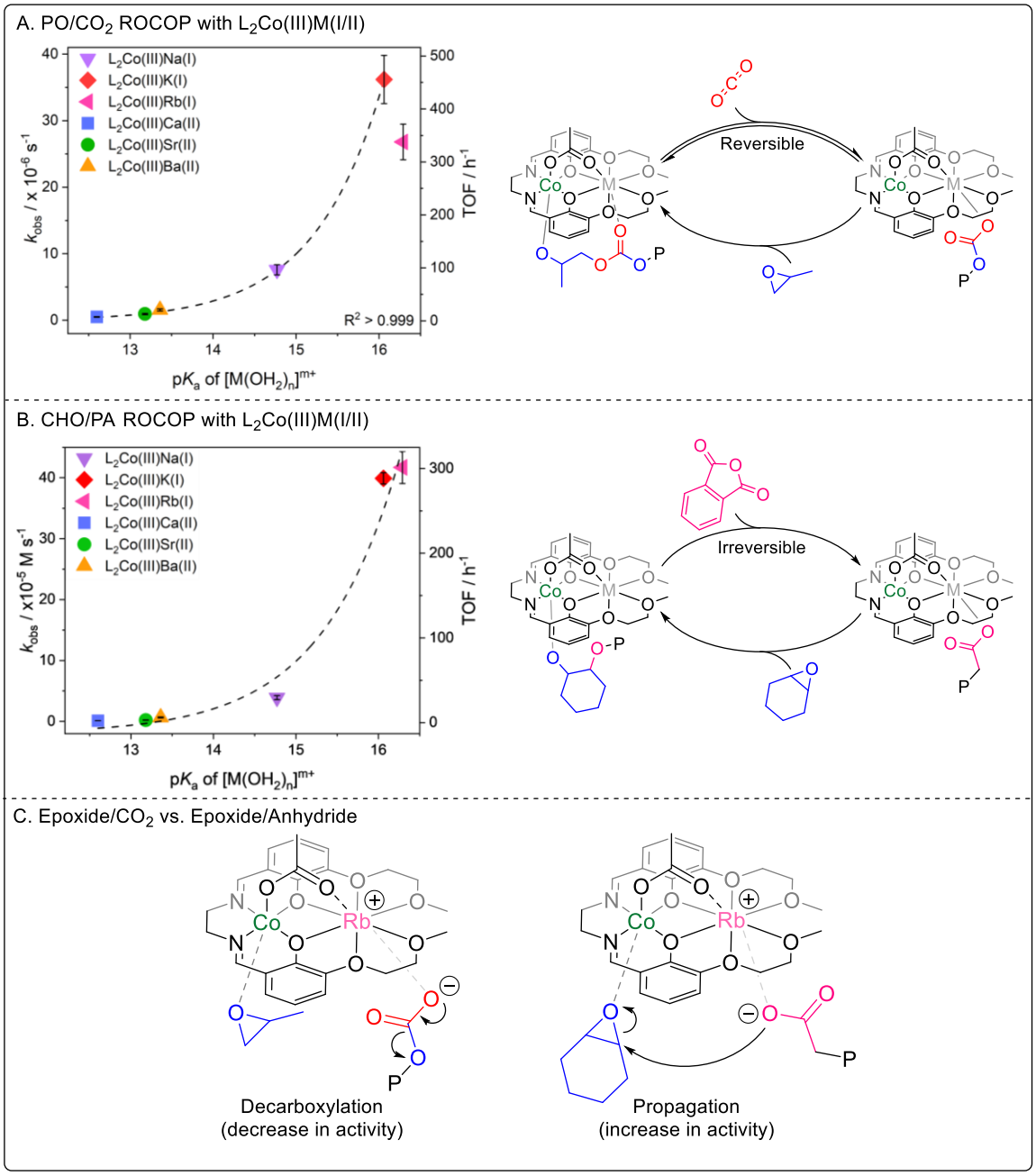


Figure 3.14. A. Plot of activity of PO/CO_2 ROCOP catalysed by L_2Co(III)M(I/II) against pK_a of the incorporated s-block metal aqua complex, alongside a simplified mechanism for the polymerisation, highlighting the reversible nature of CO_2 insertion; B. Plot of activity of CHO/PA ROCOP catalysed by L_2Co(III)M(I/II) against pK_a of the incorporated s-block metal aqua complex, alongside a simplified mechanism for the polymerisation, highlighting the irreversible nature of PA insertion; C. Structures of key rate-determining intermediates for PO/CO_2 (LHS) and CHO/PA (RHS) ROCOP, showing that the weak Lewis acidity of Rb(I) leads to decarboxylation for PO/CO_2 ROCOP but an enhancement in activity for CHO/PA ROCOP.

This can perhaps be explained by considering the pre-rate-determining equilibrium, which is present in epoxide/CO_2 ROCOP, but not in epoxide/anhydride ROCOP. Perhaps, in both cases, the weak Lewis acidity of the Rb(I) centre results in a very weakly-bound carbonate/carboxylate

intermediate. In the case of PO/CO_2 ROCOP, the instability of this carbonate chain end may result in the equilibrium shifting away from the carbonate intermediate and towards the alkoxide, decreasing the concentration of the active catalyst (Figure 3.14C). In CHO/PA ROCOP, the highly nucleophilic carboxylate chain end only increases the rate of reaction, as anhydride insertion is irreversible. These results emphasise the need to tailor catalysts for specific polymerisations, even when they share similar mechanisms.

3.4 Conclusions and Future Work

Two series of M(III)M(I/II) (M(III) = Al(III), Co(III); M(I/II) = s-block metals) catalysts were synthesised and tested for the ROCOP of epoxides with CO_2, and/or of epoxides with anhydrides. All catalysts showed correlations between activity and, where relevant, selectivity, against pK_a of the s-block metal aqua complex (used as a measure of Lewis acidity).

The catalyst systems, L_1Al(III)M(I/II) and L_2Co(III)M(I/II), featured s-block metals bound within flexible ether binding pockets, allowing the incorporation of Rb(I), which is large and weakly Lewis acidic. The L_1Al(III)M(I/II) series was tested for CHO/PA ROCOP and the most active catalyst was L_1Al(III)Rb(I). When the L_2Co(III)M(I/II) series was tested for PO/CO_2 ROCOP, the most active catalyst was L_2Co(III)K(I); a drop in activity is seen when the pK_a of the s-block metal aqua complex was increased between K(I) and Rb(I). When the selectivity of the catalysts were plotted against pK_a, a linear increase is observed from L_2Co(III)Ca(II) and L_2Co(III)Na(I), after which a plateau is observed.

When the same L_2Co(III)M(I/II) series was tested for CHO/PA ROCOP, the L_2Co(III)Rb(I) catalyst was marginally more active than the L_2Co(III)K(I) catalyst, indicating that the optimal Lewis acidity for PO/CO_2 and CHO/PA ROCOP are not the same. This was attributed to the weakly Lewis acidic nature of Rb(I) resulting in highly labile carbonate/carboxylate intermediates for PO/CO_2 and CHO/PA ROCOP, respectively. For PO/CO_2 ROCOP, this might result in decarboxylation of the carbonate chain-end, decreasing the activity of the catalyst, whereas for CHO/PA ROCOP this results in an increase in activity, perhaps due to the fact that PA incorporation into the polymer chain is irreversible.

Studying the relationship between the activity of each catalyst system against the Lewis acidity of the incorporated s-block metal has allowed an insight into the mechanisms of each of the catalysts for epoxide/CO_2 and/or epoxide/anhydride ROCOP which would not be easily achievable through

more traditional methods, e.g. kinetic measurements. The findings in this chapter show the generality of these correlations between catalyst performance and s-block metal Lewis acidity, while also demonstrating that the subtle differences in the nature of these correlations between different catalyst systems and/or polymerisations can provide key insights into the mechanisms at play.

Future work for these catalyst systems should focus primarily on trying to understand the differences observed between epoxide/CO_2 and epoxide/anhydride ROCOP for L_1Al(III)M(I/II) and L_2Co(III)M(I/II). Both catalyst systems should be tested for CHO/CO_2 ROCOP, and PO/PA ROCOP to determine the optimal s-block metal Lewis acidity to investigate whether this changes only between epoxide/CO_2 and epoxide/anhydride ROCOPs broadly, or whether the specific epoxide choice also has an effect. The complexes should also be characterised further (e.g. UV-Vis, cyclic voltammetry and single crystal X-ray diffractometry for L_2Co(III)M(I/II)) to explore whether correlations can be found between measured properties of the complexes and s-block metal Lewis acidity and therefore, by extension, polymerisation activity.

We propose that this method of mechanistic analysis, where the metal Lewis acidity is systematically varied to study the effect on activity and selectivity, should be broadly used when synthesising heteronuclear catalysts featuring s-block metals. Other catalyst systems should also be investigated, such as those containing lanthanides, to determine how general these trends are.

3.5 References

(1) Fiorentini, F.; Diment, W. T.; Deacy, A. C.; Kerr, R. W. F.; Faulkner, S.; Williams, C. K. Understanding catalytic synergy in dinuclear polymerization catalysts for sustainable polymers. *Nat. Commun.* **2023**, *14* (1), 4783.

(2) Diment, W. T.; Gregory, G. L.; Kerr, R. W. F.; Phanopoulos, A.; Buchard, A.; Williams, C. K. Catalytic Synergy Using Al(III) and Group 1 Metals to Accelerate Epoxide and Anhydride Ring-Opening Copolymerizations. *ACS Catal.* **2021**, *11* (20), 12532-12542.

(3) Abel, B. A.; Lidston, C. A. L.; Coates, G. W. Mechanism-Inspired Design of Bifunctional Catalysts for the Alternating Ring-Opening Copolymerization of Epoxides and Cyclic Anhydrides. *J. Am. Chem. Soc.* **2019**, *141* (32), 12760-12769.

(4) Eisenhardt, K. H. S.; Fiorentini, F.; Lindeboom, W.; Williams, C. K. Quantifying CO2 Insertion Equilibria for Low-Pressure Propene Oxide and Carbon Dioxide Ring Opening Copolymerization Catalysts. *J. Am. Chem. Soc.* **2024**, *146* (15), 10451-10464.

(5) Kumar, A.; Blakemore, J. D. On the Use of Aqueous Metal-Aqua pK_a Values as a Descriptor of Lewis Acidity. *Inorg. Chem.* **2021**, *60* (2), 1107-1115.

(6) Shannon, R. D. Revised effective ionic radii and systematic studies of interatomic distances in halides and chalcogenides. *Acta Crystallographica Section A* **1976**, *32* (5), 751-767.

(7) Diment, W. T.; Lindeboom, W.; Fiorentini, F.; Deacy, A. C.; Williams, C. K. Synergic Heterodinuclear Catalysts for the Ring-Opening Copolymerization (ROCOP) of Epoxides, Carbon Dioxide, and Anhydrides. *Acc. Chem. Res.* **2022**, *55* (15), 1997-2010.

(8) Gruszka, W.; Garden, J. A. Advances in heterometallic ring-opening (co)polymerisation catalysis. *Nat. Commun.* **2021**, *12* (1), 3252.

(9) Gruszka, W.; Sha, H.; Buchard, A.; Garden, J. A. Heterometallic cooperativity in divalent metal ProPhenol catalysts: combining zinc with magnesium or calcium for cyclic ester ring-opening polymerisation. *Catal. Sci. Technol.* **2022**, *12* (4), 1070-1079.

(10) Deacy, A. C.; Moreby, E.; Phanopoulos, A.; Williams, C. K. Co(III)/Alkali-Metal(I) Heterodinuclear Catalysts for the Ring-Opening Copolymerization of CO_2 and Propylene Oxide. *J. Am. Chem. Soc.* **2020**, *142* (45), 19150-19160.

(11) Kerr, R. W. F.; Williams, C. K. Zr(IV) Catalyst for the Ring-Opening Copolymerization of Anhydrides (A) with Epoxides (B), Oxetane (B), and Tetrahydrofurans (C) to Make ABB- and/or ABC-Poly(ester-alt-ethers). *J. Am. Chem. Soc.* **2022**, *144* (15), 6882-6893.

(12) Deacy, A. C.; Phanopoulos, A.; Lindeboom, W.; Buchard, A.; Williams, C. K. Insights into the Mechanism of Carbon Dioxide and Propylene Oxide Ring-Opening Copolymerization Using a Co(III)/K(I) Heterodinuclear Catalyst. *J. Am. Chem. Soc.* **2022**, *144* (39), 17929-17938.

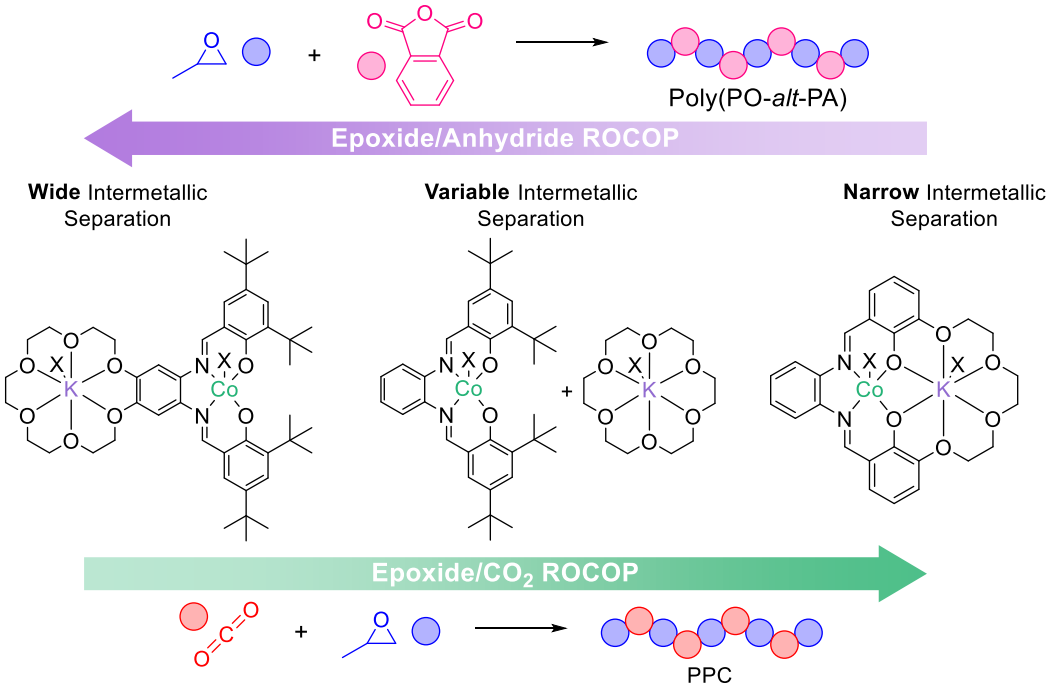
Chapter Four

The Effect of Intermetallic Separation in Co(III)K Heterodinuclear Polymerisation Catalysts

The work described in this chapter is reported in "*Synergic catalysis: the importance of intermetallic separation in Co(III)K catalysts for ring-opening copolymerizations*"

F. Fiorentini, K.H.S. Eisenhardt, A.C. Deacy, C.K. Williams

J. Am. Chem. Soc., 2024, 146, 23517 – 23538



4.1 Introduction

While Chapters Two and Three explores the influence of the s-block metal in mediating the activity of heterodinuclear Co(III)M(I/II) and Al(III)M(I/II) catalysts, the influence of the intermetallic separation, i.e. the distance between the M(III) and M(I/II) centres, was not explored as it is dictated by the ancillary ligand structure. Nonetheless, analysis of the ROCOP catalyst literature suggests that it could be a useful parameter to control catalytic performance.[1-4]

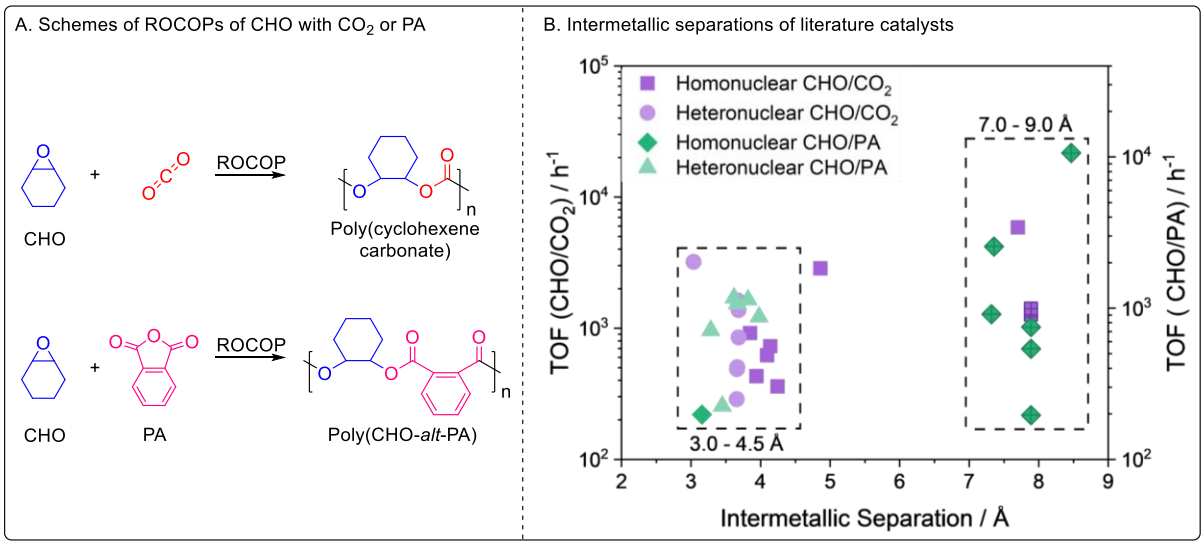


Figure 4.1. A. Schemes for the ring-opening copolymerisation of cyclohexene oxide (CHO) with CO_2 or phthalic anhydride (PA); B. Analysis of literature dinuclear catalysts for CHO/CO_2 or CHO/PA ROCOP, identifying optimal intermetallic separations within those structures. Activity (turn over frequency, TOF) for catalysts for CHO/CO_2 ROCOP (CO_2 pressures > 5 bar) (LHS y-axis, purple squares and circles) and for CHO/PA ROCOP (RHS y-axis, green diamonds and triangles) is plotted against intermetallic separation (from solid-state structures or calculated by DFT). Catalysts requiring co-catalysts (e.g PPNCl) have an added cross.[2, 3, 5-15]

We analysed data for multinuclear catalysts reported for epoxide/anhydride and/or epoxide/carbon dioxide ROCOP (Figure 4.1A).[2, 3, 5-15] To measure the intermetallic separation, data from single crystal X-ray diffraction experiments was used, or for catalysts where XRD was not reported the distances were estimated from DFT calculations. The majority of catalysts are evaluated for the ROCOP of cyclohexene oxide (CHO) used with phthalic anhydride (PA) or carbon dioxide; CHO is often studied due to its high ring-strain, high boiling point which allows for copolymerisations at higher temperatures and, for

carbon dioxide ROCOP, its higher barriers to cyclic carbonate (by-product) formation particularly when compared with alkylene oxide/CO_2 ROCOP. Thus, we plotted the activity for high-performance multinuclear catalysts for CHO/PA and CHO/CO_2 ROCOP against the intermetallic separation (Figure 4.1B). The plot reveals that the best catalysts show two typical regions for the intermetallic separation, either between 3.0 – 4.5 Å or 7.0 – 9.0 Å (Figure 4.1; Figures S4.1. and S4.2, Tables S4.1 and S4.2).

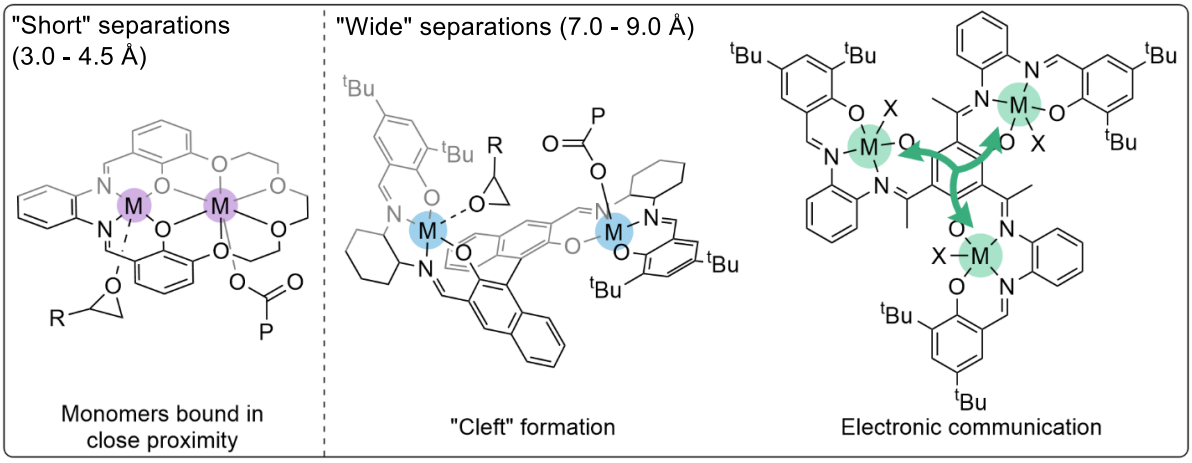


Figure 4.2. Leading catalysts by their intermetallic separations and the proposed rationale for metallic synergy. [4, 16-18]

Rationalizing the two 'separations' is challenging, with difference explanations only relevant to specific catalysts. Most authors rationalize high-performance 'narrow' separation catalysis by a chain shuttling mechanism, where close intermetallic separations reduce barriers in the rate limiting step by cooperation between the 'nucleophilic' polymer chain end group which attacks a monomer coordinated at the second metal (Figures 4.2 LHS, S4.3 and S4.4).[4] For catalysts with wider intermetallic separations, synergy explanations depend upon the ligand. For conjugated planar ligands, it is generally claimed that there may be some 'electronic communication' between metals which enhances rates (Figure 4.2 RHS).[3] For non-planar ligands the rationale tends to invoke ligand flexibility allowing access to a catalytic 'cleft' (specific conformation) where the metals point towards each other and undergo cooperative catalysis in an analogous way to the mechanisms proposed for narrow separation catalysts

(Figure 4.2, middle).[5, 17] One challenge with applying these concepts to new catalyst design is that explanations are specific to particular catalysts; there is a need for systematic investigation of the influence of metallic separation and, in particular, it would be desirable for such studies to vary only the metal separations, while keeping the nature of the metals and ligand systems the same.

4.2 Aims

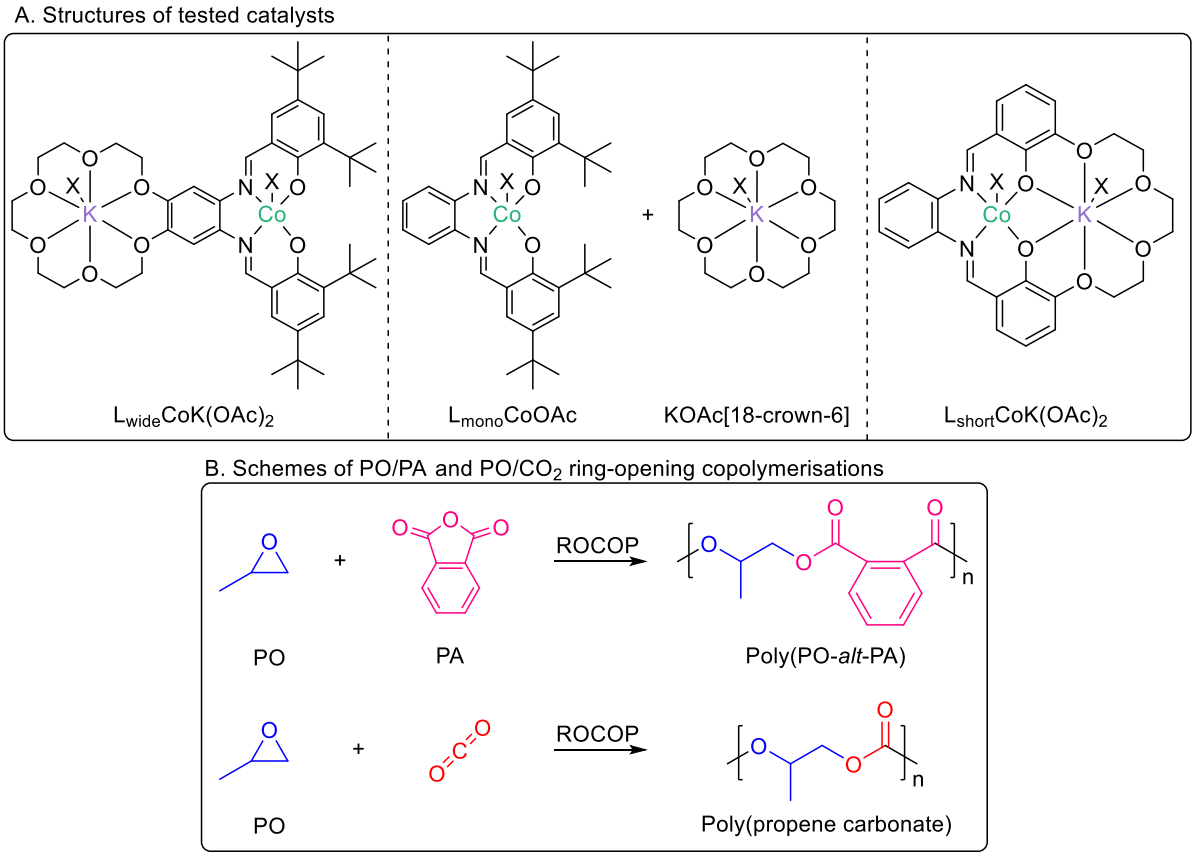


Figure 4.3. A. Structures of the catalysts tested for PO/PA and PO/CO_2 ROCOP. X = OAc. B. Schemes for the tested ring-opening polymerizations of propene oxide with phthalic anhydride or CO_2.

In this chapter, Co(III)K(I) heterodinuclear catalysts with separations in the two key intermetallic regions identified from the literature analyses, i.e. 7.0 – 9.0 Å ($L_{wide}CoK(OAc)_2$) or 3.0 – 4.5 Å ($L_{short}CoK(OAc)_2$) are targeted (Figure 4.3A). These catalysts should operate effectively without any co-catalyst or additive since the goal is to control and understand intermetallic separation influences. To investigate a catalyst with the potential for variable intermetallic separations, a bicomponent catalyst is targeted where a Co(III) complex ($L_{mono}CoOAc$) is applied with an equivalent of a potassium carboxylate salt (KOAc[18-crown-6]). These catalysts are prioritised for ROCOP using PO with PA or CO_2 (Figure 4.3B). These monomers are already produced and used on a very large scale globally, have strong

potential to be bioderived or, in the case of CO_2, is an existing waste. The monomer combinations are also very demanding and hence require better catalysts, with typical activities and selectivity values being lower than when using CHO (lower temperatures are necessary and CO_2/PO ROCOP may form propene carbonate by-product). The investigation objective is to understand the influences of intermetallic separations in both polyester (PO/PA) and polycarbonate (PO/CO_2) polymerization catalysts.

4.3 Results and Discussion

4.3.1 Catalyst Synthesis and Characterisation

4.3.1.1 Synthesis and Characterisation of $L_{wide}CoK(OAc)_2$

4.3.1.1.1 Synthesis

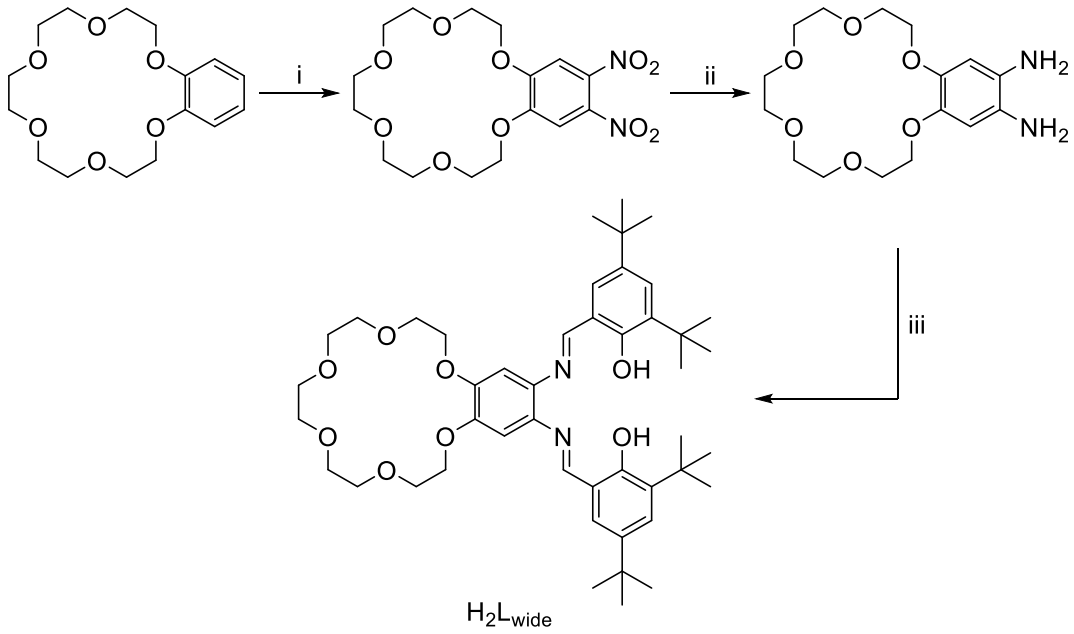


Figure 4.4. Synthesis of H_2L_{wide} from benzo-18-crown-6. i) H_2SO_4, HNO_3, $CHCl_3$, 0 °C to rt, 2 days, 84% ; ii) Pd/C, 1.5 bar H_2, MeOH, rt, 5 days iii) 3,5-ditertbutylbenzaldehyde, MeOH, N_2, 65 °C, 3 days, 87% (from dinitrobenzo-18-crown-6).

The wide intermetallic separation pro-ligand (H_2L_{wide}) was synthesised in two steps from benzo-18-crown-6, with an overall yield of 73% using a modified literature procedure (Figure 4.4).[19] In brief, benzo-18-crown-6 was doubly nitrated by the dropwise addition of a mixture of sulphuric and nitric acid at 0 °C, after which the solution was allowed to warm to room temperature and was stirred for two days. Dinitrobenzo-18-crown-6 was isolated in 84% yield and used without further purification. Dinitrobenzo-18-crown-6 was hydrogenated using Pd/C under 1.5 bar H_2 in methanol for five days. The resultant diaminobenzo-18-crown-6 was not isolated due to its air- and light-sensitivity. Instead, the

solution was filtered directly into an ampoule containing 3,5-ditertbutylbenzaldehyde and the resultant solution heated at 60 °C for three days. H_2L_2 formed as a yellow-orange precipitate, and was isolated by filtration in 87% yield (Figure 4.4).

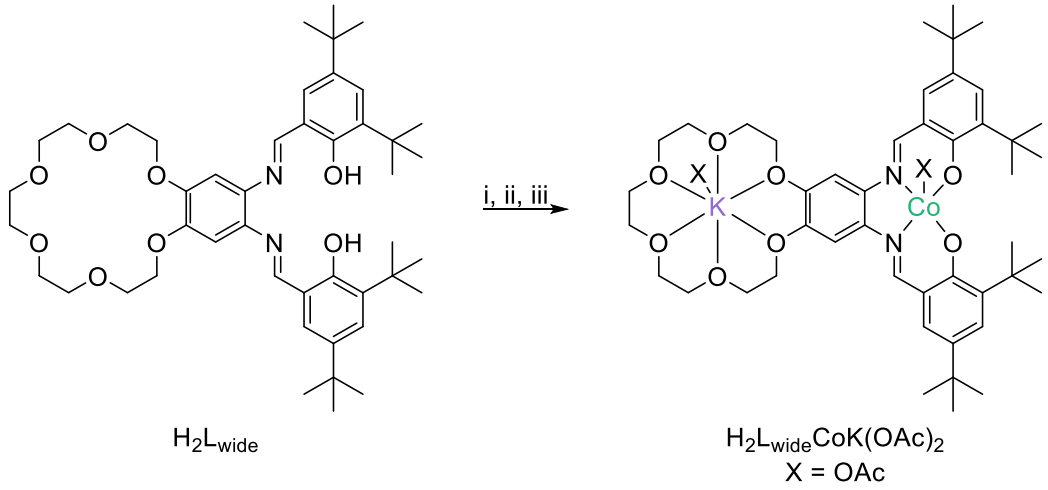


Figure 4.5. Synthesis of $L_{wide}CoK(OAc)_2$ from H_2L_{wide}; i) KOAc, MeOH, N_2, reflux, 1 h, ii) $Co(OAc)_2$, N_2, rt iii) AcOH, MeOH, air, rt, 4 h.

The novel $L_{wide}CoK(OAc)_2$ catalyst was synthesised by addition of KOAc to a suspension of the ligand in methanol, followed by refluxing under a nitrogen atmosphere for an hour (Figure 4.5). The solution was allowed to cool and $Co(OAc)_2$ added under a flow of nitrogen, followed by stirring for 16 h. The Co(II) complex was oxidised to the desired Co(III) complex by opening the solution to air, and stirring for 4 h. The target catalyst was purified by precipitation (toluene/hexane) and isolated as a very dark red-purple powder in 62% yield. The catalyst was characterised by ^{1}H, $^{13}C\{^{1}H\}$, COSY, HSQC, HMBC NMR, IR and UV-vis spectroscopy, and MALDI-TOF mass spectrometry (Figures S4.6 – S4.14). Purity of the catalyst was confirmed by elemental analysis.

4.3.1.1.2 NMR spectroscopy

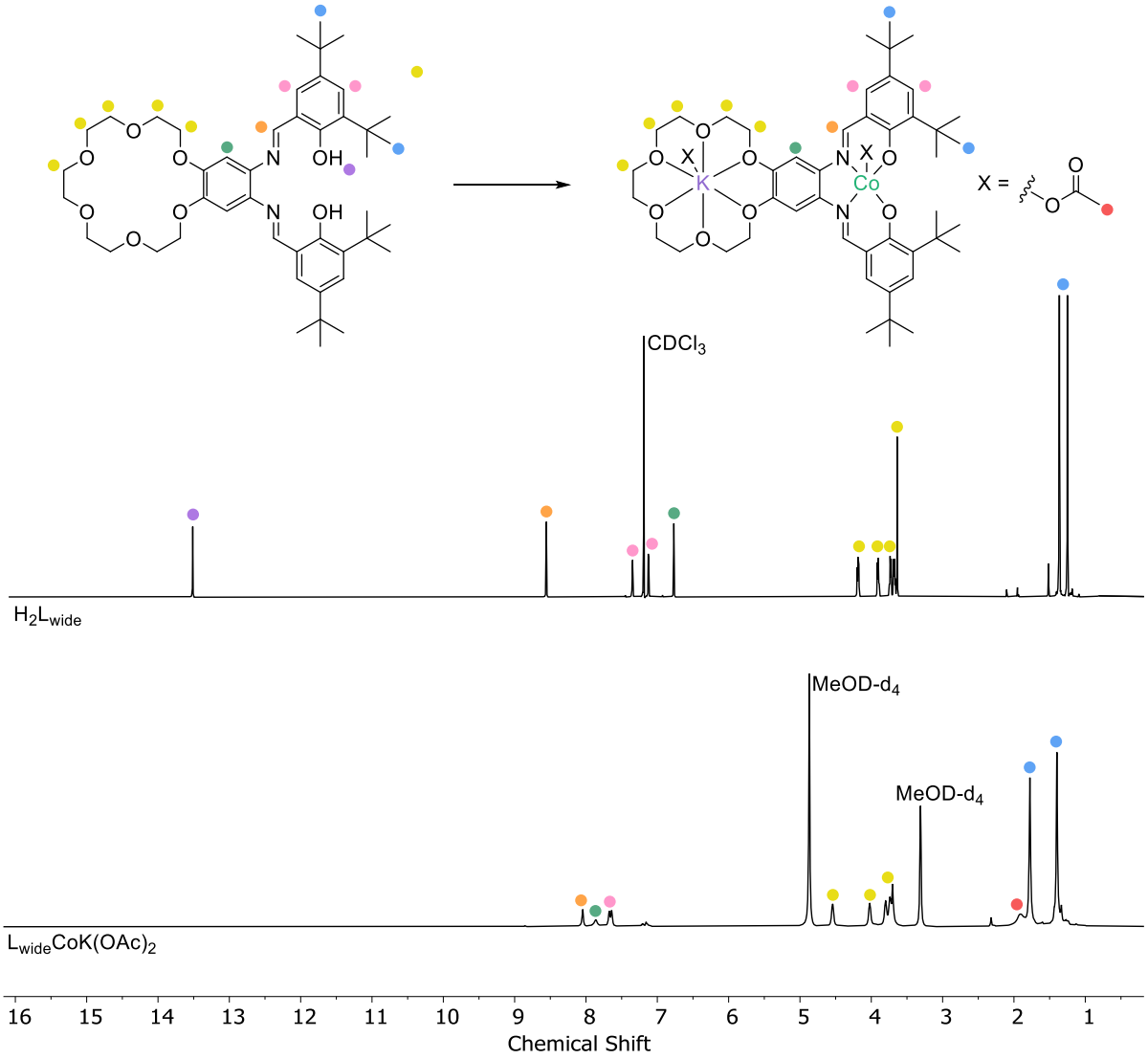


Figure 4.6.Comparison of ^{1}H NMR spectra of H_2L_{wide} (top) and $L_{wide}CoK(OAc)_2$ (bottom) showing the disappearance of the phenol resonance (purple), appearance of the acetate resonance (red), and broadening of the crown ether resonances (yellow circles)

Successful synthesis of the $L_{wide}CoK(OAc)_2$ complex was confirmed by disappearance of the pro-ligand phenol resonance (13.51 ppm; purple circle in Figure 4.5) and appearance of the acetate resonance (1.91 ppm). The crown ether (3.70 – 4.55 ppm; yellow circles in Figure 4.5) resonances broaden in the complex, indicating coordination of the K centre.

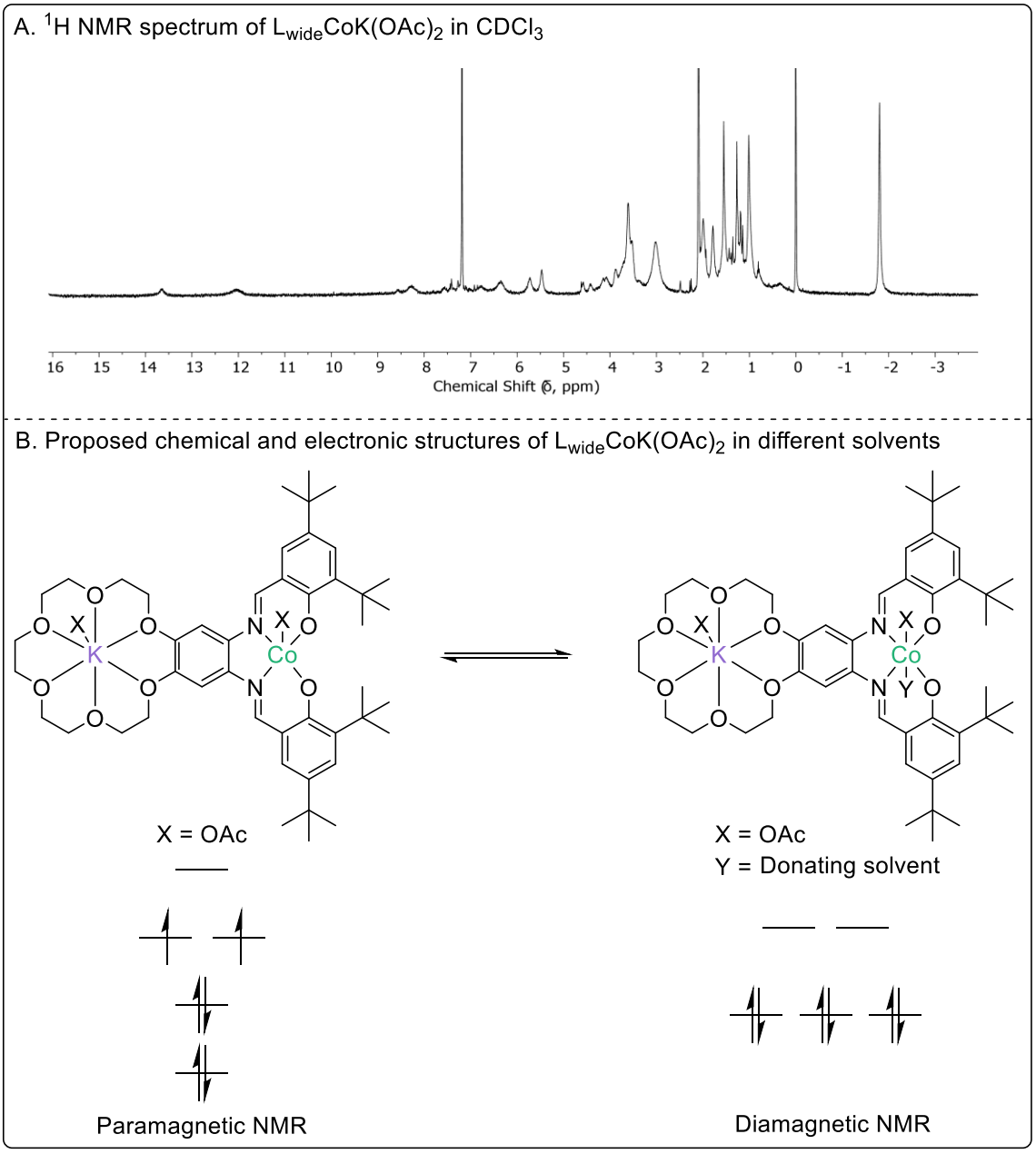


Figure 4.7. A. ^{1}H NMR spectrum of $L_{wide}CoK(OAc)_2$ in $CDCl_3$ showing broad and paramagnetically-shifted peaks; B. Proposed structures of $L_{wide}CoK(OAc)_2$ in non-donating (LHS) and donating (RHS) solvents.

When the ^{1}H NMR spectrum of $L_{wide}CoK(OAc)_2$ is recorded in MeOD-d_4, sharp, assignable resonances within the "typical region" (0 – 12 ppm) are observed, indicating a diamagnetic complex, which is consistent with a low-spin, octahedral Co(III) centre (Figures 3.6 and S3.15). In contrast, when the ^{1}H NMR spectrum of the complex is recorded in non-donating solvents, such as $CDCl_3$, the resonances are

broad and some are paramagnetically-shifted (Figure 4.7A). This is proposed to be due to the interconversion between a paramagnetic, five-coordinate Co(III) centre, and a diamagnetic, six-coordinate Co(III) centre in non-donating and donating solvents respectively (Figure 4.7B).

4.3.1.1.3 SQUID Magnetometry

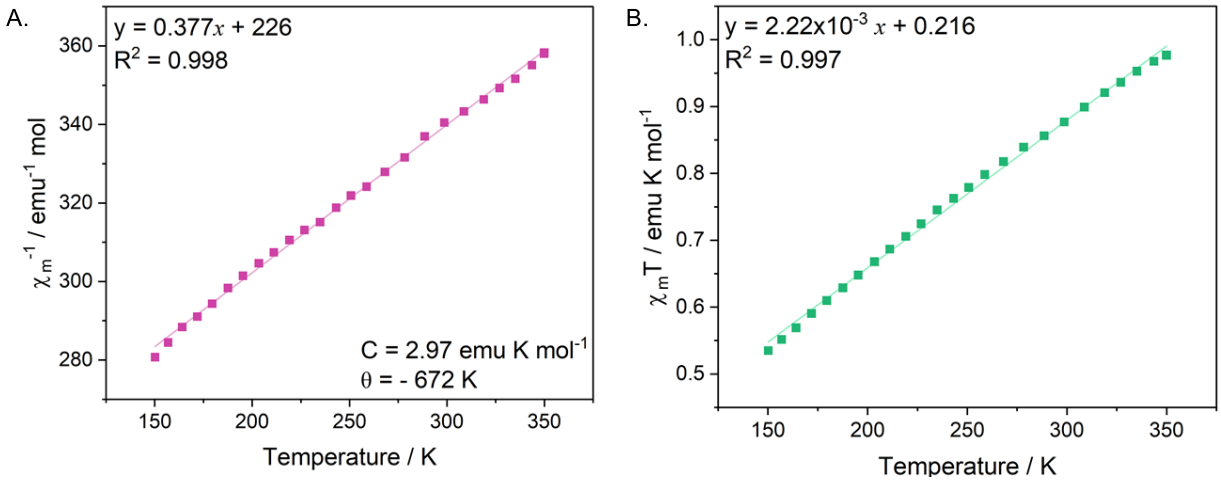


Figure 4.8. Plots of inverse of molar susceptibility (χ_m) against temperature (A) and molar susceptibility and temperature ($\chi_m T$) against temperature (B) for $L_{wide}CoK(OAc)_2$.

To investigate the electronic structure of $L_{wide}CoK(OAc)_2$, SQUID magnetometry was performed on the solid complex. The plot of inverse molar susceptibility against temperature between 150 to 350 K is linear, which shows that $L_{wide}CoK(OAc)_2$ is paramagnetic, with an effective magnetic moment of 2.65 μ_B (Figure 4.8A). This value is slightly lower than the spin-only value predicted for a low-spin, d^6 trigonal bipyramidal complex (S = 1; μ_{SO} = 2.83 μ_B). This plot also shows that $L_{wide}CoK(OAc)_2$ has a strongly negative Weiss constant (Θ = - 672 K), which indicates anti-ferromagnetic ordering of spins. This is reinforced by the plot of the sum of molar susceptibility and temperature against temperature, which shows a linear increase, indicating electronic communication between Co(III) centres (Figure 4.8B). As such, the SQUID magnetometry data is consistent with the proposed structure of the complex in the absence of donating solvent, with the relatively low effective magnetic moment due to anti-

ferromagnetic coupling of spins in the solid-state. This is also in agreement with a previously-reported five-coordinate *N*-*o*-hydroxy-benzamido-*meso*-tetraphenyl porphyrin Co(III) complex (μ_{eff} = 2.84 μ_B).[20]

4.3.1.1.4 Infrared Spectroscopy

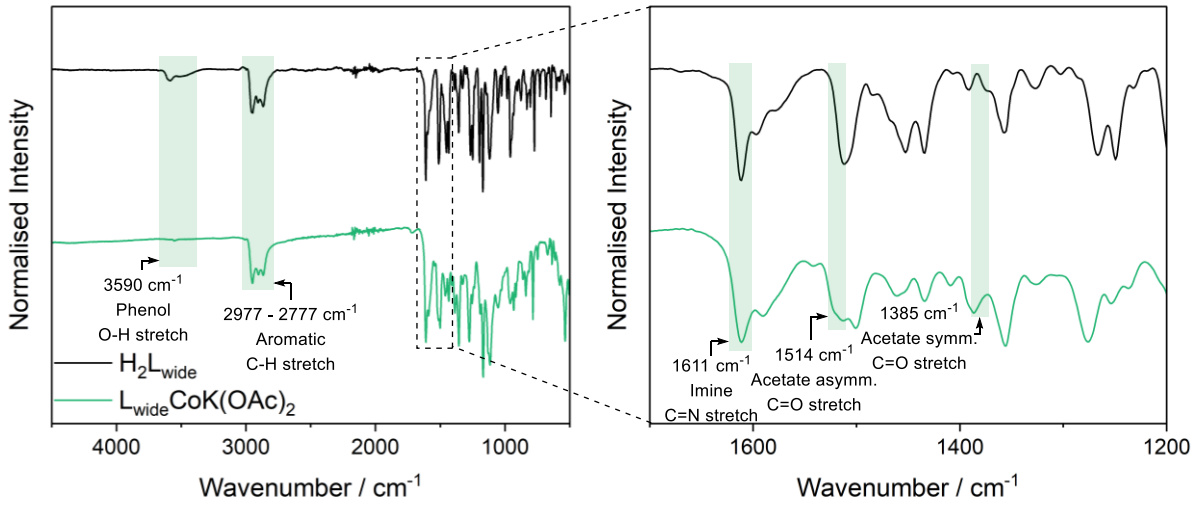


Figure 4.9. RHS: Solid-state IR spectrum of H_2L_{wide} (top; black) and $L_{wide}CoK(OAc)_2$ (bottom; green) between 4500 – 500 cm^{-1} showing all peaks; LHS: IR spectrum of H_2L_{wide} and $L_{wide}CoK(OAc)_2$ between 1700 – 1200 cm^{-1} to show imine and acetate stretches.

IR spectroscopy was also used to confirm the synthesis of the desired $L_{wide}CoK(OAc)_2$ complex. Comparing the solid-state IR spectra of the H_2L_{wide} proligand to $L_{wide}CoK(OAc)_2$ the phenol resonance of the proligand at 3590 cm^{-1} disappears, indicating successful coordination of the Co centre (Figure 4.9). New stretches at 1514 and 1385 cm^{-1} can be observed, which are assigned to acetate C=O asymmetric and symmetric stretches respectively. Peaks corresponding to aromatic C-H stretches, between 2977 – 2777 cm^{-1}, and the imine stretch at 1611 cm^{-1}, are conserved.

4.3.1.1.5 UV-Vis Spectroscopy

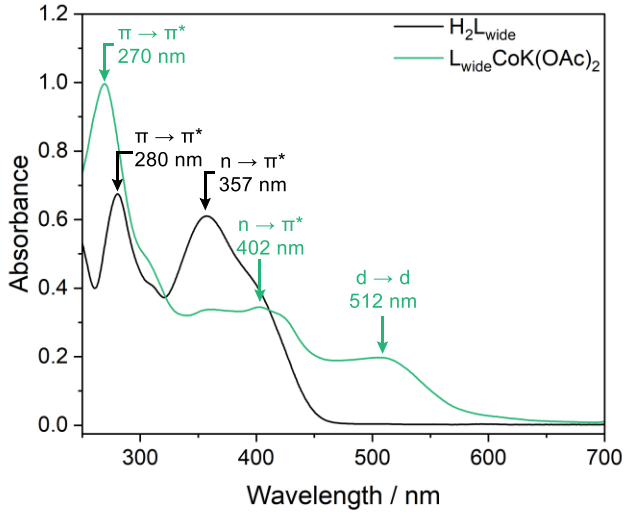


Figure 4.10. Overlaid UV-vis spectra of H_2L_{wide} (black) and $L_{wide}CoK(OAc)_2$ (green) in DCM.

Successful synthesis of the desired $L_{wide}CoK(OAc)_2$ complex can also be confirmed by UV-vis spectroscopy (Figure 4.10). The peak absorption, λ_{max}, which is assigned as a $\pi \rightarrow \pi^*$ transition, shifted from 280 to 270 nm. A peak, assigned as a ligand $n \rightarrow \pi^*$ transition, shifts from 357 nm in the proligand to 402 nm in the complex. This red-shifting is proposed to be due to weakening of the imine C=N bond due to coordination of the Co centre. A new transition at 512 nm is also observed in the complex UV-vis spectrum, which is tentatively assigned as a d → d transition. The relatively high intensity of this d → d transition (ε = 3900 $dm^3\ mol^{-1}\ cm^{-1}$) is proposed to be due to the non-centrosymmetric, five-coordinate geometry of the Co(III) centre, which results in the d → d transition being both Laporte and spin-allowed.

4.3.1.1.5 MALDI-ToF Mass Spectrometry

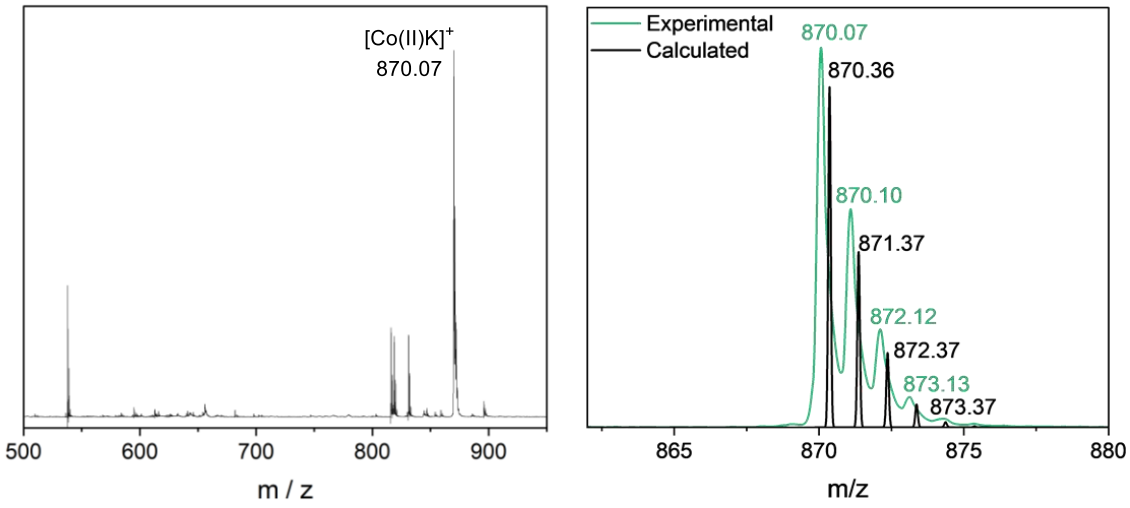


Figure 4.11. MALDI-ToF mass spectrometry of $L_{wide}CoK(OAc)_2$. The predominant peak at 870.07 m/z corresponds to $[L_{wide}Co(II)K(I)]^+$ (LHS), the isotopic distribution of which is in agreement with the calculated distribution (RHS).

MALDI-ToF mass spectrometry of $L_{wide}CoK(OAc)_2$ shows a predominant peak at 870.07 m/z, which corresponds to $[L_{wide}Co(II)K]^+$, where the acetate co-ligands have been removed, and the Co(III) centre has been reduced to Co(II) under the conditions of the mass spectrometry (Figure 4.11A). This reduction is unsurprising and has been observed before in similar Co(III) complexes.[21] No peaks corresponding to the ligand, monodinuclear, or homonuclear complexes could be observed. The isotopic distribution of the peak at 870.07 m/z is in agreement with the calculated distribution (Figure 4.11B)

4.3.1.1.6 Single Crystal Diffractometry

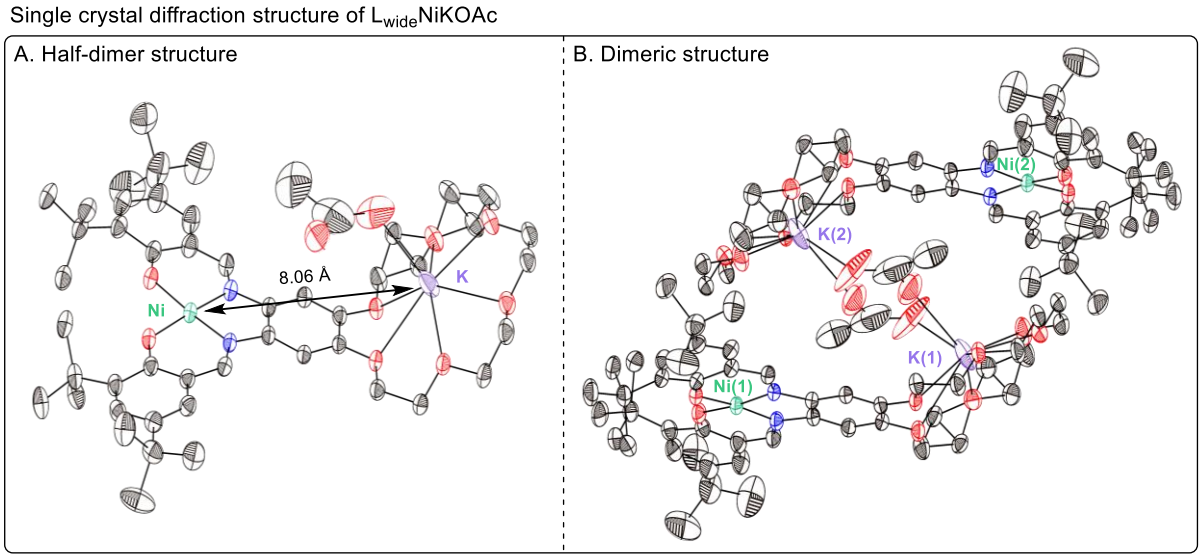


Figure 4.12. Solid-state structures of L_{wide}NiKOAc obtained by single crystal diffraction showing the half-dimer (A) and dimeric structure (B) of the complex. Solvent molecules and hydrogen atoms omitted for clarity, ellipsoids drawn at 40% probability.

While single crystals could not be grown of $L_{wide}CoK(OAc)_2$ complex, a structurally-equivalent L_{wide}NiKOAc complex was synthesized and single crystals suitable for X-ray diffraction experiments were grown by vapour diffusion of hexane into a chloroform solution of the complex.[22] L_{wide}NiKOAc crystallises as a dimeric species, where the K centres "share" two acetate co-ligands (Figure 4.12). The Ni centres are four-coordinate, coordinating to the two Schiff-base imines and two phenoxides of the salphen pocket. The K centre are both eight-coordinate, binding within the tethered crown ether binding pocket, and to two acetate co-ligands. The Ni – K separation within the complex is 8.06 Å, and it is proposed that the intermetallic separation will be very similar to that of the $L_{wide}CoK(OAc)_2$ catalyst, as the ligand framework is the same and the ionic radii of the metals are similar.

4.3.1.2 Synthesis of $L_{mono}CoOAc$

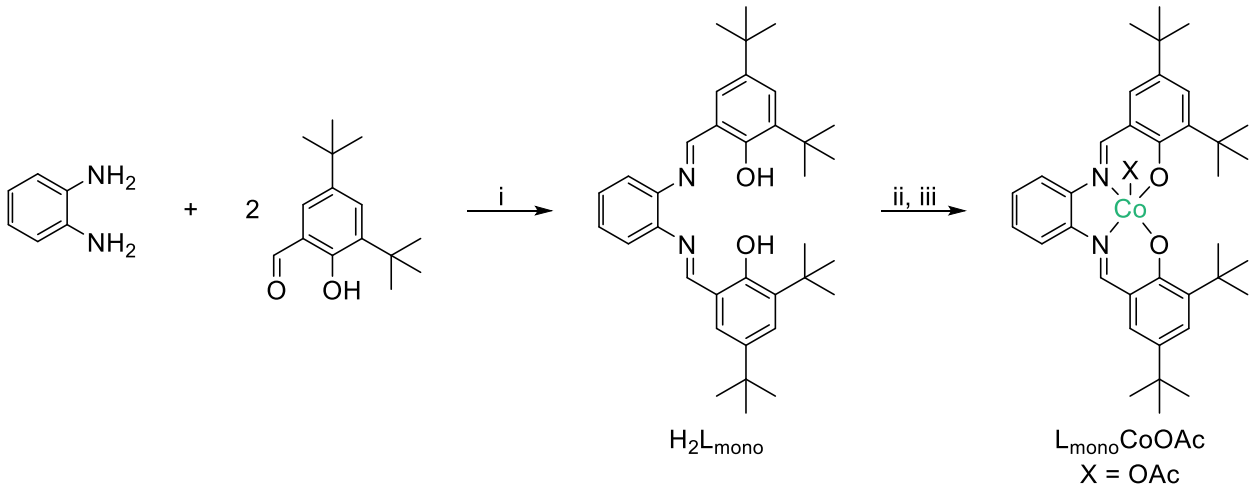


Figure 4.13. Synthesis of $L_{mono}CoOAc$: i) MeOH, reflux, N_2, 2 h, 72% yield; ii) $Co(OAc)_2$, MeOH, reflux, N_2, 1 h; iii) AcOH, air, rt, 16 h, 92% yield.

$L_{mono}CoOAc$ was synthesised following a modified literature procedure (Figure 4.13).[23] First, the proligand, H_2L_{mono}, was synthesised by stirring *ortho*-phenylene diamine with two equivalents of 3,5-di-*tert*-butyl-2-hydroxybenzaldehyde in methanol, under reflux, for 24 h. The proligand formed as a yellow precipitate, which was isolated by filtration in 77% yield, and used without further purification. $L_{mono}CoOAc$ was subsequently synthesised by combining H_2L_{mono} with $Co(OAc)_2$ in dichloromethane and refluxing for 2 h. The Co(II) centre was then oxidised to Co(III) by the addition of acetic acid and stirring under air for 16 h. Azeotropic distillations were performed with toluene to remove the excess acetic acid, followed by pentane to remove traces of toluene, to give the $L_{mono}CoOAc$ complex as a dark purple-red solid in 92% yield. Characterisation by IR spectroscopy and MALDI-ToF mass spectrometry matched that reported in the literature, and elemental analysis proved the purity of the complex.

4.3.1.3 Synthesis of $L_{short}CoK(OAc)_2$

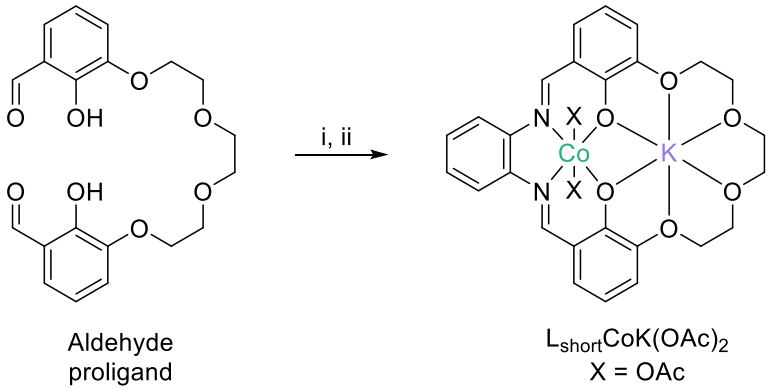


Figure 4.14. Synthesis of $L_{short}CoK(OAc)_2$ from the dialdehyde proligand: i) $Co(OAc)_2$, KOAc, MeCN, rt, 1 h, N_2; ii) *ortho*-phenylene diamine, rt, 16 h, N_2; iii) AcOH, air, rt, 72 h, 64% yield.

$L_{short}CoK(OAc)_2$ was synthesised following a literature procedure (Figure 4.14).[24] The dialdehyde proligand was combined with $Co(OAc)_2$ and KOAc in MeCN and stirred for 1 h under a N_2 atmosphere. This allows coordination of the metals within their respective pockets, allowing them to pre-organise the dialdehyde proligand for selective formation of the macrocycle in the next step. Next, *ortho*-phenyelene diamine was added in a single portion under a flow of N_2 and the resultant solution was stirred for 16 h. Acetic acid was then added, and the solution stirred open to air, to oxidise the Co(II) centre to Co(III) over three days. The final $L_{short}CoK(OAc)_2$ product was isolated following precipitation (chloroform/pentane) as a pale brown powder in 64% yield. Characterisation by ^1H NMR spectroscopy and MALDI-TOF mass spectrometry agreed with those reported in the literature, and elemental analysis proved the purity of the complex.

4.3.2 Ring-Opening Copolymerisation Results

4.3.2.1 Ring-Opening Copolymerisation of Propene Oxide and Phthalic Anhydride

The three catalyst systems were tested for PO/PA ROCOP under the following reaction conditions: 1:20:400:1000 [catalyst]$_0$:[1,3-benzene dimethanol (BDM)]$_0$:[PA]$_0$:[PO]$_0$ in neat PO at 60 °C. BDM is used as a chain transfer agent to control the molar mass of the polymer produced, to give the desired short-chained polyols. These conditions are challenging; catalysts for epoxide/anhydride ROCOP are generally reported with significantly lower anhydride loadings (generally up to 100 equivalents relative to catalyst) as the trace acid impurities invariably present in the anhydride can deactivate the catalyst.

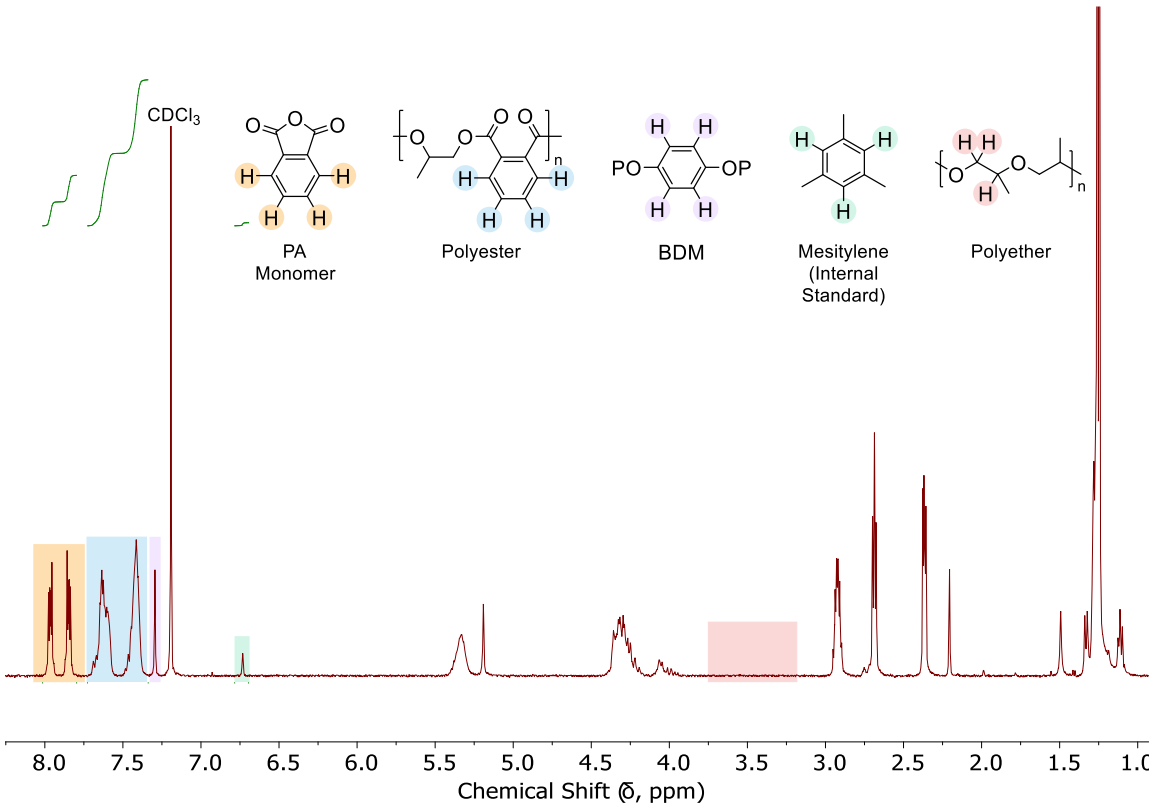


Figure 4.15. ^{1}H NMR spectrum of a representative PO/PA ROCOP reaction showing integrals and/or regions for PA monomer, polyester, BDM, mesitylene (10 eq. used as an internal standard), and polyether for the calculation of conversion, which is in turn used to calculate the turnover number (TON) and turnover frequency (TOF), and selectivity for polyester. P = polymer.

Each reaction was conducted in an air-tight vial, from which aliquots were removed at regular intervals in a N_2 glovebox to determine conversion by ^{1}H NMR spectroscopy (Figure 4.15). Conversion was determined by comparison of the integrals for the aromatic PA protons within the polyester (7.4 – 7.8 ppm) to the integrals of PA monomer (7.9 – 8.1 ppm) and mesitylene as an internal standard (6.8 ppm). Alongside conversion, ^{1}H NMR spectroscopy was used to determine whether the catalysts resulted in the formation of any polyether linkages (3.4 – 3.6 ppm).

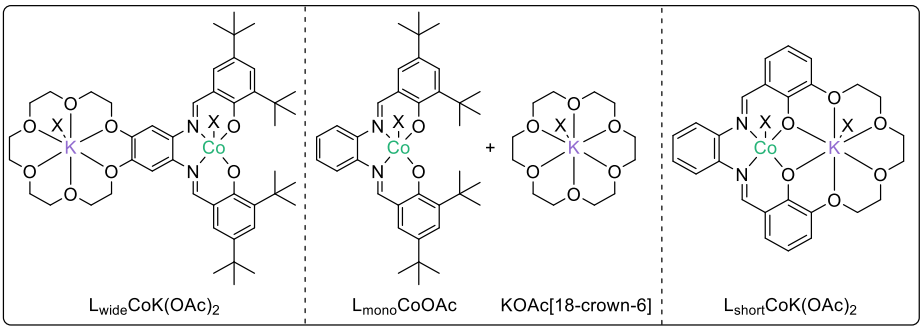


Table 4.1. Data for the ROCOP of propene oxide (PO) and phthalic anhydride (PA) for the three catalysts. [a]

	Catalyst	Time / h	TON [b]	TOF [c] / h^{-1}	M_n [$Đ$] [e] / g mol^{-1}
1	L_{wide}CoK(OAc)$_2$	0.2	281	1686	2900 [1.11]
2[f]	L_{wide}CoK(OAc)$_2$	0.8	1184	1480	12900 [1.07]
3	L_{mono}CoOAc	6	316	53	2800 [1.10]
4	KOAc[18-crown-6]	8	289	36	2100 [1.22]
5	L_{mono}CoOAc + KOAc[18-crown-6]	0.4	275	1238	2700 [1.08]
6[f]	L_{mono}CoOAc + KOAc[18-crown-6]	22.5	837	37	6500 [1.18]
7	L_{short}CoK(OAc)$_2$	1.2	270	231	2100 [1.11]

[a] Reaction conditions: PO/PA 1:20:400:1000 [cat]$_0$:[BDM]$_0$:[PA]$_0$:[PO]$_0$, neat, 60 °C. [b] Turnover number (TON) determined by number of moles of converted PO divided by moles of catalyst, where conversions are determined by ^{1}H NMR spectroscopy. [c] Turnover frequency (TOF) calculated from TON divided by time between 20 – 80% conversion. [d] Determined by comparison of the integrals for any ether resonances (3.4 – 3.6 ppm) with the resonances for polyester (7.3 ppm), using ^{1}H NMR spectroscopy. [e] Determined by GPC, in THF, using narrow dispersity polystyrene standards to calibrate. [f] Reaction conditions: PO/PA 1:20:1600:4000 [cat]$_0$:[BDM]$_0$:[PA]$_0$:[PO]$_0$, neat, 60 °C.

Of the tested catalyst systems, L_{wide}CoK(OAc)$_2$ shows the best performance with an exceptional TOF of 1623 h^{-1} (Table 3.1, entry 1). It was also fully selective for polyester linkages; no ether linkages are

observed by ^{1}H NMR spectroscopy. The polyester shows a molar mass value close to that predicted theoretically (2900 vs. 2800 g mol^{-1}). It also has a monomodal, narrow dispersity molar mass distribution, as assessed by GPC (Figure 4.16A). Higher molar mass polyesters were synthesized by reducing (or removing) the quantity of BDM (chain-transfer agent) used in the catalysis (Figure 4.16B). Both features indicate rapid and reversible chain transfer, and are indicative of catalysis with a high degree of polymerization control. The control is further supported by the linear fit to plots of polyester M_n vs. conversion, where M_n values are always close to theoretical values (Figure 4.16C).

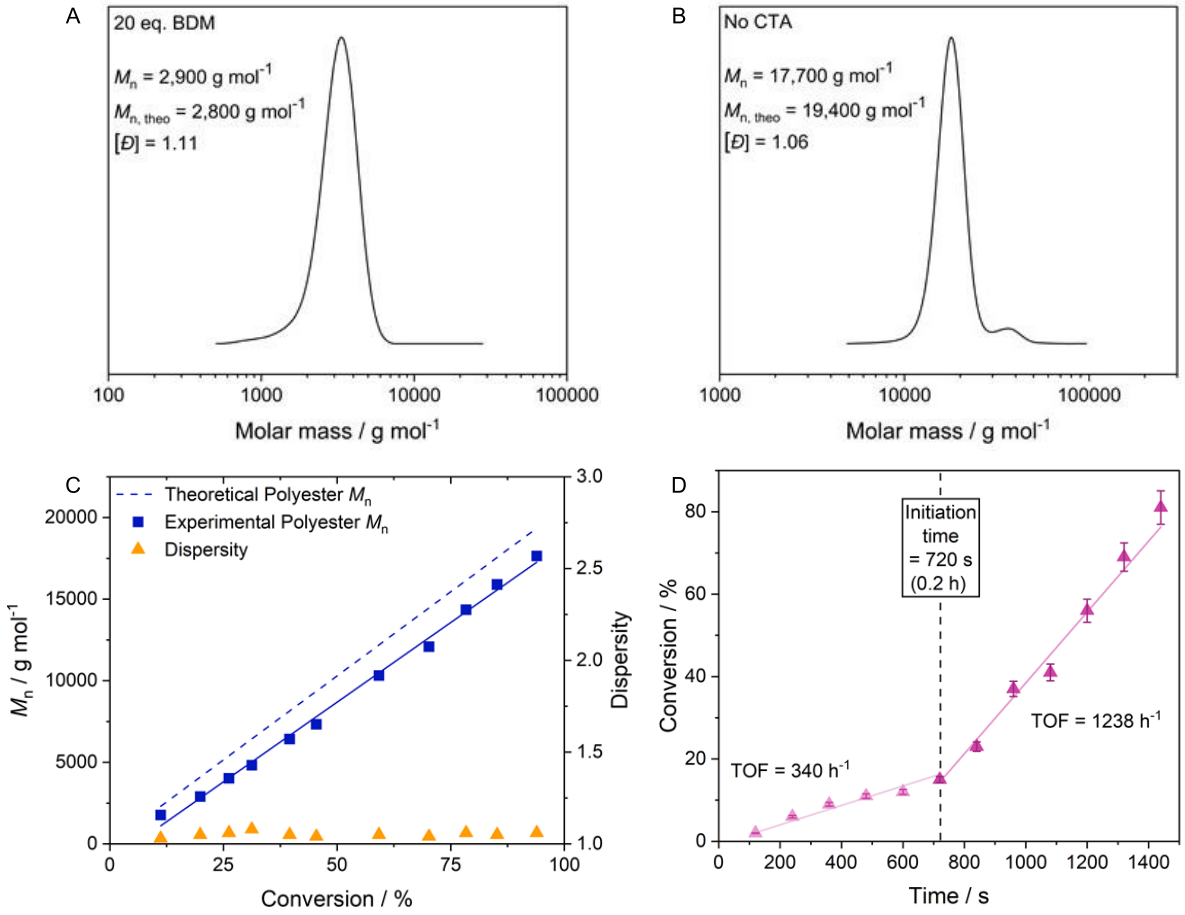


Figure 4.16. Representative molar mass distributions of poly(PO-*alt*-PA) formed by L$_{wide}$CoK(OAc)$_2$ with 20 equivalents of BDM (A) and no chain transfer agent (B) added to the polymerisation; representative plot of experimental and theoretical molar mass, and dispersity against conversion for poly(PO-*alt*-PA) formation by L$_{wide}$CoK(OAc)$_2$ (C); plot of PA conversion against time for PO/PA ROCOP polymerised by L$_{mono}$CoOAc + KOAc[18-crown-6] showing its initiation time (D).

The two components of the bicomponent system (i.e. L_{mono}CoOAc and KOAc[18-crown-6) were first tested separately (Table 4.1, entries 3 and 4 respectively). Both species showed relatively low activities of 53 h^{-1} and 36 h^{-1} respectively. Nonetheless, both catalysts were fully selective for polyester and produced polyesters with narrow dispersities.

When the two monometallic components were tested as a bicomponent system (i.e. 1:1 L_{mono}CoOAc:KOAc[18-crown-6]) a significant improvement in the activity was observed, with a TOF of 1238 h^{-1} (Table 4.1, entry 5). This increase in the activity upon combining the two monometallic components highlights the importance of heterodinuclear synergy. Again, the catalyst system was fully selective for polyester, the polyester produced had a molar mass close to the theoretical value, and a narrow dispersity, all indicating a well-controlled polymerisation. The bicomponent system does show a significant initiation time; its reported activity of 1238 h^{-1} is achieved if the initiation time is excluded, i.e. if the TOF is calculated between 20 – 80% conversion (Figure 4.16D). If only single time-point activity is considered then the TOF is reduced to 749 h^{-1}. This initiation time may be due to the necessity of the bicomponent system to form a dinuclear species in solution. While the bicomponent system has a reduced activity compared to L_{wide}CoK$(OAc)_2$, its activity is nonetheless very high for PO/PA ROCOP. One disadvantage of bicomponent catalysts is that they cannot be applied under low catalyst loadings. Indeed, when this bicomponent system is applied under more forcing conditions, 1:20:1600:4000 $[cat]_0$:$[BDM]_0$:$[PA]_0$:$[PO]_0$, its activity drops from 1238 h^{-1} to 37 h^{-1}(Table 4.1, entry 6). On the other hand, the single-component dinuclear catalyst L_{wide}CoK$(OAc)_2$ largely maintains its activity under these same forcing conditions, the rate decreases slightly from 1686 h^{-1} to 1480 h^{-1} (Table 4.1, entry 2). L_{wide}CoK$(OAc)_2$ has a 40 times greater activity than the bicomponent analogue at this concentration.

L_{short}CoK$(OAc)_2$ had a significantly lower activity compared to the two other bicomponent systems, with a TOF of 231 h^{-1}.

4.3.2.2 Ring-Opening Copolymerisation of Propene Oxide and CO_2

The three heterodinuclear catalyst systems were also tested for the ROCOP of PO and CO_2 using the following conditions: 1:20:4000 $[catalyst]_0$:[*trans*-1,2-cyclohexane diol (CHD)]$_0$:$[PO]_0$ in neat PO, at 50 °C under 20 bar CO_2 pressure.

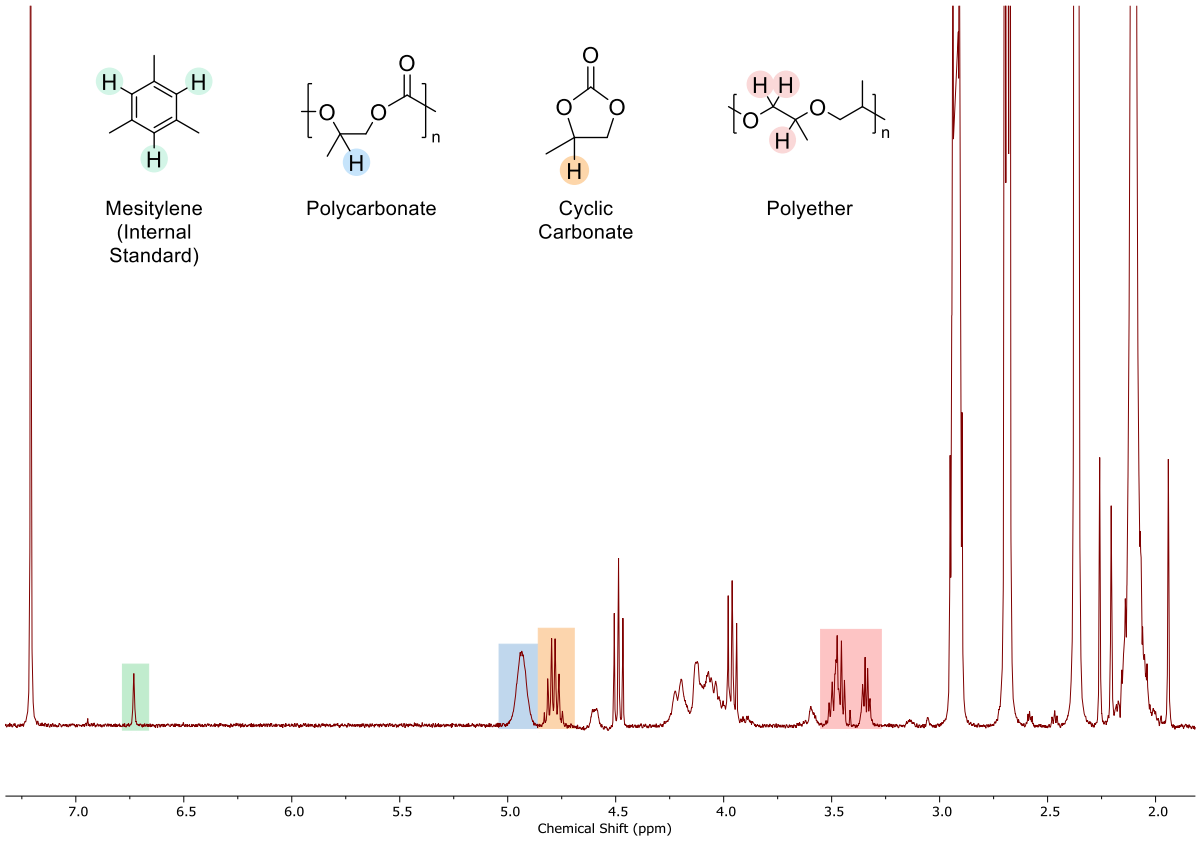


Figure 4.17. ^{1}H NMR spectrum of a representative PO/CO_2 ROCOP reaction showing integrals for mesitylene (10 eq. used as an internal standard), polycarbonate, cyclic carbonate, and polyether for the calculation of conversion, which is in turn used to calculate the turnover number (TON) and turnover frequency (TOF), and selectivity for CO_2 and polymer.

Reactions were conducted in a Parr reactor fitted with an *operando* ATR-IR spectroscopy probe to allow monitoring of formation of polycarbonate (1750 cm^{-1}) and cyclic carbonate (1810 cm^{-1}). Final conversion to polycarbonate, cyclic carbonate, and polyether was determined by ^{1}H NMR spectroscopy of an aliquot of the crude reaction, using mesitylene as an internal standard (Figure 4.17).

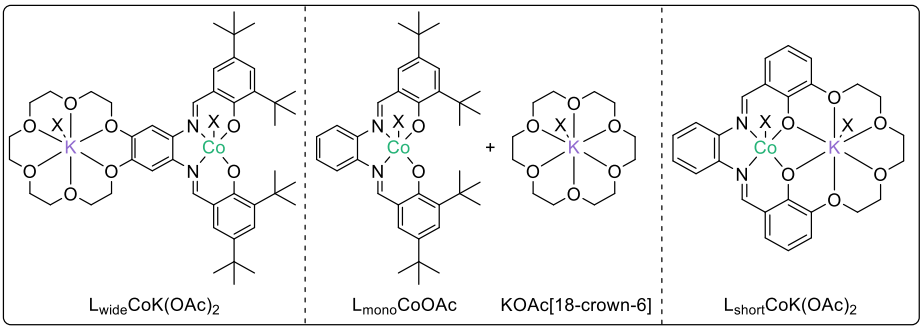


Table 4.2. Data for the ROCOP of propene oxide (PO) and CO_2 for the three catalysts.[a]

	Catalyst	Time / h	TON[b]	TOF_{PPC}[c] / h^{-1}	PPC[d] / %	PC[e] / %	PPO[f] / %	M_n [$Đ$][g] / g mol^{-1}
1	$L_{wide}CoK(OAc)_2$	27.5	207	0	0	97	3	-
2	$L_{mono}CoOAc$+KOAc[18-crown-6]	25.0	405	16	53	36	11	< 1000
3[h]	$L_{mono}CoOAc$+KOAc[18-crown-6]	0.4	112	231	82	1	17	< 1000
4[24]	$L_{short}CoK(OAc)_2$	2.5	973	389	> 99	0	0	4000 [1.06]

[a] Reaction conditions: 1:20:4000 [catalyst]$_0$:[CHD]$_0$:[PO]$_0$, neat, 50 °C, 20 bar CO_2. [b] Turnover number (TON) = moles of PO consumed/moles of catalyst, determined by ^{1}H NMR spectroscopy (Figure S28). [c] Turnover frequency for PPC production (TOF_{PPC}) = TON for PPC production / time. [d - f] Selectivity for poly(propene carbonate) (PPC), propene carbonate (cyclic by-product; PC), and polypropene oxide (polyether; PPO) determined by measuring the integrals for PPC or PC or PPO compared to all other products in the reaction by 1H NMR spectroscopy (Figure 4.16). [g] Determined by GPC, in THF, using narrow dispersity polystyrene standards. [h] Reaction conditions: 1:20:1000 [catalyst]$_0$:[CHD]$_0$:[PO]$_0$, neat, 50 °C, 20 bar CO_2.

For PO/CO_2 ROCOP, the most active catalyst of the three tested is $L_{short}CoK(OAc)_2$, which has an excellent TOF of 389 h^{-1} (Table 3.2, entry 4). It is fully selective for polycarbonate; no cyclic carbonate or polyether can be observed by ^{1}H NMR spectroscopy.

On the other hand, $L_{wide}CoK(OAc)_2$ is completely inactive for PO/CO_2 ROCOP (Table 3.2, entry 1). Over the course of the reaction, it only makes small quantities of cyclic carbonate, and trace quantities of polyether.

The bicomponent system is active for PO/CO_2 ROCOP under the tested reaction conditions, but it has a poor activity of 16 h^{-1}, and a low selectivity for polycarbonate of 53% (Table 3.1, entry 2). It should be noted, that the tested conditions are relatively dilute (4000 equivalents of PO per equivalent of catalyst), which is, as previously discussed, detrimental for the performance of bicomponent catalyst systems.

Conducting the polymerization with an increased catalyst concentration (1:20:1000 $[catalyst]_0:[BDM]_0:[PO]_0$) results in a greater than 14-fold increase in TOF to 231 h^{-1} (Table 4.1, entry 3). The selectivity for polycarbonate also increases to 82%. While the proportion of cyclic carbonate formed decreased from 36% to only 1%, the proportion of polyether increased from 11% to 17%. This is perhaps unsurprising, as $L_{mono}CoOAc$ has been reported as an efficient catalyst for the ROP of PO to form polyether.[23]

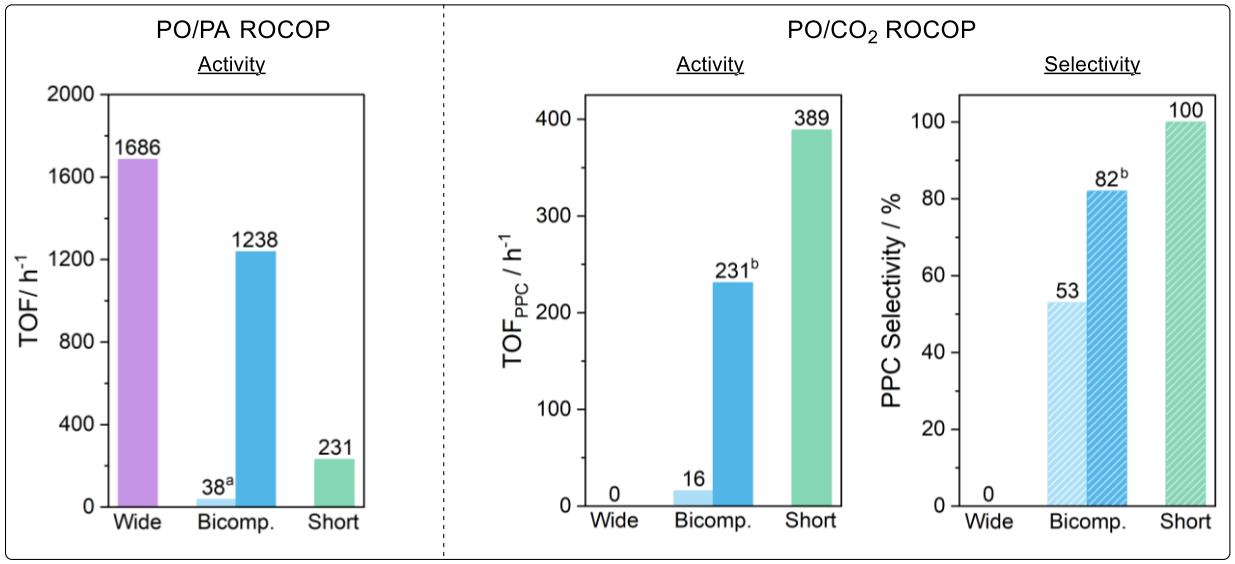


Figure 4.18. Top: Comparison of the three catalysts in terms of activities (and selectivities, where relevant) for PO/PA ROCOP (LHS) and PO/CO_2 ROCOP (RHS). Reaction conditions: PO/PA ROCOP: 1:20:400:1000 ([a] 1:20:400:4000) $[catalyst]_0:[BDM]_0:[PA]_0:[PO]_0$, neat, 60 °C; PO/$CO_2$ ROCOP: 1:20:4000 ([b]1:20:1000) $[catalyst]_0:[CHD]_0:[PO]_0$, neat, 50 °C, 20 bar CO_2.

These data are opposite to those seen for PO/PA ROCOP. While $L_{wide}CoK(OAc)_2$ showed the best performance for PO/PA ROCOP, it is completely inactive for PO/CO_2 ROCOP. On the contrary, $L_{short}CoK(OAc)_2$ had a significantly lower activity for PO/PA ROCOP, but a high activity for PO/CO_2 ROCOP. The bicomponent system has, in both cases, an activity and (where relevant) selectivity between the fixed narrow and wide intermetallic separation catalysts, provided the catalyst concentration is sufficiently high (Figure 4.18).

4.3.3 Electronic vs. Intermetallic Separation Effects

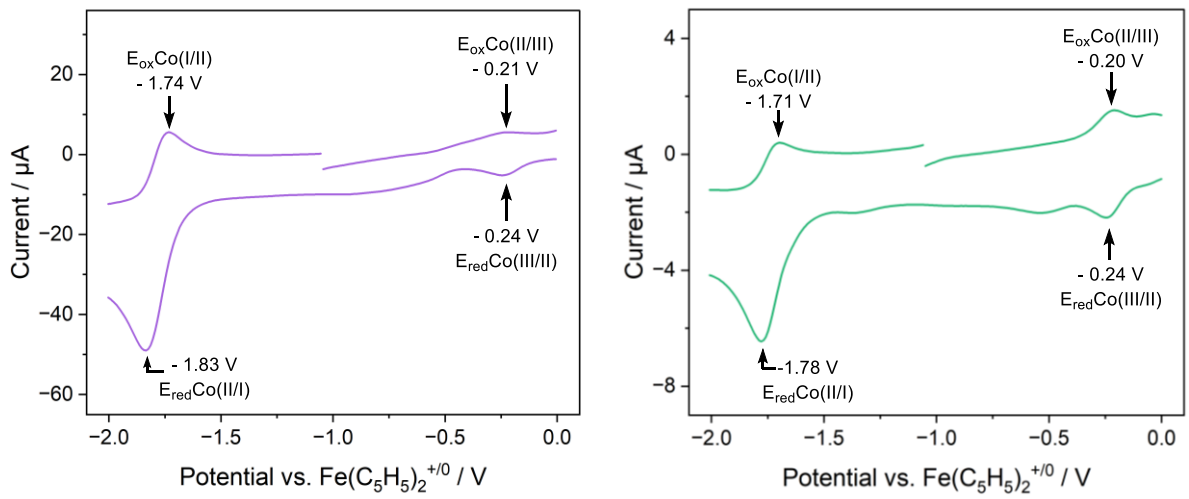


Figure 4.19. Cyclic voltammetry traces for $L_{wide}CoK(OAc)_2$ (LHS) and $L_{mono}CoOAc$ (RHS).

Recently, our group reported a series of narrow separation catalysts, including $L_{short}CoK(OAc)_2$, where the ancillary ligand was modified to include electron withdrawing and electron donating groups.[24] The investigation revealed that the most electron-rich Co(III) complexes (as determined by Co(III/II) redox potentials, determined by cyclic voltammetry) were also the most active and selective for PO/CO_2 ROCOP. To understand whether the catalytic performance differences in PO/CO_2 ROCOP between these three catalysts might correlate with electronic factors, the Co(III/II) redox potentials were measured (Figure 4.19, Table 4.3).

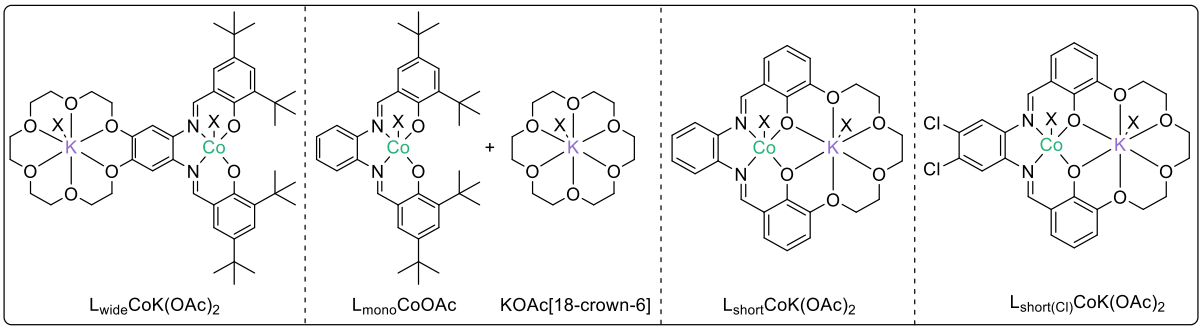


Table 4.3. Summary of Co(III/II) redox potentials and ROCOP activities/selectivities for the three tested catalysts, and for an analogue of $L_{short}CoK(OAc)_2$ with a chlorinated phenyl amine backbone.[a]

	Catalyst	$E_{1/2}$ Co(II/III) / V	PO/PA ROCOP	PO/CO_2 ROCOP	
			TOF / h^{-1}	TOF / h^{-1}	PPC / %
1	$L_{wide}CoK(OAc)_2$	- 0.23	1686	0	0
2[b]	$L_{mono}CoOAc$+KOAc[18-crown-6]	- 0.22	1238	231	82
3[24]	$L_{short}CoK(OAc)_2$	- 0.41	231	389	>99
4[24]	$L_{short(Cl)}CoK(OAc)_2$	- 0.25	N.D.	62	75

[a] Reaction conditions: PO/PA ROCOP: 1:20:400:1000 [catalyst]$_0$:[BDM] $_0$:[PA] $_0$:[PO] $_0$, 60 °C; PO/CO_2 ROCOP: 1:20:4000 [catalyst]$_0$:[CHD]$_0$:[PO]$_0$, 50 °C, 20 bar CO_2 pressure. [b] Reaction conditions: PO/PA ROCOP: 1:20:400:1000 [catalyst]$_0$:[BDM]$_0$:[PA]$_0$:[PO]$_0$, 60 °C; PO/CO_2 ROCOP: 1:20:1000 [catalyst]$_0$:[CHD]$_0$:[PO]$_0$, 50 °C, 20 bar CO_2 pressure.

The Co(III/II) redox potentials of the wide and bicomponent catalysts, $L_{wide}CoK(OAc)_2$ and $L_{mono}CoOAc$, are nearly identical, with values of – 0.23 and – 0.22 V (vs. ferrocene/ferrocenium), respectively (Table 4.3, entries 1 and 2 respectively). On the other hand, the equivalent Co(III/II) redox potential for the narrow separation catalyst, $L_{short}CoK(OAc)_2$, was significantly lower at – 0.41 V (vs. ferrocene/ferrocenium), indicating it has a more electron-rich Co(III) center (Table 3.3, entry 3).[24] While this might initially seem to explain the differences in activity observed for PO/CO_2 ROCOP, it does not explain the difference in activity observed between $L_{wide}CoK(OAc)_2$ and the bicomponent system, as they have near-identical Co(III/II) redox potentials. Further, a narrow separation catalyst analogous to $L_{short}CoK(OAc)_2$ but with a chlorinated phenylene amine linker was reported in the previously-discussed article ($L_{short(Cl)}CoK(OAc)_2$; Table 3.3, entry 4).[24] This catalyst has a very similar Co(III/II) redox potential to $L_{wide}CoK(OAc)_2$ and $L_{mono}CoOAc$ of – 0.24 V (vs. ferrocene/ferrocenium) but has an activity of 62 h^{-1} and a selectivity for polycarbonate of 75% (1:20:4000 [catalyst]$_0$:[CHD]$_0$:[PO]$_0$, neat, 50 °C, 20 bar CO_2;

Table 3.3). This is significantly faster and more selective than both $L_{wide}CoK(OAc)_2$ and the bicomponent system under the same conditions.

As such, the activity differences between $L_{wide}CoK(OAc)_2$, the bicomponent catalyst, and $L_{short}CoK(OAc)_2$ seem unlikely to be related to only different Co(III) electronics factors, and more likely relate to the difference in intermetallic separation.

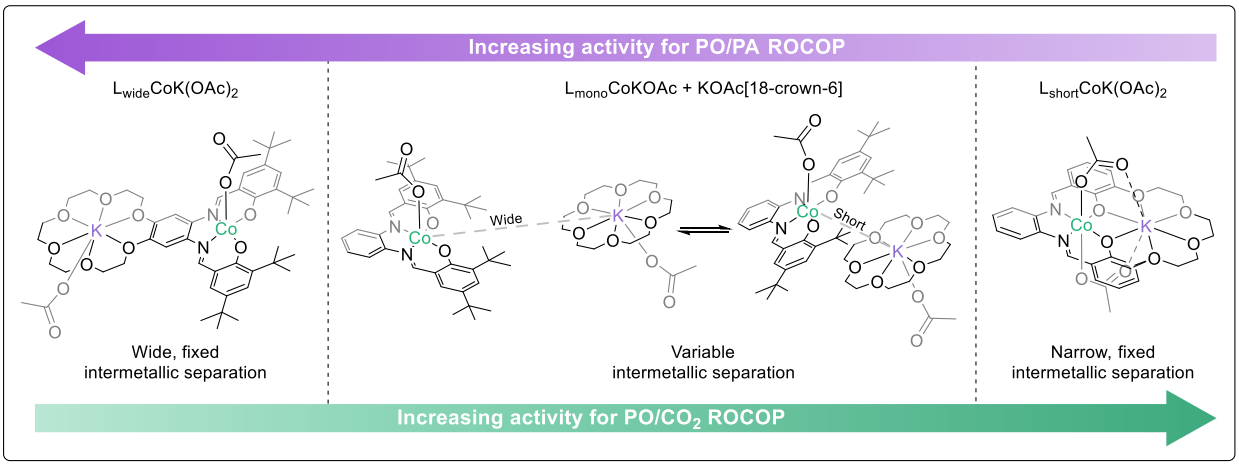


Figure 4.20. Proposed structures of the three dinuclear catalyst systems during polymerization with changing intermetallic separation

To rationalise the observed performance of each of the tested catalysts, it is proposed that while $L_{wide}CoK(OAc)_2$ and $L_{short}CoK(OAc)_2$ have fixed intermetallic separations of 8.06 Å and 3.59 Å respectively, the bicomponent catalyst system forms a dinuclear species under the polymerization conditions and may be able to do so with a variable intermetallic separation.

For PO/PA ROCOP, the large intermetallic separation found in $L_{wide}CoK(OAc)_2$ seems to result in a high activity, while the narrow intermetallic separation found in $L_{short}CoK(OAc)_2$ results in a relatively poor performance for this polymerisation. The opposite trend is seen for PO/CO_2 ROCOP: $L_{wide}CoK(OAc)_2$ is inactive for this polymerisation, while $L_{short}CoK(OAc)_2$ shows a high activity and selectivity. It is proposed that the bicomponent system is able to form a dinuclear species in solution with a variable

intermetallic separation that is optimized to the polymerization, so long as the catalyst concentration is sufficiently high (Figure 4.20). Perhaps, for PO/PA ROCOP it forms a species in solution with a relatively wide intermetallic separation, while for PO/CO_2 ROCOP it forms a species with a relatively narrow intermetallic separation, allowing it to achieve high performances for both. Perhaps the differing intermetallic separations result in different mechanisms which are highly active for PO/PA ROCOP or PO/CO_2 ROCOP, but not both.

4.3.4 Kinetic and Mechanistic Investigations of $L_{wide}CoK(OAc)_2$

The rate law for PO/PA ROCOP catalysed by $L_{wide}CoK(OAc)_2$ was determined to investigate the mechanism. To determine the rate dependence of the polymerisation with respect to the concentration of PA and PO, polymerisations were conducted with varying concentration of the monomer under investigation (0.7 – 2.9 M for PA, and 5.8 – 14.3 M for PO), while the initial concentration of the other monomer was kept constant (1.4 M for PA, and 14.3 M for PO (i.e. neat)), and the catalyst concentration was kept constant at 14.3 mM. Reactions were conducted at 60 °C and were monitored by regular aliquoting which were analysed by ^{1}H NMR spectroscopy to determine conversion.

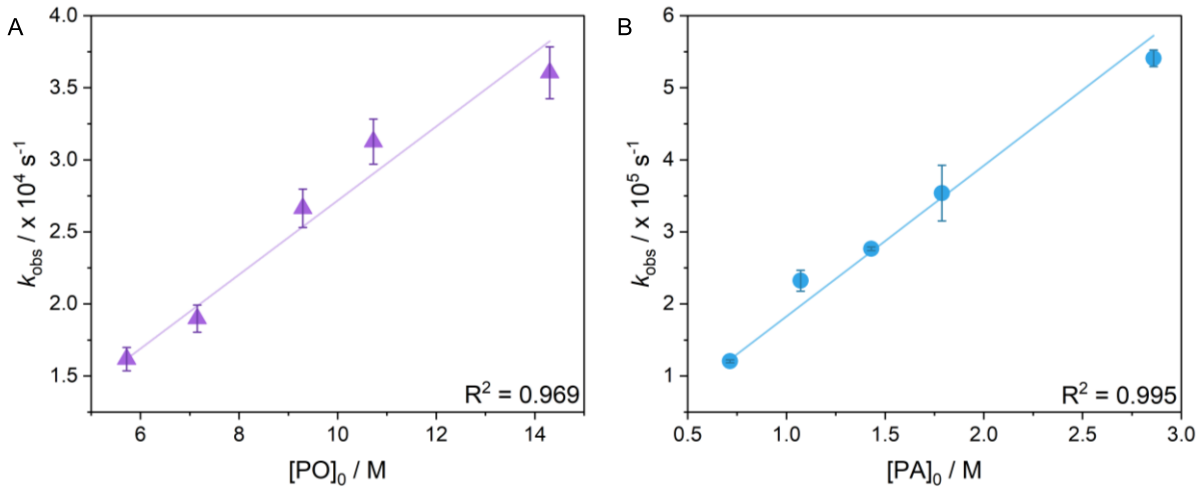


Figure 4.21. Plots of k_{obs} against $[PO]_0$ (A) and $[PA]_0$ (B) showing linear correlations, indicating first-order dependencies of rate on the concentration of each monomer.

For both monomers tested, plots of k_{obs} against the starting concentration of the relevant monomer (i.e. $[PO]_0$ or $[PA]_0$) are linear, indicating first-order rate-dependencies in both cases (Figure 4.21A and B). This is further supported by the fact that each polymerisation shows an exponential decay in PO or PA concentration against time, which is confirmed by linear plots of $\ln([PO]_t/[PO]_0)$ and $\ln([PA]t/[PA]_0)$ against time for each polymerisation (Figure 4.22A and B, respectively and Figure S4.16A and B, respectively). Finally, plots of $\ln(k_{obs})$ against $\ln[PA]_0$ or $\ln[PO]_0$ are linear with gradients of 1.10 and 0.93

respectively, and the half-life of each polymerisation remains constant with changing concentrations of both PO and PA (Figure 4.22C and D, respectively, and Figure S4.16C and D, respectively).

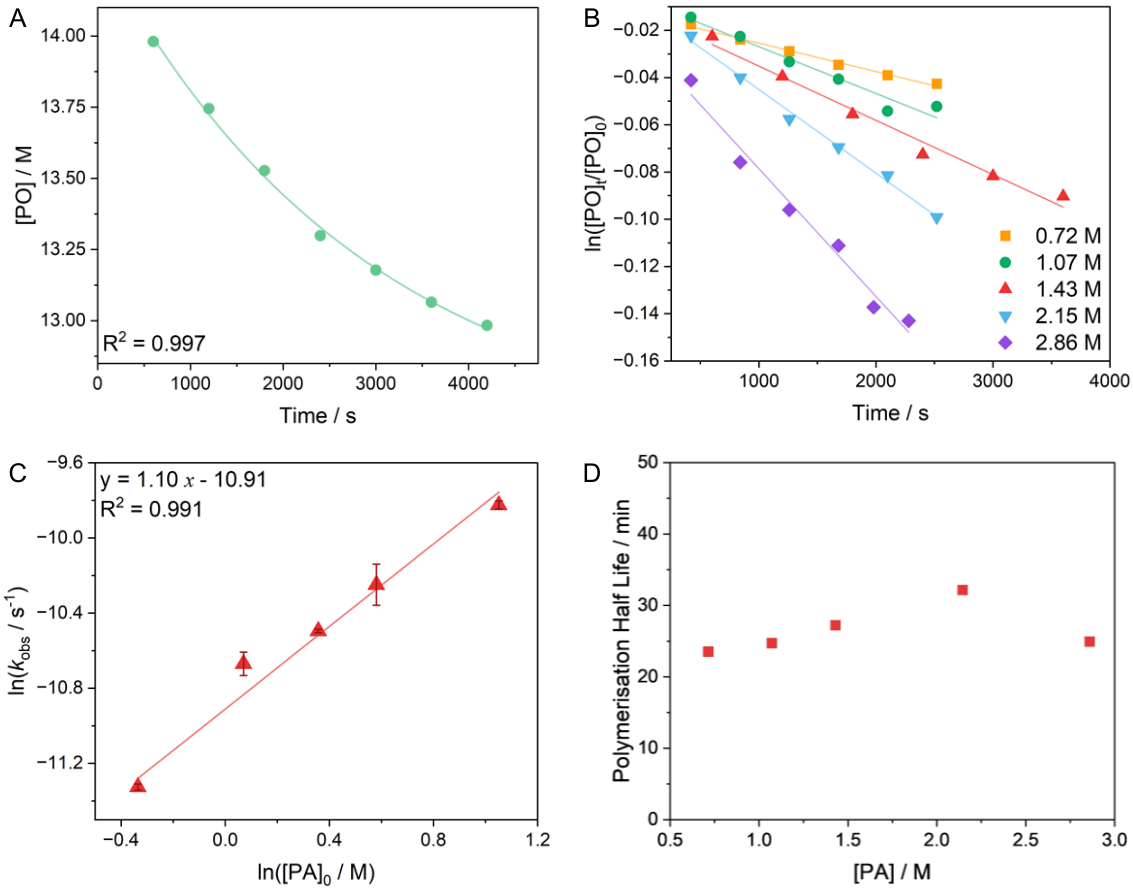


Figure 4.22. Plots used for the determination of polymerisation rate dependence with respect to the concentration of PA. A: Exponential decay of [PO] against time; B: linear plots of ln($[PO]_t/[PO]_0$) with varying concentrations of PA; C: plot of ln(k_{obs}) against ln($[PA]_0$) with a gradient of 1.10; D: polymerisation half-life against [PA] showing it stays constant with varying [PA].

The rate dependence of the polymerisation with respect to catalyst concentration was determined by conducting polymerisations in neat epoxide ($[PO]_0$ = 14.3 M) and with $[PA]_0$ = 1.43 M, at 60 °C with varying catalyst concentrations of between 3.58 – 17.9 mM (i.e. X:100:1000 $[catalyst]_0$:$[PA]_0$:$[PO]_0$, in neat epoxide, with X = 0.25 – 1.25). Increasing the concentration of catalyst results in an increase in rate, and the plot of k_{obs} against $[catalyst]_0$ is linear, which is consistent with a first-order rate dependence.

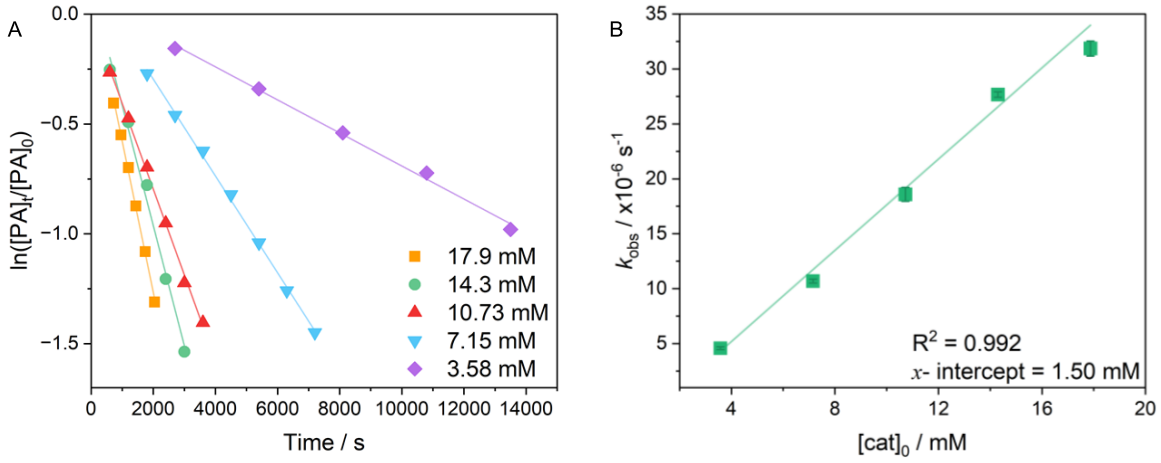


Figure 4.23. Plots used for the determination of the rate dependence with respect to catalyst concentration. A: plots of $\ln[PA]_t/[PA]_0$) against time with varying catalyst concentrations; B: plot of k_{obs} against initial catalyst concentration.

As such, an overall third-order rate law was determined for PO/PA ROCOP catalysed by $L_{wide}CoK(OAc)_2$, with a rate equation as follows:

$$rate = k_P[\text{catalyst}]^1[PO]^1[PA]^1 \qquad \text{Eq. 4.1}$$

This rate law is unusual, as catalysts for epoxide/anhydride ROCOP are almost exclusively found to operate through a mechanism which is first-order in catalyst and PO concentration, but zero-order with respect to the concentration of anhydride.[4, 25] This is rationalised by a mechanism where the rate-determining step is ring-opening of epoxide by the nucleophilic carboxylate polymer chain end.[4, 25]

To the best of our knowledge, only one other catalyst has been reported with a non-zero order in anhydride concentration.[26] As discussed in Chapters One to Three, for Co(III)K catalysts, such as $L_{short}CoK(OAc)_2$, the Co(III) centre is proposed to bind epoxide while K binds the carboxylate chain end, in the rate-determining step (Figure S4.17). Chen and co-workers reported a trinuclear Al(III) catalyst for the polymerisation of PO and PA without co-catalyst, which shows first-order kinetics with respect to the concentration of catalyst, PO, and PA.[26] However, the kinetic data was not explored in depth, and

the authors did not propose a mechanism which differs from that which is typically reported for epoxide/anhydride ROCOP.

Following from this rate law (Equation 4.1), a catalyst mechanism which features the catalyst, epoxide, and anhydride in the rate-determining step must be considered.

DFT calculations of various catalysts for epoxide/anhydride ROCOP find that the barrier for epoxide ring-opening is significantly greater than the barrier to cyclic anhydride ring-opening ($\Delta G^{\ddagger}_{ep}$ - $\Delta G^{\ddagger}_{anh}$ = 6.9 – 25.8 kcal mol^{-1}).[25, 27-31] This is found consistently across different types of catalysts (hetero- and homodinuclear catalysts with wide or short intermetallic separations, monometallic catalysts utilised with co-catalyst, organocatalysts) for varying combinations of epoxides and anhydrides. We do not expect the changes in catalyst structure detailed herein to favour epoxide ring-opening and/or disfavour anhydride ring-opening to the extent that the barriers to these two steps become energetically equivalent. As such, the rate-law is interpreted to be due to anhydride playing a key role in activating the catalyst, without being ring-opened in the rate-determining step.

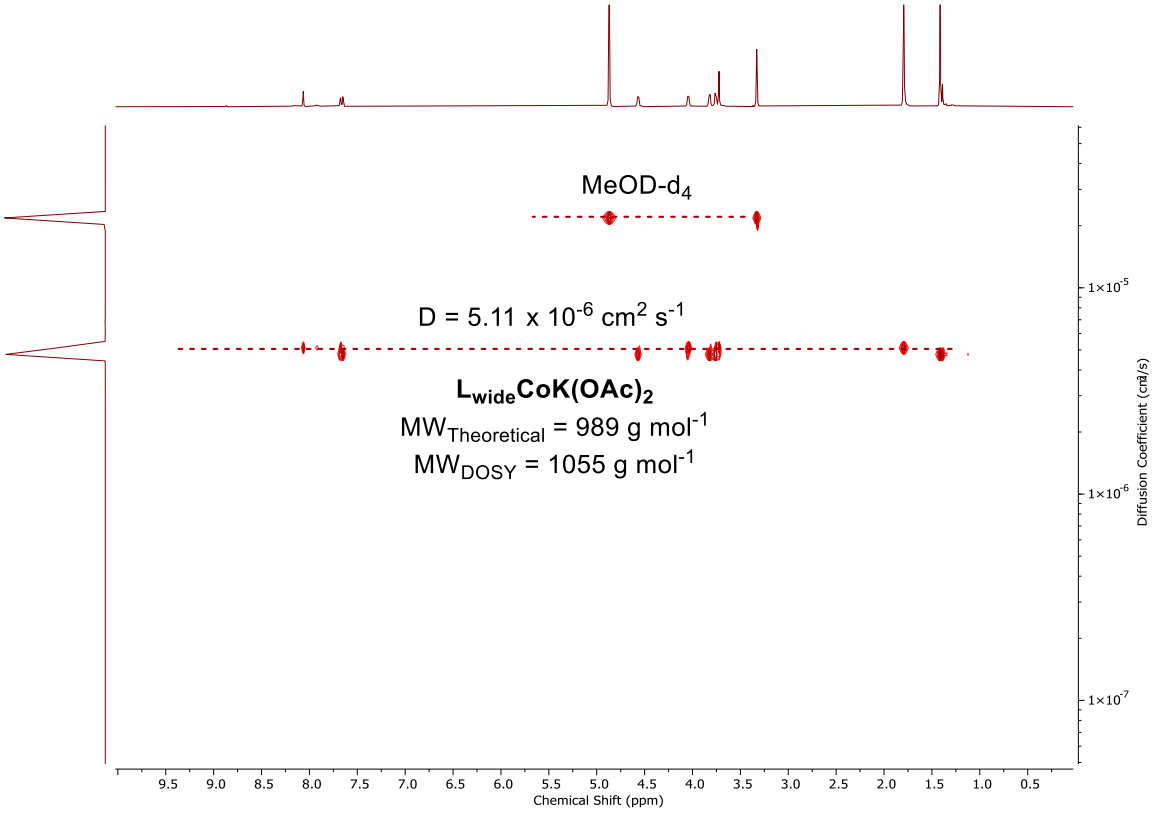


Figure 4.24. DOSY NMR experiment of $L_{wide}CoK(OAc)_2$ in MeOD-d_4 indicating a monomeric species.

A mechanism featuring two catalyst molecules working in synergy is also not considered due to the first-order rate dependence on catalyst (excluding monomer-dimer equilibria within the catalytic cycle) and a DOSY NMR experiment of the catalyst in methanol, which shows a single species with a diffusion coefficient which is consistent with the monomeric catalyst (Figure 4.24).[32] Since MeOD-d_4 is a polar, donating solvent it is used as a model for epoxide, which is used as the solvent in ROCOP polymerisations.

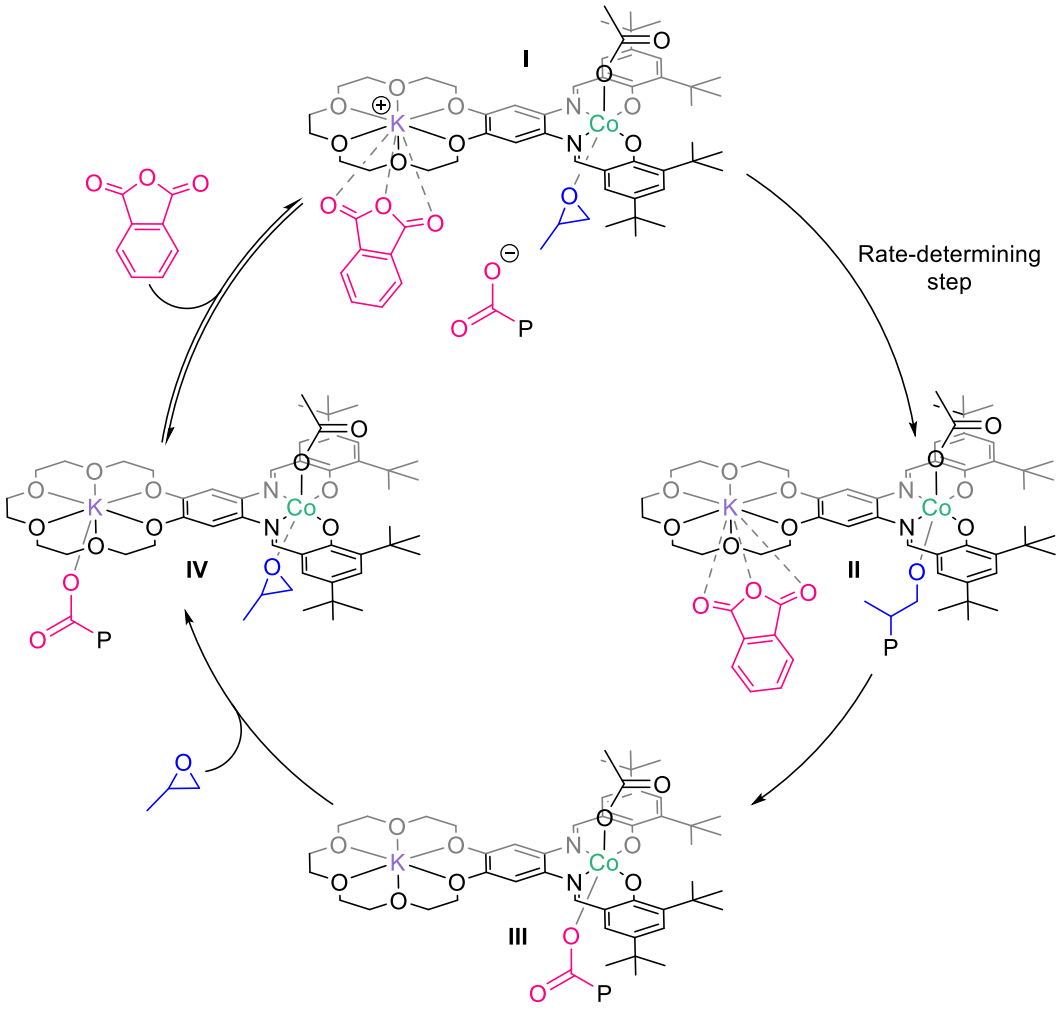


Figure 4.25. Proposed mechanism for PO/PA ROCOP catalysed by $L_{wide}CoK(OAc)_2$.

We propose a mechanism where the "usual" catalyst resting-state, IV, with epoxide bound to the Co(III) centre and the carboxylate polymer chain-end bound to the K centre is inactive due to the large intermetallic separation, which is too great for the nucleophile and electrophile to react (Figure 4.25). Perhaps, an equilibrium exists where anhydride coordination to the K centre displaces an anionic chain-end, which is then able to approach and ring-open the Co(III)-bound epoxide, I. The alkoxide intermediate formed from the epoxide ring-opening, II, is then proposed to rapidly react with an anhydride molecule, reforming the carboxylate intermediate, III.

The formation of an anionic, free carboxylate intermediate in the rate-determining step may explain the high rates for PO/PA ROCOP, since such species should be strongly nucleophilic compared to metal-bound carboxylates. Indeed, recent studies have proposed that polymerization rates are accelerated by increasingly weak coordination of the anionic chain end to the catalyst species. The existence of an equilibrium between the active species I, and inactive IV, might explain the observation that the activity of the catalyst is directly proportional to PA concentration. At high concentrations, the equilibrium is pushed towards the active species, I. As the reaction progresses, and PA is consumed, the equilibrium shifts back towards the inactive species IV, resulting in the exponential decay of PA concentration that is characteristic of first-order kinetics.

4.3.5 Literature Catalyst Comparison

The catalyst activities, both in terms of mole of polymer produced per mole of catalyst per hour (TOF), and gram per gram per hour activity, were evaluated against some of the best catalysts reported in the literature (Figure 4.26).

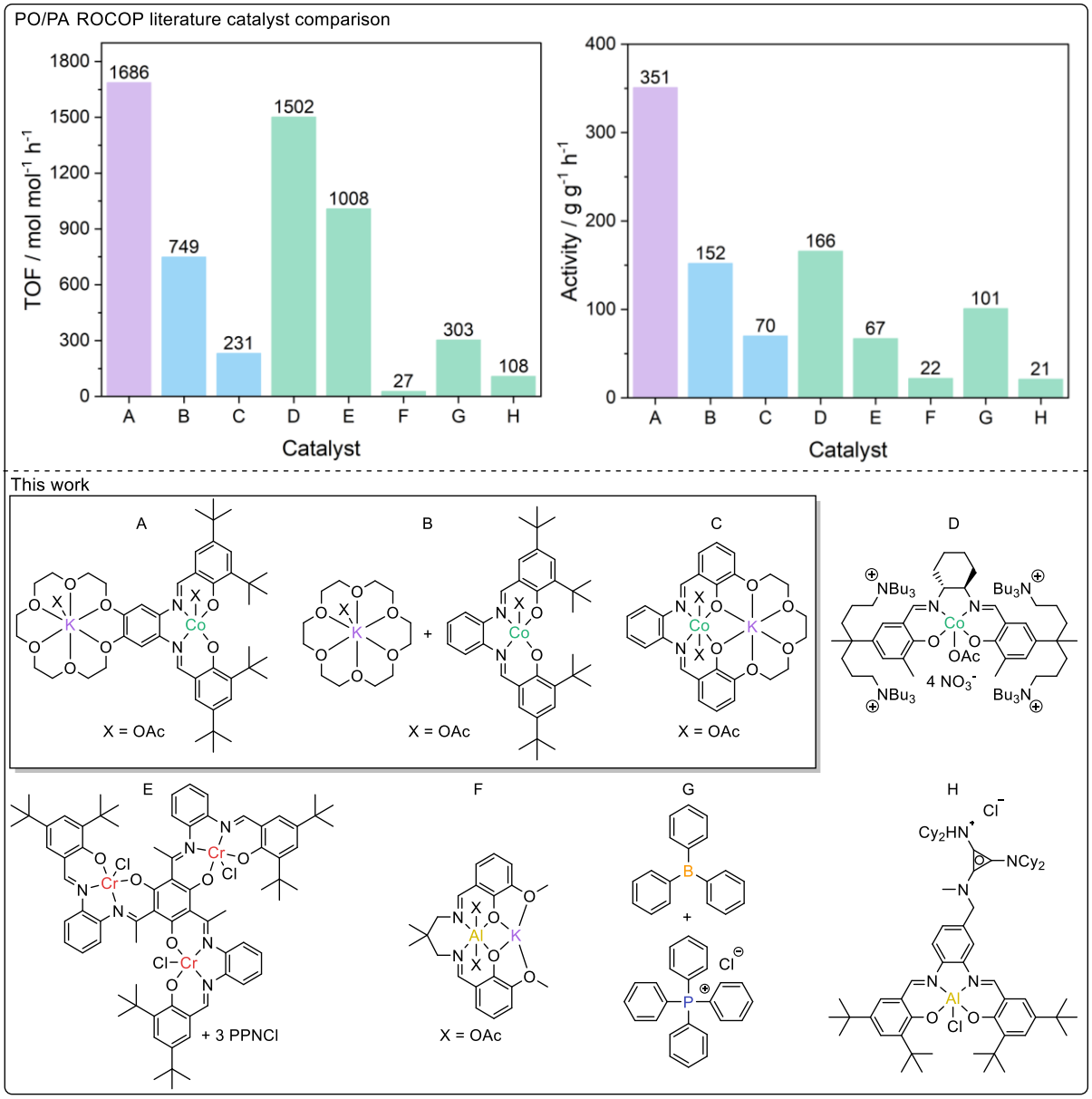


Figure 4.26. Comparison of the three Co(III)K(I) catalysts against high-performance literature catalysts for PO/PA ROCOP (for conditions see Figure S4.18). [3, 7, 33-35]

$L_{wide}CoK(OAc)_2$ is amongst the best performing catalysts reported to-date, with its TOF of 1686 h^{-1}. (A, Figure 4.26). Other excellent catalysts for PO/PA ROCOP include a cobalt salen with four tethered quaternary ammonium "arms", reported by Lee and co-workers, which shows a molar TOF of 1502 h^{-1}, and a trimetallic $Cr(III)_3$ Schiff base complex, reported by Lu and co-workers, which shows a molar TOF of 1008 h^{-1} (D and E, respectively, in Figure 4.26; 1:242:7508:100,000 $[cat]_0$:$[EtOH]_0$:$[PA]_0$:$[PO]_0$, 80 °C, neat; 1:3:600:3000 $[cat]_0$:$[PPNCl]_0$:$[PA]_0$:$[PO]_0$, 60 °C, neat).[3, 35]

It should be noted that $L_{wide}CoK(OAc)_2$ is simpler to synthesise than the tethered ammonium cobalt salen complex (which requires eight synthetic steps), and achieves its high activity at 60 °C, compared to the tethered salen's 80 °C. It also does not require the addition of PPNCl as a co-catalyst, unlike the tri-Cr(III) catalyst, which is desirable as this co-catalyst is expensive, corrosive, and toxic.

When considering the activity in terms of the mass, in grams, of polymer produced per gram of catalyst per hour, the high molar masses for these two catalysts relative to $L_{wide}CoK(OAc)_2$ is a further disadvantage (RMM D = 1674 g mol^{-1}, E = 3107 g mol^{-1} vs 989 g mol^{-1} for $L_{wide}CoK(OAc)_2$, A in Figure 7). As such, the per gram activity of $L_{wide}CoK(OAc)_2$ is twice that of the tethered ammonium, cobalt salen catalyst, and five times greater than that of the tris-Cr(III) salen catalyst (351 h^{-1} vs. 166 h^{-1} and 351 h^{-1} vs. 67 h^{-1} respectively; Figure 7). $L_{wide}CoK(OAc)_2$ also has superior activities, either mol mol^{-1} h^{-1} or g g^{-1} h^{-1}, compared to other excellent catalysts, including a Al(III)K(I) heterodinuclear catalyst (E), a organoborane/phosphonium chloride system (F), or a cationic Al(III) Schiff base catalyst (G) (for polymerisation conditions for all the discussed catalysts see Figure S4.18). [7, 33, 34]

The bicomponent catalyst system, $L_{mono}CoKOAc$ + KOAc[18-crown-6] (B) also performs very well in comparison to the literature catalysts. The simplicity of its synthesis might make it an interesting future candidate for PO/PA ROCOP, especially when relatively high catalyst loadings are acceptable.

4.3.6 Monomer Scope of $L_{wide}CoK(OAc)_2$

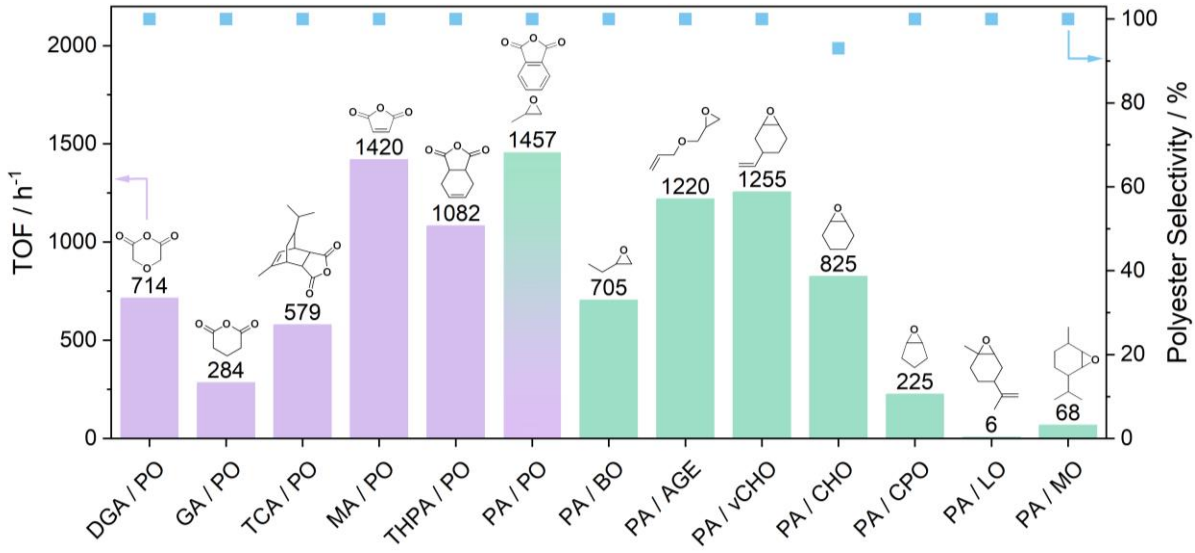


Figure 4.27. Turnover frequencies (TOFs) and polyester selectivity for polymerizations using different monomer pairs, from LHS reactions combine PO with different anhydride (purple data), whilst the RHS show PA with various epoxides (green data).

An attraction of epoxide/anhydride ROCOP is the large number of commercially available epoxides and anhydrides which could be used to make polyesters with rigid, aromatic or flexible backbone substituents. It is important to evaluate that the best catalysts are also tolerant to a range of different monomers. $L_{wide}CoK(OAc)_2$ was tested for the ROCOP of PO with various anhydrides (Figure 8 LHS) and of PA with various epoxides (Figure 8 RHS). In each case, the polymerizations were conducted with 14.3 mM catalyst, 1.43 M anhydride, 0.29 M BDM, and 0.75 mL of the epoxide at 70 °C. For PO/PA ROCOP, these conditions correspond to 1:20:100:1000 $[catalyst]_0:[BDM]_0:[PA]_0:[PO]_0$.

The catalyst was active under all conditions and showed good performance with different anhydrides, including those featuring C3 carboxylate separations (six-membered rings: DGA or GA), C2-carboxylate separations (five-membered rings: MA, THPA and PA) and also using rigid, bio-derived tricyclic anhydrides (TCA). In general, the five-membered cyclic anhydrides showed faster rates than the six-membered anhydrides. This may be due to the higher anhydride torsion angle which increases its basicity and may shift the coordination equilibria with K(I) in the rate determining step. The tricyclic anhydride TCA was least active amongst the five membered ring anhydrides, and is likely due to the

increase in steric bulk. $L_{wide}CoK(OAc)_2$ was also very effective using different epoxides, including for terminal epoxides (PO, BO), six-membered cyclic epoxides (CHO, vCHO, LO, MO) and also for the five-membered cyclic epoxide (CPO). Epoxides with high steric congestion proved less active, for example slower rates using LO or MO than for CHO or vCHO. Overall, the catalyst is highly active across the range of commonly applied epoxides and anhydrides and its low temperature activity makes it well-suited to ROCOP using PO.

4.4 Conclusions and Future Work

A series of three Co(III)/K(I) heterodinuclear catalysts were tested for propene oxide ring opening copolymerizations with phthalic anhydride or with carbon dioxide. The catalysts feature closely related Schiff base ancillary ligands but have different and controllable intermetallic separations. The catalyst with a wide intermetallic separation, $L_{wide}CoK(OAc)_2$, showed the highest activity for PO/PA ROCOP, it also showed quantitative selectivity for ester linkage formation and good polymerization control and impurity tolerance. The same catalyst was, however, nearly completely inactive for PO/CO_2 ROCOP. In contrast, the catalyst with the narrow intermetallic separation, $L_{short}CoK(OAc)_2$ showed the highest activity and selectivity for PO/CO_2 ROCOP, it was also well controlled and tolerant to impurities, but was not very active for PO/PA ROCOP. A bicomponent catalyst system, comprising a monometallic Co(III) complex applied with a potassium salt showed high activities for both PO/PA and PO/CO_2 ROCOP but required high catalyst concentrations and was not very effective at low loadings. The bicomponent catalyst may be useful but only for polymerizations where high catalyst loading can be tolerated (i.e. catalyst cost is not a barrier and effective removal strategies are developed).

The $L_{wide}CoK(OAc)_2$ catalyst rate law was determined to be first order in catalyst, anhydride and epoxide concentrations. It was also highly effective in the polymerization of a range of different anhydrides and epoxides. The rate data were compared for the two different classes of polymerizations with some useful guiding principles for catalyst design emerging from the investigation. For epoxide/carbon dioxide ROCOP, catalyst separations are most effective in the 'shorter' range (3-4 Å) and ancillary ligands which position metals accordingly should be prioritized. For epoxide/anhydride ROCOP, catalysts featuring more widely separately metals (8-9 A) should be prioritized in the future.

In the future, the proposed equilibrium in the catalytic cycle for PO/PA ROCOP catalysed by $L_{wide}CoK(OAc)_2$ should be explored further. This could include spectroscopic characterisation techniques (e.g. UV-vis, NMR spectroscopy) to try to identify key intermediates and/or the equilibrium.

For example, coordination of anhydride to the catalyst could be investigated by UV-vis titration studies, and/or by ^{19}F NMR spectroscopy using an anhydride with a fluorinated backbone.

The generality of the observed intermetallic separation – activity trends for epoxide/anhydride ROCOP should also be explored further by synthesising related complexes using L_{wide}, These could include the complexes of Al(III), Cr(III), and/or Fe(III) with K.

4.5 References

(1) Nakano, K.; Hashimoto, S.; Nozaki, K. Bimetallic mechanism operating in the copolymerization of propylene oxide with carbon dioxide catalyzed by cobalt–salen complexes. *Chem. Sci.* **2010**, *1* (3), 369-373.

(2) Moore, D. R.; Cheng, M.; Lobkovsky, E. B.; Coates, G. W. Mechanism of the Alternating Copolymerization of Epoxides and CO2 Using β-Diiminate Zinc Catalysts: Evidence for a Bimetallic Epoxide Enchainment. *J. Am. Chem. Soc.* **2003**, *125* (39), 11911-11924.

(3) Cui, L.; Ren, B.-H.; Lu, X.-B. Trinuclear salphen–chromium(III)chloride complexes as catalysts for the alternating copolymerization of epoxides and cyclic anhydrides. *J. Polym. Sci.* **2021**, *59* (16), 1821-1828.

(4) Diment, W. T.; Lindeboom, W.; Fiorentini, F.; Deacy, A. C.; Williams, C. K. Synergic Heterodinuclear Catalysts for the Ring-Opening Copolymerization (ROCOP) of Epoxides, Carbon Dioxide, and Anhydrides. *Acc. Chem. Res.* **2022**, *55* (15), 1997-2010.

(5) Liu, Y.; Ren, W.-M.; Liu, J.; Lu, X.-B. Asymmetric Copolymerization of CO_2 with meso-Epoxides Mediated by Dinuclear Cobalt(III) Complexes: Unprecedented Enantioselectivity and Activity. *Angew. Chem. Int. Ed.* **2013**, *52* (44), 11594-11598.

(6) Lee, B. Y.; Kwon, H. Y.; Lee, S. Y.; Na, S. J.; Han, S.-i.; Yun, H.; Lee, H.; Park, Y.-W. Bimetallic Anilido-Aldimine Zinc Complexes for Epoxide/CO2 Copolymerization. *J. Am. Chem. Soc.* **2005**, *127* (9), 3031-3037.

(7) Diment, W. T.; Gregory, G. L.; Kerr, R. W. F.; Phanopoulos, A.; Buchard, A.; Williams, C. K. Catalytic Synergy Using Al(III) and Group 1 Metals to Accelerate Epoxide and Anhydride Ring-Opening Copolymerizations. *ACS Catal.* **2021**, *11* (20), 12532-12542.

(8) Asaba, H.; Iwasaki, T.; Hatazawa, M.; Deng, J.; Nagae, H.; Mashima, K.; Nozaki, K. Alternating Copolymerization of CO_2 and Cyclohexene Oxide Catalyzed by Cobalt–Lanthanide Mixed Multinuclear Complexes. *Inorg. Chem.* **2020**, *59* (12), 7928-7933.

(9) Deacy, A. C.; Kilpatrick, A. F. R.; Regoutz, A.; Williams, C. K. Understanding metal synergy in heterodinuclear catalysts for the copolymerization of CO_2 and epoxides. *Nat. Chem.* **2020**, *12* (4), 372-380.

(10) Li, J.; Liu, Y.; Ren, W.-M.; Lu, X.-B. Asymmetric Alternating Copolymerization of Meso-epoxides and Cyclic Anhydrides: Efficient Access to Enantiopure Polyesters. *J. Am. Chem. Soc.* **2016**, *138* (36), 11493-11496.

(11) Thevenon, A.; Garden, J. A.; White, A. J. P.; Williams, C. K. Dinuclear Zinc Salen Catalysts for the Ring Opening Copolymerization of Epoxides and Carbon Dioxide or Anhydrides. *Inorg. Chem.* **2015**, *54* (24), 11906-11915.

(12) Diment, W. T.; Rosetto, G.; Ezaz-Nikpay, N.; Kerr, R. W. F.; Williams, C. K. A highly active, thermally robust iron(iii)/potassium(i) heterodinuclear catalyst for bio-derived epoxide/anhydride ring-opening copolymerizations. *Green Chem.* **2023**, *25* (6), 2262-2267.

(13) Bok, T.; Yun, H.; Lee, B. Y. Bimetallic Fluorine-Substituted Anilido−Aldimine Zinc Complexes for CO2/(Cyclohexene Oxide) Copolymerization. *Inorg. Chem.* **2006**, *45* (10), 4228-4237.

(14) Plajer, A. J.; Williams, C. K. Heterotrinuclear Ring Opening Copolymerization Catalysis: Structure–activity Relationships. *ACS Catal.* **2021**, *11* (24), 14819-14828.

(15) Lehenmeier, M. W.; Kissling, S.; Altenbuchner, P. T.; Bruckmeier, C.; Deglmann, P.; Brym, A.-K.; Rieger, B. Flexibly Tethered Dinuclear Zinc Complexes: A Solution to the Entropy Problem in CO2/Epoxide Copolymerization Catalysis? *Angew. Chem. Int. Ed.* **2013**, *52* (37), 9821-9826.

(16) Buchard, A.; Jutz, F.; Kember, M. R.; White, A. J. P.; Rzepa, H. S.; Williams, C. K. Experimental and Computational Investigation of the Mechanism of Carbon Dioxide/Cyclohexene Oxide Copolymerization Using a Dizinc Catalyst. *Macromolecules* **2012**, *45* (17), 6781-6795.

(17) Liu, Y.; Ren, W.-M.; Liu, C.; Fu, S.; Wang, M.; He, K.-K.; Li, R.-R.; Zhang, R.; Lu, X.-B. Mechanistic Understanding of Dinuclear Cobalt(III) Complex Mediated Highly Enantioselective Copolymerization of meso-Epoxides with CO2. *Macromolecules* **2014**, *47* (22), 7775-7788.

(18) Thomas, R. M.; Widger, P. C. B.; Ahmed, S. M.; Jeske, R. C.; Hirahata, W.; Lobkovsky, E. B.; Coates, G. W. Enantioselective Epoxide Polymerization Using a Bimetallic Cobalt Catalyst. *J. Am. Chem. Soc.* **2010**, *132* (46), 16520-16525.

(19) Pike, Jay D.; Rosa, Dell T.; Coucouvanis, D. Lipophilic Metal−Salicylideneimine−Crown Ether Hybrids — Ditopic Carriers in the Facilitated Transport of Amphiphilic Molecules Across Bulk Liquid Membranes. *Eur. J. Inorg. Chem.* **2001**, *2001* (3), 761-777.

(20) Cho, C.-H.; Chien, T.-Y.; Chen, J.-H.; Wang, S.-S.; Tung, J.-Y. Intermediate (S = 1) spin state in five-coordinate cobalt(iii): Magnetic properties of N-o-hydroxy-benzamido-meso-tetraphenylporphyrin cobalt(iii), Co(N-NCO(o-O)C6H4-tpp). *Dalton Trans.* **2010**, *39* (10), 2609-2614.

(21) Deacy, A. C.; Moreby, E.; Phanopoulos, A.; Williams, C. K. Co(III)/Alkali-Metal(I) Heterodinuclear Catalysts for the Ring-Opening Copolymerization of CO_2 and Propylene Oxide. *J. Am. Chem. Soc.* **2020**, *142* (45), 19150-19160.

(22) Coucouvanis, D. Crown-Ether-Functionalized Nickel Salicylaldimine Complexes. Structural Characterization of Their Potassium, Cesium, and Hexylammonium Derivatives and Their Use in the Transport of Amino Acids. *Inorg. Chem.* **1998**, *37* (10), 2328-2329.

(23) Peretti, K. L.; Ajiro, H.; Cohen, C. T.; Lobkovsky, E. B.; Coates, G. W. A Highly Active, Isospecific Cobalt Catalyst for Propylene Oxide Polymerization. *J. Am. Chem. Soc.* **2005**, *127* (33), 11566-11567.

(24) Lindeboom, W.; Deacy, A. C.; Phanopoulos, A.; Buchard, A.; Williams, C. K. Correlating Metal Redox Potentials to Co(III)K(I) Catalyst Performances in Carbon Dioxide and Propene Oxide Ring Opening Copolymerization. *Angew. Chem. Int. Ed.* **2023**, *62* (37), e202308378.

(25) Fieser, M. E.; Sanford, M. J.; Mitchell, L. A.; Dunbar, C. R.; Mandal, M.; Van Zee, N. J.; Urness, D. M.; Cramer, C. J.; Coates, G. W.; Tolman, W. B. Mechanistic Insights into the Alternating Copolymerization of Epoxides and Cyclic Anhydrides Using a (Salph)AlCl and Iminium Salt Catalytic System. *J. Am. Chem. Soc.* **2017**, *139* (42), 15222-15231.

(26) Duan, R.; Zhou, Y.; Huang, Y.; Sun, Z.; Zhang, H.; Pang, X.; Chen, X. A trinuclear salen–Al complex for copolymerization of epoxides and anhydride: mechanistic insight into a cocatalyst-free system. *Chem. Commun.* **2021**, *57* (1), 133-136.

(27) Jiang, L.; Wu, Y.; Tian, X.; Xue, W.; Li, H.; Kang, X.; Li, B. Mechanistic Insights into the Effects of Ureas and Monomers on the Ring-Opening Alternating Copolymerization of Epoxides and Anhydrides Catalyzed by Organic Base/Urea. In *Polymers*, 2024; Vol. 16.

(28) He, G.-H.; Ren, B.-H.; Wang, S.; Liu, Y.; Lu, X.-B. Sequence Control in Asymmetric Terpolymerizations of meso-Epoxides, CO2, and Phthalic Anhydride: Unprecedented Statistical Ester–Carbonate Distributions. *Angew. Chem. Int. Ed.* **2023**, *62* (27), e202304943.

(29) Shaw, M. S.; Bates, M. R.; Jones, M. D.; Ward, B. D. Metallocene catalysts for the ring-opening co-polymerisation of epoxides and cyclic anhydrides. *Polym. Chem.* **2022**, *13* (22), 3315-3324.

(30) Jeong, Y.; Cho, M. K.; Seo, S.; Cho, H.; Son, K.-s.; Kim, H. Electronic Tuning of Iminotriphenolate Ligands for Titanium(IV)-catalyzed Ring-opening Copolymerization of Cyclic Anhydrides and Epoxides. *ChemCatChem* **2023**, *15* (3), e202201086.

(31) Romain, C.; Zhu, Y.; Dingwall, P.; Paul, S.; Rzepa, H. S.; Buchard, A.; Williams, C. K. Chemoselective Polymerizations from Mixtures of Epoxide, Lactone, Anhydride, and Carbon Dioxide. *J. Am. Chem. Soc.* **2016**, *138* (12), 4120-4131.

(32) Alamillo-Ferrer, C.; Hutchinson, G.; Burés, J. Mechanistic interpretation of orders in catalyst greater than one. *Nature Reviews Chemistry* **2023**, *7* (1), 26-34.

(33) Abel, B. A.; Lidston, C. A. L.; Coates, G. W. Mechanism-Inspired Design of Bifunctional Catalysts for the Alternating Ring-Opening Copolymerization of Epoxides and Cyclic Anhydrides. *J. Am. Chem. Soc.* **2019**, *141* (32), 12760-12769.

(34) Hu, L.-F.; Zhang, C.-J.; Wu, H.-L.; Yang, J.-L.; Liu, B.; Duan, H.-Y.; Zhang, X.-H. Highly Active Organic Lewis Pairs for the Copolymerization of Epoxides with Cyclic Anhydrides: Metal-Free Access to Well-Defined Aliphatic Polyesters. *Macromolecules* **2018**, *51* (8), 3126-3134.

(35) Jeon, J. Y.; Eo, S. C.; Varghese, J. K.; Lee, B. Y. Copolymerization and terpolymerization of carbon dioxide/propylene oxide/phthalic anhydride using a (salen)Co(III) complex tethering four quaternary ammonium salts. *Beilstein J. Org. Chem.* **2014**, *10*, 1787-1795.

Chapter Five

Outlook and Future Work

5.1 Outlook and Challenges

5.1.1 Renewable Feedstocks

While many examples of ROCOP and ROP catalysts have been reported that can (co-)polymerise bio-derived monomers, the majority of studied polymerisations feature monomers which are derived from petrochemicals.

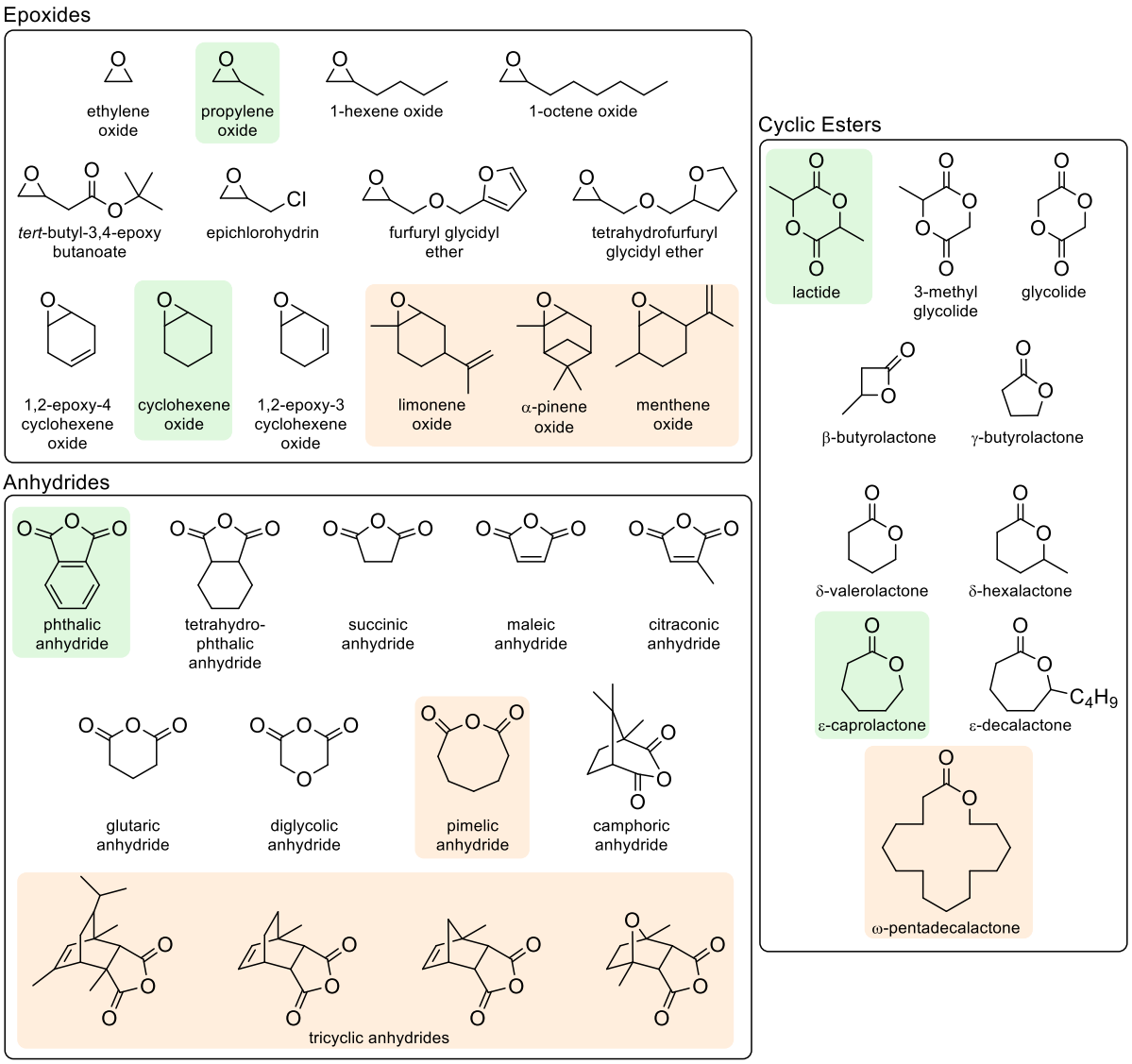


Figure 5.1. Bio-derived epoxides, anhydrides, and cyclic esters which have been reported for ring-opening co-polymerisations and ring-opening polymerisations.[1-8]

Figure 5.1 shows examples of epoxides, anhydrides, and cyclic esters which can be bio-derived, and have been reported for ROCOP or ROP. Some of these monomers have been widely studied, and

literature catalysts are able to rapidly and selectively polymerise them (e.g. propene oxide, cyclohexene oxide, phthalic anhydride, lactide, and ε-decalactone; green in Figure 5.1).[9-13] However, there remain a large number of monomers which can be bio-derived, or combinations thereof, which remain very challenging to polymerise, often due to steric congestion which hinders nucleophilic attack in the rate-determining step (e.g. limonene oxide, α-pinene oxide, menthene oxide, and tricyclic anhydrides), or low ring-strain due to large ring size (e.g. pimelic anhydride, ω-pentadecalactone; orange in Figure 5.1).[1-8] Further catalyst development is needed to improve the available scope of bio-derived monomers for ROCOP and ROP, allowing the synthesis of a wider range of polymers with diverse mechanical properties.

5.1.2 Measuring and Using Metal Synergy

5.1.2.1 Measuring Lewis Acidity

The results presented in Chapters Two and Three demonstrate the importance of optimising s-block metal Lewis acidity to the polymerisation targeted during catalyst design. A limitation of the current trends of activity and selectivity with changing s-block metal Lewis acidity is that pK_a of the aqua complex of the s-block metal is intrinsic to the s-block metal, and does not take into account electron donation effects of the ligand. Measuring the Lewis acidity of the bound s-block metal would be highly desirable, as it would allow the comparison of the strength of electron-donation from the ligands. This will be important to quantify, as ligands with strongly electron-donating s-block metal binding pockets should be targeted in the future, with the aim to make catalysts with more "K(I)-like" Na(I) centres (i.e. more weakly Lewis acidic).

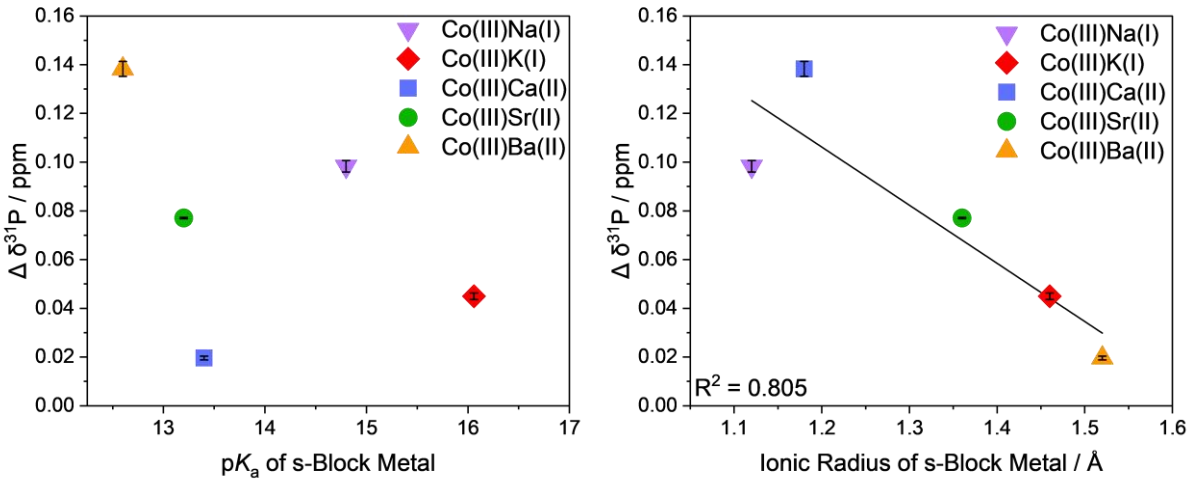


Figure 5.2. Representative results from Gutmann-Beckett studies using TPPO in MeCN-d_4.

Preliminary studies were conducted using a Gutmann-Beckett method on the catalysts described in Chapter Two in MeCN-d_3 and $CDCl_3$, with triphenylphosphine oxide (TPPO), triethylphosphine oxide (TEPO), and trimethylphosphine oxide (TMPO).[14] There were two problems with this method: 1) the changes in chemical shift of the phosphine oxide probe in the presence of the catalysts compared to the probe alone were very small ($\Delta\delta^{31}P < 0.2$ ppm), indicating issues with probe molecule coordination (Figure 5.2, LHS). Such small changes in chemical shift are within the error of ^{31}P NMR spectroscopy, and as such are not reliable for Gutmann-Beckett experiments; 2) no correlations could be seen between $\Delta\delta^{31}P$ and s-block metal Lewis acidity. Instead, correlations could be seen between $\Delta\delta^{31}P$ and the ionic radius of the s-block metal (Figure 5.2, RHS). This might suggest that the limiting factor for coordination of the phosphine oxide probe to the s-block metal is steric in nature, even with varying steric bulk of the phosphine oxide. The latter issue could be overcome by synthesising the catalysts with non-coordination co-ligands, e.g. triflate, but the former problem might be more difficult to overcome. To address the issues with probe molecule coordination, other probe molecules which are relevant to the catalysis could be investigated (e.g. epoxides, carbonates) using UV-vis spectroscopy titration studies, for example.

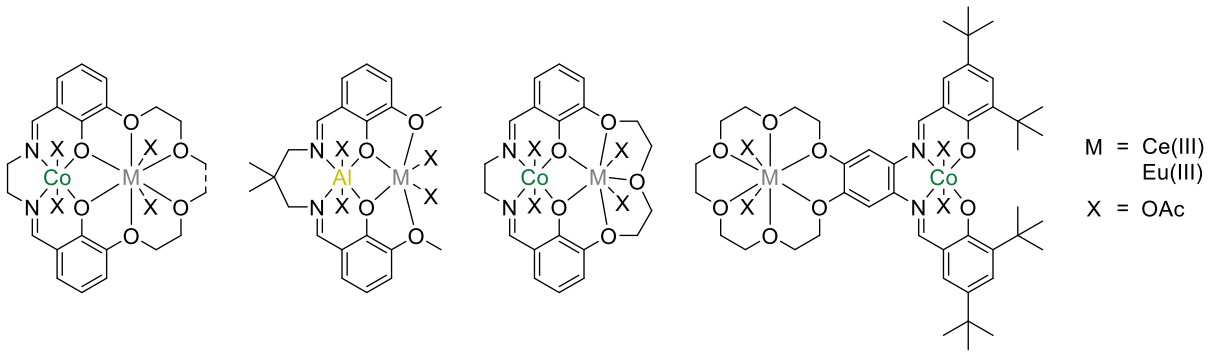


Figure 5.3. Proposed structures of complexes featuring Co(III) or Al(III) in combination with Ce(III) or Eu(III) in different ligand scaffolds, with the aim of exploring electron donation from the ligand ether moieties into the f-block elements.

Cyclic voltammetry has been used in the literature for the estimation of metal electron density; the more electron-dense the metal, the easier it is to oxidise/the harder it is to reduce, and so determination of metal redox potentials can allow determination of metal electron density.[15] Our group has used cyclic voltammetry to explore Co(III) electron density with changing ligand structures, but clearly the electron density of the s-block metals cannot be explored in the same way, as they are redox-inactive.[16] Another method of determining and comparing s-block metal Lewis acidity within different ligands could be to incorporate redox-active lanthanides (e.g. Eu(III), Ce(III)) with similar ionic radii to the s-block metals used in the catalysts (ionic radii: Eu(III) = 1.12, Ce(III) = 1.20, Na(I) = 1.12, K(I) = 1.46) and exploring how their redox potentials vary with changing ligand structures (Figure 5.3).[17]

5.1.2.2 Exploiting Intermetallic Separation

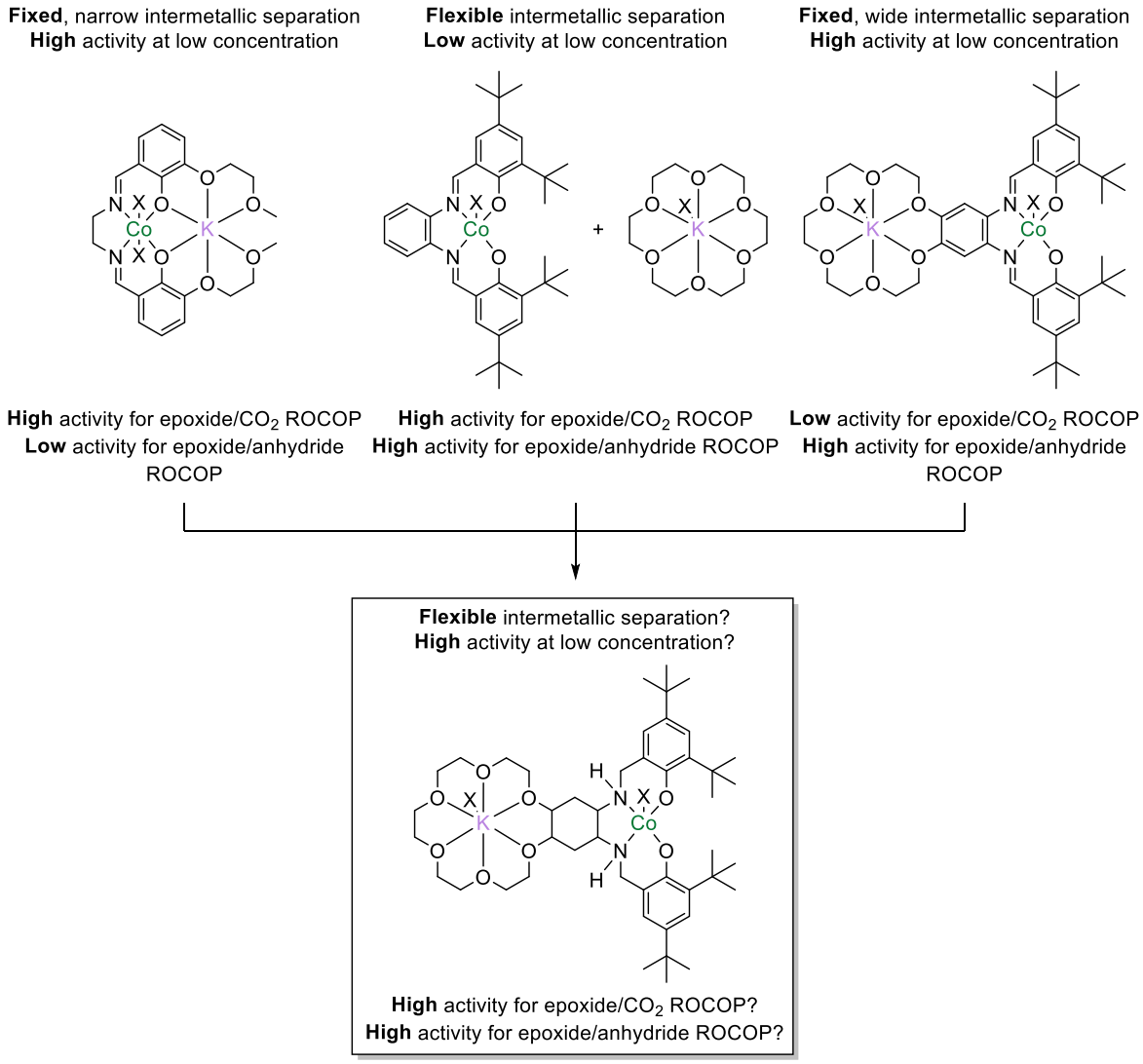


Figure 5.4. Proposed novel Co(III)K(I) catalyst structure which may have a flexible intermetallic separation.

The results discussed in Chapter Three show the utility of Co(III)K(I) heterodinuclear catalysts with wide and narrow intermetallic separations for epoxide/anhydride, and epoxide/CO_2 ROCOP respectively. It follows that designing catalysts with high activities for both epoxide/CO_2 and epoxide/anhydride ROCOP may be challenging, as they seem to have different optimum intermetallic separations.

The bicomponent system, made up of a Co(III) salen complex with KOAc bound in 18-crown-6, was able to achieve high activities for both polymerisations. This was proposed to be due to its ability to

form species in solution with variable intermetallic separations. However, these high activities could only be achieved with relatively high catalyst concentrations, since the two components were not tethered together. Perhaps by joining the two catalyst components with a flexible tether, a single component catalyst could be developed with variable intermetallic separations. This catalyst may be able to show high activities for both polymerisations, while maintaining its activity at low catalyst concentrations.

5.2 References

(1) Shao, X.; Su, L.; Zhang, J.; Tian, Z.; Zhang, N.; Wang, Y.; Wang, H.; Cui, X.; Hou, X.; Deng, T. Green Production of Phthalic Anhydride from Biobased Furan and Maleic Anhydride by an Acid Resin Catalyst. *ACS Sustain. Chem. Eng.* **2021**, *9* (43), 14385-14394.

(2) Yu, Z.; Xu, L.; Wei, Y.; Wang, Y.; He, Y.; Xia, Q.; Zhang, X.; Liu, Z. A new route for the synthesis of propylene oxide from bio-glycerol derivated propylene glycol. *Chem. Commun.* **2009**, (26), 3934-3936.

(3) Hardouin Duparc, V.; Shakaroun, R. M.; Slawinski, M.; Carpentier, J.-F.; Guillaume, S. M. Ring-opening (co)polymerization of six-membered substituted δ-valerolactones with alkali metal alkoxides. *Eur. Polym. J.* **2020**, *134*, 109858.

(4) Diment, W. T.; Rosetto, G.; Ezaz-Nikpay, N.; Kerr, R. W. F.; Williams, C. K. A highly active, thermally robust iron(iii)/potassium(i) heterodinuclear catalyst for bio-derived epoxide/anhydride ring-opening copolymerizations. *Green Chem.* **2023**, *25* (6), 2262-2267.

(5) Hornberger, L.-S.; Weingarten, P.; Lange, P. L.; Schleid, T.; Adams, F. Connecting 16- with 4-Membered Rings: Ring-Opening Polymerization of Bio-Based ω-Pentadecalactone with Amino-Alkoxy-Bis(phenolate) Yttrium Initiators and Copolymerization with β-Butyrolactone. *Eur. Polym. J.* **2023**, *199*, 112449.

(6) Young, M. S.; LaPointe, A. M.; MacMillan, S. N.; Coates, G. W. Highly Enantioselective Polymerization of β-Butyrolactone by a Bimetallic Magnesium Catalyst: An Interdependent Relationship Between Favored and Unfavored Enantiomers. *J. Am. Chem. Soc.* **2024**, *146* (26), 18032-18040.

(7) Poland, S. J.; Darensbourg, D. J. A quest for polycarbonates provided via sustainable epoxide/CO2 copolymerization processes. *Green Chem.* **2017**, *19* (21), 4990-5011.

(8) Thaore, V.; Chadwick, D.; Shah, N. Sustainable production of chemical intermediates for nylon manufacture: A techno-economic analysis for renewable production of caprolactone. *Chem. Eng. Res. Des.* **2018**, *135*, 140-152.

(9) Deacy, A. C.; Moreby, E.; Phanopoulos, A.; Williams, C. K. Co(III)/Alkali-Metal(I) Heterodinuclear Catalysts for the Ring-Opening Copolymerization of CO_2 and Propylene Oxide. *J. Am. Chem. Soc.* **2020**, *142* (45), 19150-19160.

(10) Deacy, A. C.; Kilpatrick, A. F. R.; Regoutz, A.; Williams, C. K. Understanding metal synergy in heterodinuclear catalysts for the copolymerization of CO_2 and epoxides. *Nat. Chem.* **2020**, *12* (4), 372-380.

(11) Diment, W. T.; Gregory, G. L.; Kerr, R. W. F.; Phanopoulos, A.; Buchard, A.; Williams, C. K. Catalytic Synergy Using Al(III) and Group 1 Metals to Accelerate Epoxide and Anhydride Ring-Opening Copolymerizations. *ACS Catal.* **2021**, *11* (20), 12532-12542.

(12) Sulley, G. S.; Gregory, G. L.; Chen, T. T. D.; Peña Carrodeguas, L.; Trott, G.; Santmarti, A.; Lee, K.-Y.; Terrill, N. J.; Williams, C. K. Switchable Catalysis Improves the Properties of CO_2-Derived Polymers: Poly(cyclohexene carbonate-b-ε-decalactone-b-cyclohexene carbonate) Adhesives, Elastomers, and Toughened Plastics. *J. Am. Chem. Soc.* **2020**, *142* (9), 4367-4378.

(13) Yolsal, U.; Shaw, P. J.; Lowy, P. A.; Chambenahalli, R.; Garden, J. A. Exploiting Multimetallic Cooperativity in the Ring-Opening Polymerization of Cyclic Esters and Ethers. *ACS Catal.* **2024**, *14* (2), 1050-1074.

(14) Kumar, A.; Blakemore, J. D. On the Use of Aqueous Metal-Aqua pK_a Values as a Descriptor of Lewis Acidity. *Inorg. Chem.* **2021**, *60* (2), 1107-1115.

(15) Lionetti, D.; Suseno, S.; Shiau, A. A.; de Ruiter, G.; Agapie, T. Redox Processes Involving Oxygen: The Surprising Influence of Redox-Inactive Lewis Acids. *JACS Au* **2024**, *4* (2), 344-368.

(16) Lindeboom, W.; Deacy, A. C.; Phanopoulos, A.; Buchard, A.; Williams, C. K. Correlating Metal Redox Potentials to Co(III)K(I) Catalyst Performances in Carbon Dioxide and Propene Oxide Ring Opening Copolymerization. *Angew. Chem. Int. Ed.* **2023**, *62* (37), e202308378.

(17) Shannon, R. D. Revised effective ionic radii and systematic studies of interatomic distances in halides and chalcogenides. *Acta Crystallographica Section A* **1976**, *32* (5), 751-767.

Chapter Six

Experimental

6.1 General Procedures

All manipulations were performed using either a dual manifold nitrogen-vacuum Schlenk line or a nitrogen-filled glovebox. Solvents were collected from a solvent purification system, degassed using three freeze-pump-thaw cycles and stored over 3 Å molecular sieves in a nitrogen-filled glovebox. All reagents were obtained from commercial sources and used as received. Epoxide monomers were bought from Sigma Aldrich and dried overnight over calcium hydride and purified by fractional distillation, followed by degassing with nitrogen and stored under nitrogen. Phthalic anhydride was bought from Sigma Aldrich and purified by stirring in dry toluene overnight. The supernatant was removed by filtration and the toluene removed *in vacuo*. The resultant white solid was recrystallised from hot chloroform and sublimed under vacuum at 80 °C. *rac*-Lactide monomer was purchased from Purac and recrystallised three times, from toluene, under a N_2 atmosphere, followed by sublimation three times, under vacuum. Research-grade CO_2 (BOC, 99.99 %) was dried through a Drierlite column and two additional drying columns (Micro Torr, model number: MC1-804FV) in series before use.

6.1.1 NMR Spectroscopy

^{1}H NMR spectroscopic analysis was performed using a Bruker AV 400 MHz spectrometer, at 298 K. $^{13}C\{^{1}H\}$ NMR spectroscopy, and variable temperature ^{1}H NMR spectroscopy, were performed using a Bruker AV III 500 MHz spectrometer, at 298 K ($^{13}C\{^{1}H\}$) or at the stated temperature (variable temperature ^{1}H).

6.1.2 Elemental Analysis

Elemental analysis was carried out by the Elemental Analysis Service at London Metropolitan University, 29 Hornsey Road, London, N7 7DD.

6.1.3 Mass Spectrometry

MALDI-ToF mass spectrometry was performed on a Waters MALDI Micro MX spectrometer in positive ion reflectron mode. Samples were prepared by using 10 mg/mL solutions of the complex, matrix (*trans*-2-[3-(4-*tert*-butylphenyl)-2-methyl-2-propenylidene]-malonitrile), and KI in THF. The solutions were spotted onto MALDI plates sequentially and allowed to dry.

6.1.4 UV-Visible Spectroscopy

UV-visible spectra were collected using a Cary 60 UV-Vis spectrophotometer (Agilent Technologies).

6.1.5 SQUID Magnetometry

Magnetic measurements on solid samples were carried out using a Quantum Design MPMS-5 magnetometer, at a field of 0.1 T, at temperatures from 2-300 K. Weighed samples (ca. 20 mg) were placed into gelatine capsules and then loaded into a diamagnetic plastic straw before being put in the cryostat. Values of the magnetic susceptibility were corrected for the underlying diamagnetic increment by using tabulated Pascal constants.

6.1.6 X-Ray Diffractometry

Crystalline samples were isolated in a glovebox, under a pool of fluorinated oil, and mounted on MiTeGen MicroMounts. The crystals were then cooled to 150 K, with an Oxford Cryosystems nitrogen cooling device. Data collection was carried out with an Oxford Diffraction Supernova diffractometer using Cu Kα (λ = 1.5417 Å) radiation. The resulting raw data was processed using CrysAlisPro. Structures were solved by SHELXT and full-matrix least squares refinements based on F2 were performed in SHELXL-14, as incorporated in the WinGX package. All crystal structures were collected and solved by myself, with the exception of Co(III)Ca(II) in Chapter Two, which was collected and solved by Dr. Ryan W.F. Kerr.

6.1.7 Cyclic Voltammetry

Cyclic voltammetry measurements were performed using a PalmSens EmStat Blue potentiostat under computer control with a Au disc (2.0 mm^2) working electrode, a graphite wire counter electrode, and a Ag wire pseudo-reference electrode. Measurements were typically performed using a solution of the complex (1.6 mM) and $^nBu_4N\,PF_6$ (0.1 M) as the supporting electrolyte in MeCN (10 mL). Measurements were referenced against the ferroceneium/ferrocene redox couple, measured by adding ferrocene (~ 1 mg) to the solution after the measurements were taken.

6.1.8 Gel Permeation Chromatography

Gel permeation chromatography (GPC) analysis was performed using a Shimadzu LC-20AD instrument, at 30 °C, with two mixed bed PSS SDV linear S columns, in series, and with THF as eluent, at a flow rate of 1 mL/min. Molar mass values were calibrated using narrow molar mass polystyrene standards.

6.1.9 Epoxide/CO_2 Ring-Opening Copolymerisations

A solution of catalyst, 1,2-cyclohexane diol, together with mesitylene (10 eq. as an internal standard for PO polymerisations), in epoxide (5 mL) was prepared in a N_2 glovebox. The solution was injected into a 100 mL Parr reactor, fitted with a DiComp sentinel probe attached to an ATR-IR spectrometer, under a stream of CO_2. The reactor was pressurized to the desired pressure of CO_2 and heated to the desired temperature. Conversion to polycarbonate (PPC) and cyclic carbonate (PC) were followed using *in situ* ATR-IR spectroscopy by observing the development of peaks at 1750 cm^{-1} and 1810 cm^{-1} for polycarbonate and cyclic carbonate, respectively. The copolymerization was stirred for the reaction duration, allowed to cool upon completion, and quenched by addition of benzoic acid (~ 2 mg, 0.018 mmol). Conversions to polycarbonate, cyclic carbonate and ether linkages were determined by ^1H NMR spectroscopy of the crude sample, using mesitylene as an internal standard, and molar masses and

dispersities of the crude polycarbonate were determined by GPC, in THF. The polymer product was purified by dissolving in chloroform and precipitating with methanol. Polymerizations were run in triplicate to allow determination of errors.

6.1.10 Epoxide/Anhydride Ring-Opening Copolymerisations

A solution of catalyst, anhydride, and, if used, 1,4-benzene dimethanol (BDM) in epoxide was prepared in a dried vial, inside a N_2 glovebox. The vial was sealed, with a melamine cap containing a Teflon inlay, and further sealed with electrical insulation tape. The sealed vial was then heated to 50 °C for the time stated. Aliquoting was performed by cooling the polymerization vial in an ice/water bath, before removing ~ 10 μL of the mixture with a syringe in a N_2 glovebox. Aliquots were analysed by ^{1}H NMR spectroscopy ($CDCl_3$) to determine conversion, and by GPC in THF to determine the molar mass and dispersity of the resultant polyester. The polymerizations were quenched by addition of benzoic acid (~ 2 mg, 0.018 mmol), and the polyesters purified by precipitation from chloroform with methanol and dried under vacuum. Polymerizations were run in triplicate to allow determination of errors.

6.1.11 *rac*-Lactide Ring-Opening Polymerisations

A solution of catalyst (0.014 mmol) and *rac*-LA (0.143 mmol) in PO (1 mL) was prepared in a dried vial inside a N_2 glovebox. The vial was sealed, with a melamine cap containing a Teflon inlay, and further sealed with electrical insulation tape. The sealed vial was then heated to 50 °C for the time stated. Aliquoting was performed by cooling the polymerization vial in an ice/water bath, before removing ~ 10 μL of the mixture with a syringe, in a N_2 glovebox. Aliquots were analysed by ^{1}H NMR spectroscopy ($CDCl_3$) to determine conversion, and by GPC in THF to determine the molar mass and dispersity of the resultant polyester. The polymerizations were quenched by addition of benzoic acid (2 mg, 0.018 mmol) and the PLA purified by precipitation from chloroform with methanol and dried under vacuum. Polymerizations were run in triplicate to allow determination of errors.

6.2 Chapter Two

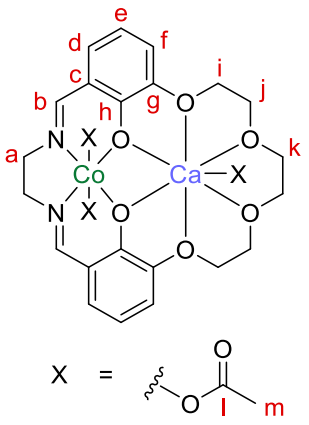
6.2.1 Co(III)M(I) (M(I) = Na, K, Rb, Cs) Catalysts

General procedure: The Co(III)M(I) (M(I) = Na, K, Rb, Cs) catalysts were synthesised following a modified literature procedure.[1] Spectroscopic characterisation and elemental analysis were in agreement with those previously reported in the literature.

6.2.2 Co(III)M(II) (M(II) = Ca, Sr, Ba) Catalysts

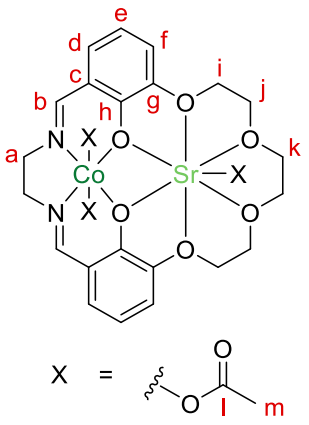
General procedure: The Co(III)M(II) catalysts were synthesised following a modified literature procedure.[1] The dialdehyde pro-ligand (400 mg, 1.02 mmol), $Co(OAc)_2$ (181 mg, 1.02 mmol) and the respective metal acetate salt (1.02 mmol) were combined in dry acetonitrile (15 mL) to form a yellow-orange suspension and stirred at room temperature for 30 mins under a nitrogen atmosphere. To the suspension was added ethylene diamine (68 μL, 1.02 mmol), immediately giving a deep red-brown solution. The solution was stirred overnight at room temperature under a nitrogen atmosphere before adding acetic acid (117 μL, 2.04 mmol) and stirring for three days, with the reaction open to air. The solution was evaporated *in vacuo* to give the crude product. Azeotropic distillations were performed on the solid with toluene (3 x 50 mL) to remove residual acetic acid, and hexane (3 x 50 mL) to remove residual toluene. The solid was purified by precipitation from a chloroform solution using diethyl ether, and then dried *in vacuo* for 16 h. Single crystals suitable for X-ray diffraction experiments were grown by slow evaporation of hexane into a solution of the complex in chloroform at room temperature.

6.2.2.1 Co(III)Ca(II)



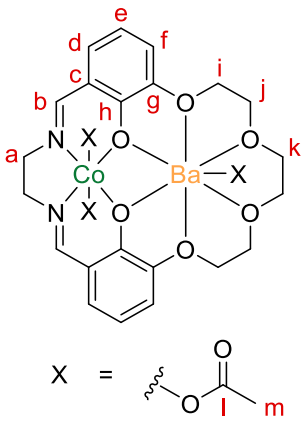
Synthesised with $Ca(OAc)_2.H_2O$. Brown solid, obtained in 390 mg yield (0.57 mmol, 56%). ^{1}H NMR (400 MHz, 298 K, $CDCl_3$, 298 K) δ (ppm): 7.84 (s, 2H, N=C**H** (**b**)), 6.95 (t, 4H, $^3J_{H\text{-}H}$ = 8.5 Hz), *meta*-Ar**H** (**d**, **f**)), 6.60 (t, 2H, $^3J_{H\text{-}H}$ = 7.78 Hz, *para*-Ar**H** (**e**)), 3.54 – 4.87 (m, 12 H, C$\mathbf{H_2}$, (**i – k**)), 4.05 (s, 4 H, NC$\mathbf{H_2}$, (**a**)), 1.38 (s, 6 H, O=C-C$\mathbf{H_3}$ (**m**)); ^{13}C {^{1}H} NMR (151 MHz, 298 K, $CDCl_3$) δ (ppm): 180.0 (s, O=**C** (**l**)), 165.2 (s, N=**C**H (**b**)), 154.6 (s, *ipso*-**C** (**h**)), 151.7 (s, *ortho*-**C** (**g**)), 127.0 (s, *meta*-**C**H (**d**)), 119.3 (s, *meta*-**C**-CH=N (**c**)), 117.7 (s, *para*-**C**H (**f**)), 114.9 (s, *meta*-**C**H (**f**)), 69.9 (O-**C**H_2 (**i** or **j** or **k**)), 69.7 (O-**C**H_2 (**i** or **j** or **k**)), 68.3 (O-**C**H_2 (**i** or **j** or **k**)), 59.0 (s, N-**C**H_2 (**a**)), 25.0 (s, O=C-**C**H_3 (**m**));)); ν_{max}/cm^{-1} 2926 (C-H stretch), 1647 (acetate asymmetric C-O stretch), 1580 (imine C=N stretch), 1455 (acetate symmetric C-O stretch), 1242 (aromatic C-O stretch), 1086 (aliphatic C-O stretch); Anal. Calc. for $C_{28}H_{33}CaCoN_2O_{12}$: C 48.84, H 4.83, N 4.07; Found: C 47.30, H 5.21, N 4.16 %.

6.2.2.2 Co(III)Sr(II)



Synthesised with $Sr(OAc)_2$. Brown solid, obtained in 0.47 g yield (0.64 mmol, 63%). ^{1}H NMR (400 MHz, $CDCl_3$, 298 K) δ (ppm): 7.75 (s, 2H, N=C**H** (**b**)), 6.86 (t, 4H, $^3J_{H\text{-}H}$ = 7.9 Hz, *meta*-C**H** (**d**, **f**)), 6.53 (m, 2H, $^3J_{H\text{-}H}$ = 7.9 Hz, *para*-C**H** (**e**)), 3.52 – 4.83 (m, 12 H, C**H**$_2$ (**i – k**), 4.01 (s, 4 H, N-C**H**$_2$ (**a**)), 1.46 (s, 4H, O=C-C**H**$_3$ (**m**)); ^{13}C {^{1}H} NMR (151 MHz, 298 K, $CDCl_3$) δ (ppm): 179.6 (s, O=**C** (**l**)), 164.7 (s, N=**C**H (**b**)), 155.2 (s, *ipso*-**C** (**h**)), 152.1 (s, *ortho*-**C** (**g**)), 126.2 (s, *meta*-**C**H (**d**)), 118.9 (s, *meta*-**C**-CH=N (**c**)), 116.1 (s, *para*-**C**H (**f**)), 114.4 (s, *meta*-**C**H (**f**)), 70.6 (O-**C**H$_2$ (**i** or **j** or **k**)), 69.0 (O-**C**H$_2$ (**i** or **j** or **k**)), 68.4 (O-**C**H$_2$ (**i** or **j** or **k**)), 59.1 (s, N-**C**H$_2$ (**a**)), 25.2 (s, O=C-**C**H$_3$ (**m**)); ν_{max}/cm^{-1} 2929 (C-H stretch), 1648 (imine C=N stretch), 1585 (acetate asymmetric C-O stretch), 1455 (acetate symmetric C-O stretch), 1227 (aromatic C-O stretch), 1086 (aliphatic C-O stretch); Anal. Calc. for $C_{28}H_{33}CoN_2O_{12}Sr$: C 45.69, H 4.52, N 3.81; Found: C 45.38, H 5.04, N 3.94%.

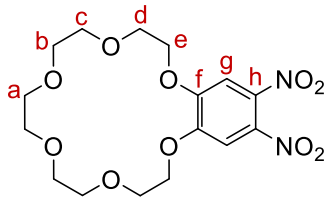
6.2.2.3 Co(III)Ba(II)



Synthesised with $Ba(OAc)_2$. Red-brown solid, obtained in 0.45 g yield (0.57 mmol, 56%). ^{1}H NMR (400 MHz, $CDCl_3$, 298 K) δ (ppm): 7.68 (s, 2H, N=C**H** (**b**)), 6.83 (d, 4H, $^3J_{H\text{-}H}$ = 7.6 Hz, *meta*-C**H** (**d**, **f**)), 6.50 (t, 2H, $^3J_{H\text{-}H}$ = 7.8 Hz, *para*-C**H** (**e**)),)), 3.75 – 4.61 (m, 12 H, C**H**$_2$ (**i – k**), 4.03 (s, 4 H, N-C**H**$_2$ (**a**)), 1.44 (s, 4H, O=C-C**H**$_3$ (**m**)); ^{13}C {^{1}H} NMR (151 MHz, 298 K, $CDCl_3$) δ (ppm): 179.0 (s, O=**C** (**l**)), 164.7 (s, N=**C**H (**b**)), 155.5 (s, *ipso*-**C** (**h**)), 152.2 (s, *ortho*-**C** (**g**)), 126.4 (s, *meta*-**C**H (**d**)), 118.9 (s, *meta*-**C**-CH=N (**c**)), 115.3 (s, *para*-**C**H (**f**)), 114.1 (s, *meta*-**C**H (**f**)), 70.6 (O-**C**H$_2$ (**i** or **j** or **k**)), 69.3 (O-**C**H$_2$ (**i** or **j** or **k**)), 67.9 (O-**C**H$_2$ (**i** or **j** or **k**)), 5921 (s, N-**C**H$_2$ (**a**)), 25.0 (s, O=C-**C**H$_3$ (**m**)); ν_{max}/cm^{-1} 3045 (C-H stretch), 2934 (C-H stretch), 1647 (imine C=N stretch), 1575 (acetate asymmetric C-O stretch), 1451 (acetate symmetric C-O stretch), 1225 (aromatic C-O stretch), 1084 (aliphatic C-O stretch); Anal. Calc. for $C_{28}H_{33}BaCoN_2O_{12}$: C 42.80, H 4.23, N 3.56; Found: C 42.18, H 4.15, N 3.34 %.

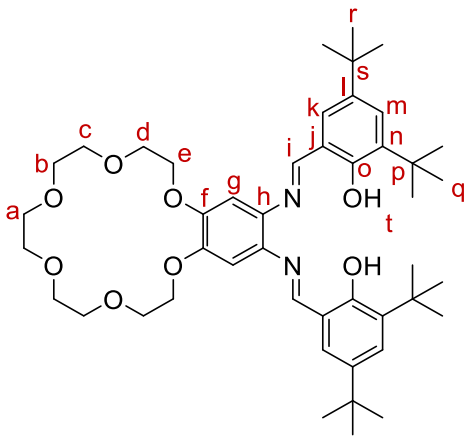
6.3 Chapter Three

6.3.1 Dinitrobenzo[18-crown-6]



To a solution of benzo-18-crown-6 (3.00 g, 9.62 mmol) in chloroform (80 mL) cooled to 0 °C was added a mixture of sulphuric acid (>95%, 10 mL) and nitric acid (70%, 20 mL) dropwise over an hour with rapid stirring. The solution gradually turned amber and nitrogen dioxide evolved. The solution was then stirred at room temperature for 48 h. Upon completion, the reaction was diluted with chloroform (60 mL) and washed with ice-cooled distilled water (3 x 40 mL). The combined aqueous phases were back-extracted with chloroform (40 mL). The organic phases were then combined and dried ($MgSO_4$), before concentrating to 10 mL *in vacuo*. Diethyl ether (approximately 200 mL) was added and the solution cooled at -12 °C for 2 h. The precipitated product was filtered from the solution and washed with cold diethyl ether, giving pure dinitrobenzo-18-crown-6 as a pale-yellow solid (3.24 g, 8.06 mmol, 84%). ^{1}H NMR (400 MHz, $CDCl_3$, 298 K) δ (ppm): 7.27 (s, 2H, Ar**H**, **g**), 4.19 – 4.24 (m, 4H, C**H**$_2$, **e**), 3.85 – 3.90 (m, 4H, C**H**$_2$, **d**), 3.65 – 3.70 (m, 4H, C**H**$_2$, **c**), 3.60 – 3.64 (m, 4H, C**H**$_2$, **b**), 3.58 (s, 4H, C**H**$_2$, **a**); ^{13}C {^{1}H} NMR (151 MHz, CD_3CN, 298 K) δ (ppm): 151.6 (**C**O, **f**), 136.7 (**C**NO_2, **h**), 108.4 (**C**H, **g**), 71.1 (**b**), 70.8 (**C**H_2, **a**), 70.5 (**C**H_2, **c**), 69.9 (**C**H_2, **e**), 68.9 (**C**H_2, **d**).

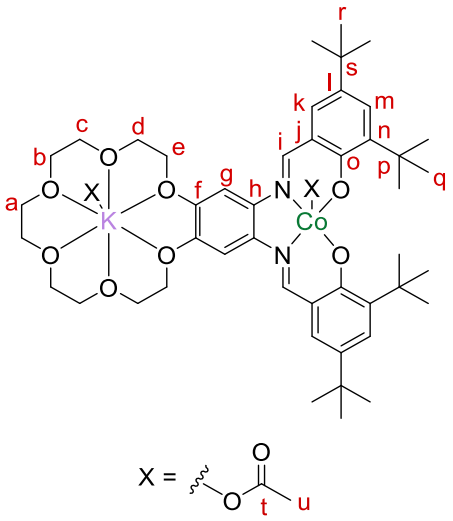
6.3.2 H_2L_{wide}



A solution of dinitrobenzo-18-crown-6 (7.00 g, 17.4 mmol) and Pd/C (10 w%, 0.46 g, 4.4 mmol) in degassed methanol (200 mL) was stirred in the dark under 1.5 bar H_2 at room temperature for 5 days. The resultant yellow solution of diaminobenzo-18-crown-6 was filtered, via cannula, into an ampoule containing 3,5-ditertbutyl-1-hydroxybenzaldehyde (8.20 g, 34.8 mmol). The resultant solution was stirred in the dark at 65 °C for 3 days. The solution immediately darkened upon heating, and eventually a yellow precipitate formed. The reaction was cooled and filtered in air, and the precipitate washed with cold methanol. The pure product H_2L_{wide} was obtained as a bright yellow solid (11.73 g, 15.1 mmol, 87%). ^{1}H NMR (400 MHz, $CDCl_3$, 298 K) δ (ppm): 13.51 (s, 2H, O**H**, **t**), 8.55 (s, 2H, N=C**H**, **i**), 7.35 (d, 2H, $^4J_{H\text{-}H}$ = 2.43 Hz, Ar**H**, **m**), 7.12 (d, 2H, $^4J_{H\text{-}H}$ = 2.34 Hz, Ar**H**, **k**), 6.76 (s, 2H, Ar**H**, **g**), 4.19 (t, 4H, $^3J_{H\text{-}H}$ = 4.54 Hz, C$\mathbf{H_2}$, **e**), 3.90 (t, 4H, $^3J_{H\text{-}H}$ = 4.50 Hz, C$\mathbf{H_2}$, **d**), 3.70 – 3.76 (m, 4H, C$\mathbf{H_2}$, **c**), 3.65-3.69 (m, 4H, C$\mathbf{H_2}$, **b**), 3.64 (s, 4H, C$\mathbf{H_2}$, **a**), 1.36 (s, 18H, C(C$\mathbf{H_3}$)$_3$, **q**), 1.25 (s, 18H, C(C$\mathbf{H_3}$)$_3$, **r**); ^{13}C {^{1}H} NMR (151 MHz, CD_3CN, 298 K) δ (ppm): 163.5 (s, N=**C**H, **i**), 158.6 (s, *ipso*-**C**, **o**), 148.6 (s, H_2CO-**C**, **f**), 140.5 (s, *para*-**C**-C(CH$_3$)$_3$, **l**), 137.3 (s, *ortho*-**C**-C(CH$_3$)$_3$, **n**), 136.1 (s, HC=N-**C**, **h**), 128.1 (s, *meta*-**C**H, **m**), 126.8 (s, *meta*-**C**H, **k**), 118.6 (s, *ortho*-**C**, **j**), 106.0 (s, **C**H, **g**), 71.1 (s, **C**H$_2$, **b** or **c**), 71.0 (s, **C**H$_2$, **a** and **b** or **c**), 69.8 (s, **C**H$_2$, **d** or **e**), 69.7 (s, **C**H$_2$, **d** or **e**), 35.3 (s, **C**(CH$_3$)$_3$, **p**), 34.4 (s, C(**C**H$_3$)$_3$, **r**), 31.7 (s, **C**(CH$_3$)$_3$, **s**), 29.6 (s, C(**C**H$_3$)$_3$, **q**); λ_{max} (DCM)/nm 280, 308sh, 357, 391sh (ε / dm^3 mol^{-1} cm^{-1} 13500, 8200, 12200, 8900); ν_{max}/cm^{-1} 3590 (phenol O-

H stretch), 2912 (C-H stretch), 1613 (imine C=N stretch), 1198 (aryl alkyl ether C-O stretch), 1121 (aliphatic ether C-O stretch). Anal. Calc. for $C_{46}H_{66}N_2O_8$: C 71.29, H 8.58, N 3.61%.

6.3.3 $L_{wide}CoK(OAc)_2$

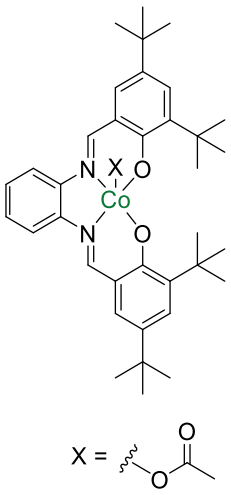


$Co(OAc)_2$ (114 mg, 0.65 mmol), KOAc (63 mg, 0.65 mmol), and H_2L_{wide} (500 mg, 0.65 mmol) were combined in dry MeCN (15 mL) under N_2, forming a deep red-brown suspension, which was stirred for 16 h. The solution was then exposed to air, and acetic acid (74 μL, 1.30 mmol) added to the mixture. The solution was stirred for 4 h, over the course of undissolved species dissolved, and the solution turned a deep, vibrant red. Solvent was removed *in vacuo* and the resultant crude product was purified by precipitation from toluene with pentane. The final product was isolated by filtration as a red solid (400 mg; 62% yield). ^{1}H NMR (400 MHz, MeOD-d_4, 298 K) δ (ppm): 8.03 (s, 2H, N=C**H**, **i**), 7.73 (s, 2H, Ar**H**, **m** or **k**), 7.68 (s, 2H, Ar**H**, **m** or **k**), 7.63 (s, br, 2H, Ar**H**, **g**), 4.55 (m, 4H, C**H**$_2$, **e**), 4.03 (m, 4H, C**H**$_2$, **d**), 3.80 (m, 4H, C**H**$_2$, **c**), 3.74 (m, 4H, C**H**$_2$, **b**), 3.70 (s, 4H, C**H**$_2$, **a**), 1.91 (s, 8H, O=C-C**H**$_3$, **q** or **r**) 1.77 (s, 18H, C(C**H**$_3$)$_3$, **q** or **r**), 1.40 (s, 18H, C(C**H**$_3$)$_3$, **q** or **r**); ^{13}C{^{1}H} (151 MHz, MeOD-d_4, 298 K) 164.96 (s, **l**), 161.90 (s, **t**), 158.24 (s, **g**), 148.78 (s, **f**, **h**), 144.71 (s, **o**), 139.84 (s, **n**), 130.15 (s, **m**), 128.24 (s, **k**), 122.69 (s, **j**), 100.80 (s, **i**), 71.45 (s, **c**), 71.13 (s, **a**), 71.07 (s, **b**), 70.07 (s, **d**), 69.62 (s, **e**), 37.00 (s, **p**), 34.11 (s, **s**), 32.57 (s, **r**), 31.71 (s, **u**), 31.33 (s, **q**); λ_{max} (DCM)/nm 270, 301sh, 358, 402, 422sh, 512 (ε / dm^3 mol^{-1} cm^{-1} 19900,

10200, 6800, 6400, 3900); ν_{max}/cm^{-1} 2906 (C-H stretch), 1609 (imine C=N stretch), 1589 (acetate asymmetric C-O stretch), 1340 (acetate symmetric C-O stretch), 1193 (aryl alkyl ether C-O stretch), 1116 (aliphatic ether C-O stretch); MS (MALDI+) *m*/z: 870.07 $[L_{wide}Co(II)K]^+$; Anal. Calc. for $C_{50}H_{70}CoKN_2O_{12}$: C 60.71, H 7.13, N 2.83 %; Found: C 58.62*, H 6.97, N 2.66%.

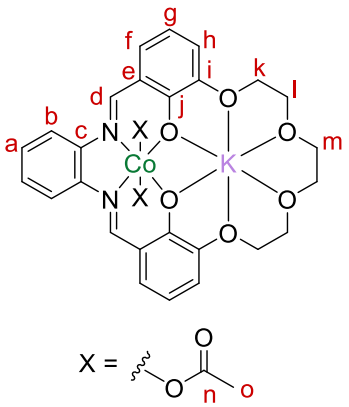
* Low C percentage for elemental analysis is proposed to be due to the formation of metal carbides.[2]

6.3.4 $L_{mono}CoOAc$



H_2L_{mono} (1.00 g, 1.85 mmol) was combined with methanol (50 mL) and refluxed, under N_2, for 2 h. $Co(OAc)_2.4H_2O$ (0.46 g, 1.85 mmol) was added, under a flow of N_2. The resultant red solution was refluxed for a further 1 h. Solvent was evaporated *in vacuo* and the resultant solid was redissolved in DCM (50 mL). To this solution, acetic acid (0.11 mL, 1.85 mmol) was added and stirred open to air for 16 h. The solvent was evaporated *in vacuo* and azeotropic distillations performed on the solid with toluene (3 x 30 mL) and pentane (3 x 30 mL). $L_{mono}CoOAc$ was isolated as a bright-red solid (1.12 g, 1.70 mmol, 92%); MS (MALDI+): 599.845 $[L_{mono}Co(II)]^+$ Anal. Calc. for $C_{38}H_{49}CoN_2O_4$: C 69.50, H 8.95, N 5.18 %; Found: C 69.83, H 7.49, N 4.12%.

6.3.5 $L_{short}CoK(OAc)_2$



The dialdehyde proligand (300 mg, 0.77 mmol), $Co(OAc)_2$ (136 mg, 0.77 mmol) and KOAc (75 mg, 0.77 mmol) were combined with dry, degassed acetonitrile (15 mL) and stirred, under a N_2 atmosphere, for 1 h. *ortho*-Phenylene diamine (83 mg, 0.77 mmol) was added in one portion, in a N_2 glovebox, and the solution was stirred for 16 h, before being opened to air and acetic acid added (44 μL, 0.77 mmol). The solution was stirred, open to air, for 3 days. Solvent was removed *in vacuo* and azeotropic distillations performed on the solid with toluene (3 x 30 mL) and pentane (3 x 30 mL). The complex was purified by precipitation (DCM/pentane), and $L_{short}CoK(OAc)_2$ was isolated as a brown powder (334 mg, 0.49 mmol, 64%). ^{1}H NMR (400 MHz, $CDCl_3$, 298 K) δ (ppm): 8.19 (s, 2H, N=C**H**, **d**), 7.99 – 8.04 (m, 2H, Ar**H**, **a** or **b**), 7.34 – 7.40 (m, 2H, Ar**H**, **a** or **b**), 7.00 (dd, 2H, $^3J_{H\text{-}H}$ = 8.11 Hz, $^4J_{H\text{-}H}$ = 1.16 Hz, Ar**H**, **f** or **h**), 6.74 (dd, 2H, $^3J_{H\text{-}H}$ = 7.78 Hz, $^4J_{H\text{-}H}$ = 1.02 Hz, Ar**H**, **f** or **h**), 6.47 (t, 2H, $^3J_{H\text{-}H}$ = 7. 87 Hz, Ar**H**, **g**), 4.18 – 4.24 (m, 4H, O-C**H**$_2$, **k**), 3.95 – 4.00 (m, 4H, O-C**H**$_2$, **l**), 3.86 (s, 4H, O-C**H**$_2$, **m**), 1.38 (s, 6H, OC(O)C**H**$_3$, **o**); ^{13}C{^{1}H} NMR (126 MHz, $CDCl_3$, 298 K) δ (ppm): 178.75 (s, **n**), 157.64 (s, **d**), 156.09 (s, **j**), 150.86 (s, **i**), 145.94 (s, **c**), 126.16 (s, **a**), 117.26 (s, **e**), 114.42 (s, **b**), 112.00 (s, **f** and **h**, or **g**), 111.98 (s, **f** and **h**, or **g**), 69.05 (s, **k**, **l**, or **m**), 68.16 (s, **k**, **l**, or **m**), 65.18 (s, **k**, **l**, or **m**), 23.42 (s, **o**); MS (MALDI+): 561.012 [L_{short}Co(II)K]$^+$; Anal. Calc. for $C_{30}H_{40}CoKN_2O_{10}$: C 53.26, H 4.47, N 4.14 %; Found: C 53.02, H 4.12, N 4.17%.

6.4 Chapter 4

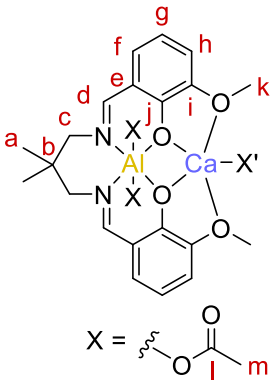
6.4.1 H_2L_1

A literature procedure was followed.[3] Spectroscopic characterisation and elemental analysis agreed with those previously reported in the literature.

6.4.2 L_1Al(III)M(I) (M(I) = Na, K, Rb) Catalysts

General procedure: A literature procedure was followed.[3] Spectroscopic characterisation and elemental analysis agreed with those previously reported in the literature.

6.4.3 L_1Al(III)Ca(II) Catalyst



H_2L_1 (400 mg, 1.08 mmol) was dissolved in THF (15 mL), under N_2. $AlEt_3$ (155 µL, 1.13 mmol) was added in one portion and the resultant solution was stirred for 1 h, under a N_2 atmosphere, during which a yellow precipitate formed. Acetic acid (62 µL, 1.08 mmol) was added in one portion under a flow of N_2, and stirred for 1 h. $CaOAc)_2.H_2O$ (190 mg, 1.08 mmol) was added to the suspension under a flow of N_2, and was stirred for 16 h. The precipitate and solution changed colour from yellow to off-white. The final L_1Al(III)Ca(II) complex was isolated by filtration, followed by washing with THF (3 x 5 mL), as a white powder in 390 mg yield (0.64 mmol, 59%). ^{1}H NMR (400 MHz, $CDCl_3$, 298 K) δ (ppm): 7.98 (s, 2H, **d**, N=C**H**), 6.91 (dd, 2H, $^3J_{H\text{-}H}$ = 8.04 Hz, $^4J_{H\text{-}H}$ = 1.01 Hz, **h**, Ar**H**), 6.84 (dd, 2H, $^3J_{H\text{-}H}$ = 7.91 Hz,

$^{4}J_{H\text{-}H}$ = 1.13 Hz, **f**, *meta*-Ar**H**), 6.65 (t, 2H, $^{3}J_{H\text{-}H}$ = 7.87 Hz, **g**, *para*-Ar**H**), 3.97 (s, 6H, **k**, OC**H**$_3$), 3.72 (s, 4H, **c**, N-C**H**$_2$), 2.13 (s, 3H, **m'**, Ca-O-C(=O)-C**H**$_3$), 1.49 (s, 6H, **m**, Al-O-C(=O)-C**H**$_3$), 1.13 (s, 6H, **a**, C(C**H**$_3$)$_2$); ^{13}C{^{1}H} NMR (126 MHz, $CDCl_3$, 298 K) δ (ppm): 182.7 (s, **l'**, Ca-O-**C**(=O)), 176.0 (s, **l**, Al-O-**C**(=O)), 167.7 (s, **d**, N=**C**H), 153.3 (s, **e**, *ortho*-Ar**C**), 150.2 (s, **i**, *ortho*-Ar**C**), 126.0 (s, **f**, *meta*-Ar**C**), 119.1 (s, **j**, *ipso*-Ar**C**), 116.4 (s, **g**, *para*-Ar**C**), 115.7 (s, **h**, *meta*-Ar**C**), 72.9 (s, **b**, **C**(CH_3)$_2$), 57.1 (s, **k**, O-**C**H_3), 35.2 (s, **c**, N-**C**H_2), 25.2 (s, **a**, C(**C**H_3)$_2$), 24.4 (s, **m**, Al-O-C(=O)-**C**H_3), 24.3 (s, **m'**, Ca-O-C(=O)-**C**H_3); ν_{max}/cm^{-1} 2939 (C-H stretch), 1635 (acetate asymmetric C-O stretch), 1555 (imine C=N stretch), 1475 (acetate symmetric C-O stretch), 1228 (aromatic C-O stretch), 1072 (aliphatic C-O stretch); Anal. Calc. for $C_{27}H_{33}AlCaN_2O_{10}$: C 52.94, H 5.43, N 4.57 %; Found: C 52.57 H 5.20 N 4.54%.

6.4.4 H_2L_2

General procedure: A literature procedure was followed.[4] Spectroscopic characterisation and elemental analysis agreed with those previously reported in the literature.

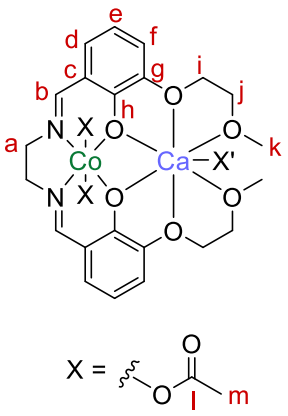
6.4.5 L_2Co(III)M(I) (M(I) = Na, K, Rb) Catalysts

General procedure: A literature procedure was followed.[4] Spectroscopic characterisation and elemental analysis agreed with those previously reported in the literature.

6.4.6 L_2Co(III)M(II) (M(II) = Ca, Sr, Ba) Catalysts

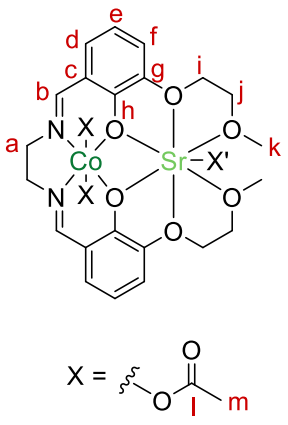
General procedure: H_2L_2 (400 mg, 0.96 mmol), $Co(OAc)_2$ (170 mg, 0.96 mmol), and M(II)$(OAc)_2$ (0.96 mmol) were combined in acetonitrile and stirred under a N_2 atmosphere for 16 h. The resultant red solution was then opened to air and stirred for 72 h, during which time it changed colour to brown. Solvent was evaporated *in vacuo* and the crude catalyst was purified by precipitation from a chloroform solution with pentane. The final catalysts were isolated as brown powders (411 – 475 mg, 56 – 67%).

6.4.6.1 $L_2Co(III)Ca(II)$



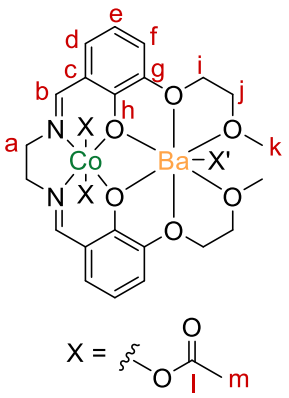
$Ca(OAc)_2.H_2O$ used (169 mg). Isolated as a brown powder in 62% yield (0.60 mmol, 411 mg). ^{1}H NMR (400 MHz, $CDCl_3$, 298 K) δ (ppm): 7.83 (s, 2H, **b**, N=C**H**), 7.13 (dd, 2H, $^3J_{H\text{-}H}$ = 8.00 Hz, $^4J_{H\text{-}H}$ = 1.07 Hz, **f**, *meta*-Ar**H**), 6.94 (dd, 2H, $^3J_{H\text{-}H}$ = 7.94 Hz, $^4J_{H\text{-}H}$ = 1.07 Hz, **d**, *meta*-Ar**H**), 6.60 (t, 2H, $^3J_{H\text{-}H}$ = 7.78 Hz, **e**, *para*-Ar**H**), 4.60 (t, 4H, **i**, $^3J_{H\text{-}H}$ = 5.06 Hz, O-C**H**$_2$), 4.25 (s, 4H, **a**, N-C**H**$_2$), 3.76 (t, 4H, **j**, $^3J_{H\text{-}H}$ = 4.87 Hz, O-C**H**$_2$), 3.40 (s, 6H, **k**, O-C**H**$_3$), 2.08 (s, 3H, **m'**, Ca-O-C(=O)-C**H**$_3$), 1.43 (s, 6H, **m**, Co-O-C(=O)-C**H**$_3$); ^{13}C{^{1}H} NMR (126 MHz, $CDCl_3$, 298 K) δ (ppm): 182.3 (s, **l'**, Ca-O-**C**(=O)), 179.4 (s, **l**, Co-O-**C**(=O)), 165.2 (s, **b**, N=**C**H), 154.3 (s, **c**, *ortho*-Ar**C**), 151.0 (s, **g**, *ortho*-Ar**C**), 126.5 (s, **d**, *meta*-Ar**C**), 119.4 (s, **h**, *ipso*-Ar**C**), 117.5 (s, **f**, *meta*-Ar**C**), 115.2 (s, **e**, *para*-Ar**C**), 70.6 (s, **j**, O-**C**H$_2$), 69.2 (s, **i**, O-**C**H$_2$), 59.4 (s, **k**, O-**C**H$_3$), 59.2 (s, **a**, N-**C**H$_2$), 24.7 (s, **m**, Co-O-C(=O)-**C**H$_3$), 24.5 (s, **m'**, Ca-O-C(=O)-**C**H$_3$); ν_{max}/cm^{-1} 2911 (C-H stretch), 1634 (acetate asymmetric C-O stretch), 1562 (imine C=N stretch), 1467 (acetate symmetric C-O stretch), 1217 (aromatic C-O stretch), 1072 (aliphatic C-O stretch); Anal. Calc. for $C_{28}H_{35}CaCoN_2O_{12}$: C 48.70, H 5.11, N 4.06 %; Found: C 48.20, H 5.16, N 4.01 %.

6.4.6.2 $L_2Co(III)Sr(II)$



$Sr(OAc)_2$ used (197 mg). Isolated as a brown powder in 67% yield (0.64 mmol, 475 mg). ^{1}H NMR (400 MHz, $CDCl_3$, 298 K) δ (ppm): 7.76 (s, 2H, **b**, N=C**H**), 6.98 (dd, 2H, $^3J_{H\text{-}H}$ = 7.97 Hz, $^4J_{H\text{-}H}$ = 1.22 Hz, **f**, *meta*-Ar**H**), 6.90 (dd, 2H, $^3J_{H\text{-}H}$ = 8.02 Hz, $^4J_{H\text{-}H}$ = 1.32 Hz, **d**, *meta*-Ar**H**), 6.56 (t, 2H, $^3J_{H\text{-}H}$ = 7.96 Hz, **e**, *para*-Ar**H**), 4.59 (t, 4H, **i**, $^3J_{H\text{-}H}$ = 4.75 Hz, O-C**H**$_2$), 4.19 (s, 4H, **a**, N-C**H**$_2$), 3.80 (t, 4H, j, $^3J_{H\text{-}H}$ = 4.36 Hz, O-C**H**$_2$), 3.49 (s, 6H, **k**, O-C**H**$_3$), 2.05 (s, 3H, **m'**, Sr-O-C(=O)-C**H**$_3$), 1.44 (s, 6H, **m**, Co-O-C(=O)-C**H**$_3$); ^{13}C{^{1}H} NMR (126 MHz, $CDCl_3$, 298 K) δ (ppm): 179.9 (s, **l'**, Sr-O-**C**(=O)), 179.3 (s, **l**, Co-O-**C**(=O)), 165.2 (s, **b**, N=**C**H), 155.5 (s, **c**, *ortho*-Ar**C**), 150.7 (s, **g**, *ortho*-Ar**C**), 127.1 (s, **d**, *meta*-Ar**C**), 119.6 (s, **h**, *ipso*-Ar**C**), 117.7 (s, **f**, *meta*-Ar**C**), 114.6 (s, **e**, *para*-Ar**C**), 69.9 (s, **j**, O-**C**H$_2$), 68.6 (s, **i**, O-**C**H$_2$), 59.5 (s, **k**, O-**C**H$_3$), 58.9 (s, **a**, N-**C**H$_2$), 24.7 (s, **m**, Co-O-C(=O)-**C**H$_3$), 24.5 (s, **m'**, Sr-O-C(=O)-**C**H$_3$); ν_{max}/cm^{-1} 2915 (C-H stretch), 1638 (acetate asymmetric C-O stretch), 1571 (imine C=N stretch), 1445 (acetate symmetric C-O stretch), 1222 (aromatic C-O stretch), 1071 (aliphatic C-O stretch); Anal. Calc. for $C_{28}H_{35}CoN_2O_{12}Sr$: C 45.56, H 4.78, N 3.80 %; Found: C 46.17, H 4.06, N 3.54%.

6.4.6.3 $L_2Co(III)Ba(II)$



$Ba(OAc)_2$ used (245 mg). Isolated as a brown powder in 56% yield (0.54 mmol, 424 mg). ^{1}H NMR (400 MHz, $CDCl_3$, 298 K) δ (ppm): 7.81 (s, 2H, **b**, N=C**H**), 6.90 (dd, 2H, $^3J_{H\text{-}H}$ = 7.94 Hz, $^4J_{H\text{-}H}$ = 1.23 Hz, **f**, *meta*-Ar**H**), 6.86 (dd, 2H, $^3J_{H\text{-}H}$ = 8.04 Hz, $^4J_{H\text{-}H}$ = 1.27 Hz, **d**, *meta*-Ar**H**), 6.52 (t, 2H, $^3J_{H\text{-}H}$ = 8.06 Hz, **e**, *para*-Ar**H**), 4.46 – 4.51 (m, 4H, **i**, O-C**H**$_2$), 4.06 (s, 4H, **a**, N-C**H**$_2$), 3.89 – 3.95 (m, 4H, **j**, O-C**H**$_2$), 3.53 (s, 6H, **k**, O-C**H**$_3$), 2.02 (s, 3H, **m'**, Ba-O-C(=O)-C**H**$_3$), 1.45 (s, 6H, **m**, Co-O-C(=O)-C**H**$_3$); ^{13}C{^{1}H} NMR (126 MHz, $CDCl_3$, 298 K) δ (ppm): 179.3 (s, **l**, O-**C**(=O)), 164.9 (s, **b**, N=**C**H), 156.1 (s, **c**, *ortho*-Ar**C**), 151.6 (s, **g**, *ortho*-Ar**C**), 127.0 (s, **d**, *meta*-Ar**C**), 119.2 (s, **h**, *ipso*-Ar**C**), 117.2 (s, **f**, *meta*-Ar**C**), 114.3 (s, **e**, *para*-Ar**C**), 69.8 (s, **j**, O-**C**H$_2$), 68.2 (s, **i**, O-**C**H$_2$), 59.0 (s, **k**, O-**C**H$_3$), 58.9 (s, **a**, N-**C**H$_2$), 24.8 (s, **m**, O-C(=O)-**C**H$_3$); ν_{max}/cm^{-1} 2914 (C-H stretch), 1641 (acetate asymmetric C-O stretch), 1573 (imine C=N stretch), 1443 (acetate symmetric C-O stretch), 1215 (aromatic C-O stretch), 1074 (aliphatic C-O stretch); Anal. Calc. for $C_{28}H_{35}BaCoN_2O_{12}$: C 42.69, H 4.48, N 3.56 %; Found: C 44.09, H 4.31, N 3.82%.

6.5 References

(1) Deacy, A. C.; Moreby, E.; Phanopoulos, A.; Williams, C. K. Co(III)/Alkali-Metal(I) Heterodinuclear Catalysts for the Ring-Opening Copolymerization of CO_2 and Propylene Oxide. *J. Am. Chem. Soc.* **2020**, *142* (45), 19150-19160.

(2) Arnold, P. L.; Turner, Z. R.; Bellabarba, R.; Tooze, R. P. Carbon–Silicon and Carbon–Carbon Bond Formation by Elimination Reactions at Metal N-Heterocyclic Carbene Complexes. *J. Am. Chem. Soc.* **2011**, *133* (30), 11744-11756.

(3) Diment, W. T.; Gregory, G. L.; Kerr, R. W. F.; Phanopoulos, A.; Buchard, A.; Williams, C. K. Catalytic Synergy Using Al(III) and Group 1 Metals to Accelerate Epoxide and Anhydride Ring-Opening Copolymerizations. *ACS Catal.* **2021**, *11* (20), 12532-12542.

(4) Eisenhardt, K. H. S.; Fiorentini, F.; Lindeboom, W.; Williams, C. K. Quantifying CO2 Insertion Equilibria for Low-Pressure Propene Oxide and Carbon Dioxide Ring Opening Copolymerization Catalysts. *J. Am. Chem. Soc.* **2024**, *146* (15), 10451-10464.

Appendix

Chapter Two

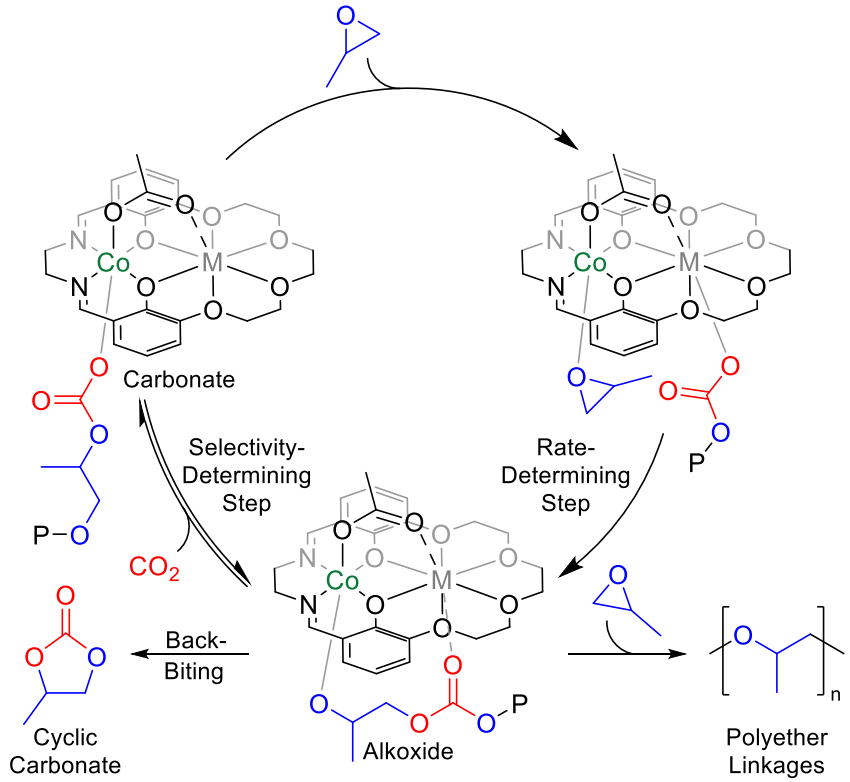


Figure S2.1. Dinuclear metallate mechanism for PO/CO_2 ROCOP catalysed by Co(III)K(I) catalyst.

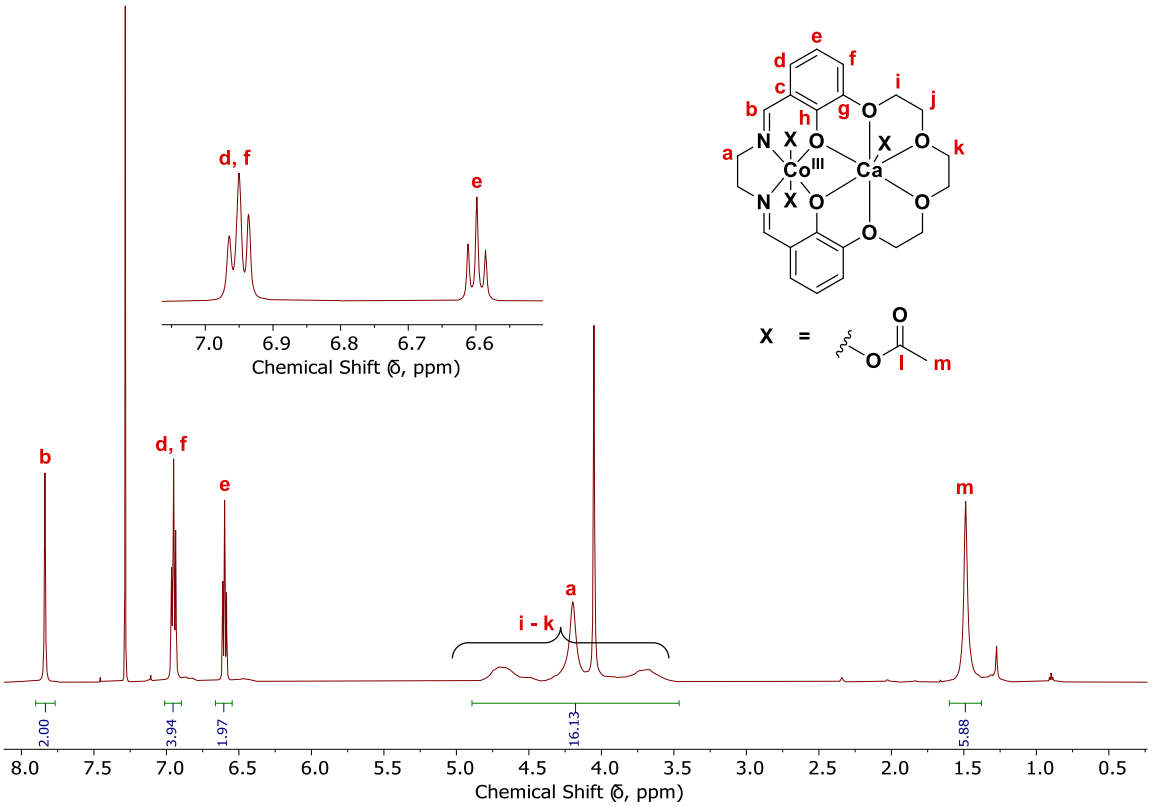


Figure S2.2. ^{1}H NMR spectrum of Co(III)Ca(II).

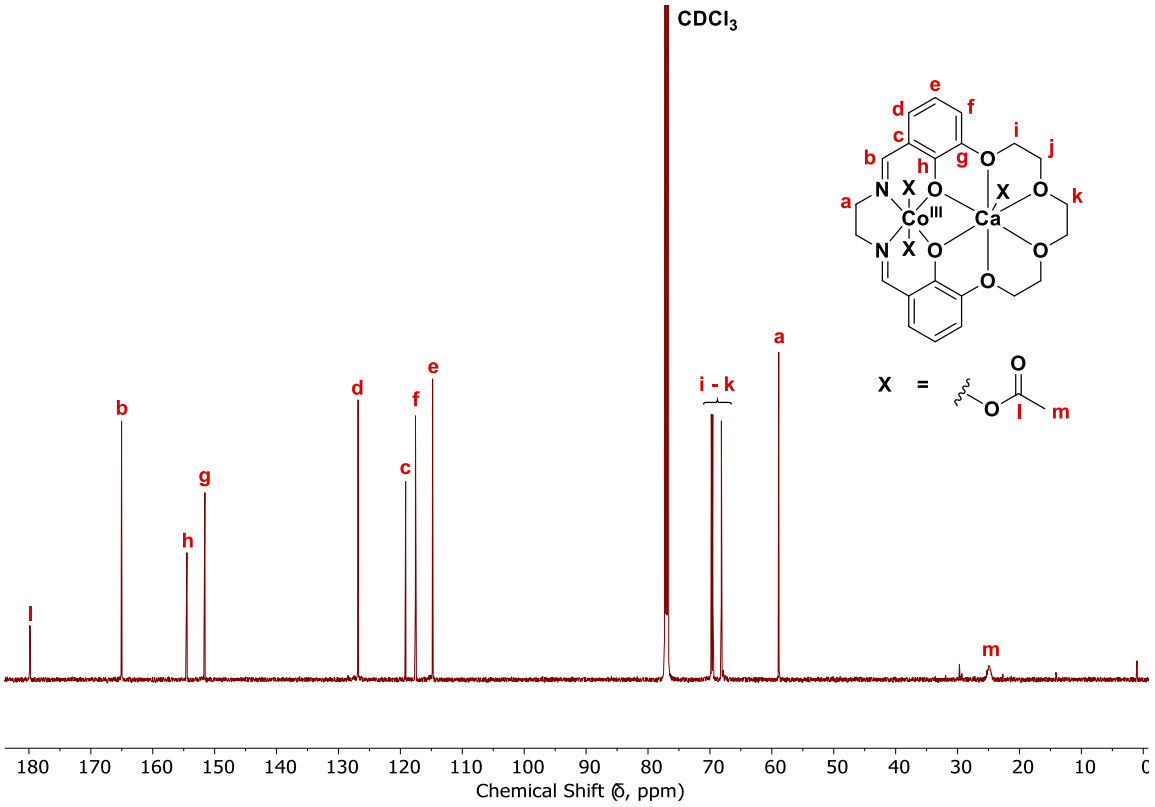


Figure S2.3. $^{13}C\{^{1}H\}$ NMR spectrum of Co(III)Ca(II).

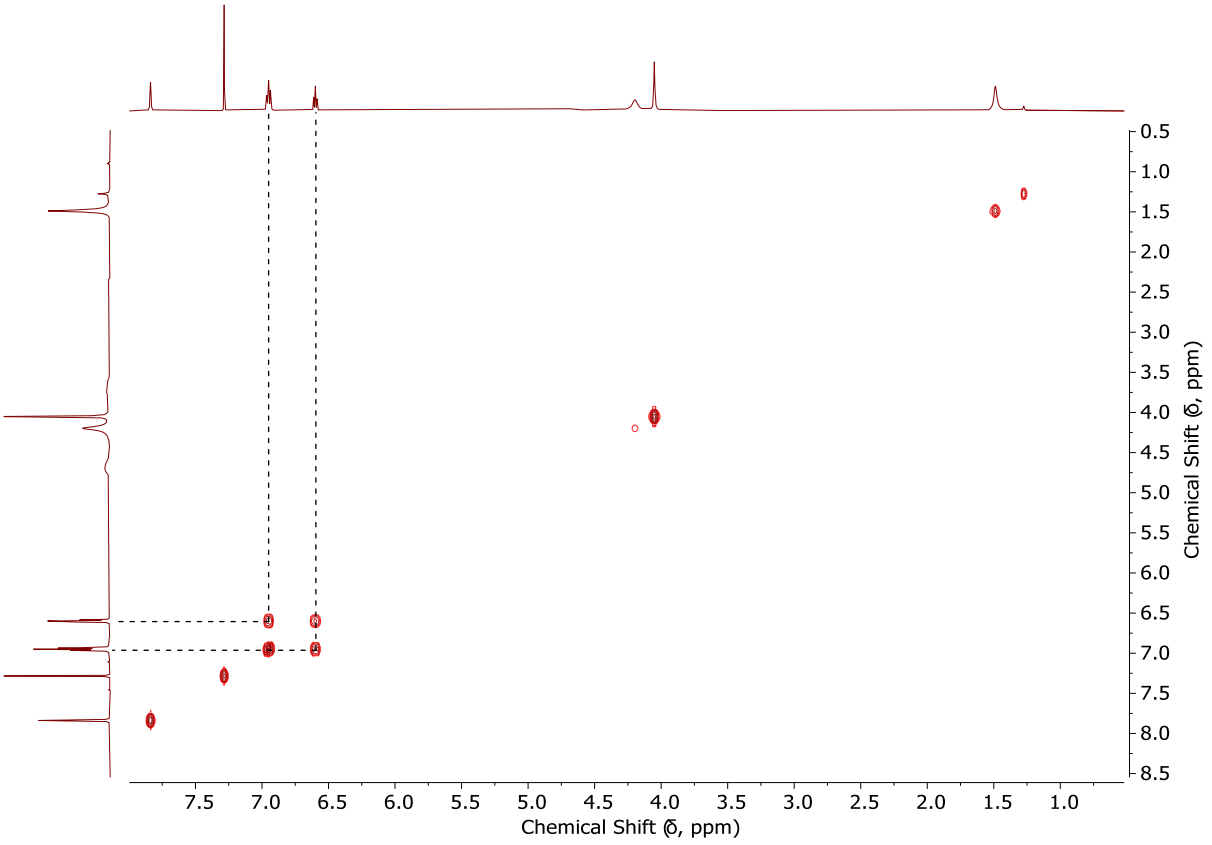


Figure S2.4. COSY NMR spectrum of Co(III)Ca(II).

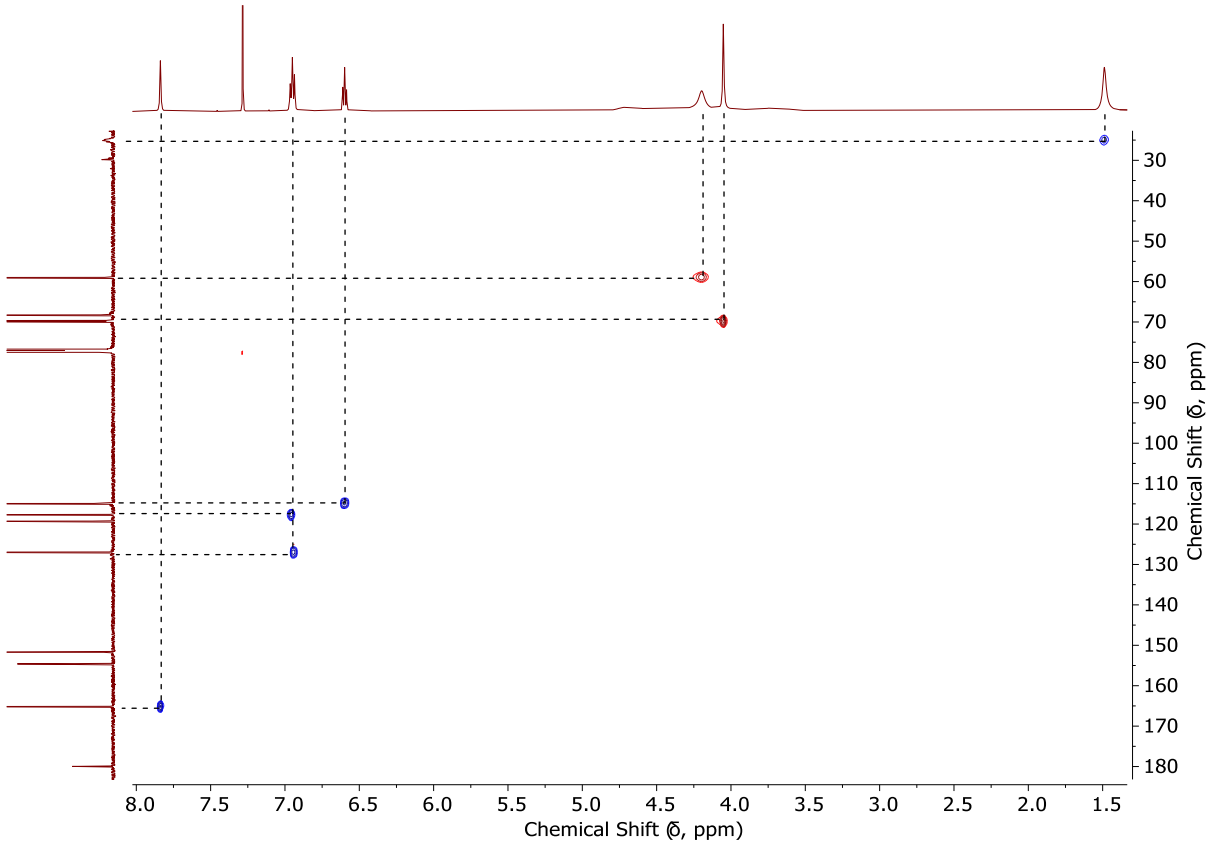


Figure S2.5. HSQC NMR spectrum of Co(III)Ca(II).

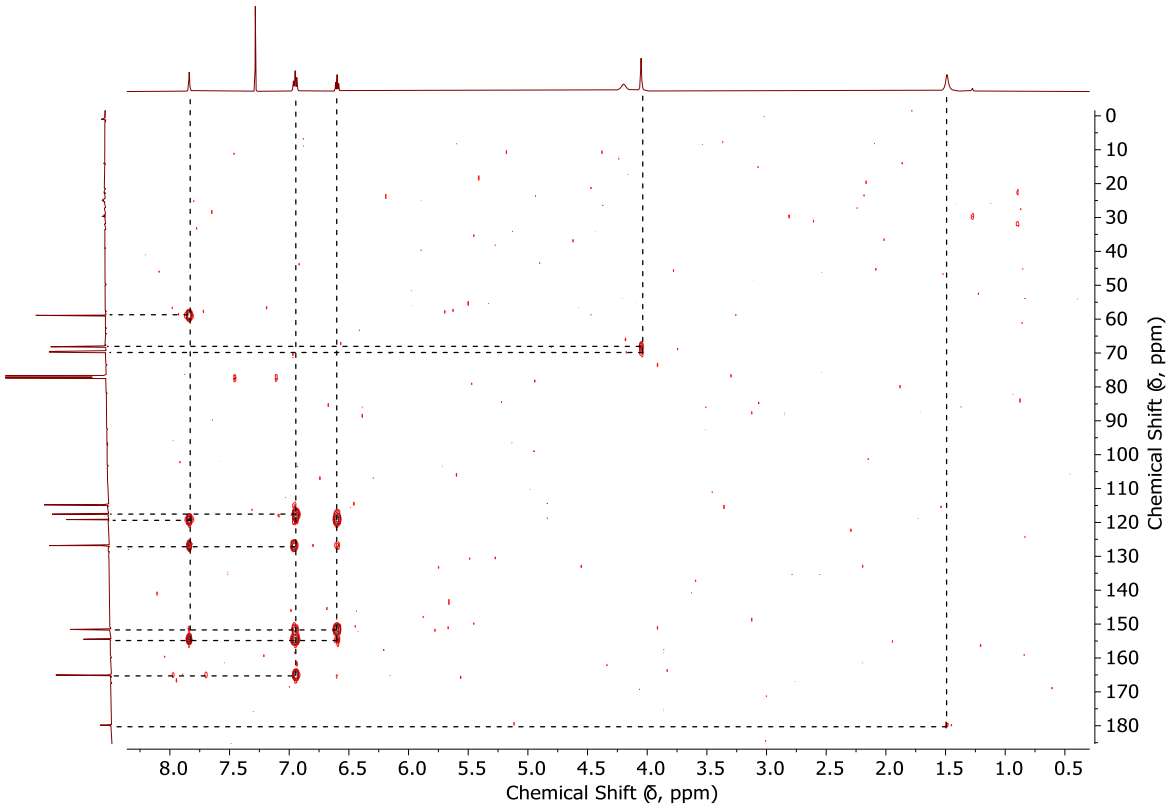


Figure S2.6. HMBC NMR spectrum of Co(III)Ca(II).

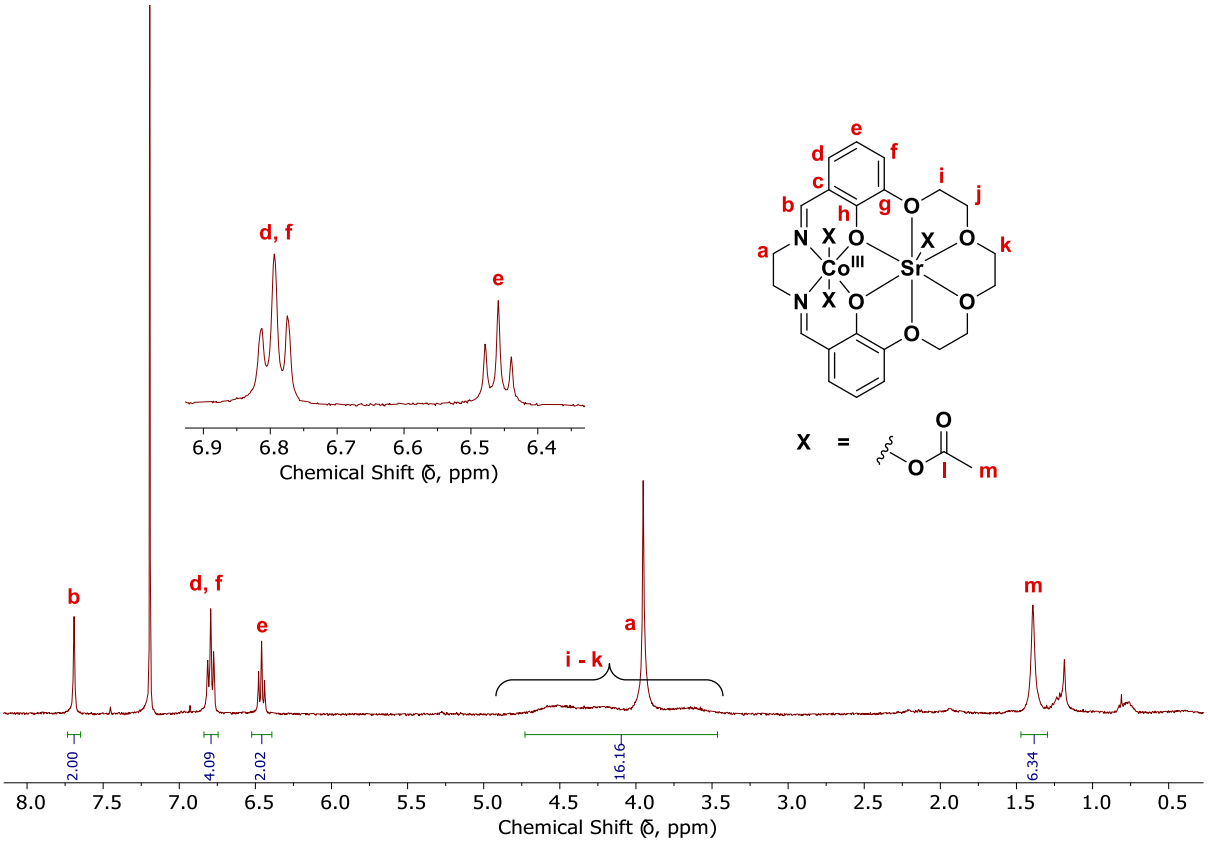


Figure S2.7. ^{1}H NMR spectrum of Co(III)Sr(II).

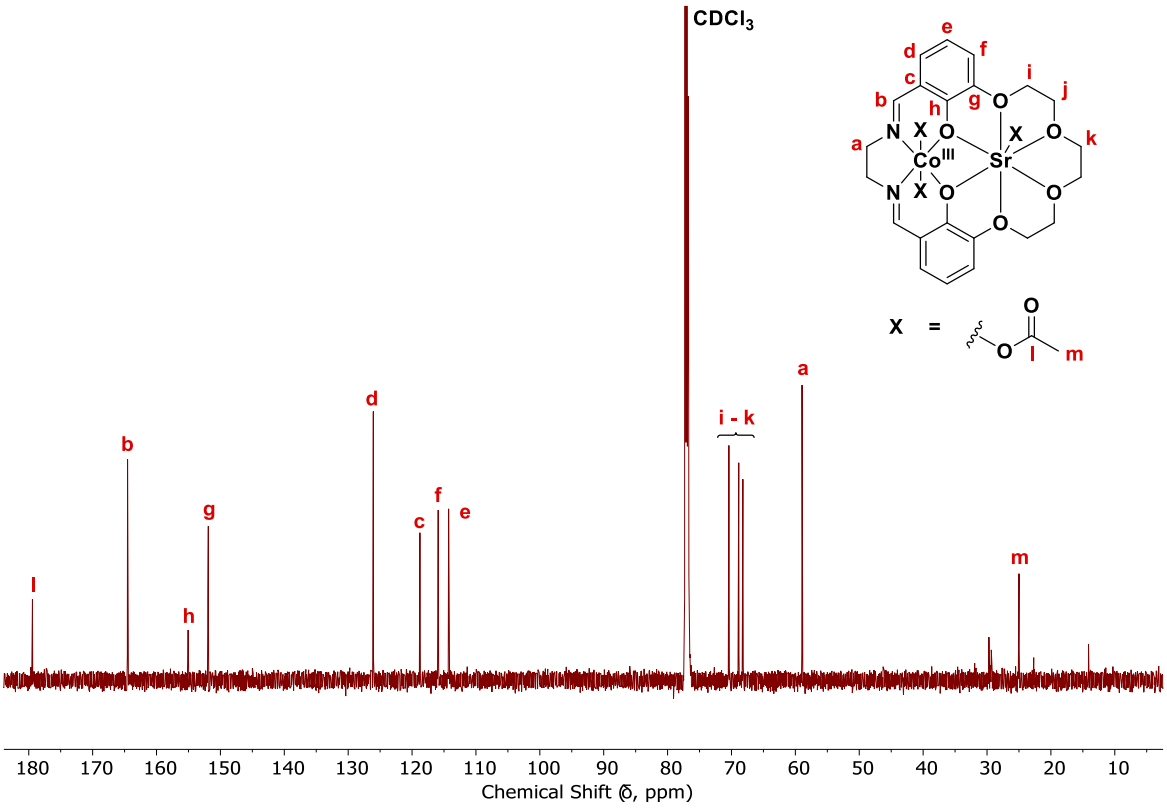


Figure S2.8. $^{13}C\{^{1}H\}$ NMR spectrum of Co(III)Sr(II).

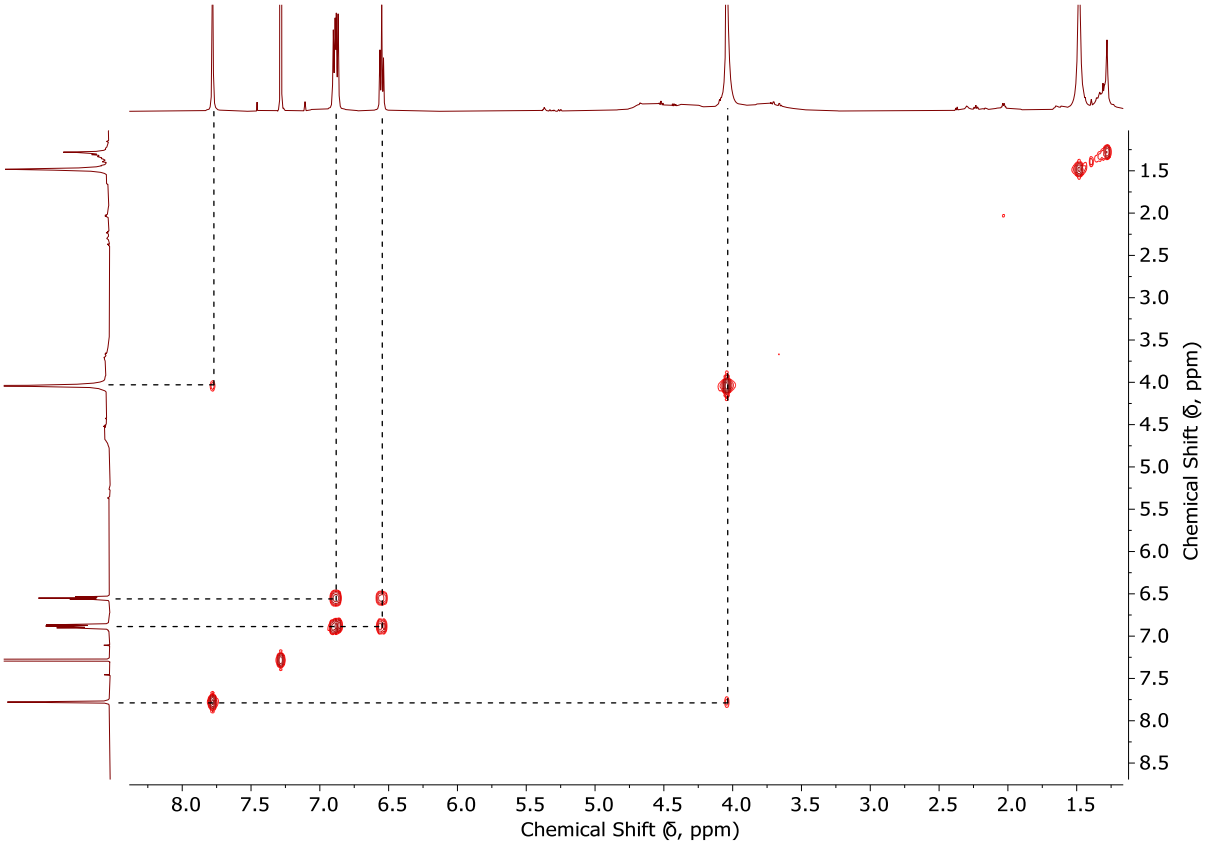


Figure S2.9. COSY NMR spectrum of Co(III)Sr(II).

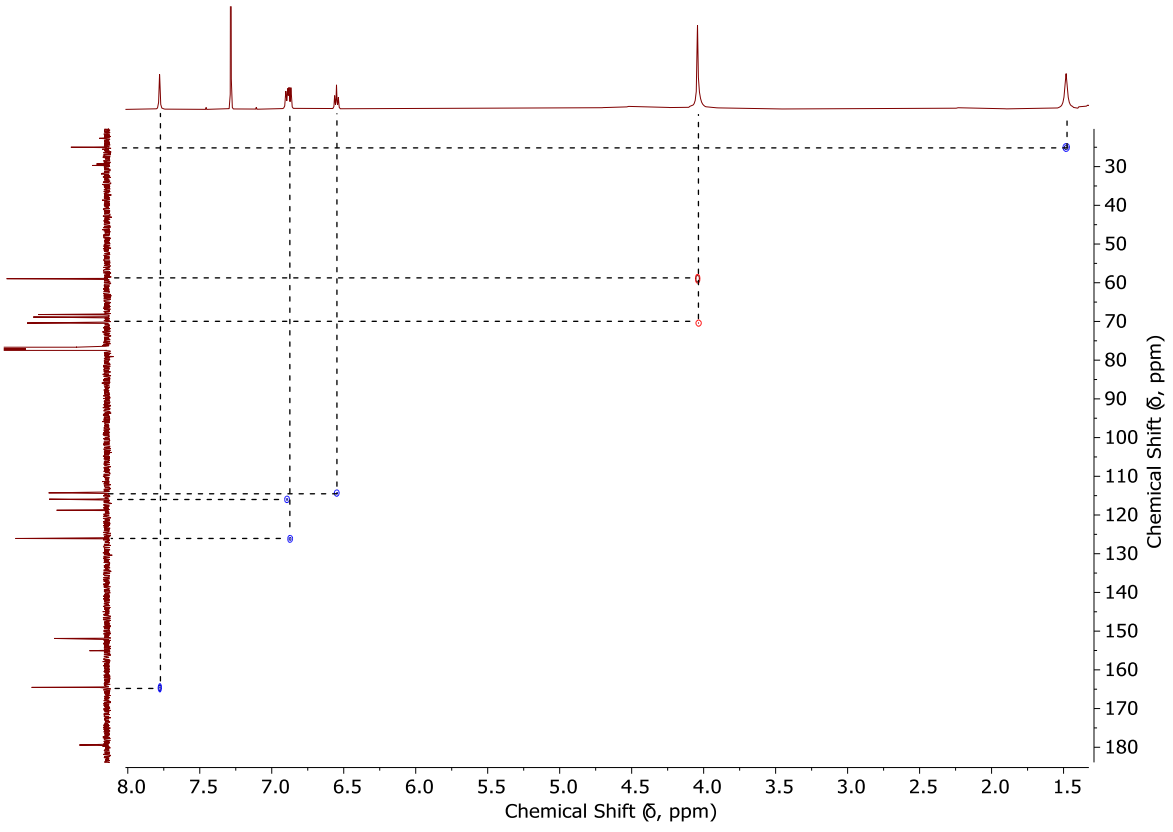


Figure S2.10. HSQC NMR spectrum of Co(III)Sr(II).

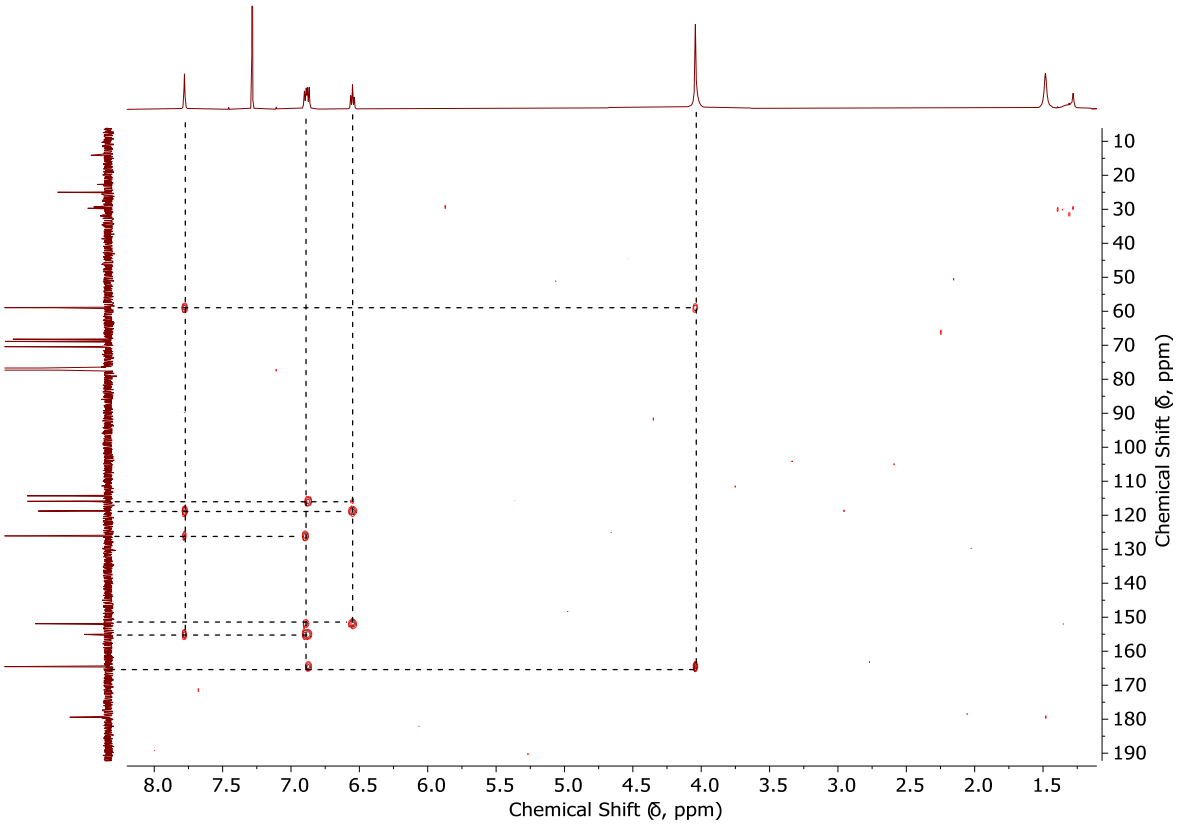


Figure S2.11. HMBC NMR spectrum of Co(III)Sr(II).

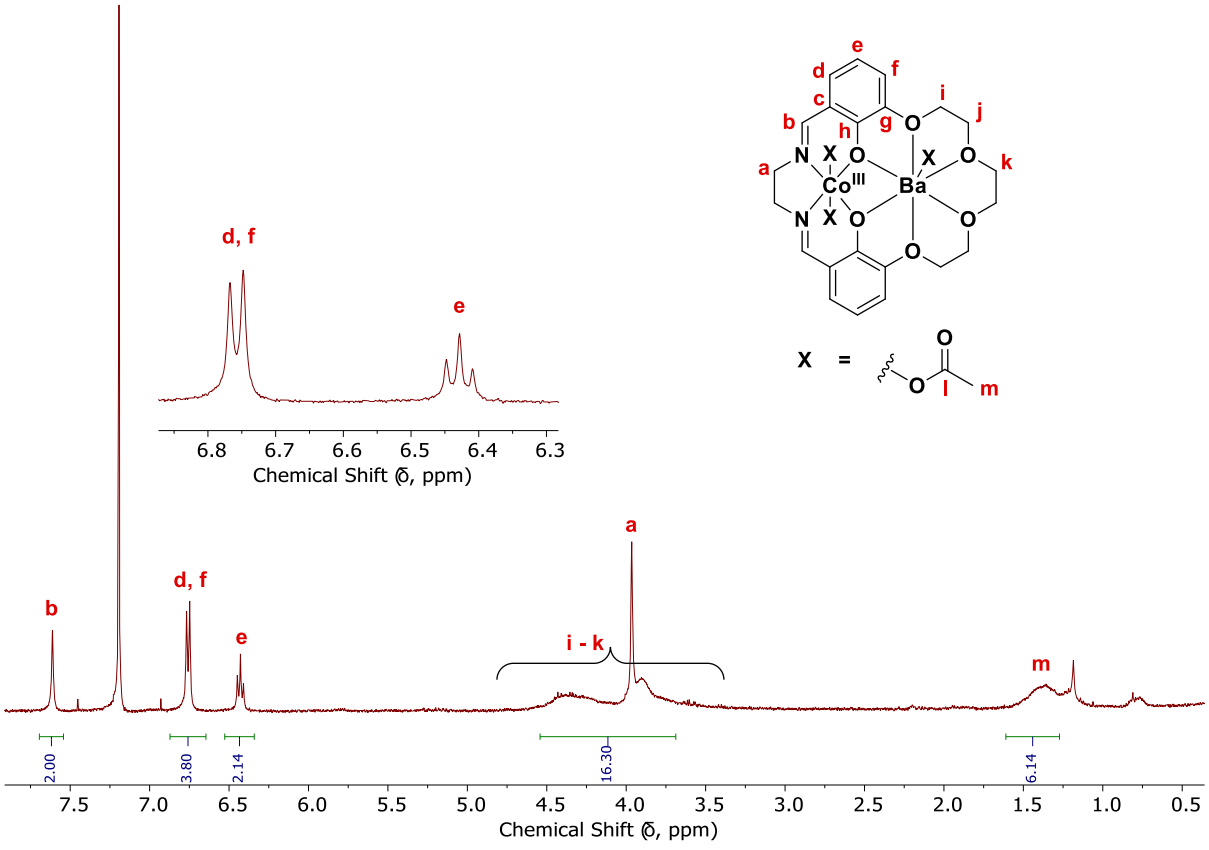


Figure S2.12. ^{1}H NMR spectrum of Co(III)Ba(II).

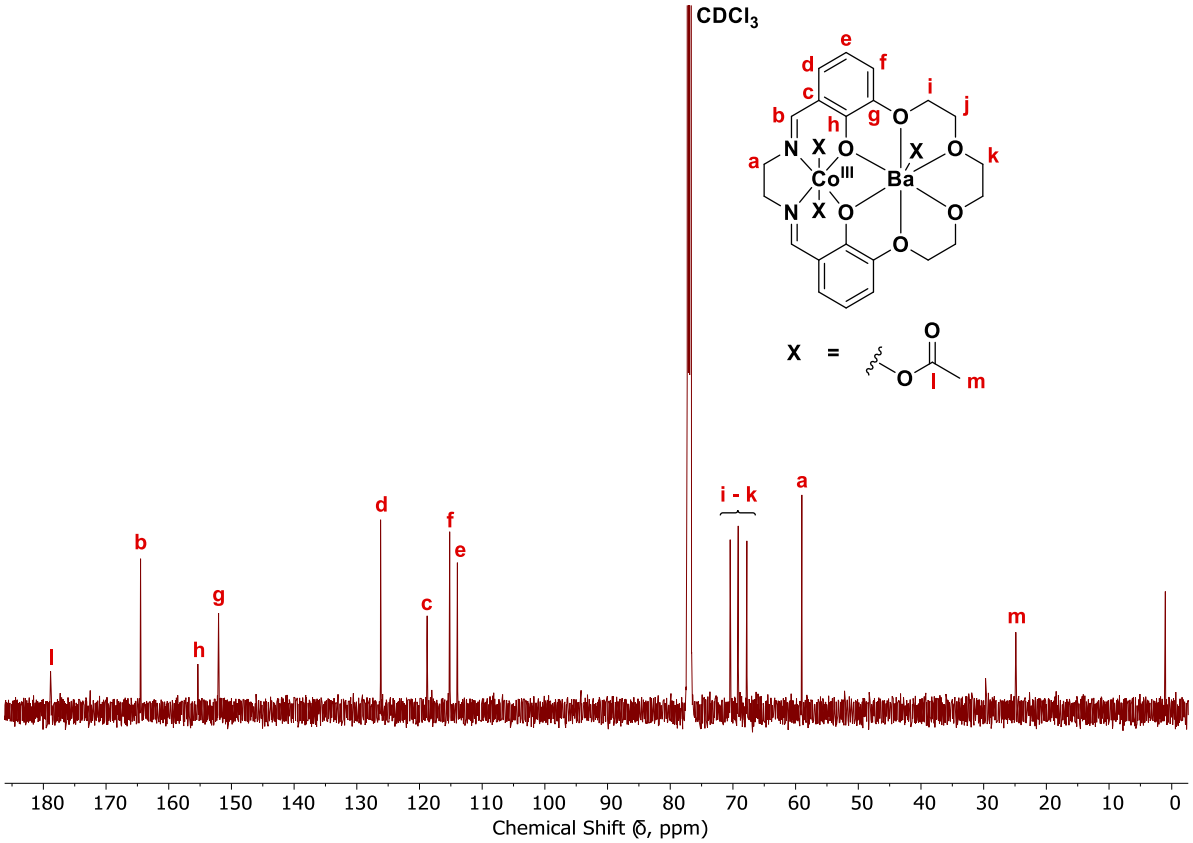


Figure S2.13. ^{13}C{^{1}H} NMR spectrum of Co(III)Ba(II).

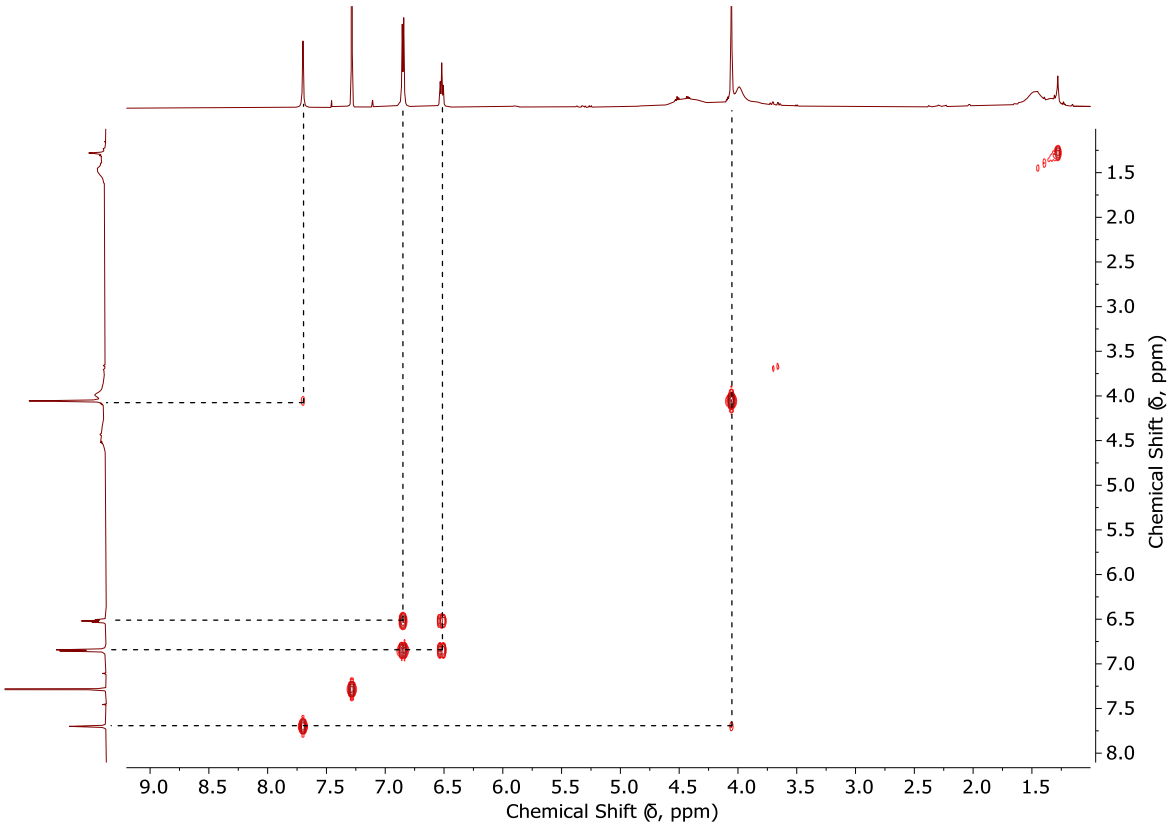


Figure S2.14. COSY NMR spectrum of Co(III)Ba(II).

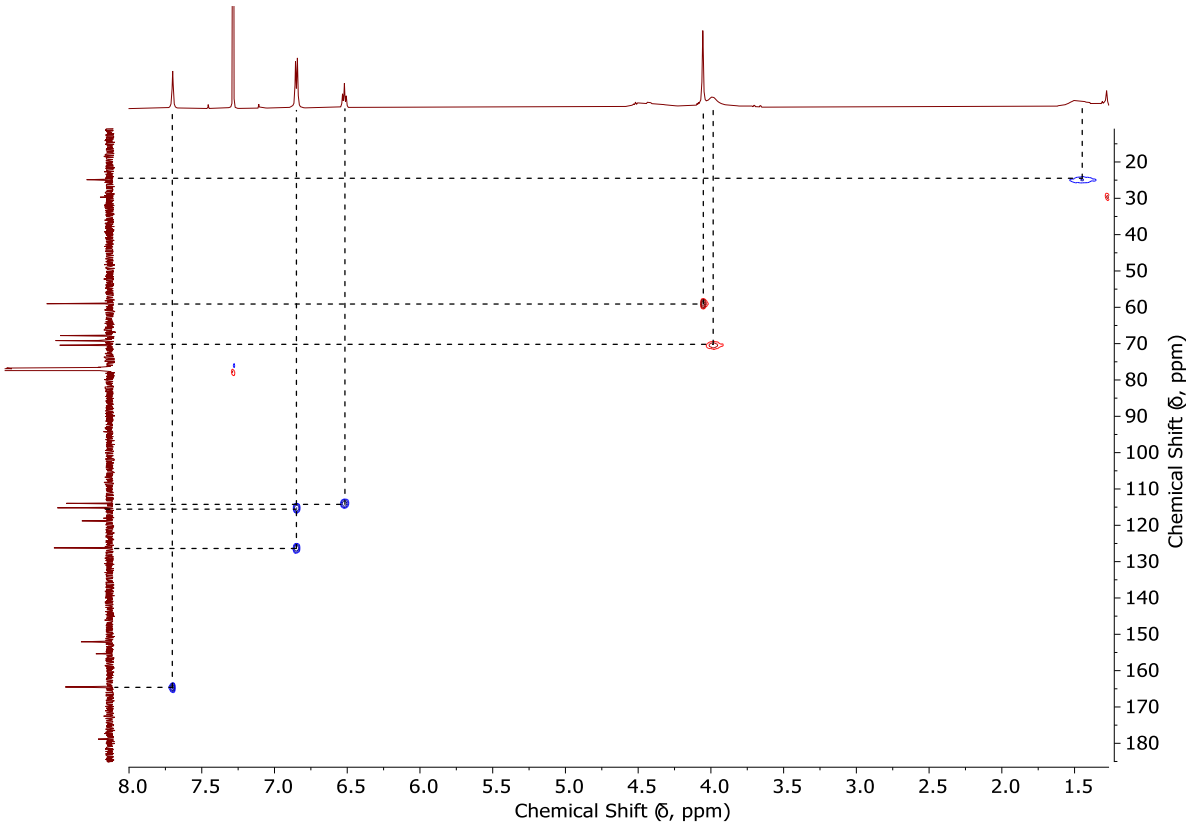


Figure S2.15. HSQC NMR spectrum of Co(III)Ba(II).

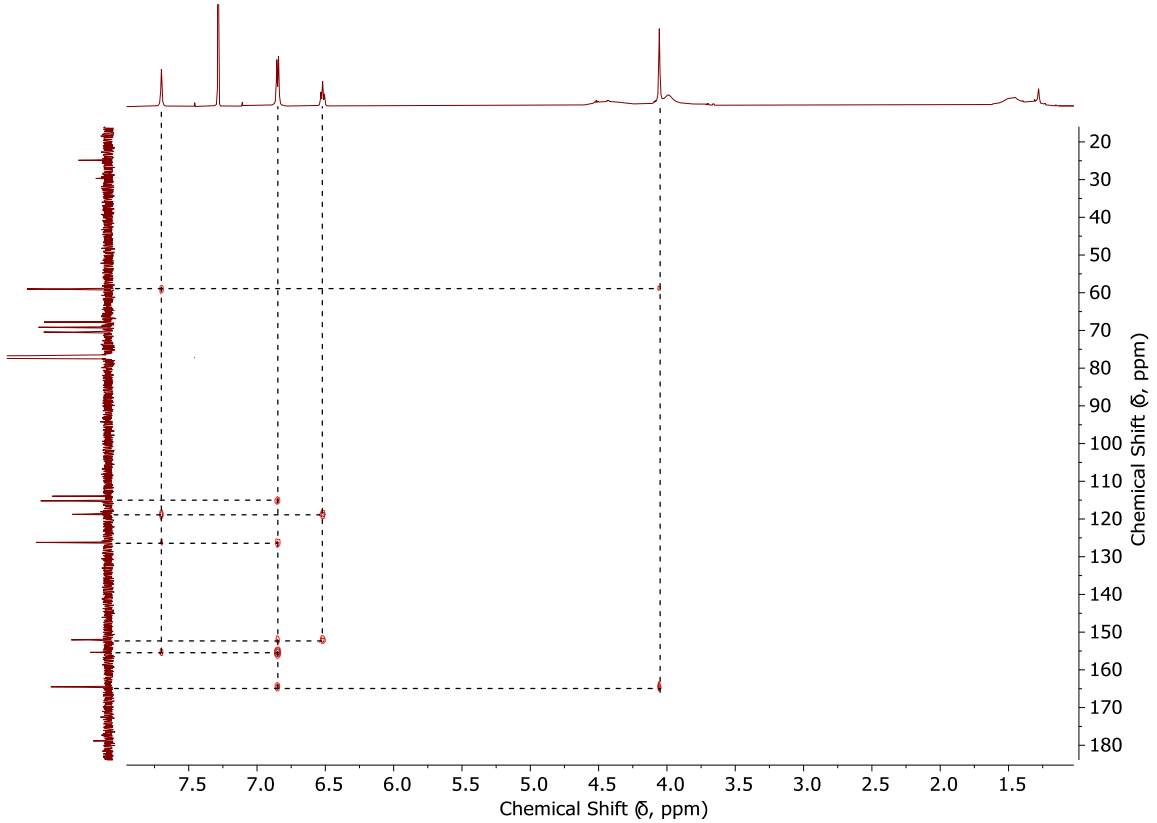


Figure S2.16. HMBC NMR spectrum of Co(III)Ba(II).

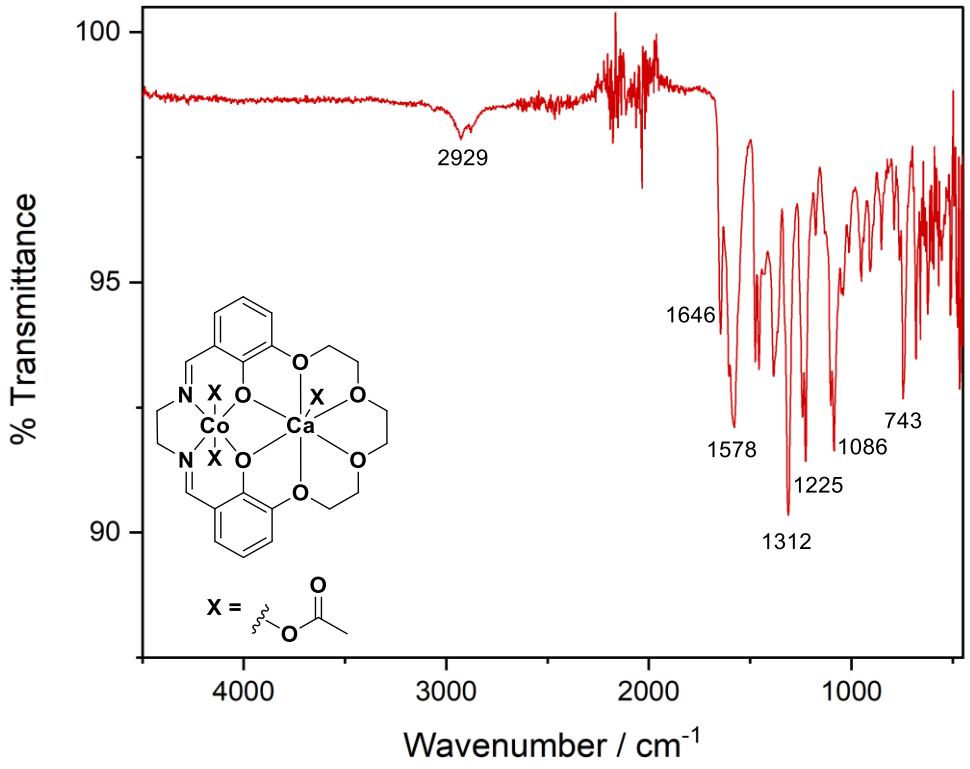


Figure S2.17. IR spectrum of Co(III)Ca(II).

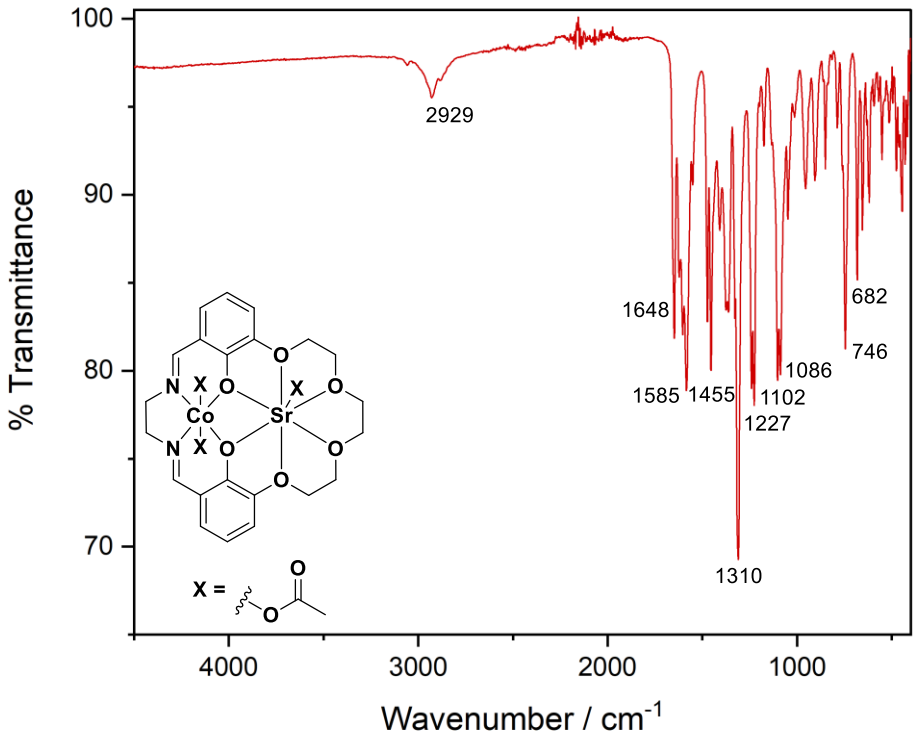


Figure S2.18. IR spectrum of Co(III)Sr(II).

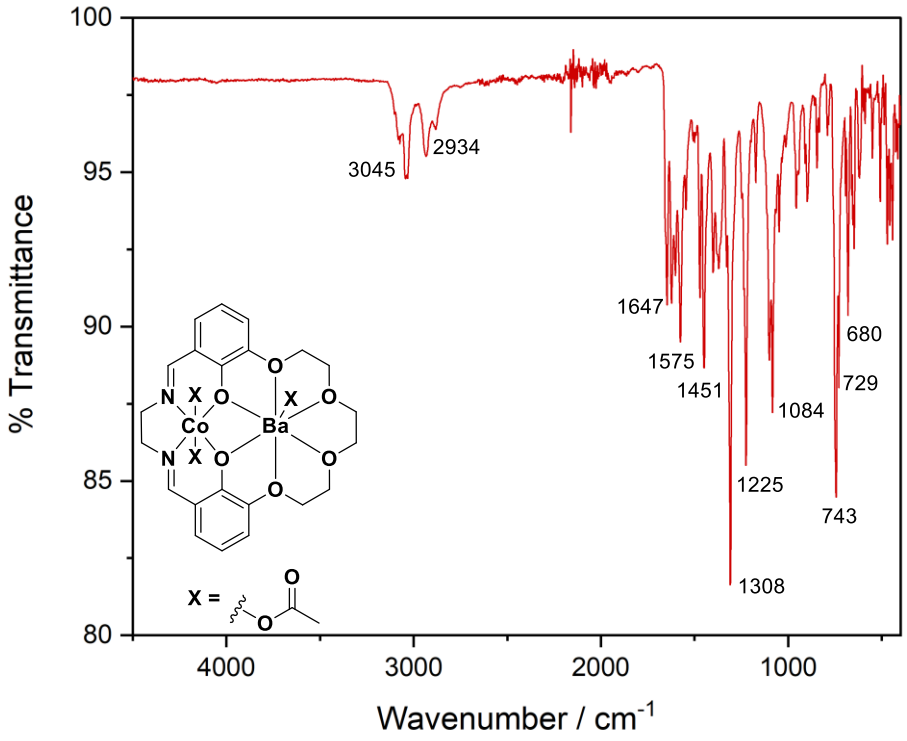


Figure S2.19. IR spectrum of Co(III)Ba(II).

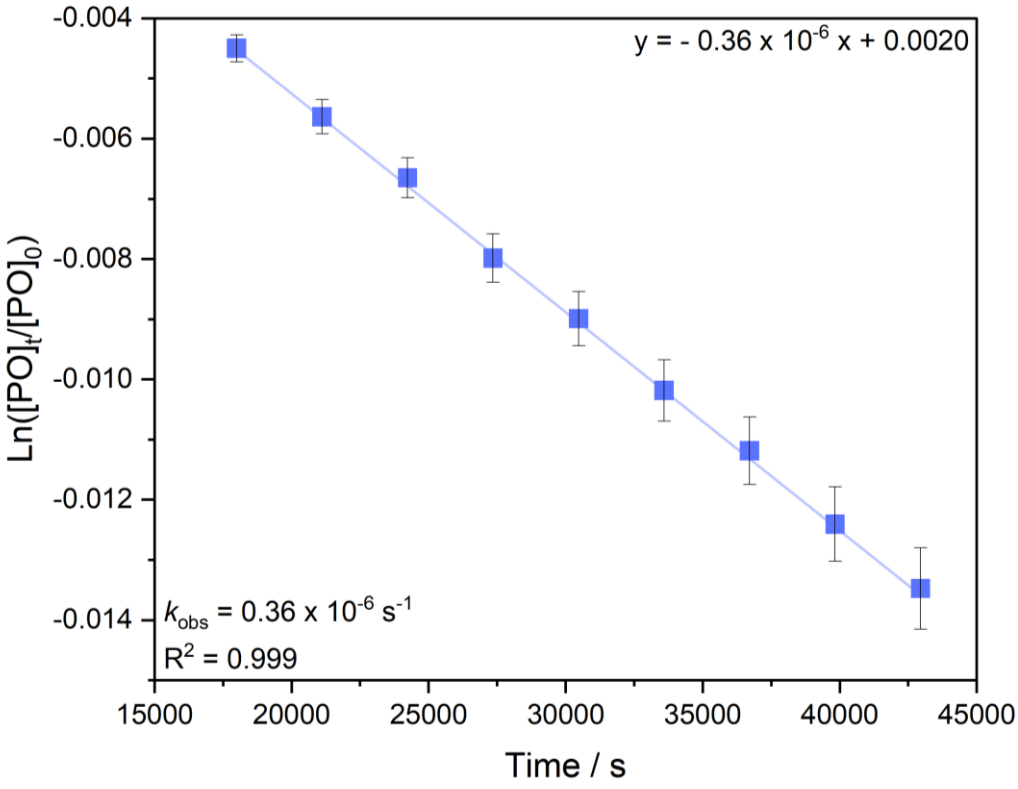


Figure S2.20: Plot of $Ln([PO]_t/[PO]_0)$ against time for PO/CO_2 ROCOP catalysed by Co(III)Ca(II) to calculate k_{obs}. (Every 52nd point shown).

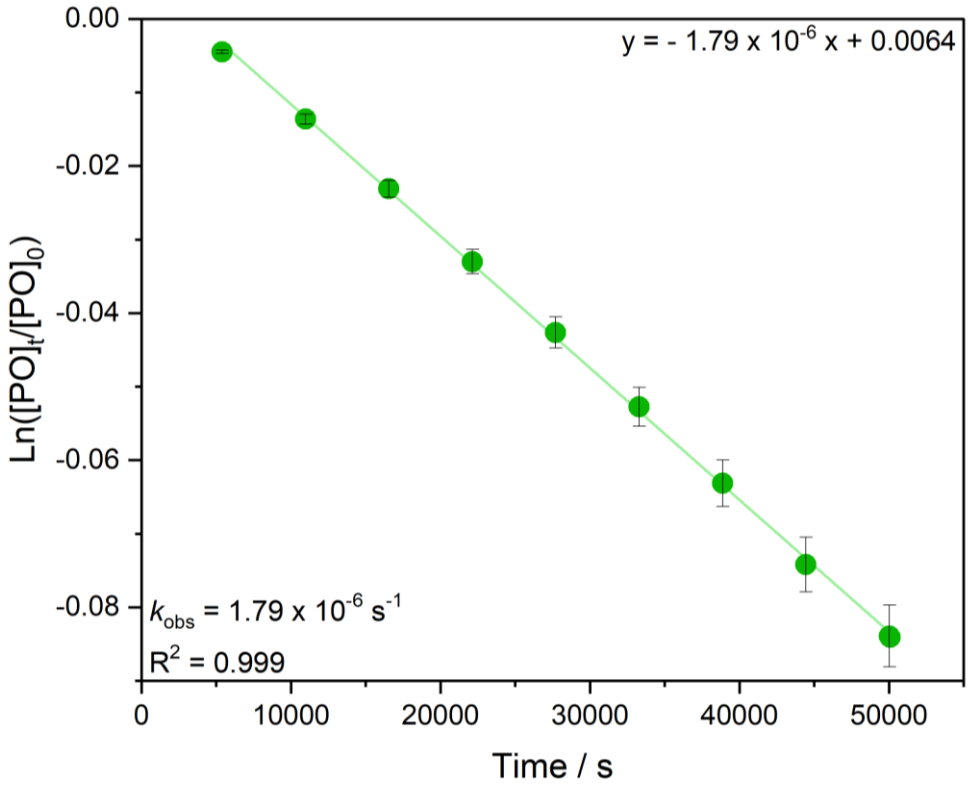


Figure S2.21: Plot of $Ln([PO]_t/[PO]_0)$ against time for PO/CO_2 ROCOP catalysed by Co(III)Sr(II) to calculate k_{obs}. (Every 75th point shown)

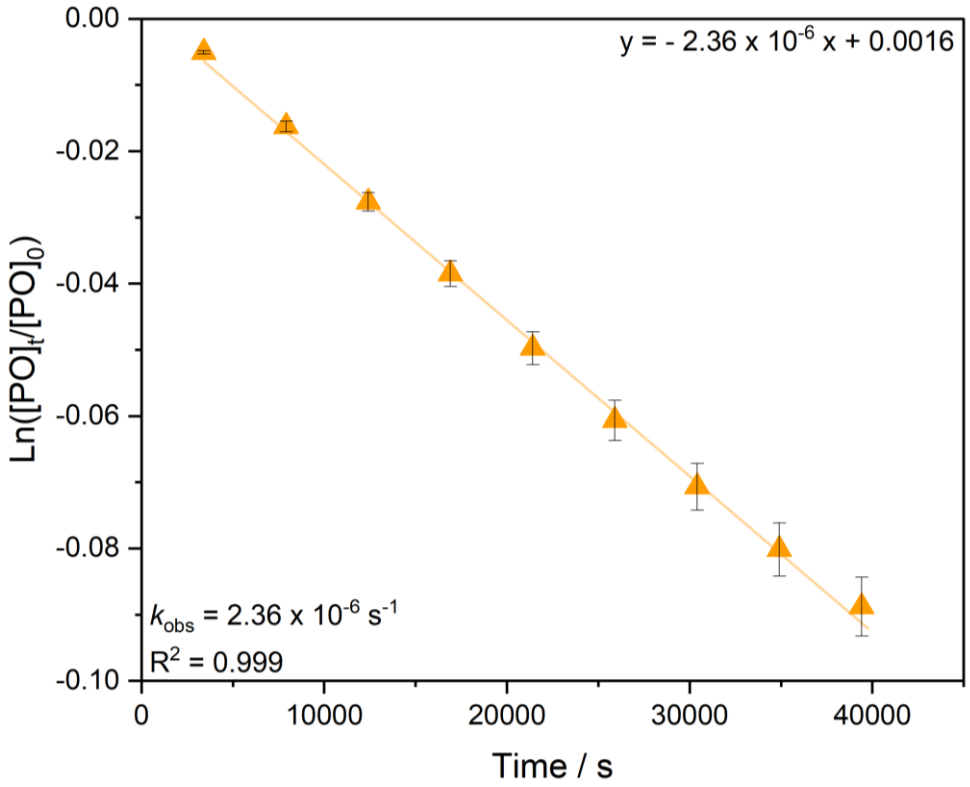


Figure S2.22: Plot of $Ln([PO]_t/[PO]_0)$ against time for PO/CO_2 ROCOP catalysed by Co(III)Ba(II) to calculate k_{obs}. (Every 75th point shown).

Table S2.1: Values for derivation of equation S1

Conversion / %	TON	$[PO]_t$ / M	$\ln([PO]_t/[PO]_0)$
5	200	13.59	- 0.0513
20	800	12.14	- 0.2231

Table S2.2: Description of parameters used for the derivation of equation S1.

Parameters	Description
$[PO]_t$	Concentration of PO at time *t*
$[PO]_0$	Starting concentration of PO (i.e. at time = 0 s)
k_{obs}	Observed rate coefficient
t	Time
t_i	Initiation time
$TOF_{5\text{-}20\%}$	Turnover frequency between 5 and 20% conversion
$TON_{20\%}$	Turnover number at 20% conversion
$TON_{5\%}$	Turnover number at 5% conversion
$t_{20\%}$	Time at 20% conversion
$t_{5\%}$	Time at 5% conversion

Derivation of Equation S2.1:

$$\ln\frac{[PO]_t}{[PO]_0} = -k_{obs}t + t_i$$

$$TOF_{5-20\%} = \frac{TON_{20\%} - TON_{5\%}}{t_{20\%} - t_{5\%}} = \frac{800 - 200}{t_{20\%} - t_{5\%}} = \frac{600}{t_{20\%} - t_{5\%}}$$

$$t = \frac{\ln\frac{[PO]_t}{[PO]_0} - t_i}{-k_{obs}}$$

$$t_{5\%} = \frac{0.05 - t_i}{-k_{obs}} \quad t_{20\%} = \frac{0.22 - t_i}{-k_{obs}}$$

$$t_{20\%} - t_{5\%} = \frac{0.22 - t_i}{-k_{obs}} - \frac{0.05 - t_i}{-k_{obs}} = \frac{0.17}{k_{obs}}$$

$$TOF_{5-20\%} = \frac{600 \times k_{obs} \times 3600\ h^{-1}}{0.17} = \boldsymbol{k_{obs} \times 12.71 \times 10^6\ h^{-1}} \qquad \text{Eq. S2.1}$$

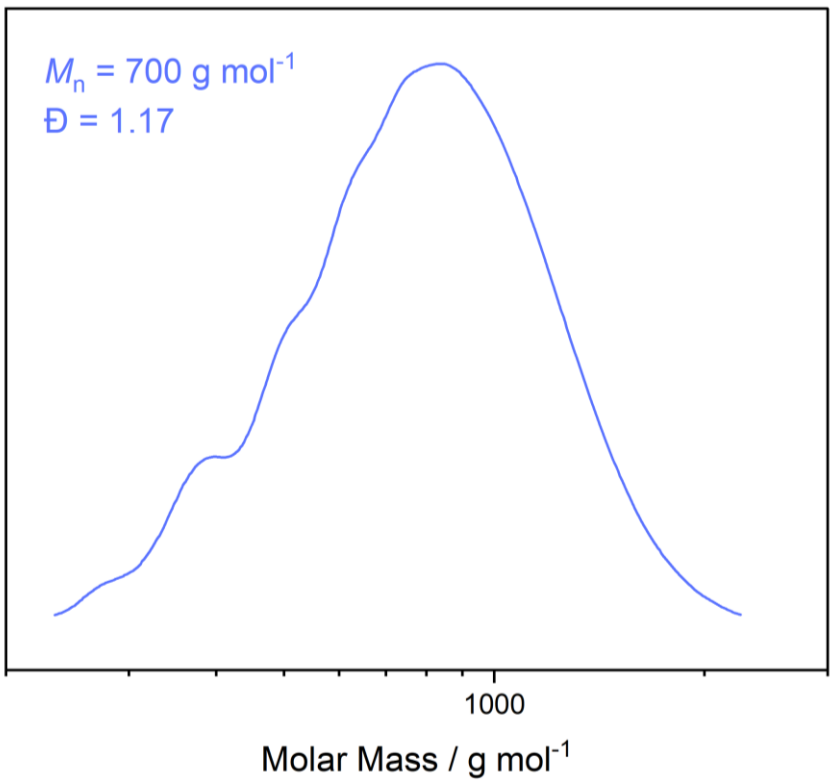


Figure S2.23. GPC trace for PO/CO_2 polymerisation with Co(III)Ca(II) in THF, using narrow dispersity polystyrene standards.

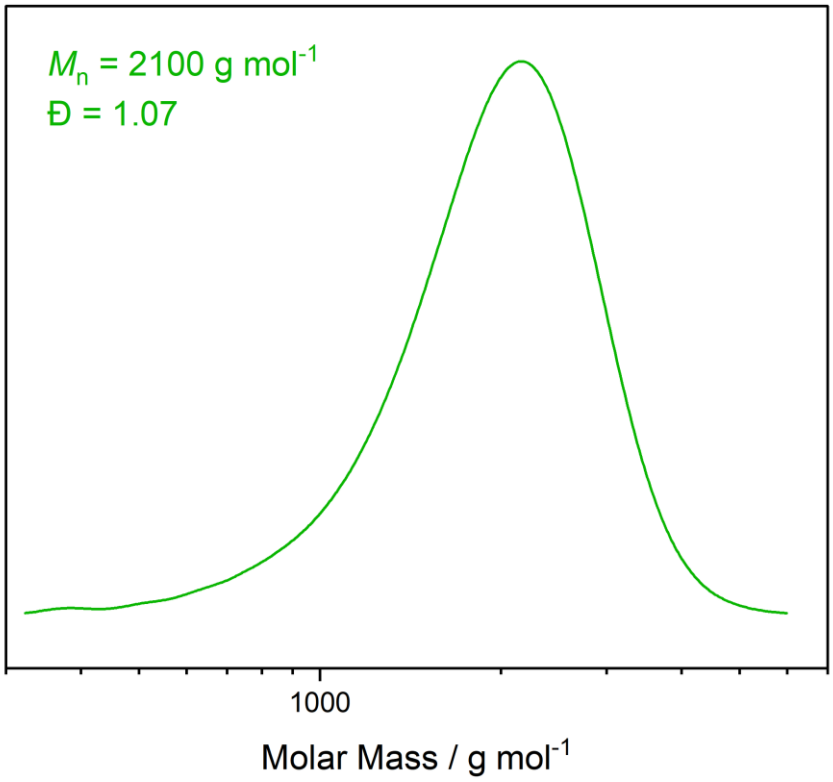


Figure S2.24. GPC trace for PO/CO_2 polymerisation with Co(III)Sr(II) in THF, using narrow dispersity polystyrene standards.

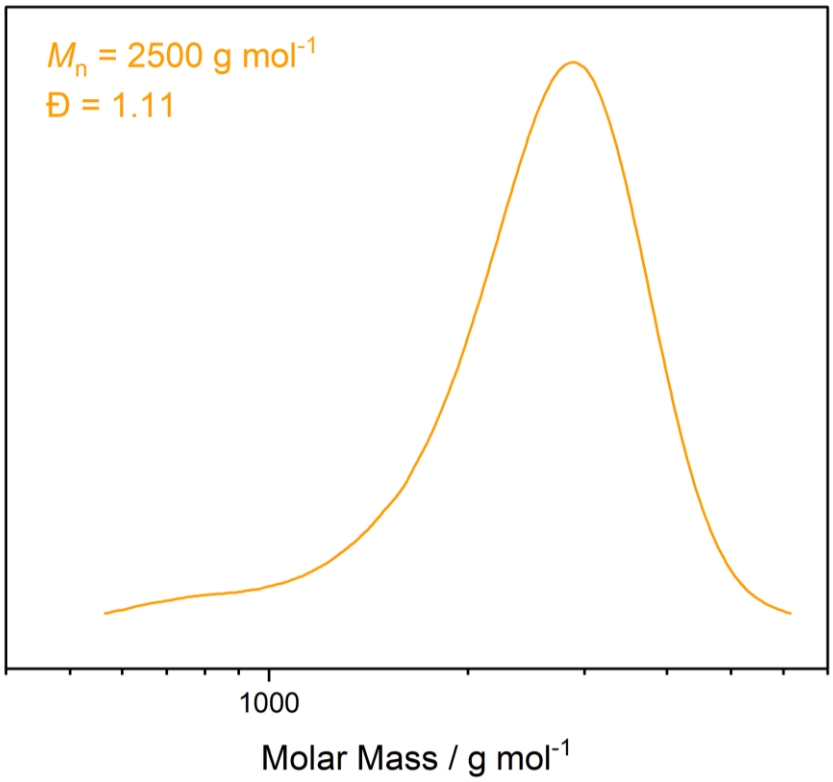


Figure S2.25. GPC trace for PO/CO_2 polymerisation with Co(III)Ba(II) in THF, using narrow dispersity polystyrene standards.

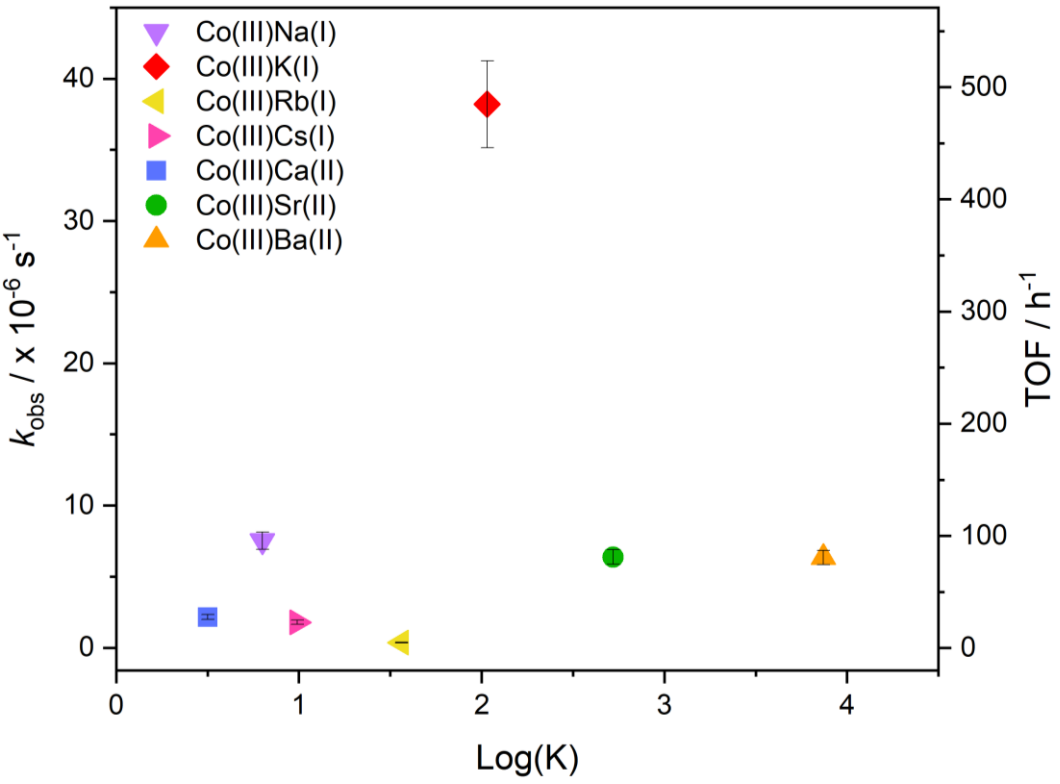


Figure S2.26. Plot of TOF against Log(K) (where K is the equilibrium constant for M(I/II) coordination within 18-crown-6 for a 1:1 reaction in aqueous solution at 25 °C) for PO/CO_2 ROCOP catalysed by Co(III)M(I/II).

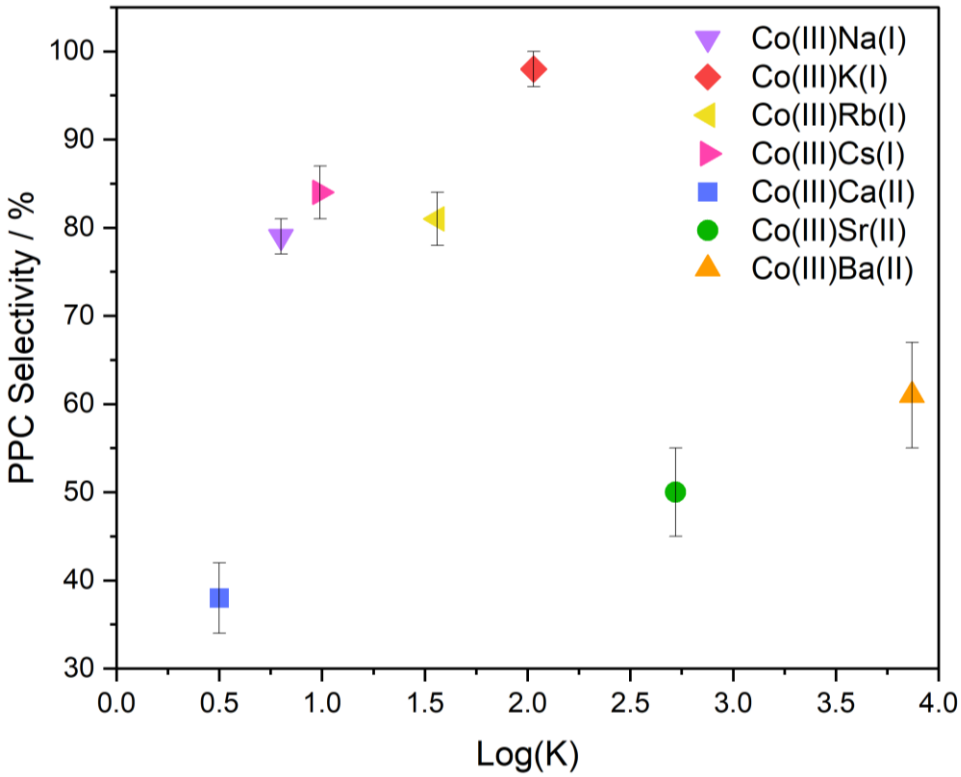


Figure S2.27. Plot of selectivity for PPC against Log(K) (where K is the equilibrium constant for M(I/II) coordination within 18-crown-6 for a 1:1 reaction in aqueous solution at 25 °C) for PO/CO_2 ROCOP catalysed by Co(III)M(I/II).

Table S2.3: Values for derivation of equation S2

Conversion / %	TON	$[PA]_t$ / M
5	5	1.36
7	70	0.43

Table S2.4: Description of parameters used for the derivation of equation S2.

Parameters	Description
$[PA]_t$	Concentration of PA at time *t*
$[PA]_0$	Starting concentration of PA (i.e. at time = 0 s)
k_{obs}	Observed rate coefficient
t	Time
t_i	Initiation time
$TOF_{5\text{-}70\%}$	Turnover frequency between 5 and 70% conversion
$TON_{70\%}$	Turnover number at 70% conversion
$TON_{5\%}$	Turnover number at 5% conversion
$t_{70\%}$	Time at 70% conversion
$t_{5\%}$	Time at 5% conversion

Derivation of Equation S2.2:

$$[\mathrm{PA}]_t = -k_{obs}t + c$$

$$\mathrm{TOF}_{5-70\%} = \frac{\mathrm{TON}_{70\%} - \mathrm{TON}_{5\%}}{t_{70\%} - t_{5\%}} = \frac{70 - 5}{t_{70\%} - t_{5\%}} = \frac{65}{t_{70\%} - t_{5\%}}$$

$$t = -\frac{[\mathrm{PA}]_t + c}{k_{obs}}$$

$$t_{5\%} = \frac{1.36 - t_i}{-k_{obs}} \quad t_{70\%} = \frac{0.43 - t_i}{-k_{obs}}$$

$$t_{70\%} - t_{5\%} = \frac{0.43 - t_i}{-k_{obs}} - \frac{1.36 - t_i}{-k_{obs}} = \frac{0.93}{k_{obs}}$$

$$\mathrm{TOF}_{5-70\%} = \frac{65 \times k_{obs} \times 3600\ \mathrm{h}^{-1}}{0.93} = \boldsymbol{k_{obs} \times 251.61 \times 10^3\ h^{-1}} \qquad \text{Eq. S2.2}$$

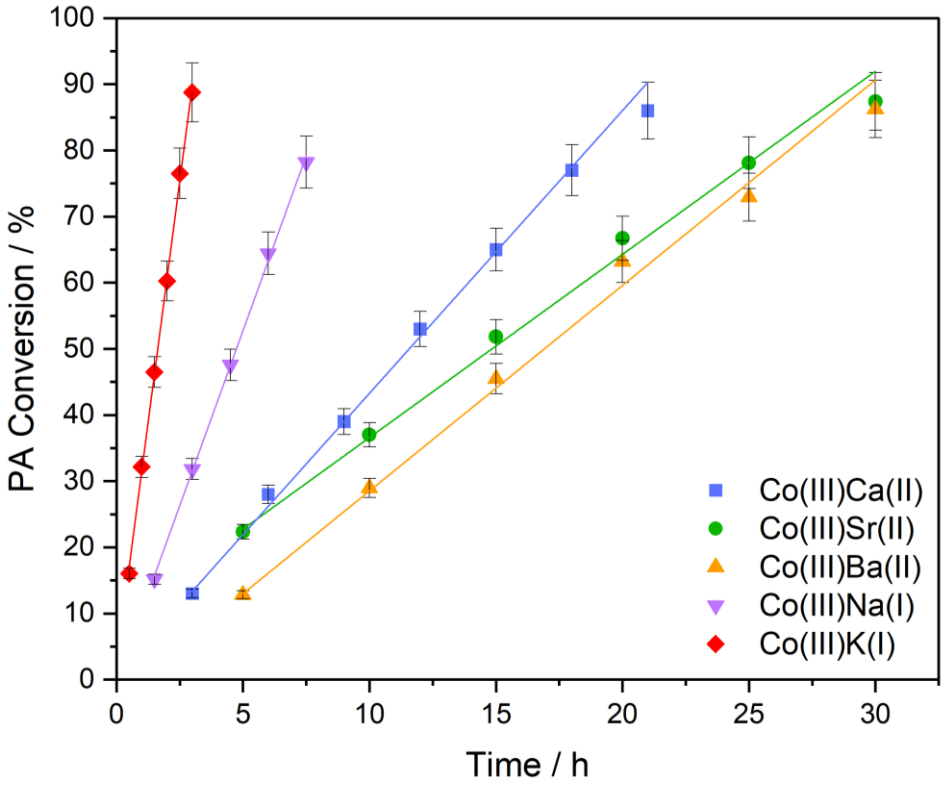


Figure S2.28. Representative conversion vs. time plots for PO/PA ROCOP catalysed by Co(III)M(I/II) (M(I/II) = Na(I), K(I), Ca(II), Sr(II), Ba(II)).

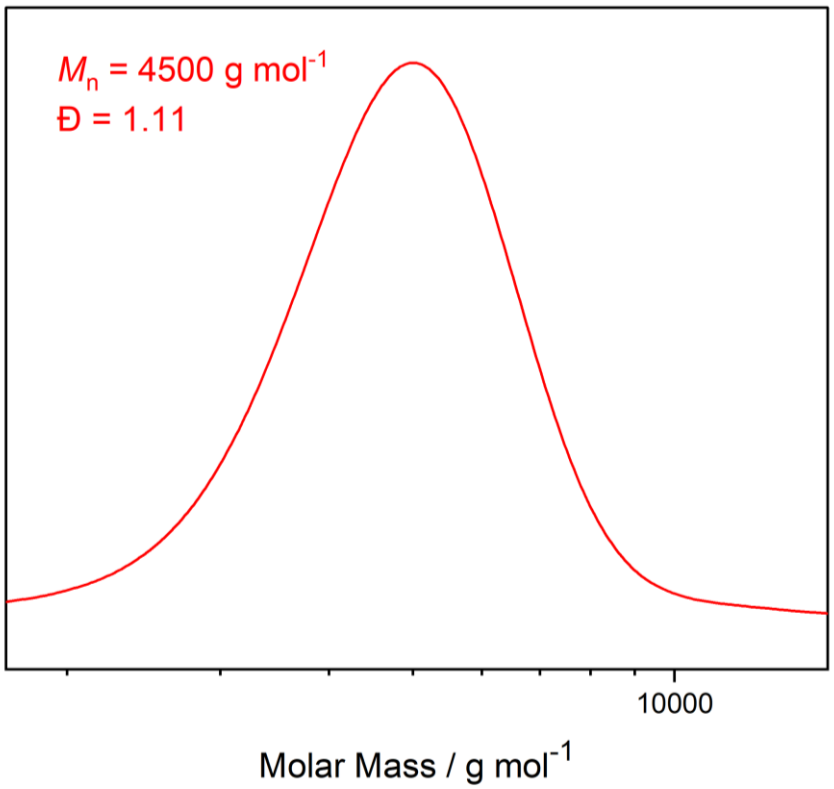


Figure S2.29. GPC trace for PO/PA co-polymerisation catalysed by Co(III)K(I).

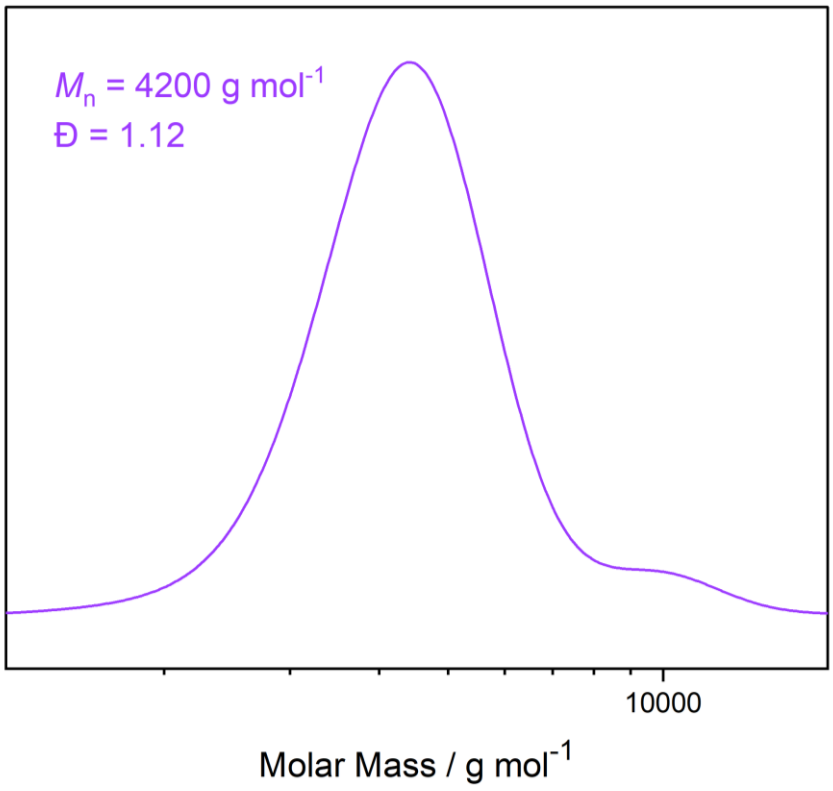


Figure S2.30. GPC trace for PO/PA co-polymerisation catalysed by Co(III)Na(I).

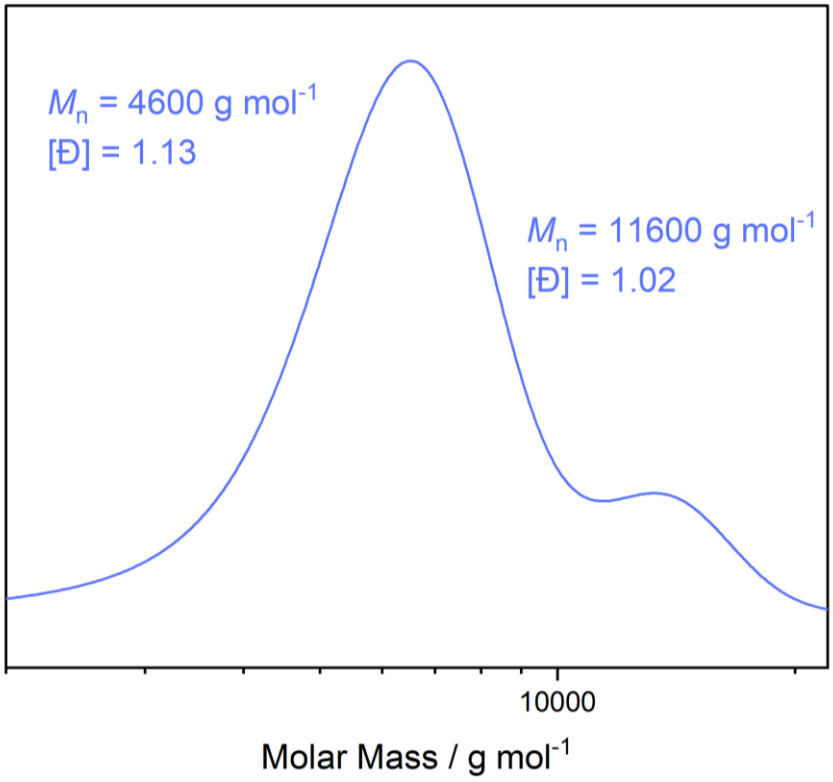


Figure S2.31. GPC trace for PO/PA co-polymerisation catalysed by Co(III)Ca(II).

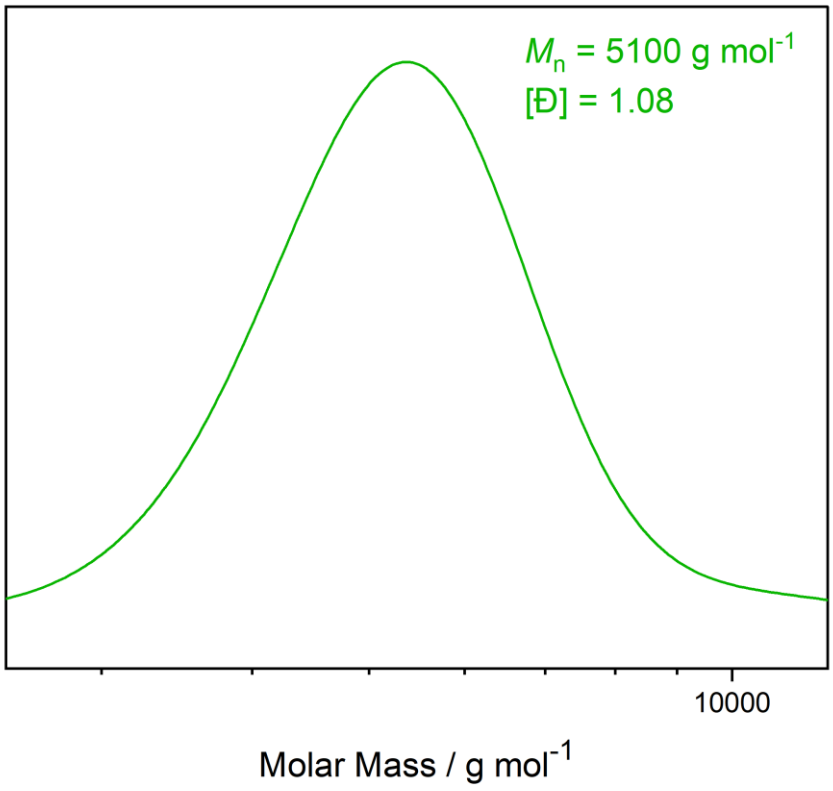


Figure S2.32. GPC trace for PO/PA co-polymerisation catalysed by Co(III)Sr(II).

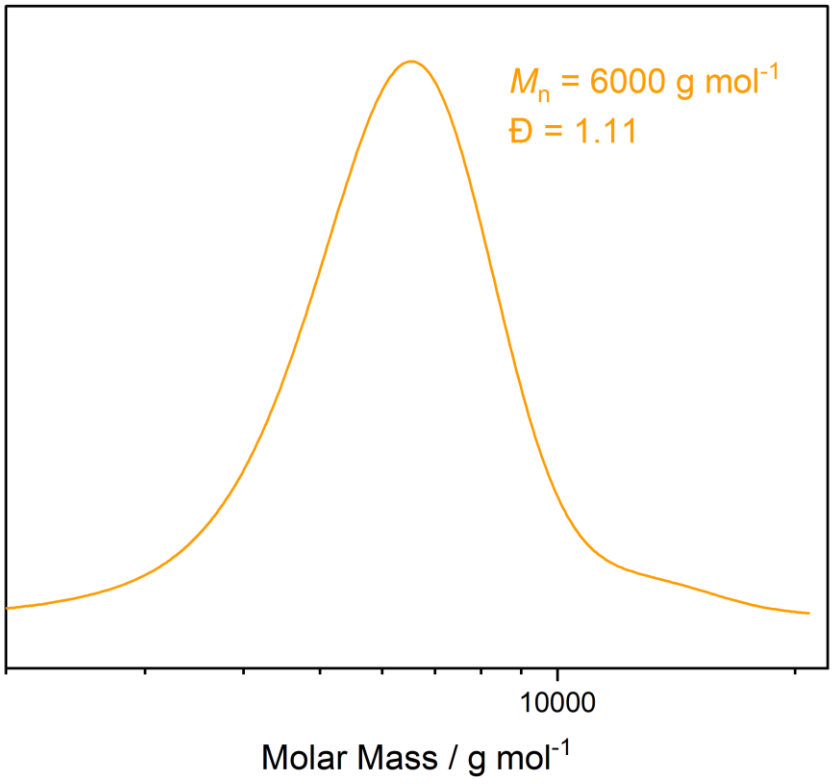


Figure S2.33. GPC trace for PO/PA co-polymerisation catalysed by Co(III)Ba(II).

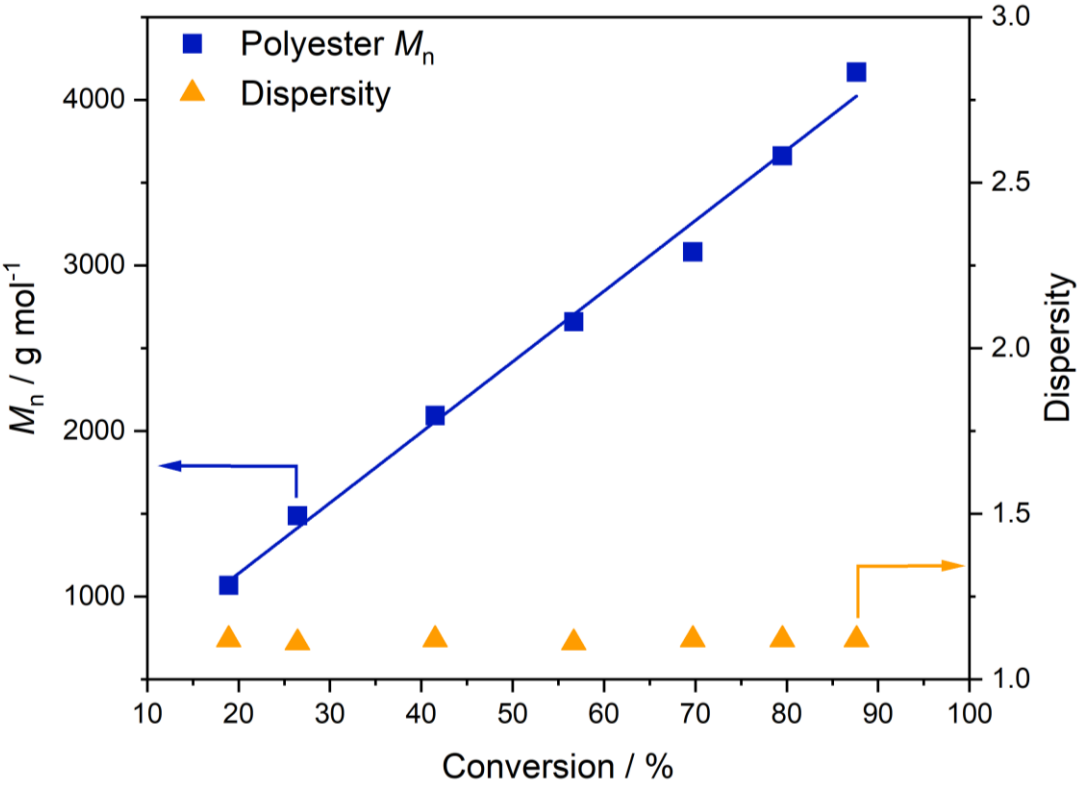


Figure S2.34. Plots polyester molar masses (blue squares and line) and dispersity (orange triangles) of polyester against conversion for PO/PA ROCOP catalysed by Co(III)Na(I).

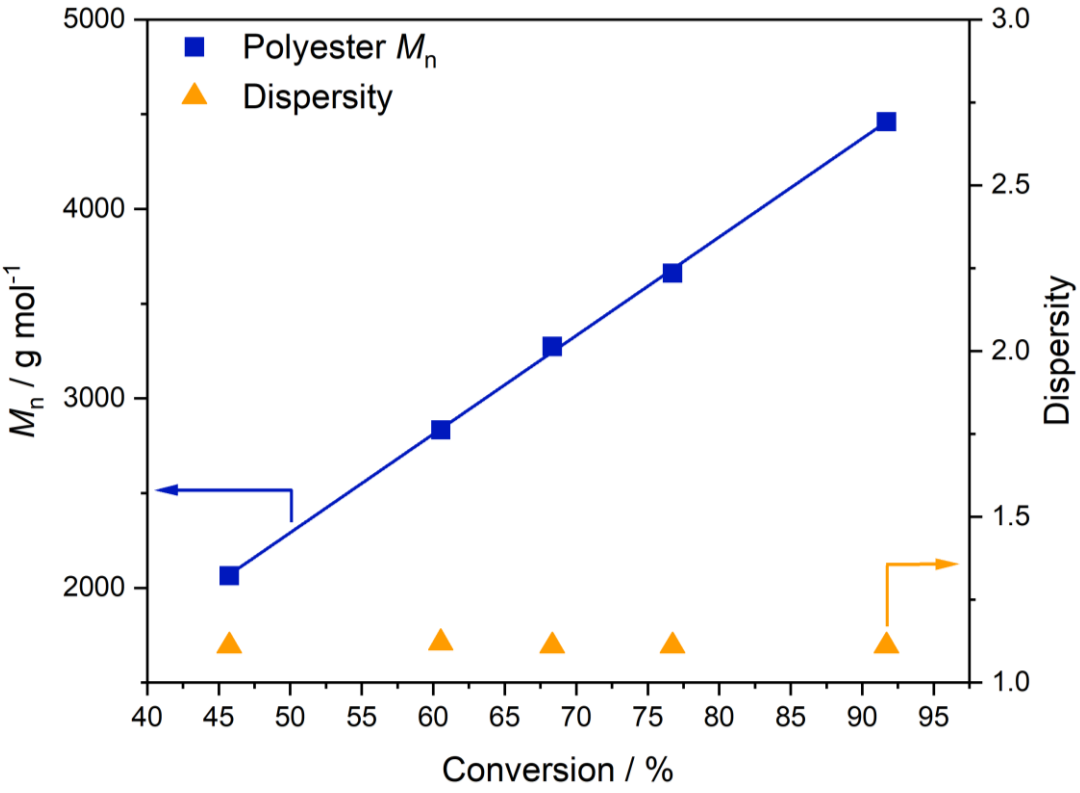


Figure S2.35. Plots polyester molar masses (blue squares and line) and dispersity (orange triangles) of polyester against conversion for PO/PA ROCOP catalysed by Co(III)K(I).

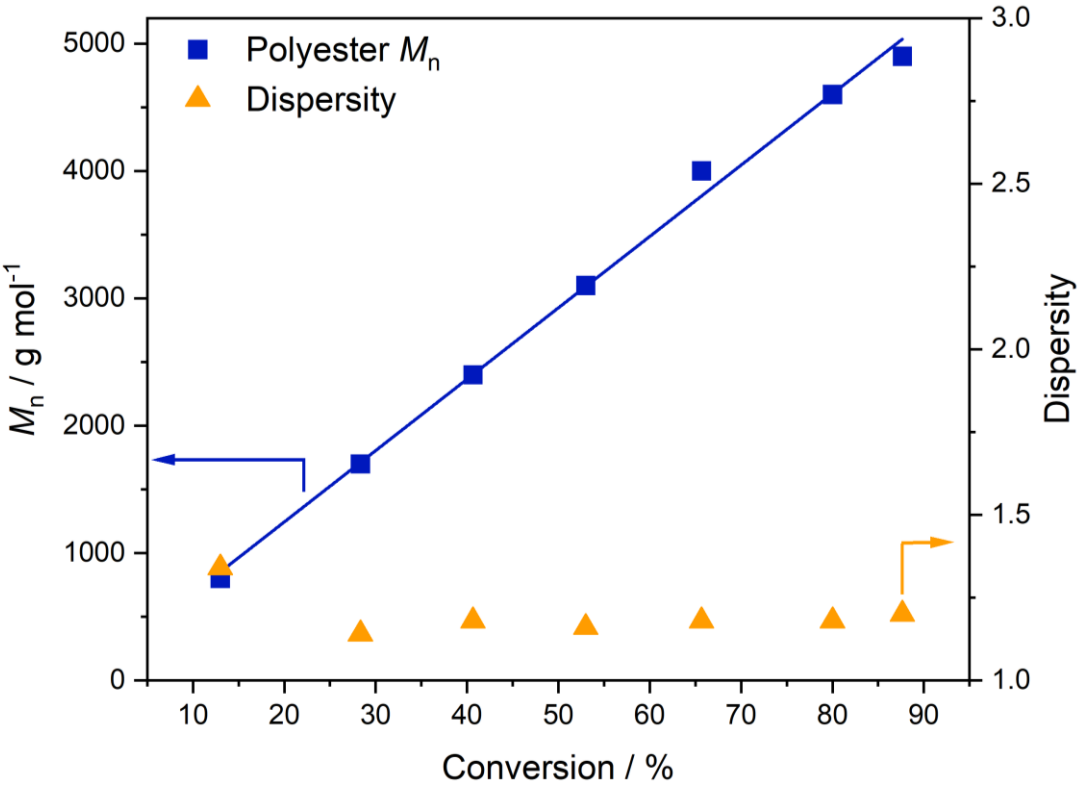


Figure S2.36. Plots of molar masses (blue squares and line) and dispersity (orange triangles) of polyester against conversion for PO/PA ROCOP catalysed by Co(III)Ca(II).

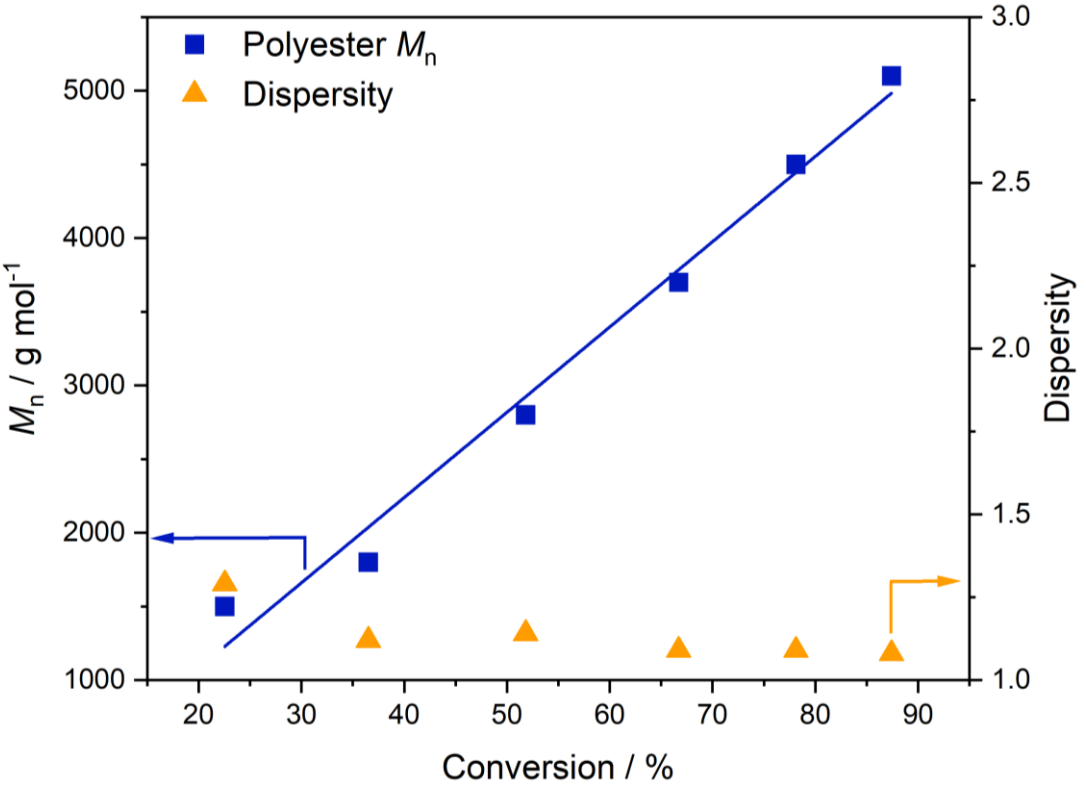


Figure S2.37. Plots of theoretical (dashed blue line) and experimental (solid blue squares and line) molar masses and dispersity (orange triangles) of polyester against conversion for PO/PA ROCOP catalysed by Co(III)Sr(II).

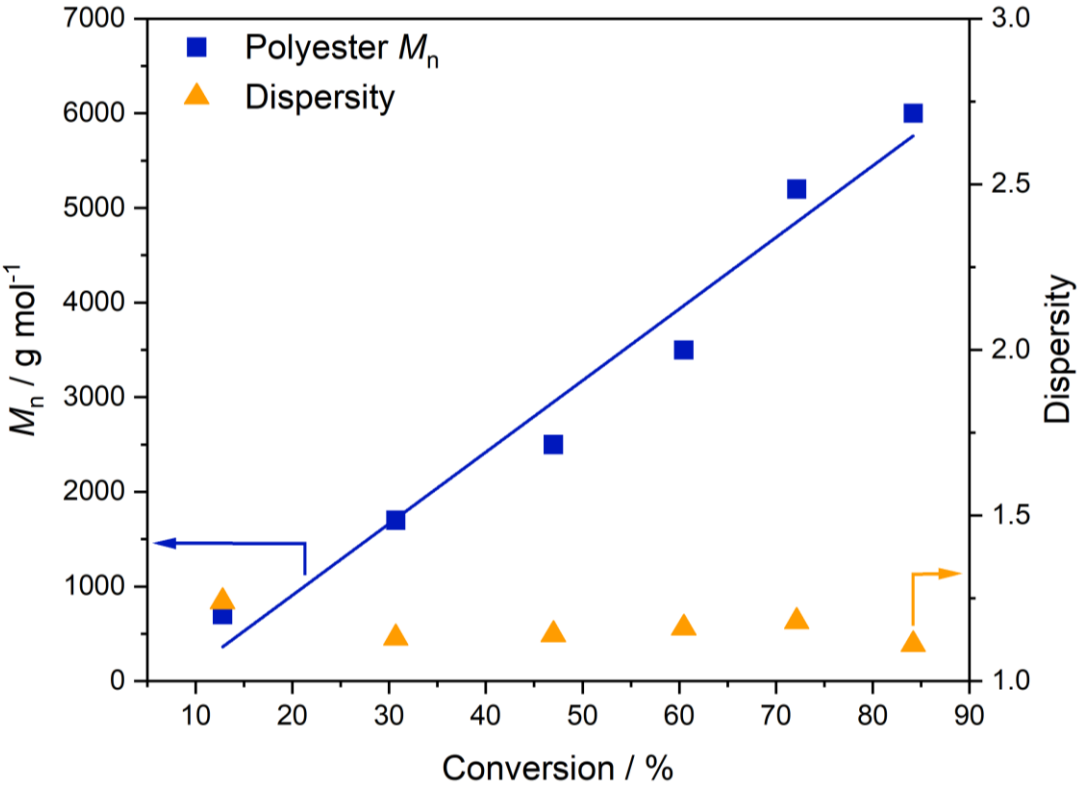


Figure S2.38. Plots of theoretical (dashed blue line) and experimental (solid blue squares and line) molar masses and dispersity (orange triangles) of polyester against conversion for PO/PA ROCOP catalysed by Co(III)Ba(II).

Table S2.5: Values for derivation of equation S3.

Conversion / %	TON	$[LA]_t$ / M	$\ln([LA]_t/[LA]_0)$
5	5	1.36	-0.05
7	70	0.43	-1.20

Table S2.6: Description of parameters used for the derivation of equation S3.

Parameters	Description
$[LA]_t$	Concentration of LA at time *t*
$[LA]_0$	Starting concentration of LA (i.e. at time = 0 s)
k_{obs}	Observed rate coefficient
t	Time
t_i	Initiation time
$TOF_{5\text{-}70\%}$	Turnover frequency between 5 and 70% conversion
$TON_{20\%}$	Turnover number at 20% conversion
$TON_{5\%}$	Turnover number at 5% conversion
$t_{20\%}$	Time at 20% conversion
$t_{5\%}$	Time at 5% conversion

Derivation of Equation S2.3:

$$\ln\frac{[\mathrm{LA}]_t}{[\mathrm{LA}]_0} = -k_{obs}t + t_i$$

$$\mathrm{TOF}_{5-70\%} = \frac{\mathrm{TON}_{70\%} - \mathrm{TON}_{5\%}}{t_{70\%} - t_{5\%}} = \frac{70 - 5}{t_{70\%} - t_{5\%}} = \frac{65}{t_{70\%} - t_{5\%}}$$

$$t = \frac{\ln\frac{[\mathrm{LA}]_t}{[\mathrm{LA}]_0} - t_i}{-k_{obs}}$$

$$t_{5\%} = \frac{0.05 - t_i}{-k_{obs}} \quad t_{70\%} = \frac{1.20 - t_i}{-k_{obs}}$$

$$t_{70\%} - t_{5\%} = \frac{1.20 - t_i}{-k_{obs}} - \frac{0.05 - t_i}{-k_{obs}} = \frac{1.15}{k_{obs}}$$

$$\mathrm{TOF}_{5-70\%} = \frac{65 \times k_{obs} \times 3600\ \mathrm{h}^{-1}}{1.15} = \boldsymbol{k_{obs} \times 203.48 \times 10^3\ \mathrm{h}^{-1}} \qquad \text{Eq. S2.3}$$

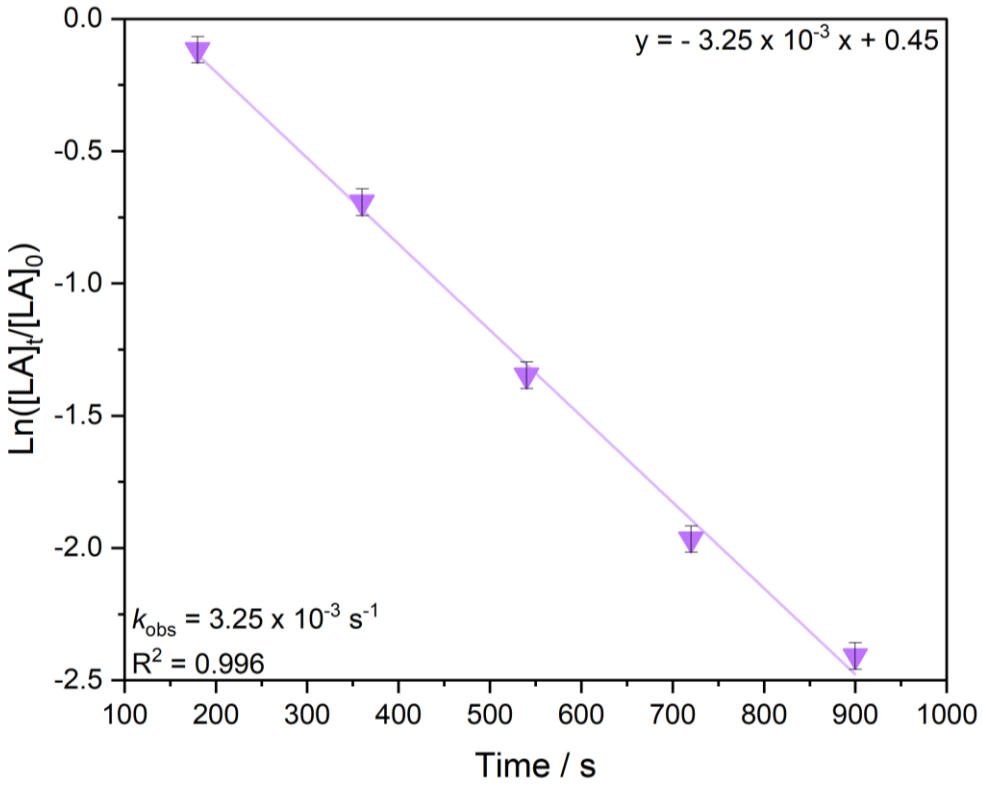


Figure S2.39. Representative semi-logarithmic plot for *rac*-LA ROP using Co(III)Na(I), k_{obs} calculated from the gradient of the straight line.

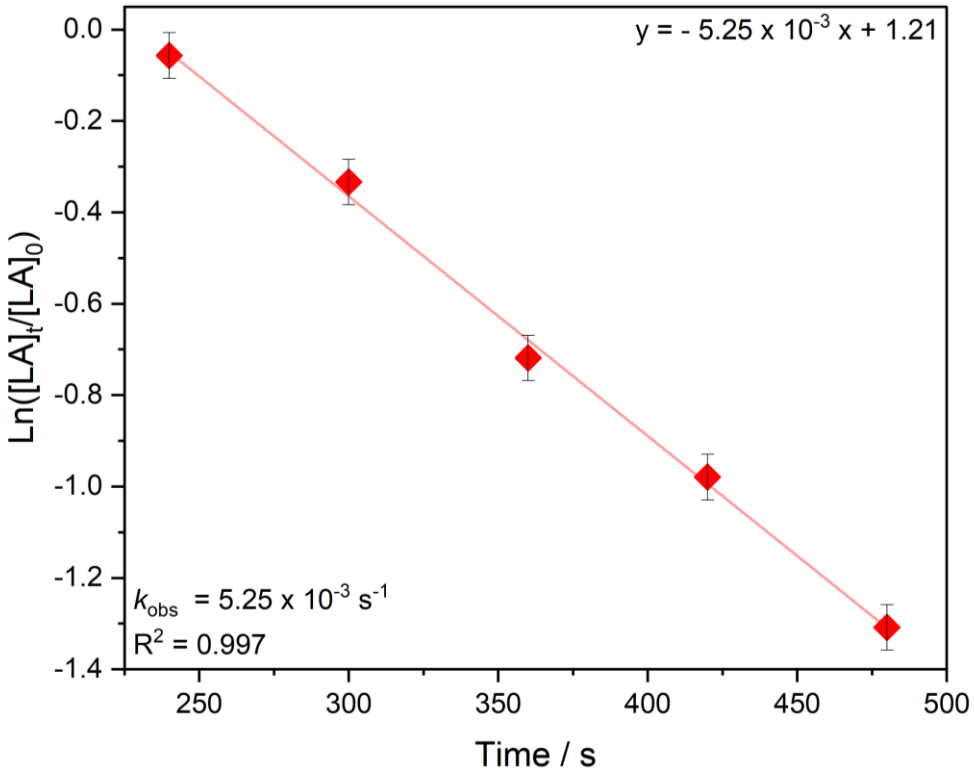


Figure S2.40. Representative plot of [LA] against time for *rac*-LA ROP using Co(III)K(I), conversion determined by ^{1}H NMR spectroscopy.

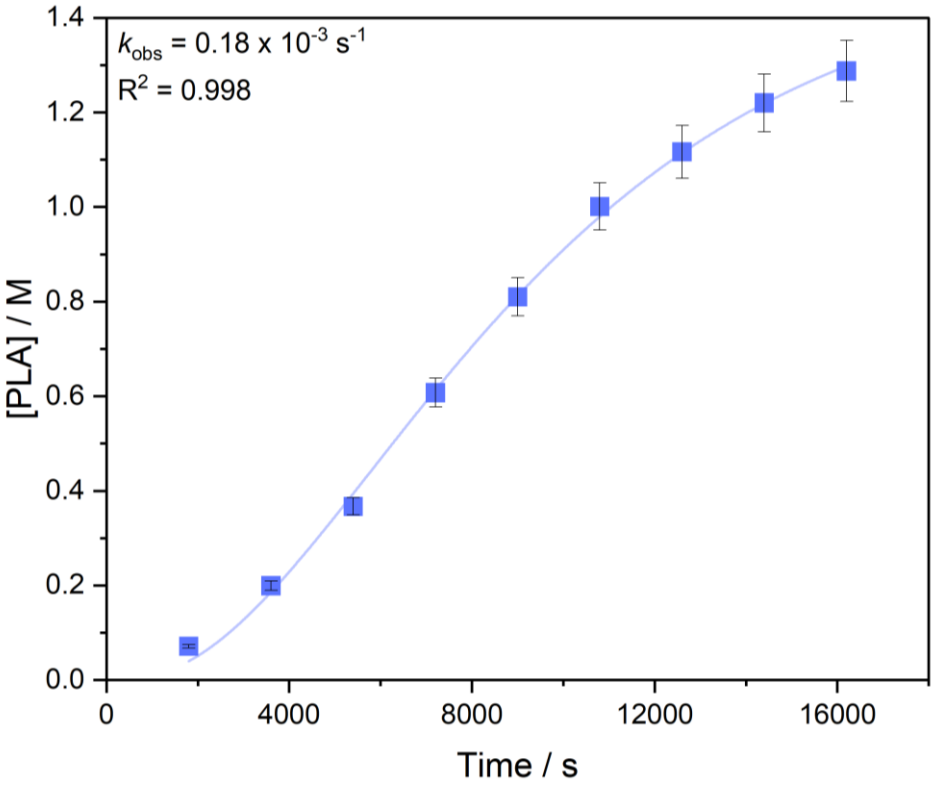


Figure S2.41. Representative plot of [PLA] against time for *rac*-LA ROP using Co(III)Ca(II), conversion determined by ^{1}H NMR spectroscopy. k_{obs} is determined by fitting a sigmoidal function of the form [PLA] = A(1-exp(-k_{obs}t))^s.

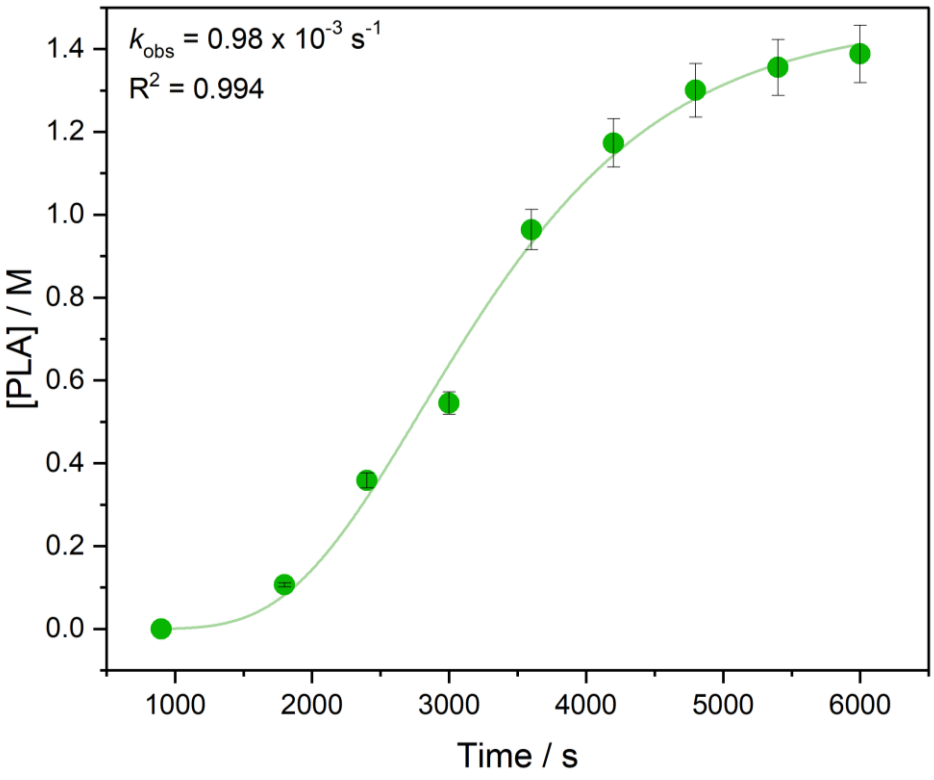


Figure S2.42. Representative plot of [PLA] against time for *rac*-LA ROP using Co(III)Sr(II), conversion determined by ^{1}H NMR spectroscopy. k_{obs} is determined by fitting a sigmoidal function of the form [PLA] = A(1-exp(-k_{obs}t))^s.

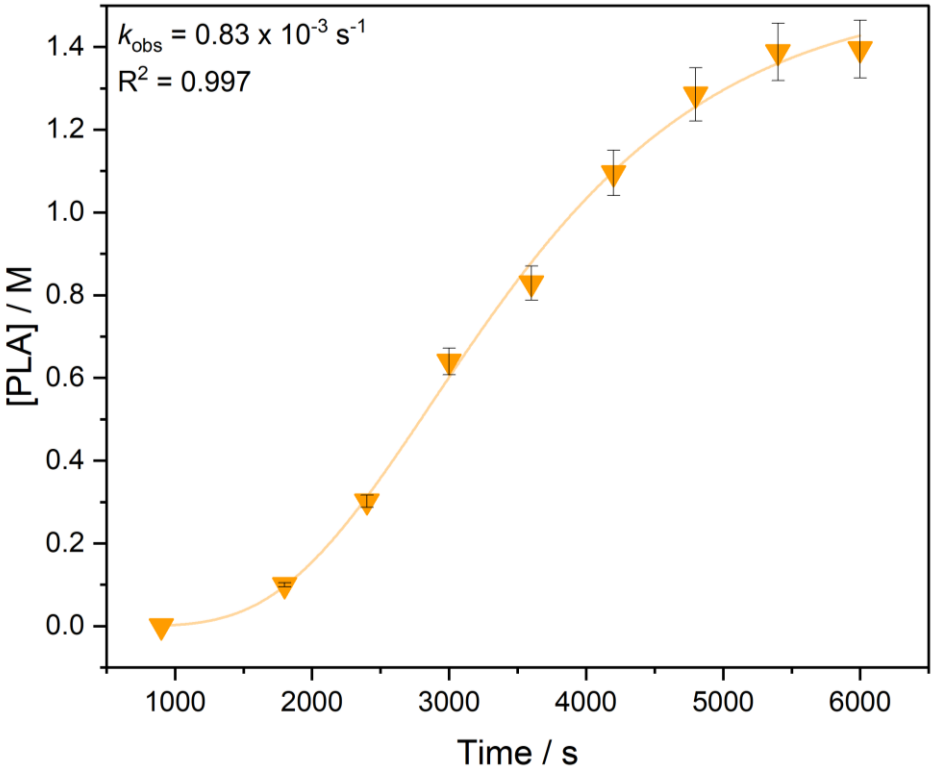


Figure S2.43. Representative plot of [PLA] against time for *rac*-LA ROP using Co(III)Ba(II), conversion determined by ^{1}H NMR spectroscopy. k_{obs} is determined by fitting a sigmoidal function of the form [PLA] = A(1-exp(-k_{obs}t))^s.

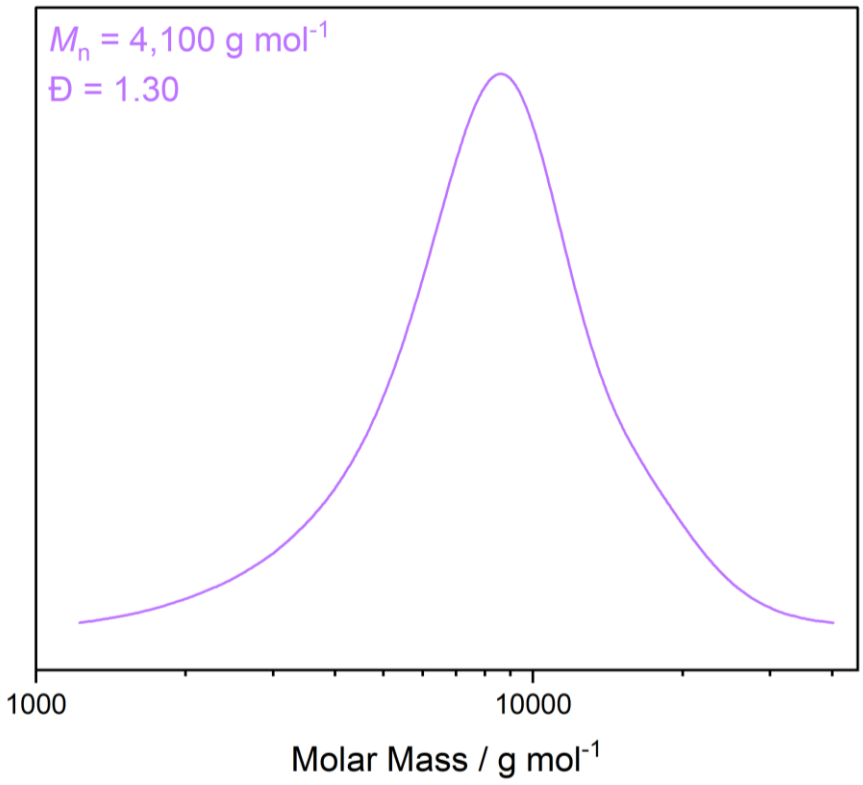


Figure S2.44. GPC trace for *rac*-LA ROP catalysed by Co(III)Na(I)

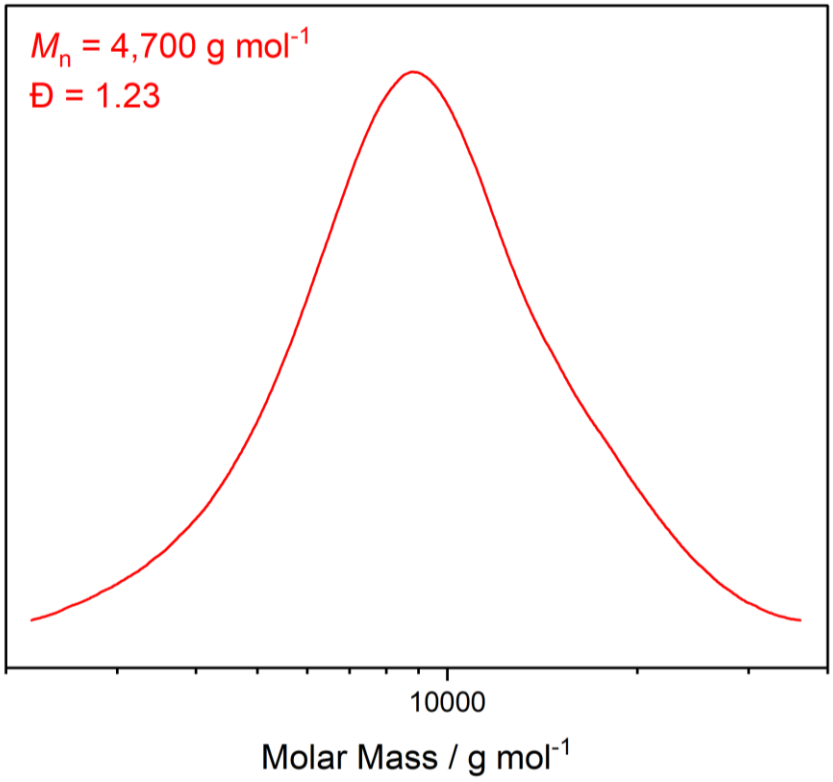


Figure S2.45. GPC trace for *rac*-LA ROP catalysed by Co(III)K(I)

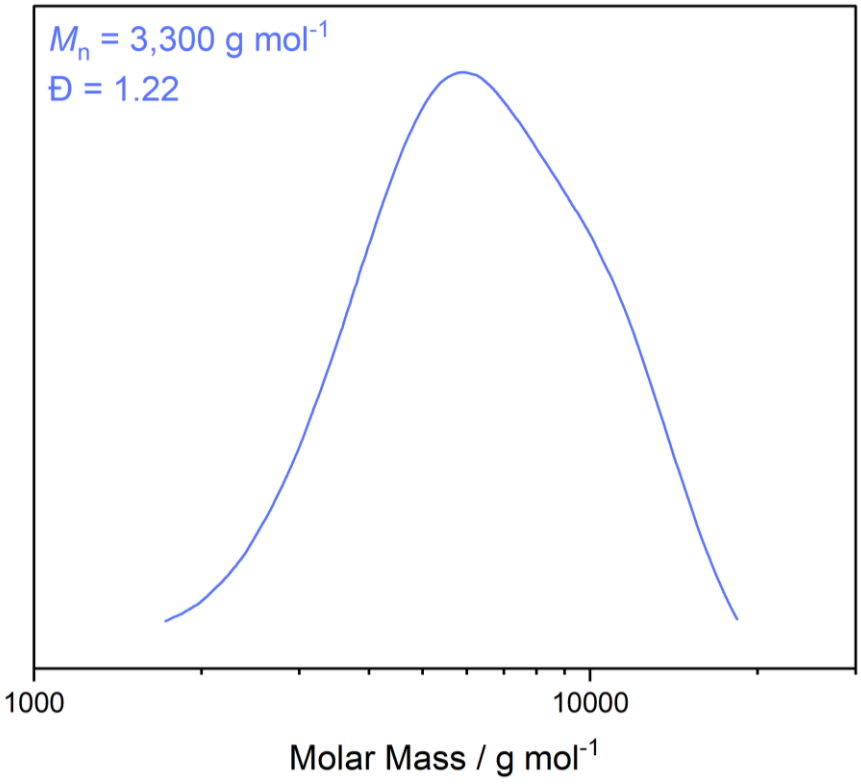


Figure S2.46. GPC trace for *rac*-LA ROP catalysed by Co(III)Ca(II)

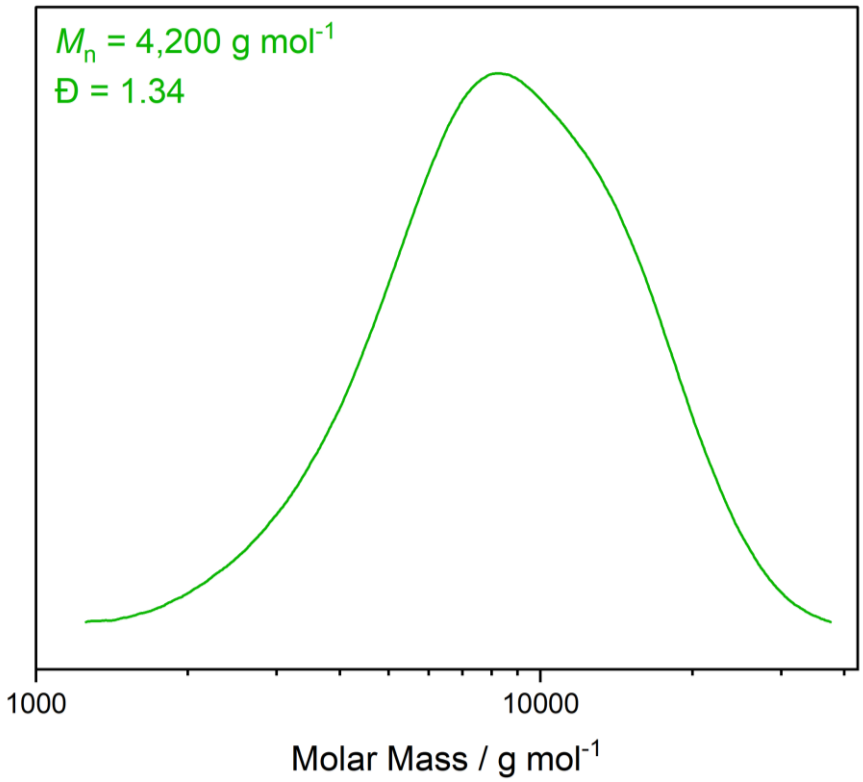


Figure S2.47. GPC trace for *rac*-LA ROP catalysed by Co(III)Sr(II)

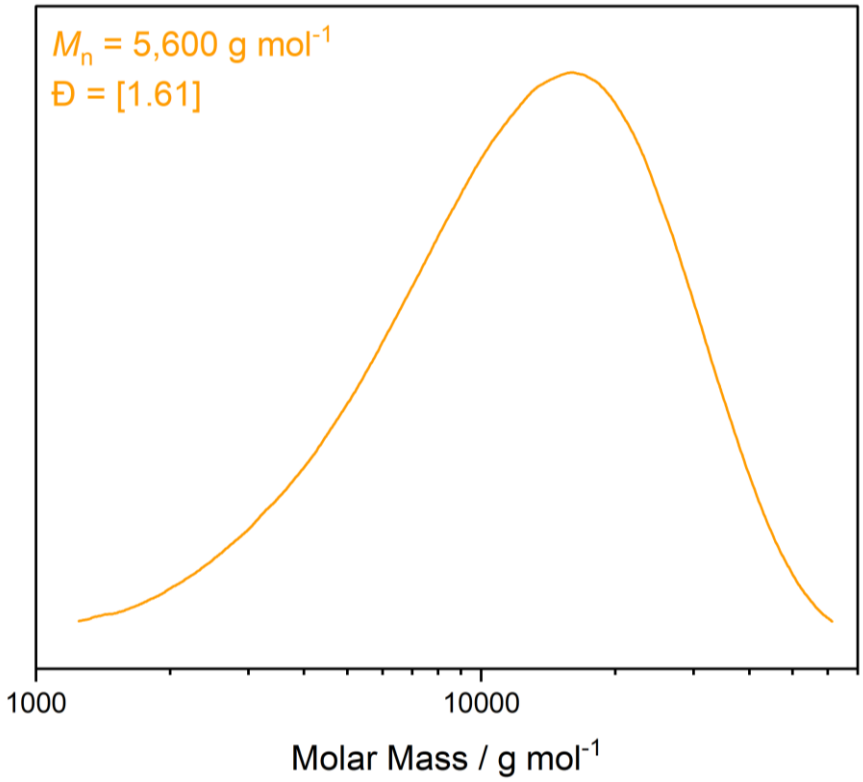


Figure S2.48: GPC trace for *rac*-LA ROP catalysed by Co(III)Ba(II)

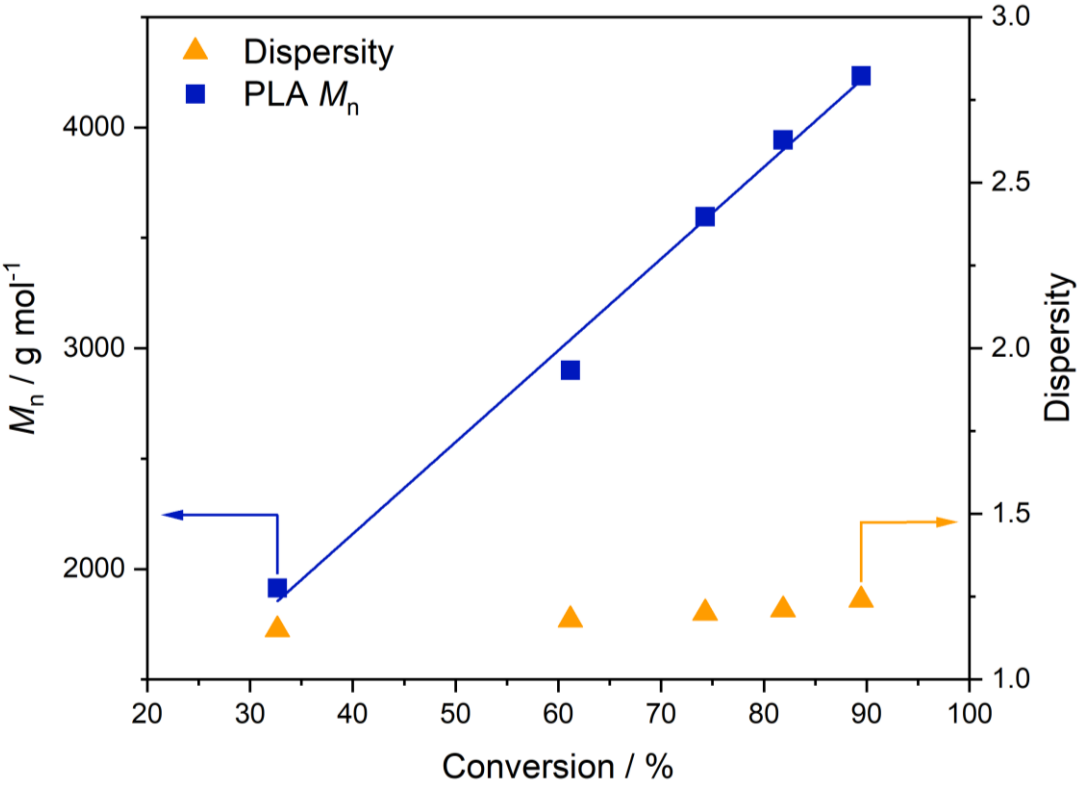


Figure S2.49. Plots of molar masses (blue squares and line) and dispersity (orange triangles) of PLA against conversion for *rac*-LA ROP catalysed by Co(III)Na(I).

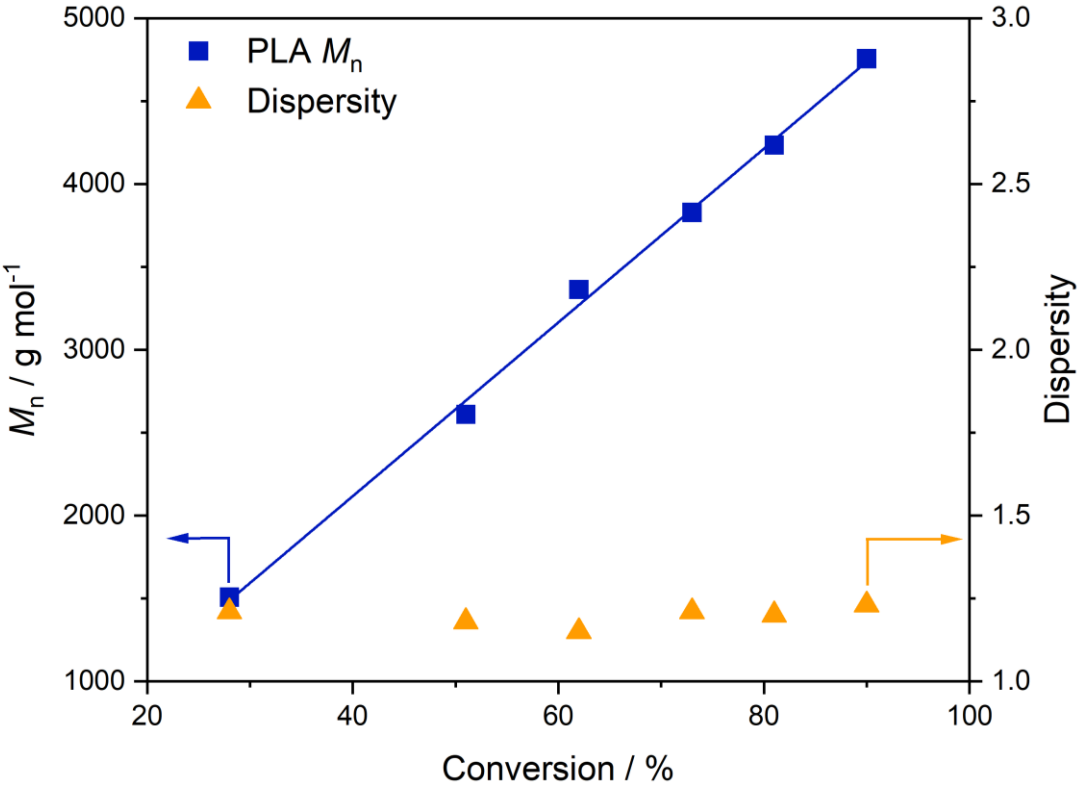


Figure S2.50. Plots of molar masses (blue squares and line) and dispersity (orange triangles) of PLA against conversion for *rac*-LA ROP catalysed by Co(III)K(I).

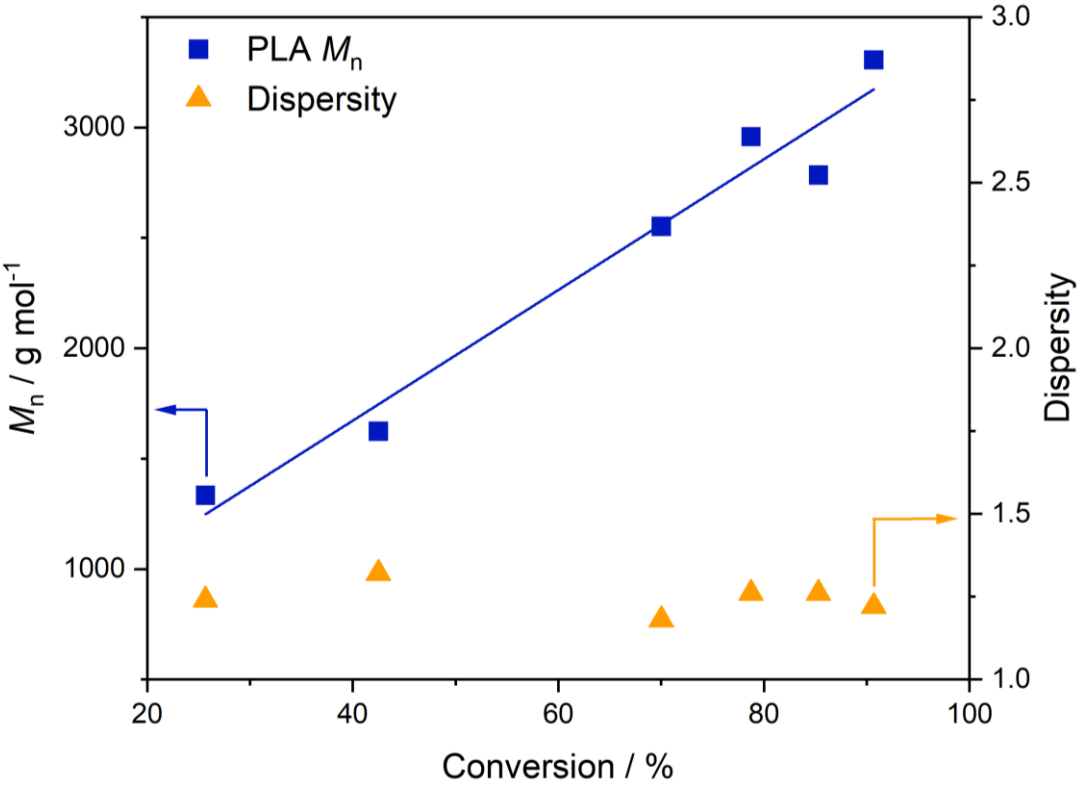


Figure S2.51. Plots of molar masses (blue squares and line) and dispersity (orange triangles) of PLA against conversion for *rac*-LA ROP catalysed by Co(III)Ca(II).

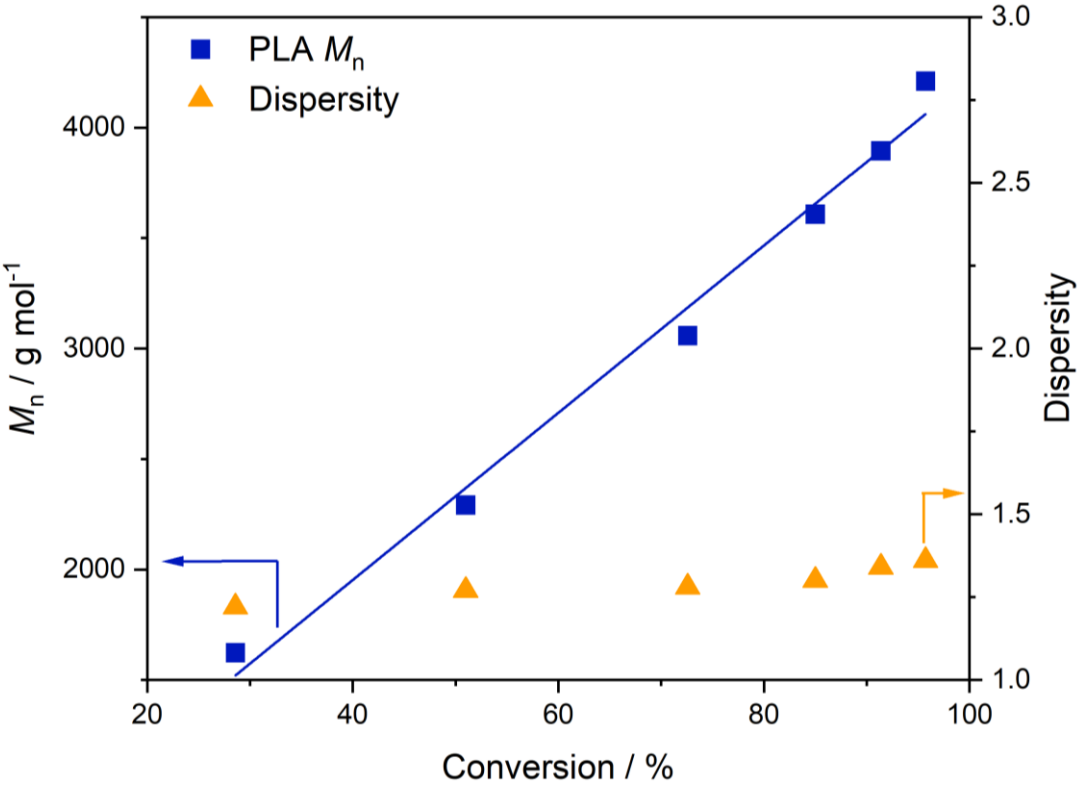


Figure S2.52. Plots of molar masses (blue squares and line) and dispersity (orange triangles) of PLA against conversion for *rac*-LA ROP catalysed by Co(III)Sr(II).

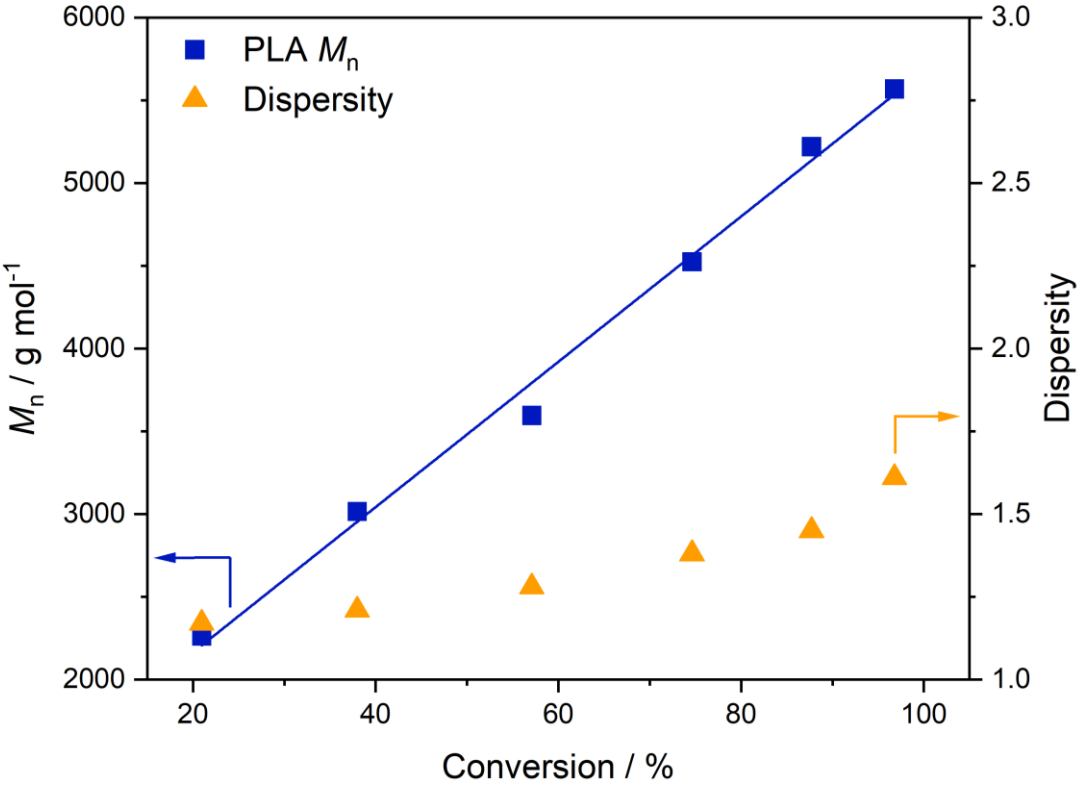


Figure S2.53. Plots of molar masses (blue squares and line) and dispersity (orange triangles) of PLA against conversion for *rac*-LA ROP catalysed by Co(III)Ba(II).

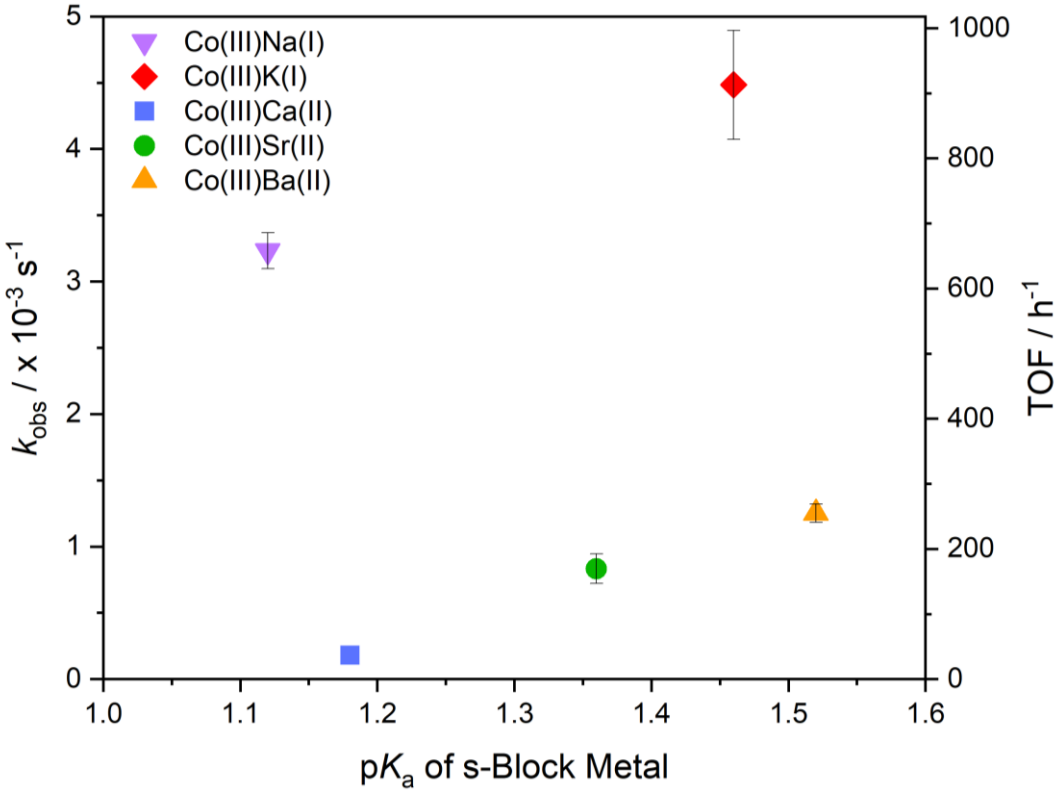


Figure S2.54. Plot of k_{obs} against ionic radius of the s-block metal for *rac*-LA ROP catalysed by Co(III)M(I/II).

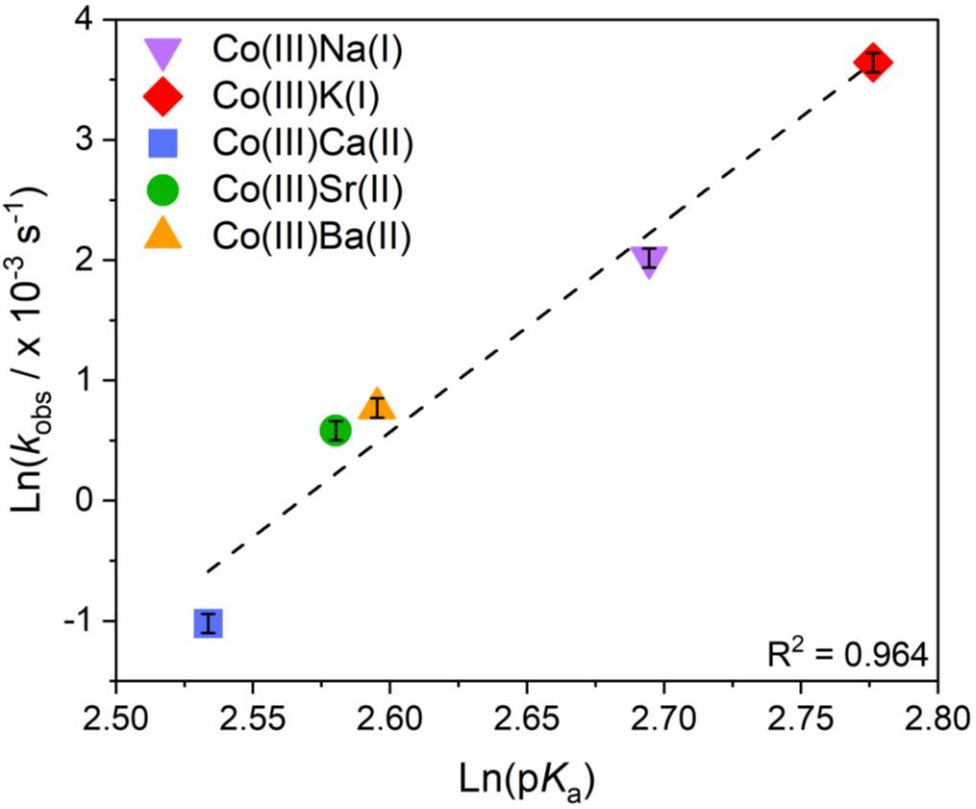


Figure S2.55. Plot of Ln(k_{obs}) vs. Ln(pK_a) for PO/CO_2 ROCOP catalysed by Co(III)M(I/II) (M(I/II) = Na(I), K(I), Ca(II), Sr(II), Ba(II)). The linear fit shows that an exponential fit of k_{obs} vs. pK_a is appropriate.

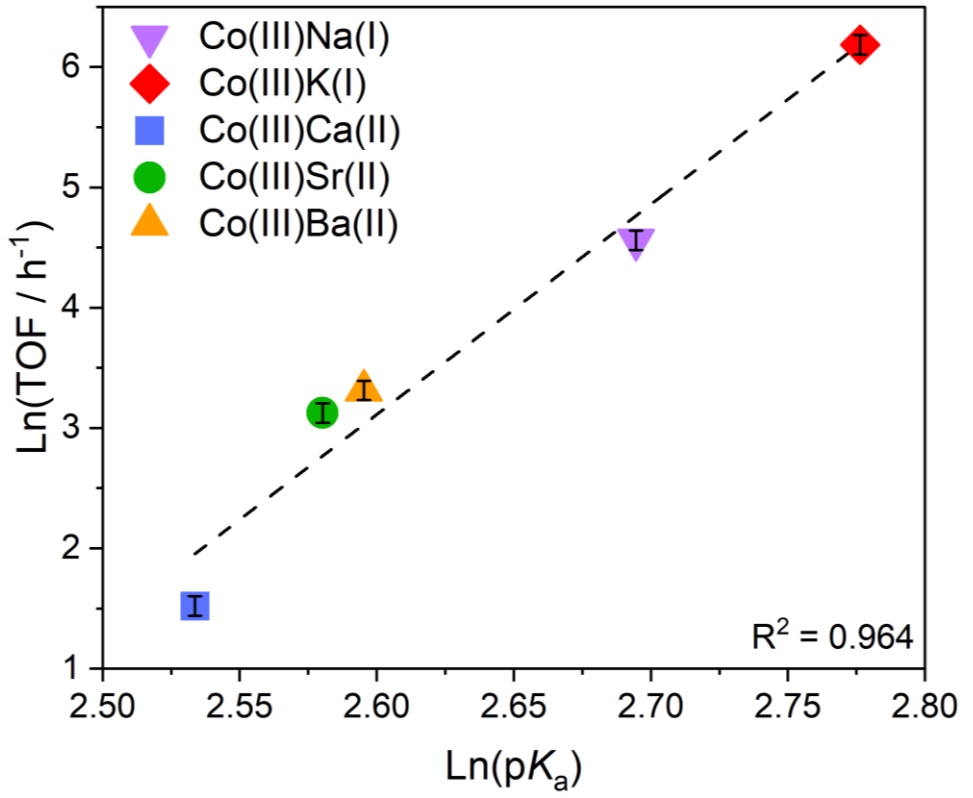


Figure S2.56. Plot of Ln(TOF) vs. Ln(pK_a) for PO/CO_2 ROCOP catalysed by Co(III)M(I/II) (M(I/II) = Na(I), K(I), Ca(II), Sr(II), Ba(II)). The linear fit shows that an exponential fit of TOF vs. pK_a is appropriate.

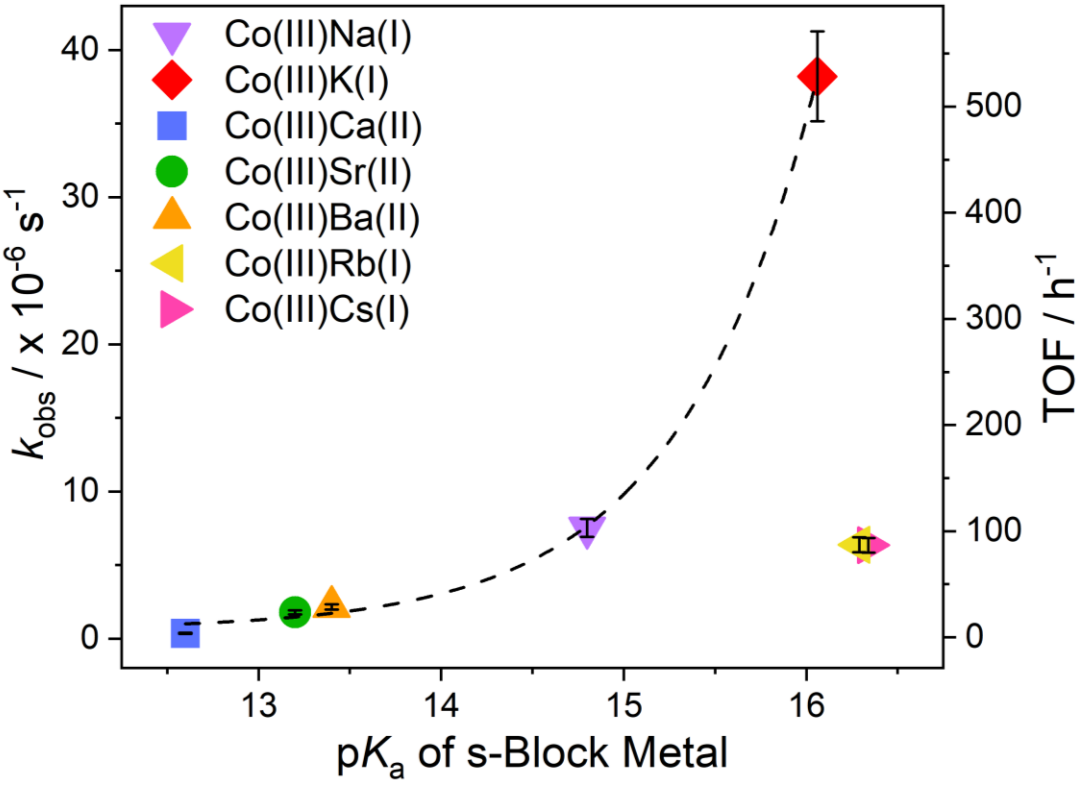


Figure S2.57: Plot of TOF against pK_a of the s-block metal for Co(III)M(I/II)-catalysed PO/CO_2 ROCOP, including values for Co(III)Cs(I) and Co(III)Rb(I).

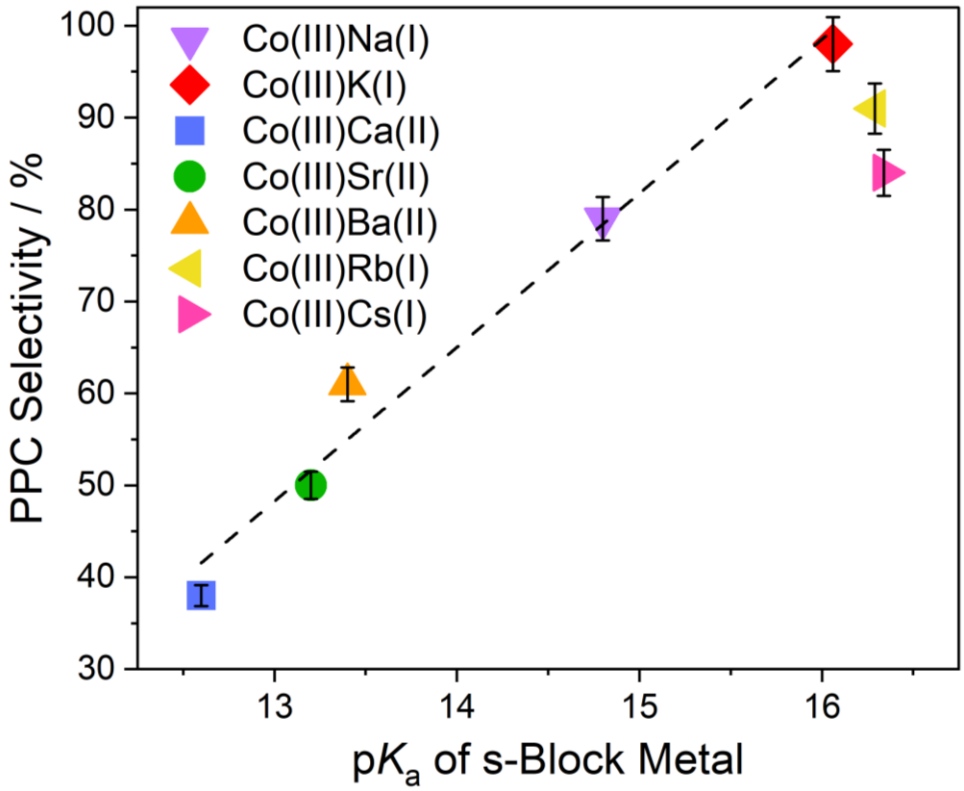


Figure S2.58. Plot of selectivity against pK_a of the s-block metal for Co(III)M(I/II)-catalysed PO/CO_2 ROCOP, including values for Co(III)Cs(I) and Co(III)Rb(I).

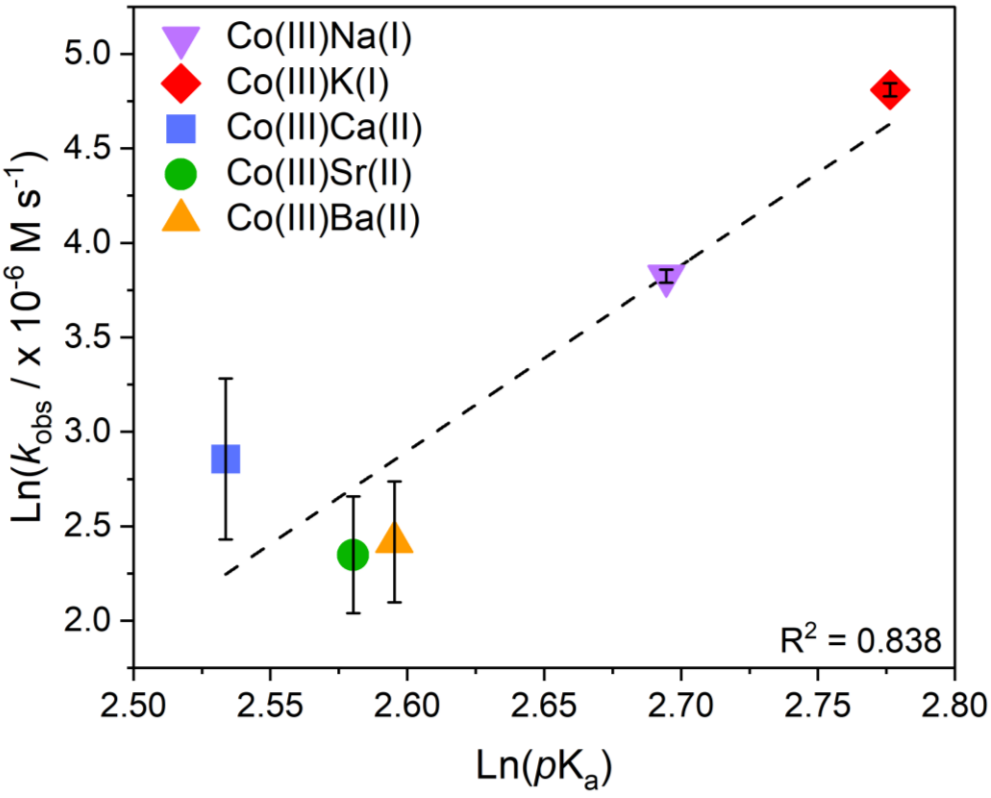


Figure S2.59. Plot of Ln(k_{obs}) vs. Ln(pK_a) for PO/PA ROCOP catalysed by Co(III)M(I/II) (M(I/II) = Na(I), K(I), Ca(II), Sr(II), Ba(II)). The linear fit shows that an exponential fit of k_{obs} vs. pK_a is appropriate.

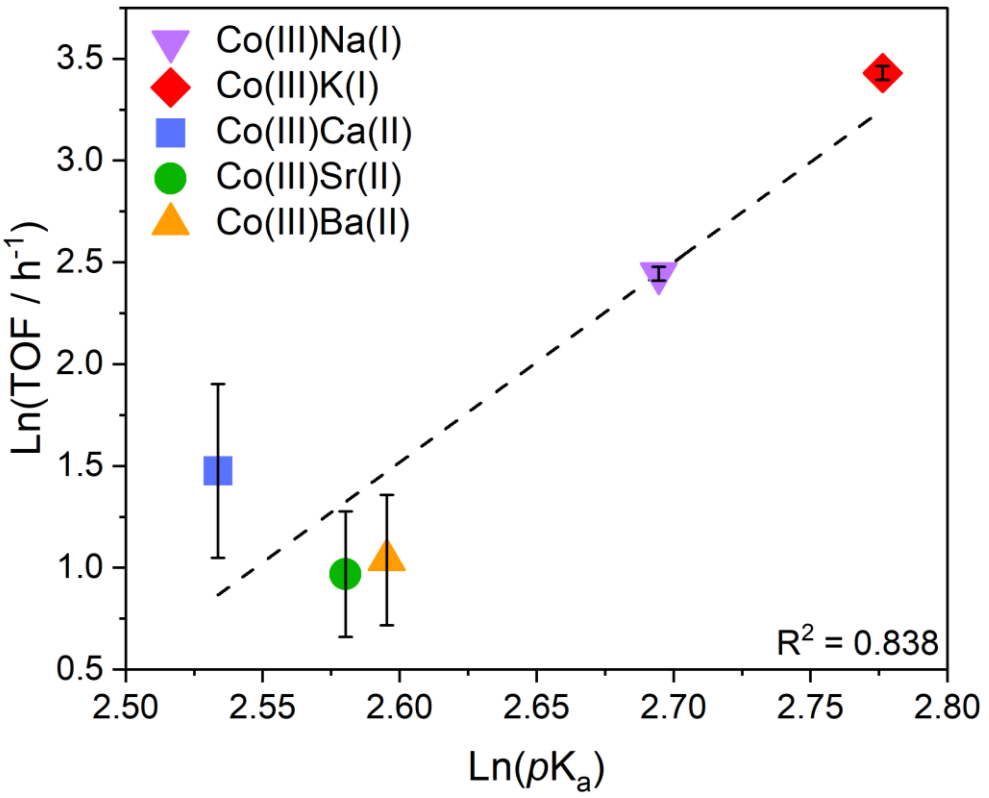


Figure S2.60. Plot of Ln(TOF) vs. Ln(pK_a) for PO/PA ROCOP catalysed by Co(III)M(I/II) (M(I/II) = Na(I), K(I), Ca(II), Sr(II), Ba(II)). The linear fit shows that an exponential fit of TOF vs. pK_a is appropriate.

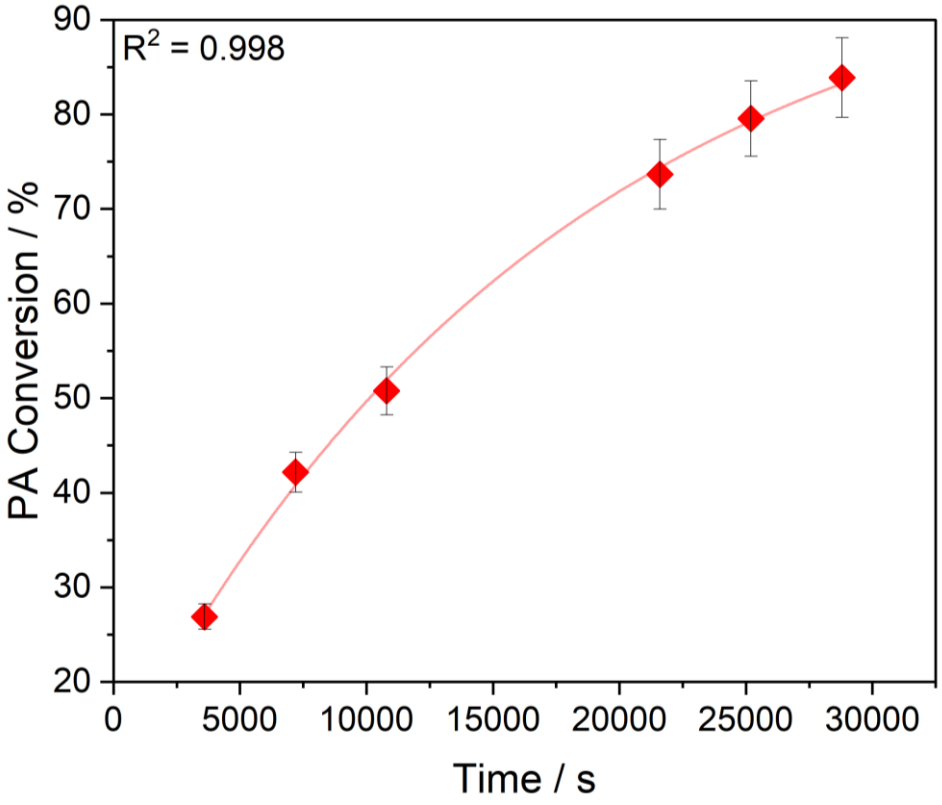


Figure S2.61. Plot of [PA] against time for PO/PA ROCOP catalysed by Co(III)K(I) using 1:100:150 $[Cat]_0$:$[PA]_0$:$[PO]_0$ in THF.

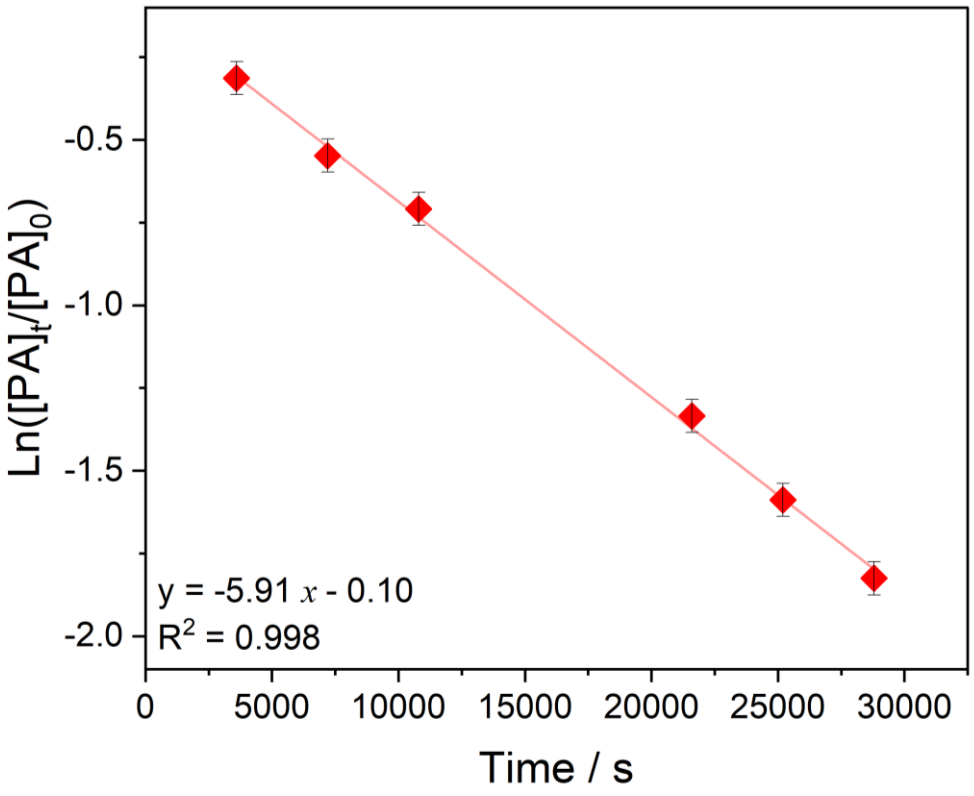


Figure S2.62. Plot of $Ln([PA]_t/[PA]_0)$ against time for PO/PA ROCOP catalysed by Co(III)K(I) using 1:200:250 $[Cat]_0$:$[PA]_0$:$[PO]_0$ in THF.

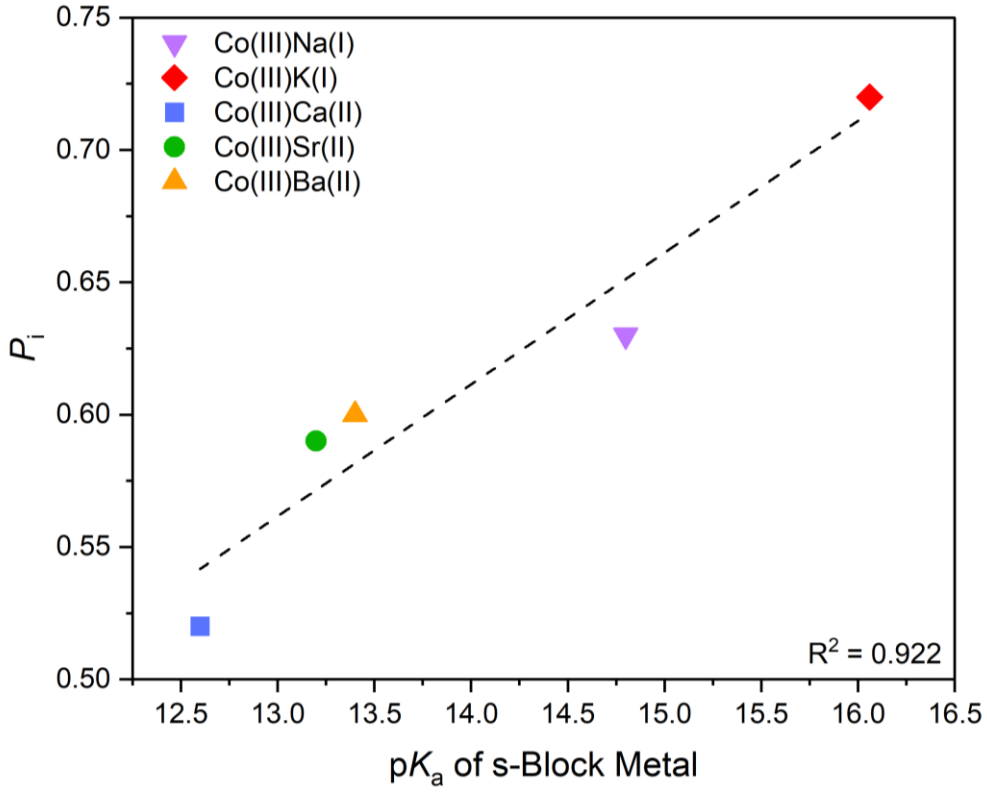


Figure S2.63. Plot of P_i of PLA vs. the pK_a of the s-block metal for *rac*-LA ROP catalysed by Co(III)M(I/II) (M(I/II) = Na(I), K(I), Ca(II), Sr(II), Ba(II)).

Crystallographic Data for Co(III)M(II) (M(II) = Ca(II), Sr(II) and Ba(II))

Table S2.7: Selected bond lengths for Co(III)M(II) (M(II) = Ca(II), Sr(II), Ba(II)).

Co(III)Ca(II) (022rwfk21)		Co(III)Sr(II) (006ff22_ff)		Co(III)Ba(II) (003ff21-ff)	
Bond/Separation	Length (°)	Bond/Separation	Length (°)	Bond/Separation	Length (°)
Co1—Ca1	3.2744 (7)	Sr1—Co1	3.4742 (6)	Ba1—Co1	3.6198 (8)
Co1—O1	1.893 (2)	Sr1—O1	2.549 (2)	Ba1—O1	2.692 (3)
Co1—O7	1.915 (2)	Sr1—O6	2.529 (2)	Ba1—O6	2.663 (3)
Co1—O6	1.901 (2)	Sr1—O8	2.618 (2)	Ba1—O2	2.795 (3)
Co1—O9	1.917 (2)	Sr1—O5	2.764 (2)	Ba1—O8	2.718 (4)
Co1—N2	1.904 (3)	Sr1—O10	2.676 (2)	Ba1—O10	2.884 (4)
Co1—N1	1.902 (3)	Sr1—O2	2.704 (2)	Ba1—O5	2.819 (4)
Ca1—O1	2.348 (2)	Sr1—O4	2.772 (3)	Ba1—O4	2.839 (4)
Ca1—O6	2.404 (2)	Sr1—O3	2.751 (3)	Ba1—O3	2.832 (4)
Ca1—O5	2.743 (2)	Sr1—C27	3.111 (7)	Ba1—O12	2.830 (6)
Ca1—O8	2.578 (2)	Sr1—O12	2.698 (5)	Ba1—O11	2.892 (6)
Ca1—O2	2.689 (2)	Sr1—O11	2.793 (5)	Ba1—C27	3.212 (8)
Ca1—O10	2.378 (2)	Co1—O1	1.898 (2)	Co1—O1	1.902 (3)
Ca1—O3	2.707 (2)	Co1—O6	1.916 (2)	Co1—O6	1.914 (3)
Ca1—O4	2.652 (2)	Co1—O7	1.914 (2)	Co1—O9	1.910 (3)
Ca1—O11	2.280 (3)	Co1—O9	1.911 (2)	Co1—O7	1.924 (3)
O7—C23	1.297 (4)	Co1—N2	1.900 (3)	Co1—N1	1.900 (4)
O9—C25	1.287 (4)	Co1—N1	1.898 (3)	Co1—N2	1.896 (4)
O8—C23	1.239 (4)	O7—C23	1.293 (4)	O9—C25	1.285 (6)
O10—C25	1.238 (4)	O8—C23	1.238 (4)	O8—C23	1.235 (7)
N2—C3	1.276 (5)	O9—C25	1.285 (4)	O7—C23	1.289 (6)
N1—C22	1.275 (5)	O10—C25	1.243 (4)	O10—C25	1.247 (6)
O11—C27	1.221 (5)	N2—C3	1.274 (5)	N1—C22	1.276 (7)
		N1—C22	1.276 (5)	N2—C3	1.283 (7)
		C27—O12	1.160 (7)	O12—C27	1.211 (10)
		C27—O11	1.192 (7)	O11—C27	1.200 (10)

Table S2.8: Selected bond angles for Co(III)M(II) (M(II) = Ca(II), Sr(II), Ba(II)).

Co(III)Ca(II) (022rwfk21)		Co(III)Sr(II) (006ff22_ff)		Co(III)Ba(II) (003ff21-ff)	
Bond	Angle (°)	Bond	Angle (°)	Bond	Angle (°)
O1—Co1—N1	175.89 (11)	O1—Sr1—O4	144.94 (8)	O1—Ba1—O4	139.99 (11)
O7—Co1—O9	178.30 (9)	O2—Sr1—O5	175.17 (8)	O6—Ba1—O3	156.78 (12)
O6—Co1—N2	177.52 (10)	O6—Sr1—O3	157.38 (10)	O2—Ba1—O5	165.90 (11)
O1—Ca1—O4	142.29 (8)	O9—Co1—O7	177.06 (10)	O9—Co1—O7	175.84 (15)
O6—Ca1—O3	148.85 (7)	N1—Co1—O1	175.91 (13)	N1—Co1—O6	176.94 (17)
O2—Ca1—O5	169.91 (7)	N2—Co1—O6	177.45 (11)	N2—Co1—O1	175.49 (19)

Table S2.9. Summary of crystallographic refinement data for Co(III)M(II) M(II) = Ca, Sr, Ba.

Complex	**Co(III)Ca(II)**	**Co(III)Sr(II)**	**Co(III)Ba(II)**
Local Code	022rwfk21	006ff22_ff	003ff21-ff
CCDC Deposition Number	2250536	2250537	2250538
Crystal data			
Chemical formula	$C_{28}H_{33}CaCoN_2O_{12}\cdot H_2O$	$C_{28}H_{33}CoN_2O_{12}Sr$	$C_{28}H_{33}BaCoN_2O_{12}$
M_r	706.59	736.11	785.83
Crystal system, space group	Monoclinic, $P2_1/c$	Tetragonal, $P4/n$	Tetragonal, $P4/n$
a, b, c **(Å)**	9.8086 (2), 18.7781 (3), 16.0772 (3)	27.1904 (1), 27.1904 (1), 9.8214 (1)	27.3281 (3), 27.3281 (3), 9.8247 (2)
α, β, γ **(°)**	90, 91.328 (2), 90	90, 90, 90	90, 90, 90
V **(Å^3)**	2960.41 (9)	7261.14 (9)	7337.3 (2)
Z	4	8	8
μ (mm^{-1})	6.69	6.00	12.31
Crystal size (mm)	0.29 × 0.16 × 0.09	0.27 × 0.20 × 0.14	0.12 × 0.07 × 0.06
Data collection			
Absorption correction	Gaussian *CrysAlis PRO* 1.171.40.53 (Rigaku Oxford Diffraction, 2019) Numerical absorption correction based on gaussian integration over a multifaceted crystal model Empirical absorption correction using spherical harmonics, implemented in SCALE3 ABSPACK scaling algorithm.	Multi-scan *CrysAlis PRO* 1.171.41.117a (Rigaku Oxford Diffraction, 2021) Empirical absorption correction using spherical harmonics, implemented in SCALE3 ABSPACK scaling algorithm.	Multi-scan *CrysAlis PRO* 1.171.41.117a (Rigaku Oxford Diffraction, 2021) Empirical absorption correction using spherical harmonics, implemented in SCALE3 ABSPACK scaling algorithm.
T_{min}, T_{max}	0.476, 1.000	0.541, 1.000	0.166, 1.000
No. of measured, independent and observed [$I > 2\sigma(I)$] reflections	17176, 6137, 5143	182489, 7602, 6671	80806, 7677, 5819
R_{int}	0.036	0.064	0.094
(sin θ/λ)$_{max}$ (Å^{-1})	0.630	0.630	0.630
Refinement			
$R[F^2 > 2\sigma(F^2)]$, $wR(F^2)$, S	0.048, 0.139, 1.02	0.047, 0.133, 1.04	0.049, 0.116, 1.03
No. of reflections	6137	7602	7677
No. of parameters	412	415	400
No. of restraints	0	18	18
	$w = 1/[\sigma^2(F_o^2) + (0.0766P)^2 + 2.3292P]$ where $P = (F_o^2 + 2F_c^2)/3$	$w = 1/[\sigma^2(F_o^2) + (0.0693P)^2 + 8.4614P]$ where $P = (F_o^2 + 2F_c^2)/3$	$w = 1/[\sigma^2(F_o^2) + (0.0408P)^2 + 17.2275P]$ where $P = (F_o^2 + 2F_c^2)/3$
$\Delta\rho_{max}$, $\Delta\rho_{min}$ **(e Å^{-3})**	0.61, −0.69	0.72, −0.56	0.83, −0.46

Chapter Three

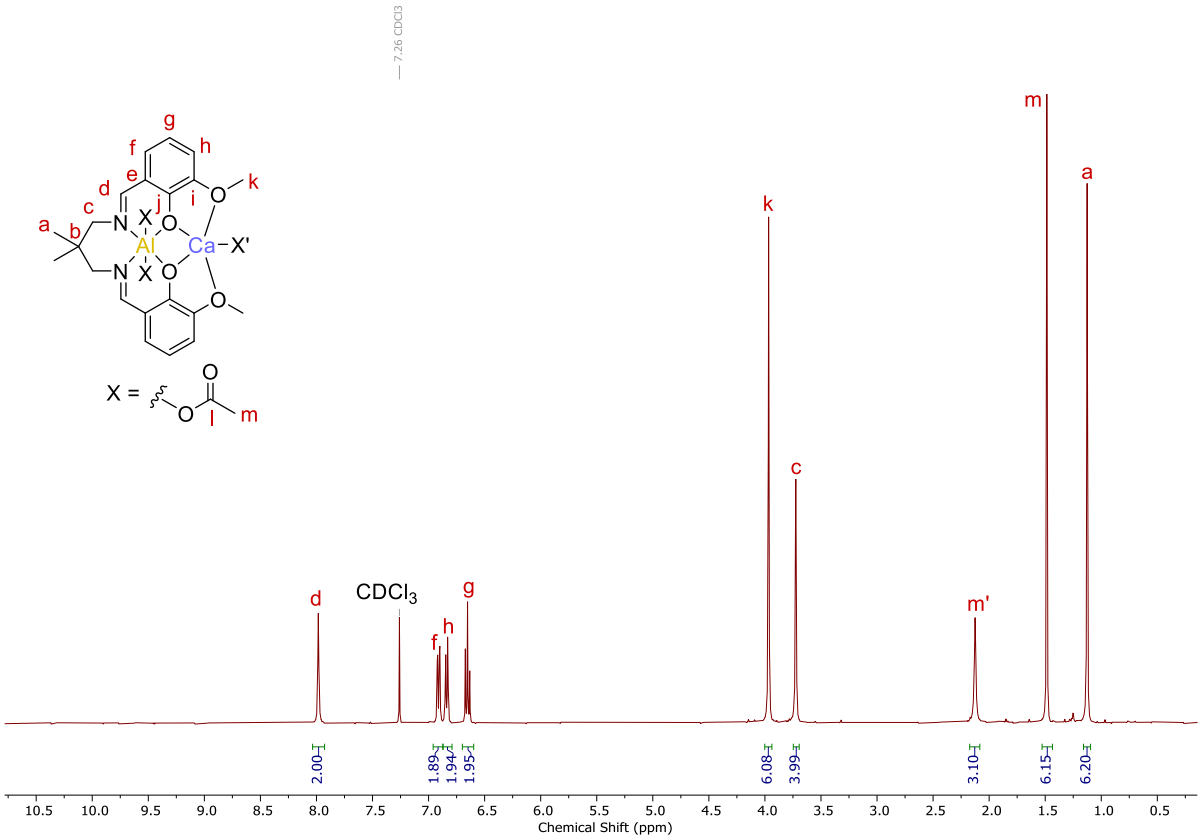


Figure S3.1. ^{1}H NMR spectrum of L_1Al(III)Ca(II) in $CDCl_3$.

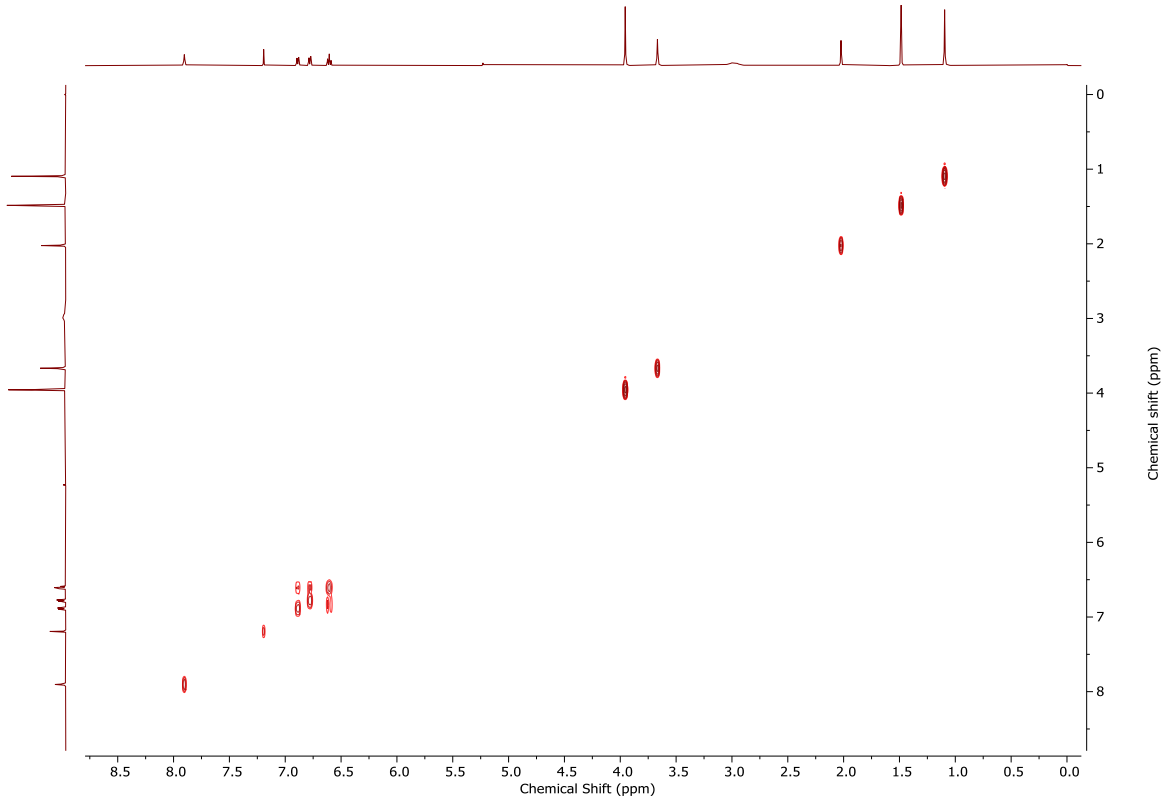


Figure S3.2. COSY NMR spectrum of L_1Al(III)Ca(II) in $CDCl_3$.

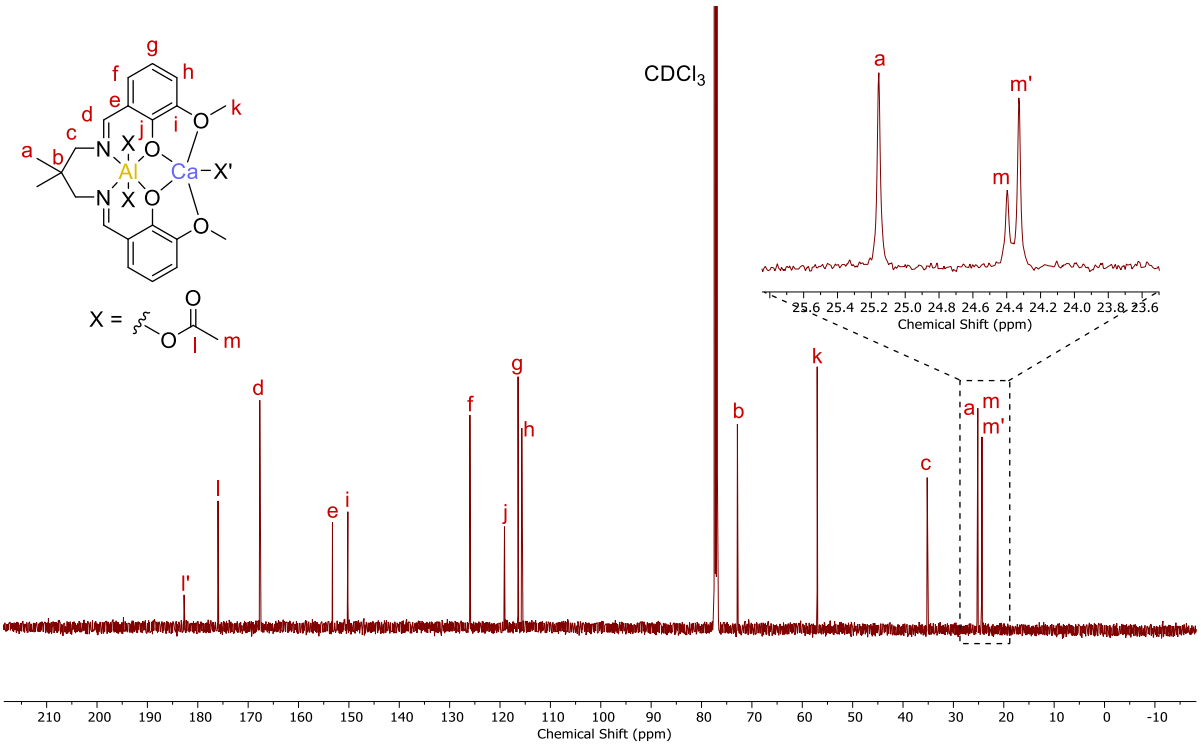


Figure S3.3. $^{13}C\{^{1}H\}$ NMR spectrum of $L_1Al(III)Ca(II)$ in $CDCl_3$.

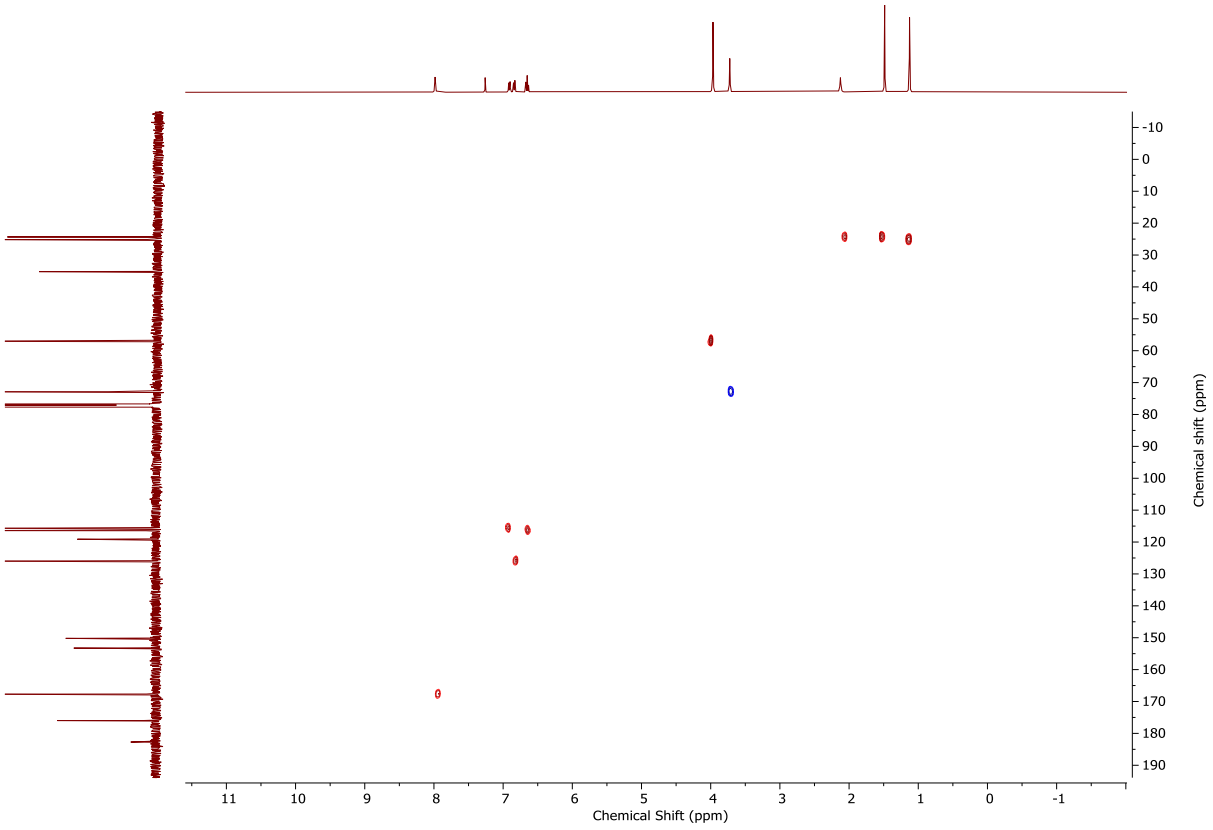


Figure S3.4. HSQC NMR spectrum of $L_1Al(III)Ca(II)$ in $CDCl_3$.

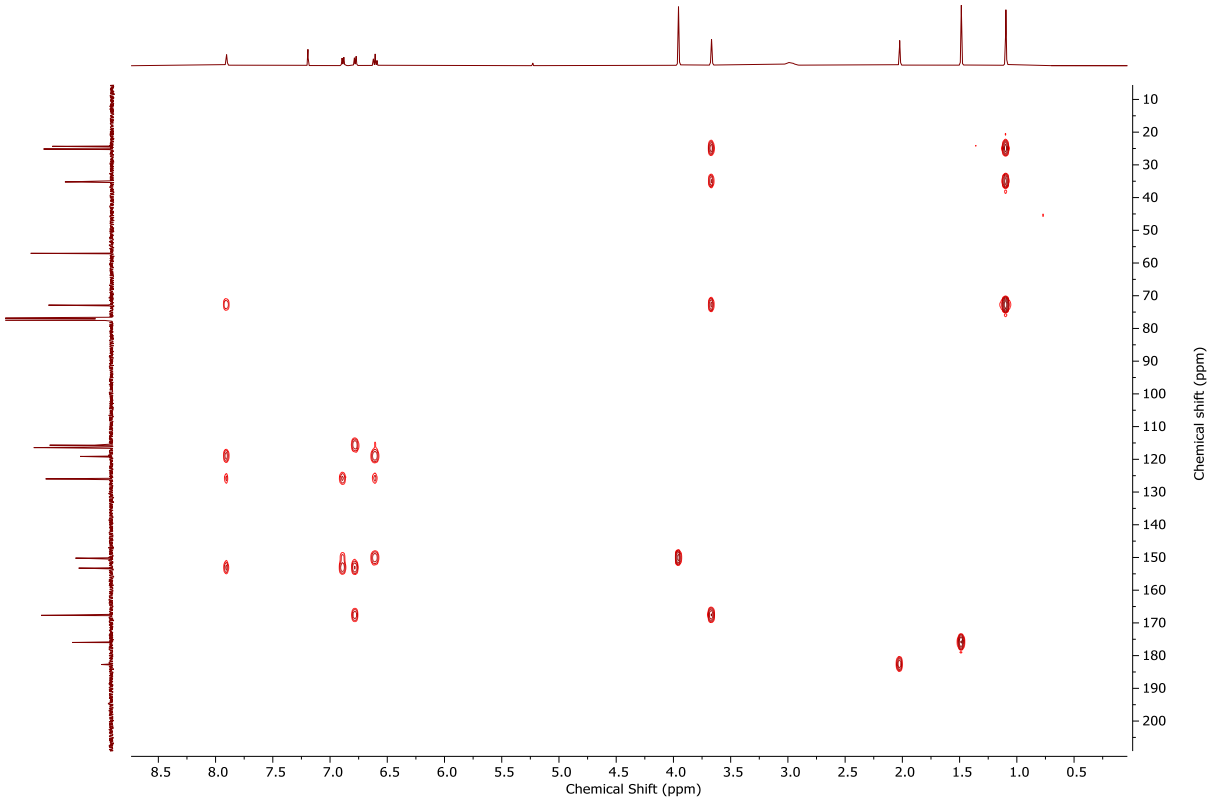


Figure S3.5. HMBC NMR spectrum of $L_1Al(III)Ca(II)$ in $CDCl_3$.

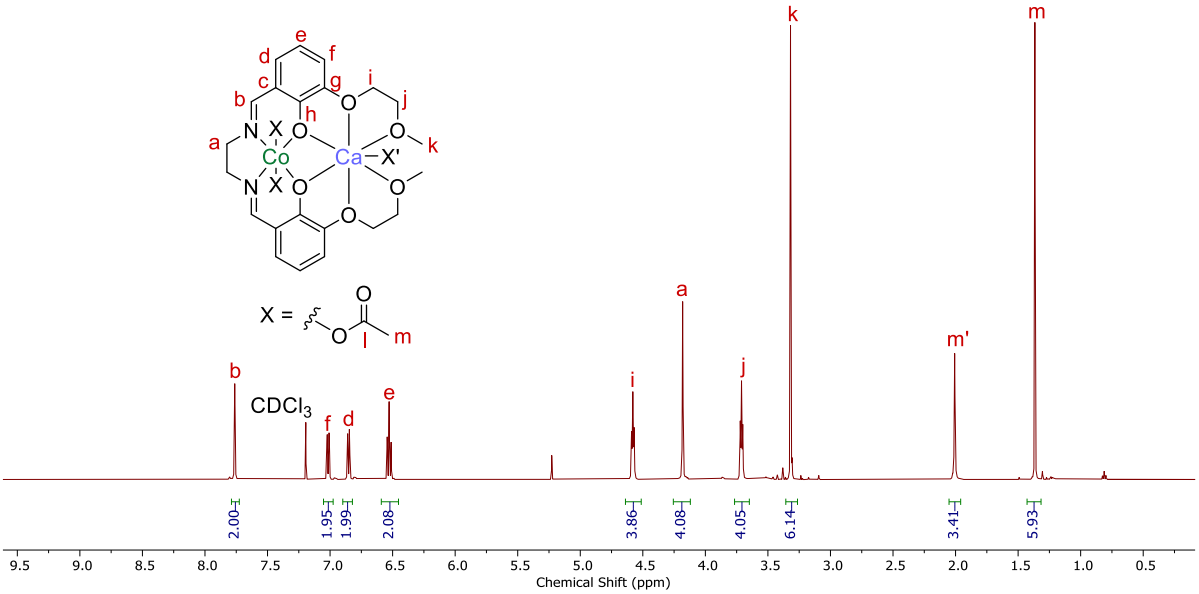


Figure S3.6. ^1H NMR spectrum of $L_2Co(III)Ca(II)$ in $CDCl_3$.

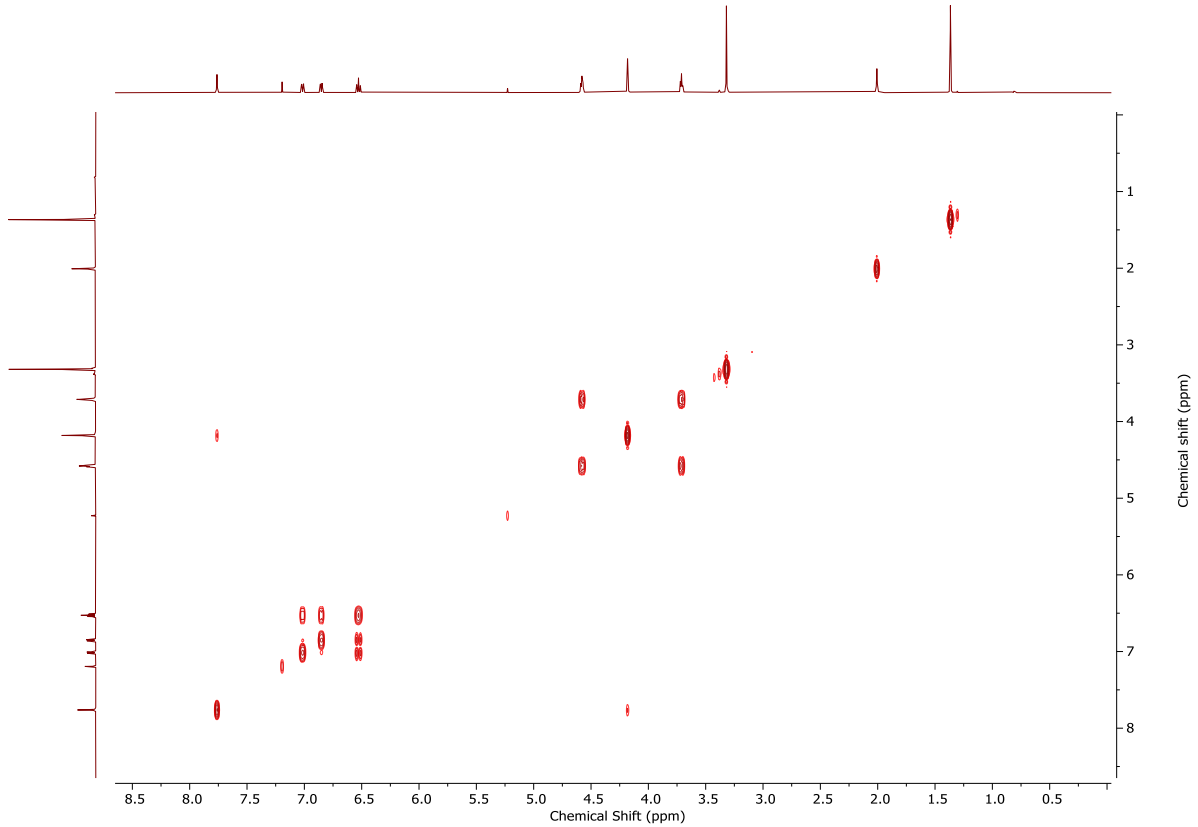


Figure S3.7. COSY NMR spectrum of $L_2Co(III)Ca(II)$.

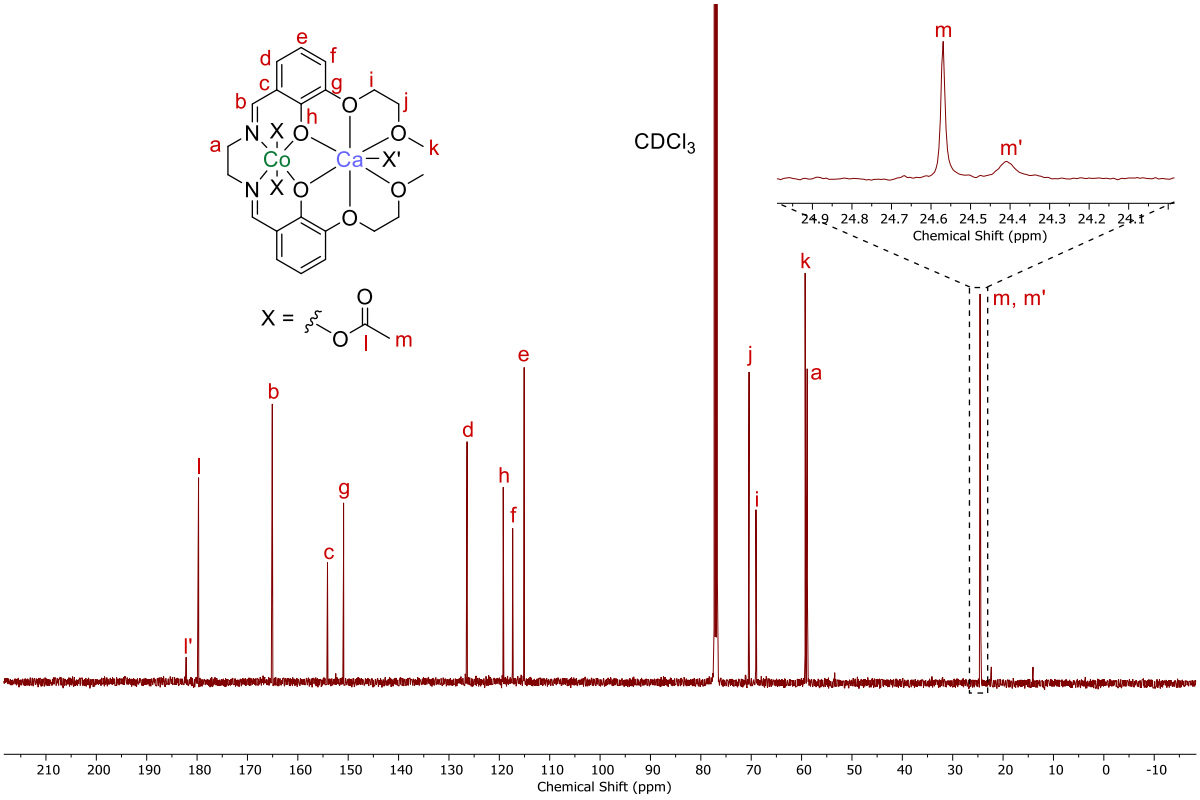


Figure S3.8. $^{13}C\{^1H\}$ NMR spectrum of $L_2Co(III)Ca(II)$ in $CDCl_3$.

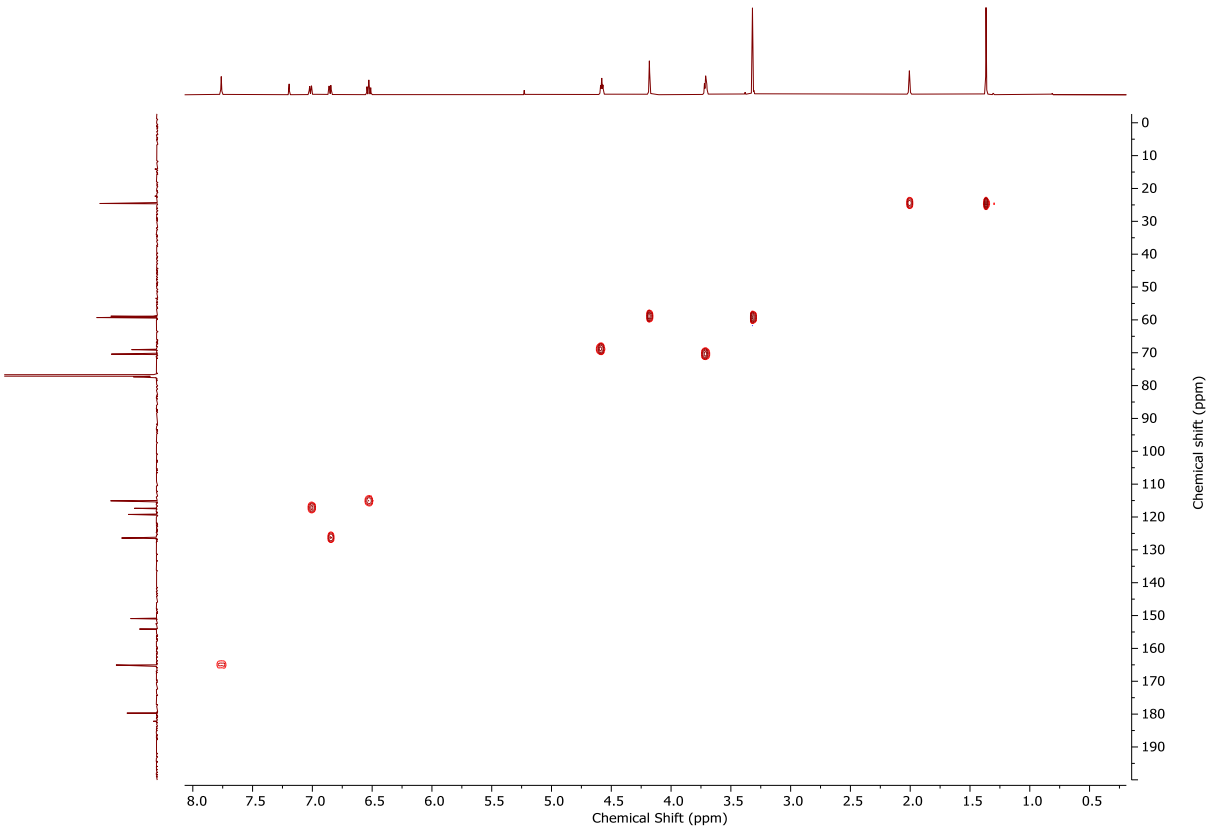


Figure S3.9. HSQC NMR spectrum of $L_2Co(III)Ca(II)$.

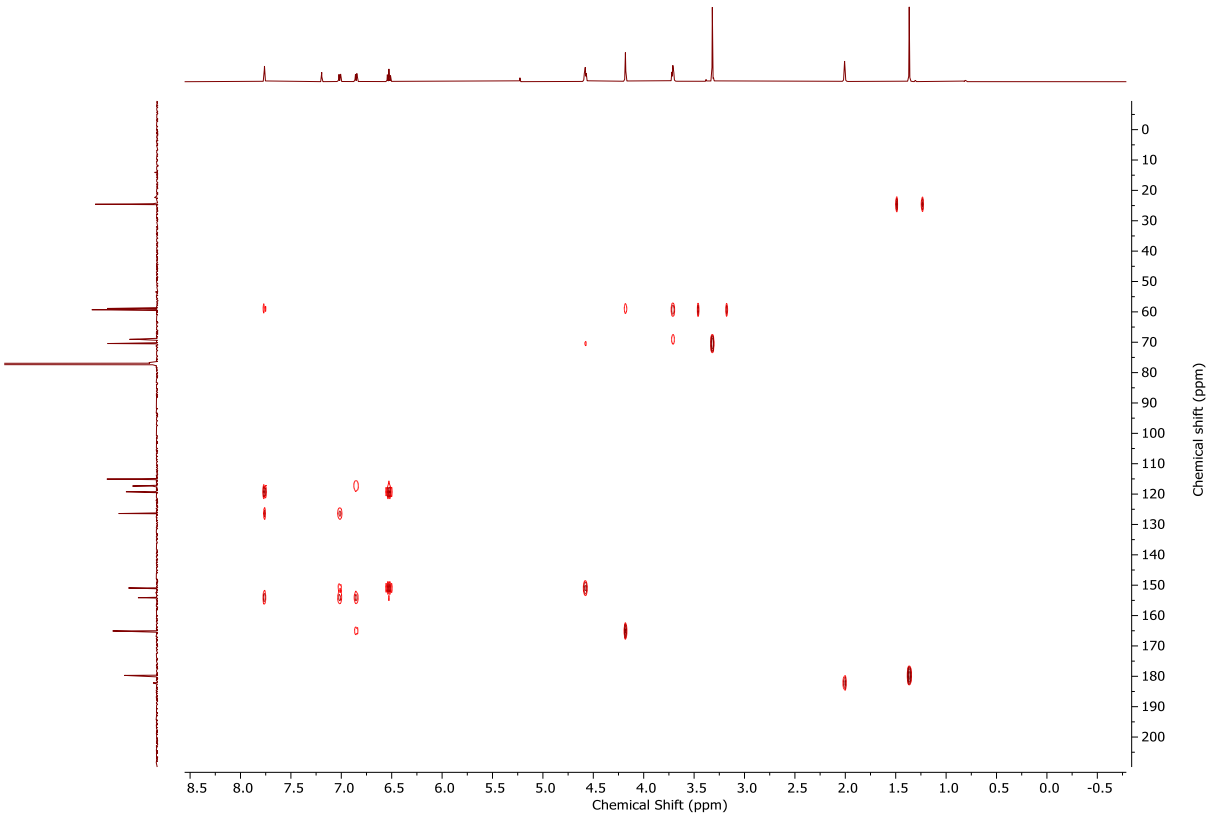


Figure S3.10. HMBC NMR spectrum of $L_2Co(III)Ca(II)$.

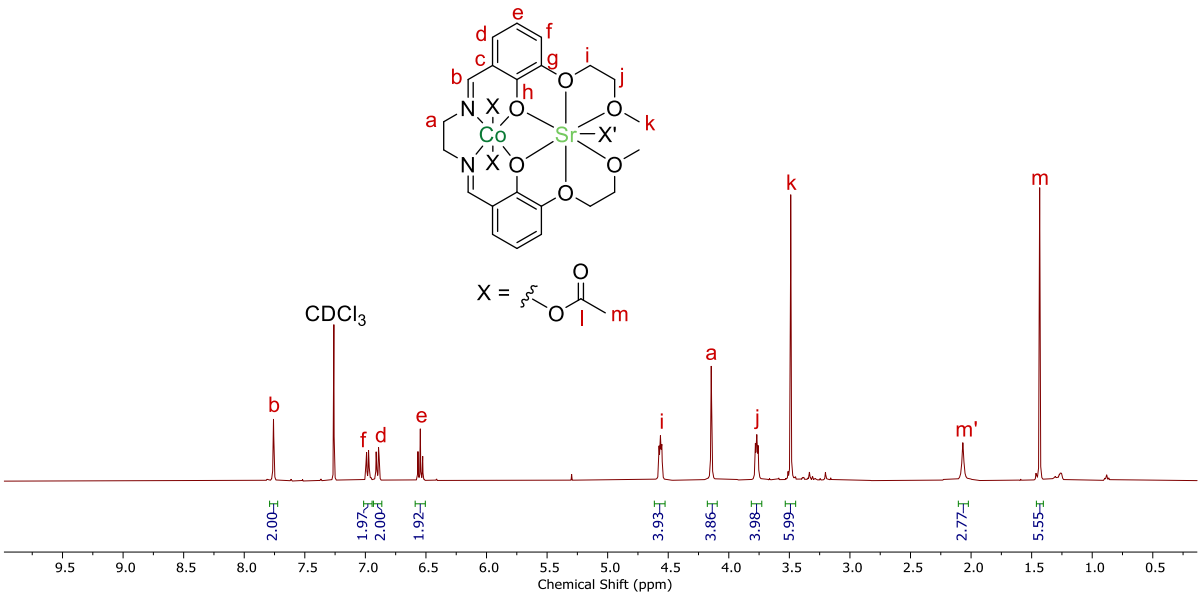


Figure S3.11. ^{1}H NMR spectrum of $L_2Co(III)Sr(II)$ in $CDCl_3$.

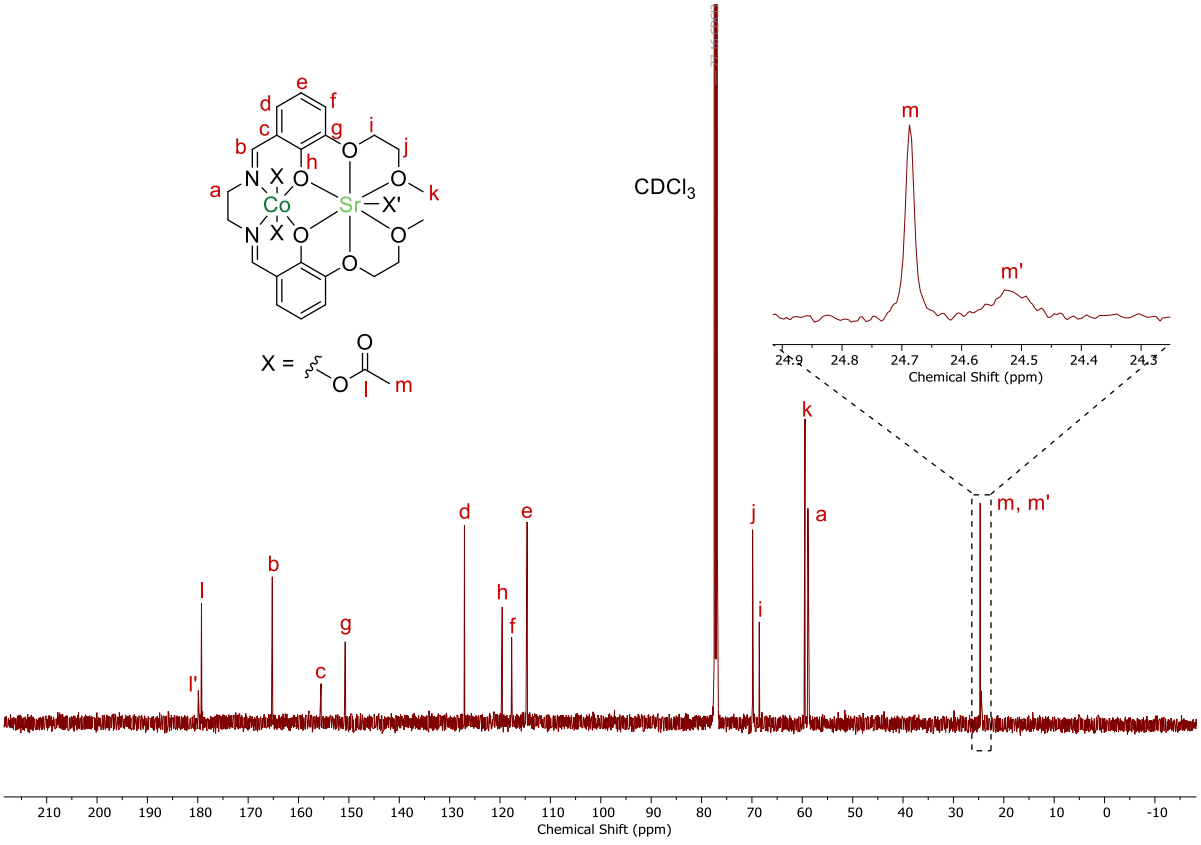


Figure S3.12. $^{13}C\{^{1}H\}$ NMR spectrum of $L_2Co(III)Sr(II)$ in $CDCl_3$.

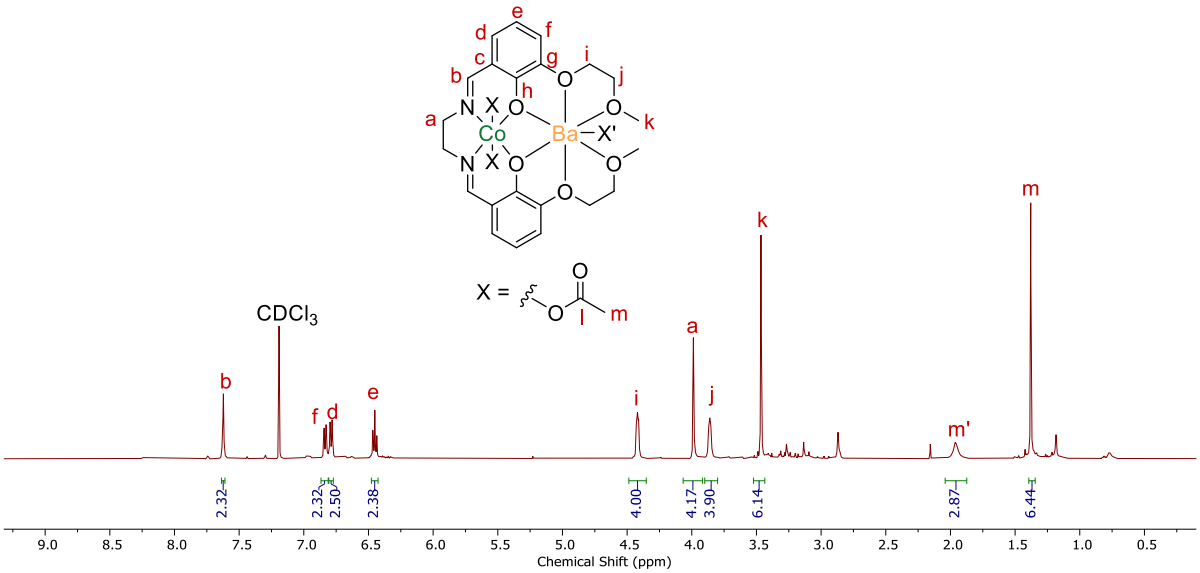


Figure S3.13. ^{1}H NMR spectrum of $L_2Co(III)Ba(II)$ in $CDCl_3$.

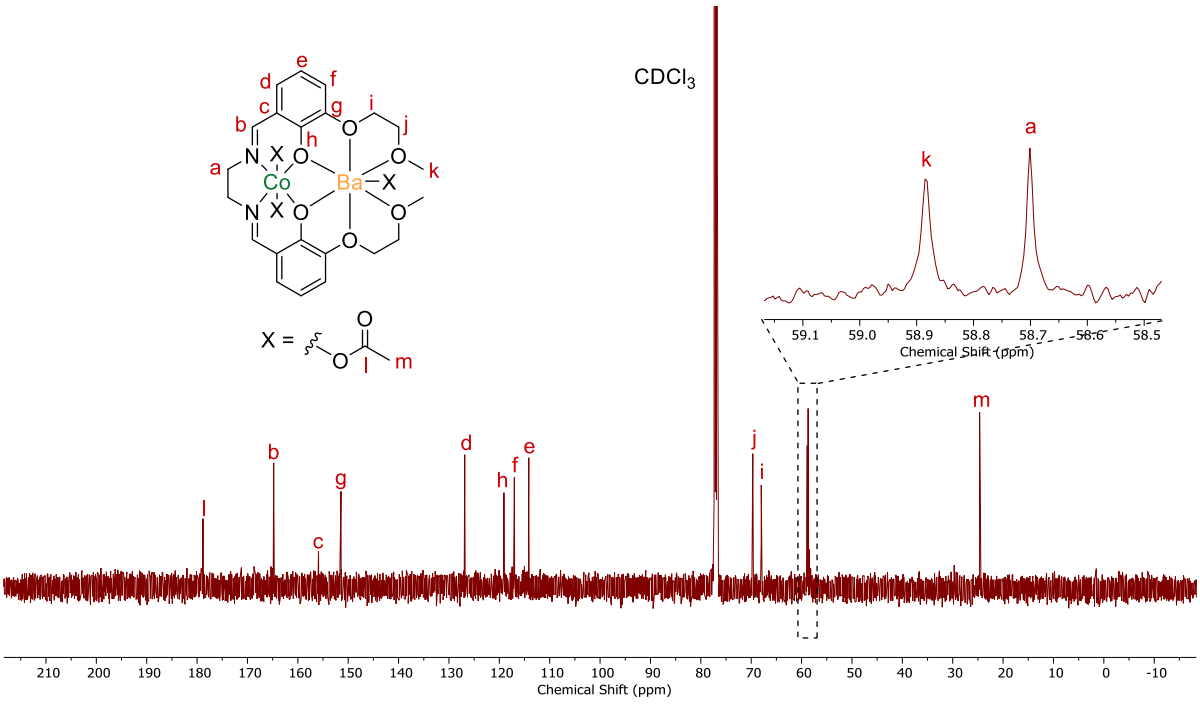


Figure S3.14. $^{13}C\{^{1}H\}$ NMR spectrum of $L_2Co(III)Ba(II)$ in $CDCl_3$.

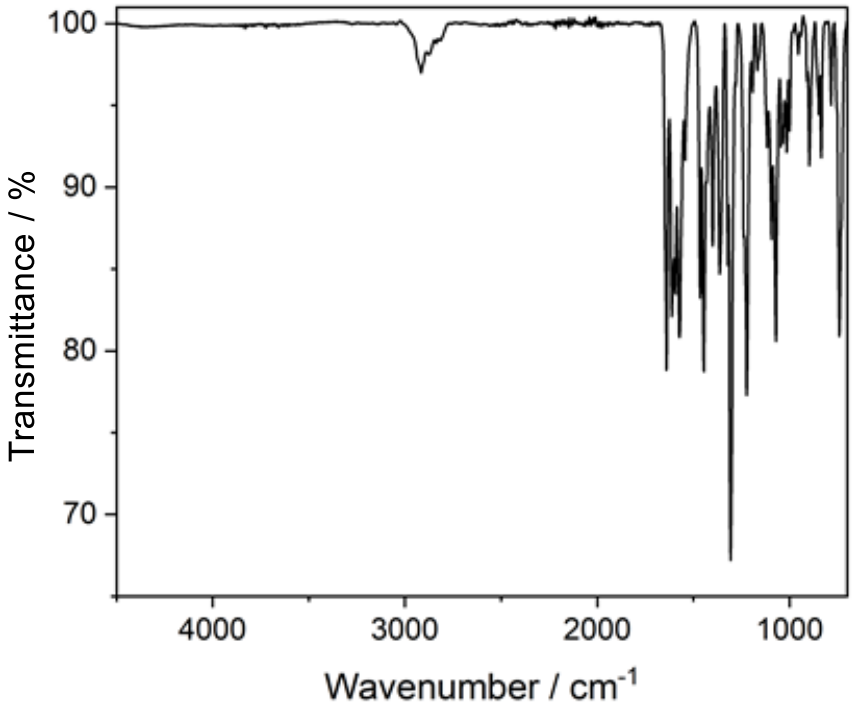


Figure S3.15. Solid-state IR spectrum of L_2Co(III)Sr(II).

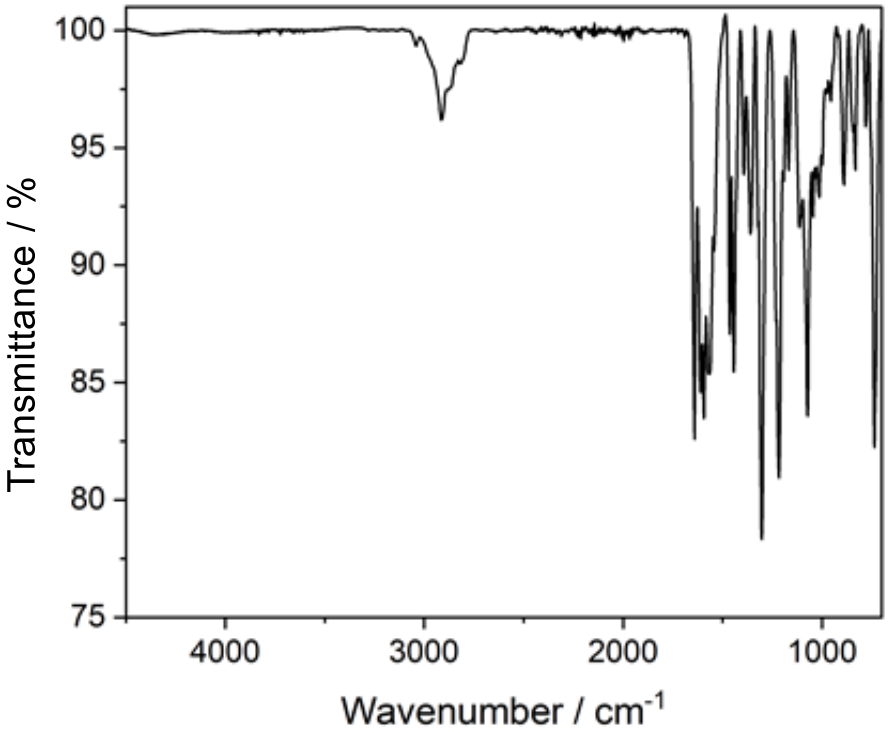


Figure S3.16. Solid-state IR spectrum of L_2Co(III)Ba(II).

Table S3.1. Values for derivation of equation S3.1.

Conversion / %	TON	$[PA]_t$ / M
5	20	1.9
70	280	0.6

Table S3.2: Description of parameters used for the derivation of equation S3.1.

Parameters	Description
$[PA]_t$	Concentration of PA at time *t*
$[PA]_0$	Starting concentration of PA (i.e. at time = 0 s)
k_{obs}	Observed rate coefficient
t	Time
t_i	Initiation time
$TOF_{5\text{-}70\%}$	Turnover frequency between 5 and 70% conversion
$TON_{70\%}$	Turnover number at 70% conversion
$TON_{5\%}$	Turnover number at 5% conversion
$t_{70\%}$	Time at 70% conversion
$t_{5\%}$	Time at 5% conversion

Derivation of Equation S3.1:

$$[\mathrm{PA}]_\mathrm{t} = -k_{\mathrm{obs}}t + t_i$$

$$\mathrm{TOF}_{5-70\%} = \frac{\mathrm{TON}_{70\%} - \mathrm{TON}_{5\%}}{t_{70\%} - t_{5\%}} = \frac{280 - 20}{t_{70\%} - t_{5\%}} = \frac{260}{t_{70\%} - t_{5\%}}$$

$$\mathrm{t} = \frac{[\mathrm{PA}]_\mathrm{t} - t_i}{-k_{\mathrm{obs}}}$$

$$t_{5\%} = \frac{1.9 - t_i}{-k_{\mathrm{obs}}} \qquad t_{70\%} = \frac{0.6 - t_i}{-k_{\mathrm{obs}}}$$

$$t_{70\%} - t_{5\%} = \frac{0.6 - t_i}{-k_{\mathrm{obs}}} - \frac{1.9 - t_i}{-k_{\mathrm{obs}}} = \frac{1.3}{k_{\mathrm{obs}}}$$

$$\mathrm{TOF}_{5-70\%} = \frac{260 \times k_{\mathrm{obs}} \times 3600\ \mathrm{h}^{-1}}{0.13} = \boldsymbol{k_{\mathrm{obs}} \times 7.2 \times 10^5\ \mathrm{h}^{-1}} \qquad \text{Eq. S3.1}$$

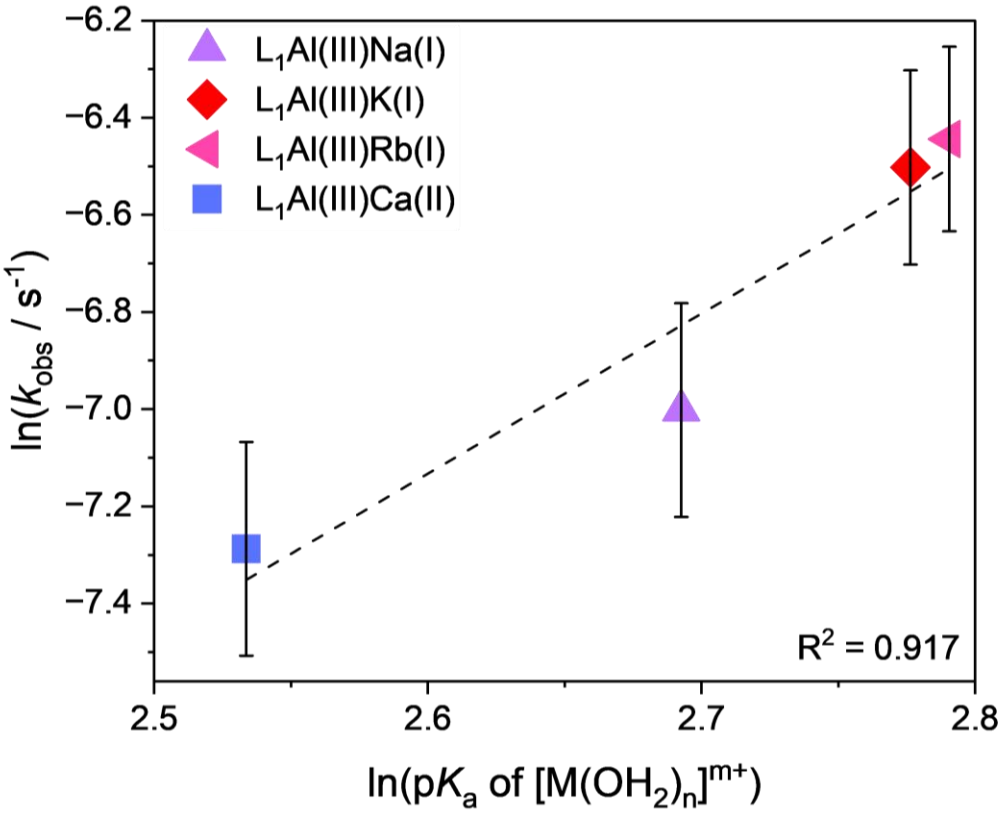


Figure S3.17. Plot of ln(k_{obs}) against ln(pK_a of $[M(OH_2)_n]^{m+}$) for CHO/PA ROCOP catalysed by L_1Al(III)M(I/II) showing the suitability of an exponential fit for the plot of activity against pK_a of $[M(OH_2)_n]^{m+}$.

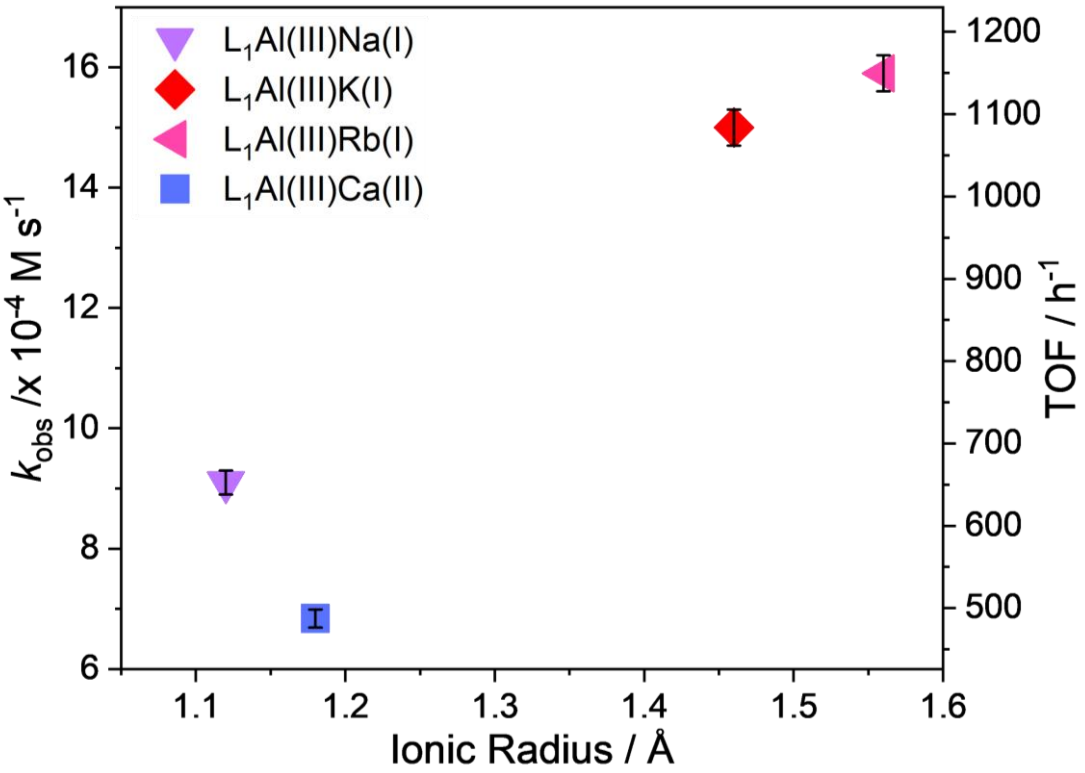


Figure S3.18. Plots of activity (k_{obs} and TOF) for the L_1Al(III)M(I/II) catalyst series for CHO/PA ROCOP against the ionic radius of the s-block metal.

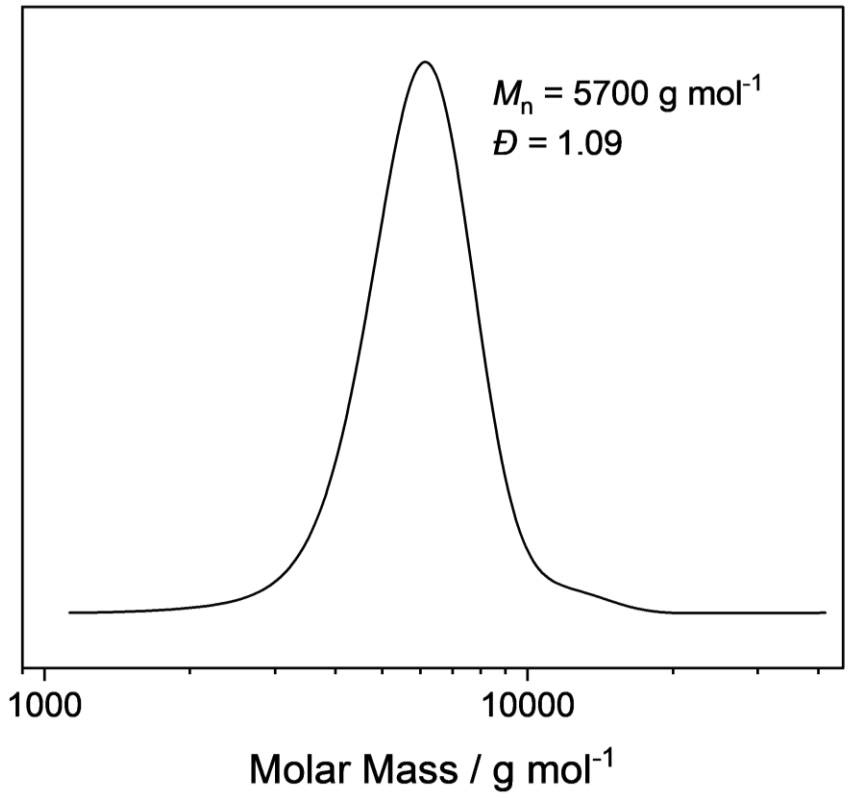


Figure S3.19. Representative GPC of poly(CHO-*alt*-PA) from the ROCOP of CHO and PA catalysed by L_1Al(III)M(I/II) catalysts.

Tables S3.3: Values for derivation of equation S3.2.

Conversion / %	TON	$[PO]_t$ / M	$\ln([PO]_t/[PO]_0)$
5	200	13.59	- 0.0513
20	800	12.14	- 0.2231

Table S3.4: Description of parameters used for the derivation of equation S3.2.

Parameters	Description
$[PO]_t$	Concentration of PO at time *t*
$[PO]_0$	Starting concentration of PO (i.e. at time = 0 s)
k_{obs}	Observed rate coefficient
t	Time
t_i	Initiation time
$TOF_{5\text{-}20\%}$	Turnover frequency between 5 and 20% conversion
$TON_{20\%}$	Turnover number at 20% conversion
$TON_{5\%}$	Turnover number at 5% conversion
$t_{20\%}$	Time at 20% conversion
$t_{5\%}$	Time at 5% conversion

Derivation of Supplementary Equation S3.2:

$$\ln\frac{[\mathrm{PO}]_\mathrm{t}}{[\mathrm{PO}]_0} = -k_\mathrm{obs}t + t_i$$

$$\mathrm{TOF}_{5-20\%} = \frac{\mathrm{TON}_{20\%} - \mathrm{TON}_{5\%}}{t_{20\%} - t_{5\%}} = \frac{800 - 200}{t_{20\%} - t_{5\%}} = \frac{600}{t_{20\%} - t_{5\%}}$$

$$\mathrm{t} = \frac{\ln\frac{[\mathrm{PO}]_\mathrm{t}}{[\mathrm{PO}]_0} - t_i}{-k_\mathrm{obs}}$$

$$t_{5\%} = \frac{0.05 - t_i}{-k_\mathrm{obs}} \quad t_{20\%} = \frac{0.22 - t_i}{-k_\mathrm{obs}}$$

$$t_{20\%} - t_{5\%} = \frac{0.05 - t_i}{-k_\mathrm{obs}} - \frac{0.22 - t_i}{-k_\mathrm{obs}} = \frac{0.17}{k_\mathrm{obs}}$$

$$\mathrm{TOF}_{5-20\%} = \frac{600 \times k_\mathrm{obs} \times 3600\ \mathrm{h}^{-1}}{0.17} = \boldsymbol{k_\mathrm{obs} \times 12.71 \times 10^6\ \mathrm{h}^{-1}} \qquad \text{Eq. S3.2}$$

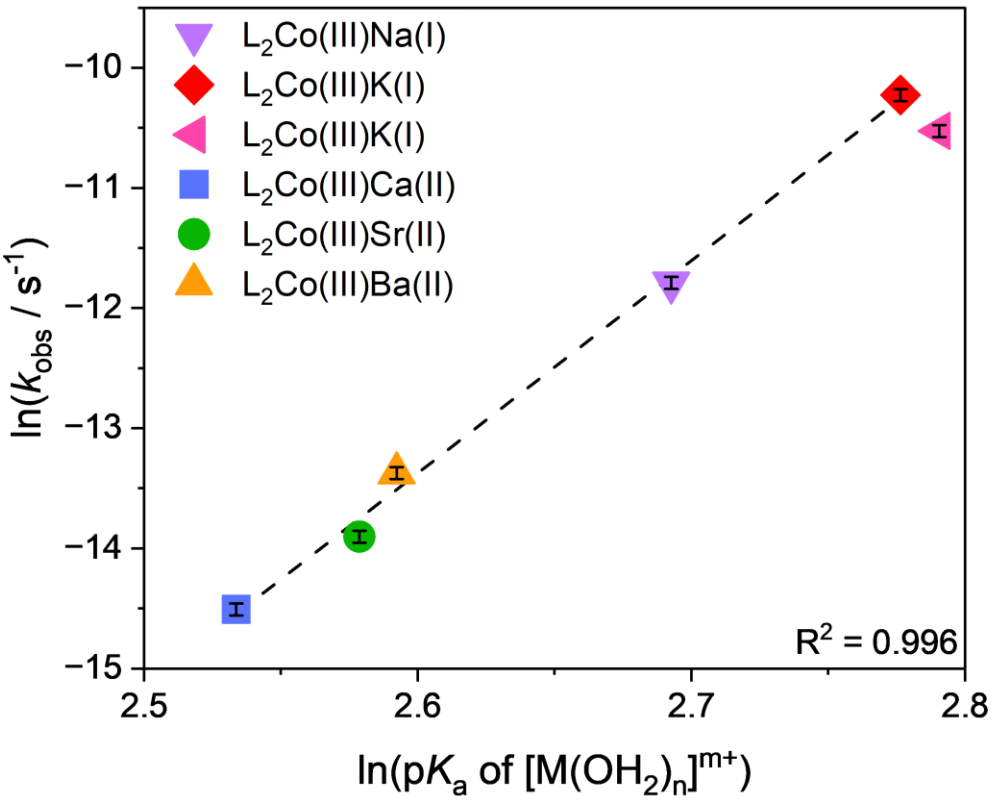


Figure S3.20. Plot of ln(k_{obs}) against ln(pK_a of $[M(OH_2)_n]^{m+}$) for PO/CO_2 ROCOP catalysed by L_2Co(III)M(I/II) showing the suitability of an exponential fit for the plot of activity against pK_a of $[M(OH_2)_n]^{m+}$ for catalysts with M(I/II) = Na(I), K(I), Ca(II), Sr(II), and Ba(II).

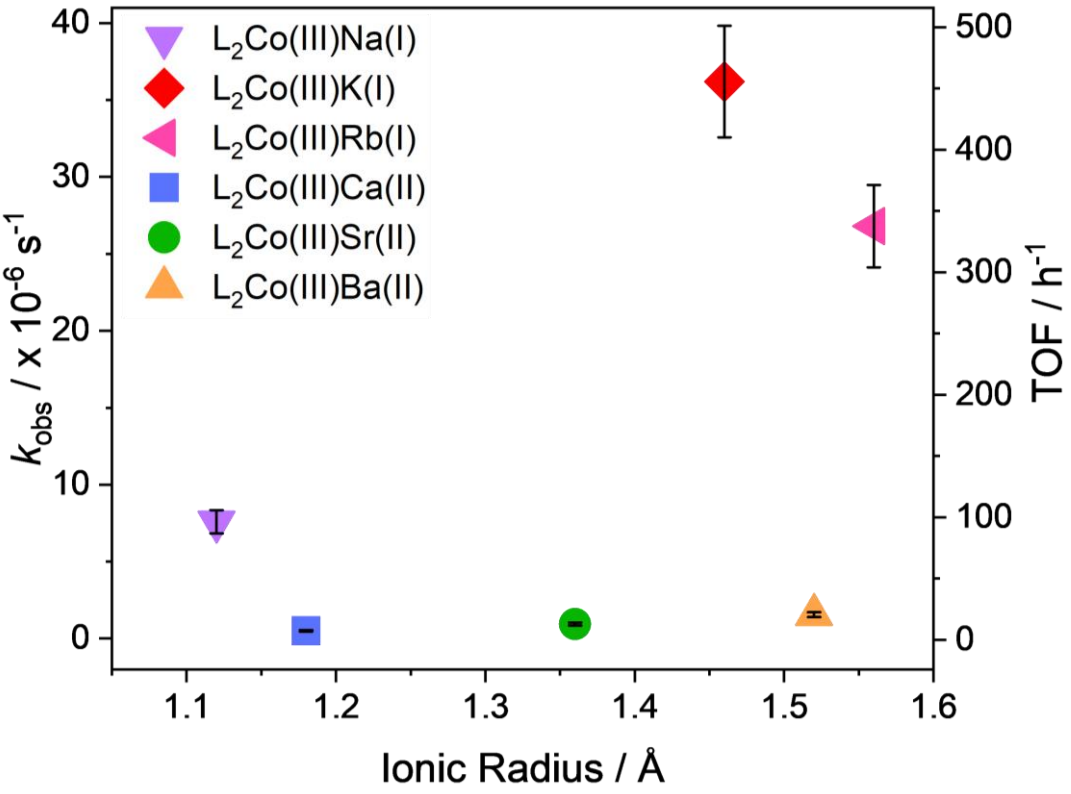


Figure S3.21. Plots of activity (k_{obs} and TOF) for the $L_2Co(III)M(I/II)$ catalyst series for PO/CO_2 ROCOP against the ionic radius of the s-block metal.

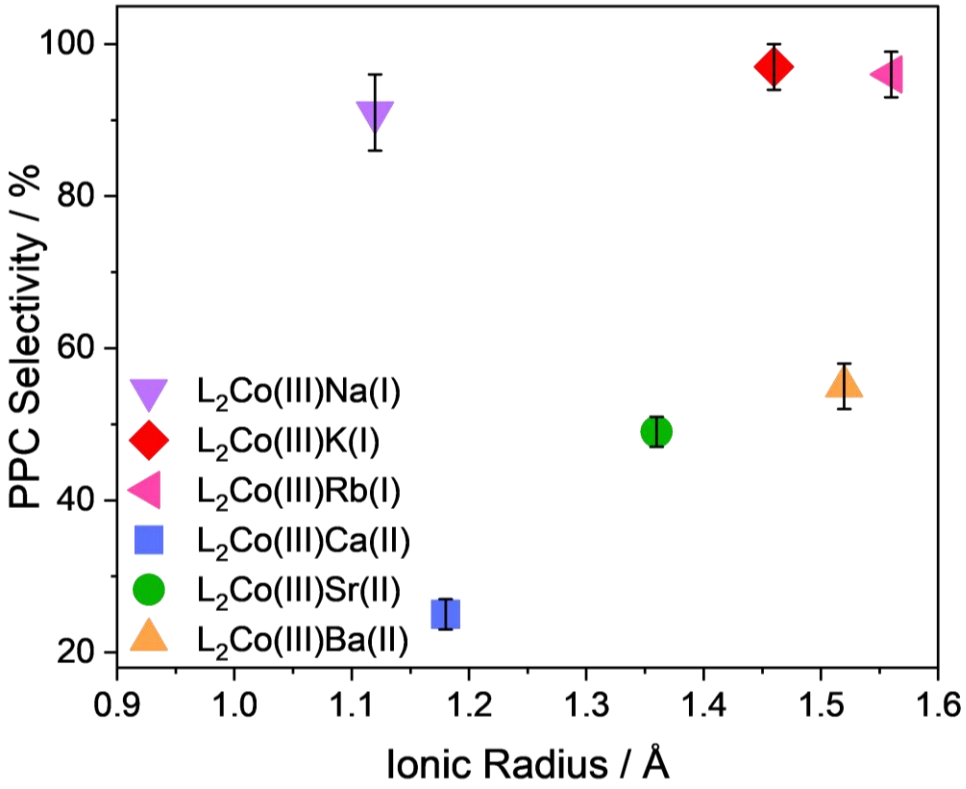


Figure S3.22. Plots of PPC selectivity for the $L_2Co(III)M(I/II)$ catalyst series for PO/CO_2 ROCOP against the ionic radius of the s-block metal.

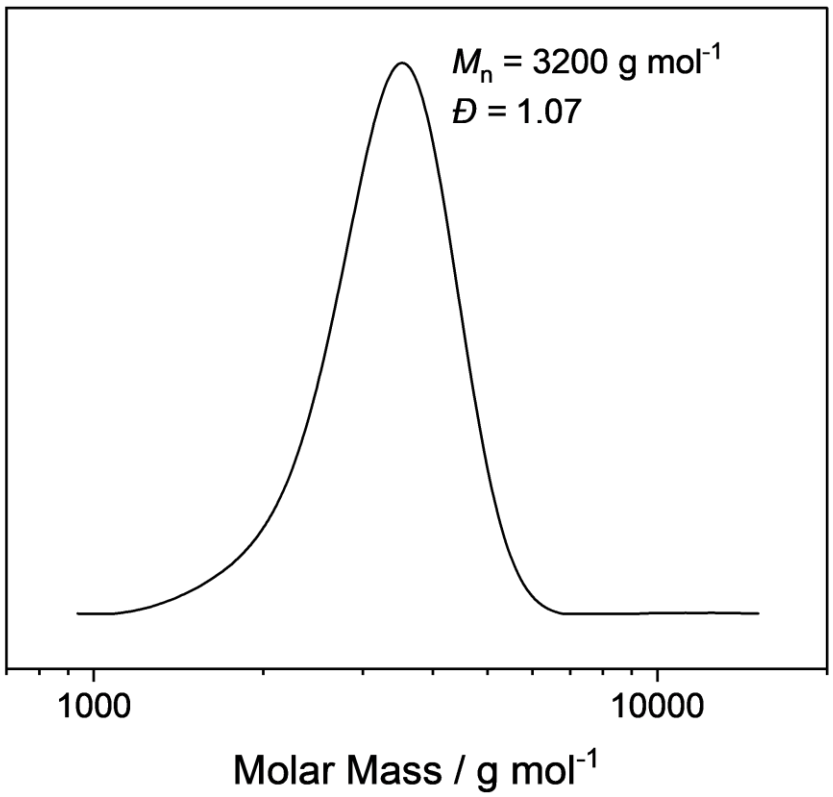


Figure S3.23. Representative GPC for poly(propylene carbonate) produced from the ROCOP of PO and CO_2 catalysed by L_2Co(III)M(I/II) catalysts.

Table S3.5. Values for derivation of equation S3.1.

Conversion / %	TON	$[PA]_t$ / M
5	10	0.95
70	140	0.30

Table S3.6: Description of parameters used for the derivation of equation S3.3.

Parameters	Description
$[PA]_t$	Concentration of PA at time *t*
$[PA]_0$	Starting concentration of PA (i.e. at time = 0 s)
k_{obs}	Observed rate coefficient
t	Time
t_i	Initiation time
$TOF_{5\text{-}70\%}$	Turnover frequency between 5 and 70% conversion
$TON_{70\%}$	Turnover number at 70% conversion
$TON_{5\%}$	Turnover number at 5% conversion
$t_{70\%}$	Time at 70% conversion
$t_{5\%}$	Time at 5% conversion

Derivation of Equation S3.3:

$$[\mathrm{PA}]_\mathrm{t} = -k_\mathrm{obs} t + t_i$$

$$\mathrm{TOF}_{5-70\%} = \frac{\mathrm{TON}_{70\%} - \mathrm{TON}_{5\%}}{t_{70\%} - t_{5\%}} = \frac{140 - 10}{t_{70\%} - t_{5\%}} = \frac{130}{t_{70\%} - t_{5\%}}$$

$$\mathrm{t} = \frac{[\mathrm{PA}]_\mathrm{t} - t_i}{-k_\mathrm{obs}}$$

$$t_{5\%} = \frac{0.95 - t_i}{-k_\mathrm{obs}} \qquad t_{70\%} = \frac{0.30 - t_i}{-k_\mathrm{obs}}$$

$$t_{70\%} - t_{5\%} = \frac{0.30 - t_i}{-k_\mathrm{obs}} - \frac{0.95 - t_i}{-k_\mathrm{obs}} = \frac{0.65}{k_\mathrm{obs}}$$

$$\mathrm{TOF}_{5-70\%} = \frac{130 \times k_\mathrm{obs} \times 3600\ \mathrm{h}^{-1}}{0.65} = \boldsymbol{k_\mathrm{obs} \times 7.2 \times 10^5\ \mathrm{h}^{-1}} \qquad \text{Eq. S3.3}$$

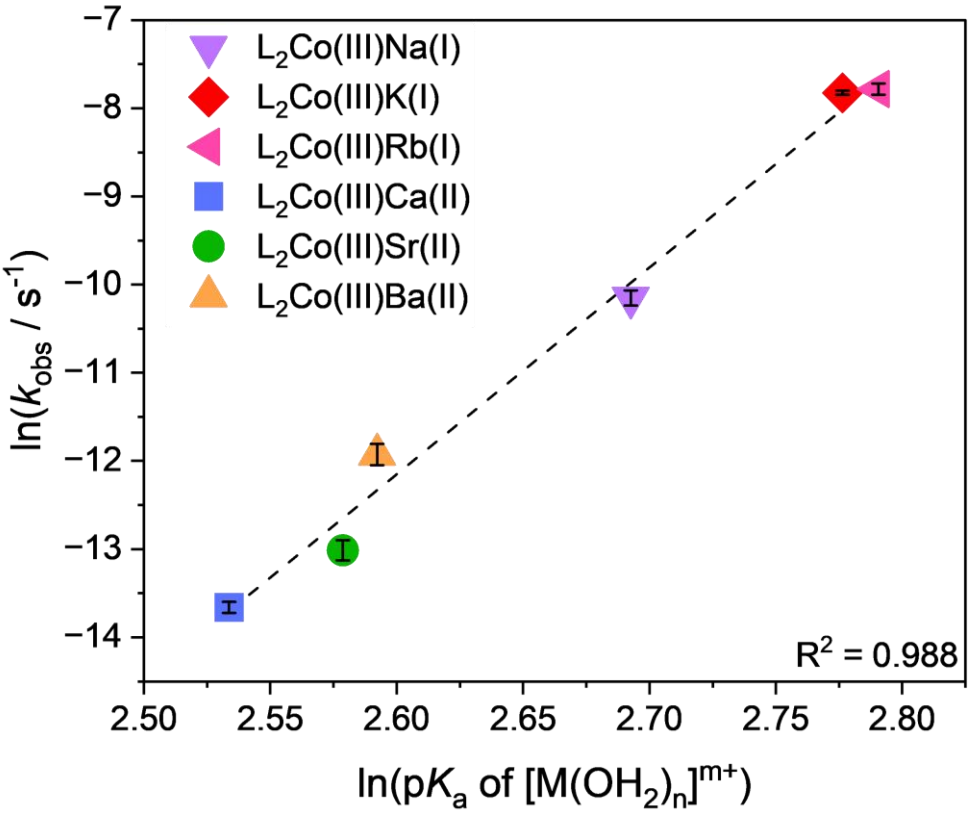


Figure S3.24. Plot of ln(k_{obs}) against ln(pK_a of $[M(OH_2)_n]^{m+}$) for CHO/PA ROCOP catalysed by L_2Co(III)M(I/II) showing the suitability of an exponential fit for the plot of activity against pK_a of $[M(OH_2)_n]^{m+}$.

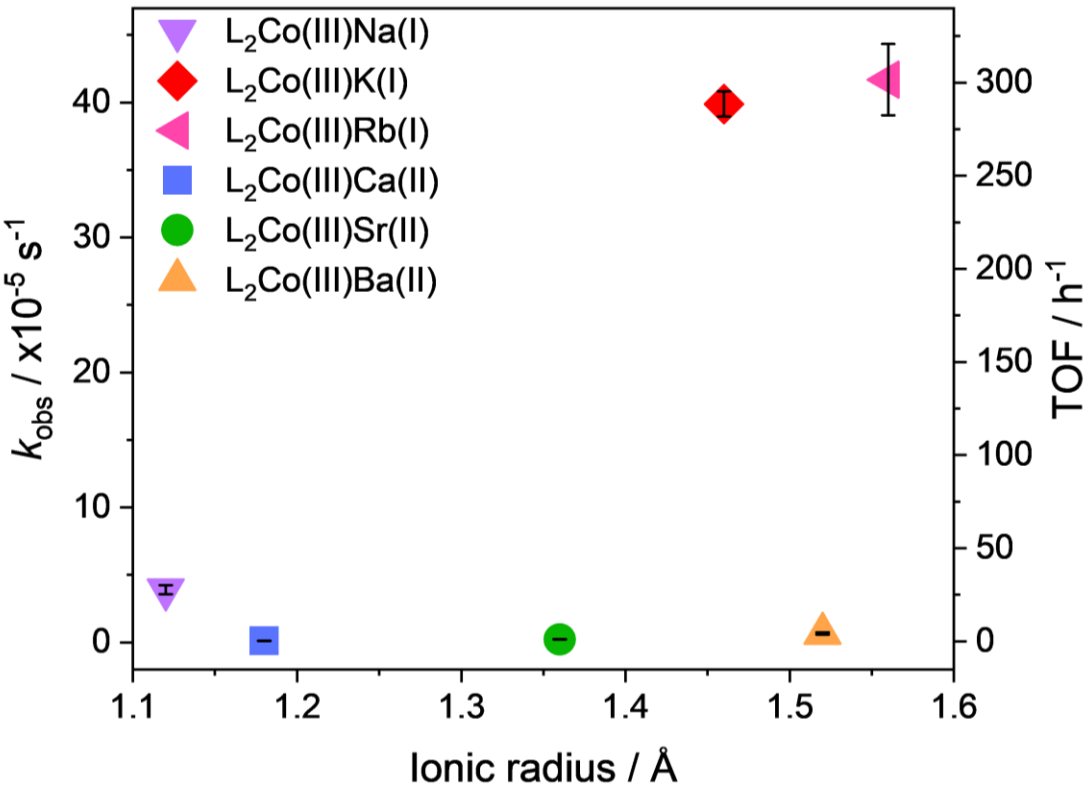


Figure S3.25. Plots of activity (k_{obs} and TOF) for the L2Co(III)M(I/II) catalyst series for CHO/PA ROCOP against the ionic radius of the s-block metal.

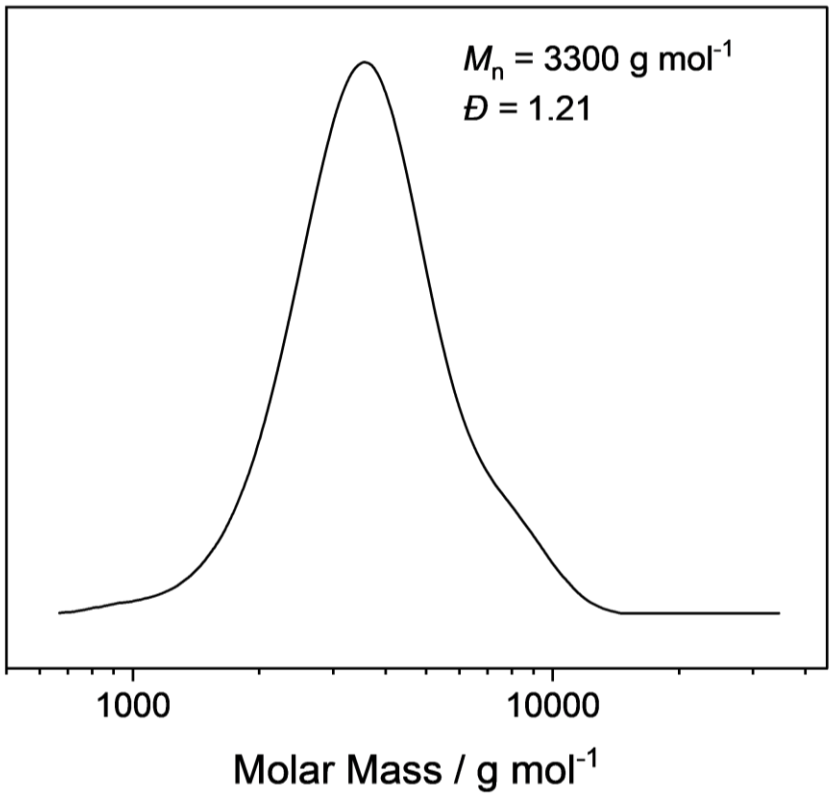


Figure S3.26. Representative GPC for poly(CHO-*alt*-PA) produced from CHO/PA ROCOP catalysed by L2Co(III)M(I/II) catalysts.

Table S3.7. Selected bond lengths and angles for L_1Al(III)Ca(II).

Bond	Length / Å	Bond	Angle / °
Ca00—Al02	3.3487 (5)	O003—Al02—O005	88.76 (5)
Ca00—O003	2.4159 (10)	O003—Al02—N00C	90.15 (5)
Ca00—O004	2.4133 (10)	O003—Al02—N00D	174.45 (5)
Ca00—O006	2.3956 (11)	O004—Al02—O003	89.21 (5)
Ca00—O008	2.4591 (11)	O004—Al02—O005	89.88 (5)
Ca00—O009	2.2580 (11)	O004—Al02—N00C	178.02 (5)
Ca00—O00A	2.5032 (11)	O004—Al02—N00D	90.56 (5)
Ca00—O00B^{i}	2.3094 (11)	O003—Al02—O005	88.76 (5)
Al02—O003	1.8787 (10)	O003—Al02—N00C	90.15 (5)
Al02—O004	1.8696 (11)	O005—Al02—N00D	85.69 (5)
Al02—O005	1.9299 (11)	O007—Al02—O003	93.39 (5)
Al02—N00C	2.0247 (13)	O007—Al02—O004	93.36 (5)
Al02—N00D	2.0406 (13)	O007—Al02—O005	176.14 (5)
O005—C00F	1.2822 (18)	O007—Al02—N00C	88.55 (5)
O006—C00F	1.2471 (18)	O007—Al02—N00D	92.16 (5)
O007—C00S	1.293 (2)	N00C—Al02—N00D	89.89 (5)
O009—C00Q	1.2592 (19)	O005—Al02—N00D	85.69 (5)
O00B—C00Q	1.2547 (19)	O007—Al02—O003	93.39 (5)
N00C—C00J	1.285 (2)		
N00C—C00N	1.4698 (19)		
N00D—C00P	1.287 (2)		
N00D—C00Y	1.4756 (19)		

L_1Al(III)Ca(II)	
Local code	0088ff23
CCDC Deposition Number	2373015
Crystal data	
Chemical formula	$C_{27}H_{33}AlCaN_2O_{10}$
M_r	612.61
Crystal system, space group	Triclinic, *P*1
Temperature (K)	139
a, *b*, *c* (Å)	9.6953 (4), 12.6810 (4), 12.7539 (5)
α, β, γ (°)	82.367 (3), 70.362 (4), 75.107 (3)
V (Å^3)	1425.37 (10)
Z	2
Radiation type	Cu *Kα*
μ (mm^{-1})	2.72
Crystal size (mm)	0.12 × 0.1 × 0.06
Data collection	
Diffractometer	SuperNova, Dual, Cu at home/near, Atlas
Absorption correction	Multi-scan *CrysAlis PRO* 1.171.42.72a (Rigaku Oxford Diffraction, 2022) Empirical absorption correction using spherical harmonics, implemented in SCALE3 ABSPACK scaling algorithm.
T_{min}, T_{max}	0.878, 1.000
No. of measured, independent and observed [$I > 2\sigma(I)$] reflections	29603, 5894, 5169
R_{int}	0.039
$(\sin\theta/\lambda)_{max}$ (Å^{-1})	0.630
Refinement	
$R[F^2 > 2\sigma(F^2)]$, $wR(F^2)$, *S*	0.032, 0.087, 1.03
No. of reflections	5894
No. of parameters	398
No. of restraints	449
H-atom treatment	H-atom parameters constrained
$\Delta\varrho_{max}$, $\Delta\varrho_{min}$ (e Å^{-3})	0.31, −0.27

Chapter Four

Table S4.1. Catalysts for high pressure (>5 bar) CHO/CO_2 ROCOP used for Figure 1, showing the TOF, intermetallic separation (from solid-state structures), and polymerisation conditions.

Catalyst	TOF / h^{-1}	Solid-State M – M Separation / Å	[CHO]/[cat]	[CHO]	Additives?	CO_2 pressure / bar	Temp. / °C
Zn(II) BDI-**1**[2]	360	4.24	1,000	Neat	No	7	50
Zn(II) BDI-**2**[2]	431	3.94					
Zn(II) BDI-**4**[2]	622	4.09					
Zn(II) BDI-**6**[2]	729	4.14					
Zn(II) BDI-**7**[2]	917	3.85					
Di-Zn(II) Tethered BDI[3]	5880	7.70	4,000	Neat	No	30	100
Di-Co(III) **1a**[4]	1269	7.89*	1,000	Neat	PPNX 2 equiv. to catalyst	20	25
Di-Co(III) **1b**[4]	1356	7.89*					
Di-Co(III) **1c**[4]	1409	7.89*					
Di-Zn(II) anilido-aldimine [5]	2860	4.86	100,000	Neat	No	14	80
Al(III)K(I) *o*-vanillin [6]	505	3.67	2000	Neat	No	20	100
Tri-Co(III)Ce(III)[7]	850	3.68	21,250	Neat	No	20	130
Tri-Co(III)Nd(III) [7]	1625	3.67*					
Tri-Co(III)Sm(III)[7]	488	3.66					
Tri-Co(III)Eu(III)[7]	288	3.66					
Tri-Co(III)La(III)[7]	1375	3.68					
Co(II)Mg(II) [8]	3100	3.04	4000	Neat	1,2-cyclohexane diol 20 equiv. to catalyst	20	100

* When intermetallic separations for the catalyst are not available (i.e. no reported molecular structure available), intermetallic separations for related systems (e.g. same ligand but different metals) are used as an approximation.

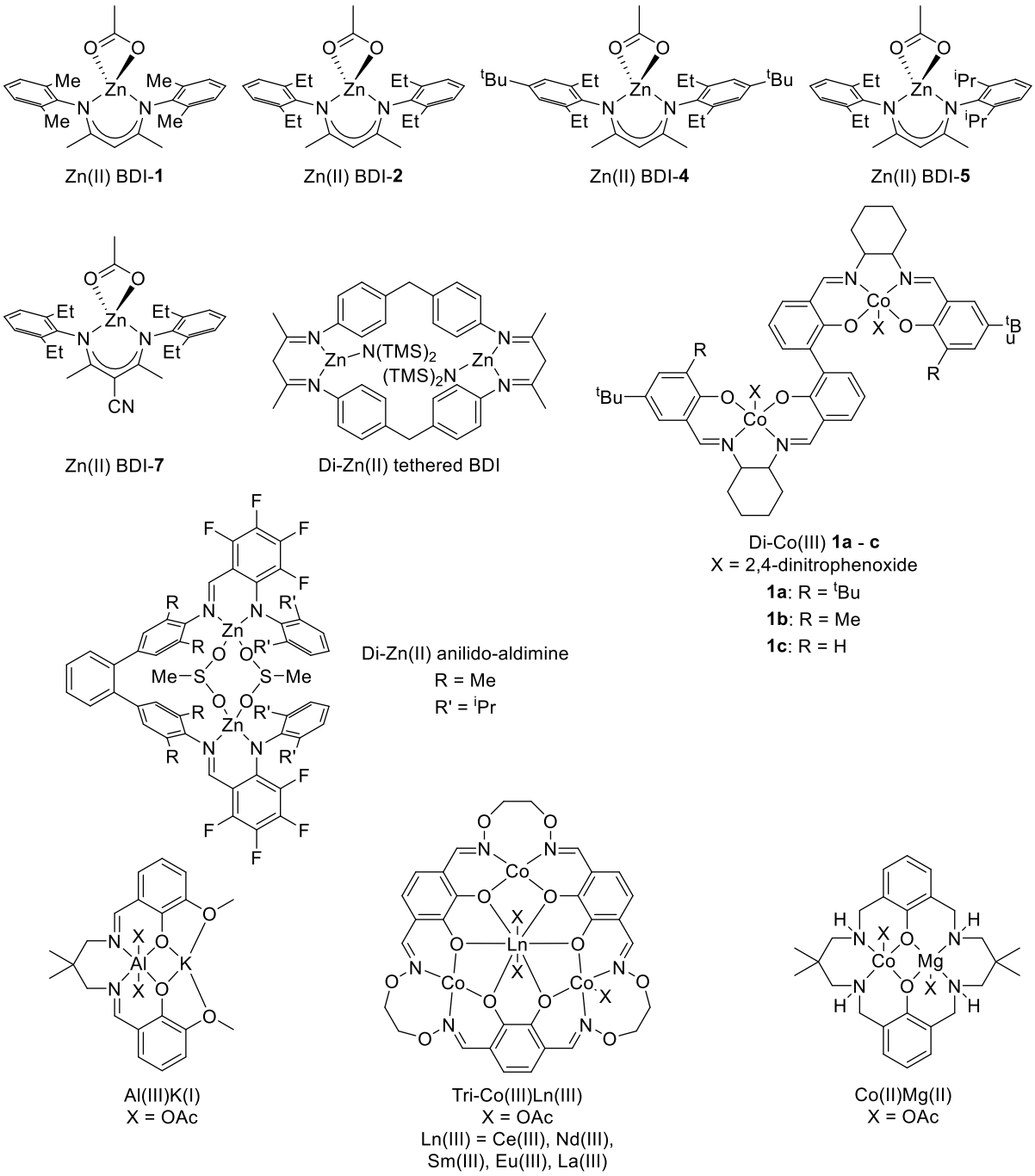
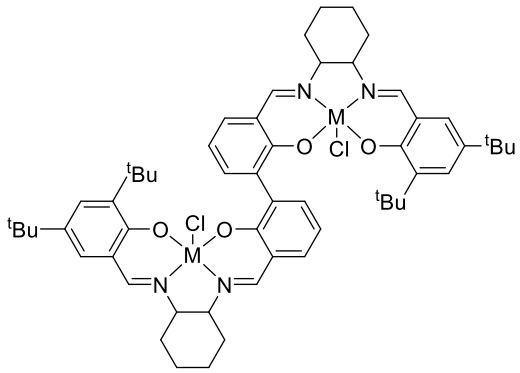


Figure S4.1. Structures of high pressure (> 5 bar) CHO/CO_2 ROCOP catalysts used in Figure 1 and Table S1.[2-8]

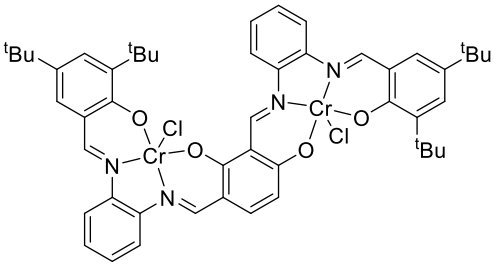
Table S4.2. Catalysts CHO/PA ROCOP used for Figure 1, showing the TOF, intermetallic separation (from solid-state structures), and polymerisation conditions.

Catalyst	TOF / h^{-1}	Solid-State M – M Separation / Å	[CHO]/[cat]	[CHO]	[PA]/[cat]	Additives?	Temp. / °C
Di-Al(III) **1** [9]	750	7.89*	1,000	Neat	250	PPNCl 2 equiv. to catalyst	50
Di-Co(III) **1** [9]	539	7.89*					
Di-Cr(III) **1** [9]	196	7.89*					
Di-Cr(III) **2** [10]	912	7.32	2,000	Neat	400	PPNCl 1 equiv. to catalyst	60
Tri-Cr(III) **1** [10]	2556	7.36	4,000	Neat	800	PPNCl 1 equiv. to catalyst	60
Tri-Cr(III) **2** [10]	10620	8.47	30,000	Neat	6,000	PPNCl 3 equiv. to catalyst	100
Di-Zn(II) *o*-vanillin [11]	198	3.1557	800	Neat	100	No	100
Fe(III)K(I) *o*-vanillin [12]	1168	3.618	8,000	Neat	400	No	100
Di-Zn(II)Na(I) [13]	225	3.45	4,000	Neat	200	1,2-cyclohexane diol 20 equiv. to catalyst	100
Al(III) Na(I) *o*-vanillin [6]	1072	3.665	2,000	Neat	400	No	100
Al(III) K(I) *o*-vanillin [6]	1136	3.819					
Al(III) Rb(I) *o*-vanillin [6]	712	3.284					
Al(III) Cs(I) *o*-vanillin [6]	875	3.979					

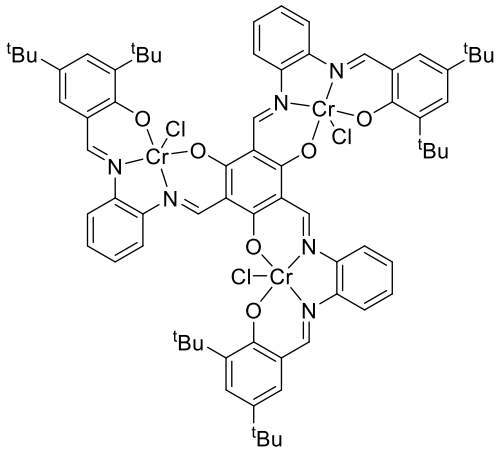
* When intermetallic separations for the catalyst are not available (i.e. no reported molecular structure available), intermetallic separations for related systems (e.g. same ligand but different metals) are used as an approximation.



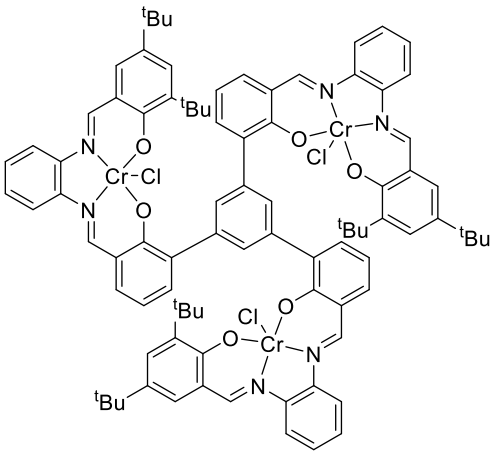
Di-M(III) 1
M = Al(III), Co(III), Cr(III)



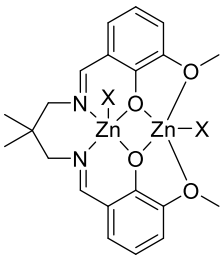
Di-Cr(III) **2**



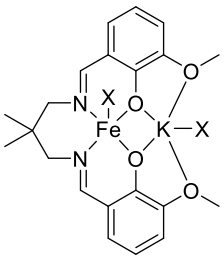
Tri-Cr(III) **1**



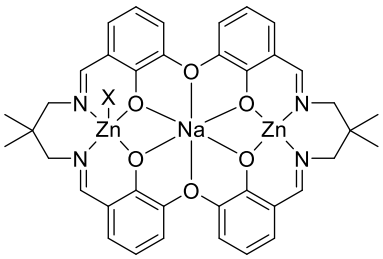
Tri-Cr(III) **2**



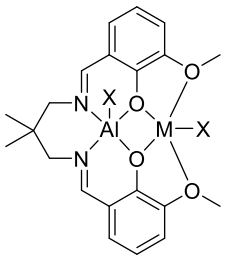
Di-Zn(II) *o*-vanillin
X = OAc



Fe(III)K(I) *o*-vanillin
X = OAc



Di-Zn(II)Na(I)
X = $CO_2C_6H_4CF_3$



Al(III)M(I) *o*-vanillin
M(I) = Na(I), K(I),
Rb(I), Cs(I)
X = OAc

Figure S4.2. CHO/PA ROCOP catalyst structures used in Figure 1 and Table S2. [6, 9-13]

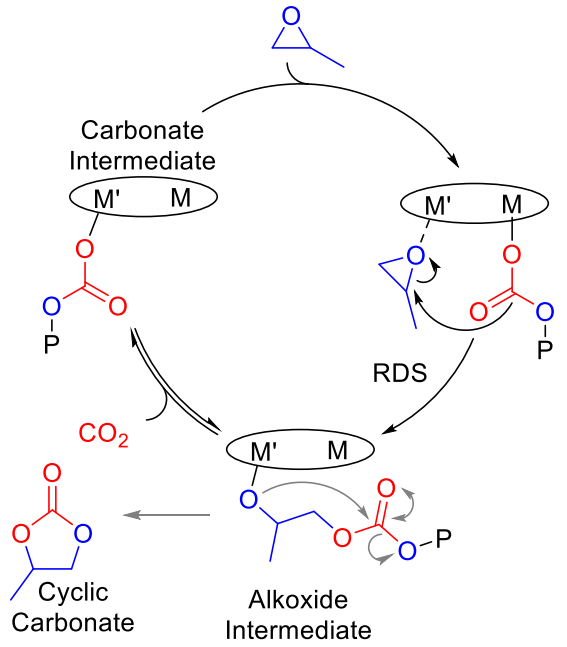


Figure S4.3. General dinuclear mechanism for epoxide/CO_2 ROCOP (showing PO/CO_2 ROCOP).

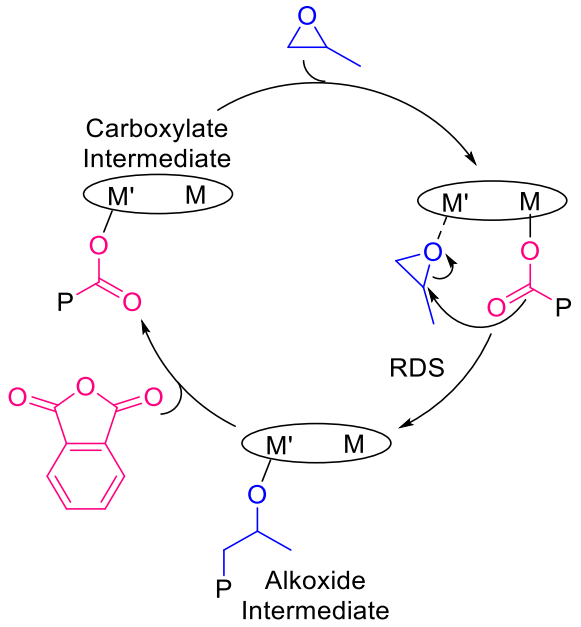


Figure S4.4. General dinuclear mechanism for epoxide/anhydride ROCOP (showing PO/PA ROCOP).

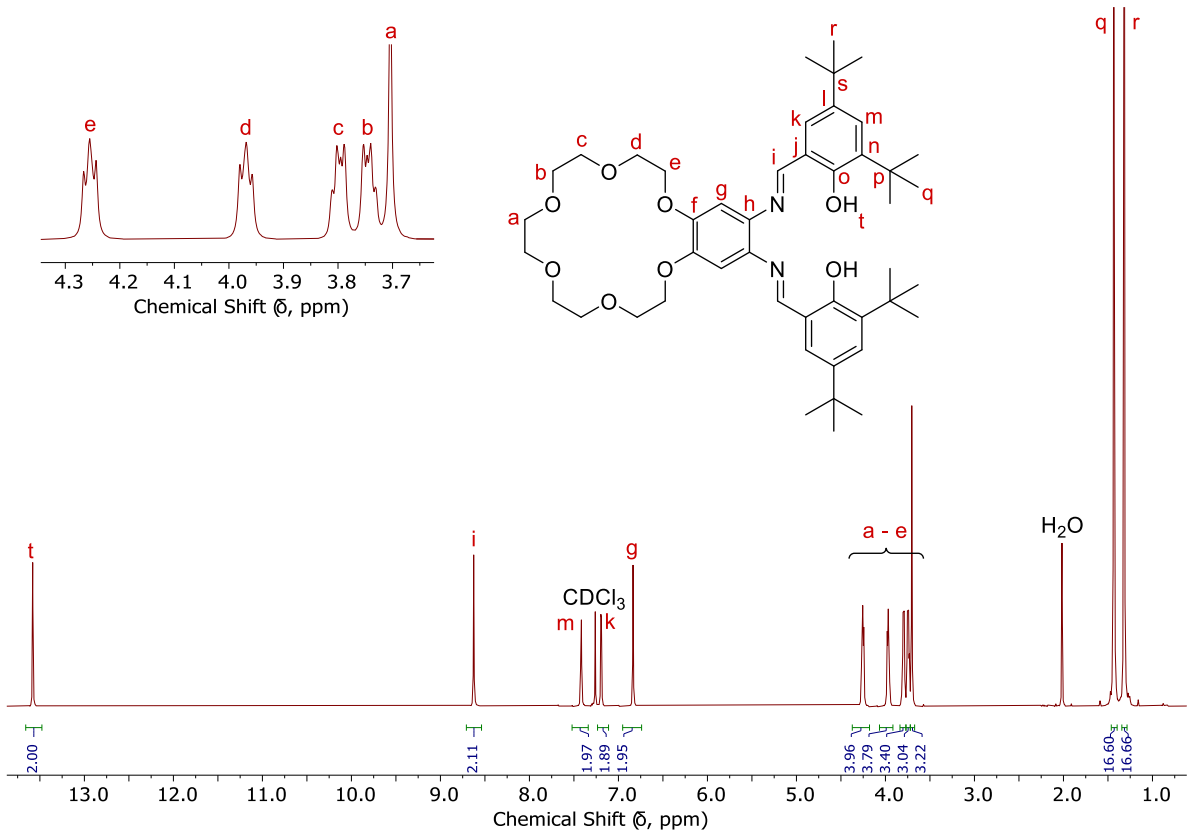


Figure S4.5. ^{1}H NMR spectrum of H_2L_{wide}

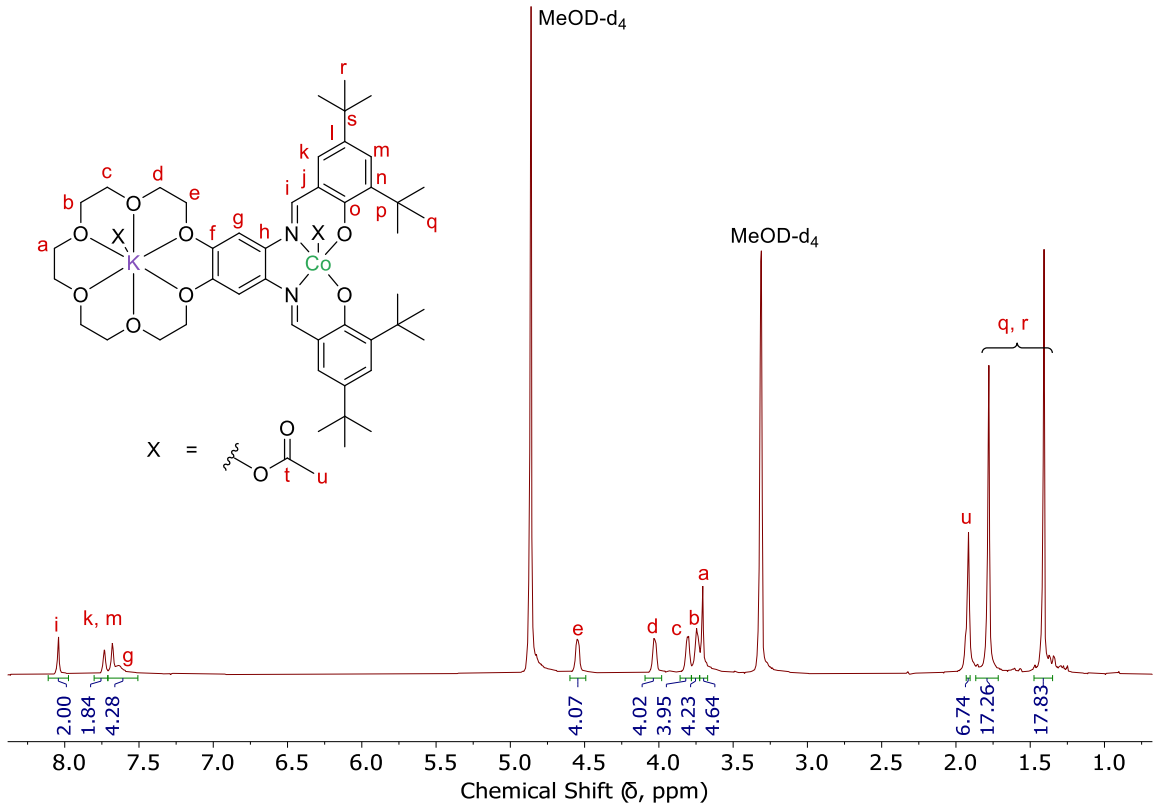


Figure S4.6. ^{1}H NMR spectrum of $L_{wide}CoK(OAc)_2$ in MeOD-d_4.

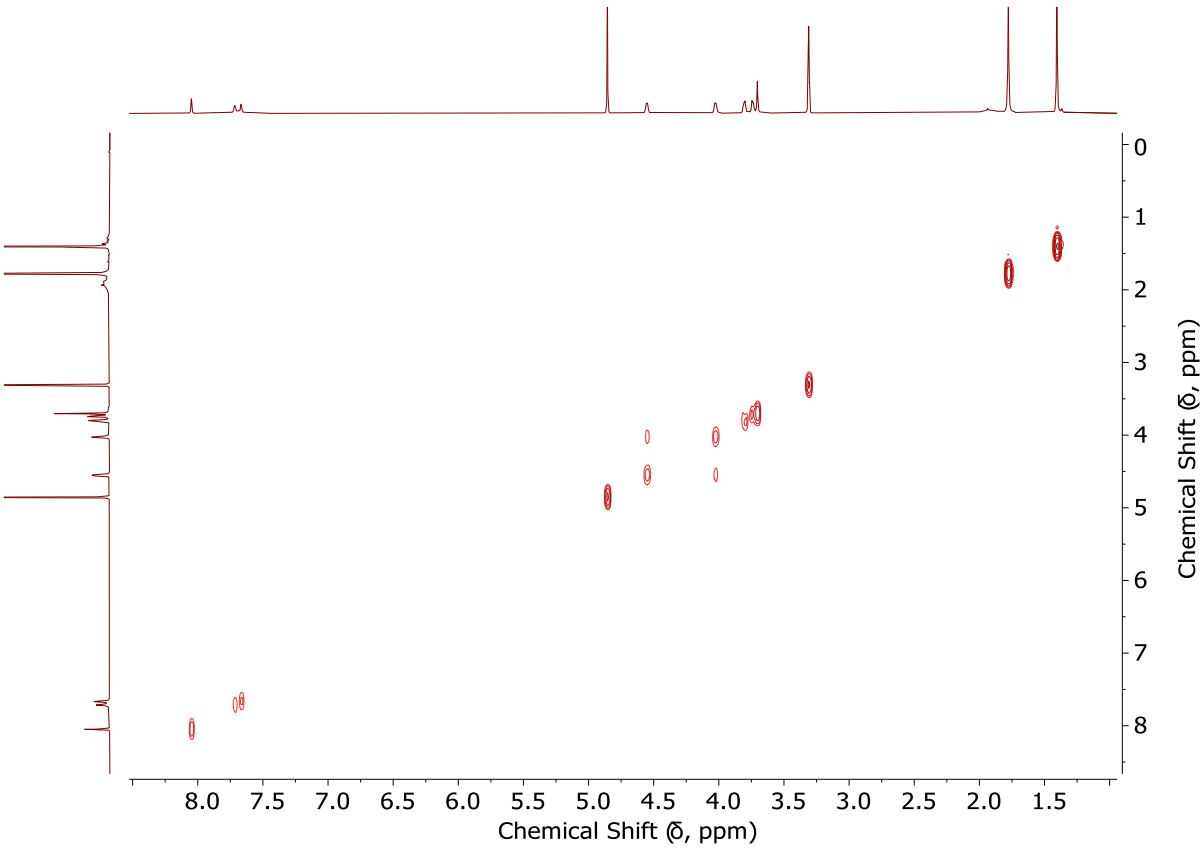


Figure S4.7. COSY NMR spectrum of $L_{wide}CoK(OAc)_2$ in MeOD-d_4

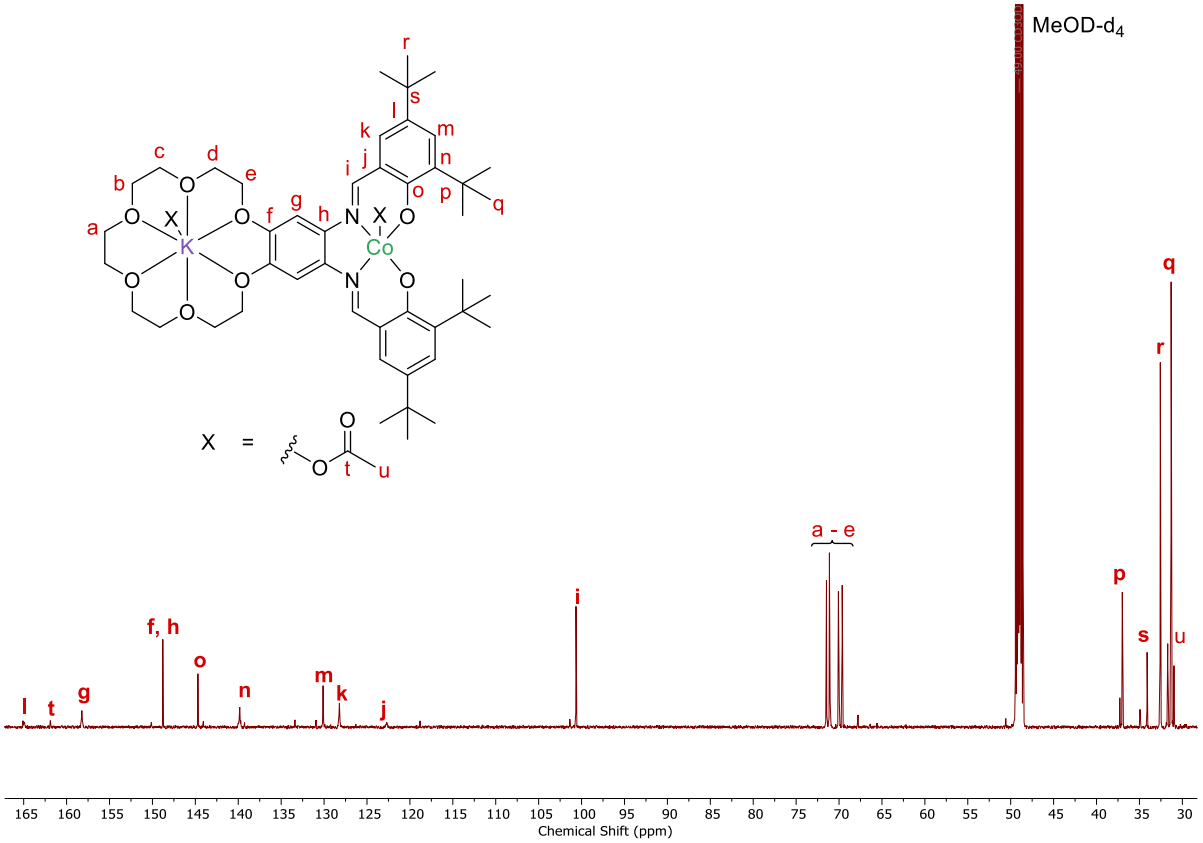


Figure S4.8. $^{13}C\{^1H\}$ NMR spectrum of $L_{wide}CoK(OAc)_2$ in MeOD-d_4

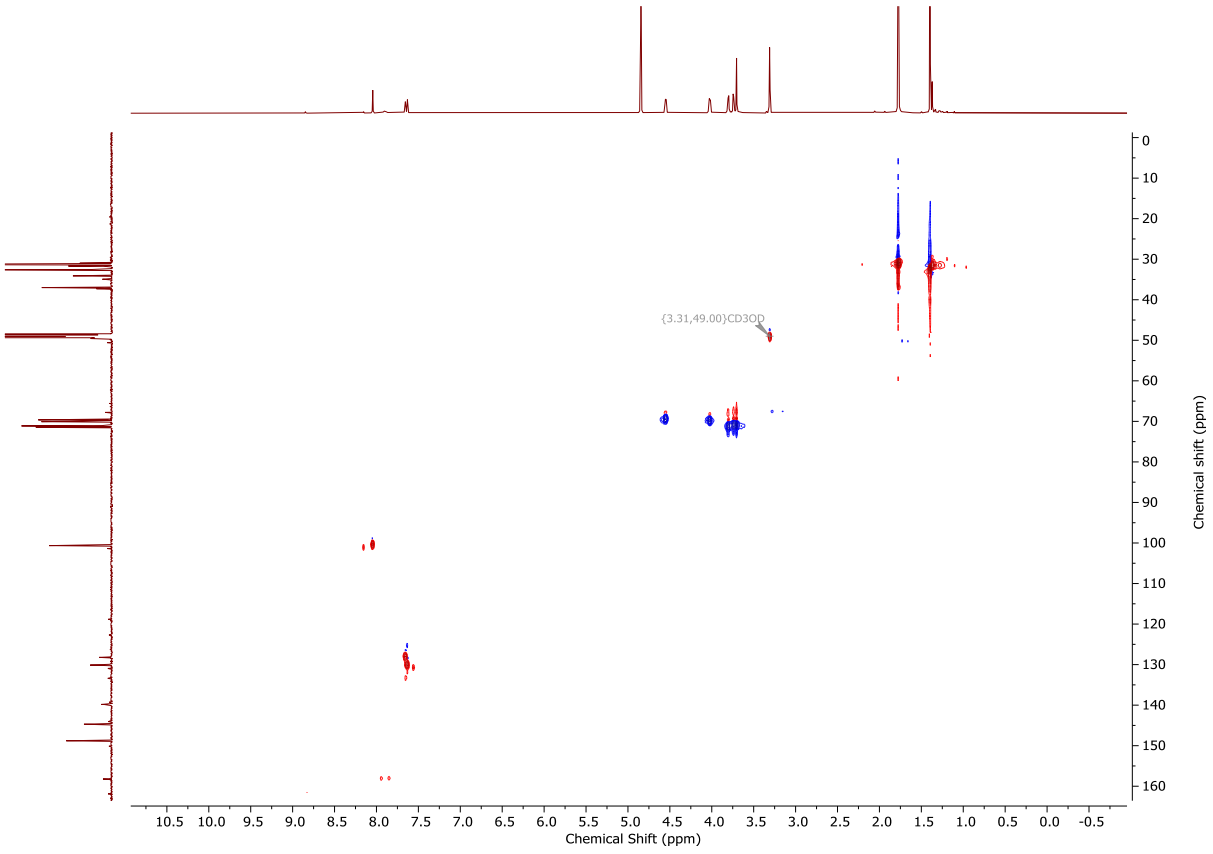


Figure S4.9. HSQC NMR spectrum of $L_{wide}CoK(OAc)_2$ in MeOD-d_4

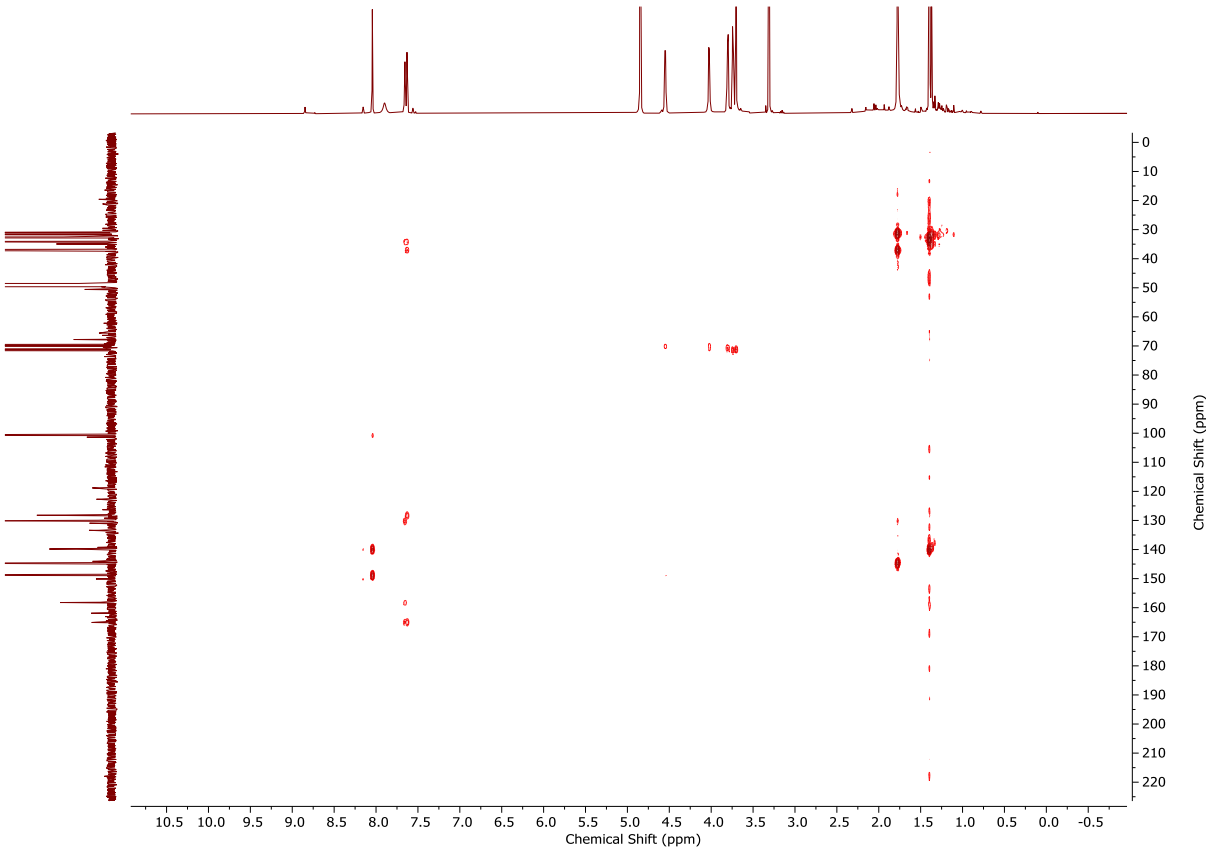


Figure S4.10. HMBC NMR spectrum of $L_{wide}CoK(OAc)_2$ in MeOD-d_4

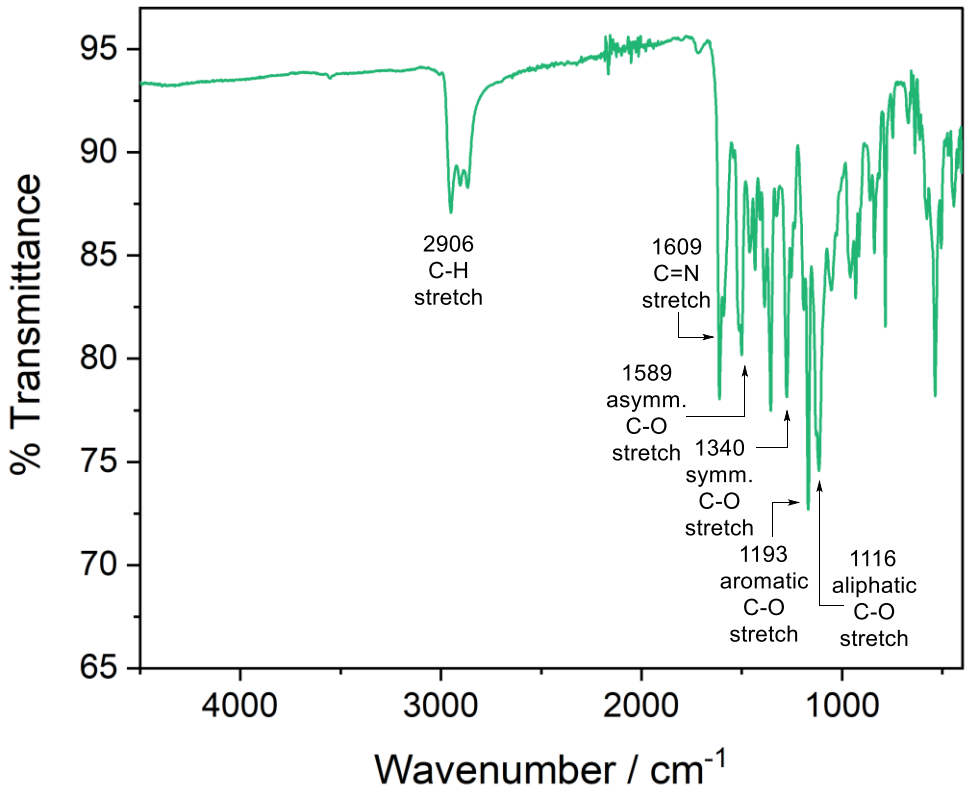


Figure S4.11. Solid state IR spectrum of $L_{wide}CoK(OAc)_2$.

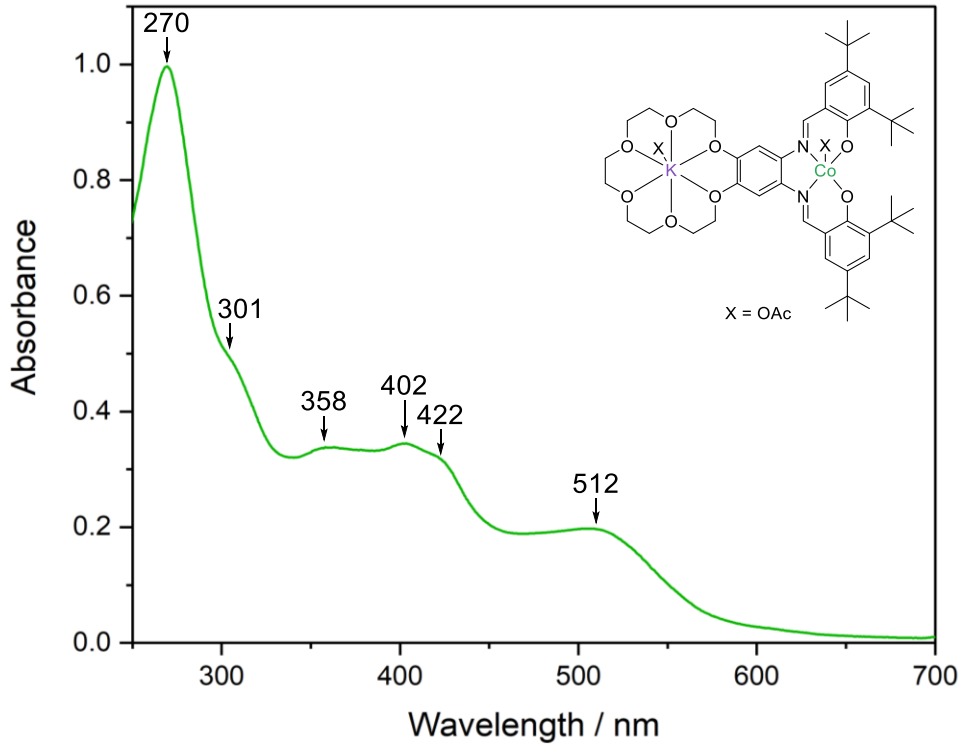


Figure S4.12. UV-vis spectrum of $L_{wide}CoK(OAc)_2$ in DCM.

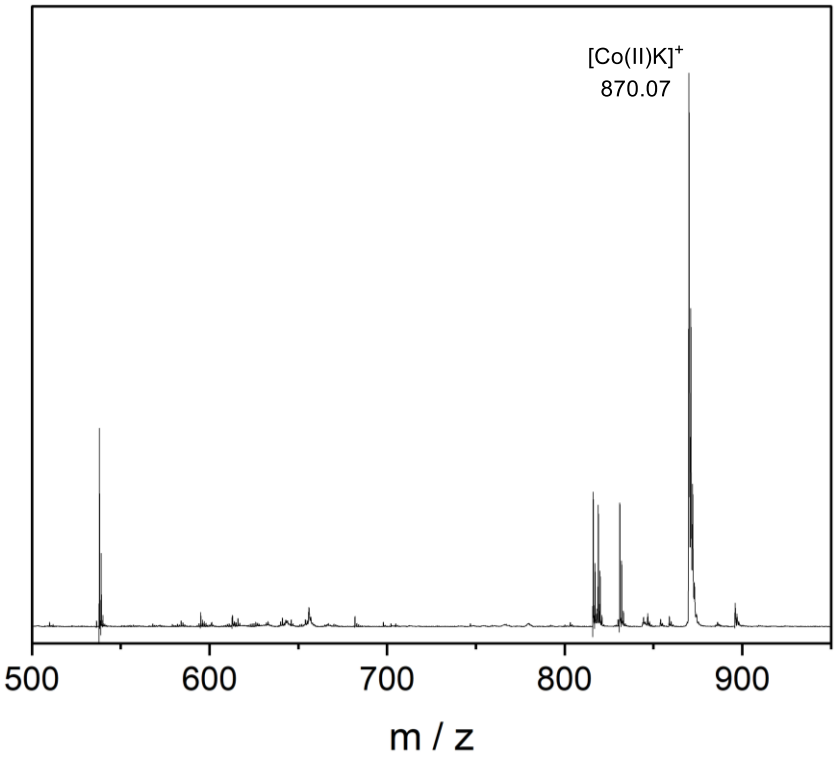


Figure S4.13. MALDI-TOF mass spectrometry trace of $L_{wide}CoK(OAc)_2$

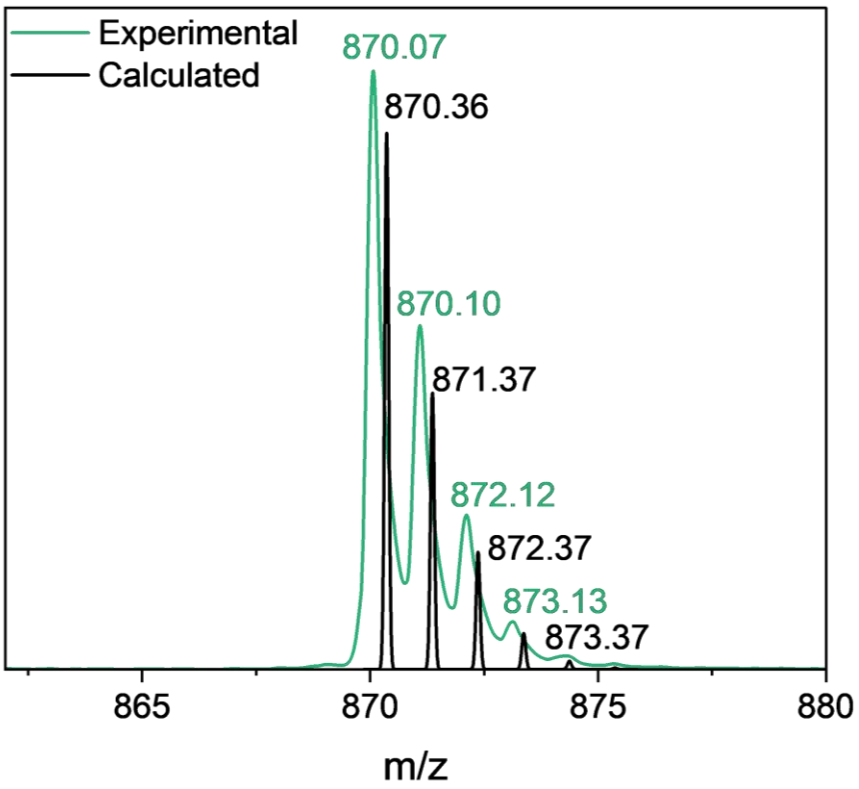


Figure S4.14. Experimental (green) and calculated (black) isotopic distributions of the $[Co(II)K(I)]^+$ peak

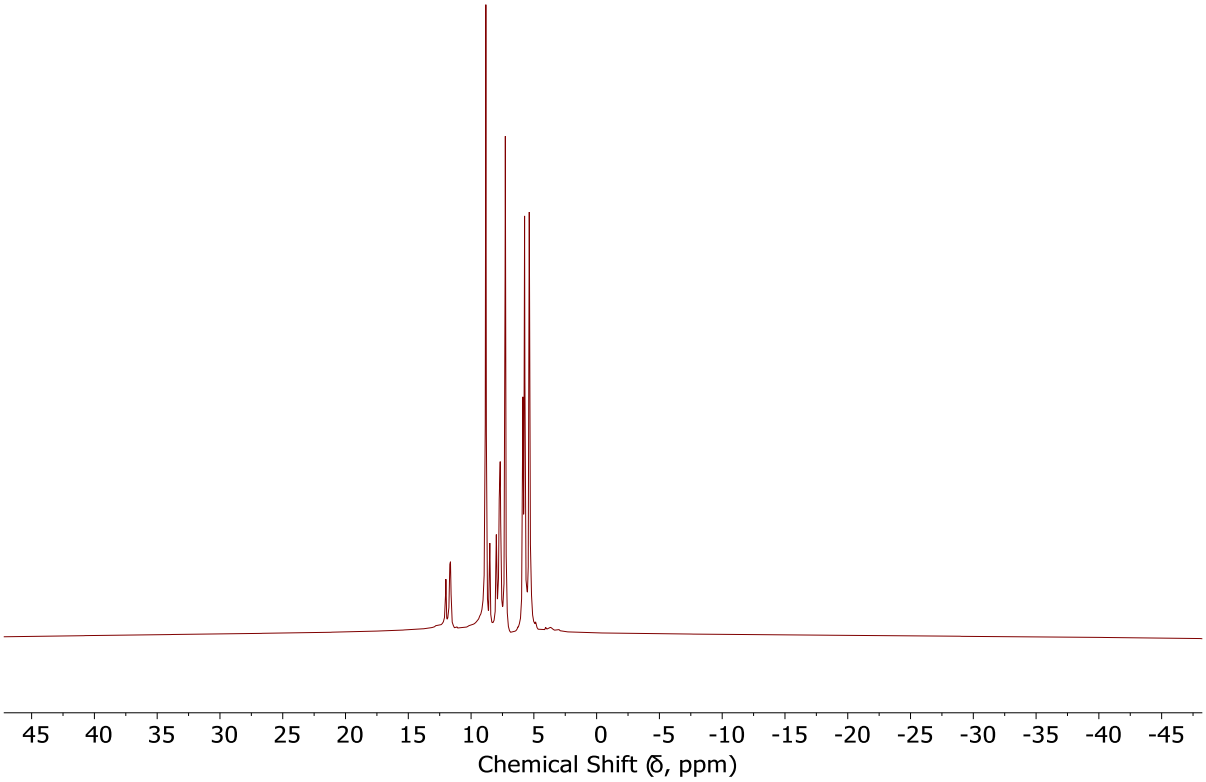


Figure S4.15. ^{1}H NMR spectrum of $L_{wide}CoK(OAc)_2$ in MeOD-d_4 between 50 to -50 ppm showing the absence of peaks outside of the typical range.

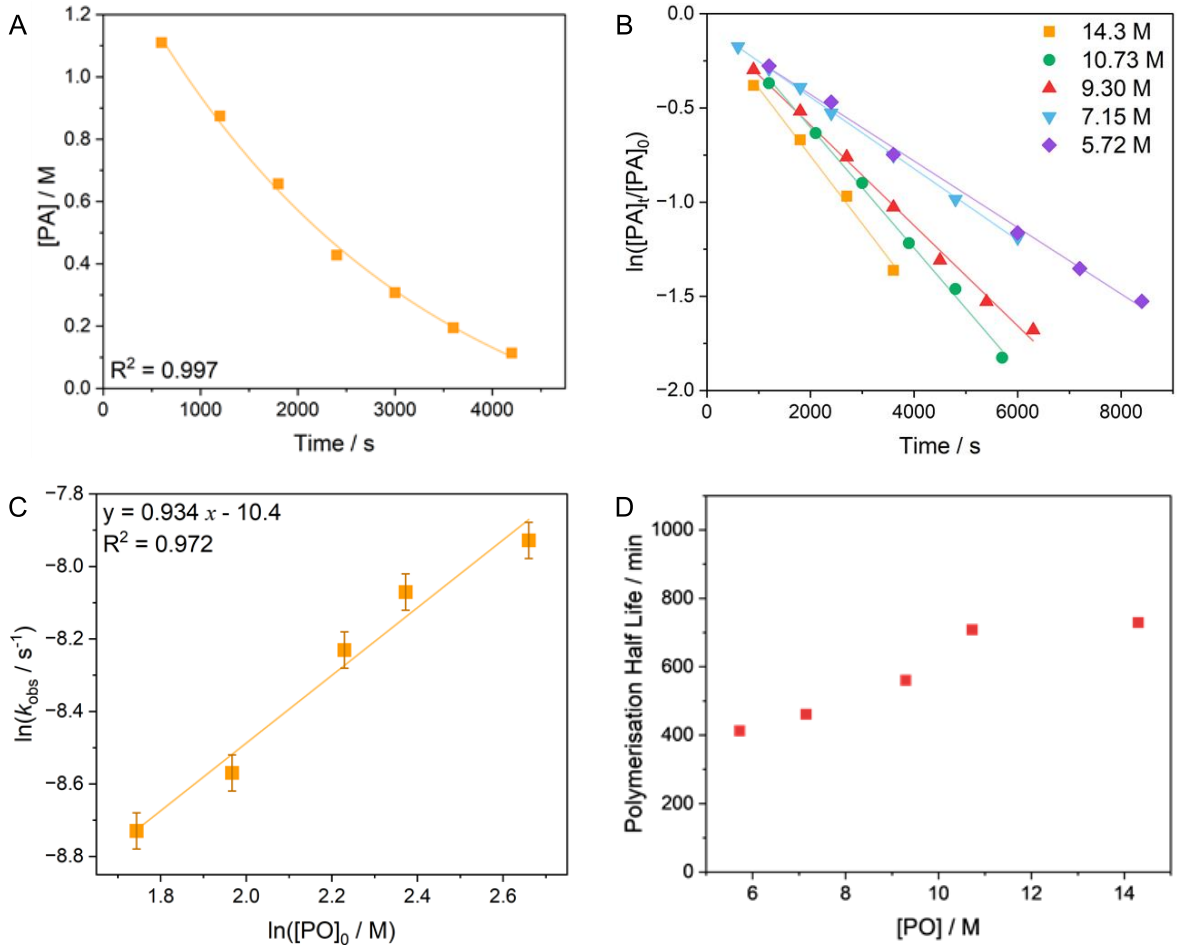


Figure S4.16. Plots used for the determination of polymerisation rate dependence with respect to the concentration of PO. A: Exponential decay of [PA] against time; B: linear plots of $\ln([PA]_t/[PA]_0)$ with varying concentrations of PO; C: plot of $\ln(k_{obs})$ against $\ln([PO]_0)$ with a gradient of 1.10; D: polymerisation half-life against [PO] showing it stays constant with varying [PO].

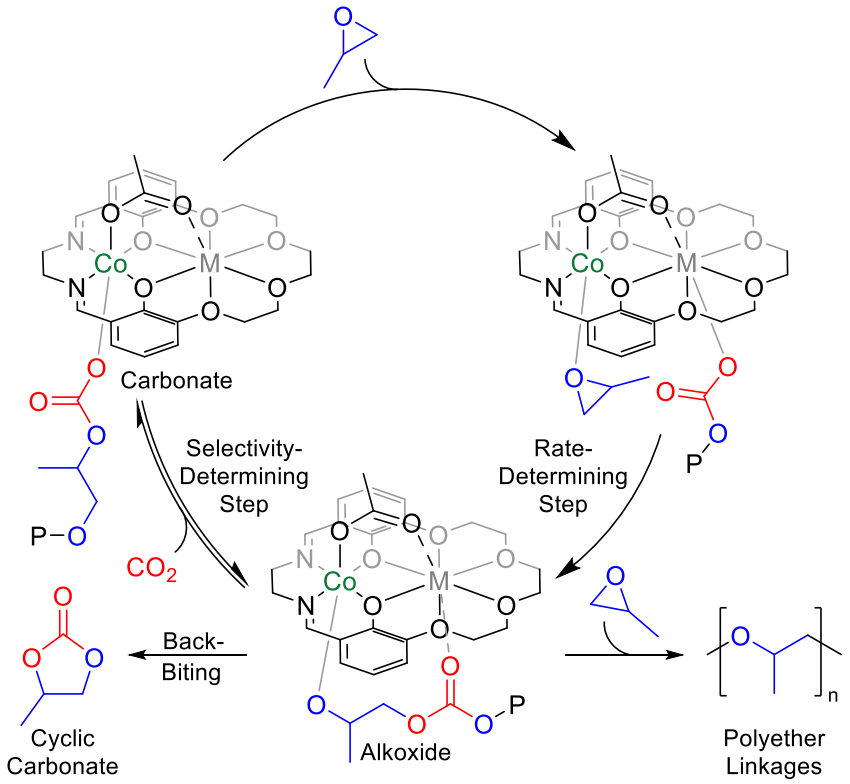


Figure S4.17. Dinuclear metallate mechanism for PO/CO_2 ROCOP catalysed by Co(III)K(I) catalyst.

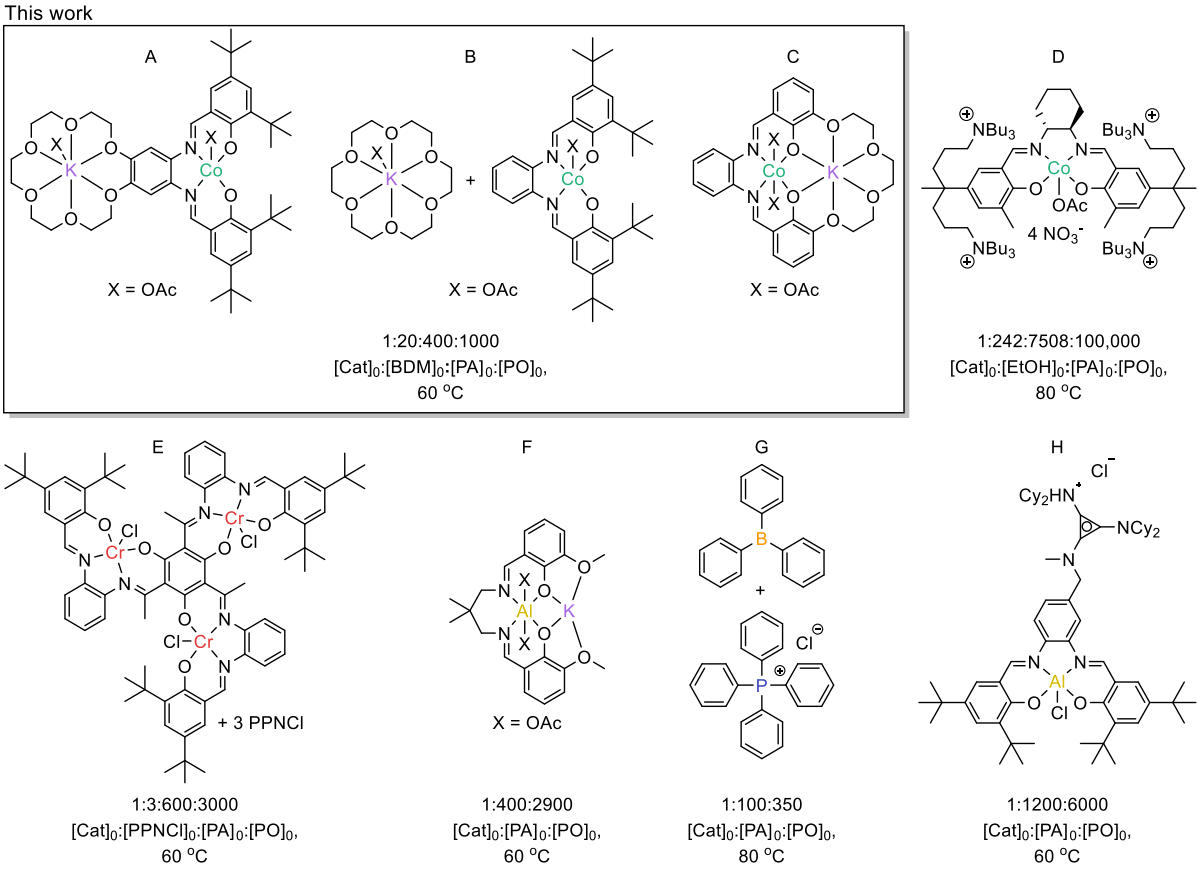


Figure S4.18. Literature catalysts for PO/PA ROCOP used for comparison.[6, 10, 14, 15]

The vials were tested to ensure that they were able to contain the pressure associated with PO heated to well above its boiling point of 34 °C, by weighing the vial containing the polymerization solution before and after each period of heating. No change in weight was observed, indicating that no PO was evaporating from the vial over the course of the polymerization (Table S5). Before removing each aliquot, the polymerization was cooled in an acetone/dry ice bath to ensure that no evaporation of PO occurred during the aliquoting process.

Table S4.3. Table of weights of the vial containing the polymerization solution of PO/GA at 70 °C demonstrating that no PO is evaporating from the vial during heating of the polymerization mixture.

Time heated / min	Weight before aliquot / g	Weight after aliquot / g
0	7.742	-
3	7.743	7.733
6	7.733	7.727
9	7.727	7.716
15	7.717	7.692

Crystallographic Data for L_{wide}NiKOAc

Table S4.4. Selected bond lengths and angles for L_{wide}NiKOAc.

Bond	Length	Bond	Angle
Ni1—O8	1.8500 (16)	**K1—O5**	2.813 (3)
Ni1—O7	1.8464 (17)	**K1—O6**	2.768 (2)
Ni1—N1	1.8551 (19)	**K1—O9**	2.750 (5)
Ni1—N2	1.853 (2)	**N1—C17**	1.299 (3)
K1—O3	2.8333 (18)	**N2—C32**	1.295 (3)
K1—O4	2.8651 (19)	**O10—C47**	1.356 (11)
K1—O2	2.832 (2)	**O9—C47**	1.410 (13)
K1—O1	2.849 (2)	**N2—Ni1—N1**	86.19 (8)
O8—Ni1—N1	174.46 (8)	**O1—K1—O4**	140.81 (7)
O8—Ni1—N2	94.38 (8)	**O5—K1—O2**	149.14 (7)
O7—Ni1—O8	85.25 (8)	**O6—K1—O3**	165.01 (8)
O7—Ni1—N1	94.67 (8)		
O7—Ni1—N2	174.94 (8)		

Table S4.5. Summary of crystallographic refinement data for L_{wide}NiKOAc.

Complex	L_{wide}NiKOAc
Local Code	005ff23_autored-ff
CCDC Deposition Number	2342581
Crystal data	
Chemical formula	$C_{48}H_{67}KN_2NiO_{10}$
M_r	929.84
Crystal system, space group	Triclinic, *P*1
Temperature (K)	150
***a*, *b*, *c* (Å)**	10.6691 (2), 17.0018 (3), 17.7820 (3)
α, β, γ (°)	94.563 (1), 102.757 (1), 104.684 (2)
***V* (Å^3)**	3011.61 (10)
Z	2
Radiation type	Cu *K*α
μ (mm^{-1})	1.46
Crystal size (mm)	0.165 x 0.169 x 0.445
Data Collection	
Diffractometer	SuperNova, Dual, Cu at home/near, Atlas
Absorption correction	Multi-scan *CrysAlis PRO* 1.171.42.72a (Rigaku Oxford Diffraction, 2022) Empirical absorption correction using spherical harmonics, implemented in SCALE3 ABSPACK scaling algorithm.
T_{min}, T_{max}	0.402, 1.000
No. of measured, independent and observed [$I > 2\sigma(I)$] reflections	74081, 12546, 10375
R_{int}	0.052
(sin θ/λ)max (Å−1)	0.631
Refinement	
$R[F^2 > 2\sigma(F^2)]$, $wR(F^2)$, S	0.064, 0.184, 1.05
No. of reflections	12546
No. of parameters	593
No. of restraints	22
H-atom treatment	H-atom parameters constrained
$(\Delta/\sigma)_{max}$	0.776
$\Delta\rho_{max}$, $\Delta\rho_{min}$ (e Å^{-3})	0.94, −1.38